# Physique statistique de la matière active

Alexandre Solon

**Université Paris Diderot (Paris 7) - Sorbonne Paris Cité**
**École Doctorale "Physique en Île-de-France"**

# Thèse de doctorat

Discipline : Physique théorique

présentée par

**Alexandre Solon**

---

# Physique statistique de la matière active

---

dirigée par Julien Tailleur

Soutenue le 8 septembre 2015 devant le jury composé de messieurs

| | |
|---|---|
| Jean-Louis Barrat | examinateur |
| Ludovic Berthier | rapporteur |
| Lydéric Bocquet | examinateur |
| David Dean | rapporteur |
| Jean-Baptiste Fournier | examinateur |
| Clément Sire | examinateur |
| Julien Tailleur | directeur de thèse |
| Raphaël Voituriez | examinateur |

# Remerciements

J'ai eu la chance de ne jamais me sentir seul ou perdu pendant cette thèse grâce à toutes les personnes formidables qui m'entouraient. Je voudrais surtout remercier mon directeur de thèse, Julien Tailleur, qui n'a pas ménagé ses efforts pour transformer l'étudiant que j'étais en chercheur. Il a réussi à me transmettre à la fois la passion et la rigueur et j'espère que notre collaboration/amitié durera encore longtemps.

Je voudrais ensuite remercier chaudement Hugues Chaté, Yariv Kafri et Mike Cates que j'ai eu la chance de côtoyer et qui ont eu une grande influence sur moi. Les interactions que j'ai pu avoir avec Joseph d'Alessandro, Denis Bartolo, Thierry Bodineau, Jean-Baptiste Caussin, Cécile Cottin-Bizonne, Félix Ginot, Vincent Hakim, Vivien Lecomte, Takahiro Nemoto, Aurelio Patelli, Fernando Peruani, Joakim Stenhammar, Hugo Touchette, Chantal Valeriani et Frédéric van Wijland m'ont été à la fois agréables et profitables.

Merci également à tous les membres du laboratoire MSC qui rendent les jours plus courts, en particulier à Clément, Pauline, Kelly, Mourtaza, Adrien, Étienne, Gwen, Florent, Thomas, Simon, Iris et Loudgy (désolé pour ceux que j'oublie). Et tout spécialement Tanguy et Agnese pour leur soutien, chacun à leur manière, pendant la rédaction de cette thèse.

Enfin, je voudrais remercier les membres du jury qui ont évalué cette thèse pour le temps qu'ils m'ont consacré, les idées intéressantes soulevées pendant le soutenance et leurs encouragements.

# Table des matières

# Chapitre 1

# Introduction

## 1.1 Physique statistique : à l'équilibre et au-delà

La physique statistique a pour but de décrire les propriétés thermodynamiques de systèmes composés d'un grand nombre de particules à partir de leur dynamique microscopique. Pour les systèmes « à l'équilibre », la dynamique peut être complètement oubliée et la valeur d'une observable macroscopique statique est donnée par une moyenne d'ensemble. Calculer cette moyenne peut être extraordinairement difficile en pratique, mais conceptuellement, le problème est bien compris.

Le formalisme de la physique statistique d'équilibre permet d'étudier, avec les mêmes outils théoriques, des systèmes très différents, des cristaux liquides aux superfluides. Cela a permis de nombreuses avancées industrielles au XX$^{\text{ème}}$ siècle, de l'utilisation des cristaux liquides pour l'affichage aux applications de la matière molle dans l'industrie agro-alimentaire et cosmétique.

Le concept d'équilibre n'est cependant pas univoque et on peut en donner deux définitions aux implications différentes.

### 1.1.1 Deux définitions de l'équilibre

Pour la plupart des manuels de physique statistique [1, 2], un système a atteint l'équilibre lorsqu'il est décrit par la distribution de Boltzmann (ou son équivalent dans l'ensemble statistique approprié). Par exemple, dans l'ensemble canonique, un système est à l'équilibre quand la probabilité d'un micro-état $\mathcal{C}$ est donnée par $P(\mathcal{C}) = e^{-\beta\mathcal{H}(\mathcal{C})}/Z$ où $\mathcal{H}$ est l'Hamiltonien du système et $Z$ la fonction de partition. La connaissance de la fonction de partition permet de retrouver toutes les relations de la thermodynamique, faisant ainsi le lien entre la dynamique microscopique et les propriétés macroscopiques d'un système (pression, température, entropie, etc.).

Si, conceptuellement, la fonction de partition contient toute la thermodynamique d'un système, en pratique elle est souvent impossible à calculer analytiquement. On peut alors recourir à des simulations numériques. On est dans ce cas libres d'utiliser des dynamiques « non physiques » qui ne représentent pas la dynamique microscopique du système (comme les algorithmes de Monte-Carlo) si elles conduisent à la même distribution d'équilibre, le but étant simplement de l'échantillonner de la façon la plus efficace possible.

Une définition alternative considère à l'équilibre tout système dont la dynamique vérifie le bilan détaillé par rapport à sa distribution stationnaire [3]. Cette symétrie de la dynamique permet d'obtenir des relations de fluctuation-dissipation. En particulier, la théorie de la réponse linéaire permet d'exprimer la réponse d'une observable à une petite perturbation du système comme une fonction de corrélation calculée à l'équilibre.

Pour les systèmes isolés dont la dynamique microscopique est celle de la mécanique classique, le bilan détaillé est naturellement satisfait dans l'état stationnaire comme conséquence de la réversibilité des équations du mouvements. Toutefois, la définition d'un système à l'équilibre comme satisfaisant le bilan détaillé est bien plus générale, et ne se limite pas aux systèmes hamiltoniens. En particulier, pour certains systèmes dont on ne connaît pas les détails microscopiques, on peut vouloir écrire une dynamique effective à une échelle plus grande (comme nous le ferons, par exemple, pour une bactérie). Si à cette échelle mésoscopique la dynamique satisfait le bilan détaillé, on peut alors définir une énergie libre effective et la dynamique autour de l'état d'équilibre est contrainte par des relations de fluctuation-dissipation. Cependant, l'énergie libre effective n'est pas reliée à un Hamiltonien. Elle n'a donc *a priori* pas d'interprétation physique, et ses dérivées ne sont pas associées à des forces thermodynamiques.

On distinguera donc dans la suite l'équilibre thermique caractérisé par la distribution de Boltzmann de la propriété de bilan détaillé.

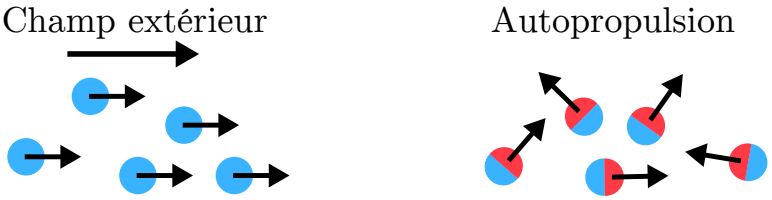


**Figure 1.1** – Contrairement à l'application d'un champ extérieur (par exemple un champ électrique sur des particules chargées), les particules actives sont propulsées chacune par des forces internes.

### 1.1.2 Différentes physiques statistiques hors d'équilibre

L'idée qu'on pourrait étendre le formalisme de Gibbs et Boltzmann pour rendre compte de façon unifiée des systèmes hors d'équilibre semble utopique car cette dénomination regroupe des situations diverses. En effet, un système peut être hors d'équilibre de différentes manières.

Un système hamiltonien, même isolé, est hors d'équilibre si le temps de relaxation vers son état stationnaire diverge. C'est le cas des verres qui restent piégés dans un paysage d'énergie accidenté sans pouvoir relaxer vers un état d'équilibre [4]. Un système hamiltonien peut également être maintenu hors d'équilibre par ses conditions aux limites. Par exemple, une barre de métal maintenue à des températures différentes à ses extrémités est traversée par un flux de chaleur et atteint un état stationnaire hors d'équilibre. D'une façon similaire, un flux d'énergie traverse un écoulement turbulent en trois dimensions des grandes échelles vers l'échelle microscopique où l'énergie est dissipée.

On trouve ensuite une infinité de modèles dont la dynamique brise le bilan détaillé à l'échelle microscopique, de différentes façons. Certains partagent un comportement commun et peuvent être regroupés dans des classes d'universalité. Sans chercher l'exhaustivité, on trouve par exemple les modèles de gaz sur réseau soumis à un champ extérieur [5], la classe KPZ pour la croissance d'interfaces [6] ou la percolation dirigée [7]. Dans cette thèse nous nous intéresserons à une autre classe de systèmes ayant une dynamique microscopique irréversible : la matière active.

## 1.2 La matière active

Les systèmes actifs sont composés de particules capables de transformer l'énergie stockée dans leur environnement pour s'autopropulser. Contrairement à l'application d'un champ extérieur, l'autopropulsion correspond à un degré de liberté interne (une direction de déplacement), propre à chaque particule (voir figure 1.1).

### 1.2.1 Intérêt des physiciens pour la matière active

L'engouement assez récent des physiciens pour l'étude de la matière active, dont témoignent les multiples revues parues ces dernières années [8–12], tient en partie au fait que les systèmes actifs présentent une phénoménologie riche dont on peut rendre compte par des modèles simples.

Le modèle proposé par Vicsek et ses collaborateurs en 1995 [13] est fondateur. Celui-ci décrit des particules ponctuelles qui se déplacent dans le plan à vitesse constante et alignent imparfaitement leur direction de déplacement avec leurs voisins. Quand le bruit sur l'interaction d'alignement est diminué, on observe une transition de phase d'un état désordonné vers un état de mouvement collectif avec un ordre à longue portée. Cette transition serait impossible à l'équilibre thermique, le théorème de Mermin-Wagner [14] interdisant de briser une symétrie continue en 2d si l'on a seulement des interactions à courte portée. Elle est donc intrinsèquement liée au caractère actif des particules qui rend possible une phénoménologie plus riche qu'à l'équilibre.

La phénoménologie de la matière active ne se limite pas aux mouvements collectifs et nous essaierons d'en donner un rapide aperçu dans la suite de cette introduction.

### 1.2.2 Réalisations expérimentales

L'excitation pour l'étude de la matière active tient également aux nombreuses expériences qui sont réalisées dans le domaine. Celles-ci couvrent des systèmes très différents, biologiques ou inertes, micro- ou macroscopiques.

On trouve les réalisations les plus évidentes de systèmes actifs dans le monde vivant, à différentes échelles (voir figure 1.2 pour quelques illustrations). Les déplacements en groupe d'animaux, des nuées d'oiseaux aux bancs de poissons en passant par les troupeaux de moutons et les foules humaines, sont les exemples les plus communs de mouvement collectifs. Certains de ces comportements ont été étudiés *in vivo* comme les mouvements d'une nuée d'étourneaux [15–17] ou ceux des spectateurs d'un concert de heavy metal [18], d'autres dans des expériences plus contrôlées, par exemple sur des poissons en aquarium [19–21].

À plus petite échelle, la motilité cellulaire est très étudiée [27], notamment pour son rôle dans la migration collective de cellules à l'oeuvre dans le développement de métastases cancéreuses [28] ou dans la cicatrisation de tissus après une plaie [25]. De plus, de nombreuses souches de bactéries comme *Escherichia coli* ou *Bacillus subtilis* s'autopropulsent, ce qui conduit dans certaines conditions à des comportements d'agrégation [23], la formation de motifs [26] ou des écoulements chaotiques [29]. L'autopropulsion est également importante à l'échelle subcellulaire. Dans la cellule, les moteurs moléculaires utilisent l'énergie libérée par

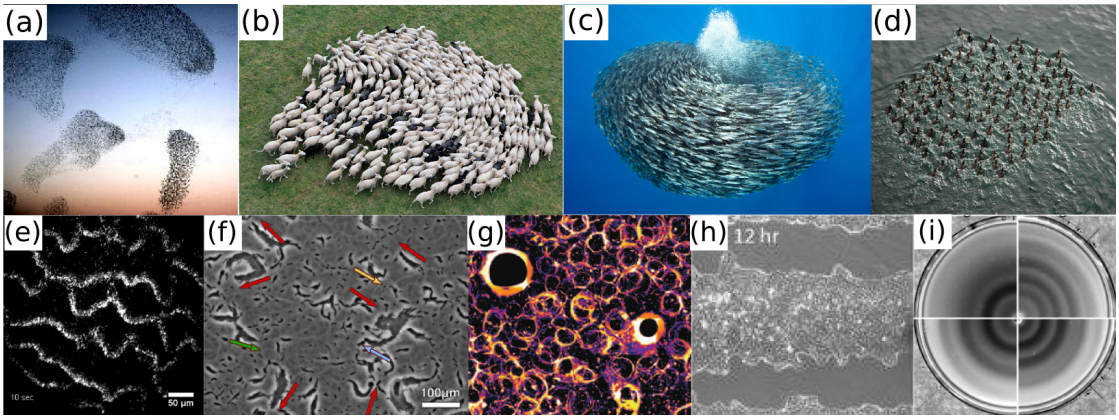


**Figure 1.2** – Exemples de mouvements collectifs à l'échelle macroscopique (haut) et (sub)cellulaire (bas). (a) Vol d'étourneaux [15], (b) troupeau de moutons, (c) banc de maquereaux, (d) groupe de canards, (e) propagation de bandes de filaments d'actine [22], (f) agrégats de myxobactéries [23], (g) vortex de microtubules [24], (h) cicatrisation d'un tissu [25], (i) formation de motifs dans des colonies de bactéries [26]

l'hydrolyse de l'ATP pour se déplacer le long de filaments d'actine ou de microtubules. À l'inverse, si des moteurs moléculaires sont attachés à un substrat, comme dans les expériences de *motility assay*, ils exercent des forces mettant en mouvement les filaments du cytosquelette. Utilisés à l'origine pour étudier les propriétés des moteurs moléculaires et du cytosquelette, les *motility assays* permettent en outre d'observer des comportements collectifs intéressant comme la formation de vortex [24, 30] ou d'écoulements macroscopiques [22, 31].

De nombreux types de particules actives inertes ont également été étudiés en laboratoire. Plusieurs mécanismes peuvent être utilisés pour engendrer l'autopropulsion. Les colloïdes Janus ont, comme le dieu Janus de la mythologie romaine, deux faces aux propriétés différentes. Ainsi, des billes micrométriques de latex recouvertes de platine sur la moitié de leur surface et placées dans une solution de peroxyde d'hydrogène s'autopropulsent par diffusiophorèse [1], un mécanisme illustré à la figure 1.3. Ces colloïdes été utilisés pour étudier, par exemple, la sédimentation et l'agrégation de particules actives [34–39]. L'autopropulsion peut aussi être induite mécaniquement dans des systèmes de grains vibrés [40–42], par une instabilité hydrodynamique pour des gouttes autopropulsées [43] ou par un champ électrique extérieur induisant une instabilité électro-hydrodynamique [44]. Toutes ces particules actives inertes peuvent être fabriquées en grand nombre et per-

1. Il existe cependant un débat sur les différents mécanismes qui participent à l'autopropulsion de ces colloïdes [32]

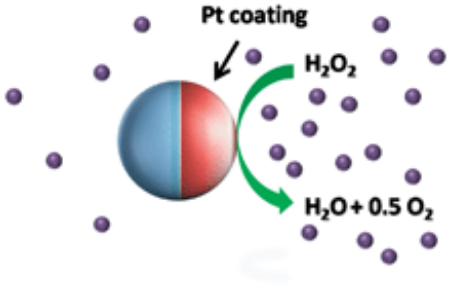


**Figure 1.3** – Autopropulsion par diffusiophorèse de colloïdes Janus recouverts de platine sur la moitié de leur surface. La réaction chimique entre le platine et le peroxyde d'hydrogène $H_2O_2$ crée un gradient de concentration qui propulse la particule. Reproduite de [33].

mettent d'explorer la phénoménologie de la matière active de façon souvent mieux contrôlée que dans les systèmes biologiques.

Des avancées techniques permettent de créer des systèmes actifs dans lesquels les interactions microscopiques peuvent être ajustées très finement. Citons deux exemples récents. Les progrès de l'ingénierie génétique permettent d'inclure dans des organismes vivants des réseaux génétiques visant à remplir différentes fonctions. On peut ainsi observer la formation de motifs (représentés à la figure 1.2) dans des colonies de bactéries auxquelles un circuit a été ajouté pour qu'elles adaptent leur motilité suivant la concentration d'une molécule dans le milieu [26]. Dans un autre registre, une intense recherche vise à la création de nuées de robots auto-organisées, dont les éléments interagissent localement. Ceux-ci sont envisagés pour remplir diverses tâches comme dépolluer les océans ou explorer de nouvelles planètes, et des prototypes atteignent déjà le millier d'individus [45]. Les interactions entre robots sont alors facilement programmables.

On voit donc qu'il est possible de contrôler de plus en plus finement les interactions microscopiques de certains systèmes actifs. Dans ce contexte, comprendre la physique de larges classes de systèmes laisserait plus de liberté pour concevoir des matériaux aux propriétés nouvelles.

### 1.2.3 Outils d'étude

Plusieurs outils sont à notre disposition pour étudier les systèmes actifs. Expérimentalement, les situations sont souvent complexes. Il nous faut donc isoler les phénomènes pertinents liés à l'activité pour pouvoir les comprendre dans un cadre simple.

Une approche consiste à postuler des équations hydrodynamiques phénoménologiques incluant tous les termes autorisés par la symétrie d'un problème. Étant

définies à l'échelle mésoscopique, ces équations peuvent rendre compte de systèmes qui ont des interactions microscopiques différentes mais qui conduisent à un même type d'interaction effective. Par exemple, une interaction d'alignement peut résulter d'une interaction « sociale » pour des groupes d'animaux, d'interactions stériques entre des particules anisotropes (par exemple dans des modèles de bâtonnets autopropulsés [46]), ou d'interactions hydrodynamiques [44]. L'enjeu est ensuite de faire le lien entre les équations hydrodynamiques et les modèles microscopiques. Les (rares) cas où il est possible de construire les équations hydrodynamiques par *coarse graining* sont alors précieux.

Les équations phénoménologiques qui contiennent tous les termes autorisés peuvent toutefois s'avérer extrêmement complexes et donc dures à analyser. Une approche différente, dans l'esprit de la théorie de Landau des transitions de phase, consiste à écrire les équations phénoménologiques les plus simples possibles rendant compte d'un certain comportement. C'est dans cet esprit que le modèle B actif [47] et le modèle H actif [48] ont été introduits, en étendant les classes d'universalité dynamiques de Hohenberg et Halperin [49]. Ils décrivent la séparation de phase d'une suspension décrite par une théorie $\phi^4$ sur un substrat ou dans un solvant pour les modèles B et H respectivement. L'unique addition par rapport à la théorie d'équilibre est un terme de gradient ne dérivant pas d'une énergie libre dont les effets peuvent être analysés.

Enfin, de nombreuses études théoriques sont consacrées à des modèles minimaux. Ils seront au coeur de cette thèse. Une possibilité pour les construire est de partir de modèles d'équilibre dont la phénoménologie est bien connue et de regarder l'effet de l'introduction de l'activité. Ces modèles sont souvent très éloignés de la réalité expérimentale mais permettent de comprendre certains phénomènes en détail. Ils guident alors notre intuition pour la compréhension de cas plus complexes.

---

Dans la suite de cette introduction nous commencerons par décrire les dynamiques de particules autopropulsées qui seront utilisées dans le reste du manuscrit (section 1.3). Nous présenterons ensuite les deux transitions de phase de la matière active qui sont au centre de notre travail (section 1.4) et terminerons cette introduction par l'idée directrice du travail de thèse : la tentative de construction d'une thermodynamique de la matière active (section 1.5).

## 1.3 Dynamiques actives

Dans cette thèse, nous considérerons de la matière active dite « sèche », pour laquelle le substrat sur lequel les particules se déplacent agit comme un réservoir

de quantité de mouvement. Tout se passe alors comme si l'autopropulsion était une force extérieure appliquée à chaque particule et l'on ne se préoccupe pas de la dynamique du substrat liée aux forces qui lui sont imposées par les particules. De nombreux systèmes expérimentaux rentrent naturellement dans cette catégorie : cellules qui rampent sur la matrice extracellulaire ou dans un gel d'agar [25–27], colloïdes roulant sur une surface [39, 44], *motility assays* [22, 24], etc. Nous considérerons deux cas : des particules propulsées par une force active constante ou par une force fluctuant selon un processus d'Ornstein-Uhlenbeck.

Pour des particules nageant en solution (par exemple des bactéries ou des colloïdes Janus), il faut parfois adopter une description plus fine. Les nageurs exercent une force sur le fluide qui est alors mis en mouvement et peu donner lieu à des interactions hydrodynamiques à longue portée. Quand ces interactions sont importantes il faut prendre en compte la dynamique du fluide dans la description du système. On distingue typiquement deux classes de nageurs suivant le type d'écoulement de champ lointain qu'ils induisent dans le fluide : les *pushers*, comme la plupart des bactéries, qui s'autopropulsent par l'arrière, et les *pullers*, comme l'algue *Chlamydomonas*, qui se propulsent par l'avant. Il est possible de simuler numériquement des suspensions de nageurs, par exemple en utilisant la méthode de *lattice Boltzmann* pour calculer les interactions hydrodynamiques de champ lointain [50] ou le modèle de *squirmers* [51] qui tient compte des interactions de champ proche en considérant des particules circulaires à la surface desquelles le fluide a une vitesse imposée. Dans cette thèse, nous resterons au niveau de description de la matière active sèche. Ce choix sera motivé à la section 1.4.

### 1.3.1 Particules autopropulsées à vitesse constante

En première approximation, l'autopropulsion peut être modélisée par une force d'amplitude constante $F_a$ suivant la direction de déplacement $\mathbf{e}_\theta$ d'une particule. En l'absence de force extérieure autre qu'une dissipation visqueuse avec un coefficient de frottement $\gamma$, la dynamique d'une particule active s'écrit alors

$$m\ddot{\mathbf{r}} = -\gamma\dot{\mathbf{r}} + F_a\mathbf{e}_\theta \tag{1.1}$$

Dans la limite suramortie, pertinente pour la plupart des systèmes expérimentaux, la particule se déplacera donc à vitesse constante $v = F_a/\gamma$.

Distinguons deux types de particules autopropulsées à une vitesse constante $v$ qui diffèrent par leurs mécanismes de réorientation, illustrés par la figure 1.4. Ces deux dynamiques correspondent à deux types de particules actives fréquemment rencontrées en laboratoire : les bactéries et les colloïdes autopropulsés.

Les particules browniennes actives (ou ABPs pour *Active Brownian Particles*) se réorientent par une diffusion rotationnelle qui peut être due au mouvement

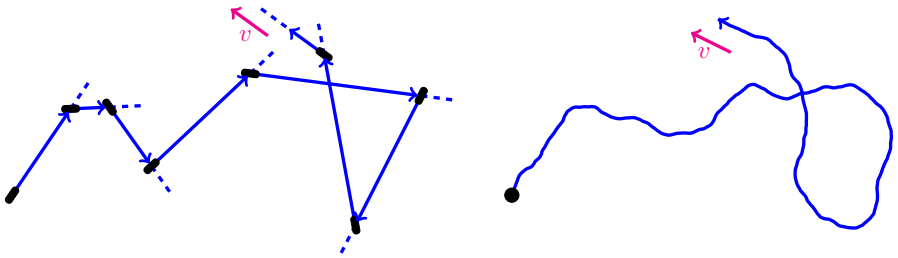


**Figure 1.4** – Exemples de trajectoires d'une RTP (gauche) et d'une ABP (droite). Reproduite de [52]

brownien environnant ou à un bruit actif dans le mécanisme d'autopropulsion. La dynamique de ces particules s'écrit alors en 2d

$$\dot{\mathbf{r}} = v\mathbf{e}_\theta \qquad \dot{\theta} = \sqrt{2D_r}\eta \tag{1.2}$$

où $D_r$ est le coefficient de diffusion rotationnelle et $\eta$ un bruit blanc gaussien de variance unité. C'est un modèle minimal permettant de décrire les colloïdes Janus propulsés par une réaction chimique que nous avons évoqués plus haut, ou encore les particules vibrées étudiées dans [42].

Les RTPs (pour *Run and Tumble Particles*) ont une dynamique différente, caractéristique de bactéries comme *E.Coli*. Celles-ci nagent en ligne droite et prennent aléatoirement une nouvelle direction de déplacement à des instants discrets (les culbutes). La durée des culbutes étant courte devant le temps de nage entre deux culbutes, on peut la négliger en première approximation et considérer des culbutes instantanés. De même, nous ne tiendrons jamais compte dans cette thèse du fait que les culbutes ne sont en réalité pas parfaitement isotropes [53].

### 1.3.2 Mouvement brownien corrélé

L'autopropulsion peut également être modélisée comme un mouvement brownien corrélé dans le temps [54–56]. À la différence de l'approche précédente, la force qui s'applique sur les particules fluctue suivant un processus d'Ornstein-Uhlenbeck

$$\dot{\mathbf{r}} = \mu\mathbf{f} \qquad \tau\dot{\mathbf{f}} = -\mathbf{f} + \sqrt{2D_f}\boldsymbol{\eta} \tag{1.3}$$

où $\tau$ est un temps de relaxation et $\boldsymbol{\eta}$ un bruit blanc gaussien de variance unité. L'équation sur $\mathbf{f}$ peut être résolue et la dynamique de $\mathbf{r}$ est alors un mouvement brownien corrélé sur un temps $\tau$ avec

$$\langle f_i(t) f_j(s)\rangle = \frac{D_f}{\tau} e^{-|t-s|/\tau}\delta_{ij} \tag{1.4}$$

Le coefficient $D_f$ fixe l'amplitude de la force active, $D_f = \tau\langle f_i^2\rangle$. Dans la limite $\tau \to 0$, on retrouve un mouvement purement brownien.

En l'état, l'équation (1.3) peut être interprétée comme un mouvement brownien inertiel, la force $\mathbf{f}$ jouant le rôle de la vitesse. Le caractère hors d'équilibre de ce système apparaît lorsqu'on ajoute des forces extérieures. Celles-ci entrent dans l'équation sur $\dot{\mathbf{r}}$, le système étant considéré dans la limite suramortie. Fussent-elles ajoutées sur $\dot{\mathbf{f}}$ (interprétée comme une accélération), nous obtiendrions l'équation de Kramers qui satisfait le bilan détaillé par rapport à la distribution de Boltzmann.

Les particules autopropulsées par la force fluctuante $\mathbf{f}$ présentent quelques différences qualitatives par rapport aux particules se déplaçant à vitesse constante. En particulier, la probabilité $P(\dot{\mathbf{r}})$ d'observer une vitesse $\dot{\mathbf{r}}$ est une Gaussienne centrée en zéro. Cela peut expliquer, par exemple, que dans un piège harmonique très confinant, la densité de particules propulsées par la force d'Ornstein-Uhlenbeck est toujours gaussienne, centrée au milieu du piège [54]. Au contraire, les particules propulsées par une force constante s'accumulent sur les bords du piège, comme nous le verrons au chapitre 2.

## 1.4 Transitions de phases

Parmi les phénomènes variés observés dans la matière active, nous nous intéresserons plus particulièrement à deux transitions de phases qui sont spécifiques aux systèmes actifs : la séparation de phase induite par la motilité (ou MIPS pour *Motility-Induced Phase Separation*) et la transition vers le mouvement collectif. Ces deux transitions peuvent être capturées par des modèles simples qui sont à la base de notre compréhension de ces phénomènes.

### 1.4.1 Séparation de phase induite par la motilité

Les particules actives, contrairement aux particules browniennes, tendent à s'accumuler dans les régions de l'espace où leur vitesse est plus faible. Si, de plus, la vitesse d'autopropulsion diminue quand la densité de particules augmente, cela crée une boucle de rétroaction menant à une séparation de phase entre une phase dense, où les particules se déplacent lentement, et une phase diluée où leur motilité est élevée (voir fig. 1.5, gauche).

Cette séparation de phase fut décrite pour la première fois par Tailleur et Cates [57] dans un modèle où la dépendance de la vitesse d'autopropulsion avec la densité est explicite. Les particules se déplacent à une vitesse $v(\rho)$ où $\rho$ est la densité locale de particules actives. Pour ce système, la séparation de phase intervient lorsque $v(\rho)$ décroît suffisamment rapidement.

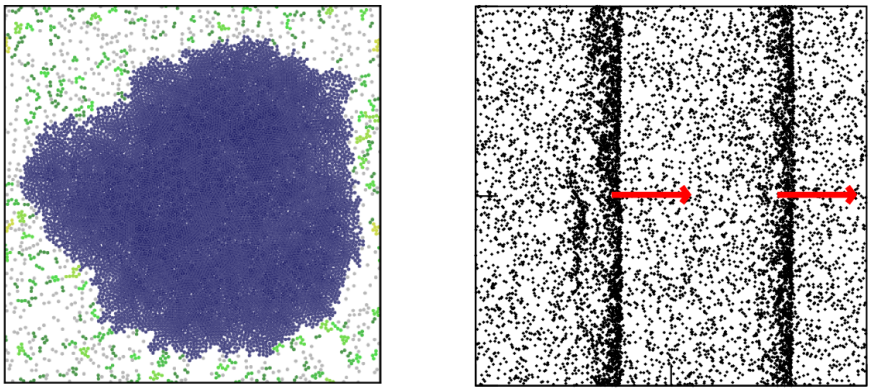

**Figure 1.5** – Transitions de phase dans la matière active. **Gauche** : séparation de phase induite par la motilité dans un système de sphères dures autopropulsées. Reproduite de [58]. **Droite** : phase inhomogène du modèle de Vicsek. Des bandes ordonnées de haute densité se propagent dans un gaz désordonné de particules. Reproduite de [68].

La dépendance de la vitesse avec la densité peut également être implicite, résultat d'interactions stériques. À haute densité, l'effet des collisions, dans la limite suramortie, est d'entraîner une diminution effective de la vitesse. Ainsi, la MIPS est observée dans des modèles de sphères dures autopropulsées, qui ont attiré beaucoup d'attention ces dernières années [58–67].

Ces deux approches correspondent à deux types d'interaction présentes dans des systèmes expérimentaux. L'interaction $v(\rho)$ est typique du comportement de bactéries qui sondent la densité locale par *quorum sensing*, en mesurant la concentration d'une molécule dans le milieu, et répondent en modifiant leur propriétés cinématiques [26]. Les interactions de coeur dur sont importantes, par exemple, dans des suspensions de colloïdes autopropulsés.

Les deux types d'interaction engendrent des comportements macroscopiques très similaires. Elles produisent par exemple la même dynamique de *coarsening* [60]. Cependant, la possibilité de décrire complètement les sphères dures par une vitesse effective $v(\rho)$ est un problème ouvert dont nous discuterons au chapitre 4.

### 1.4.2 Transition vers le mouvement collectif

Le modèle de Vicsek, déjà mentionné à la section 1.2.1, fait figure de paradigme pour l'étude de la transition vers le mouvement collectif [13, 68, 69]. Celui-ci peut être vu comme un modèle XY dynamique dans lequel des particules autopropulsées possèdent un spin vectoriel (leur direction de déplacement) qu'elles alignent via des interactions ferromagnétiques. Quand le bruit sur l'interaction d'alignement (la

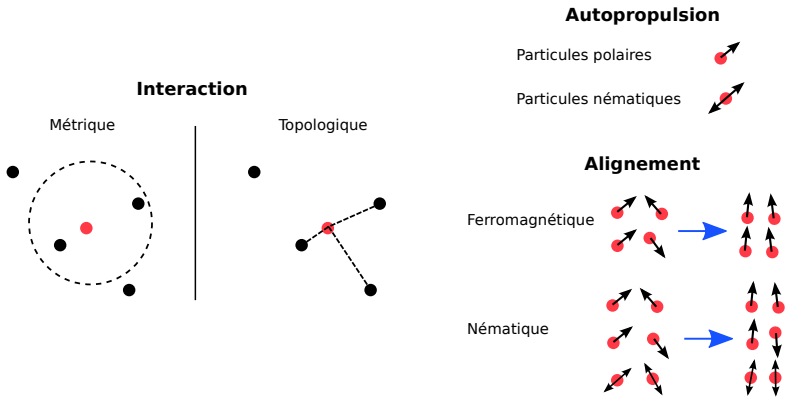


**Figure 1.6** – Variations autour du modèle de Vicsek étudiées dans la littérature [68–71]. L'interaction peut être métrique ou topologique (ici avec les trois plus proches voisins). L'autopropulsion est polaire ou nématique et l'alignement ferromagnétique ou nématique.

température dans un modèle XY) diminue, ou que la densité augmente, on observe une transition d'un état désordonné vers un état inhomogène où des bandes denses et ordonnées se propagent dans un gaz désordonné de particules (voir fig. 1.5, droite). À plus haute densité, ou plus faible bruit, on observe un état homogène ordonné, toutes les particules se déplaçant en moyenne dans la même direction.

Plusieurs variantes du modèle de Vicsek, considérant toujours des particules ponctuelles se déplaçant à vitesse constante, ont été proposées pour décrire différents types d'alignement que nous illustrons à la figure 1.6. Dans le modèle de Vicsek « topologique », les particules s'alignent avec leurs $n$ plus proches voisins, peu importe leur distance. Ce type d'interaction a été suggéré suite à des mesures faites dans des nuées d'oiseaux [15]. L'alignement peut également être nématique [70], au lieu de ferromagnétique, pour décrire, par exemple, des bactéries allongées qui s'alignent par interaction stérique [46]. Enfin, dans les modèles de nématiques actifs, l'alignement *et* la propulsion sont nématiques [71]. On a alors des particules qui oscillent le long d'un axe sans être vraiment autopropulsées, une situation qui permet de décrire des grains vibrés [40, 41]. Tous ces modèles présentent une transition vers un état ordonné, avec cependant des différences notables. Les phases inhomogènes sont différentes dans chaque modèle et absentes du modèle topologique. De plus, la phase homogène de basse température du modèle de nématiques actifs est seulement quasi-ordonnée en 2d, avec un paramètre d'ordre qui décroît avec la taille du système comme une loi de puissance [71].

Un point commun est que tous ces modèles possèdent dans leur phase (quasi) ordonnée des corrélations à longue portée. Ces corrélations, qui sont anisotropes, sont dures à mesurer précisément mais peuvent être mises en évidence en mesurant

les fluctuations de densité. Pour cela, on mesure le nombre moyen $n$ de particules dans des boîtes de tailles variables et la taille typique $\Delta n$ des fluctuations de $n$. Dans un système qui possède des corrélations à courte portée, pour des boîtes dont la taille linéaire est grande devant la longueur de corrélation, le théorème central limite impose $\Delta n \sim \sqrt{n}$. Au contraire, pour le modèle de Vicsek et ses dérivés, $\Delta n$ croît avec un exposant anormal (environ $\Delta n \sim n^{0.8}$ dans le modèle original [68]). Ces « fluctuations géantes » de densité sont une des propriétés spécifiques de la matière active et sont également observées expérimentalement [22, 40, 72]. Les équations hydrodynamiques phénoménologiques de Toner et Tu [73–75], qui comprennent tous les termes autorisés par la symétrie du problème, permettent, moyennant certaines approximations, de calculer les exposants associés aux fonctions de corrélations.

Bertin et collaborateurs ont proposé une version simplifiée du modèle de Vicsek ne prenant en compte que des collisions binaires [76]. On peut alors construire l'équation de Boltzmann associée au modèle. Celle-ci peut être être étudiée numériquement [77] mais permet surtout de construire des équations hydrodynamiques relativement simples en partant de la dynamique microscopique [76, 78–81]. Une tentative pour étendre cette approche à des collisions multiples par une procédure de Chapman-Enskog conduit quant à elle à des équations bien plus complexes [82, 83]. L'étude de la stabilité linéaire des équations hydrodynamiques permet de retrouver une partie du diagramme des phases du modèle de Vicsek et d'expliquer l'existence d'une phase inhomogène. Nous verrons cependant au chapitre 5 qu'elles n'expliquent pas la diversité des phases inhomogènes observées dans les modèles microscopiques. En effet, nous montrerons que les fluctuations jouent un rôle crucial dans la sélection de la forme de ces phases inhomogènes.

### 1.4.3 Importance des interactions hydrodynamiques

Dans cette thèse nous considérerons toujours des interactions locales et négligerons en particulier les interactions hydrodynamiques. Malgré les nombreuses situations physiques où l'hydrodynamique est prépondérante, l'importance des interactions hydrodynamiques a parfois été surestimée dans la matière active. Par exemple, l'hydrodynamique de champ lointain a été invoquée pour expliquer l'accumulation de particules actives près de parois [84], ce que des modèles négligeant les interactions hydrodynamiques expliquent très bien [85–87]. De plus, une mesure précise du flot créé par la nage d'une bactérie *E.Coli* [88] a montré que les interactions hydrodynamiques à longue portée sont négligeables devant les interactions stériques entre bactéries et avec les parois. Les interactions hydrodynamiques peuvent toutefois avoir des effets importants en déstabilisant des états ordonnés [89, 90], en arrêtant le *coarsening* dans la séparation de phase induite par la motilité [48, 91, 92], en induisant un mouvement circulaire pour des bactéries

près d'une surface [93] ou en modifiant la viscosité du milieu [94–96].

La théorie des gels actifs permet, sans décrire explicitement la dynamique du fluide, de prendre en compte les interactions hydrodynamiques de façon effective [8, 97, 98]. Basée sur la théorie des cristaux liquides, les interactions hydrodynamiques apparaissent comme une contribution supplémentaire au tenseur des contraintes, différente suivant le type de nageur, *pusher* ou *puller*. Ces équations phénoménologiques permettent, entre autres, de décrire l'apparition d'un écoulement et de défauts topologiques dans des suspensions actives denses et pourraient être pertinentes pour décrire le mouvement de cellules se déplaçant en étirant des lamellipodes [8] ou la cytocinèse [99] (le moment de la séparation d'une cellule en deux dans le cycle de division cellulaire).

Comme nous le verrons, les interactions hydrodynamiques ne sont pas nécessaires pour observer les phénomènes qui vont nous intéresser dans cette thèse. Toutefois, étendre les modèles qui seront présentés ici pour les inclure permettrait d'avoir une modélisation plus exacte de certains systèmes expérimentaux et pourrait révéler des effets intéressants.

## 1.5 Thermodynamique de la matière active

Pourrait-on construire une thermodynamique de la matière active qui permettrait de prédire de façon unifiée le comportement de larges classes de systèmes actifs ? Notre approche, qui s'appuie sur des modèles minimaux pour les relier à des équations hydrodynamiques, mettra en évidence l'universalité des phénomènes étudiés. En outre, la forte ressemblance de certains comportements, individuels ou collectifs, avec la phénoménologie de systèmes d'équilibre amène à se poser cette question.

### 1.5.1 De la matière active d'équilibre ?

En effet, certains systèmes actifs peuvent être décrits comme des systèmes d'équilibre. Le mouvement d'une particule autopropulsée, à des échelles de temps grandes devant son temps de persistance, est diffusif. La particule se comporte alors comme un colloïde chaud à une température effective dépendant de la vitesse d'autopropulsion [100]. La séparation d'échelle est ici importante, de la même façon que pour une particule passive dans un fluide, qui est décrite par un mouvement brownien à une échelle grande devant l'échelle nanométrique des collisions avec les molécules du fluide.

Le concept de température effective reste également valable pour des particules actives dans un potentiel extérieur $V$ de taille caractéristique grande devant la longueur de persistance [100]. La densité de particules en un point $\mathbf{r}$ de l'espace

est alors donnée par la distribution de Boltzmann

$$\rho(\mathbf{r}) \propto \exp\left(-\frac{V(\mathbf{r})}{k_B T_{\text{eff}}}\right) \tag{1.5}$$

On a ainsi un système à l'équilibre thermique et les différentes définitions de la température effective (par le théorème de fluctuation-dissipation, la distribution de Boltzmann ou le coefficient de diffusion) coïncident, comme nous le verrons au chapitre 2.

Les modèles décrivant des particules dont la vitesse dépend explicitement de la densité par un $v(\rho)$ sont également proches de systèmes d'équilibre. En première approximation dans un développement en gradients du champ de densité, la dynamique de ces systèmes vérifie le bilan détaillé par rapport à une énergie libre de Landau qui permet de prédire la séparation de phase MIPS [57, 101]. La probabilité d'observer un champ de densité $\rho$ est alors donnée par $P[\rho] \propto \exp(-\mathcal{F}[\rho])$. Toutefois, nous verrons au chapitre 4 qu'il est indispensable de prendre en compte des termes d'ordre supérieur pour décrire précisément la séparation de phase. On définira alors une nouvelle énergie libre, plus complexe, gouvernant la coexistence de phase.

On peut se demander jusqu'où il est possible de pousser la comparaison avec des systèmes d'équilibre. En effet, MIPS et la transition vers le mouvement collectif peuvent toutes deux être comprises comme des coexistences de type liquide-gaz ayant une phénoménologie proche de l'équilibre. Cependant, nous verrons au chapitre 3 que la pression mécanique d'un fluide actif n'admet en général pas d'équation d'état. Même pour les cas où la dynamique vérifie le bilan détaillé par rapport à une énergie libre effective, la distribution stationnaire n'est pas celle de Boltzmann et l'énergie libre n'est donc pas reliée de façon simple à la pression mécanique. Une thermodynamique de la matière active sera donc nécessairement assez différente de la thermodynamique d'équilibre, l'énergie libre ne contrôlant plus les propriétés mécaniques du système.

## 1.6 Organisation de la thèse

Nous nous sommes intéressés pendant cette thèse à différents aspects de la matière active. Les résultats obtenus seront présentés en s'appuyant sur les articles publiés pendant la thèse, qui seront reproduits dans le corps du texte. Deux autres publications sont reproduites en annexe [102, 103] pour ne pas introduire de redondance dans le texte.

Nous commencerons par étudier au chapitre 2 des particules actives sans interaction, soumises à un potentiel extérieur. Les cas de la sédimentation et d'un piège harmonique circulaire seront traités en détail. Nous verrons que nos résultats

peuvent être comparés de façon quantitative à une expérience de sédimentation de colloïdes autopropulsés [39].

Le chapitre 3 sera consacré à l'étude de la pression mécanique d'un fluide de particules actives, avec ou sans interaction entre particules. Nous définirons la pression mécanique comme la force exercée sur les parois du récipient dans lequel les particules sont confinées. La pression ainsi définie a des propriétés très différentes de la pression d'un fluide à l'équilibre. À part quelques exceptions notables, la pression dépend des détails de l'interaction entre particules et parois et n'est donc pas donnée par une équation d'état.

La séparation de phase induite par la motilité sera abordée au chapitre 4 par les deux voies évoquées plus haut : sphères dures et particules dont la vitesse dépend explicitement de la densité. Nous montrerons comment des équations hydrodynamiques fluctuantes peuvent être construites dans les deux cas. Les sphères dures autopropulsées sont un des cas particulier pour lesquels la pression mécanique satisfait une équation d'état. Comme pour un fluide d'équilibre, lorsque l'on observe une coexistence de phase, la pression mécanique est la même dans les deux phases, ce qui impose une contrainte sur les densités de coexistence. L'équation d'état nous permettra également de décrire partiellement les sphères dures comme des particules propulsées à une vitesse $v(\rho)$.

Finalement, le chapitre 5 sera consacré à la transition vers le mouvement collectif. Notre étude sera décomposée en trois étapes :

1. Nous introduirons le modèle d'Ising actif qui présente une phénoménologie plus simple que celle du modèle de Vicsek et dans lequel la transition vers la mouvement collectif peut être comprise comme une transition liquide-gaz.
2. Nous étudierons une classe d'équations hydrodynamiques décrivant la transition vers le mouvement collectif. Ces équations contiennent de façon générique toutes les solutions inhomogènes observées dans les modèles microscopiques (Ising actif et Vicsek en particulier) mais ne permettent pas d'expliquer comment telle ou telle solution est sélectionnée dans chaque modèle.
3. Nous montrerons que les fluctuations sont essentielles pour comprendre la forme des phases inhomogènes. La séparation de phase observée dans le modèle d'Ising actif devient une séparation en microphases dans le modèle de Vicsek, ce que l'on peut relier à la présence des fluctuations géantes de densité (absentes du modèle d'Ising actif). Cela nous conduira à définir deux classes d'universalité pour la transition sur la base de la symétrie de l'interaction d'alignement.

# Chapitre 2

# Particule active dans un potentiel extérieur

Avant de s'attaquer au problème plus complexe des comportements collectifs, il semble judicieux de commencer par une situation très simple : une particule active dans un potentiel extérieur. Des potentiels extérieurs, comme des parois ou des pinces optiques, peuvent être employés pour manipuler des particules autopropulsées. Il s'agit donc de comprendre la réponse d'une particule à ce type de manipulation. De plus, l'étude de l'état stationnaire d'une particule active dans un potentiel est un premier pas naturel si l'on espère découvrir des comportements génériques dans la matière active.

À l'équilibre thermique, le problème d'une particule brownienne dans un potentiel $V$ est complètement résolu. La probabilité de trouver la particule à une position $\mathbf{r}$ est donnée en toute généralité par la distribution de Boltzmann

$$\rho(\mathbf{r}) \propto \exp\left(-\frac{V(\mathbf{r})}{k_B T}\right) \tag{2.1}$$

Le même problème pour une particule autopropulsée peut sembler lié — il s'agit après tout d'un mouvement brownien persistant — mais n'admet pas de solution générale.

Les deux cas qui vont nous intéresser particulièrement, et qui seront traités en détail dans l'article A, sont la sédimentation (potentiel constant) et le confinement dans un potentiel harmonique de particules ABP et RTP se déplaçant à vitesse constante.

Le cas de la sédimentation est intéressant pour sa phénoménologie proche d'un système à l'équilibre thermique. En effet, si l'on reproduit l'expérience de Jean

Perrin avec des particules actives, on observe également une atmosphère exponentielle [36, 39, 100]. À une distance $z$ du fond du récipient, $\rho(z) \propto \exp(-z/\kappa)$ (où $\kappa$ est la longueur de sédimentation), comme pour des particules passives. Cependant, un régime d'équilibre effectif n'est atteint que lorsque la vitesse de sédimentation $v_s = \mu m g$ (où $\mu$ est la mobilité et $m$ la masse d'une particule) est faible devant la vitesse d'autopropulsion $v$ [100]. La distribution stationnaire est alors une distribution de Boltzmann, soit $\kappa^{-1} = mg/(k_B T_{\text{eff}})$ [100, 104]. Au contraire, quand $v_s \sim v$, on sort du régime d'équilibre effectif. On peut donc étudier dans ces systèmes le passage d'une distribution de Boltzmann à un autre état stationnaire en variant $v_s$ ou $v$.

Nous verrons que le régime d'équilibre effectif s'étend de façon plus générale à tous les potentiels qui varient sur une échelle grande devant le temps de persistance. Dans ce cas, la séparation d'échelle est telle que le mouvement local des particules est diffusif. Elles se comportent alors exactement comme des colloïdes « chauds ».

L'étude d'un piège harmonique circulaire nous permettra d'observer le phénomène très étudié de l'accumulation de particules actives près de parois [85–87]. Ce phénomène est propre aux particules autopropulsées. En effet, si l'on modélise un mur par un potentiel répulsif, la distribution de Boltzmann prédit que, pour des particules passives, la densité est toujours décroissante près du mur. C'est ce qui est observé pour des particules actives dans un piège peu confinant, dans le régime d'équilibre effectif. Au contraire, pour des potentiels très confinants, les particules s'accumulent sur les bords, de façon différente pour les ABP et les RTP (c'est un des cas où l'on observe une différence qualitative entre ces deux systèmes).

Quelques résultats exacts sont déjà présents dans la littérature. La longueur de sédimentation a été calculée par Tailleur et Cates pour des RTP en dimension $d = 1$ et 3 [100]. Nous étendrons ces résultats en calculant la distribution stationnaire complète pour des RTP (pour $d = 2, 3$) et ABP (pour $d = 2$). Pour des particules propulsées par une force fluctuant suivant un processus d'Ornstein-Uhlenbeck, la distribution stationnaire pour la sédimentation et un potentiel harmonique a été calculée par Szamel [54]. Notons que dans le cas du potentiel harmonique, la physique est qualitativement différente de celle des particules à $v = \text{cte}$ : la densité reste toujours gaussienne et aucune accumulation sur les bords n'est observée.

Nous introduirons d'abord l'équation maîtresse qui décrit le mouvement d'une particule active ABP ou RTP dans un potentiel extérieur (section 2.1) et nous l'utiliserons pour calculer exactement la distribution stationnaire d'une RTP en 1d dans un potentiel quelconque (section 2.2). Nous reproduirons ensuite l'article A à la section 2.3, dans lequel les cas de la sédimentation et du piège harmonique en 2d, ainsi que le régime d'équilibre effectif pour un potentiel arbitraire, seront traités. (La dernière partie de cet article concerne la séparation de phase induite par la motilité et sera donc reproduite au chapitre correspondant.) Nous compléterons

cette section par une comparaison de nos résultats avec des expériences de sédimentation sur des colloïdes Janus [39] et aborderons le cas $d = 3$ à la section 2.4.

## 2.1 Équation maîtresse

Écrivons l'équation maîtresse qui permet de décrire, en dimension d'espace arbitraire, une particule autopropulsée à une vitesse constante $v$ dans un potentiel $V$. Pour être le plus général possible on considère des particules ayant les deux types de réorientation, diffusion rotationnelle et culbutes :

$$\partial_t \mathcal{P}(\mathbf{r},\mathbf{u},t) = -\nabla \cdot [(v\mathbf{u} - \mu\nabla V)\,\mathcal{P}] - \alpha\mathcal{P} + \frac{\alpha}{\Omega}\int \mathcal{P}(\mathbf{r},\mathbf{u}',t)d\mathbf{u}' + D_r\Delta_{\mathbf{u}}\mathcal{P} + D_t\Delta\mathcal{P} \tag{2.2}$$

où $\mathcal{P}(\mathbf{r},\mathbf{u},t)$ est la probabilité de trouver la particule à la position $\mathbf{r}$ avec l'orientation $\mathbf{u}$ à l'instant $t$ et $\mu$ est la mobilité de la particule. La réorientation des ABP est donnée par le Laplacien rotationnel $D_r\Delta_{\mathbf{u}}\mathcal{P}$. Les culbutes sont prises en compte par les termes de perte et de gain proportionnels à $\alpha$ ; l'intégration par rapport à $\mathbf{u}'$ est faite sur la sphère unité $|\mathbf{u}'| = 1$, d'aire $\Omega$. Les ABP et RTP correspondent respectivement aux cas limites $\alpha = 0$ et $D_r = 0$. Le terme $D_t\Delta\mathcal{P}$ rend compte du mouvement brownien passif sur la position des particules. Contrairement au cas d'une particule passive, $D_t$ et $D_r$ ne sont pas reliés car ils sont en général d'origine différente : $D_t$ provient des collisions avec les molécules (passives) environnantes tandis que $D_r$ est en général dominé par le bruit sur le mécanisme d'autopropulsion.

### 2.1.1 Coefficient de diffusion effectif

En l'absence de potentiel extérieur, le mouvement d'une particule active est isotrope et diffusif sur une échelle de temps grande devant le temps de persistance d'une particule. L'équation maîtresse (2.2) peut être utilisée pour calculer le coefficient de diffusion effectif. Nous présentons simplement ici l'idée de la démonstration. La méthode utilisée a été introduite dans [101] et sera détaillée dans l'article C.

On commence par développer la distribution de probabilité $\mathcal{P}$ en harmoniques angulaires (en 2d) ou sphériques (en 3d)

$$\mathcal{P}(\mathbf{r},\mathbf{u},t) = \rho + \mathbf{p}\cdot\mathbf{u} + \mathbf{Q} : (\mathbf{uu} - \frac{\mathbf{I}}{d}) + \Theta(\mathcal{P}) \tag{2.3}$$

où $\rho$, $\mathbf{p}$ et $\mathbf{Q}$ sont des foncions de $\mathbf{r}$ et $t$ mais pas de $\mathbf{u}$. L'opérateur $\Theta$ projette $\mathcal{P}$ sur les harmoniques d'ordre supérieur. $\mathbf{I}$ est la matrice identité.

Les équations d'évolution de $\rho$, $\mathbf{p}$ et $\mathbf{Q}$ sont ensuite obtenues en projetant l'équation (2.2) sur les harmoniques d'ordre 0, 1 et 2 respectivement. La densité $\rho$ est un mode lent tandis que $\mathbf{p}$ et $\mathbf{Q}$ sont des modes rapides qui relaxent en un temps de l'ordre $1/\alpha, 1/D_r$. À l'ordre $\nabla^2$, l'équation sur la densité s'écrit alors

$$\partial_t \rho = \nabla \cdot (D_{\text{eff}} \nabla \rho) \,, \qquad D_{\text{eff}} = D_t + \frac{v^2}{d\,(\alpha + (d-1)D_r)} \tag{2.4}$$

On voit qu'à cette échelle les ABP et les RTP sont équivalentes, au remplacement $\alpha \leftrightarrow (d-1)D_r$ près. La contribution de la diffusion passive est découplée de celle de l'autopropulsion et vient simplement s'ajouter au coefficient de diffusion effectif.

On peut définir la température effective d'une particule active, qui sera rencontrée à plusieurs reprises dans ce chapitre et le suivant, par

$$D_{\text{eff}} = \mu k_B T_{\text{eff}} \qquad k_B T_{\text{eff}} = \frac{D_t}{\mu} + \frac{v^2}{\mu d\,(\alpha + (d-1)D_r)} \tag{2.5}$$

Notons qu'à ce point, $T_{\text{eff}}$ n'a *a priori* aucune raison de jouer un rôle « thermodynamique » [105].

## 2.2 Particules actives à une dimension

Les RTP en 1d sont le seul cas où l'on sait calculer la distribution de densité stationnaire exactement, pour un potentiel arbitraire. Notons qu'en 1d, seules deux directions sont possible $\mathbf{u} = \pm\hat{\mathbf{x}}$, les ABP n'existent donc pas dans cette dimension.

On notera $\mathcal{P}_+(x,t)$ et $\mathcal{P}_-(x,t)$ les densités de particule se déplaçant vers la droite et la gauche, et $\rho(x,t) = \mathcal{P}_+ + \mathcal{P}_-$ et $m(x,t) = \mathcal{P}_+ - \mathcal{P}_-$ la densité et l'orientation locales. L'équation maîtresse (2.2) s'écrit en 1d

$$\partial_t \mathcal{P}_+ = -\partial_x \left[(v - \mu \partial_x V)\, \mathcal{P}_+\right] - \frac{\alpha}{2}(\mathcal{P}_+ - \mathcal{P}_-) \tag{2.6}$$

$$\partial_t \mathcal{P}_- = -\partial_x \left[(-v - \mu \partial_x V)\, \mathcal{P}_-\right] + \frac{\alpha}{2}(\mathcal{P}_+ - \mathcal{P}_-) \tag{2.7}$$

$$\tag{2.8}$$

Dans l'état stationnaire, les dérivées temporelles sont nulles. En prenant la somme et la différence des deux équations précédentes, on obtient

$$0 = -\partial_x \left[vm - \mu(\partial_x V)\rho\right] \tag{2.9}$$

$$0 = -\partial_x \left[v\rho - \mu(\partial_x V)m\right] - \alpha m \tag{2.10}$$

La première équation impose que le flux de particule $J = vm - \mu(\partial_x V)\rho$ soit constant. Pour des particules confinées dans un potentiel, on a $J = 0$ et donc $vm = \mu(\partial_x V)\rho$. En reportant ceci dans la seconde équation, on obtient

$$0 = -\partial_x \left[ \left( v^2 - \mu^2 (\partial_x V)^2 \right) \rho \right] - \mu\alpha(\partial_x V)\rho \tag{2.11}$$

Utilisons maintenant l'Ansatz $\rho(x) = \rho_0 e^{-Q}$ qui donne

$$0 = \left[ v^2 - \mu^2 (\partial_x V)^2 \right] \partial_x Q + 2\mu^2 (\partial_x V)(\partial_x^2 V) - \mu\alpha(\partial_x V) \tag{2.12}$$

On peut intégrer cette équation pour trouver

$$Q = \ln \left[ \frac{v^2 - (\mu \partial_x V(x))^2}{v^2 - (\mu \partial_x V(0))^2} \right] + \int_0^x \frac{\mu\alpha \partial_x V(x')}{v^2 - (\mu \partial_x V(x'))^2} dx' \tag{2.13}$$

La densité de probabilité stationnaire est donc donnée par une fonction non-locale du potentiel, différente de la distribution de Boltzmann.

Ce n'est que dans la limite $|\mu \partial_x V| \ll v$ que l'équation (2.13) se simplifie pour donner

$$Q = \frac{\mu\alpha \left[ V(x) - V(0) \right]}{v^2} \tag{2.14}$$

La densité est alors donnée par la distribution de Boltzmann à la température $T = T_{\text{eff}}$.

## 2.3 Sédimentation et piège harmonique en deux dimensions

Dans l'article reproduit ci-après, nous traitons en détail les cas de la sédimentation et du confinement harmonique de particules actives, ABP et RTP, en dimension 2. Pour la sédimentation, nous montrons que l'on peut obtenir la distribution stationnaire, de densité et d'orientation, exactement. De plus, le régime d'équilibre effectif, mis en évidence pour des RTP en $d = 1$ à la section précédente, sera étendu de façon générale aux ABP et RTP pour $d \leq 3$.

**EPJ manuscript No.**
(will be inserted by the editor)

# Active Brownian Particles and Run-and-Tumble Particles: a Comparative Study

A. P. Solon[1], M. E. Cates[2], J. Tailleur[1]
[1] Univ Paris Diderot, Sorbonne Paris Cité, MSC, UMR 7057 CNRS, F75205 Paris, France
[2] SUPA, School of Physics and Astronomy, University of Edinburgh, Edinburgh EH9 3FD, United Kingdom

**Abstract.** Active Brownian particles (ABPs) and Run-and-Tumble particles (RTPs) both self-propel at fixed speed $v$ along a body-axis $\mathbf{u}$ that reorients either through slow angular diffusion (ABPs) or sudden complete randomisation (RTPs). We compare the physics of these two model systems both at microscopic and macroscopic scales. Using exact results for their steady-state distribution in the presence of external potentials, we show that they both admit the same effective equilibrium regime perturbatively that breaks down for stronger external potentials, in a model-dependent way. In the presence of collisional repulsions such particles slow down at high density: their propulsive effort is unchanged, but their average speed along $\mathbf{u}$ becomes $v(\rho) < v$. A fruitful avenue is then to construct a mean-field description in which particles are ghost-like and have no collisions, but swim at a variable speed $v$ that is an explicit function or functional of the density $\rho$. We give numerical evidence that the recently shown equivalence of the fluctuating hydrodynamics of ABPs and RTPs in this case, which we detail here, extends to microscopic models of ABPs and RTPs interacting with repulsive forces.

## 1 Introduction

Outside the realm of exact results, and despite recent progress [1], non-equilibrium statistical mechanics largely remains (paraphrasing Harish-Chandra [2]) messy, elusive and non-rigorous. However, we may say (paraphrasing Dyson [2]) that this is precisely why it is such an interesting research field. While a fully general extension of the well-established framework of equilibrium statistical physics remains out of reach, there are important classes of non-equilibrium systems for which progress towards a comprehensive theory seems achievable. Colloidal self-propelled particles (SPPs), which represent a central focus of research into active matter [3,4,5,6], arguably offer such a prospect. This applies at least in some simplified limits, such as spherical SPPs interacting by central forces only (a restriction that excludes hydrodynamic interactions). In developing theories of such systems, an important general question is how far macroscopic behaviour is sensitive to the detailed dynamical rules. For thermal systems, steady-state properties are governed by Boltzmann equilibrium, and hence sensitive to the energy landscape but not the dynamics used to explore it – so long as this dynamics obeys the principle of detailed balance (as it must do in

such cases). For non-equilibrium systems, such as SPPs, the question must be asked afresh. In this article we address this issue, by studying two classes of active particles, ABPs and RTPs. These have related but distinct dynamics, and have become two major workhorses of recent simulation and theoretical studies of active matter. We will find instances where their dynamical differences disappear on coarse-graining, to give the same macroscopic physics; and other instances where these differences remain important – typically when there is short-scale structure in the problem, such as confinement in small traps.

In active matter, a continuous supply of energy destroys microscopic time-reversal symmetry (TRS) and allows phenomena to arise that are impossible in thermal equilibrium systems, where detailed balance restores TRS in the steady state. Inspired in large part by experiments on synthetic self-propelled colloidal particles [7,8,9,10,11,12,13,14], many recent theory and simulation papers have addressed the physics of a simplified model comprising spherical active Brownian particles (ABPs) [15,16,17,18,19,20,21,22,23,24,25]. In parallel, growing experimental interest in bacterial motion [26,27,28,29,30,31,32] has brought run-and-tumble particles (RTPs) to the fore as a second prototypical model of self-propelled particles at the colloidal scale.

In these models, each particle feels a constant external force $\zeta v_0$ oriented along its swim direction $\mathbf{u}$. At low density this is equal and opposite to the local drag force felt by a particle moving at speed $v_0$. (At high density the external force may be partly opposed instead by conservative interparticle forces.) This is a one-body drag and thus the models entirely omit hydrodynamic interactions and all the other physics associated with the presence of an incompressible solvent. These can have important effects, for instance generating self-pumping states [33,34] or causing rotation by collision [35,36]. On the contrary, in the spherical ABP model the angular dynamics comprises rotational diffusion with a fixed diffusivity $D_r$. Idealized RTPs differ from ABPs only in their rotational relaxation; instead of continuous diffusion, RTPs undergo discrete tumbling events of short duration that completely randomize their swimming direction; these events occur randomly in time at mean rate $\alpha$ and the mean time between two tumbles is therefore exponentially distributed [1]. Both models share an important simplification, which would be inadmissible for any particles capable of exerting significant torques on one another (such as non-spherical SPPs at high density). Specifically, the angular dynamics of each particle remains unperturbed by interactions of any kind, and proceeds independent of the positions or orientations of all other particles in the system. In what follows, the terms ABP and RTP refer to this spherical, torque-free case unless stated otherwise.

Another key feature of these two models is that each particle exchanges momentum with external driving and drag forces, not with a suspending solvent. The resulting non-conservation of momentum within the system greatly complicates the discussion of the macroscopic force balances that normally underly mechanical properties such as pressure [22,23,24]. Indeed, the force per unit area on a wall in general depends on the wall-particle interactions [39]; this dependence does cancel out for the case of spherical (torque-free) ABPs moving with constant propulsive force [40], but not if the propulsive force is itself density-dependent [39] (a case we return to below).

In this paper, we present a comparative study of these simplified models of self-propelled particles. We first consider the steady-state distribution of non-interacting SPPs submitted to an external potential $V_{\text{ext}}$. Using exact results on the sedimentation of active particles, we show that ABPs and RTPs each admit an "effective temperature" regime when the Stokes speed $v_s \equiv -\nabla V_{\text{ext}}/\zeta$ is small compared to the swim speed $v$. We show how the effective temperature concept breaks down

[1] Other type of distributions, possibly with large tails, may also be considered. See, e.g., [37,38]

outside this regime in model-specific ways; this issue has attracted lots of interest recently [10,34,41,42,43]. We then consider the confinement of SPPs in circular or spherical traps, and show how the different angular dynamics between the two systems result in qualitatively different behaviours outside the effective equilibrium regime.

We then turn to interacting SPPs and consider models that replace interparticle collisions with a density-dependent propulsion force. Therefore we avoid any detailed discussion of the mechanical pressure, although it may offer an interesting alternative perspective on phase equilibria [24,40,44]. We explore an approximation scheme for torque-free SPPs with collisional interactions whereby the conservative forces responsible for collisional slow-down of the particles are replaced at mean-field level by a "programmed" slow-down, that is, an effective reduction in the propulsive force at high density. This path was first sketched out in [45] and pursued further in [17,19,46,47,48]. In a more general context it is both legitimate and interesting to consider, in its own right, the case with no conservative force field between particles, and ask about the effects of programmed slow-down among such "ghost" particles. While not forgetting its original motivation in the collisional case, we will often adopt this viewpoint here. Indeed, the concept of a programmed slow-down is well established in biological systems such as bacteria, where density-dependent dynamics can be effectively introduced through a biochemical pathway called quorum sensing [4,30,49,50]. This causes bacteria to change behaviour in response to the concentration of a short-lived chemical that they also emit. Because of the short lifetime, the response is then directly sensitive to the number of neighbours within a short but finite distance, and hence to a local coarse-grained density. Note that this is distinct from chemotaxis [51,52] in which organisms swim preferentially up or down *gradients* of a long-lived chemical signal—effectively creating a long-range repulsion or attraction. (Chemotaxis might also arise in synthetic, self-phoretic colloids [53].) An interesting study of chemotactic interactions in ABPs, showing some features resembling phase separation of the type discussed below, can be found in [54].

In bacteria such as *E. coli* angular relaxation is an RTP process, for which the consequences of density-dependent speed were first worked out in [45]. However, some bacterial types, including mutant strains of *E. coli* known as "smooth swimmers", do not tumble. In practice the genetic engineering strategies used in [30,49] to give density-dependent slow-down primarily achieve this by altering tumble times and frequencies (reducing the time-averaged speed). However, were it possible to directly link the actual propulsion speed of bacteria to their local density in a smooth-swimming strain, then this would offer an unambiguous physical realization of ABPs (as opposed to RTPs) with a density dependent speed. As in [30,49], this could probably be made to happen at densities too low for collisional or crowding effects to be important.

In summary, the study of SPPs with density-dependent propulsion speed is motivated (i) as an approximate representation of the collisional slow-down in SPPs with pairwise repulsions; (ii) as a representation of smooth-swimming or run-and-tumble bacteria with slow-down caused by quorum sensing or a related, non-collisional mechanism; and (iii) as a model in its own right, with which to explore generic collective phenomena in active matter systems. In the last context, it offers further insights into the degree to which macroscopic outcomes depend on local dynamical rules, and we shall focus on this below in comparing the ABP and RTP cases in some detail.

The most striking many-body phenomenon seen in this class of models is motility-induced phase separation, or MIPS. This is by now a well-established concept [4,45,46,47,48,55,56,57,58,59] and is the result of two effects in combination. First, the mean speed of a motile particle along its propulsion direction decreases with density (in contrast to the equilibrium case where the velocity statistics of a particle are separable, and fixed solely by equipartition). Second, particles tend to accumulate in spatial regions where they move slowly (a possibility ruled out, in isothermal equilibrium, by the fact that the

speed distribution cannot depend on position). This combination creates a positive feedback which is the origin of MIPS [4,45,56].

In what follows, after exploring in Section 2 the one-body behaviour of ABPs and RTPs in external potentials, we turn in Section **??** to their many-body physics, showing first how the large-scale dynamics with density-dependent $v(\rho)$ can in each case be mapped on the equilibrium dynamics of passive particles with attractive forces, and then outlining how gradient terms affect this mapping. Sections 2 and **??** offer a more complete presentation of results reported in [41,46] respectively. In fact we add substantially to these results: our discussion of ABPs in traps and of angular distributions for ABPs and RTPs under gravity are both new to the current paper. In the many-body section we carefully compare our approach with recent work by others on the role of leading order nonlocality (gradient corrections) in an effective free energy picture. We show further that, somewhat surprisingly, the large-scale equivalence between ABPs and RTPs established at the level of fluctuating hydrodynamics for particles with density-dependent swim speed [46] effectively extends to *microscopic simulations* of ABPs and RTPs interacting with *repulsive forces*.

## 2 Steady-state of active particles in external potential

Consider the classical experimental geometry, devised by Jean Perrin, in which dilute colloidal particles are allowed to sediment under gravity in a cuvette. Equilibrium statistical mechanics asserts that we can forget all details of the diffusive dynamics of the colloids: the steady-state probability of finding a particle at a given height $z$ is a Boltzmann distribution, $P(z) \propto \exp(-\delta m g z/kT)$, where $\delta m$ is the mass difference between the particle and a corresponding volume of liquid [2]. Let us now replace the Brownian random-walk diffusion of the colloids by an active random walk, powered by some microscopic non-equilibrium process. In the SPP context the latter is a persistent random walk of fixed speed, with either continuous (ABP) or discrete (RTP) changes of direction. (Its persistence length is much longer than for true Brownian motion, although the latter is finite in principle. More importantly, the instantaneous speed of true Brownian motion is not fixed, but has unbounded fluctuations given by the Maxwell-Boltzmann distribution.) Though not identical, clearly the equilibrium and non-equilibrium diffusive processes cannot be completely unrelated, at least in a limit where the persistence length is much smaller than the sedimentation length. Outside this regime, however, very different physics may be encountered.

Previous studies of sedimenting active particles confirm this line of reasoning. Exact results for RTPs in one, two and three spatial dimensions have shown the density profile to be exponential $\rho(z) \propto \exp(-\lambda z)$ far away from the containing boundaries [41,45]. The sedimentation length reduces to $\lambda^{-1} = kT_{\rm eff}/\delta m g$, with $T_{\rm eff} = v^2\zeta/d\alpha$ and $\zeta$ the inverse mobility of the particle; this result holds in the limit where the sedimentation speed $v_s = \zeta^{-1}\delta m g$ is much smaller than the swim speed $v$.

This effective equilibrium regime, where the sedimentation profile is given by a Boltzmann weight with a temperature $T_{\rm eff}$ independent of the potential $V_{\rm ext}$, was observed experimentally for ABPs in [10,43] and derived analytically in [34]. Its breakdown for stronger confinement, predicted in [41], was not observed experimentally so far [10,43], triggering a debate about the generic sedimentation behaviour for SPPs [42]. Below, for both RTPs and ABPs (Sections 2.1,2.2) we derive in 2D the full probability distribution $P(z,\theta)$ for finding a particle at height $z$ swimming in direction $\theta$. The outcome is that ABPs and RTPs both admit the same effective

[2] Note that in all this article but the sedimentation sections, we silently assume the mass of particles to be equal to one.

equilibrium regime – up to a simple parameter mapping between $\alpha$ and $D_r$. However, beyond this regime the density profiles are dynamics-dependent, and various definitions of the "effective temperature", which all coincide within the regime of small $v_s$, are found to differ beyond it.

In Section 2.4 we turn from sedimentation (which has $v_s$ uniform in space) to address the steady-state distributions of ABPs and RTPs in harmonic traps, where $v_s(r) = -\kappa r$. Again, ABPs and RTPs yield the same limiting effective equilibrium regime but lead to very different physics once the persistence length (respectively $v/\alpha$ or $v/D_r$) is much larger than the trap radius $v/\kappa$. In this regime, the cases of continuous (ABP) and discrete (RTP) angular rotation give entirely different statistics for the density at the centre of the trap, for reasons we discuss.

### 2.1 Sedimentation of 2D RTPs

Let us consider the dynamics of a 2D RTP in the presence of an external potential $V_{\rm ext}(\mathbf{r}) = \delta mgz$. The self-propulsion velocity $v\mathbf{u}(\theta)$ is supplemented by a sedimentation velocity $-v_s\mathbf{e}_z = -\zeta^{-1}\nabla V_{\rm ext}(\mathbf{r})$ so that the master equation reads

$$\dot{P}(\mathbf{r},\theta) = -\nabla\cdot[(v\mathbf{u}(\theta) - v_s\mathbf{e}_z)P(\mathbf{r},\theta)] - \alpha P(\mathbf{r},\theta) + \frac{\alpha}{2\pi}\int d\theta' P(r,\theta') \qquad (1)$$

We consider a system which is not free-falling, i.e. such that a wall at $z = 0$ prevents the particles from crossing this plane. A number of boundary conditions can be used to model the relevant interaction; for example, one can simply cancel the $z$ component of the particles velocity [60], or take into account the torque that a wall would exert on actual bacteria [41]. Different boundary layer structures then arise proximal to the wall, depending on the details of the dynamics and the boundary condition, which typically show strong particle accumulation in this region [61,62]. Beyond this proximal regime (typically a few run lengths in height) a stationary profile is reached at larger $z$ whose form is independent of the boundary condition.

In what follows we consider only this distal part of the profile. Its form can be found by assuming a factorized steady-state $P(z,\theta) = \rho(z)f(\theta)$; from Eq. 1, the factors must then satisfy

$$\frac{\rho'(z)}{\rho(z)} = \frac{\alpha}{v\cos\theta - v_s}\left(\frac{1}{2\pi f} - 1\right) \equiv -\lambda \qquad (2)$$

where $\lambda$ is a constant, a priori unknown. Eqs. (2) directly give

$$\rho(z) = \rho_0 e^{-\lambda z}; \qquad f(\theta) = \frac{1}{2\pi\left[1 - \frac{\lambda}{\alpha}(v\cos\theta - v_s)\right]} \qquad (3)$$

The constant $\lambda$ can then be fixed by the normalization condition $\int_0^{2\pi} f(\theta)d\theta = 1$, which yields

$$\alpha\sqrt{\frac{\lambda(v_s+v)+\alpha}{\lambda(v_s-v)+\alpha}} = \lambda(v_s+v)+\alpha \qquad (4)$$

Finally, the inverse sedimentation length is given by

$$\lambda = \frac{2\alpha v_s}{v^2 - v_s^2} \qquad (5)$$

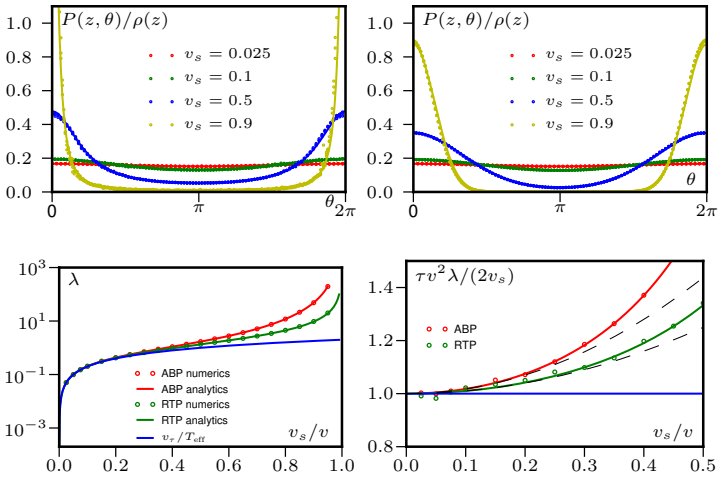


**Fig. 1.** Sedimentation of RTPs and ABPs ($\alpha = D_r = v = 1$). Symbols correspond to simulations data and full lines to analytical predictions. The conditional probability $P(\theta|z)$ for ABPs (top left) and RTPs (top right) is independent of $z$ in the distal part of the profile. (For each value of $v_s$, several $P(\theta|z)$ are constructed for different $z$ in the distal region; they show perfect overlap.) The simulation data matches the theoretical predictions given by (6) and (10). Bottom left: Inverse sedimentation length $\lambda$ as $v_s/v$ is varied. The equivalence between ABPs and RTPs breaks down as soon as one leaves the effective equilibrium regime (bottom right). The dashed lines correspond to the first order corrections of the two systems given in (12) and (15).

so that

$$f(\theta) = \frac{1 - \frac{v_s^2}{v^2}}{2\pi\left[1 - 2\frac{v_s}{v}\cos\theta + \frac{v_s^2}{v^2})\right]} \tag{6}$$

These exact results extend those of [41] where only $\rho(z)$ was computed; they perfectly fit simulations of sedimenting RTPs, as shown in figure 1.

## 2.2 Sedimentation of 2D ABPs

A similar path can be followed for sedimenting ABPs in 2D, starting from the master equation

$$\dot{P}(\mathbf{r},\theta) = -\nabla\cdot[(v\mathbf{u}(\theta) - v_s\mathbf{e}_z)P(\mathbf{r},\theta)] + D_r\partial_{\theta\theta}P(r,\theta) \tag{7}$$

Again, a separation of spatial and angular variables is confirmed numerically beyond a boundary layer proximal to the wall. The steady-state $P(z,\theta)$ is found by using the ansatz $P(z,\theta) = \rho(z)f(\theta)$ in Eq.7, to give

$$0 = -\partial_z[(v\cos\theta - v_s)P(z,\theta)] + D_r\partial_{\theta\theta}P(z,\theta) \tag{8}$$

which yields

$$\rho'(z) = -\lambda\rho(z) \qquad f''(\theta) = -\frac{\lambda}{D_r}(v\cos\theta - v_s)f(\theta) \tag{9}$$

As before, this yields an exponential atmosphere $\rho(z) = \rho_0\exp(-\lambda z)$ where the inverse sedimentation length $\lambda$ is set by the normalisation of $f(\theta)$. The equation for $f(\theta)$ is

the Mathieu equation. Given that $f(\theta)$ is even, it admits the general solution

$$f(\theta) = c_1 C\left(-\frac{4\lambda v_s}{D_r}, -\frac{2\lambda v}{D_r}, 2\theta\right) \tag{10}$$

where $C(a, q, \vartheta)$ is the cosine Mathieu function [64]. For fixed $q$, this is $\pi$-periodic in $\vartheta$ only for a countable subset of $a$ values, $a = a_n(q)$, which satisfy $a_n(0) = n^2$. Since $\lambda \to 0$ when $v_s \to 0$, the solution of interest has $n = 0$ which implies

$$-4\frac{\lambda v_s}{D_r} = a_0\left(-2\frac{\lambda v}{D_r}\right) \tag{11}$$

Solving this numerically gives $\lambda(v_s, v, D_r)$. (The numerics can be done using either a formal solver like Mathematica or by procedures based on series expansion of the $a_n$'s [65].) The resulting values of $\lambda$ match perfectly the results found by simulating sedimenting ABPs; the full distribution is then obtained by plotting the corresponding Mathieu function, and also agrees very well with the numerics (see Fig 1).

### 2.3 Effective equilibrium regimes

**Boltzmann distributions.** When $v_s/v \ll 1$, both ABPs and RTPs admit an effective equilibrium regime. This is most easily seen for RTPs where $\lambda$ can be readily expanded:

$$\lambda \underset{v_s \ll v}{\simeq} \frac{2\alpha v_s}{v^2}(1 + \frac{v_s^2}{v^2}) \tag{12}$$

Keeping only the dominant contribution, the steady-state thus reduces to the Boltzmann form

$$\rho(z) = \rho_0 e^{-V_{\rm ext}(z)/kT_{\rm eff}}; \qquad kT_{\rm eff} = \frac{v^2\zeta}{2\alpha} \tag{13}$$

where the last equality is an effective Stokes-Einstein relation that connects the mobility $\zeta^{-1}$ to the diffusivity $D_0 = v^2/(2\alpha)$ through an effective temperature $T_{\rm eff}$.

For ABPs, one can use the expansion

$$a_0(q) \underset{q \ll 1}{\simeq} -\frac{1}{2}q^2 + \frac{7}{128}q^4 \tag{14}$$

to get

$$\lambda \underset{v_s \ll v}{\simeq} \frac{2D_r v_s}{v^2}(1 + \frac{7v_s^2}{4v^2}) \tag{15}$$

Again, the system admits a Boltzmann distribution as steady-state, at the dominant order in $v_s/v$, with an effective temperature

$$kT_{\rm eff} = \frac{v^2\zeta}{2D_r} \tag{16}$$

Equating the mean time $\tau = \alpha^{-1}$ between two tumbles in RTPs and the rotational diffusion time $\tau = D_r^{-1}$ in ABPs, the two effective equilibrium regimes match. (In general dimensions, the parameter mapping is from $\alpha^{-1}$ to $(d-1)D_r^{-1}$, which are the angular autocorrelation times for RTPs and ATPs respectively [46].) However, even the first order corrections in (12) and (15) are different in form (see Fig. 1). Matching the angular relaxation times gives exponential decay of the angular correlator

$\langle \mathbf{u}(t)\mathbf{u}(0)\rangle = \exp[-t/\tau]$ in both cases, but unless $v_s/v \ll 1$ the sedimentation length depends on the details of the angular dynamics.

Note that one can also expand the angular distribution $f(\theta)$ close to the effective temperature regime $v_s \ll v$. For 2d RTPs, this gives (using the normalisation $\int \mathrm{d}\theta f(\theta) = 1$)

$$2\pi f(\theta) = 1 + \left(\frac{\kappa v}{\alpha} + \frac{3\kappa^2 v v_s}{\alpha^2}\right)\cos\theta + \frac{\kappa^2 v^2}{2\alpha^2}\cos 2\theta + O(\kappa^2) \tag{17}$$

$$= 1 + \frac{2v_s}{v}\cos\theta + \frac{2v_s^2}{v^2}\cos 2\theta + O(\Big(\frac{v_s}{v}\Big)^3) \tag{18}$$

where on the last line we used that

$$\kappa \underset{v_s \ll v}{\simeq} \frac{2\alpha v_s}{v^2}(1 + \frac{v_s^2}{v^2}) \tag{19}$$

We can do the same for 2d ABPs using the Fourier expansion of characteristic Mathieu functions [64], to get

$$2\pi f(\theta) = 1 + \frac{\kappa v}{D_r}\cos\theta + \frac{\kappa^2 v^2}{8D_r^2}\cos 2\theta + O(\kappa^2) \tag{20}$$

$$= 1 + \frac{2v_s}{v}\cos\theta + \frac{v_s^2}{2v^2}\cos 2\theta + O(\Big(\frac{v_s}{v}\Big)^3) \tag{21}$$

where on the last line we used that

$$\kappa \underset{v_s \ll v}{\simeq} \frac{2D_r v_s}{v^2}(1 + \frac{7v_s^2}{4v^2}) \tag{22}$$

The difference between $f(\theta)$ for ABPs and RTPs can thus be seen at the level of the second harmonics. As for the difference between the density profiles of RTPs and ABPs, it appears at second order in $v_s/v$. Note that the first order correction to $f(\theta) = 1/(2\pi)$ however suffices to distinguish these distributions from equilibrium ones.

**Fluctuation-dissipation relations.** A quantity that is frequently looked at in non-equilibrium statistical physics is the ratio between correlation and response functions [66]. Here we examine this for active particles in a sedimentation setup. For simplicity we only consider RTPs where we have explicit formulae, but conceptually what follows applies equally to ABPs. Let us consider a small force $f$ applied along $\mathbf{e}_z$ and compute the response function

$$R = \left.\frac{\partial\langle z\rangle}{\partial f}\right|_{f=0} \tag{23}$$

The steady-state distribution is then $\rho(z) \propto \lambda(f)\exp[-\lambda(f)z]$ where $\lambda(f)$ is obtained by replacing $v_s \to v_s - \zeta^{-1}f$ in Eq. (5). Since $\langle z\rangle = \lambda(f)^{-1}$, $R$ is given by

$$R = -\frac{\lambda'(0)}{\lambda(0)^2} \tag{24}$$

Since the correlation function $C \equiv \langle z^2\rangle - \langle z\rangle^2 = \lambda(0)^{-2}$, one directly gets

$$\frac{C}{R} = -\frac{1}{\lambda'(0)} \tag{25}$$

In the effective equilibrium regime, where $\lambda(f) = 2(v_s - f/\zeta)/\tau v^2$ this gives

$$\frac{C}{R} = \frac{\zeta v^2 \tau}{2} = kT_{\text{eff}} \tag{26}$$

which is the usual form for a system with an effective temperature; the system satisfies a fluctuation dissipation theorem (as it should) governed by that temperature.

For larger $v_s$, the same ratio can be computed explicitly for RTPs using the exact result 5, yielding

$$\frac{C}{R} = \zeta\tau \frac{v^2 - v_s^2}{2} \frac{v^2 - v_s^2}{v^2 + v_s^2} \tag{27}$$

In this regime, there is no longer an FDT at temperature $T_{\text{eff}}$ for the response to a force along $z$. Moreover, an alternative definition of the effective temperature (which coincides with the fluctuation-dissipation ratio in the effective equilibrium regime) is found by applying a force instead along $\mathbf{e}_x$, and asserting a Stokes-Einstein relation between the mobility $\zeta^{-1}$ and the lateral diffusivity defined via the mean-square displacement along $x$. This yields $kT_{\text{eff}} = \zeta v^2 \tau/2$, just as in Eq.(26), with no dependence at all on $v_s$. For large $v_s$, the resulting "horizontal" effective temperature controls neither the density profile nor the fluctuation-dissipation in the $z$ direction.

In summary, outside the effective equilibrium regime, the three equally plausible definitions

$$kT_{\text{eff}} \equiv \frac{C}{R} \quad \text{and} \quad kT_{\text{eff}} = -\frac{V_{\text{ext}}(z)}{\log P(z)} \quad \text{and} \quad kT_{\text{eff}} \equiv \zeta \lim_{t\to\infty} \langle x^2(t)/t \rangle \tag{28}$$

yield three different effective temperatures. It follows that none is really effective, in the sense that if a new one is needed to describe each property measured, the concept of effective temperature is itself ineffective. In contrast, for both ABPs and RTPs within the effective equilibrium regime (arising in the limit of weak gravity) all three definitions of temperature coincide and the dynamics effectively reduces to an equilibrium problem. For this reason we prefer the term "effective equilibrium" to describe this regime over the less explicit "effective temperature" name used earlier [41].

Interestingly it was recently shown experimentally, by measuring density profiles, that the addition of repulsive interactions between the particles does not immediately destroy the effective equilibrium regime [43]. Note that observing its breakdown experimentally requires a rather large ratio of $v_s/v$ (for $v_s/v \simeq 0.4$, the difference in $\lambda$ is only 40% for ABPs). This may explain why this breakdown has not been reported experimentally so far. The more general question of effective equilibrium in active particles remains a subtle one. For instance, if the fixed self-propulsion speed $v$ is replaced by a fluctuating one, using an Ornstein-Uhlenbeck process [42,43], the effective equilibrium regime extends to arbitrary sedimentation speed $v_s$, which clearly differs from the RTP and ABP cases treated here. As discussed in [41], fixed propulsion speed is qualitatively different from any dynamics that can sample very high speeds, even if these are rare (as they are in the thermal Maxwell-Boltzmann distribution). One reason for this is clear: if there is a fixed maximum speed, then when $v_s$ exceeds this, all particles are moving only downwards and the sedimentation length must be strictly zero (in the absence of particle-particle interactions). Rare sampling of high molecular speeds is why, in thermal equilibrium, a nonzero sedimentation length $\lambda^{-1} = kT/\delta mg$ is maintained even for very large $v_s = \delta mg/\zeta$.

### 2.4 Trapping of SPPs

Apart from RTPs in one dimension [45], there are no exact results available for the full steady-state distribution of ABPs and RTPs in a harmonic trap. While the approach

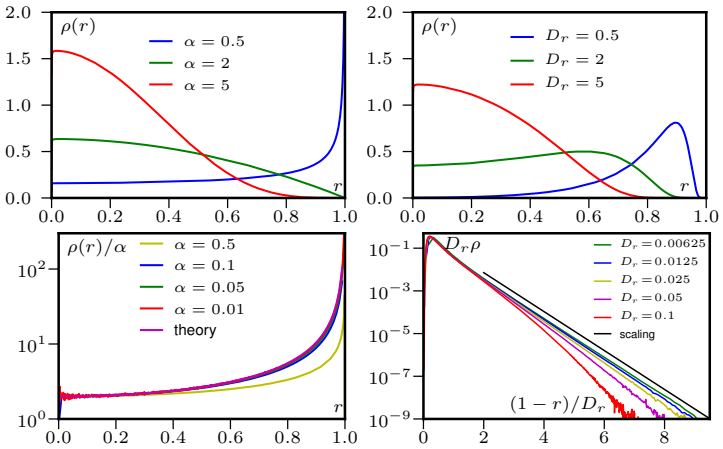


**Fig. 2.** SPPs in a harmonic trap ($v = \kappa = 1$ in simulation units). As $\Phi = \kappa\tau$ increases, $\rho(r)$ goes from a Gaussian centered on $r \simeq 0$ to a distribution peaked at $r \simeq v/\kappa$; this holds for both RTPs (top left) and for ABPs (top right). As $\Phi$ diverges, the density of RTPs in the bulk scales as $1/\Phi$ (bottom left), while the density of ABPs in the bulk scales exponentially with $D_r$, and the profile $\rho(r)$ decreases exponentially with the distance to the trap boundary (bottom right).

presented in the previous section does not apply here, because $P(\mathbf{r}, \theta)$ is not factorized, some progress is still possible as we show below. The Stokes velocities of SPPs are now position-dependent and read $\mathbf{v}_s = -\kappa\mathbf{r}/\zeta$, where $\mathbf{r}$ is measured from the center of the trap. The physics is very different from the sedimentation case since the particles are effectively confined to $r < r_T \equiv v/\kappa$; At $r = r_T$ the trapping and propulsive forces compensate exactly, hence preventing the particles from moving further outside.

The effective equilibrium regimes correspond to $\tau \ll \lambda^{-1}$ and, as expected, are the same for ABPs and RTPs, with Boltzmann weights for the steady-state distribution $\rho(\mathbf{r})$ (see Fig. 2)

$$\rho(\mathbf{r}) \propto \exp\Big(-\frac{\kappa\,\mathbf{r}^2}{2kT_{\rm eff}}\Big); \qquad kT_{\rm eff} = \frac{v^2\tau\zeta}{2} \tag{29}$$

As the ratio $\Phi \equiv \kappa\tau$ between the persistence-length $v\tau$ and the trap radius $r_T = v/\kappa$ increases, the time needed for the particles to cross the trap becomes much smaller than the mean reorientation time. Particles thus accumulate at the outskirts of the trap where, on average, they point outward radially. How long they persist in this state depends on the dynamical details; in consequence, the density distributions of RTPs and ABPs differ in this regime, particularly in the central region of the trap. Note that, once again, this scenario differs from the fluctuating speed model of [42] where the steady-state in a harmonic trap is always a Gaussian, with fast enough particles reaching arbitrarily large distances and slow enough particles remaining in the center of the trap.

**RTP in a harmonic trap.** RTPs pointing outward at the trap boundary undergo instantaneous tumble events at rate $\alpha$ whereafter they move across the trap along a certain path. Despite the trap force, and somewhat surprisingly, we show below this path to be a straight line segment, which fully crosses the trap for large $\Phi$; In this limit, the trajectory is thus a succession of chords of the circle in 2D. The fraction of

time spent by a particle in the bulk then corresponds to the fraction of its run-time needed to reach the other side of the trap; this time is proportional to $1/\Phi$. (This scaling is correct although in practice the path is not followed at constant speed.)

Beyond the scaling $\rho(r) \propto \alpha/\kappa$ in the bulk, one can furthermore compute a limiting shape of $\rho(r)$ as $\alpha/\kappa \to 0$. Let us consider a particle at position $\mathbf{r}_0$ on the trap boundary which tumbles to make an angle $\theta$ with the horizontal axis. Its trajectory until the next tumble is simply given by

$$\mathbf{r}(t) = \mathbf{r}_0 e^{-\kappa t} + \frac{v}{\kappa}(1 - e^{-\kappa t})(\cos\theta, \sin\theta) \tag{30}$$

which generalizes the intuitive result $r = (v/\kappa)(2\exp[-\kappa t] - 1)$ for $\mathbf{r}_0 = (v/\kappa, 0)$ and $\cos\theta = -1$. (The latter describes overdamped relaxation across a diameter of the circle to a new equilibrium position opposite the previous one, and applies in the case where the tumble exactly reverses the swim direction.) Eq. (30) describes a linear trajectory joining $\mathbf{r}_0$ to $\frac{v}{\kappa}u(\theta)$, where the trap force balances again the propulsion force. The angular momentum $L(t) = (\mathbf{r}(t) - \mathbf{r}_0) \wedge \dot{\mathbf{r}}(t)$ about the initial position $\mathbf{r}_0$ satisfies $L(0) = 0$ and $\dot{L} = -\kappa L$ so that $L(t) = 0$. The velocity $\dot{\mathbf{r}}$ and $\mathbf{r} - \mathbf{r}_0$ are thus always parallel: the torques about $\mathbf{r}_0$ exerted by the trap force and the propulsion force balance to produce a straight trajectory at an angle intermediate between $\mathbf{u}$ and $\mathbf{r}_0$; Only the speed $|\dot{r}(t)| \propto \exp(-\kappa t)$ is thus varying.

Let us now consider $\mathbf{r}_0 = (v/\kappa, 0)$. As shown in Fig. 3, the distance to the center of the trap first decreases from $r \sim v/\kappa$ to $r_{\min}(\theta) = v|\cos\frac{\theta}{2}|/\kappa$, which is reached after a time $t = (\log 2)/\kappa$. The distance then increases again until (almost) reaching $r \sim v/\kappa$ before the next tumble happens. (Since the speed $|\mathbf{v} + \mathbf{v}_s|$ vanishes as $r \to v/\kappa$, the particle never reaches exactly the trap boundary.) The trajectory thus crosses twice any annulus of radius $r > r_{\min}(\theta)$ within the trap, where it spends a fraction of its duration $\propto \alpha(1/|\dot{\mathbf{r}}[t_+(\theta)]| + 1/|\dot{\mathbf{r}}[t_-(\theta)]|)$. Here, we have assumed that the total duration of the trajectory is $1/\alpha$ and $t_\pm(\theta)$ are the times at which the particle reaches $|\mathbf{r}| = r$. These times satisfy

$$(v^2 - \kappa^2 r^2)\exp(\kappa t_\pm) = v^2(1 - \cos\theta) \pm \sqrt{2\lambda^2(1 - \cos\theta)(r^2 - r_{\min}^2)} \tag{31}$$

so that the probability of finding a particle at position $r$ can be computed as

$$\rho(r) = Z\frac{1}{2\pi}\int_{2\arccos(\kappa r/v)}^{2\pi - 2\arccos(\kappa r/v)} \left(\frac{\alpha}{|\dot{\mathbf{r}}(t_1)|} + \frac{\alpha}{|\dot{\mathbf{r}}(t_2)|}\right) d\theta \tag{32}$$

Note that $\rho(r)$ formally diverges as $r \to v/\kappa$; in practice this is cut off because the finite duration ($\sim 1/\alpha$) of the trajectory ensures that no particle exactly reaches the maximal radius $r = v/\kappa$ at which its net speed vanishes. The smaller $\alpha$, the closer to the trap boundary this cut-off takes place. We have taken $\alpha$ out of the normalization $Z$ to make the scaling of $\rho(r)$ apparent; $Z$ is then independent of $\alpha$ and equals $Z \simeq \pi/2$. The bottom-left quadrant of Fig 2 shows a very good agreement between Eq. (32) and simulations of RTPs for $\alpha/\kappa \leq 0.1$.

**ABP in a harmonic trap.** Contrary to RTPs, the orientation of ABPs diffuse slowly so that, as $\theta$ varies, they simply slide along the boundary of the trap, rarely visiting its inner region. This was used recently [67,68] to compute the distribution of ABPs along the boundary of small traps of arbitrary shapes, assuming that the particles effectively never leave the boundary of the trap. As we show below, this asumption is a sound one since the density of particles decreases exponentially as one moves away

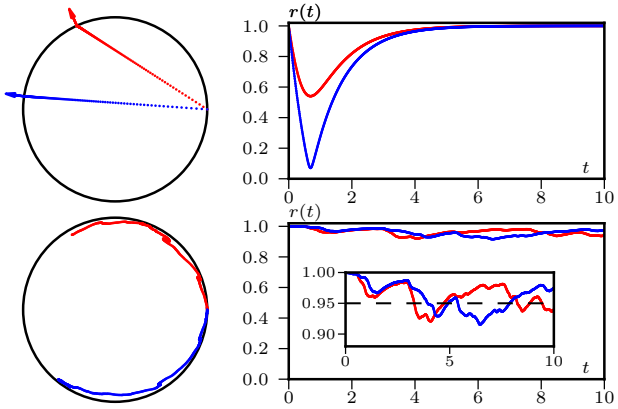


**Fig. 3.** SPPs in a harmonic trap ($\alpha = D_r = 0.1$, $v = \kappa = 1$ in simulation units). Left and right plots correspond to real-space trajectories and the evolution of $r(t)$, respectively. The arrows in the top left panel show the orientations of the particles. Top and bottom correspond to RTPs and ABPs, on similar time-scales. The dashed line in the bottom right panel correspond to $r = v[1 - D_r/(2\kappa)]/\kappa$.

from the boundary and is exponentially small in $\Phi$ at the trap centre. Introducing the angle $\varphi$ between the direction of the particle and the normal to the trap $\mathbf{e}_r$, the dynamics in the $(r, \varphi)$ variables become

$$\dot{r} = -\kappa r + v\cos\varphi \qquad \dot{\varphi} = \sqrt{2D_r}\eta(t) - \frac{v}{r}\sin\varphi \tag{33}$$

where $\eta(t)$ is a Gaussian unit white noise. Using dimensionless variables $\tau = tD_r$, $\tilde{r} = r\kappa/v$, and $\tilde{\eta}(\tau) = \eta(t)/\sqrt{D_r}$, Eqs. (33) become

$$\dot{\tilde{r}} = -\frac{\kappa}{D_r}(\tilde{r} - \cos\varphi) \qquad \dot{\varphi} = \sqrt{2}\tilde{\eta} - \frac{\kappa}{\tilde{r}D_r}\sin\varphi \tag{34}$$

where $\tilde{\eta}(\tau)$ is also a Gaussian unit white noise. The angle $\varphi$ thus undergoes rotational diffusion in an effective potential $\frac{\kappa}{\tilde{r}D_r}(1-\cos\varphi)$ whose amplitude diverges as $D_r/\kappa \to 0$. In this limit, $\varphi$ oscillates around $\varphi = 0$ with Gaussian fluctuations $\langle\varphi^2\rangle = D_r/\kappa$. Consequently, $\tilde{r} \simeq 1 - D_r/(2\kappa)$: the particle is almost always at the border of the trap, although the fluctuations of $\varphi$ prevent it from reaching exactly $r = v/\kappa$ (see Fig. 3). The density of particles in the bulk of the trap is thus much smaller than in the RTP case since in a time $t \sim 1/D_r$, the particles are exponentially unlikely to escape the trap boundary while RTPs would typically cross the trap in times $t \sim 1/\alpha$. (Recall that these two times are interchangeable in the effective equilibrium regime.) The occurrence of an effective potential, preventing particles from diffusing in angle away from the outward normal direction, at first seems to violate the fact that the dynamics of ABPs is torque-free. Note however that there is no real potential for the angle $\theta$; the effective potential for $\varphi$ arises not because there is a torque, but because the translational motion of a particle along the trap boundary naturally leads it towards a location where the outward normal is parallel to the current orientation, hence leading to $\varphi \simeq 0$. This effect is also present for RTPs but the discrete angular dynamics effectively allows the RTP to immediately escape the reorientation potential.

To reach the bulk part of the trap, Eq. (34) tells us that $\varphi$ needs to climb the effective potential to turn and face its destination. In principle, there are many stochastic

paths leading from the boundary to some inner target point at distance $r$ from the center. As $\kappa/D_r \to 0$, however, the transition probability is dominated by the most probable path leading to such a point [69] (an instanton). The probability of this path will be given by $\exp \kappa \Delta E/D_r$, where $\Delta E(r/r_T)$ is a geometric function depending on the exact location of the target. Since reaching the center of the trap requires a fluctuation of $\varphi$ much larger than any required to reach another point close to the trap boundary, the energy barrier increases as the distance of a target from the boundary increases. In practice, a linear function $\Delta E(r/r_T)$ fits very well the effective energy barrier:

$$\rho(\mathbf{r}) \simeq \frac{C}{2\pi r_T^2} \Phi \exp\big[C\Phi(r/r_T - 1)\big] \tag{35}$$

where $C$ is a dimensionless constant. The density in the center of the trap indeed decreases much faster than for RTPs, as $\Phi \exp(-C\Phi)$. Somewhat surprisingly, this simple argument gives reasonably good agreement, with a geometric factor $C$ whose fit yields $C \simeq 2.15$, with the bulk density measured in numerical simulations (See Fig. 2).

### 2.5 Effective equilibrium for generic potentials

In this section we show that for generic potentials $V_{\text{ext}}$, sufficient conditions to observe an effective equilibrium regime are given by

$$|\xi^{-1} \nabla V_{\text{ext}}(\mathbf{r})| \ll v; \qquad \text{and} \qquad |\xi^{-1} \Delta V_{\text{ext}}(\mathbf{r})| \ll \alpha,\, D_r(d-1) \tag{36}$$

To show this, let us consider a system for which (36) holds. The fluctuating hydrodynamics for ABPs and RTPs in the presence of external drifts derived in [46] reads:

$$\dot{\rho} = -\tfrac{\Omega}{d} \nabla (v\mathbf{p}) + \nabla \cdot [\xi^{-1} \nabla V_{\text{ext}} \rho] + \nabla (D_t \nabla \rho) \tag{37}$$

$$A p_a = -\nabla_a (v\rho/\Omega) + \nabla_b (\xi^{-1} \nabla_b V_{\text{ext}} p_a) + \mathcal{O}(\nabla^2) \tag{38}$$

where $\Omega$ is the surface of the unit sphere in $d$ dimensions and $A$ equals $\alpha$ for RTPs and $D_r(d-1)$ for ABPs. This description is valid at times $t \gg A^{-1}$ and for fields $\rho, \mathbf{p}$ whose gradients are small on the scale of the persistence length of SPPs, $|\nabla\rho|/\rho$, $|\nabla \mathbf{p}|/|\mathbf{p}| \ll A/v$; its derivation in the isotropic case is the subject of section **??**, whose notation differs slightly through introduction of a quantity $\varphi = \rho/\Omega$.

Expanding the second term of the r.h.s of Eq. (38) then yields

$$(A - \xi^{-1} \Delta V_{\text{ext}}) p_a = -\nabla_a (v\rho/\Omega) + \xi^{-1} \nabla_b V_{\text{ext}} \cdot \nabla_b p_a + \mathcal{O}(\nabla^2) \tag{39}$$

Equation (39) thus shows that $p_a \simeq \mathcal{O}(\nabla)$. Using (36), the Laplacian of $V_{\text{ext}}$ can then be neglected and (39) simplifies into

$$p_a = -\frac{v}{A} \nabla_a (\rho/\Omega) + \mathcal{O}(\nabla^2) \tag{40}$$

The dynamics of $\rho$ is then given by

$$\dot{\rho} = \nabla \cdot \Big[ \big(D_t + \frac{v^2}{A}\big) \nabla \rho + \xi^{-1} \nabla V_{\text{ext}} \rho \Big] \tag{41}$$

which is nothing but the equilibrium Fokker-Planck equation of a colloid of mobility $\xi$ subject to an external potential $V_{\text{ext}}$, at a temperature

$$k T_{\text{eff}} = \xi \big[ D_t + \frac{v^2}{A} \big] \tag{42}$$

The steady-state solution of this equation is the Boltzmann weight $\rho(x) \propto \exp[-\beta_{\rm eff} V_{\rm ext}]$, which satisfies

$$\left| \frac{v}{A} \frac{\nabla \rho}{\rho} \right| = \left| \frac{v}{A} \frac{\xi^{-1} \nabla V_{\rm ext}}{D_t + \frac{v^2}{A}} \right| < \left| \frac{\xi^{-1} \nabla V_{\rm ext}}{v} \right| \tag{43}$$

which is indeed small, thanks to (36).

The two conditions (36) are enough to show the long time dynamics of the SPP to amount to the equilibrium dynamics of a colloid subject to an external potential $V_{\rm ext}$. Physically, they require that the Stokes speed $v_s = -\nabla V$ be much smaller that the self-propulsion speed $v$ of the SPP, but also that its variations over a run-length $\nabla v_s . v/A$ be much smaller than $v$.

## References

1. B. Derrida, *J. Stat. Mech.* P07023 (2007).
2. M. Kac. *Enigmas of Chance: an Autobiography*, Univ of California Press (1985).
3. S. Ramaswamy, *Annu. Rev. Cond. Mat. Phys.* **1**, 323 (2010).
4. Cates M. E., *Rep. Prog. Phys.* **75**,042601 (2012).
5. P. Romanczuk, M. Baer, W. Ebeling, B. Lindner, L. Schimansky-Geier, *Eur. Phys. J. Special-Topics* **202**, 1 (2012).
6. M. C. Marchetti, J.-F. Joanny, S. Ramaswamy, T. B. Liverpool, J. Prost, M. Rao, R. A. Simha, *Rev. Mod. Phys.* **85**, 1143 (2013).
7. W. F. Paxton, S. Sundararajan, T. E. Mallouk, A. Sen, *Ang. Chimie - Int. Ed.* **45**, 5420 (2006).
8. J. R. Howse, R. A. L. Jones, A. J. Ryan, T. Gough, R. Vafabakhsh, R. Golestanian, *Phys. Rev. Lett.* **99**, 048102 (2007).
9. R. Golestanian, T. B. Liverpool, A. Ajdari, *New J. of Phys.* **9**, 126 (2007).
10. J. Palacci, C. Cottin-Bizonne, C. Ybert, L. Bocquet, *Phys. Rev. Lett.* **105**, 088304 (2010).
11. I. Theurkauff, C. Cottin-Bizonne, J. Palacci, C. Ybert, L. Bocquet, *Phys. Rev. Lett.* **108**, 268303 (2012).
12. I. Buttinoni, J. Bialké, F. Kümmel, H. Löwen, C. Bechinger, T. Speck, *Phys. Rev. Lett.* **110**, 238301 (2013)
13. J. Palacci, S. Sacanna, A. P. Stenberg, D. J. Pine, P. M. Chaikin, *Science* **339**, 936 (2013).
14. S. Thutupalli, R. Seeman, S. Herminghaus, *New J. Phys.* **13**, 073021 (2011).
15. Y. Fily, M. C. Marchetti, *Phys. Rev. Lett.* **108**, 235702 (2012).
16. G. S. Redner, M. F. Hagan, A. Baskaran, *Phys. Rev. Lett.* **110**, 055701 (2013).
17. J. Stenhammar, A. Tiribocchi, R. J. Allen, D. Marenduzzo, M. E. Cates, *Phys. Rev. Lett.* **111**, 147502 (2013).
18. A. Wysocki, R. G. Winkler, G. Gompper, *Europhys. Lett.* **105**, 48004 (2014).
19. J. Stenhammar, D. Marenduzzo, R. J. Allen, M. E. Cates, *Soft Matter* **10**, 1489 (2014).
20. T. Speck, J. Bialké, A. M. Menzel, H. Löwen, *Phys. Rev. Lett.* **112**, 218304 (2014).
21. G. S. Redner, A. Baskaran, M. F. Hagan, *Phys. Rev. E* **88**, 012305 (2013).
22. S. A. Mallory, A. Saric, C. Valeriani, A. Cacciuto, *Phys. Rev. E* **89**, 052303 (2014).
23. X. B. Yang, L. M. Manning, M. C. Marchetti, *Soft Matter* **10**, 6477 (2014).
24. S. C. Takatori, W. Yan, J. F. Brady, *Phys. Rev. Lett.* **113**, 028103 (2014).
25. Y. Fily, S. Henkes, M. C. Marchetti, *Soft Matter* **10**, 2132 (2014).
26. P. Galajda, J. Keymer, P. Chaikin, R. Austin, *J. Bacteriol.* **189**, 8704 (2007); P. Galajda *et al.*, *J. Modern Optics* **55**, 3413-3422 (2008).
27. R. Di Leonardo, L. Angelani, D. DellArciprete, G. Ruocco, V. Iebba, S. Schippa, M. P. Conte, F. Mecarini, F. De Angelis, E. Di Fabrizio, *Proc. Natl. Acad. Sci. USA* **107**, 9541 (2010).
28. A. Sokolov, M. M. Apodaca, B. A. Grzybowski, I. S. Aranson, *Proc. Natl. Acad. Sci. USA* **107**, 969 (2010).

29. J. Saragosti, V. Calvez, N. Bournaveas, B. Perthame, A. Buguin, P. Silberzan, *Proc. Natl. Acad. Sci. USA* **108**, 16235 (2011).
30. C. Liu, X. Fu, L. Liu, X. Ren, C. K. L. Chau, S. Li, L. Xiang, H. Zeng, G. Chen, L.-H. Tang, P. Lenz, X. Cui, W. Huang, T. Hwa, J.-D. Huang,*Science* **334**, 238 (2011).
31. I. D. Vladescu, E. J. Marsden, J. Schwarz-Linek, V. A. Martinez, J. Arlt, A. N. Morozov, D. Marenduzzo, M. E. Cates, W. C. K. Poon, *Phys. Rev. Lett.* **113**, 268101 (2014).
32. J. Schwarz-Linek, C. Valeriani, A. Cacciuto, M. E. Cates, D. Marenduzzo, A. N. Morozov, W. C. K. Poon, *Proc. Natl. Acad. Sci. USA* **109**, 4052 (2012).
33. R. W. Nash, R. Adhikari, J. Tailleur, M. E. Cates, *Phys. Rev. Lett.* **104**, 258101 (2010).
34. M. Enculescu, H. Stark, *Phys. Rev. Lett.* **107** 058301 (2011).
35. R. Matas-Navarro, R. Golestanian, T. B. Liverpool, S. M. Fielding, *Phys. Rev. E.* **90**, 032304 (2014).
36. A. Zoettl, H. Stark, *Phys. Rev. Lett.* **112**, 118101 (2014).
37. E. Korobkova, T. Emonet, J. M. G. Vilar, T.S. Shimizu, P. Cluzel, *Nature* **428**, 574 (2004).
38. F. Thiel, L. Schimansky-Geier, I. M. Sokolov, *Phys. Rev. E* **86**, 021117 (2012).
39. A. P. Solon, Y. Fily, A. Baskaran, M. E. Cates, Y. Kafri, M. Kardar, J. Tailleur, arXiv:1412.3952 (2014).
40. A. P. Solon, J. Stenhammar, R. Wittkowski, M. Kardar, Y. Kafri, M. E. Cates, J. Tailleur, *Phys. Rev. Lett.*, In press, arXiv:1412.5475 (2014).
41. J. Tailleur, M.E. Cates, *EPL* **86**, 60002 (2009).
42. G. Szamel, *Phys. Rev. E* **90**, 012111 (2014).
43. F. Ginot, I. Theurkauff, D. Levis, C. Ybert, L. Bocquet, L. Berthier, C. Cotton-Bizonne, *Phys. Rev. X* **5** 011004 (2015).
44. S. C. Takatori, J. F. Brady, *Phys. Rev. E* **91**, 032117 (2015).
45. J. Tailleur, M. E. Cates, *Phys. Rev. Lett.***100**, 218103 (2008).
46. M. E. Cates, J. Tailleur, *EPL* **101**, 20010 (2013).
47. A. G. Thompson, J. Tailleur, M. E. Cates, R. A. Blythe, *J Stat. Mech.* P02029 (2011).
48. R. Wittkowski, A. Tiribocchi, J. Stenhammar, R. J. Allen, D. Marenduzzo, M. E. Cates, *Nature Commun.* **5**, 4351 (2014).
49. Fu X. et al, *Phys. Rev. Lett.* **108**, 198102 (2012).
50. M. B. Miller, B. L. Bassler, *Ann. Rev. Microbiol.* **55**, 165 (2001).
51. H. C. Berg, *E. coli in Motion* Springer, NY (2004).
52. M. J. Schnitzer, *Phys. Rev. E* **48**, 2553 (1993).
53. S. Saha, R. Golestanian, S. Ramaswamy, *Phys. Rev. E* **89**, 062316 (2014)
54. M. Meyer, L. Schimansky-Geier, P. Romanczuk, *Phys. Rev. E* **89**, 022711 (2014).
55. F. D. C. Farrell, J. Tailleur, D. Marenduzzo, M. C. Marchetti, *Phys. Rev. Lett.* **108**, 248101 (2012).
56. M. E. Cates, J. Tailleur, *Ann. Rev. Cond. Matt. Phys.* **6**, 219 (2015).
57. M. E. Cates, D. Marenduzzo, I. Pagonabarraga, J. Tailleur, *Proc. Nat. Acad. Sci. USA* **107**, 11715 (2010).
58. J. Bialké, T. Speck, H. Löwen, *Phys. Rev. Lett.* **108**, 168301 (2012).
59. T. Speck, J. Bialk, A. M. Menzel, H. Löwen, *Phys. Rev. Lett.* **112**, 218304 (2014).
60. M. B. Wan, C. O. Reichhardt, Z. Nussinov, C. Reichhardt, *Phys. Rev. Lett.* **101**, 018102 (2008).
61. J. Elgeti, G. Gompper *EPL (Europhysics Letters)* **85**, 38002 (2009).
62. J. Elgeti, G. Gompper, *EPL (Europhysics Letters)* **101**, 48003 (2013).
63. J. Elgeti, G. Gompper, *EPL (Europhysics Letters)* **109**, 58003 (2015).
64. The Digital Library of Mathematical Functions, http://dlmf.nist.gov/28
65. F. A. Alhargan, *SIAM Review* **38**, 239-255 (1996).
66. L. F. Cugliandolo, *J. Phys. A* **44**, 3001 (2011). D. Loi, S. Mossa, L. F. Cugliandolo, *Physical Review E* **77** 051111 (2008); D. Loi, S. Mossa, L. F. Cugliandolo, *Soft Matter* **7** 3726 (2011).
67. Y. Fily, A. Baskaran, M. F. Hagan, *Soft Matt.* **10**, 5609 (2014).
68. Y. Fily, A. Baskaran, M. F. Hagan, *Phys. Rev. E* **91**, 012125 (2015).
69. J. Tailleur, J. Kurchan, V. Lecomte, *J. Phys. A* **41**, 50500 (2008).

70. P. Romanczuk, L. Schimansky-Geier, *Interface focus* **2**, 746 (2012).
71. J. Barré, R. Chétrite, M. Muratori, F. Peruani, *J. Stat. Phys.* **158** 589 (2015).
72. D. S. Dean, *J. Phys. A. Math. Gen.* **29**, L613 (1996).
73. H. Risken, *The Fokker-Planck Equation: Methods of Solution and Applications*, Springer Verlag, Berlin (1996).
74. B. K. Oksendal, *Stochastic Differential Equations: An Introduction with Applications*, 5th Edn., Springer Verlag, Berlin (2000)
75. E. Bertin et al., *New J. Physics* **15**, 085032 (2013).

### 2.3.1 Sédimentation en deux dimensions avec diffusion translationnelle

On peut étendre les résultats de l'article A sur la sédimentation en 2d pour inclure un mouvement brownien passif de coefficient $D_t$ sur la position des particules. Cela nous permettra ensuite de comparer avec une meilleure précision nos résultats et des données expérimentales sur les colloïdes autopropulsés.

Pour $D_t = 0$, on observe un effondrement gravitationnel lorsque la vitesse de sédimentation tend vers la vitesse d'une particule $v_s \to v$. L'autopropulsion ne peut alors plus contrebalancer la gravité et la longueur de sédimentation tombe à 0. Si l'on ajoute un mouvement brownien passif, on s'attend à retrouver une longueur de sédimentation finie pour $v_s \geq v$, contrôlée par la diffusion brownienne.

La démonstration suit exactement le même chemin que pour $D_t = 0$. Pour les RTP, la distribution stationnaire satisfait maintenant l'équation

$$0 = -\partial_z \left[(v\cos\theta - v_s)P(z,\theta)\right] + D_t\partial_z^2 P(z,\theta) - \alpha P(z,\theta) + \frac{\alpha}{2\pi}\rho(z) \tag{2.15}$$

On peut toujours supposer que l'état stationnaire est factorisé $P(z,\theta) = \rho(z)f(\theta)$. L'équation (2.15) nous donne alors

$$\rho(z) = \rho_0 e^{-\lambda z}, \qquad f(\theta) = \frac{\alpha}{2\pi(a - v\lambda\cos\theta)} \tag{2.16}$$

avec $a = \alpha + v_s\lambda - D_t\lambda^2$. La constante $\lambda$ est fixée par la condition de normalisation $\int_0^{2\pi} f(\theta)d\theta = 1$. Cette équation se réduit à un polynôme du $4^{\text{ème}}$ ordre en $\lambda$ qui admet une seule solution réelle telle que $\lambda \to 0$ quand $v_s \to 0$. Cette solution a une expression compliquée qu'il est inutile de reproduire ici. Elle est tracée à la figure 2.1, où elle est comparée avec des simulations.

Dans la limite $v_s \ll v$, l'expression de $\lambda$ se simplifie :

$$\lambda = \frac{2\alpha v_s}{v^2 + 2D_t\alpha} + \frac{2\alpha v^4 v_s^3}{(v^2 + 2D_t\alpha)^4} + \mathcal{O}\left[\left(\frac{v_s}{v}\right)^5\right] \tag{2.17}$$

Le premier ordre correspond au régime de température effective $\lambda = mg/k_BT_{\text{eff}}$ avec $k_BT_{\text{eff}} = \mu^{-1}\left(\frac{v^2}{2\alpha} + D_t\right)$, où $\mu$ est la mobilité.

Dans la limite $v_s \to \infty$, on trouve $\lambda = (v_s - v)/D_t + O(1/v_s)$, ce qui correspond à une particule brownienne à la température du fluide $k_BT = \mu^{-1}D_t$ dans un champ de gravité effectif $g' = g - v/(\mu m)$. Comme on peut le voir sur la figure 2.1, on interpole donc entre un régime d'équilibre effectif dominé par l'activité à petit $v_s$ et un régime d'équilibre passif à grand $v_s$.

Les ABP montrent la même phénoménologie. Par le même calcul que dans l'article A, $\lambda$ est donné par la solution de

$$a_0(-2\lambda/D_r) = -\frac{4\lambda}{D_r}(v_s - D_t\lambda) \tag{2.18}$$

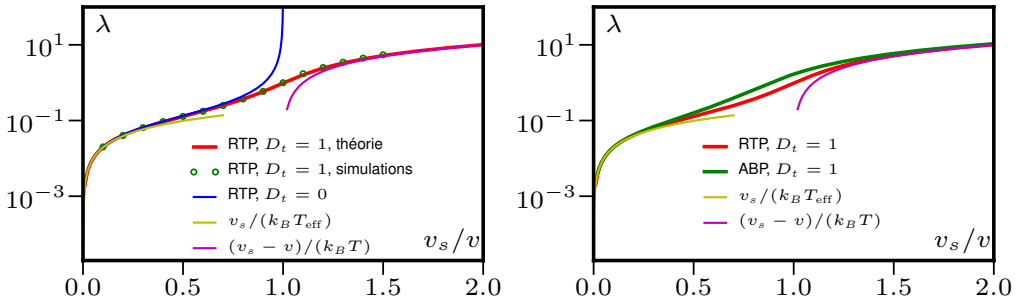


**Figure 2.1** – Longueur inverse de sédimentation $\lambda$ pour des ABP et RTP en 2d. **Gauche** : Simulations avec $D_t = 1$ montrant un accord parfait avec la prédiction théorique. On voit que $D_t \neq 0$ permet d'éviter l'effondrement gravitationnel à $v_s = v$ que l'on observe quand $D_t = 0$. **Droite** : Comparaison entre ABP et RTP. Les limites d'équilibre effectif à petit et grand $v_s/v$ sont identiques entre les deux types de particules. $v_s/v$ est varié en changeant $v_s$ à $v$ constant. Paramètres : $v = 10$, $\alpha = D_r = 1$.

où $a_0$ est la première valeur caractéristique de l'équation de Mathieu. La distribution angulaire est donnée par la fonction de Mathieu paire

$$f(\theta) = c_1 C\left[-\frac{4\lambda}{D_r}(v_s - D_t\lambda), -2\lambda/D_r, 2\theta\right] \tag{2.19}$$

où $c_1$ est fixé par la normalisation de $f$. On peut utiliser les développements connus de la fonction $a_0$ pour obtenir $\lambda$ dans les limites de petit et grand $v_s$. Pour $v_s \ll v$ on trouve

$$\lambda = \frac{2D_r v_s}{v^2 + 2D_t D_r} + \frac{7D_r v^4 v_s^3}{2(v^2 + 2D_t D_r)^4} + \mathcal{O}\left[\left(\frac{v_s}{v}\right)^5\right] \tag{2.20}$$

En comparant avec l'équation (2.17), on voit qu'à l'ordre $v_s/v$ (dans le régime de température effective) les ABP et RTP ont la même longueur de sédimentation, la première différence apparaissant à l'ordre suivant. À grand $v_s$ on trouve, comme pour les RTP, $\lambda = (v_s - v)/D_t$. Les deux limites (petit et grand $v_s$) sont donc identiques pour les deux types de particules qui ne diffèrent que dans le régime intermédiaire comme on peut le voir à la figure 2.1 (droite).

Intéressons-nous également à la distribution angulaire, $f(\theta)$, dans la limite de petit $v_s$, qui sera ensuite comparée à l'expérience. À l'ordre $(v_s/v)^2$, on obtient

$$2\pi f_{\text{RTP}}(\theta) = 1 + \frac{2vv_s}{v^2 + 2D_t\alpha}\cos\theta + \frac{2v^2v_s^2}{(v^2 + 2D_t\alpha)^2}\cos 2\theta + \mathcal{O}\left[\left(\frac{v_s}{v}\right)^3\right] \tag{2.21}$$

$$2\pi f_{\text{ABP}}(\theta) = 1 + \frac{2vv_s}{v^2 + 2D_t D_r}\cos\theta + \frac{v^2v_s^2}{2(v^2 + 2D_t D_r)^2}\cos 2\theta + \mathcal{O}\left[\left(\frac{v_s}{v}\right)^3\right] \tag{2.22}$$

Comme pour la longueur de sédimentation, au premier ordre en $v_s/v$ (*i.e.* en tronquant les expressions après le terme en $\cos\theta$), les ABP et les RTP ont la même distribution angulaire lorsque $\alpha = D_r$. La différence entre les deux types de particules n'apparaît qu'à l'ordre $(v_s/v)^2$.

### 2.3.2 Sédimentation de colloïdes Janus

Nous voulons maintenant comparer les distributions angulaires obtenues analytiquement pour la sédimentation d'ABP en 2d, équation (2.22), à l'expérience de Ginot et collaborateurs sur des colloïdes autopropulsés [39].

Les colloïdes étudiés dans [39] sont recouverts de platine sur la moitié de leur surface et propulsés par la réaction du platine avec le peroxyde d'hydrogène présent en solution, qui crée un gradient de concentration de $O_2$ et $H_2O_2$ entre les deux faces de la particules (voir figure 1.3). Les colloïdes sont alors mis en mouvement par diffusiophorèse. L'autre face des colloïdes étant en or, des effets d'électrophorèse s'ajoutent probablement à la diffusiophorèse, ce qui expliquerait leur vitesse plus élevée que les colloïdes platine-latex considérés dans [36]. La vitesse d'autopropulsion peut être ajustée en changeant la concentration en peroxyde d'hydrogène de la solution dans laquelle les particules sont immergées. Le système expérimental, schématisé à la figure 2.2, est incliné légèrement par rapport à l'horizontale (d'un angle de l'ordre de $10^{-3}$ radians) de telle sorte que les colloïdes forment une monocouche sur la surface inférieure de la chambre d'observation. Ce dispositif permet d'observer le comportement des colloïdes sur toute une gamme de densité, de l'empilement compact jusqu'à un gaz très dilué (voir figure 2.2).

Nous nous intéresserons ici aux profils d'orientation dans la phase diluée, où l'on peut négliger les interactions. Toutes les quantités présentes dans l'équation (2.22) peuvent être mesurées indépendamment. La vitesse de sédimentation $v_s$ est mesurée sur des particules passives en cours de sédimentation. $D_r$ et $v$ sont mesurés sur des particules libres à plat. Pour le coefficient de diffusion passive $D_t$ nous utiliserons la valeur donnée par la relation de Stokes-Einstein pour une sphère dans l'eau $D_t = k_B T/(6\pi\eta R)$, le rayon d'une particule étant mesuré par microscopie électronique. Notons qu'une mesure (peu précise) de $D_t$ utilisant le déplacement quadratique moyen des particules donne une valeur compatible avec la prédiction théorique, bien que les particules soient proches d'une surface.

On peux donc comparer les prédictions de l'équation (2.22) avec les données expérimentales sans aucun paramètre ajustable. Cette comparaison est montrée à la figure 2.3 pour deux valeurs de $v_s/v$, obtenues en variant $v$ à $v_s$ constant. À $v_s/v = 0.08$, dans le régime d'équilibre effectif, les distributions angulaires données par l'équation (2.22), tronquées au premier ou au deuxième ordre, avec $D_t = 0$ ou $D_t \neq 0$, sont toutes indistinguables à l'échelle de la figure et donnent un bon accord avec l'expérience. À $v_s/v = 0.28$, les prédictions à l'ordre 1 et 2 sont toujours très

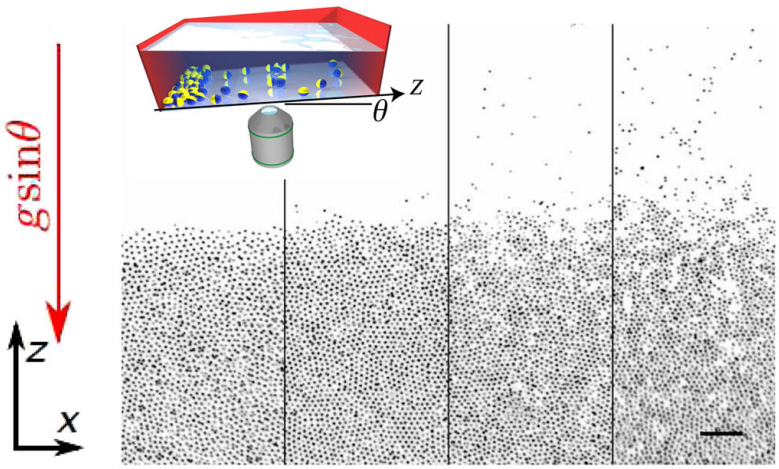


**Figure 2.2** – Le système expérimental est incliné d'un petit angle $\theta$, induisant un champ de gravité $g \sin\theta$. De gauche à droite : profils de sédimentation pour une activité de plus en plus grande, l'image de gauche correspondant au cas passif. La barre d'échelle est de 20$\mu$m. Figure reproduite de [39].

proches. L'effet de la diffusion brownienne n'est cependant pas du tout négligeable et prendre en compte $D_t \neq 0$ permet d'avoir un meilleur accord avec les données. On peut quantifier la qualité de l'accord entre les données expérimentales et les prédictions théoriques en calculant la quantité

$$R^2 = \frac{2\pi}{N_p} \sum_i \left[ f_{\text{exp}}(\theta_i) - f_{\text{th}}(\theta_i) \right]^2 \tag{2.23}$$

où $N_p$ est le nombre de points expérimentaux $\theta_i$. La normalisation est telle que $R^2$ soit l'analogue discret de la norme $||f_{\text{exp}} - f_{\text{th}}||_2 = \int_{-\pi}^{\pi} \left[ f_{\text{exp}}(\theta) - f_{\text{th}}(\theta) \right]^2 d\theta$. Les valeurs de $R^2$ pour les différentes prédictions théoriques sont reportées sur la figure 2.3.

Notons qu'il est expérimentalement difficile de se placer à des ratios $v_s/v$ plus grands, qui permettraient de montrer la différence entre l'équation (2.22) développée à l'ordre 2 en $v_s/v$ et la distribution angulaire complète donnée par l'équation (2.19). En effet, à grand $v_s/v$, la longueur de sédimentation est trop petite pour permettre d'obtenir assez de statistiques sur la durée de vie de l'expérience.

Notons finalement que ceci est un travail en cours, la prochaine étape étant de comparer les longueurs de sédimentation mesurées expérimentalement avec les prédictions pour $\lambda^{-1}$ données dans ce chapitre.

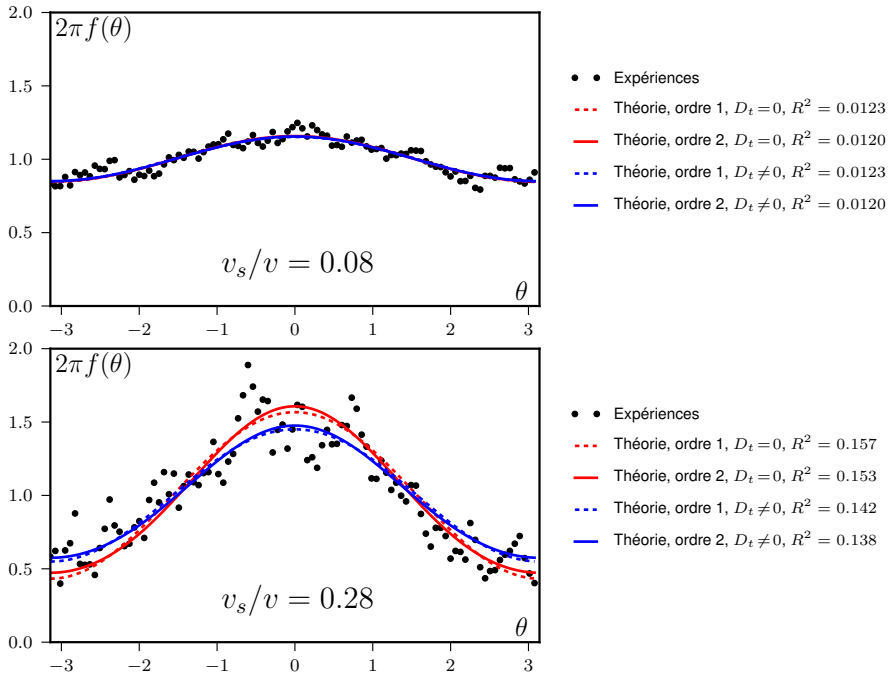


**Figure 2.3** – Comparaison entre les distributions angulaires expérimentales et théoriques, sans paramètre d'ajustement, pour deux valeurs de $v_s/v$. $R^2$, donné par l'équation (2.23), quantifie la qualité de l'accord entre expérience et théorie. $D_r = 0.64\,\mathrm{s}^{-1}$, $D_t = 0.274\,\mu\mathrm{m}^2.\mathrm{s}^{-1}$, $v_s = 0.33\,\mu\mathrm{m}.\mathrm{s}^{-1}$.

## 2.4 Sédimentation en trois dimensions

Attaquons-nous pour terminer au cas $d = 3$. Pour la sédimentation, tout se passe dans une direction de l'espace, celle du champ de gravité. On peut donc espérer résoudre le problème en 3d comme en deux dimensions. C'est le cas pour les RTP mais pas pour les ABP, pour lesquelles la solution en 2d repose sur notre connaissance des fonctions de Mathieu.

En 3d, la direction $\mathbf{u}$ d'une particule est paramétrée en coordonnées sphériques par deux angles $\theta$ et $\phi$ tels que $\mathbf{u} = (\sin\theta\cos\phi, \sin\theta\sin\phi, \cos\theta)$. Le champ de gravité sera toujours pris suivant $\hat{z}$. Par symétrie, la distribution stationnaire ne dépend que de $z$ et $\theta$ et l'équation maîtresse se réduit alors pour des RTP à

$$0 = -\partial_z\left[(v\cos\theta - v_s)P\right] - \alpha P + \frac{\alpha}{4\pi}\int_0^\pi d\theta' \int_0^{2\pi} d\phi' \sin\theta' P(z,\theta',\phi') \tag{2.24}$$

En utilisant $P(z,\theta,\phi) = P(z,\theta)/(2\pi)$, on peut intégrer sur $\phi$ et réécrire l'équation précédente

$$0 = -\partial_z\left[(v\cos\theta - v_s)P(z,\theta)\right] - \alpha P(z,\theta) + \frac{\alpha}{2}\int_0^\pi d\theta' \sin\theta' P(z,\theta') \tag{2.25}$$

Le calcul se poursuit comme en 2d, en séparant les variables $P(z,\theta) = \rho(z)f(\theta)$, avec la condition de normalisation $\int_0^\pi f(\theta)\sin\theta d\theta = 1$. L'équation (2.25) donne alors

$$\rho(z) = C\exp(-\lambda z) \tag{2.26}$$

$$f(\theta) = \frac{1}{2\left[1 - \frac{\lambda}{\alpha}(v\cos\theta - v_s)\right]} \tag{2.27}$$

et la condition sur la normalisation de $f$ donne l'équation

$$\operatorname{arctanh}\left(\frac{\lambda v}{\lambda v_s + \alpha}\right) = \frac{\lambda v}{\alpha} \tag{2.28}$$

qui peut être résolue numériquement pour fixer la longueur de sédimentation. En développant l'équation (2.28) à petit $\lambda$, on retrouve le régime d'équilibre effectif

$$\lambda = \frac{mg}{k_B T_{\text{eff}}} + \mathcal{O}\left[\left(\frac{v_s}{v}\right)^2\right], \qquad k_B T_{\text{eff}} = \mu^{-1}\left(\frac{v^2}{3\alpha}\right) \tag{2.29}$$

Pour des ABP en 3d, après les simplifications liées à la symétrie du problème, l'équation maîtresse donne pour l'état stationnaire

$$0 = -\partial_z\left[(v\cos\theta - v_s)P(z,\theta)\right] + \frac{D_r}{\sin\theta}\partial_\theta(\sin\theta\partial_\theta P(z,\theta)) \tag{2.30}$$

et après séparation des variables

$$\rho'(z) = -\lambda\rho(z) \tag{2.31}$$

$$f''(\theta) + D_r \tan\theta f'(\theta) + \frac{\lambda}{D_r}(v\cos\theta - v_s)f(\theta) = 0 \tag{2.32}$$

Le profile de densité reste bien exponentiel mais l'équation sur $f$ n'est plus une équation de Mathieu comme en 2d, à cause du terme en $f'(\theta)$. Pour obtenir une équation fixant $\lambda$, il faudrait donc construire une théorie analogue à celle des valeurs caractéristiques de l'équation de Mathieu pour ce nouveau type d'équation, ce que nous réservons pour un travail futur.

On peut aussi comparer les RTP et ABP en 3d en utilisant des simulations numériques. Pour les RTP il n'y a pas de problème particulier, les culbutes sont toujours distribuées exponentiellement avec un taux $\alpha$. À chaque culbute, une nouvelle direction est tirée sur la sphère unité. Pour simuler des ABP, il nous faut obtenir l'équation de Langevin pour la diffusion rotationnelle. Celle-ci doit être équivalente au Laplacien rotationnel

$$\dot{P}(\theta,\varphi) = \Delta_{\mathbf{u}} D_r P(\theta,\varphi) = D_r \left[\frac{1}{\sin\theta}\frac{\partial}{\partial\theta}\left(\sin\theta\frac{\partial}{\partial\theta}\right) + \frac{1}{\sin\theta^2}\frac{\partial^2}{\partial\varphi^2}\right] P \tag{2.33}$$

Dans la littérature sur les ABP [62, 64, 66], on lit généralement que l'équation de Langevin en 3d est donnée par

$$\frac{d\mathbf{u}}{dt} = \sqrt{2D_r}\,(\mathbf{u}\times\mathbf{\Lambda}) \tag{2.34}$$

où $\mathbf{\Lambda}$ est un bruit blanc gaussien dont les composantes vérifient, en coordonnées cartésiennes, $\langle\Lambda_i(\mathbf{r},t)\Lambda_j(\mathbf{r}',t')\rangle = \delta_{ij}\delta(\mathbf{r}-\mathbf{r}')\delta(t-t')$. Le bruit dans l'équation (2.34) est multiplicatif et il est donc important de spécifier la discrétisation que l'on choisit, ce qui est rarement discuté [62, 64, 66].

En pratique, c'est la discrétisation d'Itō qui est utilisée en simulation numérique car le terme de bruit ne dépend alors pas des coordonnées futures ; elle permet donc d'utiliser une intégration temporelle explicite, comme la méthode d'Euler. Or, il est facile de voir que l'équation (2.34) ne décrit pas la diffusion rotationnelle dans l'interprétation d'Itō. En particulier, elle ne conserve pas la norme du vecteur $\mathbf{u}$ :

$$\left\langle\frac{d|\mathbf{u}|^2}{dt}\right\rangle = \langle 2\mathbf{u}\cdot\dot{\mathbf{u}}\rangle + 2D_r\sum_i\sigma_{ii} \tag{2.35}$$

où la matrice $\boldsymbol{\sigma}$ contient les corrélations du bruit $\mathbf{u}\times\mathbf{\Lambda}$ :

$$\sigma_{xx} = \langle(u_y\Lambda_z - u_z\Lambda_y)^2\rangle = u_z^2 + u_y^2, \quad \sigma_{xy} = \langle(u_y\Lambda_z - u_z\Lambda_y)(u_z\Lambda_x - u_x\Lambda_z)\rangle = -u_x u_y \tag{2.36}$$

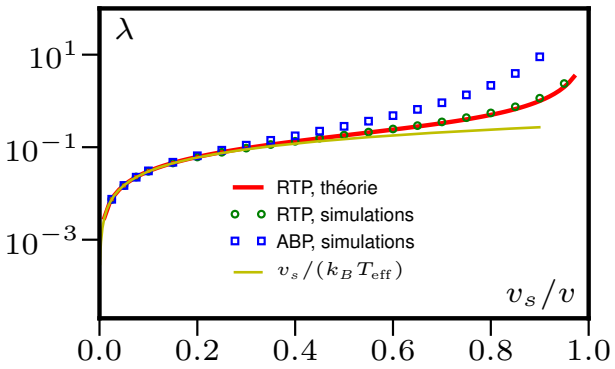


**Figure 2.4** – Longueur inverse de sédimentation $\lambda$ pour les ABP et RTP en 3d. Paramètres des simulations : $v = 10$, $\alpha = 1$ $D_r = 0.5$.

et des expressions analogues pour les autres composantes. Le premier terme du membre de droite de l'équation (2.35) s'annule en interprétation d'Itō et on trouve alors

$$\left\langle \frac{d|\mathbf{u}|^2}{dt} \right\rangle = 2D_r \sum_i \sigma_{ii} = 4D_r|\mathbf{u}|^2 \tag{2.37}$$

Nous montrons à l'annexe A que l'équation (2.34) correspond en fait à une diffusion rotationnelle dans l'interprétation de Stratonovich. L'équation correcte dans l'interprétation d'Itō s'écrit

$$\frac{d\mathbf{u}}{dt} = \sqrt{2D_r}\,(\mathbf{u} \times \mathbf{\Lambda}) - 2D_r\mathbf{u} \tag{2.38}$$

et conserve la norme du vecteur $\mathbf{u}$ :

$$\left\langle \frac{d|\mathbf{u}|^2}{dt} \right\rangle = \langle 2\mathbf{u} \cdot \dot{\mathbf{u}} \rangle + 4D_r|\mathbf{u}|^2 = 0 \tag{2.39}$$

Nous avons donc utilisé cette équation de Langevin pour simuler des ABP en 3d et ainsi comparer les longueurs de sédimentation des ABP et RTP. Les résultats sont montrés à la figure 2.4. Comme en 2d, les deux types de particules sont équivalents dans la limite d'équilibre effectif, à la substitution $\alpha = (d-1)D_r$ près.

# Chapitre 3

# Pression d'un fluide actif

Les forces actives qui s'exercent dans les tissus biologiques, que ce soit à l'échelle intracellulaire ou au niveau du groupe de cellules, sont l'objet d'une intense recherche. Elles sont essentielles pour comprendre la motilité cellulaire qui trouve son origine dans les forces exercées par les moteurs moléculaires sur le cytosquelette et qui joue un rôle clé dans l'apparition de métastases cancéreuses, la morphogenèse ou la cicatrisation de blessures [25, 106, 107]. Ces systèmes sont toutefois très complexes et beaucoup moins d'attention a été portée à des questions beaucoup plus simples, telles que la pression exercée par un fluide de particules actives sur les parois de son contenant. Comme nous allons le voir dans ce chapitre, cette question est néanmoins subtile et réserve de nombreuses surprises.

Différentes définitions de la pression d'un fluide coexistent. La pression « mécanique » est définie comme la force par unité de surface qu'un fluide exerce sur son contenant. Une définition alternative, fréquemment rencontrée en mécanique des fluides, est reliée au tenseur des contraintes $\boldsymbol{\sigma}$ qui apparaît par exemple dans les équations de Navier-Stokes. Cette pression « hydrodynamique » est définie par $P = -\operatorname{Tr}\boldsymbol{\sigma}/d$, où $d$ est la dimension de l'espace. Enfin, pour un système à l'équilibre thermique, on peut définir une pression « thermodynamique » par $P = -\partial F/\partial V$, où $F$ est l'énergie libre et $V$ le volume du système.

Pour un système passif, l'équivalence des pressions mécanique et hydrodynamique découle de la conservation de la quantité de mouvement. Cette équivalence traduit le fait qu'on peut mentalement diviser un fluide en petites boîtes en équilibre mécanique les unes avec les autres et avec les parois. De plus, pour un système décrit par la distribution de Boltzmann, on peut montrer que les deux définitions

mécanique et hydrodynamique de la pression sont équivalentes à la définition thermodynamique (voir les suppléments de l'article B pour une démonstration). L'énergie libre étant extensive, et donc proportionnelle au volume, la contribution des interactions particules-parois, proportionelle à la surface, est sous-dominante dans la limite thermodynamique. La pression est alors donnée par une équation d'état : elle ne dépend que de quantités physiques mesurées dans le coeur du système et non pas du détail des interactions entre les particules et les parois.

Dans les systèmes actifs, aucune des équivalences entre les trois définitions de la pression données plus haut n'est vraie *a priori*. En effet, la quantité de mouvement n'est pas conservée du fait de l'autopropulsion et, à part dans le régime d'équilibre effectif étudié au chapitre précédent (pour des particules sans interaction dans un potentiel peu confinant), les systèmes actifs ne sont pas décrits par une distribution de Boltzmann. Il n'y a donc pas de raison non plus de supposer l'existence d'une équation d'état.

Des études théoriques récentes sur la pression de systèmes de sphères dures autopropulsées [65–67, 108–110] semblent toutefois indiquer, sans le démontrer, que la pression peut être définie de façon équivalente comme la trace du tenseur des contraintes ou comme la force exercée par unité de surface sur le contenant. Elle est alors donnée par une équation d'état. En outre, une équation d'état a été mesurée expérimentalement, de façon indirecte, en reliant la pression à des profils de sédimentation [39].

Nous montrerons dans l'article B qu'une équation d'état existe dans des cas exceptionnels mais qu'en général, la pression mécanique exercée par un fluide actif sur son contenant dépend des interactions microscopiques avec les parois. Le même fluide dans deux récipients différents exercera alors des pressions différentes. C'est le cas dès que des couples s'exercent entre particules ou entre les particules et les murs. La majorité des systèmes expérimentaux sont concernés. En effet, des interactions d'alignement sont induites par la répulsion stérique pour toutes les particules asymétriques. De plus, des particules actives en solution (mêmes sphériques), s'autopropulsent en appliquant un dipôle de force, qui a une symétrie axiale, au fluide environnant. Les interactions hydrodynamiques vont donc générer des couples à longue distance entre particules et avec les parois (voir par exemple [111]). D'autres interactions, comme des particules se déplaçant à une vitesse $v(\rho)$, conduisent aussi à une absence d'équation d'état.

Une équation d'état existe néanmoins dans deux cas particuliers notables : le gaz parfait et les sphères dures autopropulsées. Pour un gaz parfait de particules sphériques (ne s'alignant pas avec les murs), la pression est donnée par la loi du gaz parfait à la température effective calculée au chapitre 2. Nous montrerons à la section 3.2 que ce résultat est valide pour plusieurs types de dynamiques. Le cas des sphères dures sera, quant à lui, traité en détail dans l'article D, au chapitre

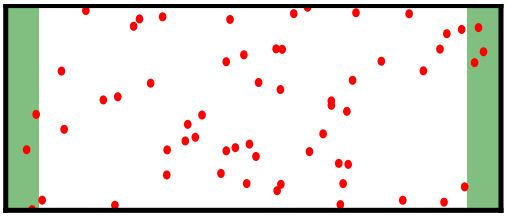

**Figure 3.1** – Géométrie utilisée pour calculer la pression d'un fluide actif. Les particules sont confinées, suivant l'axe $\hat{x}$, par un potentiel répulsif (schématisé par les régions vertes). Le système est considéré comme infini dans la direction $\hat{y}$.

sur la séparation de phase induite par la motilité, l'équation d'état donnant alors une relation entre les densités des deux phases en coexistence. Nous montrons également dans l'article B que, même dans les cas où une équation d'état existe, la pression peut avoir des propriétés inhabituelles. Elle peut par exemple être anisotrope ou inhomogène sans que cela ne génère d'écoulement dans le système.

À la section 3.3, nous calculerons la pression pour un système satisfaisant le bilan détaillé, mais dont la distribution stationnaire n'est pas une distribution de Boltzmann. Dans ce cas, la pression mécanique n'est pas donnée par une équation d'état, ce qui montre la nécessité de bien faire la différence entre les deux définitions d'un système d'équilibre discutées en introduction de cette thèse.

Notons que plusieurs études s'intéressent à la pression dans des systèmes très confinants pour lesquels la taille du récipient est comparable à la longueur de persistance des particules [66, 67, 109, 110]. Pour des parois mobiles, cela conduit à des interactions à courte portée, décroissant exponentiellement sur une longueur de l'ordre de la longueur de persistance des particules [112]. Au contraire, nous ne considérerons ici que des systèmes grands devant la longueur de persistance.

Le dispositif que nous utiliserons dans tout ce chapitre est schématisé à la figure 3.1. Par soucis de simplicité, on considérera des particules en 2d confinées suivant l'axe $\hat{x}$ par un potentiel et un système infini (ou des conditions aux bords périodiques en simulation) suivant l'axe $\hat{y}$. Tous les résultats présentés ici s'étendent trivialement si l'on rajoute une troisième direction $\hat{z}$ infinie (ou avec des conditions aux bords périodiques). Il serait néanmoins intéressant, pour aller plus loin, d'étudier d'autres géométries comme une cavité sphérique ou, plus généralement, des murs non plans.

On peut tester le dispositif de la figure 3.1 en calculant la pression mécanique exercée par un gaz parfait passif. La densité de particules à une abscisse $x$ est alors donnée par la distribution de Boltzmann $\rho(x) = e^{-V(x)/(k_B T)}/Z$ où $V$ est le potentiel répulsif modélisant les bords de la boîte. La pression mécanique s'exprime simplement comme la force par unité de longueur exercée par les particules sur ce

potentiel

$$P = \int_0^{+\infty} \rho(x)(\partial_x V)dx, \tag{3.1}$$

le point $x = 0$ étant choisi dans le coeur du système, loin des parois. En remplaçant $\rho(x)$ par son expression, on peut calculer l'intégrale de l'équation (3.1)

$$P = \int_0^{+\infty} \frac{e^{-V(x)/(k_B T)}}{Z}(\partial_x V)dx = k_B T \frac{e^{-V(0)/(k_B T)}}{Z} = k_B T \rho_0 \tag{3.2}$$

où $\rho_0$ est la densité au coeur du système. On retrouve donc, sans surprise, la loi du gaz parfait. On voit que le potentiel $V$ est présent dans la définition de la pression mais disparaît du résultat final, traduisant le fait que la pression est donnée par une équation d'état.

## 3.1 La pression d'un fluide actif n'est en général pas une fonction d'état

# Pressure is not a state function for generic active fluids

Alexandre P. Solon,[1] Y. Fily,[2] A. Baskaran,[2] M. E. Cates,[3] Y. Kafri,[4] M. Kardar,[5] and J. Tailleur[1]

[1]*Université Paris Diderot, Sorbonne Paris Cité, MSC, UMR 7057 CNRS, 75205 Paris, France*
[2]*Martin Fisher School of Physics, Brandeis University, Waltham, MA 02453, USA*
[3]*SUPA, School of Physics and Astronomy, University of Edinburgh, JCMB, Peter Guthrie Tait Road, Edinburgh EH9 3FD, UK*
[4]*Department of Physics, Technion, Haifa 32000, Israel*
[5]*Department of Physics, Massachusetts Institute of Technology, Cambridge, Massachusetts 02139, USA*

(Dated: June 6, 2015)

Pressure is the mechanical force per unit area that a confined system exerts on its container. In thermal equilibrium, it depends only on bulk properties (density, temperature, etc.) through an equation of state. Here we show that in a wide class of active systems the pressure depends on the precise interactions between the active particles and the confining walls. In general, therefore, active fluids have no equation of state; their mechanical pressures exhibit anomalous properties that defy the familiar thermodynamic reasoning that holds in equilibrium. The pressure remains a function of state, however, in some specific and well-studied active models that tacitly restrict the character of the particle-wall and/or particle-particle interactions.

For fluids in thermal equilibrium, the concept of pressure, $P$, is familiar as the force per unit area exerted by the fluid on its containing vessel. This primary, mechanical definition of pressure *seems* to require knowledge of the interactions between the fluid's constituent particles and its confining walls. But we learn from statistical mechanics that $P$ can also be expressed thermodynamically, as the derivative of a free energy with respect to volume. The pressure therefore obeys an equation of state, which only involves bulk properties of the fluid (temperature $T$, number density $\rho$, etc.). Hydrodynamics provides a third definition of $P$, as the trace of the bulk thermodynamic stress tensor, whose microscopic definition in terms of momentum fluxes is again well known [1]. In thermal equilibrium, all these definitions of pressure coincide. The corresponding physical insight is that the fluid may be divided into blocks that are in mechanical equilibrium with each other and with any confining walls, so bulk and wall-based pressure definitions must agree.

Purely thermodynamic concepts, like temperature, are well known to be ill-defined in systems far from equilibrium [2]. However, one could hope that mechanical properties, like pressure, are less problematic. Here we investigate this question for active fluids, in which energy dissipation at the microscopic level drives the motion of each particle to give strong non–equilibrium effects [3]. Assemblies of self-propelled particles (SPPs) have been proposed as simplified models for systems ranging from bacteria [4, 5] and active colloidal 'surfers' [6–8], to shaken grains [9–11] and bird flocks [12]. We define the mechanical pressure $P$ of an active fluid as the mean force per area exerted by its constituent particles on a confining wall. This was studied numerically for a number of active systems, showing some surprising effects for finite-size, strongly confined fluids [13–19]. Alternatively, when describing the dynamics of such active fluids at larger scales, some authors have introduced a bulk stress tensor and defined pressure as its trace [3, 17–19], leading to recent experimental measurements [20]. Since we are far from equilibrium, an equivalence between these different definitions, as seen numerically in [13, 17, 18], requires explanation.

In this article, we show analytically and numerically that the pressure $P$ exerted on a wall by generic active fluids *directly depends* on the microscopic interactions between the fluid and the wall. Unless these interactions, as well as the interactions between the fluid particles, obey strict and exceptional criteria, there is no equation of state relating the mechanical pressure to bulk properties of the fluid. Therefore, all connections to thermodynamics and to the bulk stress tensor are lost. Nevertheless, we provide analytical formulas to compute the wall-dependent pressure for some of the most studied classes of active systems. Exceptional models for which an equation of state is recovered include the strictly spherical SPPs considered in [13, 17, 18]. Below we find that such simplified models are structurally unstable: small orientation-dependent interactions (whether wall-particle or particle-particle) immediately destroy the equation of state. Such interactions are present in every experimental system we know of.

A clear distinction exists between the present work and that of Ref [21]. The latter includes an explicit proof that pressure is, after all, well defined within a narrow class of models: spherical SPPs with torque-free wall interactions and torque-free pairwise interparticle forces. Because this class has been a major focus of theory and simulation studies, that finding is important, creating in those cases a direct link between pressure and correlation functions that can be exploited in future theoretical advances. However, in general terms it is even more important to know that an equation of state for the pressure is the exception, rather than the rule, in active matter systems. This we establish here.

To appreciate the remarkable consequences of the generic absence of an equation of state, consider the quasi-static compression of an active fluid by a piston. Since the mechanical pressure depends on the piston, compressing with a very soft wall—into which particles bump gently—or with a very hard one requires different forces and hence different amounts of work to reach the same final density. This is not the only way our thermodynamic intuition can fail for active systems. We will show both that pressure can be anisotropic, and that active particles admit flux-free steady-states in which the pressure is inhomogeneous. Finally, in the models we consider (which best describe, e.g., crawling bacteria [4] or colloidal surfers or rollers near a supporting

surface [22, 23]) there are situations in which the confinement forces at the edges of a sample do not sum to zero. We show how this unbalanced force is compensated by momentum transfer to the support. The issue of whether an equation of state exists in so-called "wet" active matter [3]—in which full momentum conservation applies throughout the interior of the system—remains open.

## NON–INTERACTING PARTICLES

We consider a standard class of models for SPPs in which the independent Brownian motion of each particle (diffusivity $D_t$) is supplemented by self-propulsion at speed $v$ in direction $\mathbf{u}$,

$$\frac{d\mathbf{r}}{dt} = v\mathbf{u} + \sqrt{2D_t}\,\boldsymbol{\eta}(t)\ , \tag{1}$$

with $\boldsymbol{\eta}(t)$ a Gaussian white noise of unit variance. The reorientation of the direction of motion $\mathbf{u}$ then occurs with a system-specific mechanism: active Brownian particles (ABPs) undergo rotational diffusion, while run-and-tumble particles (RTPs) randomly undergo complete reorientations ('tumbles') at a certain rate. These well-established models have been used [5, 7, 24–28] to describe respectively active colloids [6, 8, 22, 23], or bacterial motion [4, 28] and cell migration [29]. Such models neglect any coupling to a momentum conserving solvent, and are thus best suited to describe particles whose locomotion exploits the presence of a gel matrix or supporting surface as a momentum sink. This is true of many active systems, such as crawling cells [30], vibrated disks or grains [9, 10, 31], and colloidal rollers [23] or sliders [22].

We address a system of SPPs with spatial coordinates $\mathbf{r} = (x, y)$ in 2D; we assume periodic boundary conditions, and hence translational invariance, in the $\hat{y}$ direction. The system is confined along $\hat{x}$ by two walls at specified positions, which exert forces $-\nabla V(x)$ on particles at $x$; these forces have finite range and thus vanish in the bulk of the system. The propulsion direction of a particle is $\mathbf{u} = (\cos\theta, \sin\theta)$ with $\theta = 0$ along the $\hat{x}$ direction. In the absence of interactions between the particles, the master equation for the probability $\mathcal{P}(\mathbf{r}, \theta, t)$ of finding a particle at position $\mathbf{r}$ at time $t$ pointing along the $\theta$ direction reads

$$\partial_t \mathcal{P} = -\nabla \cdot [(\mathbf{v} - \mu_t \nabla V(x))\mathcal{P} - D_t \nabla \mathcal{P}] - \partial_\theta [\mu_r \Gamma(x, \theta)\mathcal{P} - D_r \partial_\theta \mathcal{P}] - \alpha \mathcal{P} + \frac{\alpha}{2\pi} \int \mathcal{P}\, d\theta' \ . \tag{2}$$

Here $\mu_t$ and $D_t$ are the translational mobility and diffusivity; likewise $\mu_r$ and $D_r$ for rotations. The propulsive velocity is $\mathbf{v} = v\mathbf{u}(\theta)$, and $\alpha$ is the tumble rate. ABPs correspond to $\alpha = 0$ and RTPs to $D_r = 0$. Here we allow all intermediate combinations, to test the generality of our results. In addition to the external force $-\nabla V(x)$, we include an external torque $\Gamma(x, \theta)$, which may, for example, describe the well–documented alignment of bacteria along walls [32]. Generically, just as in passive fluids, a wall–torque will arise whenever the particles are not spherical and its absence is thus strictly exceptional. Obviously, the asphericity of (say) water molecules does not violate the thermodynamical precepts of pressure; remarkably, we show below that, for active particles, it does so.

Since our setup is invariant along the $\hat{y}$ direction, the mechanical pressure can be computed directly from the force exerted by the system on a wall (which we place at $x = x_w \gg 0$), as

$$P = \int_0^\infty \rho(x) \partial_x V(x)\, dx \ . \tag{3}$$

Here an origin $x = 0$ is taken in the bulk, and $\rho(x) = \int_0^{2\pi} \mathcal{P}(x, \theta) d\theta$ is the steady-state density of particles at $x$. As stated previously, for a passive equilibrium system ($v = 0$) with the same geometry, the mechanical definition (3) of pressure is equivalent to the thermodynamic definition, as proved for completeness in the Supplementary Information (SI). Note that Eq. (3) still applies in the presence of other particles, such as solvent molecules, so long as those particles do not themselves exert any direct force on the wall (which is thus semi-permeable). Under such conditions $P$ is, by definition, an *osmotic* pressure; the results below will still apply to it, whenever Eq.(2) remains valid.

As described in the SI, the pressure can be computed analytically from Eq. (2) as:

$$P = \left[\frac{v^2}{2\mu_t(D_r + \alpha)} + \frac{D_t}{\mu_t}\right] \rho_0 - \frac{v\mu_r}{\mu_t(D_r + \alpha)} \int_0^\infty dx \int_0^{2\pi} \Gamma(x, \theta) \sin\theta\, \mathcal{P}(x, \theta)\, d\theta \ . \tag{4}$$

This is a central result, and exact for all systems obeying Eq. (2). Clearly, $\Gamma(x, \theta)$ in general depends on the wall-particle interactions, as does $\mathcal{P}(x, \theta)$ which is sensitive to both $\Gamma(x, \theta)$ and $V(x)$. Thus the mechanical pressure $P$ obeying Eq. (4) is likewise sensitive to these details: it follows that *no equation of state exists* for active particle systems in the general case.

To illustrate this effect and show that (4) can indeed be used to compute the pressure, we study a model of ABPs with elliptical shape (see SI for details). We choose a harmonic confining potential, $V(x) = \frac{\lambda}{2}(x - x_w)^2$ for $x > x_w$, with $V = 0$ otherwise,

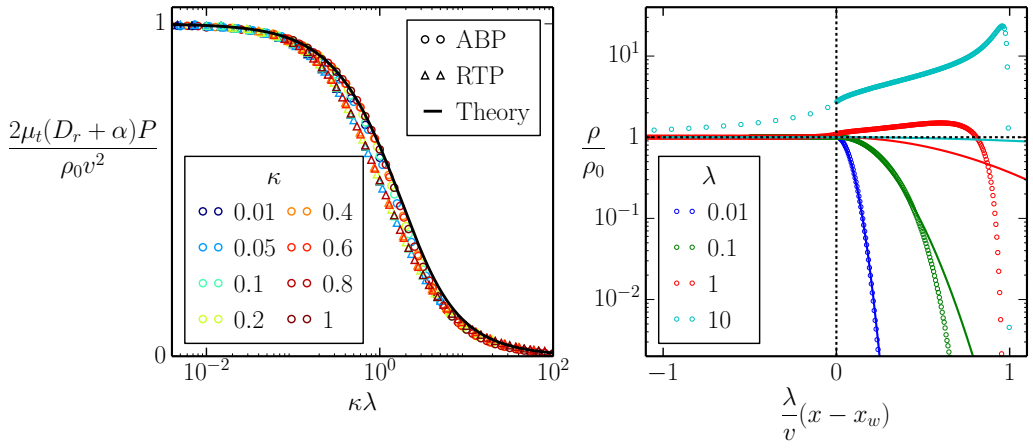


FIG. 1. **Non–interacting self-propelled ellipses. Left:** Normalized pressure as the particle anisotropy $\kappa$ and the wall stiffness $\lambda$ are varied for ABPs and RTPs. The theoretical prediction for ABPs correspond to Eq. (5) **Right**: Density profiles for spherical particles for four different wall stiffness all yielding a pressure equal to $\rho k T_{\text{eff}}$. The full lines are Boltzmann distributions at $kT_{\text{eff}}$, showing that the pressure is given by the effective temperature far outside the Boltzmann regime $\lambda \ll D_r$. $v = D_r = 1$ and $D_t = 0$, with box size $L_x \times L_y = 10 \times 1$.

accompanied by a torque $\Gamma = \lambda\kappa \sin 2\theta$ (again, for $x > x_w$ and zero otherwise). With $\kappa = (a^2 - b^2)/8$, this is the torque felt by an elliptical particle of axial dimensions $a, b$ and unit area $\pi ab$, subject to the linear force field $-\nabla V(x)$ distributed across its body. Assuming the steady-state distribution $\mathcal{P}(x, \theta)$ to relax to its bulk value outside the range of the wall potential, $\mathcal{P}(x_w, \theta) = \rho_0/2\pi$, the pressure in such an ABP fluid (for $D_t = 0$) is given by

$$P = \frac{\rho_0 v^2}{2\lambda\mu_t\mu_r\kappa}\left[1 - \exp\left(-\frac{\lambda\mu_r\kappa}{D_r}\right)\right] . \tag{5}$$

For $\kappa > 0$ the torque reduces the pressure by orienting the ABPs parallel to the wall. Equation (5) shows explicitly how walls with different spring constants $\lambda$ experience different pressures, in sharp contrast with thermodynamics. We checked this prediction by direct numerical simulations of ABPs and found good agreement (see Fig. 1). We also found similar behavior numerically for (likewise elliptical) RTPs, confirming that the failure of thermodynamics is generic.

For passive particles in thermal equilibrium, $v = 0$ and Eq. (4) reduces to the ideal gas law, $P = \rho_0 k_B T$, upon use of the Einstein relation ($D_t/\mu_t = k_B T$). Another case where an equation of state is recovered is for torque–free (e.g., spherical) particles, with $\Gamma = 0$. In that case Eq. (4) reduces to the same ideal gas law but with an effective temperature

$$\frac{P}{\rho_0} = k_B T_{\text{eff}} = \frac{v^2}{2\mu_t(D_r + \alpha)} + \frac{D_t}{\mu_t} . \tag{6}$$

This explains why previous numerical studies of torque–free, non–interacting active particle fluids gave consistent pressure measurements between impenetrable [14, 15] or harmonically soft walls [13]. Related expressions for the pressure of such fluids were found by computing the mean kinetic energy [13], or the stress tensor [17–19], possibly encouraging a belief that all reasonable definitions of pressure in active systems are equivalent. However, Eq. (4) shows that these approaches cannot yield consistent results beyond the simplest, torque–free case.

The "effective gas law" of Eq. (6) for the torque–free case is itself remarkable. For ABPs or RTPs in an external potential $V(x)$, the effective temperature concept predicts a steady-state density $\rho(x) \propto \exp[-V(x)/k_B T_{\text{eff}}]$ that is accurate *only* for weak force fields [33, 40]. Yet Eq. (6) holds even with hard-core walls for which the opposite applies and the steady-state density profile is far from a Boltzmann distribution (see the simulation results of Fig. 1 and the analytical results for one–dimensional RTPs in SI). In fact the result stems directly from the exact computation of $\int_0^\infty \rho(x)\partial_x V(x)\, dx$, which can be done at the level of the master equation and leads to Eq. (4), so that no broader validity of the $T_{\text{eff}}$ concept is required, or implied.

## INTERACTING ACTIVE PARTICLES

Equation (4) gives the pressure of non–interacting active particles and we now address the extent to which our conclusions apply to interacting SPPs. Clearly, interactions will not restore the existence of an equation of state in the presence of wall torques and we thus focus on "torque-free" walls.

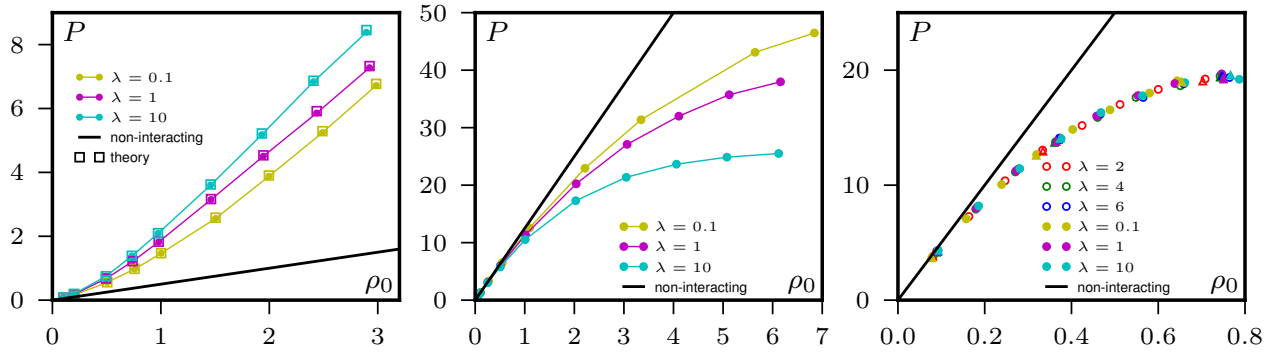


FIG. 2. **Interacting self-propelled spheres.** Pressure versus density $P(\rho_0)$ for interacting particles ($L_x \times L_y = 200 \times 50$). **Left:** Aligning ABPs. The torque exerted by particle $j$ on particle $i$ is $F(\theta_j - \theta_i, \mathbf{r}_i, \mathbf{r}_j) = \frac{\gamma}{\mathcal{N}(\mathbf{r}_i)} \sin(\theta_j - \theta_i)$ if $|\mathbf{r}_j - \mathbf{r}_i| < R$ and 0 otherwise, where $\mathcal{N}(\mathbf{r}_i)$ is the number of particles interacting with particle $i$. $v = 1$, $D_r = 1$, $D_t = 0$, $R = 1$ and $\gamma = 2$. **Center**: "Quorum sensing" interactions $v(\bar{\rho}) = v_0(1 - \bar{\rho}/\rho_m) + v_1$ with $v_0 = 10$, $v_1 = 1$, $\rho_m = 5$, $D_r = D_t = 1$. **Right** The pressure of particles interacting with repulsive WCA potentials is independant of the wall potential. Triangles and circles represent RTPs and ABPs with $v = 10$, $D_r = 1$, $\alpha = 1$ and $D_t = 0$. Open and full symbols correspond to linear and harmonic wall potentials. (See SI for numerical details.)

Interparticle alignment is probably the most studied interaction in active matter [3]. To measure its impact on pressure, we consider $N$ ABPs whose positions $\mathbf{r}_i$ and orientations $\theta_i$ evolve according to (1) and

$$\frac{d\theta_i}{dt} = \mu_r \sum_{j=1}^{N} F(\theta_j - \theta_i, \mathbf{r}_i, \mathbf{r}_j) + \sqrt{2D_r}\xi_i(t) \tag{7}$$

where $F$ is an aligning torque between the particles. As shown in SI, the pressure can be computed analytically to give

$$P = \left[\frac{v^2}{2\mu_t D_r} + \frac{D_t}{\mu_t}\right]\rho_0 - \frac{v\mu_r}{\mu_t D_r}\int_0^\infty dx \int_{-\infty}^{\infty} dy \int_0^{2\pi} d\theta \int d\mathbf{r}' \int_0^{2\pi} d\theta' F(\theta' - \theta, \mathbf{r}, \mathbf{r}') \sin\theta \langle \mathcal{P}(\mathbf{r}, \theta)\mathcal{P}(\mathbf{r}', \theta')\rangle \tag{8}$$

where the integral over $\mathbf{r}'$ is over the whole space. Since the distribution $\mathcal{P}(\mathbf{r}, \theta) = \sum_{i=1}^{N} \delta(\mathbf{r} - \mathbf{r}_i)\delta(\theta - \theta_i)$ depends (for $x > 0$) on the wall potential, so does the pressure. Therefore, even in the absence of wall torques, alignment interactions between particles destroy any equation of state. Figure 2 shows the result of ABP simulations with a particular choice of interparticle torque $F$: The measured pressure indeed depends on the wall potential and agrees with equation (8).

In active matter, more general interactions than pairwise torques often have to be considered. For example, in bacteria with "quorum sensing" (a form of chemical communication), particles at position $\mathbf{r}$ can adapt their dynamics in response to changes in the local coarse–grained particle density $\bar{\rho}(\mathbf{r})$ [37]. Also shown in Fig. 2 are simulations for the case $v(\bar{\rho}) = v_0(1 - \bar{\rho}/\rho_m) + v_1$, reflecting a pairwise speed reduction (see SI for details). This is an example where even completely torque-free particles have no equation of state. Again, we show in SI how an explicit formula for the pressure can be computed from first principles.

The case of torque–free ABPs with short range repulsive interactions [24, 25, 34, 35] was recently considered in [17, 18]. The mechanical force exerted on a wall was found to coincide with a pressure computed from the bulk stress tensor, suggesting that in this case an equation of state does exist. To check this, we choose a Weeks–Chandler–Andersen (WCA) potential: $U(r) = 4\left[\left(\frac{\sigma}{r}\right)^{12} - \left(\frac{\sigma}{r}\right)^{6}\right] + 1$ if $r < 2^{1/6}\sigma$ and $U = 0$ otherwise, where $r$ is the inter-particle distance and $\sigma$ the particle diameter. Using simulations we determined $P$ as a function of bulk density $\rho_0$ for various harmonic and linear wall potentials. As shown in Fig. 2, all our data collapses onto a wall-independent equation of state $P(\rho_0)$. An analytical expression for $P(\rho)$ in this rather exceptional case is derived and studied in [21] in the context of phase equilibria.

The cases explored above show that there is generically no equation of state in an active fluid, one exception being when wall-particle and particle-particle torques are both negligible. Given this outcome, a simple test for the presence or absence of an equation of state, in simulations or experiments, would be welcome. If the pressure is set by bulk properties of the fluid, when an asymmetrically interacting partition is used to separate the system in two parts, no force acts upon the partition and it does not move. Conversely, if the partition does move, there is no equation of state. To check this, we simulated a large box of homogeneous active fluid, introduced at its centre a mobile wall with asymmetric potentials on its two sides, and let the system reach steady state. In the cases shown above to have an equation of state, the wall remains at the center of the box so that the densities on its two sides stay equal. In the other cases, however, the partition moves to equalize the two wall–dependent pressures, resulting in a flux-free steady-state with unequal densities in the two chambers (Fig. 3).

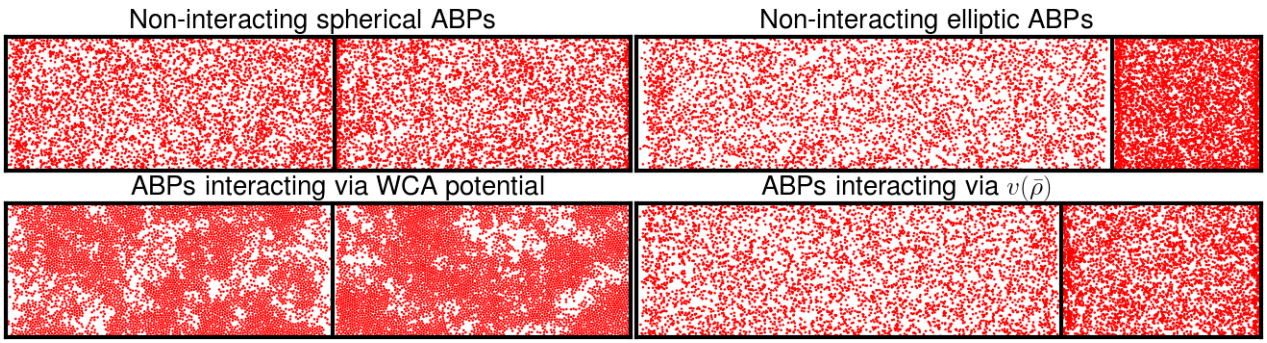


FIG. 3. **Simple test for the existence of an equation of state.** Four snapshots of the steady-state of 10 000 ABPs in a $200 \times 50$ cavity split in two by a mobile asymmetric harmonic wall ($\lambda = 1$ on the left and $\lambda = 4$ on the right, $v = 10$, $D_r = 1$, $D_t = 0$) for: non–interacting spherical ABPs (top left), non–interacting elliptic ABPs with $\mu_r = \kappa = 1$ (top right), ABPs interacting via the WCA potential (bottom left) and via $v(\bar{\rho})$ (bottom right) with $v_0 = 10$, $v_1 = 1$, $\rho_m = 4.8$. A spontaneous compression of the right half of the system is the signature of the lack of equation of state.

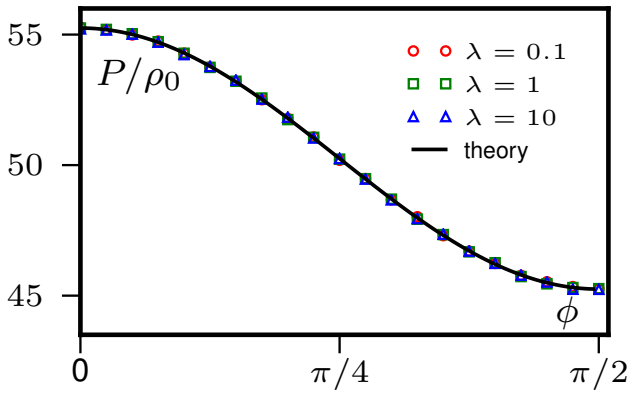


FIG. 4. **Anisotropic pressure.** RTPs with anisotropic speed $v(\theta) = v_0 + v_1 \cos(2\theta)$, with $v_0 = 10$, $v_1 = 1$, $D_t = 0$. The pressure depends on the angle $\phi$ between the wall and the axis $\hat{y}$ but not on the stiffness of the potential.

## ANOMALOUS ATTRIBUTES OF THE PRESSURE

A defining property of equilibrium *fluids* is that they cannot statically support an anisotropic stress. Put differently, the normal force per unit area on any part of the boundary is independent of its orientation. This applies even to oriented fluids (without positional order), such as nematic liquid crystals [38], but breaks down for active nematics [3].

We next show that it can also break down for active fluids with isotropic particle orientations, as long as the propulsion speed is anisotropic, i.e. $v = v(\theta)$. This could stem from an anisotropic mobility $\mu_t(\theta)$ as might arise for cells crawling on a corrugated surface. We suppose $v(\theta) = v(\theta + \pi)$ so that oppositely oriented particles have the same speed; Eq. (2) then shows that the bulk steady state particle distribution $\mathcal{P}(\mathbf{r}, \theta)$ remains isotropic. In addition, as shown in SI, the pressure $P(\phi)$ acting on a wall whose normal is at angle $\phi$ to the $\hat{x}$ axis remains independent of the wall interactions, but is $\phi$-dependent; for RTPs ($D_r = 0$) it obeys

$$P(\phi) = \frac{\rho_0 D_t}{\mu_t} + \frac{\rho_0}{2\pi\mu_t\alpha}\int_0^{2\pi} v^2(\theta)\cos^2(\theta - \phi)\, d\theta \quad . \tag{9}$$

To verify that the pressure is indeed anisotropic we performed numerical simulations for $v(\theta) = v_0 + v_1\cos(2\theta)$ which show perfect agreement with Eq. (9) (see Fig. 4).

For passive fluids without external forces, mechanical equilibrium requires that the pressure is not only isotropic, but also uniform. This follows from the Navier–Stokes equation for momentum transport [38], but also holds in (say) Brownian dynamics simulations which do not conserve momentum [1].

We now show that $P$ need not be uniform in active fluids, even when an equation of state exists. Consider non–interacting

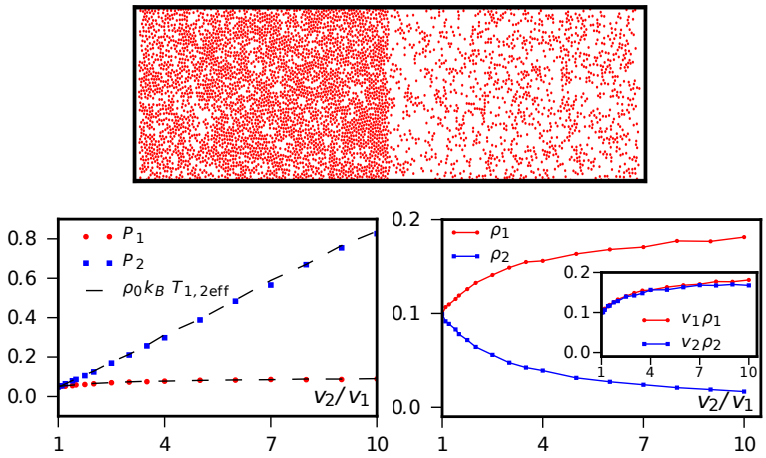


FIG. 5. **Inhomogeneous pressure**. Spherical ABPs interacting with WCA potential, with speeds $v_1$ for $x < 0$ and $v_2$ for $x > 0$. **Left:** Snapshot of the cavity in steady state ($v_1 = 1$, $v_2 = 5$). **Middle:** Pressures $P_1$ and $P_2$ as $v_2/v_1$ is varied. **Right:** As $v_2/v_1$ varies, the densities evolve to equalize $\rho v$ rather than $P \sim \rho v^2$. $D_r = 1$, $D_t = 0$, $\lambda = 1$, $L_x \times L_y = 200 \times 50$.

spherical ABPs in a closed container with different propulsion speeds in different regions, say $v = v_1$ for $x < 0$ and $v = v_2$ for $x > 0$. This is a realizable laboratory experiment in active colloids whose propulsion is light-induced [8, 22]. From Eq. 2, the flux-free steady state has $\rho \propto 1/v$ throughout [26, 27, 36], so that the pressures $P_{1,2} \propto \rho v^2$ are unequal. Though different, the pressures in the two compartments are well defined, uniform within each bulk, and independent of the wall-particle interactions. They remain different when interparticle interactions are added (see Fig 5). Indeed, if for $v_1 \neq v_2$ equality of the ideal pressure is restored by setting $D_r \propto v$, the effect of such interactions is to reinstate a pressure imbalance. Nonuniformity of $P$ is thus fully generic for nonuniform $v$.

The above example implies a remarkable result, that also holds for systems with no equation of state enclosed by spatially heterogeneous walls. In both cases *the net force acting across the system boundary is generically nonzero*. Were momentum conserved, this would require the system as a whole to be accelerating. Recall however that Eq. (2) describes particles moving on, or through, a medium that absorbs momentum and this net force is exactly cancelled by the momentum exchange with the support. The latter vanishes on average in the isotropic bulk, but is nonzero in a layer of finite polarization ($m_1 \neq 0$) close to each wall.

## DISCUSSION

Our work shows that in active fluids the concept of pressure defies many suppositions based upon concepts from thermal equilibrium. The generic absence of an equation of state is the most striking instance of this. Despite its absence, we have shown how to compute the mechanical pressure for a large class of active particle systems. Clearly, the concept of pressure is even more powerful in the exceptional cases where an equation of state does exist. This excludes any chemically-mediated variation in propulsion speed, and also requires wall–particle and interparticle torques both to be negligible. Because it can easily be achieved on a computer, though not in a laboratory, the torque-free case of spherical active Brownian particles without bulk momentum conservation has played a pivotal role in recent theoretical studies of active matter [13, 17, 18]. The proof [21] that an equation of state does exist for this system is all the more remarkable because, as we have seen, such an outcome is the exception and not the rule.

It is interesting to inquire how our results would change for systems with full momentum conservation in the bulk. As mentioned previously, if Eq. (2) still applies, our exact results for $P$ remain valid so long as this is taken as an *osmotic* pressure. For dilute systems Eq. (2) should indeed hold in bulk, even though particles now propel by exerting force multipoles on the surrounding solvent. (Since the walls of the system are semipermeable, the solvent can carry momentum across them, and effectively becomes a momentum sink for the active particles.) However, even for spherical swimmers, hydrodynamic interactions can now cause torques, both between the particles and near the wall [39], making an equation of state less likely. Its absence would then manifest as a nonzero net force on a semipermeable partition between two identical samples of (say) a swimming bacterial fluid. We predict this outcome whenever the two faces of the partition have different interactions with the swimming

particles.

[1] Allen, M. P. and Tidlesley, D. J. , *Computer Simulation of Liquids*, Oxford University Press, Oxford (1987)
[2] Cugliandolo, L. F., The effective temperature, *J. Phys. A* **44**, 483001 (2011)
[3] Marchetti, M. C. *et al.*, Hydrodynamics of soft active matter, *Rev. Mod. Phys.* **85**, 1143 (2013)
[4] Berg, H., *E. coli in Motion* Springer, Berlin (2001)
[5] Cates, M. E., Diffusive transport without detailed balance in motile bacteria: does microbiology need statistical physics?, *Repts. on Prog. in Phys.* **75**, 042601 (2012)
[6] Palacci, J., Cottin-Bizonne, C., Ybert, C. and Bocquet, L., Sedimentation and Effective Temperature of Active Colloidal Suspensions, *Phy. Rev. Lett.* **105**, 088304 (2010)
[7] Fily, Y. and Marchetti, M. C, Athermal Phase Separation of Self-Propelled Particles with No Alignment, *Phys. Rev. Lett.* **108**, 235702 (2012)
[8] Buttinoni, I. *et al.*, Dynamical Clustering and Phase Separation in Suspensions of Self-Propelled Colloidal Particles, *Phys. Rev. Lett.* **110**, 238301 (2013)
[9] Kudrolli, A., Lumay, G., Volfson, D. and Tsimring, L. S., Swarming and Swirling in Self-Propelled Polar Granular Rods, *Phys. Rev. Lett.* **100**, 058001 (2008).
[10] Narayan, V., Ramaswamy, S. and Menon, N., Long-Lived Giant Number Fluctuations in a Swarming Granular Nematic, *Science* **317**, 105-108 (2007)
[11] Deseigne, J., Dauchot, O. and Chaté, H., Collective Motion of Vibrated Polar Disks, *Phys. Rev. Lett.* **105**, 098001 (2010)
[12] Ballerini, M. *et al.*, Interaction ruling animal collective behavior depends on topological rather than metric distance: Evidence from a field study, *Proc. Natl Acad. Sci. USA* **105**, 1232-1237 (2008)
[13] Mallory, S. A., Saric, A., Valeriani, C. and Cacciuto, A., Anomalous thermomechanical properties of a self-propelled colloidal fluid, *Phys. Rev. E* **89**, 052303 (2014)
[14] Fily, Y., Baskaran, A. and Hagan, M. F., Dynamics of self-propelled particles under strong confinement, *Soft Matter* **10**, 5609 (2014)
[15] Fily, Y., Baskaran, A. and Hagan, M. F., Dynamics of strongly confined self propelled particles in non convex boundaries, arXiv:1410.5151 (2014)
[16] Ni, R., Cohen Stuart, M. A. and Bolhuis, P. G., Tunable long range forces mediated by self-propelled colloidal hard spheres, arxiv:1403.1533 (2014)
[17] Yang, X., Manning, M. L. and Marchetti, M. C., Aggregation and segregation of confined active particles, *Soft Matter* **10**, 6477 (2014)
[18] Takatori,S. C., Yan, W. and Brady, J. F., Swim Pressure: Stress Generation in Active Matter, *Phys. Rev. Lett.* **113**, 028103 (2014)
[19] Takatori, S. C. and Brady, J. F., Towards a 'Thermodynamics' of Active Matter, arxiv:1411.5776 (2014)
[20] Ginot, F. *et al.*, Nonequilibrium equation of state in suspensions of active colloids, *Phys. Rev. X* in press, arxiv:1411.7175 (2014)
[21] Solon, A.P. *et al.*, Pressure and Phase Equilibria in Interacting Active Brownian Spheres, arXiv:1412.5475 (2014)
[22] Palacci, J. *et al.*, Living Crystals of Light-Activated Colloidal Surfers, *Science* **339**, 936 (2013)
[23] Bricard, A., Caussin, J. B., Desreumaux, N., Dauchot, O. and Bartolo, D., Emergence of macroscopic directed motion in populations of motile colloids, *Nature* **503**, 95 (2013)
[24] Redner, G. S., Hagan, M. F. and Baskaran, A., Structure and Dynamics of a Phase-Separating Active Colloidal Fluid, *Phys. Rev. Lett.* **110**, 055701 (2013)
[25] Stenhammar, J. *et al.*, Continuum Theory of Phase Separation Kinetics for Active Brownian Particles, *Phys. Rev. Lett.* **111**, 145702 (2013)
[26] Schnitzer, J., Theory of continuum random walks and application to chemotaxis, *Phys. Rev. E* **48**, 2553 (1993)
[27] Tailleur, J. and Cates, M. E., Statistical Mechanics of Interacting Run-and-Tumble Bacteria, *Phys. Rev. Lett.* **100**, 218103 (2008)
[28] Cates, M. E., Marenduzzo, D., Pagonabarraga, I. and Tailleur, J., Arrested phase separation in reproducing bacteria creates a generic route to pattern formation, *Proc. Nat. Acad. Sci. USA* **107**, 11715-11729 (2010)
[29] Theveneau, E. *et al.*, Collective Chemotaxis Requires Contact-Dependent Cell Polarity, *Dev. Cell* **19**, 39 (2010)
[30] Sepulveda, N. *et al.*, Collective Cell Motion in an Epithelial Sheet Can Be Quantitatively Described by a Stochastic Interacting Particle Model, *PLoS Comp. Biol.* **9**, e1002944 (2013)
[31] Deseigne, J., Dauchot, O. and Chaté, H., Collective Motion of Vibrated Polar Disks, *Phys. Rev. Lett.* **105**, 098001 (2010)
[32] Elgeti, J. and Gompper, G., Self-propelled rods near surfaces, *EPL* **85**, 38002 (2009)
[33] Tailleur, J. and Cates, M. E., Sedimentation, trapping, and rectification of dilute bacteria, *EPL* **86**, 60002 (2009)
[34] Bialké, J., Lowen, H. and Speck, T., Microscopic theory for the phase separation of self-propelled repulsive disks, *EPL* **103**, 30008 (2013)
[35] Wysocki, A., Winkler, R. G. and Gompper, G., Cooperative motion of active Brownian spheres in three-dimensional dense suspensions, *EPL* **105**, 48004 (2014)
[36] Cates, M. E. and Tailleur, J., When are active Brownian particles and run-and-tumble particles equivalent? Consequences for motility-induced phase separation, *EPL* **101**, 20010 (2013)
[37] Liu, C. *et al.*, Sequential Establishment of Stripe Patterns in an Expanding Cell Population, Science **334**, 238-241 (2011)
[38] Chaikin, P. M. and Lubensky, T. C., *Principles of Condensed Matter Physics*, Cambridge University Press, Cambridge (2000)
[39] Berke, A. P., Turner, L., Berg, H. C. and Lauga, E., Hydrodynamic Attraction of Swimming Microorganisms by Surfaces, *Phys. Rev. Lett.* **101**, 038102 (2008)
[40] A. P. Solon, M. E. Cates and J. Tailleur, Active Brownian Particles and Run-and-Tumble Particles: a Comparative Study, arXiv:1504.07391 (2015)

**ACKNOWLEDGMENTS**

We thank K. Keren, M. Kolodrubetz, C. Marchetti, A. Polkovnikov, J. Stenhammar, R. Wittkowski and Xingbo Yang for discussions. This work was funded in part by EPSRC EP/J007404. MEC holds a Royal Society Research Professorship. YK was supported by the I-CORE Program of the Planning and Budgeting Committee and the Israel Science Foundation. MK is supported by NSF grant No. DMR-12-06323. AB and YF acknowledge support from NSF grant DMR-1149266 and the Brandeis Center for Bioinspired Soft Materials, an NSF MRSEC, DMR-1420382. Their computational resources were provided by the NSF through XSEDE computing resources and the Brandeis HPCC. YK, AS and JT thank the Galileo Galilei Institute for Theoretical Physics for hospitality. AB, MEC, YF, AS, MK and JT thank the KITP at the University of California, Santa Barbara, where they were supported through National Science Foundation Grant NSF PHY11-25925. Correspondence and requests for materials should be addressed to A.P.S. (email: alexandre.solon@univ-paris-diderot.fr).

# Supplementary Information

(Dated: May 21, 2015)

## I. DETAILS OF NUMERICAL SIMULATIONS

**Time-stepping**: Simulations were run using Euler time-discretization schemes over total times $T = 10^4$ or larger (up to $T = 10^9$).

**Non-interacting particles**: At each time step $dt$, particles update their direction of motion $\theta_i$, then their position $\mathbf{r_i}$. For ABPs, $\dot{\theta}_i = \sqrt{2D_r}\xi(t)$ where $\xi(t)$ is a Gaussian white noise of unit variance. For RTPs, the time $\Delta t$ before the next tumble is chosen using an exponential distribution $P(\Delta t) = \lambda e^{-\lambda \Delta t}$. When this time is reached, a new direction is chosen uniformly in $[0, 2\pi[$ and the next tumble time is drawn from the same distribution. This neglects the possibility to have two tumbles during $dt$. Both types of particles then move according to the Langevin equation $\dot{\mathbf{r_i}} = v\mathbf{e}_{\theta_\mathbf{i}} - \nabla V + \sqrt{2D_t}\eta(t)$ where $\eta(t)$ is a Gaussian white noise of unit variance.

**Hard-core repulsion**: To model hard-core repulsion we use a WCA potential $V(r) = 4\big[\left(\frac{\sigma}{r}\right)^{12} - \left(\frac{\sigma}{r}\right)^{6}\big] + 1$ if $r < 2^{1/6}\sigma$ and 0 otherwise. The unit of length is chosen such that the interaction radius $2^{1/6}\sigma = 1$. Because of the stiff repulsion, one needs to use much smaller time steps ($dt = 5.10^{-5}$ for the speeds considered in the paper).

**Aligning particles**: Particles exert torques on each other to align their directions of motion $\theta_i$. The torque exerted by particle $j$ on particle $i$ reads $F(\theta_j - \theta_i, \mathbf{r}_j - \mathbf{r}_i) = \frac{\gamma}{\mathcal{N}(\mathbf{r}_i)}\sin(\theta_j - \theta_i)$ if $|\mathbf{r}_i - \mathbf{r}_j| < R$ and 0 otherwise, where $\mathcal{N}(\mathbf{r}_i)$ is the number of particles interacting with particle $i$. The interaction radius $R$ is chosen as unit of length. For the parameters used in simulations $v = 1$, $\gamma = 2$, with a time-step $dt = 10^{-2}$.

**Quorum sensing** $v(\bar{\rho})$: The velocities of the particles depend on the local density $\bar{\rho}$. The unit of length is fixed such that the radius of interaction is 1. To compute the local density, we use the Schwartz bell curve $K(r) = \frac{1}{Z}\exp(-\frac{1}{1-r^2})$ for $r < 1$ and 0 otherwise, where $Z$ is a normalization constant. The average density around particle $i$ is then given by $\bar{\rho}_i = \sum_j K(|\mathbf{r_i} - \mathbf{r_j}|)$ and the velocity of particle $i$ is $v(\bar{\rho}_i) = v_0(1 - \bar{\rho}_i/\rho_m) + v_1$. We used $dt = 5.10^{-3}$.

**Asymmetric wall experiment**: The simulation box is separated in two parts by an asymmetric wall which has a different stiffness $\lambda_1$ and $\lambda_2$ on both sides. At each time step, the total force $\mathcal{F}$ exerted on the wall by the particles is computed and the wall position is updated according to $\dot{x}_{\text{wall}} = \mu_{\text{wall}}\mathcal{F}$, where $\mu_{\text{wall}} = 2.10^{-4} \ll \mu_t$ is the wall mobility.

**SI movie 1**: Asymmetric wall experiment with non-interacting ABP particles. The particles are spherical (no torque) for $t < 1000$ and $t > 3000$ and ellipses with $\kappa = 1$ for $1000 < t < 3000$. Wall potentials are harmonic and other parameters are $v = 10$, $D_r = 1$, $\lambda = 10$ (external box) and for the asymmetric mobile wall $\lambda = 1$ on the left and $\lambda = 4$ on the right.

## II. EQUILIBRIUM PRESSURE

Here, for completeness, we show that in equilibrium 1) the thermodynamic pressure equals the mechanical pressure given by Eq. (3) of the main text, and 2) that it is independent from the wall potential. For simplicity we consider a system of interacting point-like particles in one-dimension where the pressure is a force and we work in the canonical ensemble. The extension to other cases

is trivial.

The thermodynamic pressure is defined as

$$P = -\left.\frac{\partial F}{\partial L}\right|_N , \tag{1}$$

where $L$ is the system length, $F$ is the free energy, and the number of particles $N$ is kept constant. Note that since $F$ is extensive, any contribution from the potential of the wall is finite and will therefore not influence the pressure. Next, the free energy is given by

$$F = -\frac{1}{\beta}\ln \mathcal{Z} , \tag{2}$$

where

$$\mathcal{Z} = \sum_n e^{-\beta[(\mathcal{H}+\sum_i V(x_i-L)]} , \tag{3}$$

is the partition function, $\beta = 1/T$ with $T$ the temperature, and the sum runs over all micro-states. The origin of the wall is chosen at $x = L$, as opposed to $x = x_w$ in the main text. The energy function of the system is given by $\mathcal{H}+\sum_i V(x_i-L)$, where $V(x_i-L)$ is the wall potential, $x_i$ is the position of particle $i$, and $\mathcal{H}$ contains all the other interactions in the system. Using the definition of $P$ we have

$$P = -\frac{1}{\mathcal{Z}}\sum_n\sum_i \partial_L V(x_i-L)e^{-\beta(\mathcal{H}+\sum_i V(x_i-L))} = -\left\langle \int dx\rho(x)\partial_L V(x-L)\right\rangle , \tag{4}$$

where the angular brackets denote a thermal average, and $\rho(x) = \sum_i \delta(x-x_i)$ is the number density. Exchanging $\partial_L$ for $-\partial_x$, we obtain the expression from the main text

$$P = \left\langle \int dx\rho(x)\partial_x V(x-L)\right\rangle . \tag{5}$$

## III. DERIVATION OF THE PRESSURE FOR NON-INTERACTING SPPS

To compute the mechanical pressure $P$ for SPPs, we first define $m_n(x) = \int_0^{2\pi}\cos(n\theta)\mathcal{P}(x,\theta)d\theta$. Taking moments of the master equation, Eq. (2) in the main text, we find that in steady state

$$0 = -\partial_x(vm_1 - \mu_t\rho\partial_x V - D_t\partial_x\rho) , \tag{6}$$

$$(D_r+\alpha)m_1 = -\partial_x\Big(v\frac{\rho+m_2}{2} - \mu_t m_1\partial_x V - D_t\partial_x m_1\Big) - \int_0^{2\pi}\sin\theta\,\mu_r\Gamma(x,\theta)\mathcal{P}\,d\theta . \tag{7}$$

Equation (6) is tantamount to setting $\partial_x J = 0$, where $J$ is a particle current that must vanish in any confined system; while Eq. (7) expresses a similar result for the first moment $m_1$. Equation (3) of the main text and Eq. (6) together imply that

$$P = \int_0^\infty \frac{1}{\mu_t}\left[vm_1 - D_t\partial_x\rho\right] dx . \tag{8}$$

Next, from Eqs. (6,7) we see that, apart from the term involving the torque $\Gamma$, $m_1(x)$ is a total derivative. We can trivially integrate this contribution to Eq. (8), noting that at $x = 0$, isotropic bulk conditions prevail so that $m_1 = m_2 = 0$, and $\rho = \rho_0$ (say), while as $x \to \infty$, far beyond the confining wall, $\rho = m_1 = m_2 = 0$. Restoring the $\Gamma$ term we finally obtain Eq. (4) of the main text.

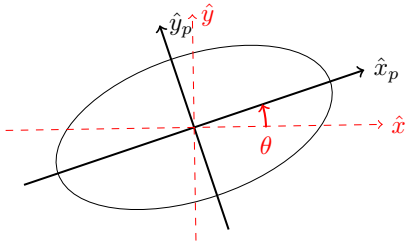


Figure 1. An illustration of the axes $(\hat{x}, \hat{x})$ and $(\hat{x}_p, \hat{x}_p)$, and the angle $\theta$.

## IV. PRESSURE FOR AN ELLIPSE IN A HARMONIC POTENTIAL

In what follows we first compute the torque applied on an ellipse in a harmonic potential. We then derive an approximate expression for the pressure, Eq. (5) of the main text, which is valid as long as the density distribution $P(r, \theta)$ equals its bulk value as soon as the wall potential vanishes (at $x = x_w$).

### A. Torque on an ellipse

We consider an ellipse of uniform density and long and short axes of lengths $a$ and $b$ respectively. We define two sets of axes: 1) $(\hat{x}, \hat{y})$ are the real space coordinates with the wall parallel to the $y$ axis, and 2) $(\hat{x}_p, \hat{y}_p)$ are the coordinates associated with the ellipse so that $x_p$ is parallel to its long axis. The angle between the two sets of coordinates is $\theta$, which is also the direction of motion of the particle (see Fig. 1). For simplicity, we assume that the particle is moving along its long principal axis.

Since the wall is perpendicular to the $\hat{x}$ axis, the force acting on an area element of the ellipse is given by $F_w(x_0 + x) = -\partial_x V(x_0 + x)$, where $x_0$ is the position of the center of mass of the ellipse and $x$ the relative coordinate of the area element within the ellipse, both along the $\hat{x}$ direction.

The torque applied by the force at a point $\mathbf{r}$ is then given by

$$\gamma = \mathbf{r} \times F_w(x_0 + x)\hat{x} \,, \tag{9}$$

$$= \begin{pmatrix} x_p \\ y_p \end{pmatrix} \times F_w(x_0 + x_p \cos\theta - y_p \sin\theta) \begin{pmatrix} \cos\theta \\ -\sin\theta \end{pmatrix} \,. \tag{10}$$

Next, we integrate over the ellipse, taking its mass density to be uniform $\rho(x_p, y_p) = m/(\pi ab)$. Rescaling the axes as $x'_p = x_p/a$ and $y'_p = y_p/b$ to transform the ellipse into a unit circle, and switching from $(x'_p, y'_p)$ to polar coordinates $(r, \varphi)$, yields

$$\Gamma = \frac{m}{\pi ab} \int dx_p dy_p \gamma \tag{11}$$

$$= \frac{m}{\pi} \int dx'_p \int dy'_p F_w(x_0 + ax'_p \cos\theta - by'_p \sin\theta) \begin{pmatrix} ax'_p \\ by'_p \end{pmatrix} \times \begin{pmatrix} \cos\theta \\ -\sin\theta \end{pmatrix}$$

$$= m \int_0^{2\pi} \frac{d\varphi}{\pi} \int_0^1 dr r F_w(x_0 + ar\cos\varphi\cos\theta - br\sin\varphi\sin\theta) \begin{pmatrix} ar\cos\varphi \\ br\sin\varphi \end{pmatrix} \times \begin{pmatrix} \cos\theta \\ -\sin\theta \end{pmatrix} \,.$$

For a harmonic wall potential $F_w(x) = -\lambda x$, the integral can be computed, and we get

$$\Gamma = \frac{m\lambda}{8}(a^2 - b^2)\sin(2\theta) \equiv \lambda\kappa\sin(2\theta) \ , \tag{12}$$

which has the expected symmetries: it vanishes for a sphere ($a = b$), and for particles moving along or perpendicular to the $x$-axis. Note that the torque is constant, independent of the position of the particle as long as the whole ellipse is within the range of the wall potential. In the main text we assume that this is always the case, which means that the ellipse is very small when compared to the typical decay length of $\rho(x)$ due to $V$. In the simulations, we thus simulated point-like ABPs with external torques $\Gamma = \pm\lambda\kappa\sin 2\theta$ for left and right walls. For real systems, the collision details would clearly be different, hence giving different quantitative predictions for the pressure $P$, but the qualitative results would be the same. We set $m = 1$ for ease of notation and define the asymetry coeficient $\kappa = (a^2 - b^2)/8$ as in the main text.

### B. Approximate expression for the pressure

We now turn to the derivation of the approximate expression Eq. (5) in the main text for the pressure. In particular we focus on the case of ABP ($\alpha = 0$) ellipses confined by a harmonic wall potential and for simplicity neglect the translational diffusion $D_t = 0$. In that case the contribution of the torque to the pressure reads

$$C = \frac{\bar{\lambda}v}{\mu_t}\int_0^{+\infty} dx \int_0^{2\pi} d\theta \sin(\theta)\sin(2\theta)\mathcal{P}(x,\theta) \ , \tag{13}$$

where we have used expression (12) for $\Gamma$ and defined $\bar{\lambda} = \mu_r\kappa\lambda/D_r$.

We will now expand the pressure $P$ as a power series in $\bar{\lambda}$. If we make the approximation $P(x_w,\theta) = \rho_0/(2\pi)$, so that the steady-state distribution relaxes to its bulk value as soon as the system is outside the range of the wall potential, we can resum the series to obtain Eq. (5) of main text.

We first expand the probability distribution $\mathcal{P}(x,\theta)$ in powers of $\bar{\lambda}$

$$\mathcal{P}(x,\theta) = \sum_{k=0}^{\infty} \bar{\lambda}^k \mathcal{P}_k(x,\theta) \ , \tag{14}$$

so that the pressure is given by

$$P = \frac{v^2}{2\mu_t D_r}\rho_0 - C = \frac{v^2}{2\mu_t D_r}\rho_0 - \frac{v}{\mu_t}\sum_{k=0}^{\infty} C_k \bar{\lambda}^{k+1} \ , \tag{15}$$

where

$$C_k = \int_{x_w}^{\infty} dx \int_0^{2\pi} d\theta \sin\theta\sin(2\theta)\mathcal{P}_k(x,\theta) \ . \tag{16}$$

#### 1. *Computation of the coefficients $C_k$*

$C_0$ is known since $\mathcal{P}_0 = \rho_0/2\pi$. Using the hypothesis $\mathcal{P}(x_w,\theta) = \rho_0/(2\pi)$, so that $\mathcal{P}_{k\geq 1}(x_w) = 0$, we can now relate $\mathcal{P}_k$ to $\mathcal{P}_{k-1}$ and then compute iteratively the $C_k$'s.

In steady-state, the master equation gives for $x > x_w$, order by order in $\bar{\lambda}$:

$$0 = -\partial_x(v\cos\theta\mathcal{P}_k - \frac{\mu_t D_r}{\kappa\mu_r}(x-x_w)\mathcal{P}_{k-1}) + D_r\partial_\theta^2\mathcal{P}_k - D_r\partial_\theta(\sin(2\theta)\mathcal{P}_{k-1}), \quad k \geq 1 \tag{17}$$

$$0 = -\partial_x(v\cos\theta\mathcal{P}_0) + D_r\partial_\theta^2\mathcal{P}_0 \ . \tag{18}$$

Multiplying Eq. (17) by an arbitrary function $f(\theta)$ and integrating over $\theta$ and $x$, one gets

$$\int_{x_w}^{\infty} dx \int_0^{2\pi} d\theta f''\mathcal{P}_k = -\int_{x_w}^{\infty} dx \int_0^{2\pi} d\theta f' \sin(2\theta)\mathcal{P}_{k-1}, \quad k \geq 1 \tag{19}$$

$$\int_{x_w}^{\infty} dx \int_0^{2\pi} d\theta f''\mathcal{P}_0 = -\frac{1}{D_r}\int_0^{2\pi} d\theta v\cos\theta f\mathcal{P}_0(x_w,\theta) = -\frac{v\rho_0}{2\pi D_r}\int d\theta\cos\theta f \ . \tag{20}$$

For conciseness, we define the operators $T$ and $T^*$

$$T(f) = \sin(2\theta)\int d\theta f \quad , \qquad T^*(f) = \cos\theta\int d\theta\int d\theta f \ , \tag{21}$$

where the integral signs refer to indefinite integrals, to rewrite Eqs. (19-20) as

$$\int_{x_w}^{\infty} dx \int_0^{2\pi} d\theta g(\theta)\mathcal{P}_k = -\int_0^{\infty} dx \int_0^{2\pi} d\theta T(g(\theta))\mathcal{P}_{k-1}, \quad k \geq 1 \tag{22}$$

$$\int_{x_w}^{\infty} dx \int_0^{2\pi} d\theta g(\theta)\mathcal{P}_0 = -\frac{1}{D_r}\int_0^{2\pi} d\theta v T^*(g(\theta))\mathcal{P}_0(x_w,\theta) = -\frac{v\rho_0}{2\pi D_r}\int d\theta T^*(g(\theta)) \ , \tag{23}$$

where $g = f''$. The $C_k$'s then reduce to the explicit integrals

$$C_k = (-1)^{k+1}\frac{v\rho_0}{2\pi D_r}\int_0^{2\pi} d\theta T^* T^{k+1}(\cos\theta) \ , \tag{24}$$

where we use $\sin\theta\sin(2\theta) = T(\cos\theta)$ so that $T^k(\sin\theta\sin(2\theta)) = T^{k+1}(\cos\theta)$.

Let us now compute the $C_k$'s. By inspection, one sees that $T^k(\cos\theta)$ is of the form

$$T^k(\cos\theta) = \sum_{i=0}^{k}\alpha_i^k\cos((2i+1)\theta) \ , \tag{25}$$

where the coefficients $\alpha_i^k$ obey the recursion

$$\alpha_0^0 = 1, \qquad \alpha_{j>0}^0 = 0 \ , \tag{26}$$

$$\alpha_0^{k+1} = \frac{\alpha_0^k}{2} + \frac{\alpha_1^k}{6} \tag{27}$$

$$\alpha_i^{k+1} = \frac{1}{2}\left(\frac{\alpha_{i+1}^k}{2i+3} - \frac{\alpha_{i-1}^k}{2i-1}\right) \ , \tag{28}$$

$$\alpha_k^{k+1} = -\frac{1}{2}\frac{\alpha_{k-1}^k}{2k-1} \ , \tag{29}$$

$$\alpha_{k+1}^{k+1} = -\frac{1}{2}\frac{\alpha_k^k}{2k+1} \ , \tag{30}$$

which solution is

$$\alpha_j^k = \frac{(-1)^j}{k+1}\frac{(2j+1)}{(k+j+1)!}\prod_{i=0}^{j}(k+1-i) \ . \tag{31}$$

After the application of $T^*$ in Eq. (24), the only term that contributes to $C_k$ in $T^k(\cos\theta)$ is $\alpha_0^k = \frac{1}{(k+1)!}$, because $\int d\theta \cos\theta \cos[(2i+1)\theta] = 0$ for $i > 0$. One thus finally gets

$$C_k = (-1)^k \frac{v\rho_0}{2\pi D_r} \int_0^{2\pi} d\theta \alpha_0^{k+1} \cos^2(\theta) = (-1)^k \frac{v\rho_0}{2D_r(k+2)!} \ . \tag{32}$$

*2. Approximate expression for the pressure*

The series (15) can now be resummed to yield

$$P = \frac{v^2}{2\mu_t D_r}\rho_0 \left(1 - \sum_{k=0}^{\infty}(-1)^k \frac{\bar{\lambda}^{k+1}}{(k+2)!}\right) = P_I \frac{1-e^{-\bar{\lambda}}}{\bar{\lambda}} \ , \tag{33}$$

where $P_I$ is the ideal gas pressure. As expected, the pressure tends to $P_I$ as $\bar{\lambda} \to 0$.

As can be seen in the right panel of Fig. 1 in the main text, the approximation that the wall does not affect the probability density for $x \leq x_w$ is not satisfied when $\bar{\lambda}$ is large. However, this happens only when $P(\bar{\lambda})$ is already very small, so that the analytic formula Eq. (33) compares very well with the $P(\bar{\lambda})$ curve obtained numerically, as shown in Figure 1 of main text.

## V. NON–BOLTZMANN DISTRIBUTION

While the analytical computation of the full distribution for RTPs and ABPs in two dimensions is beyond the scope of this paper, here we show explicitly that the steady–state density is not a Boltzmann distribution for 1D RTPs. The master equation for the probability densities of right and left-movers ($\mathcal{P}_+(x,t)$ and $\mathcal{P}_-(x,t)$) is given by (see Ref. (26) of the main text)

$$\begin{aligned} \partial_t \mathcal{P}_+ &= -\partial_x \left(v - \mu_t \partial_x V\right) - \frac{\alpha}{2}\left(\mathcal{P}_+ - \mathcal{P}_-\right) \ , \\ \partial_t \mathcal{P}_- &= -\partial_x \left(-v - \mu_t \partial_x V\right) - \frac{\alpha}{2}\left(\mathcal{P}_- - \mathcal{P}_+\right) \ . \end{aligned} \tag{34}$$

Note that $D_t = 0$ for this system. The equation for the steady-state density then reads

$$\partial_x \left[\left(v^2 - \mu_t^2 (\partial_x V)^2\right)\rho\right] + \alpha\mu_t(\partial_x V)\rho = 0 \ . \tag{35}$$

First, rescale the potential so that the equation reduces to

$$\partial_x \left[\left(1 - (\partial_x \tilde{V})^2\right)\rho\right] + g(\partial_x \tilde{V})\rho = 0 \ , \tag{36}$$

with $g = \alpha/v$ and $\tilde{V} = V\mu_t/v$. The steady state distribution is then given by

$$\rho(x) = \rho_0 e^{-Q} \ , \tag{37}$$

and

$$Q = \ln[1 - (\partial_x \tilde{V}(x))^2] + \int_0^x dx' \frac{g\partial_{x'}\tilde{V}(x')}{1 - (\partial_{x'}\tilde{V}(x'))^2} \ . \tag{38}$$

The probability distribution is non-local inside the wall and not given by a Boltzmann distribution. (Note that particles are confined within the region $[0, x^*]$ where $(\partial_x \tilde{V})^2 < 1$ and $\rho(x) = 0$ outside.)

Despite the absence of a Boltzmann distribution, the pressure is well defined (as for the 2D case considered in the text). To see this explicitly in one dimension consider the expression for the pressure

$$P = \frac{v}{\mu_t}\int_0^{x^*} \partial_x V(x)\rho(x) \ , \tag{39}$$

with $\partial_x V(x^*) = 1$. Then using the explicit expression of the steady-state distribution, $P$ can be written as

$$P = -\rho_0 \frac{v}{g\mu_t}\int_0^{x^*} dx \partial_x e^{-g\int_0^x dx' \frac{\partial_{x'}V(x')}{1-(\partial_{x'}V(x'))^2}} \ , \tag{40}$$

so that

$$P = -\rho_0 \frac{v}{g\mu_t}\left(e^{-g\int_0^{x^*} dx' \frac{\partial_{x'}V(x')}{1-(\partial_{x'}V(x'))^2}} - 1\right) \ . \tag{41}$$

Now, since at the upper bound of the integral within the exponential the integrand diverges we have

$$P = \rho_0 \frac{v}{g\mu_t} = \rho_0 \frac{v^2}{\alpha\mu_t} \ . \tag{42}$$

## VI. ANISOTROPIC PRESSURE

We consider spherical particles whose speeds depend on their direction of motion $\theta$. As discussed in the main text, such situations could arise, for example, when the motion takes place on a corrugated surface. For simplicity, we consider only run–and–tumble particles ($D_r = 0$). The case of active Brownian particles can be treated following the same argument.

In steady–state, the master equation yields

$$0 = -\partial_x\left[\left(v(\theta)\cos\theta - \mu_t\partial_x V - D_t\partial_x\right)\mathcal{P}(\theta,\mathbf{x})\right] - \alpha\mathcal{P} + \frac{\alpha}{2\pi}\int d\theta'\mathcal{P}(\theta',\mathbf{x}) \ . \tag{43}$$

We want to restrict ourselves to cases where the bulk currents along any direction vanish (the system is therefore uniform in the bulk), which we achieve by assuming that $v(\theta+\pi) = v(\theta)$. Following the same steps that lead to Eq. (4) in the main text, we get in steady state

$$0 = -\partial_x(\tilde{m}_1 - \mu_t\rho\partial_x V - D_t\partial_x\rho) \ , \tag{44}$$

$$0 = -\partial_x\left[\int_0^{2\pi} v(\theta)^2\cos^2(\theta)\mathcal{P}d\theta - \mu_t\partial_x V\tilde{m}_1 - D_t\partial_x\tilde{m}_1\right] - \alpha\tilde{m}_1 \ , \tag{45}$$

where we have defined $\tilde{m}_1 = \int_0^{2\pi} v(\theta)\cos(\theta)\mathcal{P}d\theta$ (which differs from $m_1$ in section III because it includes the speed).

From these two equations, we can express the mechanical pressure as a function of the bulk density and $v(\theta)$, as

$$P = \int_0^x \rho(x)\partial_x V dx = \frac{1}{\mu_t}\int_0^x(\tilde{m}_1 - D_t\partial_x\rho) = \left(\frac{D_t}{\mu_t} + \frac{\int_0^{2\pi} d\theta v^2(\theta)\cos^2(\theta)}{2\pi\alpha\mu_t}\right)\rho_0 \ . \tag{46}$$

This holds for a wall perpendicular to the $\hat{x}$ axis. For a wall tilted by an angle $\phi$, one obtains the anisotropic pressure

$$P(\phi) = \left( \frac{D_t}{\mu_t} + \frac{\int_0^{2\pi} d\theta v^2(\theta) \cos^2(\theta - \phi)}{2\pi\alpha\mu_t} \right) \rho_0 \ , \tag{47}$$

which is Eq. (9) of the main text.

## VII. INTERACTING ACTIVE BROWNIAN PARTICLES

In the following we study ABPs with aligning interactions (Section VII A) and quorum-sensing interactions (Section VII B). In particular, we derive exact expressions for the pressure $P$ in terms of microscopic correlators evaluated near the wall. These show $P$ to depend explicitly on the details of the interaction with the wall, hence forbidding the existence of equations of state.

### A. Aligning particles

We consider a system of $N$ spherical ABPs which can exert torque on each other, for instance to promote the alignment of their directions of motion, but which do not feel any wall-torque. The positions and orientations of the particles evolve according to the Itō-Langevin equations

$$\frac{d\mathbf{r}_i}{dt} = \mathbf{v} - \mu_t \partial_x V + \sqrt{2D_t}\eta_i(t) \tag{48}$$

$$\frac{d\theta_i}{dt} = \mu_r \sum_j F(\theta_j - \theta_i, \mathbf{r}_i, \mathbf{r}_j) + \sqrt{2D_r}\xi_i(t) \tag{49}$$

where $\eta_i$ and $\xi_i$ are uncorrelated Gaussian white noises of unit variance and appropriate dimensionality. $F(\theta_j - \theta_i, \mathbf{r}_i, \mathbf{r}_j)$ is the torque exerted by particle $j$ on particle $i$.

We now define a microscopic density field $\mathcal{P}(\mathbf{r}, \theta)$ as

$$\mathcal{P}(\mathbf{r}, \theta) = \sum_{i=1}^{N} \delta(\mathbf{r} - \mathbf{r}_i)\delta(\theta - \theta_i) \tag{50}$$

Following [1], its evolution equation is given by

$$\begin{aligned} \partial_t \mathcal{P}(\mathbf{r}, \theta) = &-\nabla\cdot[(\mathbf{v} - \mu_t \nabla V(x))\mathcal{P}(\mathbf{r}, \theta) - D_t \nabla \mathcal{P}(\mathbf{r}, \theta)] + \nabla \cdot \left( \sqrt{2D_t \mathcal{P}}\eta \right) + \partial_\theta \left( \sqrt{2D_r \mathcal{P}}\xi \right) \\ &- \partial_\theta \left[ \mu_r \int dr' \int_0^{2\pi} d\theta' F(\theta' - \theta, \mathbf{r}, \mathbf{r}')\mathcal{P}(\mathbf{r}, \theta)\mathcal{P}(\mathbf{r}', \theta') \right] + D_r \partial_\theta^2 \mathcal{P}(\mathbf{r}, \theta) \end{aligned} \tag{51}$$

where the integral $\int d\mathbf{r}'$ is performed over all space.

We then follow the same reasoning as for non-interacting particles to derive an expression for the pressure. We first average Eq. (51) in steady-state, assuming translational invariance along $y$, to get

$$\begin{aligned} 0 = &-\partial_x[(\mathbf{v} - \mu_t \partial_x V(x))\langle \mathcal{P} \rangle - D_t \partial_x \langle \mathcal{P} \rangle] - \partial_\theta \left[ \mu_r \int dr' \int_0^{2\pi} d\theta' F(\theta' - \theta, \mathbf{r}, \mathbf{r}')\langle \mathcal{P}(\mathbf{r}, \theta)\mathcal{P}(\mathbf{r}', \theta') \rangle \right] \\ &+ D_r \partial_\theta^2 \langle \mathcal{P} \rangle \end{aligned} \tag{52}$$

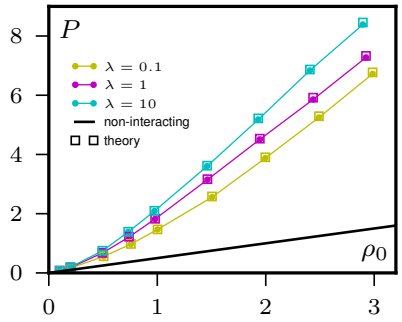


Figure 2. Lack of equation of state for ABPs with interparticle alignment interactions but no wall torques. The mechanical force per unit area $P$ exerted on the wall is equal to its theoretical expression (56) and depends on the stiffness $\lambda$ of the wall potential. The torque exerted by particle $j$ on particle $i$ is $F(\theta_j - \theta_i, \mathbf{r}_i, \mathbf{r}_j) = \frac{\gamma}{\mathcal{N}(\mathbf{r}_i)} \sin(\theta_j - \theta_i)$ if $|\mathbf{r}_j - \mathbf{r}_i| < R$ and 0 otherwise, where $\mathcal{N}(\mathbf{r}_i)$ is the number of particles interacting with particle $i$. ($v = 1$, $D_r = 1$, $D_t = 0$ and $\gamma = 2$.)

where the brackets $\langle \cdot \rangle$ denote averaging over noise realisations. Note that the noise terms average to zero due to our use of the Itō convention.

Multiplying Eq. (52) by 1 and $\cos\theta$ and then integrating over $\theta$ gives the analog of Eq. (6) and (7)

$$0 = -\partial_x[v m_1 - \mu_t \rho(\partial_x V) - D_t \partial_x \rho] \tag{53}$$

$$D_r m_1 = -\partial_x \left[ v \frac{\rho + m_2}{2} - \mu_t m_1 (\partial_x V) - D_t \partial_x m_1 \right] - \mu_r \int_0^{2\pi} \sin\theta \int dr' \int_0^{2\pi} d\theta' F(\theta' - \theta, \mathbf{r}, \mathbf{r}') \langle \mathcal{P}(\mathbf{r}, \theta) \mathcal{P}(\mathbf{r}', \theta') \rangle \tag{54}$$

where $m_n(x) = \int_0^{2\pi} \cos(n\theta) \langle \mathcal{P}(x, \theta) \rangle d\theta$ and $\rho(x) = \int_0^{2\pi} \langle \mathcal{P}(x, \theta) \rangle d\theta$.

Inserting Eq. (54) in Eq. (53) allows us to rewrite the pressure $P = \int_0^\infty dx \rho \partial_x V$ exactly as

$$P = \left[ \frac{v^2}{2\mu_t D_r} + \frac{D_t}{\mu_t} \right] \rho_0 - \frac{v\mu_r}{\mu_t D_r} \int_0^\infty dx \int_{-\infty}^\infty dy \int_0^{2\pi} d\theta \int d\mathbf{r}' \int_0^{2\pi} d\theta' F(\theta' - \theta, \mathbf{r}, \mathbf{r}') \sin\theta \langle \mathcal{P}(\mathbf{r}, \theta) \mathcal{P}(\mathbf{r}', \theta') \rangle \tag{55}$$

We see that, just as in Eq. (4) in main text, the mechanical pressure depends explicitly on the density $\mathcal{P}(\mathbf{r}, \theta)$ close to the wall, which in turn depends on the detail of the interaction $V(x)$ between the particles and the wall. There is thus no equation of state.

Using the microscopic definition of $\mathcal{P}$, Eq. (50), one can rewrite the integral in Eq. (55) as a sum over all particles, more suitable to numerical measurements:

$$P = \left[ \frac{v^2}{2\mu_t D_r} + \frac{D_t}{\mu_t} \right] \rho_0 - \frac{v\mu_r}{\mu_t D_r} \langle \sum_{i,j=1}^{N} F(\theta_j - \theta_i, \mathbf{r}_i, \mathbf{r}_j) \sin\theta_i \Theta(x_i) \rangle \tag{56}$$

where $\Theta(x_i) = 1$ if $x_i > 0$ and zero otherwise. In Fig. 2, we compare measurements of $P$ from the force applied on the confining wall and from Eq. (56), for a particular choice of $F$. They show perfect agreement, thus confirming Eq. (55).

### B. Quorum-sensing interactions

A similar path can be followed to compute the pressure exerted by ABPs that adapt their swim speed to the local density computed through a coarse-graining kernel $\bar{\rho}(\mathbf{r}) = \sum_i K(|\mathbf{r} - \mathbf{r}_i|)$, where the sum runs over all particles. The dynamics of the system is now given by the Itō-Langevin equations

$$\frac{d\mathbf{r}_i}{dt} = v(\bar{\rho})\mathbf{e}_i - \mu_t \partial_x V + \sqrt{2D_t}\eta_i(t) \tag{57}$$

$$\frac{d\theta_i}{dt} = \sqrt{2D_r}\xi_i(t) \tag{58}$$

As before, the dynamics of the density field can be obtained using Itō calculus [1]

$$\begin{aligned}\partial_t \mathcal{P}(\mathbf{r},\theta) = &-\nabla\cdot[(v(\bar{\rho})\mathbf{e}_\theta - \mu_t\nabla V(x))\mathcal{P}(\mathbf{r},\theta) - D_t\nabla\mathcal{P}(\mathbf{r},\theta)] + D_r\partial_\theta^2\mathcal{P}(\mathbf{r},\theta)\\ &+\nabla\cdot\left(\sqrt{2D_t\mathcal{P}}\eta\right) + \partial_\theta\left(\sqrt{2D_r\mathcal{P}}\xi\right)\end{aligned} \tag{59}$$

By the same procedure as for aligning particles (except that we first multiply Eq. (59) by $v(\bar{\rho})$ for the second equation) we get the two relations

$$0 = -\partial_x[\langle v(\bar{\rho})\hat{m}_1\rangle - \mu_t\rho(\partial_x V) - D_t\partial_x\rho] \tag{60}$$

$$D_r\langle v(\bar{\rho})\hat{m}_1\rangle = -\left\langle v(\bar{\rho})\partial_x\left[v(\bar{\rho})\frac{\hat{\rho}+\hat{m}_2}{2} - \mu_t\hat{m}_1(\partial_x V) - D_t\partial_x\hat{m}_1\right]\right\rangle \tag{61}$$

where $\hat{m}_n(x) = \int_0^{2\pi}\cos(n\theta)\mathcal{P}(x,\theta)d\theta$ and $\hat{\rho}(x) = \int_0^{2\pi}\mathcal{P}(x,\theta)d\theta$ are fluctuating quantities whose averages are $m_n$ and $\rho$.

We can now rewrite the pressure using these two equalities:

$$P = \int_0^\infty dx\rho\partial_x V = \frac{1}{\mu_t}\int_0^\infty dx\,[\langle v(\bar{\rho})\hat{m}_1\rangle - D_t\partial_x\rho] \tag{62}$$

$$= \frac{D_t}{\mu_t}\rho_0 - \frac{1}{D_r\mu_t}\int_0^\infty dx\left\langle v(\bar{\rho})\partial_x\left[v(\bar{\rho})\frac{\hat{\rho}+\hat{m}_2}{2} - \mu_t\hat{m}_1(\partial_x V) - D_t\partial_x\hat{m}_1\right]\right\rangle \tag{63}$$

Integrating by part the last integral, we obtain

$$\begin{aligned}P =& \frac{\langle v(\bar{\rho})^2(\hat{\rho}+\hat{m}_2)\rangle_0}{2\mu_t D_r} - \frac{D_t\langle v(\bar{\rho})\partial_x\hat{m}_1)\rangle_0}{\mu_t D_r} + \frac{D_t}{\mu_t}\rho_0\\ &+\frac{1}{D_r\mu_t}\int_0^\infty dx\left\langle\partial_x v(\bar{\rho})\left[v(\bar{\rho})\frac{\hat{\rho}+\hat{m}_2}{2} - \mu_t\hat{m}_1(\partial_x V) - D_t\partial_x\hat{m}_1\right]\right\rangle\end{aligned} \tag{64}$$

where the brackets $\langle\cdot\rangle_0$ denote an average done in the bulk of the system.

As for aligning particles, one can use Eq. (50) to obtain a "microscopic expression" for $P$ which is more suitable for numerical evaluation:

$$\begin{aligned}P =& \frac{D_t}{\mu_t}\rho_0 + \sum_{i=1}^N\left(\frac{\langle v(\bar{\rho}_i)^2(1+\cos(2\theta_i))\rangle_0}{2\mu_t D_r} + \frac{2D_t\langle\partial_{x_i}v(\bar{\rho}_i)\cos\theta_i\rangle_0}{\mu_t D_r}\right)\\ &+\sum_{i=1}^N\Theta(x_i)\frac{1}{D_r\mu_t}\left\langle\partial_{x_i}v(\bar{\rho}_i)\left[v(\bar{\rho}_i)\frac{1+\cos(2\theta_i)}{2} - \mu_t\cos\theta_i(\partial_x V)\right] + D_t(\partial_{x_i}^2 v(\bar{\rho}_i))\cos\theta_i\right\rangle\end{aligned} \tag{65}$$

Here, for ease of notation, we have written $\bar{\rho}_i = \bar{\rho}(\mathbf{r}_i)$. Again this exact formula shows that no equation of state relates the mechanical pressure to bulk properties of the system.

---

[1] Farrell, F. D. C., Tailleur, J., Marenduzzo D. and Marchetti M. C. , Pattern formation in self-propelled particles with density-dependent motility, Phys. Rev. Lett. **108**, 248101 (2012)

## 3.2 Gaz parfait pour différentes dynamiques

La fait que la pression mécanique d'un gaz parfait de particules actives satisfasse une équation d'état peut paraître surprenant. En effet, la pression est toujours donnée par la loi du gaz parfait à la température $T_{\text{eff}}$ même dans le régime où le concept de température effective n'est plus valable, *i.e.* pour un mur très confinant $|\mu\partial_x V| \sim v$. Pour s'assurer que ceci n'est pas une curiosité mathématique du modèle de particules à vitesse constante dans la limite suramortie, nous généralisons ici le résultat à deux autres cas. Nous considérerons tout d'abord des particules autopropulsées avec inertie, puis des particules propulsées par une force active fluctuant suivant un processus d'Ornstein-Uhlenbeck, qui ont attiré beaucoup d'attention récemment [54, 56, 113].

### 3.2.1 Particule active avec inertie

Considérons le cas d'une ABP sphérique (sur laquelle aucun couple ne s'exerce) en 2d, confinée par un potentiel $V$ et propulsée par une force active $F_a$ constante. La dynamique d'une telle particule s'écrit

$$\dot{\mathbf{r}} = \mathbf{v} \tag{3.3}$$

$$m\dot{\mathbf{v}} = -\gamma\mathbf{v} + F_a\mathbf{u} - \nabla V + \sqrt{2D_v}\boldsymbol{\eta} \tag{3.4}$$

$$\dot{\theta} = \sqrt{2D_r}\xi \tag{3.5}$$

où $\mathbf{u} = (\cos\theta, \sin\theta)$ est la direction d'autopropulsion et $\boldsymbol{\eta}$ et $\xi$ sont des bruits blancs gaussiens de dimension appropriée. L'équation de Fokker-Planck associée s'écrit

$$\partial_t\mathcal{P}(\mathbf{r},\mathbf{v},\theta) = -\nabla_{\mathbf{r}}\cdot[\mathbf{v}\mathcal{P}] - \nabla_{\mathbf{v}}\cdot\left[\left(-\frac{\gamma}{m}\mathbf{v} + \frac{F_a}{m}\mathbf{u} - \frac{\nabla V}{m}\right)\mathcal{P}\right] + \frac{D_v}{m^2}\Delta_{\mathbf{v}}\mathcal{P} + D_r\partial_\theta^2\mathcal{P} \tag{3.6}$$

Comme dans l'article B, on considère un système confiné suivant $\hat{\mathbf{x}}$ et infini suivant $\hat{\mathbf{y}}$. Dans l'état stationnaire, $\mathcal{P}$ est donc invariante suivant $y$. On peut alors remplacer $\nabla_{\mathbf{r}}\cdot[\mathbf{v}\mathcal{P}]$ par $\partial_x[v_x\mathcal{P}]$ et intégrer l'équation (3.6) sur $y$ et $v_y$. On obtient

$$0 = -\partial_x[v_x\mathcal{P}] - \partial_{v_x}\left[\left(-\frac{\gamma}{m}v_x + \frac{F_a}{m}\cos\theta - \frac{\partial_x V}{m}\right)\mathcal{P}\right] + \frac{D_v}{m^2}\partial_{v_x}^2\mathcal{P} + D_r\partial_\theta^2\mathcal{P} \tag{3.7}$$

où, de manière abusive, $\mathcal{P}(x,v_x,\theta) = \int dy \int dv_y \mathcal{P}(\mathbf{r},\mathbf{v},\theta)$.

On notera dans la suite pour une observable $O$

$$\langle O\rangle(x) = \int_{-\infty}^{+\infty} dv_x \int_0^{2\pi} d\theta O(x,v_x,\theta)\mathcal{P}(x,v_x,\theta) \tag{3.8}$$

où $\mathcal{P}(x,v_x,\theta)$ est la distribution stationnaire. Intégrer l'équation (3.7) suivant $v_x$ et $\theta$ donne

$$0 = -\partial_x \langle v_x \rangle \tag{3.9}$$

qui traduit un flux de particules $J = \langle v_x \rangle$ constant. Pour un système confiné suivant $\hat{x}$, on a donc $\langle v_x \rangle(x) = 0$ pour tout $x$. Multiplier l'équation (3.7) par $v_x$ et intégrer suivant $v_x$ et $\theta$ donne

$$0 = -\partial_x \langle v_x^2 \rangle + \left\langle -\frac{\gamma}{m} v_x + \frac{F_a}{m} \cos\theta - \frac{\partial_x V}{m} \right\rangle \tag{3.10}$$

où l'on a utilisé une intégration par partie pour obtenir le dernier terme. Comme montré ci-dessus, le terme $\langle \frac{\gamma}{m} v_x \rangle$ est nul. On peut alors utiliser l'équation (3.10) pour réécrire la pression

$$P = \int_0^\infty \langle \partial_x V \rangle = m \langle v_x^2 \rangle_0 + \int_0^\infty \langle F_a \cos\theta \rangle \tag{3.11}$$

où $\langle \cdot \rangle_0$ dénote une moyenne dans le coeur du système, en $x = 0$. Multiplier l'équation (3.7) par $\theta$ et intégrer suivant $v_x$ et $\theta$ donne

$$0 = -\partial_x \langle v_x \cos\theta \rangle - D_r \langle \cos\theta \rangle \tag{3.12}$$

de sorte que la pression s'écrit comme une quantité calculée dans le coeur du système

$$P = m \langle v_x^2 \rangle_0 + \frac{F_a}{D_r} \langle v_x \cos\theta \rangle_0 \tag{3.13}$$

L'équation (3.13) constitue d'ores et déjà une équation d'état qui relie la pression mécanique à des quantités physiques calculées dans le coeur du système, ne dépendant pas des interactions avec les parois.

On peut aller plus loin en utilisant le calcul d'Itō pour exprimer les moyennes de l'équation (3.13). On trouve

$$\partial_t \langle v_x^2 \rangle = \langle 2 v_x \dot{v}_x + \frac{2 D_v}{m^2} \rangle \tag{3.14}$$

$$= -\frac{2\gamma}{m} \langle v_x^2 \rangle + \frac{2 F_a}{m} \langle v_x \cos\theta \rangle + \langle \frac{2 D_v}{m^2} \rangle \tag{3.15}$$

où les moyennes sont ici sur les réalisations des bruits $\boldsymbol{\eta}$ et $\xi$. On a également

$$\partial_t \langle v_x \cos\theta \rangle = \langle \dot{v}_x \cos\theta - v \dot{\theta} \sin\theta - D_r v_x \cos\theta \rangle \tag{3.16}$$

$$= -\frac{\gamma}{m} \langle v_x \cos\theta \rangle + \frac{F_a}{m} \langle \cos^2\theta \rangle - D_r \langle v_x \cos\theta \rangle \tag{3.17}$$

On utilise ensuite $\cos^2\theta = \frac{1}{2}(1+\cos 2\theta)$ et $\langle \cos 2\theta \rangle_0 = 0$, cette dernière égalité venant du fait que la distribution angulaire est uniforme dans le coeur du système, par symétrie. Les équations (3.15) et (3.17) donnent alors

$$\langle v_x \cos\theta \rangle_0 = \frac{F_a}{2m(D_r+\gamma/m)}\rho_0, \qquad \langle v_x^2 \rangle_0 = \left[\frac{D_v}{\gamma m} + \frac{F_a^2}{2\gamma m(D_r+\gamma/m)}\right]\rho_0 \quad (3.18)$$

où l'on a noté $\rho_0 = \langle 1 \rangle_0$ la densité dans le coeur du système.

Définissons $D_t = D_v/\gamma^2$, $v = F_a/\gamma$ et $\mu_t = 1/\gamma$. En reprenant l'équation (3.13), on trouve pour la pression

$$P = \left[\frac{D_v}{\gamma} + \frac{F_a^2}{2D_r\gamma}\right]\rho_0 = \left[\frac{D_t}{\mu_t} + \frac{v^2}{2\mu_t D_r}\right]\rho_0 \quad (3.19)$$

qui est exactement le résultat donné dans l'article B pour la dynamique suramortie.

### 3.2.2 Mouvement brownien corrélé

On considère maintenant une particule propulsée par un processus d'Ornstein-Uhlenbeck, toujours dans la géométrie de la figure 3.1. La position de la particule est donnée par les équations de Langevin

$$\dot{\mathbf{r}} = \mu(\mathbf{f} - \nabla V) \qquad \tau\dot{\mathbf{f}} = -\mathbf{f} + \sqrt{2D_f}\boldsymbol{\eta} \quad (3.20)$$

où $\boldsymbol{\eta}$ est un bruit blanc gaussien. L'équation de Fokker-Planck associée s'écrit

$$\partial_t \mathcal{P}(\mathbf{r},\mathbf{f},t) = -\nabla\cdot[\mu(\mathbf{f}-\nabla V)\mathcal{P}] + \nabla_{\mathbf{f}}\cdot\left[\frac{\mathbf{f}}{\tau}\mathcal{P}\right] + \frac{D_f}{\tau^2}\Delta_{\mathbf{f}}\mathcal{P} \quad (3.21)$$

Comme précédemment, la distribution stationnaire est invariante suivant $y$ et on peut intégrer l'équation (3.21) suivant $y$ et $f_y$. La distribution stationnaire est alors donnée par

$$0 = -\partial_x\left[\mu(f_x - \partial_x V)\mathcal{P}\right] + \partial_{f_x}\left[\frac{f_x}{\tau}\mathcal{P}\right] + \frac{D_f}{\tau^2}\partial_{f_x}^2\mathcal{P} \quad (3.22)$$

où $\mathcal{P} = \mathcal{P}(x,f_x)$ est la distribution stationnaire moyennée sur $y$ et $f_y$.

On note pour une observable $O$

$$\langle O \rangle(x) = \int_{-\infty}^{+\infty} df_x O(x,f_x)\mathcal{P}(x,v_x) \quad (3.23)$$

Intégrer l'équation (3.22) sur $f_x$ donne alors

$$0 = -\partial_x\left[\mu\langle f_x\rangle - \mu\langle\partial_x V\rangle\right], \quad \text{pour tout } x \quad (3.24)$$

et donc, pour une particule confinée, $\langle \partial_x V \rangle = \langle f_x \rangle$. La pression se réécrit alors

$$P = \int_0^{+\infty} \langle \partial_x V \rangle dx = \int_0^{+\infty} \langle f_x \rangle dx \tag{3.25}$$

On peut calculer $\langle f_x \rangle$ en multipliant l'équation (3.22) par $f_x$ et en intégrant suivant $f_x$. On trouve

$$0 = -\partial_x \left[ \mu \langle f_x^2 \rangle - \mu \langle f_x \partial_x V \rangle \right] - \left\langle \frac{f_x}{\tau} \right\rangle \tag{3.26}$$

où le dernier terme est obtenu par intégration par partie. La pression s'écrit alors comme une moyenne dans le coeur du système, notée $\langle \cdot \rangle_0$

$$P = \int_0^{+\infty} -\tau \partial_x \left[ \mu \langle f_x^2 \rangle - \mu \langle f_x \partial_x V \rangle \right] = \mu \tau \langle f_x^2 \rangle_0 \tag{3.27}$$

car $\partial_x V = 0$ dans le coeur du système.

On peut finalement utiliser le calcul d'Itō pour obtenir $\langle f_x^2 \rangle_0$. De l'équation (3.20) on déduit

$$\frac{d\langle f^2(t) \rangle}{dt} = \langle 2 f \dot{f} \rangle + \langle \frac{2D_f}{\tau^2} \rangle = -\frac{2}{\tau} \langle f^2 \rangle + \frac{2D_f}{\tau^2} \rho_0 \tag{3.28}$$

Dans l'état stationnaire on a donc $\langle f^2 \rangle = D_f \rho_0 / \tau$ et la pression s'écrit

$$P = \mu \tau \langle f_x^2 \rangle_0 = \mu D_f \rho_0 \tag{3.29}$$

La pression est donc bien donnée par une loi du gaz parfait. C'est la quantité $D_f$ qui fixe la température effective $k_B T_{\text{eff}} = \mu D_f$.

## 3.3 Pression et bilan détaillé

Nous voulons mettre ici en évidence une différence entre les deux définitions d'un système à l'équilibre : satisfaire le bilan détaillé ou être décrit par une distribution de Boltzmann. La définition par le bilan détaillé est beaucoup plus faible car elle ne dit rien sur les propriétés mécaniques du système, en particulier sur la pression.

Prenons un exemple concret. Dans [57], Tailleur et Cates ont montré que des RTP en 1d se déplaçant à une vitesse $v(\rho)$, où $\rho$ est la densité locale, satisfont le bilan détaillé sur une échelle de temps grande devant le temps de persistance d'une particule. Le champ de densité est alors décrit par l'équation

$$\partial_t \rho(x,t) = \nabla \cdot \left[ \rho D(\rho) \nabla \frac{\delta \mathcal{F}}{\delta \rho} + \sqrt{2\rho D(\rho)} \boldsymbol{\eta} \right] \tag{3.30}$$

où $\boldsymbol{\eta}$ est un bruit blanc gaussien satisfaisant $\langle \eta_i(x,t)\eta_j(x',t')\rangle = \delta_{ij}\delta(x-x')\delta(t-t')$ et $D(\rho) = v(\rho)^2/(2\alpha)$. La probabilité d'observer un certain champ de densité est donnée par une énergie libre effective $\mathcal{P}(\rho) \propto e^{-\mathcal{F}[\rho]}$, différente de la distribution de Boltzmann,

$$\mathcal{F}[\rho] = \int_{-\infty}^{+\infty} dx f(\rho(x)), \qquad f(\rho) = \rho(\log\rho - 1) + \int_0^\rho \log v(u) du \tag{3.31}$$

On peut de plus confiner les particules dans un potentiel $V$ et regarder la pression qu'elles exercent sur ce potentiel. On négligera le bruit pour s'intéresser à l'évolution déterministe

$$\partial_t \rho(x,t) = \nabla \cdot \left[ \rho D(\rho) \nabla \frac{\delta \mathcal{F}}{\delta \rho} + \mu \rho \nabla V \right] = -\nabla \cdot J \tag{3.32}$$

Notons qu'il n'est pas clair qu'en présence du potentiel $V$, le système satisfasse toujours le bilan détaillé. Le courant $J$ s'annule dans l'état stationnaire et on peut alors réécrire la pression

$$P = \int_0^{+\infty} \rho(x) \nabla V dx = -\frac{1}{\mu} \int_0^{+\infty} \rho D(\rho) \nabla \frac{\delta \mathcal{F}}{\delta \rho} dx \tag{3.33}$$

L'intégration peut être menée à bien explicitement en utilisant $\nabla \frac{\delta \mathcal{F}}{\delta \rho} = \nabla f'(\rho) = f''(\rho)\nabla\rho$. Définissons $g(\rho)$ telle que $g'(\rho) = \rho D(\rho) f''(\rho)$. La pression s'écrit alors

$$P = -\frac{1}{\mu} \int_0^{+\infty} \nabla g(\rho) dx = \frac{g(\rho_0)}{\mu} \tag{3.34}$$

où $\rho_0$ est la densité dans le coeur du système. On voit donc que la pression est donnée par une équation d'état mais n'est pas reliée de la façon habituelle à l'énergie libre effective $\mathcal{F}$.

Toutefois, l'existence d'une équation d'état dans ce système est fragile. En effet, si l'on complète l'énergie libre par un terme de tension de surface

$$\mathcal{F}[\rho] = \int_{-\infty}^{+\infty} f[\rho(x)] + \frac{c}{2} |\nabla\rho|^2 dx, \tag{3.35}$$

l'équation (3.33) est inchangée et la pression s'écrit maintenant

$$P = \frac{g(\rho_0)}{\mu} + \frac{c}{\mu} \int_0^{\infty} \rho D(\rho) \nabla(\Delta\rho) dx \tag{3.36}$$

Le dernier terme n'est en général pas intégrable. On retrouve alors le résultat de l'article B : la pression mécanique dépend explicitement du profil de densité proche des parois et n'est donc pas donnée par une équation d'état.

Au contraire, lorsque $D = \text{cte}$, comme c'est le cas pour le gaz parfait actif dans lequel $v = \text{cte}$, l'existence d'une équation d'état est bien plus robuste. Cela tient au fait que le potentiel peut être écrit comme une contribution supplémentaire à l'énergie libre

$$\tilde{\mathcal{F}}[\rho] = \mathcal{F}[\rho] + \int \rho(x)V(x)dx \tag{3.37}$$

C'est cette propriété, qui est naturellement vérifiée pour les systèmes décrits par une distribution de Boltzmann, qui permet de relier la pression mécanique et la pression thermodynamique. En effet, lorsque $D = \text{cte} = \mu k_B T$, l'équation (3.34) donnant la pression mécanique se réécrit

$$P = \frac{g(\rho_0)}{\mu} = k_B T \left[\rho_0 f' - f\right] \tag{3.38}$$

où $k_B T \left[\rho_0 f' - f\right]$ est l'expression habituelle de la pression thermodynamique pour des systèmes à l'équilibre thermique.

L'ajout de la tension de surface ne modifie pas ce résultat. Le dernier terme de l'équation (3.36) devient intégrable lorsque $D = \text{cte}$

$$\int_0^\infty \rho D \nabla(\Delta\rho)dx = D\left[\rho\Delta\rho - \frac{1}{2}|\nabla\rho|^2\right]_0^\infty \tag{3.39}$$

Il ne contribue donc pas à la pression mécanique d'une phase homogène.

L'existence d'une équation d'état n'est pas directement liée au fait qu'un système vérifie ou non le bilan détaillé. La propriété déterminante est de pouvoir rendre compte de l'effet d'un potentiel extérieur par une contribution additive à l'énergie libre effective, comme c'est le cas pour une distribution de Boltzmann. Toutefois, nous avons vu que parfois la pression mécanique satisfait une équation d'état alors que cette propriété n'est pas vérifiée. L'existence d'une équation d'état est alors sensible à l'ajout d'ingrédients supplémentaires (ici, la tension de surface).

# Chapitre 4

# Séparation de phase induite par la motilité

## 4.1 Introduction

Dans ce chapitre, nous nous intéresserons à une transition de phase spécifique aux systèmes actifs : la séparation de phase induite par la motilité (que l'on désignera aussi par son acronyme anglais MIPS pour *Motility-Induced Phase Separation*). Ce phénomène peut être compris de façon assez intuitive. Il requiert deux ingrédients essentiels.

Le premier ingrédient est générique pour des particules autopropulsées : celles-ci tendent à s'accumuler dans les régions où elles se déplacent le moins vite. On peut voir cela facilement en modifiant l'équation maîtresse (2.2) décrivant des ABP et des RTP pour considérer, au lieu de particules se déplaçant à vitesse constante, une vitesse d'autopropulsion $v(\mathbf{r})$ variant spatialement. Pour des particules libres, on a

$$\partial_t \mathcal{P}(\mathbf{r},\mathbf{u},t) = -\nabla \cdot [v(\mathbf{r})\mathbf{u}\mathcal{P}] - \alpha\mathcal{P} + \frac{\alpha}{\Omega}\int \mathcal{P}(\mathbf{r},\mathbf{u}',t)d\mathbf{u}' + D_r\Delta_{\mathbf{u}}\mathcal{P} \tag{4.1}$$

La distribution stationnaire est alors isotrope et satisfait $\mathcal{P} \propto 1/v(\mathbf{r})$. On a donc une accumulation dans les régions où $v(\mathbf{r})$ est faible. Au contraire, pour des particules passives à l'équilibre thermique, l'état stationnaire n'est contrôlé que par la température et ne serait pas affecté, par exemple, par une mobilité inhomogène $\mu(\mathbf{r})$.

Le second ingrédient nécessaire pour observer la MIPS est une vitesse d'autopropulsion qui dépend de la densité. Si la vitesse d'une particule décroît suffisamment rapidement lorsque la densité augmente, les deux ingrédients se combinent dans une boucle de rétroaction qui conduit à une séparation de phase entre une région dense où les particules se déplacent lentement et une région diluée où elles se déplacent vite. Un des enjeux de l'étude de la MIPS est de comprendre comment les densités de coexistence des régions denses et diluées sont fixées. La phénoménologie de cette séparation de phase est très similaire à celle d'une séparation liquide-gaz d'équilibre, qui survient par exemple dans un fluide de Lennard-Jones. On est donc tenté de généraliser les relations de la thermodynamique d'équilibre qui fixent les densités de coexistence par la construction d'une « tangente commune » sur l'énergie libre ou, de façon équivalente, par la construction de Maxwell d'« aires égales » sur la pression thermodynamique. Bien sûr, la possibilité de construire les analogues de l'énergie libre et de la pression est une question complètement ouverte dès lors que l'on considère des systèmes hors d'équilibre.

La simplicité du mécanisme à l'origine de la MIPS est telle que celle-ci se rencontre dans de nombreux contextes. Nous considérerons dans ce chapitre deux façons d'obtenir une vitesse dépendant de la densité, qui correspondent à deux classes de systèmes que nous utiliserons pour étudier la MIPS.

### 4.1.1 Vitesse dépendant de la densité $v(\rho)$

La manière la plus évidente est d'imposer explicitement une vitesse d'autopropulsion $v(\rho)$ aux particules. C'est une bonne description des interactions entre certaines bactéries ou cellules qui interagissent par *quorum sensing*, en adaptant leur motilité à la concentration d'une molécule qu'elles sécrètent. Ces molécules diffusent dans le milieu et se dégradent, chaque individu mesurant ainsi une concentration d'autant plus grande qu'il est entouré de nombreux congénères. Une telle interaction peut également être induite chez des bactéries par ingénierie génétique [26].

La question se pose alors de savoir comment les particules mesurent la densité locale. Dans ce chapitre, nous étudierons successivement trois cas, schématisés à la figure 4.1 : un $v(\rho)$ purement local, un $v(\tilde{\rho})$ où $\tilde{\rho}$ est la densité moyennée de façon isotrope dans un certain rayon d'interaction, et un $v(\tilde{\rho})$ où la moyenne est faite de façon asymétrique par rapport à la direction d'autopropulsion d'une particule.

$$v(\rho)\ \textit{local}$$

C'est en étudiant des particules actives dont la vitesse $v(\rho)$ dépend explicitement de la densité $\rho$ que la MIPS fut décrite pour la première fois par Tailleur et Cates [57, 101] (voir aussi [52] pour une revue récente). En particulier, ils ont pu montrer

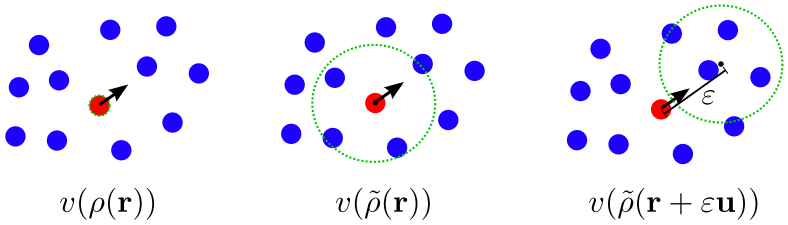


**Figure 4.1** – Les trois façons de calculer la densité au voisinage d'une particule que nous considérerons : une mesure de la densité purement locale (gauche), une moyenne isotrope dans un rayon d'interaction fini et une moyenne anisotrope effectuée à une distance $\varepsilon\mathbf{u}$ de la particule.

que pour des systèmes d'ABP ou RTP autopropulsées à une vitesse $v\left[\rho(\mathbf{r})\right]$, la probabilité d'observer un certain champ de densité $\rho(\mathbf{r})$ est donnée par une énergie libre de Landau $\mathcal{P}[\rho] \propto e^{-\mathcal{F}[\rho]}$. Le système satisfait alors le bilan détaillé par rapport à cette distribution stationnaire. Comme pour la théorie de champ moyen de la séparation liquide-gaz à l'équilibre, l'énergie libre de Landau peut s'écrire sous la forme $\mathcal{F}[\rho] = \int d\mathbf{r} f[\rho(\mathbf{r})]$. Lorsque $f(\rho)$ a une forme non-convexe, on observe une séparation de phase. On peut alors utiliser $f(\rho)$ pour prédire (toujours au niveau champ moyen) des densités de coexistence, par la construction de tangente commune.

Dans la théorie de Tailleur et Cates, l'interaction est purement locale. En effet, le champ de densité considéré est microscopique, défini formellement par

$$\rho(\mathbf{r}) = \sum_i \delta(\mathbf{r} - \mathbf{r}_i) \tag{4.2}$$

où $\mathbf{r}_i$ est la position de la particule $i$. Au niveau des équations hydrodynamiques, le rayon d'interaction nul se traduit par une absence de tension de surface. En pratique, on n'observe donc pas de *coarsening* et donc pas de séparation de phase avec ce modèle. L'interaction purement locale est donc une approximation utile dans une description continue mais ne permet pas d'observer réellement la MIPS.

De plus, il n'est pas possible d'implémenter une interaction de portée nulle dans des simulations de particules en espace continu, comme le schéma de la figure 4.1 le laisse apparaître. On peut toutefois l'implémenter sur réseau. Une particule au site $k$ se déplace dans ce cas avec une vitesse $v(\rho_k)$, où $\rho_k$ est le nombre de particules au site $k$. Le problème peut alors être résolu exactement pour des RTP [114]. L'énergie libre effective est factorisée $\mathcal{F}(\{\rho_k\}) = \sum_k f(\rho_k)$ et l'on observe une coexistence entre des sites de faible et haute densité prédite par l'énergie libre mais pas de *coarsening*, et donc pas de séparation de phase, comme illustré à la figure 4.2.

$v(\tilde{\rho})$ *isotrope*

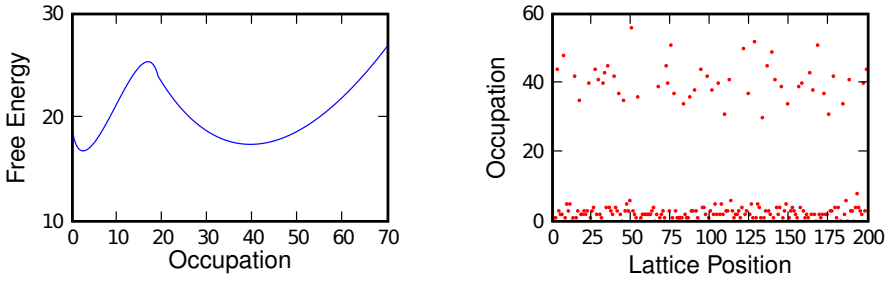


**Figure 4.2** – RTP sur un réseau 1d. Une particule au site $k$ se déplace à une vitesse $v(\rho_k)$ où $\rho_k$ dénote le nombre de particules au site $k$. **Gauche** : Énergie libre effective donnant de façon exacte la probabilité d'observer une certaine occupation $\rho_k$ sur chaque site. **Droite** : Instantané d'un système de 200 sites avec 2400 particules. Figure reproduite de [114].

Pour observer la MIPS, il faut inclure des corrélations spatiales pouvant mener à un *coarsening* et une séparation de phase. Ceci arrive naturellement lorsque l'on considère un rayon d'interaction non nul. Nous montrerons comment ceci induit l'apparition d'une tension de surface effective au niveau de l'hydrodynamique fluctuante.

Dans un premier temps, nous considérerons une densité $\tilde{\rho}$ mesurée de façon isotrope dans un rayon d'interaction $r_0$. On utilise pour ce faire une convolution entre un noyau $K(\mathbf{r})$, qui s'annule pour $|\mathbf{r}| > r_0$, et la densité microscopique $\rho(\mathbf{r})$

$$\tilde{\rho}(\mathbf{r}) = \int d\mathbf{r}' K(\mathbf{r}' - \mathbf{r})\rho(\mathbf{r}') = \sum_i K(\mathbf{r}_i - \mathbf{r}) \tag{4.3}$$

où la dernière égalité est obtenue en utilisant la définition de la densité microscopique, équation (4.2). Une particule à la position $\mathbf{r}$ se déplace alors à une vitesse $v(\tilde{\rho})$.

Concrètement, pour des bactéries interagissant par *quorum sensing*, le rôle du moyennage par le noyau $K$ est joué par la diffusion dans le milieu extérieur de la molécule qui sert d'intermédiaire pour la mesure de densité. Le rayon d'interaction est alors fixé par le coefficient de diffusion et le temps de vie de cette molécule.

Nous verrons que, par rapport au cas $v(\rho)$ local, le moyennage isotrope se traduit par une tension de surface dépendant de la densité. À l'équilibre, la tension de surface apparaît comme une contribution à l'énergie libre $\mathcal{F}_s = \int (c/2)|\nabla\rho|^2 d\mathbf{r}$. Elle contrôle alors la forme des interfaces pour un système séparé en deux phases, mais ne joue pas de rôle dans la sélection des densités de coexistence. Au contraire, nous verrons que dans notre cas la tension de surface ne peut pas être écrite comme un terme supplémentaire dans l'énergie libre, et nous devrons donc étudier ses effets sur la coexistence de phase.

### *$v(\tilde{\rho})$ asymétrique*

Nous étudierons finalement le cas où la mesure de la densité est anisotrope, dépendant de la direction de déplacement des particules. Plus particulièrement, nous considérerons que la moyenne est effectuée à une distance $\varepsilon\mathbf{u}$ de la particule (où $\mathbf{u}$ est la direction d'autopropulsion). Les particules se déplacent alors à une vitesse $v(\tilde{\rho}(\mathbf{r}+\varepsilon\mathbf{u}))$ (voir figure 4.1).

Il est assez naturel de considérer cette situation pour des particules actives. Par exemple, pour mesurer la densité d'une molécule dans le milieu, une bactérie réalise une moyenne temporelle le long de sa trajectoire. En première approximation, on peut donc considérer qu'une bactérie mesure la densité « derrière elle », la densité à l'avant n'ayant pas encore été échantillonnée. Au contraire, les sphères dures autopropulsées, que nous abordons au prochain paragraphe, interagissent par des collisions qui sont en majorité frontales. On peut donc essayer de modéliser cette situation par une densité mesurée à l'avant des particules.

## 4.1.2 Sphères dures autopropulsées

La MIPS a également été étudiée intensivement ces dernières années dans des systèmes composés de particules ABP avec des interactions de coeur dur [58–65]. Pour ces systèmes, ce sont les collisions entre particules qui, de façon indirecte, entraînent une diminution de la vitesse lorsque la densité augmente. En effet, dans la limite suramortie, deux particules actives entrant en collision frontale restent en contact jusqu'à ce qu'elles se soient réorientées pour repartir dans des directions différentes. Cet effet peut être quantifié, par exemple en mesurant la fonction de corrélation à deux points centrée sur une particule : la probabilité de trouver une particule devant soi (dans la direction de déplacement) est plus élevée que derrière [61]. On observe alors, à vitesse et densité suffisantes, une séparation de phase entre un gaz dilué et un liquide dense. Comme pour les particules nageant à une vitesse $v(\tilde{\rho})$, les deux phases sont désordonnées, les interactions stériques entre sphères ne produisant pas d'alignement.

Pour étudier analytiquement ces systèmes de sphères dures autopropulsées, on peut tenter de les modéliser comme des particules ponctuelles se déplaçant à une vitesse $v(\tilde{\rho})$. Ainsi, la vitesse effective des sphères dures, fonction de la densité, a été mesurée en simulation [58, 62]. En première approximation, elle décroît linéairement avec la densité $v(\rho) = v_0(1-\rho/\rho_0)$ où $\rho_0$ est une constante ne dépendant pas de $v_0$, la vitesse d'autopropulsion des sphères dures. On peut alors comparer un système de sphères dures autopropulsées et un système de particules ponctuelles se déplaçant à la vitesse $v(\rho)$. Les deux conduisent à la même dynamique de *coarsening* et présentent qualitativement la même séparation de phase (voir figure 4.3). Cependant, les densités de coexistence diffèrent significativement [62].

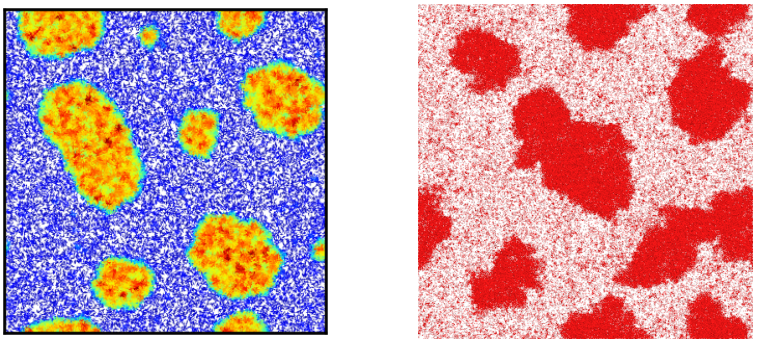

**Figure 4.3** – Exemples de MIPS pendant la phase de coarsening. **Gauche** : Pour des RTP nageant à une vitesse $v(\tilde{\rho})$ où $\tilde{\rho}$ est la densité moyenne au voisinage d'une particule. Reproduite de l'article C. **Droite** : Pour des sphères dures ABP. Reproduite de [59].

En outre, le fait même de décrire les sphères dures par un $v(\tilde{\rho})$ est une approximation forte, dont la validité n'est pas évidente. En effet, les deux systèmes présentent des différences importantes. Par exemple, comme nous l'avons montré au chapitre précédent, la pression mécanique d'un fluide de sphères dures ABP satisfait une équation d'état, contrairement à celle des systèmes avec $v(\tilde{\rho})$. De façon surprenante, c'est pourtant l'étude de la pression mécanique des sphères dures qui nous permettra, dans l'article D, de montrer rigoureusement qu'un lien existe entre les deux types de systèmes.

### 4.1.3 Expérimentalement

La MIPS est engendrée par un mécanisme relativement simple et a été observée dans de nombreuses études numériques. Cependant, les observations expérimentales sont moins nombreuses. En particulier, les colloïdes autopropulsés, qui sont la réalisation expérimentale la plus directe des sphères dures ABP, ne présentent pas toujours une séparation de phase [35, 37]. Ceux-ci forment souvent, au contraire, des agrégats ayant une taille caractéristique finie qui se cassent et se reforment continûment. L'absence de séparation de phase complète dans ces systèmes pourrait être due au fait qu'à faible densité, l'effet de l'autopropulsion serait de casser une séparation de phase induite par des interactions attractives plutôt que de la favoriser [115, 116]. Ce n'est qu'à plus haute densité, dans des régimes qui ne sont pas étudiés dans [35, 37], que la séparation de phase induite par la motilité serait observée. Cette explication est appuyée par les expériences décrites dans [117] qui montrent une transition entre des agrégats de taille finie et une séparation de phase quand la densité augmente. Les interactions hydrodynamiques peuvent également limiter la MIPS à haute densité [48, 91], en arrêtant le *coarsening* à une taille

caractéristique.

En ce qui concerne les systèmes biologiques, il est souvent difficile d'isoler un phénomène physique, comme la MIPS, des processus biochimiques complexes à l'oeuvre dans ces systèmes. La MIPS pourrait toutefois jouer un rôle dans la formation de certains agrégats cellulaires ou dans la formation de biofilms [118]. On trouve la réalisation la plus probante de MIPS chez des bactéries génétiquement modifiées pour adapter leur motilité à la concentration d'une molécule qu'elles relâchent dans le milieu [26]. Une petite colonie sphérique de ces bactéries s'étend alors en formant des anneaux concentriques dont la taille est fixée par la compétition, bien comprise [119–121], entre la MIPS et la dynamique de reproduction et de mort des bactéries.

---

Dans ce chapitre, nous aborderons en premier lieu, à la section 4.2, la théorie qui permet de décrire des particules interagissant par un $v(\rho)$ purement local. Ainsi, l'article C montrera comment construire l'hydrodynamique fluctuante et l'énergie libre effective de ces systèmes. Nous étudierons ensuite à la section 4.3 l'effet d'un $v(\tilde{\rho})$ non-local et asymétrique. Enfin, nous considérerons à la section 4.4, contenant l'article D, des sphères dures autopropulsées. Nous montrerons en particulier que l'équation d'état satisfaite par la pression mécanique permet d'expliquer en partie l'équilibre de phases de la MIPS et de relier les sphères dures aux théories en $v(\rho)$.

## 4.2 Particules avec une vitesse $v(\rho)$ : hydrodynamique fluctuante et énergie libre effective

L'article C, que nous reproduisons ici, constitue la deuxième partie de l'article A. Il présente en détail la construction de l'hydrodynamique fluctuante qui permet de décrire des ABP ou RTP interagissant par un $v(\rho)$ local. On peut diviser la démonstration en trois étapes :

1. Pour des particules se déplaçant à une vitesse $v(\mathbf{r})$ variant spatialement, un développement en harmoniques sphériques permet d'écrire, en partant de l'équation maîtresse, une équation d'advection-diffusion pour la densité de particules.
2. Remplacer la vitesse $v(\mathbf{r})$ par une dépendance indirecte $v[\rho(\mathbf{r})]$ permet alors de passer de l'équation d'advection-diffusion à une équation de Langevin décrivant des particules interagissant par un $v(\rho)$. La méthode introduite par Dean [122], généralisée au cas d'un bruit multiplicatif, permet ensuite de construire l'hydrodynamique fluctuante du champ de densité.

3. Passer de l'hydrodynamique fluctuante à l'équation de Fokker-Planck correspondante permet finalement d'écrire une condition pour l'existence d'une énergie libre effective par rapport à laquelle le système satisfait le bilan détaillé.

Les détails techniques associés à ces trois étapes sont développés dans les trois annexes de l'article, reproduites à sa suite. Cette approche, pour un $v(\rho)$ purement local, a déjà été traitée par Tailleur et Cates [57, 101], ma contribution personnelle étant limitée à l'affinement de certains points techniques. Il nous semblait toutefois important de présenter ce cas en détail ici car il constitue le point de départ pour dépasser la théorie de Landau de la transition de phase induite par la motilité, en considérant un $v(\tilde{\rho})$ non-local et asymétrique. Ces développements sont, eux, entièrement nouveaux.

La section 3.2 de l'article décrit ensuite la similarité des ABP et RTP pour la MIPS. Nous observons numériquement que pour les deux types d'interactions ($v(\rho)$ et sphères dures), les ABP et RTP ont les mêmes densités de coexistence et donc exactement le même diagramme des phases. Cela est surprenant car, les interfaces entre les phases ayant une taille de l'ordre de la longueur de persistance d'une particule, on s'attendrait à ce que la dynamique microscopique des particules soit importante. Nous verrons à la section suivante que cette observation peut s'expliquer pour les particules avec $v(\rho)$.

**EPJ manuscript No.**
(will be inserted by the editor)

# Active Brownian Particles and Run-and-Tumble Particles: a Comparative Study

A. P. Solon[1], M. E. Cates[2], J. Tailleur[1]
[1] Univ Paris Diderot, Sorbonne Paris Cité, MSC, UMR 7057 CNRS, F75205 Paris, France
[2] SUPA, School of Physics and Astronomy, University of Edinburgh, Edinburgh EH9 3FD, United Kingdom

## 3 Fluctuating Hydrodynamics of ABPs and RTPs

Following [46], we address a model using a general angular relaxation dynamics, combining smooth angular diffusion with diffusivity $D_r$ with pointwise random reorientations (tumbles) at rate $\alpha$. The model has ABPs as one limit and RTPs as another. An intrinsic translational diffusivity $D_t$ is also allowed for; the swim speed $v$ is allowed to be position-dependent in the first part of the derivation, $v(\mathbf{r})$, and we will then turn to density-dependent $v(\rho)$. For a single particle, the probability density $\psi(\mathbf{r},\mathbf{u},t)$ of finding the particle at position $\mathbf{r}$ moving in direction $\mathbf{u}$ obeys exactly (in $d=2,3$)

$$\begin{aligned}\dot{\psi}(\mathbf{r},\mathbf{u}) = &-\nabla\cdot[v\mathbf{u}\psi(\mathbf{r},\mathbf{u})] + \nabla_{\mathbf{u}}\cdot[D_r\nabla_{\mathbf{u}}\psi(\mathbf{r},\mathbf{u})]\\ &+\nabla\cdot(D_t\nabla\psi(\mathbf{r},\mathbf{u})) - \alpha\psi(\mathbf{r},\mathbf{u}) + \frac{\alpha}{\Omega}\int\psi(\mathbf{r},\mathbf{u}')\mathrm{d}\Omega'\end{aligned} \tag{44}$$

where $\nabla_{\mathbf{u}}$ is the rotational gradient acting on $\mathbf{u}$ and the integral is over the unit sphere $|\mathbf{u}'|=1$ of area $\Omega$. The first term on the right is the divergence of the advective current resulting from self propulsion and the last two terms are loss and gain due to tumbling out of and into the direction $\mathbf{u}$. The second and third terms account for rotational and translational diffusion.

### 3.1 Coarse-graining procedure

The first part of the derivation below consists in using a moment expansion to show that at large time and space scales, the dynamics (44) amount to a Langevin equation, whose drift and diffusion terms can be fully characterised. Using Itō calculus, we will then start from this single-particle Langevin dynamics to derive a collective Langevin dynamics of the density field of $N$ non-interacting active particles. Since all the computations will be done allowing for dependence of the microscopic parameters $v$, $\alpha$, $D_r$ on the spatial position $\mathbf{r}$ of the active particle, our computation applies to the case where these dependencies occur through the density field $\rho(\mathbf{r})$. This derivation will thus provide the stochastic dynamics for the density field of $N$ interacting active particles. Were we to consider purely ABPs, one could directly use Itō calculus to

construct the dynamics of the density field, as was done in [55,70,71]. In the general case, it is the presence of the tumbles that makes it necessary to take a first diffusive limit. Note that in lattice models, field theoretic methods can be used directly that bypass this limitation and give the same final result [47].

### 3.1.1 Moment expansion

We first decompose $\psi$ as

$$\psi(\mathbf{r},\mathbf{u},t) = \varphi + \mathbf{p}.\mathbf{u} + \mathbf{Q} : (\mathbf{u}\mathbf{u} - \mathbf{I}/d) + \Theta[\psi] \tag{45}$$

Here, $\varphi, \mathbf{p}, \mathbf{Q}$ are functions of $(\mathbf{r}, t)$, which parameterize the zeroth, first and second angular ($d = 2$) or spherical ($d = 3$) harmonic components of $\psi$, while $\Theta$ projects onto the higher harmonics. Note that in 2 dimensions, the angular harmonics are Fourier sine and cosine series in $\theta$; clearly

$$\mathbf{p}.\mathbf{u} = p_1 \sin\theta + p_2 \cos\theta \quad \text{and} \quad \mathbf{Q}:(u_i u_j - \frac{\delta_{ij}}{2}) = \frac{Q_{11} - Q_{22}}{2}\cos 2\theta + \frac{Q_{12} + Q_{21}}{2}\sin 2\theta$$

span the subspaces generated by the first and second harmonics, respectively. The same holds in $d = 3$, where the components of any unit vector $u_i$ are linear combinations of $Y_1^m, m = -1, 0, 1$ whereas the components of the traceless tensor $u_i u_j - \delta_{ij}/3$ are linear combinations of $Y_2^m, m = -2... + 2$.

We now proceed order by order in the harmonics. Integrating Eq. (44) over $\mathbf{u}$ gives

$$\dot{\varphi} = -\frac{1}{d}\nabla(v\mathbf{p}) + \nabla(D_t \nabla\varphi) \tag{46}$$

whereas multiplying eq. (44) by $\mathbf{u}$ and then integrating over $\mathbf{u}$ gives

$$\dot{p}_a = -\nabla_a(v\varphi) - \big(D_r(d-1) + \alpha\big)p_a + \nabla(D_t\nabla p_a) - \frac{2}{d+2}\nabla_b[vQ_{ab}] \tag{47}$$

Finally, multiplying eq. (44) by $\mathbf{u}\mathbf{u} - \mathbf{I}/d$ and integrating over $\mathbf{u}$ yields

$$\dot{Q}_{ab} = -\frac{d+2}{2}B_{abcd}\nabla_c v p_d - (2dD_r + \alpha)Q_{ab} + \nabla\cdot[D_t\nabla Q_{ab}] - \nabla_c v \chi_{abc} \tag{48}$$

where $B_{abcd} = (\delta_{ac}\delta_{bd} + \delta_{ad}\delta_{bc} - 2\delta_{ab}\delta_{cd}/d)/(d+2)$ and $\chi_{abc}$, which comes from higher order harmonics, will not play any role in the following. The derivations of Eqs. (46-48) are detailed in Appendix A.

### 3.1.2 Diffusion-drift equations

So far, beyond the assumed isotropy of $v(\mathbf{r}), D_{r,t}(\mathbf{r})$ and $\alpha(\mathbf{r})$, no approximation has been made; Eqs. (46-48) are exact results for the time evolution of the zeroth, first and second harmonics of $\psi(\mathbf{r},\mathbf{u},t)$. We then note that Eq. (46) is a mass conservation equation:

$$\dot{\varphi} = -\nabla\cdot\mathbf{J} \quad \text{with} \quad \mathbf{J} = \frac{1}{d}v\mathbf{p} - D_t\nabla\varphi \tag{49}$$

with a current $\mathbf{J}$ which involves the first harmonic $\mathbf{p}$. We will now use a large time and space scale limit to obtain $\mathbf{J}$ as a function of $\varphi$.

We first note that $\varphi$ is locally conserved and is thus a slow mode: the relaxation of a density perturbation on a scale $\ell$ occurs in a time that diverges as $\ell \to \infty$. On the contrary, $\mathbf{p}$ and $\mathbf{Q}$ are fast modes, whose relaxation rates are given by $t_{\mathbf{p}} = \alpha + D_r(d-1)$ and $t_{\mathbf{Q}} = \alpha + 2dD_r$. For times greater than $t_{\mathbf{p},\mathbf{Q}}$, one thus assumes $\dot{\mathbf{p}} = \dot{\mathbf{Q}} = \Theta[\dot{\psi}] = 0$. Eqs. (47) and (48) then give the ordinary differential equations that $\mathbf{p}$ and $\mathbf{Q}$ satisfy quasi-statically as $\varphi$ evolves on time-scales much larger than $t_{\mathbf{p},\mathbf{Q}}$. By itself, this creates a non-local constitutive relation between $\mathbf{J}$ and $\psi$ which still involves all harmonics.

Next we explicitly carry out a gradient expansion, yielding for $\mathbf{Q}$:

$$Q_{ab} = -\frac{1}{2dD_r + \alpha}\left(\frac{d+2}{2}B_{abcd}\nabla_c(vp_d) + \nabla_c(\chi_{abc})\right) + \mathcal{O}(\nabla^2) \tag{50}$$

from which the quasi-stationary $\mathbf{p}$ then follows via (47) as

$$\mathbf{p} = -\frac{1}{(d-1)D_r + \alpha}\nabla(v\varphi) + O(\nabla^2) \tag{51}$$

At this order in the gradient expansion, closure is achieved without needing further information on harmonics beyond the first; the current $\mathbf{J}$ is given by

$$\mathbf{J} = -\frac{v}{d(d-1)D_r + d\alpha}\nabla(v\varphi) - D_t\nabla\varphi \tag{52}$$

At this order, Eq.(49) corresponds to a diffusion-drift approximation of the microscopic master equation (44), given by:

$$\dot{\varphi} = -\nabla\cdot[-D\nabla\varphi + \mathbf{V}\varphi] \tag{53}$$

where the diffusivity and drift velocity obey

$$D = \frac{v^2}{d(d-1)D_r + d\alpha} + D_t \quad \text{and} \quad \mathbf{V} = \frac{-v\nabla v}{d(d-1)D_r + d\alpha} \tag{54}$$

At this level of description, though not for the exact results that preceded it, RTPs and ABPs are seen to be equivalent. That is, in (53), the tumble rate $\alpha$ and rotational diffusivity $D_t$ enter only through the combination $(d-1)D_r + \alpha$, so that the two types of angular relaxation are fully interchangeable. Conversely, given a sequence of snapshots showing the large-scale evolution of the local densities of SPPs, one cannot determine whether the system is composed of ABPs or RTPs. Note that "large scale" here excludes some of the trap problems considered in Section **??** where the confinement length is smaller than the persistence length of the self-propelled motion.

### 3.1.3 Many-body physics

Eqs. (49) and (53) give the evolution for the probability density of one particle at diffusion-drift level. Following [45] we can now consider an assembly of particles whose motility parameters $v, \alpha, D_r$ and $D_t$ depend on position both directly and indirectly, through a functional dependence on the microscopic density $\rho(\mathbf{r},t) \simeq \sum_\mu \delta(\mathbf{r} - \mathbf{r}_\mu(t))$. Since we are considering a multiplicative noise whose variance is a functional of the density field $\rho$, the construction of the Langevin equation associated to $\rho$ is technically

more involved than in the additive case [72]. First, we go from the Fokker-Planck equation (53) to the equivalent Itō-Langevin equation for an individual particle position $\mathbf{r}_\mu(t)$:

$$\dot{\mathbf{r}}_\mu(t) = \mathbf{V} + \nabla_1 D(\mathbf{r}_\mu,[\rho]) + \big(\nabla_{\mathbf{r}_\mu}\frac{\delta}{\delta\rho(\mathbf{r}_\mu)}\big)D(\mathbf{r}_\mu,[\rho]) + \sqrt{2D}\boldsymbol{\eta} \tag{55}$$

where $\nabla_1 D(\mathbf{r}_\mu,[\rho])$ represents a gradient with respect to the *first* argument of $D$ and not with respect to its implicit dependence on $\mathbf{r}_\mu$ through the field $\rho(\mathbf{r}') = \sum_\alpha \delta(\mathbf{r}'-\mathbf{r}_\alpha)$. On the contrary, the operator $\nabla_{\mathbf{r}_\mu}\frac{\delta}{\delta\rho(\mathbf{r}_\mu)}$ applies to the functional dependence of $D$ on the field $\rho(\mathbf{r}')$ and the subscript $\mathbf{r}_\mu$ shows $\nabla_{\mathbf{r}_\mu}$ to apply to dependencies on $\mathbf{r}_\mu$ and not on $\mathbf{r}'$ or $\mathbf{r}_{\alpha\neq\mu}$ that may appear in $D$. (For more technical details, see Appendix B.) The two terms $\nabla_1 D(\mathbf{r}_\mu,[\rho]) + \nabla_{\mathbf{r}_\mu}\frac{\delta}{\delta\rho(\mathbf{r}_\mu)}D(\mathbf{r}_\mu,[\rho])$ form the so-called "spurious drift" term due to the Itō time discretisation. (This term is, of course, not spurious, but necessary once one uses the Itō convention to define that discretization [73,74].) The atypical form of this spurious drift is due to $D$ depending on $\mathbf{r}_\mu$ both explicitly, which explains the first term, and implicitly—through $\rho(\mathbf{r}')$—which explains the second one. In Appendix B, we show that the density $\rho(\mathbf{r},t)$ then obeys the many-body Langevin equation [45]

$$\dot{\rho} = -\nabla.\left(\mathbf{V}[\rho]\rho - D[\rho]\nabla\rho + \big(\nabla_{\mathbf{r}}\frac{\delta}{\delta\rho(\mathbf{r})}\big)D(\mathbf{r},[\rho]) + (2D\rho)^{1/2}\boldsymbol{\Lambda}\right) \tag{56}$$

with white noise $\langle \Lambda_i(\mathbf{r},t)\Lambda_j(\mathbf{r}',t')\rangle = \delta_{ij}\delta(\mathbf{r}-\mathbf{r}')\delta(t-t')$. The gradients in (56) have no subscript '1' since there are no more ambiguities at this stage: the derivatives are taken with respect to the spatial coordinate $\mathbf{r}$, which does not enter $\rho(\mathbf{r}')$, and not with respect to the position of one of the $N$ particles as in (55). Note that when the diffusivity of particle $\mu$ does not include 'self-interaction', i.e. $D = D(\mathbf{r}_\mu,[\rho-\delta(\mathbf{r}-\mathbf{r}_\mu)]$ or is the result of a convolution between $\rho(\mathbf{r}')$ and a symmetric kernel $K(\mathbf{r})$, i.e. $D = \int \mathrm{d}\mathbf{r}' K(\mathbf{r}_\mu-\mathbf{r}')\rho(\mathbf{r}')$, then $\nabla_{\mathbf{r}_\mu}\frac{\delta}{\delta\rho(\mathbf{r}_\mu)}D(\mathbf{r}_\mu,[\rho]) = -\nabla K(0)$ vanishes (see Appendix B for details) and one recovers the more standard equation

$$\dot{\rho} = -\nabla.\left(\mathbf{V}[\rho]\rho - D[\rho]\nabla\rho + (2D\rho)^{1/2}\boldsymbol{\Lambda}\right) \tag{57}$$

The functionals $v[\rho]$, $\alpha[\rho]$ and $D_{t,r}[\rho]$ in (54) then define for the interacting particle system the many-body drift velocity and diffusivity $\mathbf{V}[\rho]$ and $D[\rho]$ for use in Eq. (56).

Starting from the many-body Itō-Langevin equation (56), one can then derive a functional Fokker-Planck equation for the evolution of the probability density $P[\rho(\mathbf{r}),t]$ of finding the system with a density field $\rho(\mathbf{r})$ at time $t$:

$$\dot{P}[\rho] = \int \mathrm{d}\mathbf{r}\frac{\delta}{\delta\rho(\mathbf{r})}\nabla\cdot\left[\rho\mathbf{V} - D\nabla\rho - D\rho\left(\nabla_{\mathbf{r}}\frac{\delta}{\delta\rho(\mathbf{r})}\right)\right]P[\rho] \tag{58}$$

The technical details, which show the importance of the atypical spurious drift, are detailed in appendix C.

### 3.1.4 Connection to large-deviation functionals; role of noise

A crucial observation, first made for RTPs in [45], is that (56) reduces, under specific conditions, to a description of passive Brownian particles (PBPs) with a specified free energy functional $\beta\mathcal{F}[\rho] = \beta\mathcal{F}_{\mathrm{ex}}[\rho] + \int \rho(\ln\rho - 1)dx$. (In what follows we use

thermal units in which $\beta = 1$.) This is best seen by noting that the Fokker-Planck equation (58) admits flux-free solution

$$\left[\rho\mathbf{V} - D\nabla\rho - D\rho\left(\nabla_{\mathbf{r}}\frac{\delta}{\delta\rho(\mathbf{r})}\right)\right]P[\rho] = 0 \tag{59}$$

whenever there exists a functional $\mathcal{F}_{\rm ex}[\rho]$ which satisfies the condition

$$\mathbf{V}([\rho],\mathbf{r})/D([\rho],\mathbf{r}) = -\nabla_{\mathbf{r}}(\delta\mathcal{F}_{\rm ex}[\rho]/\delta\rho(\mathbf{r})) \tag{60}$$

Indeed, in such a case $P[\rho] = \exp[-\beta\mathcal{F}[\rho]]$ satisfies (59). As was noted in [71,47], $s[\rho] = \beta\mathcal{F}/V$, with $V$ the volume of the system, is the large deviation function of the density profile $\rho$

$$s[\rho] = -\lim_{V\to\infty}\frac{1}{V}\log P[\rho] \tag{61}$$

It is at first sight very surprising that one can compute this object for any kind of interacting out-of-equilibrium system. However its computability depends on (60) holding true, and indeed this is not true in any general manner. It is however satisfied to leading (zeroth) order in a gradient expansion of $\mathcal{F}_{ex}$. If (60) holds, the system is completely equivalent to an equilibrium system of passive particles with excess chemical potential gradient $\delta\mathcal{F}_{\rm ex}/\delta\rho(\mathbf{r})$. This equivalence holds not only at the level of the steady-state but also at the level of the dynamics (58). This means that, at this macroscopic level, the dynamics is effectively an equilibrium one and, for instance, satisfy the Onsager-Machlup symmetry between excursion and relaxation [69]. However this does not mean that the phenomenology of the system reduces to an equilibrium one. For instance, the slowing down of active particles at high density causes an effective many-body attraction between the equivalent passive particles, characterized by a $\mathcal{F}_{\rm ex}$ whose local part has negative curvature in $\rho$. This kinetic slowdown can trigger a phase separation mechanism, which we detail in the following section, which would be impossible at equilibrium. (Making the viscous drag on each particle an increasing function of local density would generate a similar kinetic slowdown in an equilibrium system, but the Boltzmann distribution would be insensitive to this effect.)

If the condition (60) is not met, however, the dynamics is not equivalent to PBPs with conservative interactions and is therefore "irreducibly" active. As we will show later, the equivalence established above will only hold for homogeneous systems and, when the kinetic slow-down triggers a phase-separation, higher-order gradient terms comes into play at the large-deviation level, and break the mapping to equilibrium.

### 3.1.5 Mapping to equilibrium

The simplest case is where $D_t = 0$. Here the left hand side of (60) is $-\nabla\ln v[\rho]$ and we then require $\delta\mathcal{F}_{ex}[\rho]/\delta\rho(\mathbf{r}) = \ln(v([\rho];\mathbf{r})$. The simplest first approach is to assume that the functional dependence of swim speed on density is strictly local, so that $v([\rho];\mathbf{r}) = v(\rho(\mathbf{r}))$. We then have $\mathcal{F}_{ex} = \int f_{ex}(\rho(\mathbf{r}))d\mathbf{r}$ where $f_{ex} = \int_0^\rho \ln v(\lambda)d\lambda$. This structure in the free energy is equivalent to having a passive system whose chemical potential obeys $\mu = \ln(\rho v)$; the mean particle current then obeys

$$\mathbf{J} = -\rho D\nabla\ln(\rho v) \tag{62}$$

Noting that in our chosen units ($\beta = 1$) the mobility coincides with the diffusivity $D$, this is the expected form for the stated chemical potential. When $D_t\alpha$ is a nonzero constant, the result for $f_{ex}$ generalizes to

$$f_{ex} = \frac{1}{2}\int_0^\rho \ln[v(\lambda)^2 + dD_t\alpha]d\lambda \tag{63}$$

This case is explored in [56].

To approximate the excess free energy by a local function is a widely used approximation in equilibrium systems which makes sense at (Landau) mean-field level where fluctuations are neglected. (If the excess free energy were genuinely local, short-length scale fluctuations would be out of control, so to go beyond mean field theory requires treatment of nonlocality even if that is weak). The chosen form (with $D_t = 0$) leads to a spinodal instability whenever $dv/d\rho < -v/\rho$ [45,56]. The system is then equivalent to an equilibrium system undergoing liquid-gas phase separation due to attractive forces and the spinodal instability is complemented by binodals, which can be characterised analytically in some cases (See [56] for a recent review).

For ABPs with collisions, one finds empirically that $v(\rho) \simeq v_0(1 - \rho/\rho^*)$ with $\rho^*$ a near-close-packed density beyond which self-propulsion is effectively arrested. The system is then spinodally unstable for $\rho \geq \rho^*/2$ [15,17,19]. Stability is restored by packing constraints at high enough density, but in the present approach (collisions replaced by an effective density-dependent propulsion speed), empirical corrections to $\mathcal{F}_{ex}$ are needed to account for this [17]. An alternative is to impose a sharp cutoff so that $f = +\infty$ for $\rho > \rho^*$; this is used in [40].

The presence of a finite $D_t$, either due to Brownian motion or resulting from the random collision of particles (in which case $D_t$ will depend on $\rho$), alters the shape of the spinodal curves which instead obey $1 + \rho v'/v < -dD_t/(v^2\tau)$. This causes the spinodals to meet at a critical point; while in qualitative agreement with the shape of the phase diagram reported for ABPs with repulsions (see, e.g. [15,17,21]), this is somewhat accidental since the actual role of $D_t$ in the simulated dynamics is negligible. The observed critical point is better viewed in terms of the competition between slowing down at high density (promoting motility-induced phase separation) and the buildup of particle mechanical pressure [40]. The latter stems primarily from the pair interaction, rather than the small ideal gas part which is proportional to $D_t$ [24,40]. Numerically, the spinodals are hard to locate precisely, whereas binodals can be located by looking directly at the coexisting densities in phase-separated states. The point at which phase separate is seen kinetically in ABP simulations often lies in between the spinodal and binodal; it depends in general on nucleation rates and is subject to large finite-size corrections. Very large scale simulations are thus required for accurate phase diagram determination [17,19].

### 3.1.6 Beyond the local approximation

When a system phase separates, large gradients develop and the gradient expansion cannot be truncated at lowest order: the local approximation to $\mathcal{F}$ no longer yields a good approximation to the large deviation functional. In such a case, one has to look for higher order gradient terms, which stem from two different mechanisms. First, for real particles, the interactions between particles are never perfectly local: even for hard-core repulsions, the particle size defines a finite interaction range. Second, we have dropped higher angular harmonic contributions by appeal to a gradient approximation. Retaining higher order gradients thus requires two different type of terms whose impact on motility-induced phase separation we now discuss.

**Non-local $v(\rho)$.** The local form of the free energy can be used to predict the binodal densities for phase coexistence via the the common tangent construction on $f = f_{ex} + \rho(\ln\rho - 1)$ [45]. In this construction one equates the chemical potential $df/d\rho$ and the 'thermodynamic' pressure $\rho df/d\rho - f$ in the two phases; this means that a single line can be drawn on a plot of $f(\rho)$ that is tangent at the binodal densities and

lies below $f$ everywhere else. However, there is a hidden pitfall here: this construction implicitly assumes that, whatever the nonlocal terms are, these continue to obey (60). Whenever they do, a free energy still exists and, so long as it does, the binodal densities do not depend on the precise form of the nonlocal terms. Conversely, if a free energy does not exist, then the binodal conditions can depend explicitly on the nonlocal terms. This is explored in some detail, within the simplification of a $\phi^4$ effective field theory, in [48]. For ABPs, numerical evidence of the breakdown of the common tangent construction was reported in [17,19].

The lowest order nonlocal theory can be constructed by assuming that the functional dependence of swim speed on density takes the form [45]

$$v[\rho] = v(\hat{\rho}) \simeq v(\rho + \gamma^2\nabla^2\rho) \simeq v(\rho) + v'(\rho)\gamma^2\nabla^2\rho \tag{64}$$

This represents a quasi-local dependence on a quantity $\hat{\rho}$ that samples the local density isotropically in a region of size $\gamma$. For programmed slowing-down (e.g., quorum-sensing) the simplest assumption is that $\gamma$ is a density-independent constant. However for collisional slowing down in ABPs, a better estimate is $\gamma \simeq \gamma_0 v(\rho)/[(d-1)D_r + \alpha]$ which, with $\gamma_0$ of order unity, is the distance travelled during one angular relaxation time. Substituting the nonlocal form for $v$ in (62) gives to leading order

$$\mathbf{J} = -\rho D\nabla\mu \tag{65}$$

$$\mu = \ln(\rho v) - \frac{\gamma^2}{v}v'\nabla^2\rho \tag{66}$$

Only if $\gamma^2 v'/v$ is a constant, independent of density $\rho$, does this form of chemical potential support the existence of a free energy. If this combination is constant – such as for the case where $\gamma$ is constant and $v(\rho) \sim \exp[-a\rho]$ [45] – then the common tangent can legitimately be used to predict the binodal densities. In all other cases it cannot be relied upon [17,48]. Note that in practice, only quantitative differences with the local theory have been noticed when simulating models with such non-local $v([\rho])$ [17,48]: the phase separation still occurs, the coarsening law is not much affected, and one only observes quantitative shifts of the binodals. Importantly, the *concept* of a binodal is maintained: the densities of coexisting phases do not change as the global average density in the system is varied between the two coexistence values.

**Other gradient terms.** The second source of higher order gradient terms is the gradient expansion used to close the spherical harmonics expansion in Section 3.1.2. Were we to pursue this gradient expansion to higher orders, we would obtain a set of ordinary differential equations for $\mathbf{p}$, $Q$, etc. rather than the simple algebraic relation (51) between $\mathbf{p}$, $\varphi$ and $\nabla\varphi$. Solving these equations in terms of $\varphi$ and reinjecting into $\mathbf{J}$ would then not lead to a simple Fokker-Planck equation, from which we would not be able to derive a microscopic Langevin equation like (55), which is the starting point of our approach. The equivalence between ABPs and RTPs at this higher order in gradients is thus questionable. This echoes the fact that the difference between the two models becomes more important at short length scales. As we will show in Section 3.1.7, however, these differences hardly impact the phase diagram.

For ABPs, since one directly starts at the microscopic level with coupled Langevin equations, one can bypass the construction of the microscopic Langevin equation (55) and directly use Itō calculus to obtain a stochastic equation for the probability density $\rho(\mathbf{r}, \mathbf{u})$ of finding particles at $\mathbf{r}$ going in the direction $\mathbf{u}$ [55,70,71]. One then has to project this equation onto successive harmonics and use an appropriate truncation. Again, the equation (56) amounts to second order gradient expansion. It is then easier to pursue this development to higher orders, which would yield coupled stochastic

equations for $\rho$, $\mathbf{p}$, $Q$, etc.. As far as we are aware, this has not be carried out in the literature for ABPs or RTPs, but progress along this path can be found for aligning nematic particles [75].

For ABPs, a similar path has been followed at mean-field level, albeit without a proper derivation of the noise terms, to arrive at [15,25,59]

$$\begin{aligned} \dot{\rho} &= D\Delta\rho - \nabla\cdot[v\mathbf{p}] \\ \dot{p} &= -D_r\mathbf{p} - \frac{1}{2}\nabla[v\rho] + D\Delta\mathbf{p} \end{aligned} \tag{67}$$

One can then always complete these equation by adding ad-hoc Gaussian noise [15] or by assuming that, were the coupled equations (67) to be written in a gradient form (implying the existence of a free energy functional) the noise terms would be whatever is required to give an equilibrium like-dynamics. As we have shown in Section 3.1.4, however, the derivation of the noise terms is a crucial step to determine whether or not the system really maps onto an equilibrium one. Indeed, the integrability criterion (60) is derived by requiring a flux-free steady-state in the Fokker-Planck equation. This condition crucially relies on the fact that the variance of the noise obeys a fluctuation-dissipation relation with the mobility.

Nevertheless, since the derivations of these noise terms are particularly difficult, a first strategy can be to look at whether the equations (67) have the gradient structure of an equilibrium model. While analyzing the linear stability of (67) for a linearly decreasing $v(\rho)$ reveals a spinodal decomposition scenario very similar to the one described in section (3.1.5), it was explicitly shown in [59] that these equations are not of gradient form. However, expanding close to the linear instability, the authors of [59] were able to map these equations onto a Cahn-Hilliard model, but with an effective free energy which depends on where in the phase diagram the expansion is carried out. This revealed a rather surprising feature: the addition of the $\Delta\mathbf{p}$ terms breaks the global mapping to equilibrium but seems to preserve a local one. This however fundamentally changes the structure of the phase diagram: there is nothing to guarantee that the binodals stay in fixed positions as one moves along the 'tie line' between them (and without this property the concept of a binodal is inapplicable). Moreover, according to this calculation, a large part of the transition line is changed from a first order to a second order transition, in contrast to the isolated critical point usually seen in liquid-gas type phase-separation.

To test the predictions of this approach, we simulated directly the equations (67) using spectral-methods and semi-implicit time-stepping. We chose a form of $v(\rho)$ which does not lead to $v(\rho) < 0$ at any density and thus does not require an ad-hoc cut-off at the level of the effective free energies:

$$v(\rho)^2 = v_0^2 + (v_1^2 - v_0^2)(1 - e^{-\rho/\phi}) \tag{68}$$

For this choice, we can compute analytically spinodals and binodals predicted by the local theory [56] and hence evaluate precisely the impact of the $\Delta\mathbf{p}$ term. The scenario revealed by our simulations does not show any of the surprising phenomenology predicted by the methods of [59]: the binodals are quantitatively shifted by this new gradient term, in qualitative agreement with the effect of gradient terms stemming from a non-local $v(\rho)$ [48], but the binodals do not vary along the tie-line in the coexistence region (where the lever rule still applies). Also, the transition line seems to remain first-order on approach to the critical point, exhibiting the familiar hysteresis curves (see fig. 1).

In principle, this outcome could depend on our choice of $v(\rho)$; note that direct comparison with [59] is not possible since the theory developed there relies on the addition of confining terms at the level of the free energy that do not exist at the level

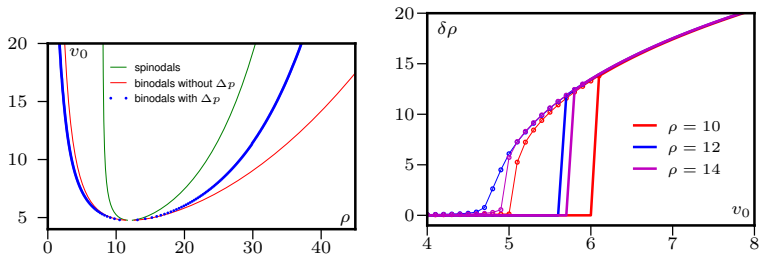


**Fig. 1.** The phase diagram (**left**) predicted by the theory without the $\Delta\mathbf{p}$ term (red and green lines) are only qualitatively affected by the $\Delta\mathbf{p}$ term (blue). Hysteresis loops (**right**), showing the first order nature of the transition, can be seen on approach to the critical point by ramping up (solid lines) or down (connected symbols). $D = 0.25$, $v_1 = 0.25$, $\phi = 4$, $\tau = 1/D_r = 1$.

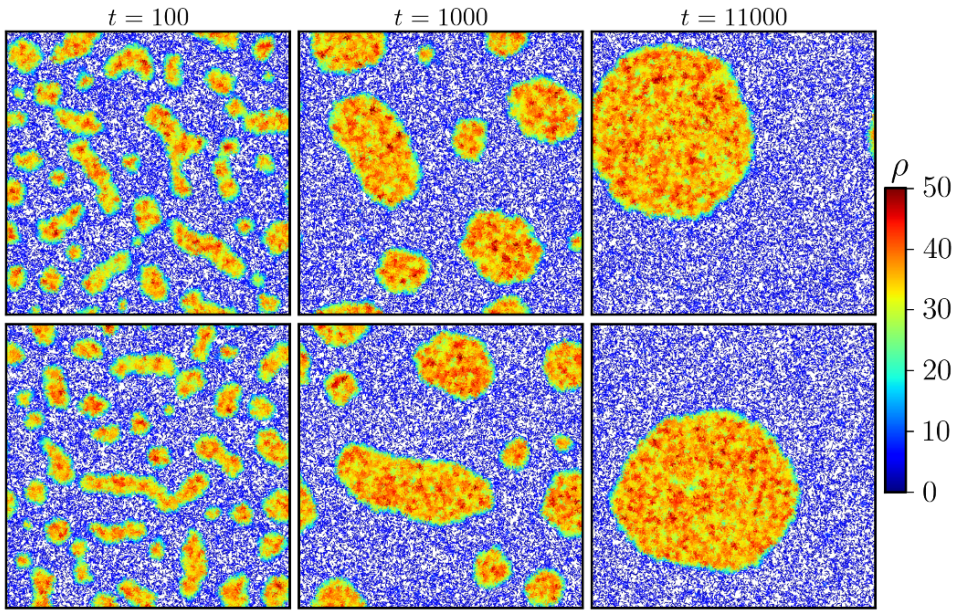


**Fig. 2.** Coarsening dynamics of RTPs (top) and ABPs (bottom) interacting via the density-dependent swim-speed (68) with $v_0 = 15$, $v_1 = 0.25$, $\varphi = 4$, $\tau = 1$, $D_t = 0.25$. Simulated for $N = 120\,000$ particles in a box of side $L = 100$.

of the PDE, Eq. (67). However this interpretation seems unlikely given the growing breadth of literature supporting the existence of well-defined binodals in MIPS. An alternative possibility is that the new and unusual phenomenology predicted from the approach of [59] is an artefact of a quasi-linear, noiseless treatement of what is in fact a noisy nonlinear transition. Further study is needed to resolve this issue, for instance by carrying out the analytical procedure in [59] for the particular $v(\rho)$ chosen in (68).

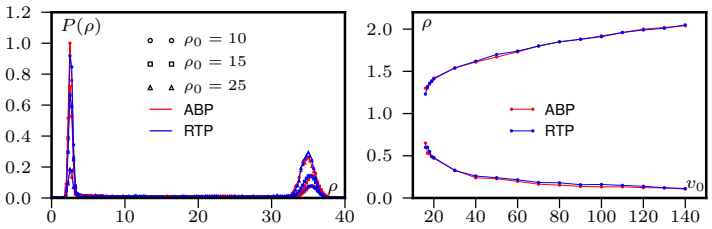


**Fig. 3. Left**: The local density distributions $P(\rho)$ of ABPs and RTPs interacting via the density-dependent swim speed Eq. (68) with $v_0 = 15$, $v_1 = 0.25$, $\varphi = 4$, $\tau = 1$, $D_t = 0.25$. The two systems overlap very well, showing that not only the mean coexistence densities in the two models but also their fluctuations are very similar. As expected, changing the mean density $\rho_0$ does not change the coexisting densities. **Right**: Phase diagrams of RTPs and ABPs interacting via WCA potential. The boundary lines are obtained by computing the binodals as a function of $v$ in the phase coexistence region for various global densities $\rho_0 = N/L^2$, to check that the binodals are indeed independent of $\rho_0$. Again, a surprisingly good overlap between the two systems is observed.

### 3.1.7 Comparison between microscopic simulations of RTPs and ABPs

Since gradient terms can alter the equivalence between ABPs and RTPs, we carried out extensive microscopic simulations of MIPS for both models in two dimensions for $N$ particles in an $L \times L$ square domain. We first compared the two models in the case of a density-dependent swim speed $v(\rho)$ given by (68). The coarsening of both phase separating systems is shown in figure 2 and shows a strikingly similar dynamics. Beyond the apparent similarity of the two dynamics, one can compute the steady-state density distributions $P(\rho)$ of the two systems in the phase separated region, which shows that both the mean densities and their fluctuations in each phase are also very similar (see Fig. 3). Note that as expected, the coexisting densities along the tie-line in the coexistence region do not depend on the mean density $\rho_0 = N/L^2$.

We then simulated both ABPs and RTPs in the case where slowing down is caused by repulsive interactions (represented as a WCA potential as in [15,16,17]). We know that the $v(\rho)$ theory correctly captures the slowdown in these models but that it lacks the direct interparticle forces which are responsible for saturating density in the high-density phase [40]. Therefore, the dynamical equivalence of ABPs and RTPs at large scales might break down for the repulsive case where much of the physics depends on short-distance collisional events taking place below the coarse-graining length scale of the fluctuating hydrodynamics theory. Suprisingly however, the phase diagrams of repulsive ABPs and RTPs collapse onto each other upon the usual rescaling $\alpha = (d-1)D_r$ (see Fig. 3). Thus, although we have shown that the details of the angular dynamics are important for SPPs confined to traps of size comparable to the run-length or smaller, the presence of short-length scale physics in the mechanism for MIPS does not create a similar dependence on details, as judged either by the qualitative kinetic observations or a quantitative study of phase diagrams.

## 4 Conclusions

Motivated by a wish to understand for active systems the relation between microscopic dynamics and macroscopic behaviour, we have in this paper compared in detail two distinct but related classes of self-propelled particles: Active Brownian particles

and run-and-tumble particles. These differ only in the details of their angular relaxation (continuous versus discrete). We considered first one-body-problems involving non-interacting particles in either uniform fields (e.g., gravity) or isotropic harmonic traps. In both cases, for weak enough forces there is an "effective equilibrium" regime in which the characteristic length scale set by the balance of external and propulsive forces is large compared to the run length, defined as the distance a free particle can travel during its orientational relaxation time. In this regime, the two types of dynamics (ABP and RTP) are equivalent modulo a simple mapping between parameters, which corresponds to equating the angular relaxation time in the two cases. However, for stronger confinement the corrections to this picture are specific to the chosen dynamics. In the case of harmonic traps, this difference is particularly striking: in the regime where the confinement length is large compared to the run length, there is an exponentially strong suppression of the density of ABPs at the trap centre when compared to RTPs of the same rotational relaxation time. This can be attributed to a subtle but physically simple mechanism whereby, in the strong trapping regime, particles tend to remain a long time at the outer edge of the trap, where external and propulsive forces balance. For RTPs this balance is suddenly destroyed with each tumble event, whereas for ABPs, which update their orientations gradually, there is a tendency to drift around the perimeter so that the balance is continually maintained, causing only an exponentially small escape rate from the surface region. We also considered the effect of the microscopic rotational dynamics on MIPs, or motility-induced phase separation. For this process we gave a fuller presentation of results summarized in our earlier papers concerning the derivation of collective equations for the particle density field, from which criteria for MIPS are easily found within a limiting approximation corresponding to neglect of gradient terms in the large deviation functional. This criterion is again insensitive to the choice of rotational dynamics. It is explicitly derived from a model where particles interact through a programmed dependence of their propulsion speed on the local density, but also describes, to reasonable accuracy, the case where slowing down is caused instead by collisions. We then considered the role of gradient corrections, arising either from nonlocality in the dependence of speed on density, or as additional terms in a combined expansion in spatial gradients and angular harmonics of the local distribution of particle orientations. Although the latter could in principle cause qualitative shifts in phase behaviour, in common with previous studies we do not find compelling evidence for anything more than a quantitative shift numerically. Specifically, although the "equilibrium" conditions for phase coexistence (those derivable from the local part of the large deviation functional) are violated, the system still exhibits conventional binodals whose defining property is that the density of coexisting phases is independent of the intermediate global density of the system. For the case where MIPS is caused by collisional rather than programmed speed reduction, we find, somewhat surprisingly, that there is once again almost no difference in phase behaviour between ABPs and RTPs with matched angular relaxation time. This is despite the fact that both the collisional dynamics, and the presence of sharp interfaces in the system, involve length scales below those at which the equivalence of the two models can be formally established by systematic coarse graining.

Acknowledgements: The authors thank Rosalind Allen, Ludovic Berthier, Cecile Cottin-Bizonne, Paul Goldbart, Davide Marenduzzo, Joakim Stenhammar and Raphael Wittkowski for discussions. MEC thanks the Royal Society for a Research Professorship. This work was supported in part by EPSRC Grant EP/J007404/1.

## A Moment-expansion

We start from the master equation on the probability density $\psi(\mathbf{r},\mathbf{u},t)$:

$$\dot{\psi} = -\nabla\cdot[v\mathbf{u}\psi] + D_r\Delta_{\mathbf{u}}\psi + \nabla\cdot[D_t\nabla\psi] - \alpha\psi + \frac{\alpha}{\Omega}\int \mathrm{d}\Omega\psi(u') \tag{69}$$

with $\Delta_{\mathbf{u}}$ the rotational part of the Laplacian acting on $\mathbf{u}$. We then use the decomposition (45) of $\psi$, which we recall here for clarity

$$\psi(\mathbf{r},\mathbf{u},t) = \varphi + \mathbf{p}\cdot\mathbf{u} + \mathbf{Q}:(\mathbf{uu}-\mathbf{I}/d) + \Theta[\psi] \tag{70}$$

In the following we will use the notation $M_{ab} = u_a u_b - \delta_{ab}/d$ and the convention that repeated indices are implictly summed upon: $f_i g_i \equiv \sum_i f_i g_i$. Because $Q$ enters $\psi$ solely through the combination $\sum_{i,j} Q_{ij}M_{ij}$, it can always be chosen traceless symmetric. (Indeed, replacing $Q$ by $(Q+Q^\dagger)/2$ or $Q - \mathbf{1}\,\mathrm{Tr}(Q)/d$ does not change this sum.)

We will use the standard notation for the scalar product on the sphere

$$\langle f,g\rangle = \int \mathrm{d}\Omega f(u)g(u) \tag{71}$$

for which spherical (and angular) harmonics are orthogonal. To obtain equations for $\dot{\varphi}$, $\dot{\mathbf{p}}$, $\dot{\mathbf{Q}}$, we take the scalar product of equation (69) with 1, $\mathbf{u}$ and $M$. To do so, we compute

$$\langle 1,\psi\rangle = \Omega\varphi; \quad \langle \mathbf{u},\psi\rangle = \frac{\Omega}{d}\mathbf{p}; \quad \langle M_{ab},\psi\rangle = \frac{\Omega}{d}B_{abcd}Q_{cd} = \frac{\Omega}{d}\frac{2}{d+2}Q_{ab} \tag{72}$$

which rely on

$$\begin{aligned} \langle u_i,u_j\rangle &= \frac{\Omega}{d}\delta_{ij}; \qquad \langle u_iu_j,u_ku_\ell\rangle = \frac{\Omega}{d(d+2)}(\delta_{ij}\delta_{k\ell}+\delta_{i\ell}\delta_{kj}+\delta_{ik}\delta_{j\ell}) \\ B_{ijk\ell} &= \frac{d}{\Omega}\langle M_{ij},M_{kl}\rangle = \frac{1}{d+2}(\delta_{ik}\delta_{j\ell}+\delta_{i\ell}\delta_{jk}-\frac{2}{d}\delta_{ij}\delta_{kl}) \end{aligned} \tag{73}$$

Projecting (69) on 1 then yields for $\dot{\varphi}$

$$\dot{\varphi} = -\frac{1}{d}\nabla[v\mathbf{p}] + \nabla\cdot[D_t\nabla\varphi] \tag{74}$$

while projecting (69) on $\mathbf{u}$ yields for $\dot{\mathbf{p}}$

$$\frac{\Omega\dot{\mathbf{p}}}{d} = -\langle\mathbf{u},\nabla[v\mathbf{u}\psi]\rangle + D_r\langle\mathbf{u},\Delta_{\mathbf{u}}\psi\rangle + \nabla\cdot[D_t\nabla\langle\mathbf{u},\psi\rangle] - \alpha\langle\mathbf{u},\psi\rangle \tag{75}$$

The last two terms are easy to compute since $\langle\mathbf{u},\psi\rangle = \Omega\mathbf{p}/d$. Then, spherical and angular harmonics of order $\ell$ are eigenvectors of $\Delta_{\mathbf{u}}$ with eigenvalues $-\ell(\ell+1)$ and $-\ell^2$, respectively, and the projection on $\mathbf{u}$ selects the $\mathbf{p}.\mathbf{u}$ term so that

$$D_r\langle\mathbf{u},\Delta_u\psi\rangle = -D_r(d-1)\Omega\frac{\mathbf{p}}{d} \tag{76}$$

The first term of the r.h.s. of (75) is harder to compute since $u\psi$ is not directly developed in harmonics. It can however be brought to a simpler form:

$$\begin{aligned} \langle u_a,\nabla_b[vu_b\psi]\rangle &= \nabla_b v\langle M_{ab},\psi\rangle + \nabla_b v\frac{\delta_{ab}}{d}\langle 1,\psi\rangle \\ &= \frac{\Omega}{d}\nabla_b v\frac{2}{d+2}Q_{ab} + \nabla_a v\frac{\Omega}{d}\varphi \\ &= \frac{2\Omega}{d(d+2)}\nabla_b vQ_{ab} + \nabla_a v\frac{\Omega}{d}\varphi \end{aligned} \tag{77}$$

Note that $\nabla$ always applies to everything on its right, unless specified otherwise. One then obtain for the evoluation of $\mathbf{p}$

$$\dot{p}_a = -\nabla_a[v\varphi] - \big(D_r(d-1)+\alpha\big)p_a + \nabla\cdot[D_t\nabla p_a] - \frac{2}{d+2}\nabla_b[vQ_{ab}] \tag{78}$$

Next, one projects (69) on $M_{ab}$ to obtain

$$\langle M_{ab}, \dot{\psi}\rangle = \frac{\Omega}{d}\frac{2}{d+2}\dot{Q}_{ab} \tag{79}$$

for the left hand side, and for the r.h.s.

$$-\langle M_{ab}, \nabla v\mathbf{u}\psi\rangle + D_r\langle M_{ab}, \Delta_{\mathbf{u}}\psi\rangle + \nabla\cdot[D_t\nabla\langle M_{ab},\psi\rangle] - \alpha\langle M_{ab},\psi\rangle \tag{80}$$

Again, the last two terms are simple since $\langle M_{ab},\psi\rangle = 2\Omega Q_{ab}/[d(d+2)]$. Only the second angular/spherical harmonics survive the projection on $M_{ab}$; they are eigenvectors of $\Delta_{\mathbf{u}}$, with eigenvalues $-\ell(\ell+1) = 2d$ for d=3 and $-\ell^2 = -2d$ for $d=2$. Hence the rotational diffusion term contributes a factor

$$D_r\langle M_{ab}, \Delta_{\mathbf{u}}\psi\rangle = -2dD_r\frac{\Omega}{d}\frac{2}{d+2}Q_{ab} \tag{81}$$

Again, the first term of (80) is slightly more difficult to handle and has to be split as

$$\begin{aligned} -\langle M_{ab}, \nabla_c v u_c\psi\rangle &= -\nabla_c v\langle M_{ab}, u_c u_d p_d\rangle - \nabla_c v\langle M_{ab}, u_c\Theta[\psi]\rangle \\ &= -\nabla_c v p_d\langle M_{ab}, (M_{cd} + \frac{d_{cd}}{d})\rangle - \nabla_c v\frac{\Omega}{d}\tilde{\chi}_{abc} \\ &= -\frac{\Omega}{d}\nabla_c v p_d B_{abcd} - \nabla_c v\frac{\Omega}{d}\tilde{\chi}_{abc} \end{aligned} \tag{82}$$

where we have introduced $\frac{\Omega}{d}\tilde{\chi}_{abc} = \langle M_{ab}, u_c\Theta[\psi]\rangle$ which comes from the projection of $u\Theta[\psi]$ on the second harmonics and whose precise expression we won't need.

Putting everything together then yields Eq. (48) of the main text

$$\dot{Q}_{ab} = -\frac{d+2}{2}\nabla_c v p_d B_{abcd} - 2dD_r Q_{ab} + \nabla\cdot[D_t\nabla Q_{ab}] - \alpha Q_{ab} - \nabla_c v\chi_{abc} \tag{83}$$

with $\chi = (d+2)\tilde{\chi}/2$.

## B From microscopic to mesoscopic Itō-Langevin equations

**Itō drift with functional dependences.** The total gradient of $D$ with respect to $\mathbf{r}_\mu$, notated as $D'(\mathbf{r}_\mu,[\rho])$ for lack of a better notation, is given by the chain rule

$$D'(\mathbf{r}_\mu,[\rho]) \equiv \nabla_1 D(\mathbf{r}_\mu,[\rho]) + \int d\mathbf{r}'\frac{\delta D(\mathbf{r}_\mu,[\rho])}{\delta\rho(\mathbf{r}')}\nabla_{\mathbf{r}_\mu}\rho(\mathbf{r}') \tag{84}$$

where the first term on the r.h.s. comes from the explicit dependence of $D$ on $\mathbf{r}_\mu$ and the second from the dependence of $D$ on $\rho(\mathbf{r}')$ which itself depends on $\mathbf{r}_\mu$. By convention, $\nabla_1 D(\mathbf{r}_\mu,[\rho])$ is thus a "partial gradient" which acts upon the explicit dependence of $D$ on $\mathbf{r}_\mu$ (its first argument) but not on its implicit dependence through $\rho$. Using the explicit expression of $\rho(\mathbf{r}')$, one has

$$\nabla_{\mathbf{r}_\mu}\rho(\mathbf{r}') = \nabla_{\mathbf{r}_\mu}\sum_j \delta(\mathbf{r}'-\mathbf{r}_j) = \nabla_{\mathbf{r}_\mu}\delta(\mathbf{r}'-\mathbf{r}_\mu) = -\nabla_{\mathbf{r}'}\delta(\mathbf{r}'-\mathbf{r}_\mu) \tag{85}$$

Equation (85) shows why the notation $\nabla_{\mathbf{r}_\mu}$, which indicates that the gradient acts on $\mathbf{r}_\mu$ and not on $\mathbf{r}'$ or $\mathbf{r}_j$, is essential—though cumbersome—to get the correct result. Inserting (85) into (84) and integrating by parts, one then finds that

$$\begin{aligned} D'(\mathbf{r}_\mu,[\rho]) &= \nabla_1 D(\mathbf{r}_\mu,[\rho]) + \int d\mathbf{r}' \delta(\mathbf{r}'-\mathbf{r}_\mu)\nabla_{\mathbf{r}'}\frac{\delta D(\mathbf{r}_\mu,[\rho])}{\delta\rho(\mathbf{r}')} \\ &= \nabla_1 D(\mathbf{r}_\mu,[\rho]) + \left(\nabla_{\mathbf{r}_\mu}\frac{\delta}{\delta\rho(\mathbf{r}_\mu)}\right) D(\mathbf{r}_\mu,[\rho]) \end{aligned} \tag{86}$$

As a consistency check, and to understand how the operator $\nabla_{\mathbf{r}_\mu}\frac{\delta}{\delta\rho(\mathbf{r}_\mu)}$ works, let us consider a simple example where the diffusivity of a particle at position $\mathbf{r}_\mu$ is a linear functional of the density of its neighbours, convoluted by some kernel $K$:

$$D(\mathbf{r}_\mu,[\rho]) = \int d\mathbf{r}'\rho(\mathbf{r}')K(\mathbf{r}_\mu-\mathbf{r}') = \sum_j K(\mathbf{r}_\mu-\mathbf{r}_j) \tag{87}$$

In such a case, the total gradient of $D$ with respect to $\mathbf{r}_\mu$ can be directly computed:

$$D'(\mathbf{r}_\mu,[\rho]) = \sum_{j\neq\mu}\nabla K(\mathbf{r}_\mu-\mathbf{r}_j), \tag{88}$$

where $\nabla K$ is the standard gradient of the function $K(\mathbf{r})$. Applying the formula (86), one finds

$$D'(\mathbf{r}_\mu,[\rho]) = \int d\mathbf{r}'\rho(\mathbf{r}')\nabla K(\mathbf{r}_\mu-\mathbf{r}') + \int d\mathbf{r}'[\nabla_{\mathbf{r}_\mu}\frac{\delta\rho(\mathbf{r}')}{\delta\rho(\mathbf{r}_\mu)}]K(\mathbf{r}_\mu-\mathbf{r}') \tag{89}$$

where the first term comes from the explicit derivative and the second one from the functional derivative. Note that, in the latter term, $\nabla_{\mathbf{r}_\mu}$ *does not* act upon $K(\mathbf{r}_\mu-\mathbf{r}')$. The computation can now be readily pursued, to give

$$D'(\mathbf{r}_\mu,[\rho]) = \int d\mathbf{r}'\sum_j \delta(\mathbf{r}'-\mathbf{r}_j)\nabla K(\mathbf{r}_\mu-\mathbf{r}') + \int d\mathbf{r}'[\nabla_{\mathbf{r}_\mu}\delta(\mathbf{r}'-\mathbf{r}_\mu)]K(\mathbf{r}_\mu-\mathbf{r}') \tag{90}$$

Using again that $\nabla_{\mathbf{r}_\mu}\delta(\mathbf{r}'-\mathbf{r}_\mu) = -\nabla_{\mathbf{r}'}\delta(\mathbf{r}'-\mathbf{r}_\mu)$ and integrating by parts, one gets

$$D'(\mathbf{r}_\mu,[\rho]) = \sum_j \nabla K(\mathbf{r}_\mu-\mathbf{r}_j) - \nabla K(0) = \sum_{j\neq\mu}\nabla K(\mathbf{r}_\mu-\mathbf{r}_j) \tag{91}$$

Interestingly, the functional derivative generates a term $-\nabla K(0)$ which will be absent whenever $K(r)$ is a symmetric kernel or when the particles are *not* self-interacting. (By this we mean that the diffusivity $D$ of particle $\mu$ is a function of $\mathbf{r}_\mu$ and a functional of $\rho(\mathbf{r}) - \delta(\mathbf{r}-\mathbf{r}_\mu)$; as such it is functionally dependent only on the density field of other particles, which differs from the total density by the $\delta$-function self-term.) For complete generality however, we must retain this term in the Langevin equation (55) and throughout the construction of the Langevin equation for $\rho(\mathbf{r})$, in order to derive a Fokker-Planck equation which is properly ordered as this is crucial to get the correct steady-state. Since the contribution of this term vanishes in many cases, it is often silently omitted in the literature.

Let us further note that, looking at the simple derivation of equation (88), all ambiguities can be overcome by coming back to the microscopic definition of $\rho(\mathbf{r})$. As often with functionals, the notational problem is present only when working at

the field level, where it stems from an underlying ambiguity concerning the gradient symbol $\nabla$, which is used in different contexts to represent either a total derivative (acting on both implicit and explicit dependences of $D(\mathbf{r},[\rho])$, and hence containing in practice a functional derivative) or a partial derivative acting only on the first argument of $D$. This ambiguity translates into an ordering problem at the level of the Fokker-Planck equation. However, at the large deviation level—which corresponds here to the large size limit—we are effectively interested in the small noise limit of our stochastic partial differential equations. The various ordering of the Fokker-Planck equation differ by terms, similar to those that distinguish Itō and Stratonovich time-discretisation, which are generally negligible [69]. This is why the issue was for instance (rightly) neglected in [71].

**Mesoscopic Langevin equation.** Let us now consider a function $f(\mathbf{r})$ and compute the time evolution of $f(\mathbf{r}_\mu(t))$ where $\mathbf{r}_\mu(t)$ is solution of the Langevin equation (55). Using Itō's formula [73,74], one finds

$$\dot{f}(\mathbf{r}_\mu(t)) = \big[\mathbf{A} + \sqrt{2D}\boldsymbol{\eta}\big]\nabla f(\mathbf{r}_\mu) + D\Delta f(\mathbf{r}_\mu) \tag{92}$$

where

$$\mathbf{A} = \mathbf{V} + \nabla_1 D(\mathbf{r}_\mu,[\rho]) + \big(\nabla_{\mathbf{r}_\mu}\frac{\delta}{\delta\rho(\mathbf{r}_\mu)}\big)D(\mathbf{r}_\mu,[\rho]) \tag{93}$$

Introducing $\rho_\mu = \delta(\mathbf{r}-\mathbf{r}_\mu)$ and using that, for any function $H$, $H(\mathbf{r}_\mu) = \int \mathrm{d}\mathbf{r}\rho_\mu H(\mathbf{r})$, Eq. (92) can be rewritten

$$\dot{f}(\mathbf{r}_\mu(t)) = \int \mathrm{d}\mathbf{r}\rho_\mu(\mathbf{r},t)[(\mathbf{A} + \sqrt{2D}\boldsymbol{\eta})\nabla f(\mathbf{r}) + D(\mathbf{r},[\rho])\Delta f(\mathbf{r})] \tag{94}$$

where the derivatives in $\nabla f(\mathbf{r})$ and $\Delta f(\mathbf{r})$ are now taken with respect to $\mathbf{r}$. The last term in (94), even though it looks harmless, requires some explanations. Indeed, $D(\mathbf{r}_\mu,[\rho])$ has dependencies on $\mathbf{r}_\mu$ both through its explicit dependence and through its functional dependence on $\rho(\mathbf{r}') = \sum_\alpha \delta(\mathbf{r}'-\mathbf{r}_\alpha)$. When going from (92) to (94), we use that

$$\delta(\mathbf{r}-\mathbf{r}_\mu)D(\mathbf{r}_\mu,[\rho])\Delta f(\mathbf{r}_\mu) = \delta(\mathbf{r}-\mathbf{r}_\mu)D(\mathbf{r},[\rho])\Delta f(\mathbf{r}), \tag{95}$$

where we have replaced all the $\mathbf{r}_\mu$'s by $\mathbf{r}$ *but the one in* $\rho$, i.e., $\rho(\mathbf{r}') = \sum_\alpha \delta(\mathbf{r}'-\mathbf{r}_\alpha)$ has not been replaced by $\delta(\mathbf{r}'-\mathbf{r}) + \sum_{\alpha\neq\mu}\delta(\mathbf{r}'-\mathbf{r}_\alpha)$. There is thus no dependence of $D$ on $\mathbf{r}$ through $\rho$. From now on, gradients $\nabla D(\mathbf{r},[\rho])$ are not ambiguous anymore: they solely apply to the first argument of $D$ which is the only place where $D$ depends on $\mathbf{r}$. There is thus no need anymore for the notation $\nabla_1$. Integrating by part Eq. (94) then leads to

$$\dot{f}(\mathbf{r}_\mu(t)) = \int \mathrm{d}\mathbf{r} f(\mathbf{r})\nabla\cdot[-(\mathbf{A} + \sqrt{2D}\boldsymbol{\eta})\rho_\mu(\mathbf{r},t) + \nabla(D\rho_\mu)] \tag{96}$$

Alternatively, $\dot{f}(\mathbf{r}_\mu)$ can also be written

$$\dot{f}(\mathbf{r}_\mu) = \int \mathrm{d}\mathbf{r}\dot{\rho}_\mu(\mathbf{r})f(\mathbf{r}) \tag{97}$$

Since the equations (96) and (97) hold for any function $f$, one gets

$$\dot{\rho}_\mu = \nabla[-(\mathbf{A} + \sqrt{2D}\boldsymbol{\eta})\rho_\mu(\mathbf{r},t) + \nabla(D\rho_\mu)] \tag{98}$$

Introducing the Gaussian white noise

$$\sqrt{2D\rho}\Lambda \equiv \sum_{\mu} \sqrt{2D}\boldsymbol{\eta}_{\mu}\rho_{\mu} \tag{99}$$

whose statistics satisfy

$$\langle \Lambda \rangle = 0; \qquad \langle \Lambda(\mathbf{r},t)\Lambda(\mathbf{r}',t')\rangle = \delta(t-t')\delta(\mathbf{r}-\mathbf{r}') \tag{100}$$

one gets

$$\dot{\rho}(\mathbf{r}) = \nabla[-\rho(\mathbf{r})\mathbf{V} + D\nabla\rho(\mathbf{r}) - \rho\big(\nabla_{\mathbf{r}}\frac{\delta}{\delta\rho(\mathbf{r})}\big)D - \sqrt{2D\rho}\Lambda] \tag{101}$$

which is Eq. (56) as required.

## C Functional Fokker-Planck Equation

The easiest way to derive the Fokker-Planck equation (58) starting from the Langevin equation (56) is to spatially discretize the latter in one spatial dimension

$$\dot{\rho}_i = A_i + \frac{1}{2}(B_{i,i+1}\eta_{i+1} + B_{i,i-1}\eta_{i-1}) \tag{102}$$

where

$$A_i = \nabla_i\big[-\rho_i V_i + \frac{1}{2}D_i(\rho_{i+1}-\rho_{i-1}) + \frac{1}{2}\big(\frac{\partial D_i}{\partial\rho_{i+1}} - \frac{\partial D_i}{\partial\rho_{i-1}}\big)\rho_i\big] \tag{103}$$

$$B_{i,i+1} = -\frac{1}{2}\sqrt{2D_{i+1}\rho_{i+1}} \qquad \text{and} \qquad B_{i,i-1} = \frac{1}{2}\sqrt{2D_{i-1}\rho_{i-1}} \tag{104}$$

Note that we use centred differences $\nabla_i O_i \equiv \frac{1}{2}(O_{i+1}-O_{i-1})$ to respect the isotropy of the equation. One can then use the general relation between Itō-Langevin dynamics and the Fokker-Planck equation [73],

$$\dot{x}_i = A_i + B_{ij}\eta_j \quad \longrightarrow \quad \dot{P}(x) = -\sum_i \frac{\partial}{\partial x_i}A_i P + \frac{1}{2}\sum_{i,j,k}\frac{\partial}{\partial x_i}\frac{\partial}{\partial x_j}B_{ik}B_{jk}P \tag{105}$$

to derive the Fokker-Planck equation satisfied by $P(\rho_i)$. To do so, we first note that

$$\begin{aligned} 2\sum_k B_{ik}B_{jk} &= \sum_k \Big[\sqrt{D_{i+1}\rho_{i+1}}\delta_{k,i+1} + \sqrt{D_{i-1}\rho_{i-1}}\delta_{k,i-1}\Big] \\ &\quad\times \Big[\sqrt{D_{j+1}\rho_{j+1}}\delta_{k,j+1} + \sqrt{D_{j-1}\rho_{j-1}}\delta_{k,j-1}\Big] \qquad (106) \\ &= \sqrt{D_{i+1}\rho_{i+1}D_{j+1}\rho_{j+1}}\delta_{i,j} - \sqrt{D_{i-1}\rho_{i-1}D_{j+1}\rho_{j+1}}\delta_{i-2,j} \\ &\quad - \sqrt{D_{i+1}\rho_{i+1}D_{j-1}\rho_{j-1}}\delta_{i+2,j} + \sqrt{D_{i-1}\rho_{i-1}2D_{j-1}\rho_{j-1}}\delta_{i,j} \qquad (107) \end{aligned}$$

To (slightly) lighten the notation, we write $\partial_{\rho_i}$ for the operator $\frac{\partial}{\partial\rho_i}$. The second order differential operator then becomes

$$\begin{aligned} 2\sum_{i,j,k}\partial_{\rho_i}\partial_{\rho_j}B_{ik}B_{jk} &= \sum_i \partial_{\rho_i}\big[\partial_{\rho_i}D_{i+1}\rho_{i+1} - \partial_{\rho_{i-2}}D_{i-1}\rho_{i-1} \\ &\qquad - \partial_{\rho_{i+2}}D_{i+1}\rho_{i+1} + \partial_{\rho_i}D_{i-1}\rho_{i-1}\big] \\ &= \sum_i \partial_{\rho_i}\big(\partial_{\rho_i} - \partial_{\rho_{i+2}}\big)D_{i+1}\rho_{i+1} - \sum_i \partial_{\rho_i}\big(\partial_{\rho_{i-2}} - \partial_{\rho_i}\big)D_{i-1}\rho_{i-1} \end{aligned}$$

Shifting by $\pm 1$ the indices in the two sums, one finally gets

$$2\sum_{i,j,k}\partial_{\rho_i}\partial_{\rho_j}B_{ik}B_{jk}=\sum_i\left(\frac{\partial}{\partial\rho_{i-1}}-\frac{\partial}{\partial\rho_{i+1}}\right)\left(\frac{\partial}{\partial\rho_{i-1}}-\frac{\partial}{\partial\rho_{i+1}}\right)D_i\rho_i \tag{108}$$

We now have to compute the drift term in the Fokker-Planck equation $\sum_i \partial_{\rho_i}A_i$. Noting that $A_i$ is a gradient, $A_i=\nabla_i C_i$, where $C_i$ can be read in (103), the drift term can be rewritten

$$\begin{aligned}2\sum_i\partial_{\rho_i}A_i&=\sum_i\partial_{\rho_i}(C_{i+1}-C_{i-1})=\sum_i(\partial_{\rho_{i-1}}-\partial_{\rho_{i+1}})C_i \\ &=\sum_i(\partial_{\rho_{i-1}}-\partial_{\rho_{i+1}})\left(-\rho_i V_i+D_i\frac{\rho_{i+1}-\rho_{i-1}}{2}+\frac{1}{2}\left(\frac{\partial D_i}{\partial\rho_{i+1}}-\frac{\partial D_i}{\partial\rho_{i-1}}\right)\rho_i\right)\end{aligned} \tag{109}$$

Putting everything together yields

$$\dot{P}=\sum_i\frac{\partial_{\rho_{i-1}}-\partial_{\rho_{i+1}}}{2}\left(\rho_i V_i-D_i\nabla_i\rho_i-\frac{\rho_i}{2}\Big(\frac{\partial D_i}{\partial\rho_{i+1}}-\frac{\partial D_i}{\partial\rho_{i-1}}\Big)+\frac{\partial_{\rho_{i-1}}-\partial_{\rho_{i+1}}}{2}D_i\rho_i\right) \tag{110}$$

Let us now note that $\rho_i$ commutes with $\partial_{\rho_{i-1}}-\partial_{\rho_{i+1}}$ but not $D_i$, since the latter is in principle a function of all the $\rho_j$'s. However, the application of $\partial_{\rho_{i-1}}-\partial_{\rho_{i+1}}$ on $D_i$ exactly cancels the one before last term in (110), so that

$$\dot{P}=\sum_i\frac{1}{2}(\partial_{\rho_{i-1}}-\partial_{\rho_{i+1}})\left(\rho_i V_i-D_i\nabla_i\rho_i+D_i\rho_i\frac{\partial_{\rho_{i-1}}-\partial_{\rho_{i+1}}}{2}\right)P$$

Taking at this stage the continuum limit and integrating once by part yields the correct Fokker-Planck equation

$$\dot{P}=-\int\mathrm{d}x\frac{\partial}{\partial\rho(x)}\nabla\left(\rho(x)V(x,[\rho])-D(x,[\rho])\nabla\rho-D(x,[\rho])\rho\nabla_x\frac{\delta}{\delta\rho(x)}\right)P \tag{111}$$

where one has recognised the operator

$$\frac{1}{2}(\partial_{\rho_{i-1}}-\partial_{\rho_{i+1}})=\nabla_i\frac{\partial}{\partial\rho_i}\longrightarrow\nabla_x\frac{\delta}{\delta\rho(x)} \tag{112}$$

Equation (112) is actually the best way to make sense of this operator and to see that the gradient really applies to the field with respect to which we are taking a functional derivative and not to the argument of this functional derivative. The equation (111) directly generalizes to (58) in higher dimensions. We note that to get the correct ordering between $\rho D$ and $\nabla_{\mathbf{r}}\frac{\delta}{\delta\rho(\mathbf{r})}$ in the Fokker-Planck equation, it was necessary to correctly account for the atypical form of the spurious Itō drift as defined in the main text.

## References

1. B. Derrida, *J. Stat. Mech.* P07023 (2007).
2. M. Kac. *Enigmas of Chance: an Autobiography*, Univ of California Press (1985).
3. S. Ramaswamy, *Annu. Rev. Cond. Mat. Phys.* **1**, 323 (2010).
4. Cates M. E., *Rep. Prog. Phys.* **75**,042601 (2012).

5. P. Romanczuk, M. Baer, W. Ebeling, B. Lindner, L. Schimansky-Geier, *Eur. Phys. J. Special-Topics* **202**, 1 (2012).
6. M. C. Marchetti, J.-F. Joanny, S. Ramaswamy, T. B. Liverpool, J. Prost, M. Rao, R. A. Simha, *Rev. Mod. Phys.* **85**, 1143 (2013).
7. W. F. Paxton, S. Sundararajan, T. E. Mallouk, A. Sen, *Ang. Chimie - Int. Ed.* **45**, 5420 (2006).
8. J. R. Howse, R. A. L. Jones, A. J. Ryan, T. Gough, R. Vafabakhsh, R. Golestanian, *Phys. Rev. Lett.* **99**, 048102 (2007).
9. R. Golestanian, T. B. Liverpool, A. Ajdari, *New J. of Phys.* **9**, 126 (2007).
10. J. Palacci, C. Cottin-Bizonne, C. Ybert, L. Bocquet, *Phys. Rev. Lett.* **105**, 088304 (2010).
11. I. Theurkauff, C. Cottin-Bizonne, J. Palacci, C. Ybert, L. Bocquet, *Phys. Rev. Lett.* **108**, 268303 (2012).
12. I. Buttinoni, J. Bialké, F. Kümmel, H. Löwen, C. Bechinger, T. Speck, *Phys. Rev. Lett.* **110**, 238301 (2013)
13. J. Palacci, S. Sacanna, A. P. Stenberg, D. J. Pine, P. M. Chaikin, *Science* **339**, 936 (2013).
14. S. Thutupalli, R. Seeman, S. Herminghaus, *New J. Phys.* **13**, 073021 (2011).
15. Y. Fily, M. C. Marchetti, *Phys. Rev. Lett.* **108**, 235702 (2012).
16. G. S. Redner, M. F. Hagan, A. Baskaran, *Phys. Rev. Lett.* **110**, 055701 (2013).
17. J. Stenhammar, A. Tiribocchi, R. J. Allen, D. Marenduzzo, M. E. Cates, *Phys. Rev. Lett.* **111**, 147502 (2013).
18. A. Wysocki, R. G. Winkler, G. Gompper, *Europhys. Lett.* **105**, 48004 (2014).
19. J. Stenhammar, D. Marenduzzo, R. J. Allen, M. E. Cates, *Soft Matter* **10**, 1489 (2014).
20. T. Speck, J. Bialké, A. M. Menzel, H. Löwen, *Phys. Rev. Lett.* **112**, 218304 (2014).
21. G. S. Redner, A. Baskaran, M. F. Hagan, *Phys. Rev. E* **88**, 012305 (2013).
22. S. A. Mallory, A. Saric, C. Valeriani, A. Cacciuto, *Phys. Rev. E* **89**, 052303 (2014).
23. X. B. Yang, L. M. Manning, M. C. Marchetti, *Soft Matter* **10**, 6477 (2014).
24. S. C. Takatori, W. Yan, J. F. Brady, *Phys. Rev. Lett.* **113**, 028103 (2014).
25. Y. Fily, S. Henkes, M. C. Marchetti, *Soft Matter* **10**, 2132 (2014).
26. P. Galajda, J. Keymer, P. Chaikin, R. Austin, *J. Bacteriol.* **189**, 8704 (2007); P. Galajda *et al.*, *J. Modern Optics* **55**, 3413-3422 (2008).
27. R. Di Leonardo, L. Angelani, D. DellArciprete, G. Ruocco, V. Iebba, S. Schippa, M. P. Conte, F. Mecarini, F. De Angelis, E. Di Fabrizio, *Proc. Natl. Acad. Sci. USA* **107**, 9541 (2010).
28. A. Sokolov, M. M. Apodaca, B. A. Grzybowski, I. S. Aranson, *Proc. Natl. Acad. Sci. USA* **107**, 969 (2010).
29. J. Saragosti, V. Calvez, N. Bournaveas, B. Perthame, A. Buguin, P. Silberzan, *Proc. Natl. Acad. Sci. USA* **108**, 16235 (2011).
30. C. Liu, X. Fu, L. Liu, X. Ren, C. K. L. Chau, S. Li, L. Xiang, H. Zeng, G. Chen, L.-H. Tang, P. Lenz, X. Cui, W. Huang, T. Hwa, J.-D. Huang,*Science* **334**, 238 (2011).
31. I. D. Vladescu, E. J. Marsden, J. Schwarz-Linek, V. A. Martinez, J. Arlt, A. N. Morozov, D. Marenduzzo, M. E. Cates, W. C. K. Poon, *Phys. Rev. Lett.* **113**, 268101 (2014).
32. J. Schwarz-Linek, C. Valeriani, A. Cacciuto, M. E. Cates, D. Marenduzzo, A. N. Morozov, W. C. K. Poon, *Proc. Natl. Acad. Sci. USA* **109**, 4052 (2012).
33. R. W. Nash, R. Adhikari, J. Tailleur, M. E. Cates, *Phys. Rev. Lett.* **104**, 258101 (2010).
34. M. Enculescu, H. Stark, *Phys. Rev. Lett.* **107** 058301 (2011).
35. R. Matas-Navarro, R. Golestanian, T. B. Liverpool, S. M. Fielding, *Phys. Rev. E.* **90**, 032304 (2014).
36. A. Zoettl, H. Stark, *Phys. Rev. Lett.* **112**, 118101 (2014).
37. E. Korobkova, T. Emonet, J. M. G. Vilar, T.S. Shimizu, P. Cluzel, *Nature* **428**, 574 (2004).
38. F. Thiel, L. Schimansky-Geier, I. M. Sokolov, *Phys. Rev. E* **86**, 021117 (2012).
39. A. P. Solon, Y. Fily, A. Baskaran, M. E. Cates, Y. Kafri, M. Kardar, J. Tailleur, arXiv:1412.3952 (2014).
40. A. P. Solon, J. Stenhammar, R. Wittkowski, M. Kardar, Y. Kafri, M. E. Cates, J. Tailleur, *Phys. Rev. Lett.*, In press, arXiv:1412.5475 (2014).

41. J. Tailleur, M.E. Cates, *EPL* **86**, 60002 (2009).
42. G. Szamel, *Phys. Rev. E* **90**, 012111 (2014).
43. F. Ginot, I. Theurkauff, D. Levis, C. Ybert, L. Bocquet, L. Berthier, C. Cotton-Bizonne, *Phys. Rev. X* **5** 011004 (2015).
44. S. C. Takatori, J. F. Brady, *Phys. Rev. E* **91**, 032117 (2015).
45. J. Tailleur, M. E. Cates, *Phys. Rev. Lett.***100**, 218103 (2008).
46. M. E. Cates, J. Tailleur, *EPL* **101**, 20010 (2013).
47. A. G. Thompson, J. Tailleur, M. E. Cates, R. A. Blythe, *J Stat. Mech.* P02029 (2011).
48. R. Wittkowski, A. Tiribocchi, J. Stenhammar, R. J. Allen, D. Marenduzzo, M. E. Cates, *Nature Commun.* **5**, 4351 (2014).
49. Fu X. et al, *Phys. Rev. Lett.* **108**, 198102 (2012).
50. M. B. Miller, B. L. Bassler, *Ann. Rev. Microbiol.* **55**, 165 (2001).
51. H. C. Berg, *E. coli in Motion* Springer, NY (2004).
52. M. J. Schnitzer, *Phys. Rev. E* **48**, 2553 (1993).
53. S. Saha, R. Golestanian, S. Ramaswamy, *Phys. Rev. E* **89**, 062316 (2014)
54. M. Meyer, L. Schimansky-Geier, P. Romanczuk, *Phys. Rev. E* **89**, 022711 (2014).
55. F. D. C. Farrell, J. Tailleur, D. Marenduzzo, M. C. Marchetti, *Phys. Rev. Lett.* **108**, 248101 (2012).
56. M. E. Cates, J. Tailleur, *Ann. Rev. Cond. Matt. Phys.* **6**, 219 (2015).
57. M. E. Cates, D. Marenduzzo, I. Pagonabarraga, J. Tailleur, *Proc. Nat. Acad. Sci. USA* **107**, 11715 (2010).
58. J. Bialké, T. Speck, H. Löwen, *Phys. Rev. Lett.* **108**, 168301 (2012).
59. T. Speck, J. Bialk, A. M. Menzel, H. Löwen, *Phys. Rev. Lett.* **112**, 218304 (2014).
60. M. B. Wan, C. O. Reichhardt, Z. Nussinov, C. Reichhardt, *Phys. Rev. Lett.* **101**, 018102 (2008).
61. J. Elgeti, G. Gompper *EPL (Europhysics Letters)* **85**, 38002 (2009).
62. J. Elgeti, G. Gompper, *EPL (Europhysics Letters)* **101**, 48003 (2013).
63. J. Elgeti, G. Gompper, *EPL (Europhysics Letters)* **109**, 58003 (2015).
64. The Digital Library of Mathematical Functions, http://dlmf.nist.gov/28
65. F. A. Alhargan, *SIAM Review* **38**, 239-255 (1996).
66. L. F. Cugliandolo, *J. Phys. A* **44**, 3001 (2011). D. Loi, S. Mossa, L. F. Cugliandolo, *Physical Review E* **77** 051111 (2008); D. Loi, S. Mossa, L. F. Cugliandolo, *Soft Matter* **7** 3726 (2011).
67. Y. Fily, A. Baskaran, M. F. Hagan, *Soft Matt.* **10**, 5609 (2014).
68. Y. Fily, A. Baskaran, M. F. Hagan, *Phys. Rev. E* **91**, 012125 (2015).
69. J. Tailleur, J. Kurchan, V. Lecomte, *J. Phys. A* **41**, 50500 (2008).
70. P. Romanczuk, L. Schimansky-Geier, *Interface focus* **2**, 746 (2012).
71. J. Barré, R. Chétrite, M. Muratori, F. Peruani, *J. Stat. Phys.* **158** 589 (2015).
72. D. S. Dean, *J. Phys. A. Math. Gen.* **29**, L613 (1996).
73. H. Risken, *The Fokker-Planck Equation: Methods of Solution and Applications*, Springer Verlag, Berlin (1996).
74. B. K. Oksendal, *Stochastic Differential Equations: An Introduction with Applications*, 5th Edn., Springer Verlag, Berlin (2000)
75. E. Bertin et al., *New J. Physics* **15**, 085032 (2013).

## 4.3 Effet d'un $v(\rho)$ asymétrique et non-local

Nous avons discuté dans l'introduction de ce chapitre la nécessité, pour décrire la MIPS, de considérer des particules autopropulsées à une vitesse $v(\tilde{\rho})$ où $\tilde{\rho}$ est la densité moyennée autour de chaque particule. Dans un premier temps (section 4.3.1), nous étudierons l'effet d'une densité calculée de façon isotrope autour des particules. Nous considérerons ensuite (section 4.3.2) l'effet d'un moyennage asymétrique de la densité, qui dépend de la direction de déplacement. À la section 4.3.3, nous verrons que, par un changement de variables, on peut définir une fonction qui joue exactement le rôle de l'énergie libre pour la coexistence de phases. Les densités de coexistence seront alors calculées par la construction de tangente commune sur cette fonction, comme à l'équilibre. À chaque étape, nous comparerons les prédictions théoriques à des simulations des modèles microscopiques correspondants. À notre connaissance, il s'agit du premier système pour lequel une théorie analytique prédit quantitativement le diagramme des phases de la transition de phase induite par la motilité mesuré numériquement.

### 4.3.1 Effet d'un moyennage isotrope de la densité

*Calcul des termes de tension de surface*

Reprenons l'hydrodynamique fluctuante construite pour un $v(\rho)$ local dans l'article C

$$\dot{\rho} = \nabla \cdot \left[ D(\rho)\nabla\rho - \rho\mathbf{V}(\rho) + \sqrt{2D(\rho)\rho}\boldsymbol{\eta} \right], \tag{4.4}$$

$$\text{où} \quad \mathbf{V} = -\frac{\tau v(\rho)\nabla v(\rho)}{d} \qquad D = \frac{\tau v(\rho)^2}{d} + D_t \tag{4.5}$$

où $\tau = (\alpha + (d-1)D_r)^{-1}$ est le temps de persistance d'une particule. Par soucis de simplicité, nous prendrons $D_t = 0$ dans la suite. Comme nous l'avons vu précédemment, l'équation (4.4) décrit un système qui satisfait le bilan détaillé par rapport à l'énergie libre

$$\mathcal{F}[\rho] = \int f\left[\rho(\mathbf{r})\right] d\mathbf{r}, \quad \text{où} \quad f(\rho) = \rho(\ln\rho - 1) + \int_0^\rho \ln v(s) ds, \tag{4.6}$$

la dynamique s'écrivant alors

$$\dot{\rho} = \nabla \cdot \left[ \rho D(\rho)\nabla\frac{\delta\mathcal{F}}{\delta\rho} + \sqrt{2D(\rho)\rho}\boldsymbol{\eta} \right] \tag{4.7}$$

Dans toutes ces équations, c'est le champ de densité microscopique $\rho(\mathbf{r}) = \sum_i \delta(\mathbf{r} - \mathbf{r}_i)$ qui intervient.

Considérons maintenant des particules qui adaptent leur vitesse à la densité $\tilde{\rho}$ moyennée de façon isotrope dans leur voisinage. Techniquement, la moyenne est effectuée par un noyau $K$

$$\tilde{\rho}(\mathbf{r}) = \int K(\mathbf{r}-\mathbf{r}')\rho(\mathbf{r}')d\mathbf{r}' = \int K(\mathbf{r}')\rho(\mathbf{r}-\mathbf{r}')d\mathbf{r}' \tag{4.8}$$

Le rayon d'interaction des particules est donné par la « taille » du noyau : le $r_0$ tel que $K(r) = 0$ pour tout $r > r_0$. Pour un $r_0$ petit devant la longueur typique des variations de $\rho$, on peut développer $\rho(\mathbf{r}-\mathbf{r}')$ dans l'équation (4.8)

$$\tilde{\rho}(\mathbf{r}) = \int K(\mathbf{r}')\left[\rho(\mathbf{r}) - \mathbf{r}'\cdot\nabla\rho + \frac{1}{2}|\mathbf{r}'|^2\Delta\rho\right]d\mathbf{r}' + \mathcal{O}(\nabla^3\rho) \tag{4.9}$$

Pour un noyau isotrope, $K(\mathbf{r}) = K(|\mathbf{r}|)$, les termes de gradient d'ordre impair sont nuls et on obtient donc

$$\tilde{\rho}(\mathbf{r}) = \rho(\mathbf{r}) + \gamma^2\Delta\rho + O\left(\nabla^4\rho\right) \tag{4.10}$$

avec $\gamma^2 = \frac{1}{2}\int|\mathbf{r}'|^2K(|\mathbf{r}'|)d\mathbf{r}'$, une constante. On peut alors développer la vitesse pour obtenir

$$v[\tilde{\rho}(\mathbf{r})] = v[\rho(\mathbf{r})] + \gamma^2 v'[\rho(\mathbf{r})]\Delta\rho + O\left(\nabla^4\rho\right) \tag{4.11}$$

On peut maintenant remplacer $v(\rho)$ par $v(\tilde{\rho})$ dans l'équation (4.4) et développer en gradients de $\rho$. $\mathbf{V}/D$ se réécrit alors

$$\frac{\mathbf{V}(\tilde{\rho})}{D} = -\frac{\nabla v(\tilde{\rho})}{v(\tilde{\rho})} = -\nabla\ln v(\tilde{\rho}) = -\nabla\left[\log v(\rho) + \frac{\gamma^2 v'(\rho)}{v(\rho)}\Delta\rho + \mathcal{O}\left(\nabla^4\rho\right)\right] \tag{4.12}$$

et l'équation complète s'écrit donc

$$\dot{\rho} = \nabla\cdot\left[\rho D(\tilde{\rho})\nabla\left(\frac{\delta\mathcal{F}}{\delta\rho} - \kappa(\rho)\Delta\rho\right) + \sqrt{2D(\tilde{\rho})\rho}\boldsymbol{\eta}\right], \tag{4.13}$$

où $\kappa(\rho) = -\gamma^2 v'(\rho)/v(\rho)$ et $\mathcal{F}$ est l'énergie libre du cas $v(\rho)$ local, donnée par l'équation (4.6). Par rapport au cas $v(\rho)$ local, l'effet de la densité moyennée est donc simplement, au premier ordre, de rajouter un terme de tension de surface proportionnel à $\kappa(\rho)$.

Notons qu'il n'est pas possible de réécrire ce terme supplémentaire comme une contribution à l'énergie libre. Ce serait le cas pour une tension de surface avec $\kappa = \text{cte}$, mais à cause de la dépendance en densité, une énergie libre $\mathcal{F}_s = \int\kappa(\rho)|\nabla\rho|^2/2d\mathbf{r}'$ générerait un terme additionnel

$$\frac{\delta\mathcal{F}_s}{\delta\rho} = -\kappa(\rho)\Delta\rho - \kappa'(\rho)|\nabla\rho|^2 \tag{4.14}$$

Le système ne satisfait donc pas le bilan détaillé quand la tension de surface est prise en compte.

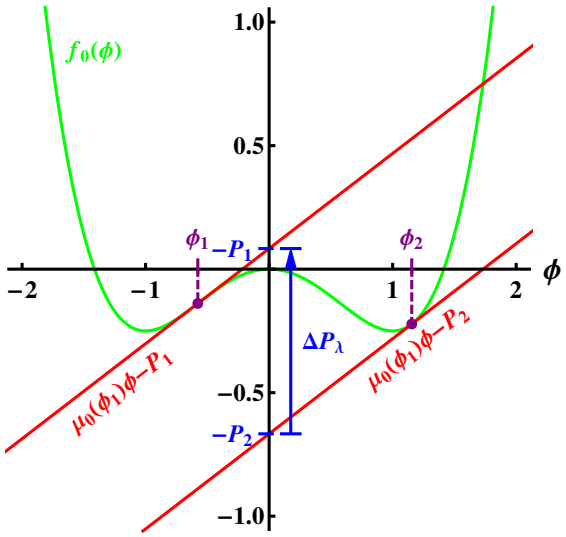


**Figure 4.4** – Schématisation de la construction de tangentes parallèles, reproduite de [47]. Les densités de coexistence ne sont pas données par la tangente commune sur l'énergie libre $f_0(\phi)$ mais par des tangentes parallèles dont l'écartement vertical, noté ici $\Delta P_\lambda$ peut être interprété comme un saut de pression thermodynamique entre les deux phases.

### *Effet d'une tension de surface non-linéaire*

Dans [47], Wittkowski et collaborateurs ont montré que l'ajout d'un terme de gradient $\lambda(\nabla\rho)^2$ avec $\lambda$ constant (à la place de notre $\kappa(\rho)\Delta\rho$) a un effet simple sur les densités de coexistence : ce terme engendre une différence de pression thermodynamique entre les deux phases. Les densités de coexistence sont alors données par une construction de tangentes parallèles, schématisée à la figure 4.4, sur l'énergie libre effective $\mathcal{F}$. Nous montrons ici que notre terme de tension de surface $\kappa(\rho)$ a le même effet et allons plus loin en donnant une formule analytique pour calculer la différence de pression, et donc les densités de coexistence.

Comme il est d'usage dans l'étude des séparations de phase, nous négligerons à présent le bruit [123]. Dans l'état stationnaire, le flux de densité s'annule, ce qui se traduit pour l'équation (4.13) par

$$\rho D(\tilde{\rho})\nabla\left(f'(\rho) - \kappa(\rho)\Delta\rho\right) = 0 \tag{4.15}$$

dont on déduit

$$f'(\rho) - \kappa(\rho)\Delta\rho = \text{cte} \equiv \mu \tag{4.16}$$

où nous avons défini la constante $\mu$ qui jouera le rôle d'un potentiel chimique dans la suite. À l'équilibre thermique, deux relations sont nécessaires pour déterminer

les densités de coexistence $\rho_g$ et $\rho_\ell$ dans le liquide et dans le gaz : l'égalité des potentiels chimiques et des pressions dans les deux phases.

L'égalité des potentiels chimiques donne, ici aussi, une première relation. En effet, les phases étant homogènes, on a directement

$$f'(\rho_g) = f'(\rho_\ell) = \mu \tag{4.17}$$

Pour une transition liquide-gaz d'équilibre, l'égalité des pressions est obtenue en multipliant l'équation (4.16) par $\nabla\rho$ et en intégrant le long d'une interface. Si l'on répète cela ici, en prenant l'interface le long de l'axe $\hat{x}$ entre un $x_g$ dans la phase gazeuse et un $x_\ell$ dans le liquide, on obtient

$$\int_{x_g}^{x_\ell} \left[f'(\rho)\nabla\rho - \mu\nabla\rho\right] dx = \int_{x_g}^{x_\ell} \kappa(\rho)\nabla\rho\Delta\rho dx \tag{4.18}$$

À l'équilibre, $\kappa$ = cte de telle sorte que le terme de droite de l'équation (4.18) s'annule. En utilisant la relation habituelle entre l'énergie libre et la pression thermodynamique, $P = f - \mu\rho$, l'équation (4.18) est alors bien équivalente à l'égalité des pressions $P(\rho_\ell) - P(\rho_g) = 0$ (elle-même équivalente à la construction de tangente commune). Cette relation n'est plus vraie en présence d'un $\kappa(\rho)$. Le terme de droite de l'équation (4.18) n'étant plus intégrable, il donne une contribution non nulle qu'on peut interpréter comme un saut de pression entre les deux phases. L'équilibre des phases est alors donné par la construction de tangentes parallèles de la figure 4.4, avec un saut de pression pour l'instant inconnu.

On peut toutefois obtenir une expression analytique pour les densités de coexistence en définissant une nouvelle « pression » qui sera égale dans les deux phases (c'est la seule caractéristique d'une pression que cette fonction possédera, d'où les guillemets). En divisant l'équation (4.16) par $\kappa(\rho)$, on a

$$\Delta\rho = \frac{f'(\rho) - \mu}{\kappa(\rho)} \tag{4.19}$$

et si on définit $\tilde{P}(\rho)$ par $\tilde{P}'(\rho) = [\mu - f'(\rho)]/\kappa$, on a bien $\tilde{P}(\rho_g) = \tilde{P}(\rho_\ell)$. Cette dernière égalité constitue la deuxième relation qui permet de fixer les densités de coexistence. Nous verrons à la section 4.3.3 que l'on peut aller plus loin, en redéfinissant le champ de densité, pour obtenir une nouvelle énergie libre sur laquelle les densités de coexistence seront données par une construction de tangente commune.

### *Vérifications numériques*

Nous voulons maintenant faire le lien entre les prédictions théoriques données plus haut et les résultats obtenus par simulation de modèles microscopiques. Pour

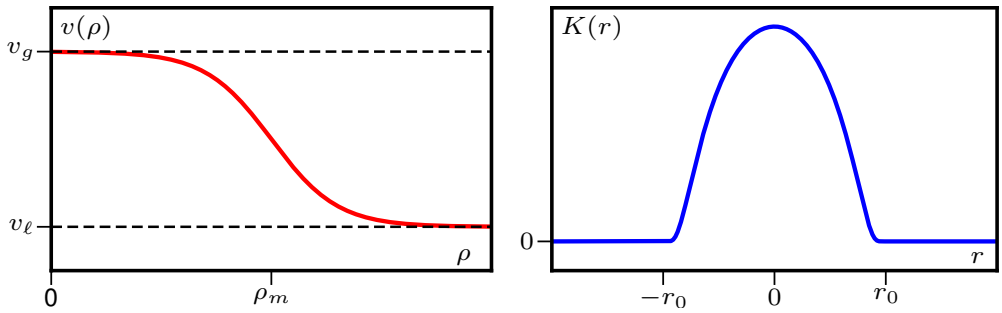


**Figure 4.5** – **Gauche** : Forme de $v(\rho)$ utilisée dans les simulations numériques, données par l'équation (4.20). **Droite** : Noyau de moyennage de rayon $r_0$ utilisé pour calculer la densité moyenne autour d'une particule, donné par l'équation (4.21).

cela, nous avons choisi d'utiliser une dépendance $v(\rho)$, représentée à la figure 4.5 (gauche), donnée par

$$v(\rho) = v_g - \frac{(v_g - v_\ell)}{2}\left[\tanh\left(\frac{\rho - \rho_m}{L_f}\right) + 1\right] \tag{4.20}$$

Cette forme interpole, de façon plus ou moins abrupte suivant la valeur de $L_f$, entre une vitesse rapide $v_g$ à basse densité et une vitesse plus lente $v_\ell$ à haute densité. En outre, cette forme permet de changer l'échelle de densité en changeant $\rho_m$ : quand $\rho_m$ augmente les densités de coexistence dans le gaz *et* le liquide augmentent aussi, ce qui nous permet de les mesurer avec précision. Le noyau de moyennage que nous utiliserons est une « cloche de Schwartz » de rayon $r_0$

$$K(r) = \frac{1}{Z}\exp\left(-\frac{1}{1-\left(\frac{r}{r_0}\right)^2}\right), \quad \text{si } r \leq r_0, \qquad K(r) = 0 \text{ sinon} \tag{4.21}$$

où $Z$ est une constante de normalisation telle que $\int K(|\mathbf{r}|)d\mathbf{r} = 1$. Cette fonction, représentée à la figure 4.5 (droite), a la particularité d'être infiniment dérivable à support compact $[-r_0,r_0]$.

Les simulations que nous présentons maintenant ont été réalisées pour des RTP sur un réseau 1d avec des conditions aux bords périodiques. C'est le modèle qui est numériquement le plus efficace, nous permettant d'obtenir les meilleures statistiques. Nous vérifierons cependant sur un autre exemple que l'on trouve les même résultats pour des particules évoluant dans un espace continu en deux dimensions. L'algorithme que nous avons utilisé sur réseau est celui de la mise à jour séquentielle aléatoire. Pour un système contenant $N$ particules, à chaque pas de temps $dt/N$, une particule est choisie au hasard. Elle saute alors sur le site voisin avec

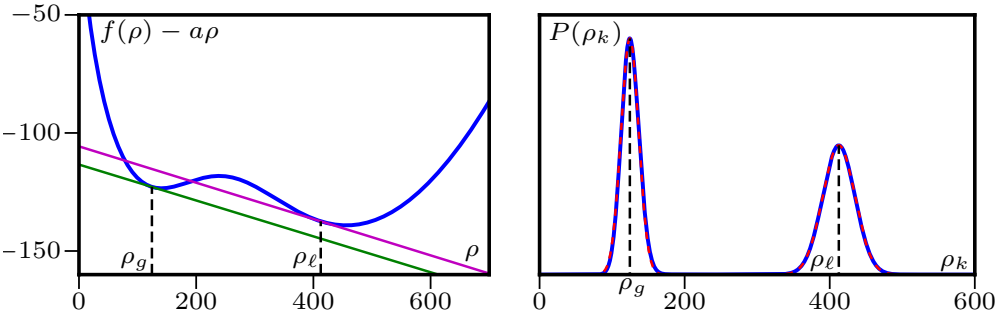


**Figure 4.6** – **Gauche** : Densité d'énergie libre $f(\rho)$ (décalée de $a\rho$ avec $a = 7.75$ pour plus de lisibilité) et tangentes aux densités de coexistence $\rho_g$ et $\rho_\ell$ mesurées dans des simulations de RTP sur réseau 1d. Les deux tangentes sont parallèles, l'erreur relative sur la pente étant $\frac{|f'(\rho_g)-f'(\rho_\ell)|}{|f'(\rho_g)|} = 10^{-4}$. **Droite** : Histogramme du nombre de particule sur un site. Les densités de coexistence sont mesurées en ajustant chaque bosse par une distribution gaussienne (les lignes pointillées rouges). Paramètres : $v_g = 20$, $v_\ell = 5$, $\alpha = 1$, $\rho_m = 200$, $L_f = 100$, $r_0 = 2$.

une probabilité $v(\tilde{\rho})dt$ et culbute avec une probabilité $\alpha dt$. La densité dans son voisinage est calculée en utilisant le noyau de l'équation (4.21). Pour une particule au site $k$,

$$\tilde{\rho}_k = \sum_{i=-r_0}^{r_0} K(i)\rho_{k+i} \tag{4.22}$$

Avant de comparer quantitativement les prédictions théoriques pour les densités de coexistence, on peut commencer par vérifier que celles-ci sont bien données par une construction de tangentes parallèles sur la densité d'énergie libre $f(\rho)$. Pour ce faire, on mesure les deux densités de coexistence dans une simulation et l'on trace les deux tangentes à l'énergie libre aux points correspondants. Le résultat est montré à la figure 4.6 (gauche) : les deux tangentes sont bien parallèles. Notons que cette construction est très sensible à la valeur des densités car celles-ci sont proches des minima de $f(\rho)$. Une petite variation de densité produit alors une grande variation de la pente, ce qui nous oblige à mesurer les densités avec précision. On choisit donc $\rho_m$ grand pour que les deux densités de coexistence soient grandes, et on les mesure en ajustant les histogrammes $P(\rho_k)$, où $\rho_k$ est le nombre de particules sur un site, à des Gaussiennes (voir figure 4.6, droite).

Nous avons vu que les densités de coexistence sont données par les égalités du potentiel chimique $f'(\rho_g) = f'(\rho_\ell) = \mu$ et par l'égalité de notre pression thermodynamique généralisée $\tilde{P}(\rho_g) = \tilde{P}(\rho_\ell)$ avec $\tilde{P}'(\rho) = (f'(\rho) - \mu)/\kappa(\rho)$. Ces deux équations peuvent être résolues numériquement pour obtenir $\rho_g$ et $\rho_\ell$, que l'on souhaite comparer aux simulations du modèle microscopique. Nous montrons la

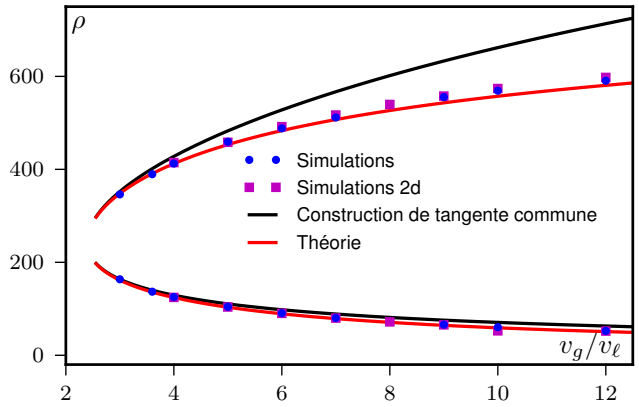


**Figure 4.7** – Densités de coexistence pour différents $v_g/v_\ell$, obtenus en variant $v_g$ à $v_\ell$ constant. Comparaison entre des simulations microscopiques de RTP (sur réseau 1d et dans le plan continu 2d), la prédiction théorique et ce qui serait donné par une construction de tangente commune. Paramètres : $v_\ell = 5$, $\alpha = 1$, $\rho_m = 200$, $L_f = 100$, $r_0 = 2$.

comparaison à la figure 4.7 sur un diagramme des phases obtenu en variant $v_g$ à $v_\ell$ constant. On voit que, sans aucun paramètre ajustable, l'accord est excellent. On peut aussi remarquer que la construction de tangente commune (qui revient à prendre $\kappa = \text{cte}$) donne des densités de coexistence acceptables quand $v_g \gtrsim v_\ell$ mais, qu'à grand $v_g/v_\ell$, il faut prendre en compte le terme de tension de surface pour prédire les binodales.

La coexistence que nous obtenons a quelques propriétés remarquables. Rappelons que les densités de coexistence sont données par les égalités de $f'$ et $\tilde{P}$, dont les expressions sont

$$f'(\rho) = \ln[\rho v(\rho)], \quad \tilde{P}(\rho) = \frac{f'(\rho) - \mu}{\kappa(\rho)}, \quad \text{où } \kappa(\rho) = -\frac{\gamma^2 v'(\rho)}{v} \tag{4.23}$$

Le noyau de moyennage $K$ intervient seulement dans la constante $\gamma$, qui apparaît en facteur dans $\kappa(\rho)$. Dans l'égalité des pressions, cette constante se simplifie et ne joue donc aucun rôle dans l'équilibre des phases, ce qui est vérifié numériquement à la figure 4.8. On obtient donc un résultat intéressant : toutes les manières de faire une moyenne isotrope de la densité conduisent à la même coexistence de phase. Pour une transition d'équilibre, la tension de surface ne joue aucun rôle dans l'équilibre des phases. Ici, la situation est plus subtile : les dépendances en $\rho$ de la tension de surface contribuent au calcul des binodales mais pas leurs préfacteurs constants. Nous verrons à la prochaine section que ce résultat survit pour une moyenne anisotrope de la densité.

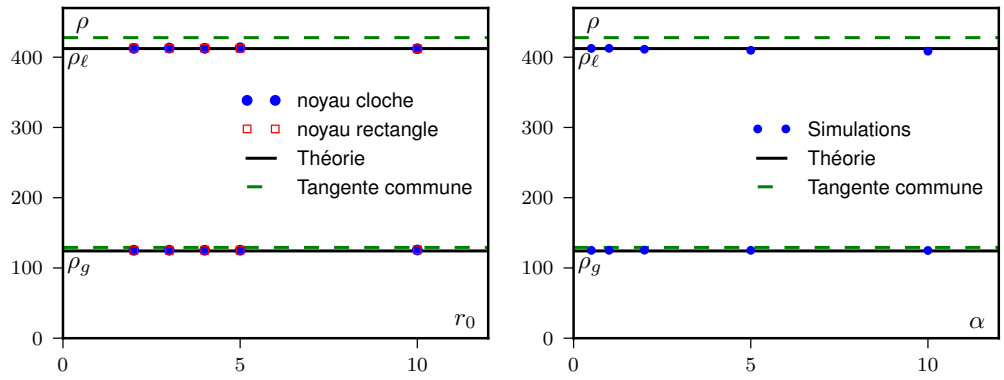


**Figure 4.8** – **Gauche** : La forme du noyau de moyennage n'influe pas sur les densités de coexistence. On considère ici deux types de noyaux (dont on varie la taille) : la cloche de l'équation (4.21) et un noyau rectangulaire ($K(r) = 1/(2r_0)$ quand $r < r_0$ et 0 sinon). **Droite** : Le temps de persistance des particules n'influe pas non plus sur les densités de coexistence. Paramètres : RTP en 1d sur réseau, $v_g = 20$, $v_\ell = 5$, $\alpha = 1$ (gauche), $\rho_m = 200$, $L_f = 100$, $r_0 = 2$ (droite).

On remarque également que le temps de persistance $\tau = (\alpha + (d-1)D_r)^{-1}$ n'apparaît pas dans les équations fixant les densités de coexistence, qui n'en dépendent donc pas (voir figure 4.8). Cela explique l'équivalence, pour des particules en $v(\rho)$, entre ABP et RTP observée dans l'article C (voir figure 6). Le fait que cette équivalence soit également vraie pour des interactions stériques reste une agréable surprise quant au pouvoir prédictif des théories en $v(\rho)$.

### 4.3.2 Effet d'un moyennage asymétrique

Intéressons-nous maintenant au cas où la densité n'est pas échantillonnée de manière isotrope autour des particules. La situation qui nous intéresse en particulier, schématisée à la figure 4.1, est celle de particules qui mesurent la densité « devant elles » (par rapport à leur direction d'autopropulsion), de la même manière que des sphères dures autopropulsées sont ralenties par les collisions avec les particules situées *devant* elles.

En pratique, nous considérerons que la densité est mesurée de façon isotrope à une distance $\varepsilon\mathbf{u}$ de la particule. Les particules se déplacent alors à la vitesse $v[\tilde{\rho}(\mathbf{r} + \varepsilon\mathbf{u})]$, où $\tilde{\rho}$ est mesurée grâce à un noyau isotrope, comme ceux considérés à la section précédente. Quand $\varepsilon$ est petit devant la longueur caractéristique des

variations de $\rho$, on peut faire l'approximation

$$v\left[\tilde{\rho}(\mathbf{r}+\varepsilon\mathbf{u})\right] \approx v\left[\tilde{\rho}(\mathbf{r})+\nabla\tilde{\rho}(\mathbf{r})\cdot\varepsilon\mathbf{u}\right] \tag{4.24}$$

$$\approx v\left[\tilde{\rho}(\mathbf{r})\right]+\nabla v\left[\tilde{\rho}(\mathbf{r})\right]\cdot\varepsilon\mathbf{u} \tag{4.25}$$

L'enjeu est alors de prendre en compte le nouveau terme $\nabla v(\tilde{\rho}(\mathbf{r}))\cdot\varepsilon\mathbf{u}$ dans notre description.

Nous montrons dans l'annexe B que l'on peut étendre le calcul de l'annexe A de l'article C pour construire une équation d'advection-diffusion décrivant des particules se déplaçant à une vitesse $v(\mathbf{r},\mathbf{u}) = v_0(\mathbf{r}) + \mathbf{v}_1(\mathbf{r})\cdot\mathbf{u}$. Cela nous permet ensuite, par le même chemin que dans l'article C, de construire l'hydrodynamique fluctuante de particules se déplaçant à la vitesse donnée par l'équation (4.25). L'hydrodynamique fluctuante est la même que pour le noyau isotrope de la section 4.3.1

$$\dot{\rho} = \nabla\cdot\left[\rho D(\tilde{\rho})\nabla\left(\frac{\delta\mathcal{F}}{\delta\rho}-\kappa(\rho)\Delta\rho\right)+\sqrt{2D(\tilde{\rho})\rho}\boldsymbol{\eta}\right] \tag{4.26}$$

L'énergie libre et la tension de surface sont cependant modifiées et incluent maintenant des contributions liées à l'asymétrie $\varepsilon$

$$\mathcal{F} = \int f[\rho(\mathbf{r})]d\mathbf{r}, \qquad f(\rho) = \rho(\ln\rho-1)+\int_0^\rho\left[\ln[v(u)]+\frac{\varepsilon}{\tau v(u)}\right]du, \tag{4.27}$$

$$\kappa(\rho) = -\gamma^2\frac{v'}{v}\left(1-\frac{\varepsilon}{\tau v}\right) \tag{4.28}$$

On peut alors déterminer les nouvelles densités de coexistence, fonctions de $\varepsilon$, de la même manière que pour un moyennage isotrope.

On montre à la figure 4.9 la comparaison entre les densités de coexistence prédites et celles mesurées en simulant des RTP sur un réseau 1d, pour des asymétries $\varepsilon = 1$ et $\varepsilon = 2$ sites du réseau. L'accord est très bon pour $\varepsilon = 1$ et pour $\varepsilon = 2$ à petit $v_g/v_\ell$, beaucoup moins à grand $v_g/v_\ell$. La raison exacte de ce désaccord n'est pas complètement claire. Des termes d'ordre supérieur dans le développement de l'équation (4.24) pourraient contribuer de façon significative à la tension de surface. Une analyse plus poussée des développements effectués ici sera l'objet d'un futur travail.

### 4.3.3 De nouvelles relations thermodynamiques

Nous allons montrer ici que l'on peut définir une nouvelle variable $R$, qui jouera le rôle d'un champ de densité, pour laquelle l'équilibre des phases est donné par les relations de thermodynamique d'équilibre. En particulier, les densités de coexistence seront données par la construction de tangente commune.

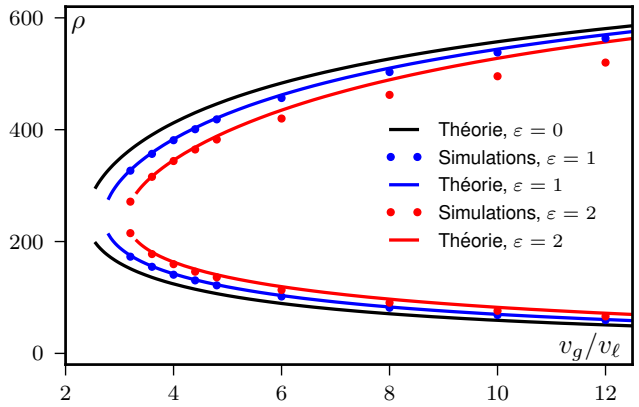


**Figure 4.9** – Comparaison entre les densités de coexistence prédites pour un moyennage asymétrique et les densités observées dans des simulations de RTP sur réseau en 1d. L'unité d'espace est la distance entre deux sites. $\varepsilon = k$ correspond donc à un moyennage décalé de $k$ sites par rapport à la particule. Paramètres : $v_\ell = 5$, $\alpha = 1$, $\rho_m = 200$, $L_f = 100$, $r_0 = 2$.

Reprenons l'équation (4.16) exprimant la nullité du flux de particules dans l'état stationnaire

$$f'(\rho) - \kappa(\rho)\Delta\rho = \text{cte} \equiv \mu \tag{4.29}$$

et définissons maintenant la variable

$$R(\rho) = \int_0^\rho \frac{1}{\kappa(s)} ds \tag{4.30}$$

qui vérifie $dR/d\rho = 1/\kappa(\rho)$.

L'équation (4.29) se réécrit alors pour la variable $R$

$$\frac{1}{\kappa}\frac{df}{dR} - \kappa^2 \Delta R - \kappa \frac{d\kappa}{dR}|\nabla R|^2 = \mu \tag{4.31}$$

qui peut s'écrire comme la dérivée d'une nouvelle énergie libre $\bar{\mathcal{F}}$

$$\mu = \frac{\delta \bar{\mathcal{F}}}{\delta R}, \qquad \bar{\mathcal{F}} = \int \left[ \bar{f}(R(\mathbf{r})) + \frac{\kappa^2}{2}|\nabla R|^2 \right] d\mathbf{r} \tag{4.32}$$

où la nouvelle densité d'énergie libre $\bar{f}$ est définie par la relation

$$\frac{d\bar{f}}{dR} = \frac{df}{d\rho} \tag{4.33}$$

Les densités de coexistence sont maintenant données par la construction de tangente commune sur la fonction $\bar{\mathcal{F}}$.

Le statut de cette fonction $\bar{\mathcal{F}}$ n'est pas évident. La variable $R$ n'est pas une quantité conservée, comme on peut le voir en écrivant sa dynamique par le calcul d'Itō

$$\dot{R} = \frac{\partial R}{\partial \rho}\dot{\rho} + \frac{1}{2}\frac{\partial^2 R}{\partial \rho^2}\sigma^2 \tag{4.34}$$

où $\sigma^2 = 2\nabla^2[\rho D(\tilde{\rho})]$ est la variance du bruit sur $\rho$. En définissant $\bar{D}(R) = \rho D(\tilde{\rho})$, on peut alors réécrire l'équation (4.34)

$$\dot{R} = \frac{1}{\kappa(R)}\nabla \cdot \left[\bar{D}(R)\nabla\frac{\delta\bar{\mathcal{F}}}{\delta R} + \sqrt{2\bar{D}(R)}\boldsymbol{\eta}\right] - \frac{1}{\kappa(R)^3}\frac{d\kappa}{dR}\Delta\bar{D}(R) \tag{4.35}$$

Il reste à déterminer si cette dynamique vérifie le bilan détaillé, ce qui sera entreprit dans le futur. Si tel était le cas, nous aurions trouvé une classe de systèmes hors de l'équilibre thermique, qui ne sont pas décrits par une distribution de Boltzmann, mais proche d'un autre type d'équilibre. Ceci constituerait un pas encourageant dans la construction d'approches génériques des systèmes actifs.

## 4.4 Sphères dures : pression et équilibre de phases

Les sphères dures ABP, qui n'interagissent que par un potentiel répulsif à courte portée, ont été beaucoup étudiées numériquement ces dernières années [58–67]. Elles permettent en effet d'observer une MIPS induite par des effets purement stériques, qui pourrait potentiellement être pertinente dans la description de systèmes comme les colloïdes Janus ou certaines bactéries qui forment des agrégats [23]. Les progrès théoriques ont cependant été assez limités et ce système est moins bien compris que les particules se déplaçant à une vitesse $v(\rho)$ étudiées aux sections précédentes.

Qualitativement, les collisions entre sphères tendent à réduire leur vitesse de déplacement. Une tentative [58, 60, 61] a donc été de quantifier ce ralentissement en fonction de la densité par un $v(\rho)$ et de comparer les sphères dures et des particules ayant explicitement une vitesse dépendant de leur densité avec la relation $v(\rho)$ mesurée en simulation. Cette approche est phénoménologique dans le sens où elle suppose que des particules se déplaçant à une vitesse $v(\rho)$ sont une bonne description des sphères dures autopropulsées.

Dans l'article D, nous donnons une expression exacte pour la pression mécanique de sphères dures autopropulsées. Cette expression comporte trois termes :

- Une pression de gaz parfait $P_0 = \rho_0 k_B T_{\text{eff}}$ où $T_{\text{eff}}$ est la température effective déjà rencontrée aux chapitres 2 et 3.
- Une pression directe $P_D$ que l'on rencontre à l'équilibre dans l'étude de sphères browniennes.

– Une pression indirecte $P_I$ qui quantifie la perte de pression due au ralentissement des particules lors des collisions et qui n'a pas d'équivalent à l'équilibre.

Nous montrons que les particules autopropulsées avec des forces répulsives correspondent à un cas exceptionnel où la pression mécanique est solution d'une équation d'état. Nous montrons par ailleurs que pour un système séparé entre une phase gazeuse et une phase liquide, les pressions dans chaque phase sont égales. Cette égalité fournit une des deux équations nécessaires pour fixer les densités de coexistence. Nous montrons que, comme pour les particules avec $v(\rho)$, la deuxième condition n'est pas fournie par les relations usuelles de thermodynamique (ici la construction de Maxwell sur la pression).

L'article D permet également de relier quantitativement les sphères dures aux particules avec $v(\rho)$. En effet, dans une phase homogène à densité $\rho$, on peut définir une vitesse moyenne $v(\rho)$ comme la projection de $\dot{\mathbf{r}}$ suivant la direction $\mathbf{u}$ d'une particule : $v(\rho) = \langle \mathbf{u} \cdot \frac{d\mathbf{r}}{dt} \rangle$. Cette vitesse est reliée de façon exacte à la pression :

$$P_0 + P_I = \frac{v_0 v(\rho)}{2D_r}\rho \tag{4.36}$$

L'équivalence entre sphères dures et particules $v(\rho)$ n'est toutefois pas complète. En effet, l'équation (4.36) laisse de côté le terme de pression directe $P_D$. De plus, la vitesse effective $v(\rho)$ est calculée dans les phases homogènes, et ne décrit donc pas les interfaces entre les phases. Ainsi la théorie en $v(\rho)$ ne permet pas, pour l'instant, de prédire le diagramme des phases des sphères dures.

PRL 114, 198301 (2015) Selected for a Viewpoint in *Physics* PHYSICAL REVIEW LETTERS week ending 15 MAY 2015

# Pressure and Phase Equilibria in Interacting Active Brownian Spheres

Alexandre P. Solon,[1] Joakim Stenhammar,[2] Raphael Wittkowski,[2] Mehran Kardar,[3] Yariv Kafri,[4] Michael E. Cates,[2] and Julien Tailleur[1]

[1]*Laboratoire, Matière et Systèmes Complexes, UMR 7057 CNRS/P7, Université Paris Diderot, 75205 Paris Cedex 13, France*
[2]*SUPA, School of Physics and Astronomy, University of Edinburgh, Edinburgh EH9 3FD, United Kingdom*
[3]*Department of Physics, Massachusetts Institute of Technology, Cambridge, Massachusetts 02139, USA*
[4]*Department of Physics, Technion, Haifa 32000, Israel*

(Received 18 December 2014; revised manuscript received 13 March 2015; published 11 May 2015)

We derive a microscopic expression for the mechanical pressure $P$ in a system of spherical active Brownian particles at density $\rho$. Our exact result relates $P$, defined as the force per unit area on a bounding wall, to bulk correlation functions evaluated far away from the wall. It shows that (i) $P(\rho)$ is a state function, independent of the particle-wall interaction; (ii) interactions contribute two terms to $P$, one encoding the slow-down that drives motility-induced phase separation, and the other a direct contribution well known for passive systems; and (iii) $P$ is equal in coexisting phases. We discuss the consequences of these results for the motility-induced phase separation of active Brownian particles and show that the densities at coexistence *do not* satisfy a Maxwell construction on $P$.

DOI: 10.1103/PhysRevLett.114.198301 PACS numbers: 82.70.Dd, 05.40.−a, 05.70.Ce, 87.18.Gh

Much recent research addresses the statistical physics of active matter, whose constituent particles show autonomous dissipative motion (typically self-propulsion), sustained by an energy supply. Progress has been made in understanding spontaneous flow [1] and phase equilibria in active matter [2–6], but as yet there is no clear thermodynamic framework for these systems. Even the definition of basic thermodynamic variables such as temperature and pressure is problematic. While "effective temperature" is a widely used concept outside equilibrium [7], the discussion of pressure $P$ in active matter has been neglected until recently [8–14]. At first sight, because $P$ can be defined mechanically as the force per unit area on a confining wall, its computation as a statistical average looks unproblematic. Remarkably, though, it was recently shown that for active matter the force on a wall can depend on details of the wall-particle interaction so that $P$ is not, in general, a state function [15].

Active particles are nonetheless clearly capable of exerting a mechanical pressure $P$ on their containers. (When immersed in a space-filling solvent, this becomes an *osmotic* pressure [8,10].) Less clear is how to calculate $P$; several suggestions have been made [9–12] whose interrelations are, as yet, uncertain. Recall that for systems in thermal equilibrium, the mechanical and thermodynamic definitions of pressure [force per unit area on a confining wall, and $-(\partial\mathcal{F}/\partial V)_N$ for $N$ particles in volume $V$, with $\mathcal{F}$ the Helmholtz free energy] necessarily coincide. Accordingly, various formulas for $P$ (involving, e.g., the density distribution near a wall [16], or correlators in the bulk [17,18]) are always equivalent. This ceases to be true, in general, for active particles [11,15].

In this Letter we adopt the mechanical definition of $P$. We first show analytically that $P$ is a state function, independent of the wall-particle interaction, for one important and well-studied class of systems: spherical active Brownian particles (ABPs) with isotropic repulsions. By definition, such ABPs undergo overdamped motion in response to a force that combines an arbitrary pair interaction with an external forcing term of constant magnitude along a body axis; this axis rotates by angular diffusion. While not a perfect representation of experiments (particularly in bulk fluids, where self-propulsion is created internally and hydrodynamic torques arise [19]), ABPs have become the mainstay of recent simulation and theoretical studies [3,5,6,20–24]. They provide a benchmark for the statistical physics of active matter and a simplified model for the experimental many-body dynamics of autophoretic colloidal swimmers, or other active systems, coupled to a momentum reservoir such as a supporting surface [24–29]. (We comment below on the momentum-conserving case.) By generating large amounts of data in systems whose dynamics and interactions are precisely known, ABP simulations are currently better placed than experiments to answer fundamental issues concerning the physics of active pressure, such as those raised in Refs. [9,10].

Our key result exactly relates $P$ to bulk correlators, powerfully generalizing familiar results for the passive case. The pressure for ABPs is the sum of an ideal-gas contribution and a nonideal one stemming from interactions. Crucially, the latter results from *two* contributions: one is a standard, "direct" term (the density of pairwise forces acting across a plane), which we call $P_D$, while the other, "indirect" term, absent in the passive case, describes the reduction in momentum flux caused by collisional slow-down of the particles. For short-ranged repulsions and high propulsive force, $P_D$ becomes important only at high

 

densities; the indirect term dominates at intermediate densities and is responsible for motility-induced phase separation (MIPS) [2–4]. The same calculation establishes that, for spherical ABPs (though not in general [15]), $P$ must be equal in all coexisting phases.

We further show that our ideal and indirect terms together form exactly the "swim pressure," $P_S(\rho)$ at density $\rho$, previously defined via a force-moment integral in Refs. [9,10], and moreover that (in 2D) $P_S$ is simply $\rho v(0) v(\rho)/(2D_r)$, where $v(\rho)$ is the mean propulsive speed of ABPs and $D_r$ their rotational diffusivity. We interpret this result and show that (for $P_D = 0$) the mechanical instability $dP_S/d\rho = 0$ coincides exactly with a diffusive one previously found to cause MIPS among particles whose interaction comprises a density-dependent swim speed $v(\rho)$ [2–4]. We briefly explain why this correspondence does not extend to phase equilibria more generally, deferring a full account to a longer paper [33].

To calculate the pressure in interacting ABPs, we follow Ref. [15] and consider the dynamics in the presence of an explicit, conservative wall-particle force $\mathbf{F}_w$. For simplicity, we work in 2D and consider periodic boundary conditions in $y$ and confining walls parallel to $\mathbf{e}_y = (0, 1)$. We start from the standard Langevin dynamics of ABPs with bare speed $v_0$, interparticle forces $\mathbf{F}$, and unit mobility [5,6,34],

$$\dot{\mathbf{r}}_i = v_0 \mathbf{u}(\theta_i) + F_w(x_i)\mathbf{e}_x + \sum_{j \neq i} \mathbf{F}(\mathbf{r}_j - \mathbf{r}_i) + \sqrt{2D_t}\boldsymbol{\eta}_i,$$
$$\dot{\theta}_i = \sqrt{2D_r}\xi_i. \tag{1}$$

Here, $\mathbf{r}_i(t) = (x_i, y_i)$ is the position and $\theta_i(t)$ the orientation of particle $i$ at time $t$; $\mathbf{u}(\theta) = (\cos(\theta), \sin(\theta))$; $F_w = \|\mathbf{F}_w\|$ is a force acting along the wall normal $\mathbf{e}_x = (1, 0)$; $D_t$ is the bare translational diffusivity; and $\boldsymbol{\eta}_i(t)$ and $\xi_i(t)$ are zero-mean unit-variance Gaussian white noises with no correlations among particles.

Following standard procedures [2,3,35,36], this leads to an equation for the fluctuating distribution function $\hat{\psi}(\mathbf{r}, \theta, t)$ whose zeroth, first, and second angular harmonics are the fluctuating particle density $\hat{\rho} = \int \hat{\psi} d\theta$, the $x$ polarization $\hat{\mathcal{P}} = \int \hat{\psi} \cos(\theta) d\theta$, and $\hat{\mathcal{Q}} = \int \hat{\psi} \cos(2\theta) d\theta$, which encodes nematic order normal to the wall,

$$\dot{\hat{\psi}} = -\boldsymbol{\nabla} \cdot \left\{ \left[ v_0 \mathbf{u}(\theta) + F_w(x)\mathbf{e}_x + \int \mathbf{F}(\mathbf{r}' - \mathbf{r}) \hat{\rho}(\mathbf{r}') d^2 r' \right] \hat{\psi} \right\} + D_r \partial_\theta^2 \hat{\psi} + D_t \nabla^2 \hat{\psi} + \boldsymbol{\nabla} \cdot \left( \sqrt{2D_t \hat{\psi}} \boldsymbol{\eta} \right) + \partial_\theta \left( \sqrt{2D_r \hat{\psi}} \xi \right), \tag{2}$$

where $\boldsymbol{\eta}(\mathbf{r}, t)$ and $\xi(\mathbf{r}, t)$ are $\delta$-correlated, zero-mean, and unit-variance Gaussian white noise fields. In the steady state, the noise averages $\rho = \langle \hat{\rho} \rangle$, $\mathcal{P} = \langle \hat{\mathcal{P}} \rangle$, and $\mathcal{Q} = \langle \hat{\mathcal{Q}} \rangle$ are, by translational invariance, functions of $x$ only, as is the wall force $F_w(x)$ [37]. Integrating (2) over $\theta$ and then averaging over noise in the steady state gives $\partial_x J = 0$, with $J$ the particle current. For any system with impermeable boundaries, $J = 0$. Writing this out explicitly gives

$$0 = v_0 \mathcal{P} + F_w \rho - D_t \partial_x \rho + I_1(x), \tag{3}$$

$$I_1(x) \equiv \int F_x(\mathbf{r}' - \mathbf{r}) \langle \hat{\rho}(\mathbf{r}') \hat{\rho}(\mathbf{r}) \rangle d^2 r'. \tag{4}$$

Applying the same procedure to the first angular harmonic gives

$$D_r \mathcal{P} = -\partial_x \left[ \frac{v_0}{2} (\rho + \mathcal{Q}) + F_w \mathcal{P} - D_t \partial_x \mathcal{P} + I_2(x) \right], \tag{5}$$

$$I_2(x) \equiv \int F_x(\mathbf{r}' - \mathbf{r}) \langle \hat{\rho}(\mathbf{r}') \hat{\mathcal{P}}(\mathbf{r}) \rangle d^2 r'. \tag{6}$$

Note that the integrals $I_1$ and $I_2$ defined in (4) and (6) are, by translational invariance, functions only of $x$.

The mechanical pressure on the wall is the spatial integral of the force density exerted upon it by the particles. The wall force obeys $F_w = -\partial_x U_w$, where an origin is chosen so that $U_w$ is nonzero only for $x > 0$. The wall is confining, i.e., $F_w \rho \to 0$ for $x \gg 0$, whereas $x = \Lambda \ll 0$ denotes any plane in the bulk of the fluid, far from the wall. By Newton's third law, the pressure is then

$$P = -\int_\Lambda^\infty F_w(x) \rho(x) dx. \tag{7}$$

In Eq. (7) we now use (3) to set $-F_w \rho = v_0 \mathcal{P} - D_t \partial_x \rho + I_1$,

$$P = v_0 \int_\Lambda^\infty \mathcal{P}(x) dx + D_t \rho(\Lambda) + \int_\Lambda^\infty I_1(x) dx. \tag{8}$$

We next use (5), in which $\mathcal{P}$ and $\mathcal{Q}$ vanish in the bulk and all terms vanish at infinity, to evaluate $\int \mathcal{P} dx$, giving

$$P = \frac{v_0}{D_r} \left( \frac{v_0}{2} \rho(\Lambda) + I_2(\Lambda) \right) + D_t \rho(\Lambda) + \int_\Lambda^\infty I_1(x) dx. \tag{9}$$

Using Newton's third law, the final integral in (9) takes a familiar form, describing the density of pair forces acting across some plane through the bulk (far from any wall),

$$\int_{x > \Lambda} dx \int_{x' < \Lambda} d^2 r' F_x(\mathbf{r}' - \mathbf{r}) \langle \hat{\rho}(\mathbf{r}') \hat{\rho}(\mathbf{r}) \rangle \equiv P_D. \tag{10}$$

Thus, in the passive limit ($v_0 = 0$) we recover in $P_D$ the standard interaction part in the pressure [18]. We call $P_D$ the "direct" contribution; it is affected by activity only through changes to the correlator. Activity also enters (via $v_0$) the well-known ideal pressure term [9,10,13,15],

$$P_0 \equiv \left(D_t + \frac{v_0^2}{2D_r}\right)\rho(\Lambda). \tag{11}$$

Having set friction to unity in (1), $D_t = k_B T$, so that within $P_0$ (only) activity looks like a temperature shift.

Most strikingly, activity in combination with interactions also brings an "indirect" pressure contribution

$$P_I \equiv \frac{v_0}{D_r} I_2(\Lambda) \tag{12}$$

with no passive counterpart. Here, $I_2(\Lambda)$ is again a wall-independent quantity, evaluated on *any* bulk plane $x = \Lambda \ll 0$. We discuss this term further below.

Our exact result for mechanical pressure is finally

$$P = P_0 + P_I + P_D, \tag{13}$$

with these three terms defined by (11), (12), and (10), respectively. $P$ is thus for interacting ABPs a state function, calculable solely from bulk correlations and independent of the particle-wall force $F_w(x)$. Because the same boundary force can be calculated using *any* bulk plane $x = \Lambda$, it follows that, should the system undergo phase separation, $P$ is the same in all coexisting phases [37]. This proves for ABPs an assumption that, while plausible [10,38], is not obvious, and indeed can fail for particles interacting via a density-dependent swim speed rather than direct interparticle forces [15].

Notably, although ABPs exchange momentum with a reservoir, (1) also describes particles swimming through a momentum-conserving bulk fluid, in an approximation where interparticle and particle-wall hydrodynamic interactions are both neglected. So long as the wall interacts *solely* with the swimmers, our results above continue to apply to what is now the *osmotic* pressure.

The physics of the indirect contribution $P_I$ is that interactions between ABPs reduce their motility as the density increases. The ideal pressure term $P_0$ normally represents the flux of momentum through a bulk plane carried by particles that *move* across it (as opposed to those that *interact* across it) [17]. In our overdamped system one should replace in the preceding sentence "momentum" with "propulsive force" (plus a random force associated with $D_t$). Per particle, the propulsive force is density independent, but the rate of crossing the plane is not. Accordingly, we expect the factor $v_0^2$ in (11) to be modified by interactions, with one factor $v_0$ (force or momentum) unaltered, but the other (speed) replaced by a density-dependent contribution $v(\rho) \leq v_0$,

$$P_0 + P_I = \left(D_t + \frac{v_0 v(\rho)}{2D_r}\right)\rho. \tag{14}$$

This requires the mean particle speed to obey

$$v(\rho) = v_0 + 2I_2/\rho. \tag{15}$$

Remarkably, (14) and (15) are *exact* results, where (15) is found from the mean speed of particle $i$ in bulk $v = v_0 + \langle \mathbf{u}(\theta_i) \cdot \sum_{j \neq i} \mathbf{F}(\mathbf{r}_j - \mathbf{r}_i)\rangle$. To see why this average involves $I_2$, note that the system is isotropic in bulk, so $x$ and $y$ can be interchanged in $I_2(x)$, and that $\cos(\theta) \equiv \mathbf{u} \cdot \mathbf{e}_x$. Relation (6) then links $v$ to $I_2$ via the $\langle \hat{\rho}\hat{\mathcal{P}}\rangle$ correlator, which describes the imbalance of forces acting on an ABP from neighbors in front and behind.

Furthermore, the self-propulsive term in (14) is exactly the "swim pressure" $P_S$ of Refs. [9,10],

$$\frac{v_0 v(\rho)}{2D_r}\rho = P_S \equiv \frac{\rho}{2}\langle \mathbf{r} \cdot \mathbf{F}^a \rangle, \tag{16}$$

with $\mathbf{F}^a = v_0 \mathbf{u}$ a particle's propulsive force and $\mathbf{r}$ its position. (The particle mobility $v_0/F^a = 1$ in our units.) The equivalence of (12), (14), and (16) is proven analytically in the Supplemental Material [39] and confirmed numerically in Fig. 1 for ABP simulations performed as in Refs. [20,21].

Thus, for $D_t = 0$, (13) may alternatively be rewritten as $P = P_S + P_D$ [9,10]. Together, our results confirm that $P_S$, defined in bulk via (16), determines (with $P_D$) the force acting on a confining wall. This was checked numerically in Ref. [9] but is not automatic [15]. Moreover, our work gives via (14) an exact kinetic expression for $P_S$ with a clear and simple physical interpretation in terms of the transport of propulsive forces. This illuminates the nature of the

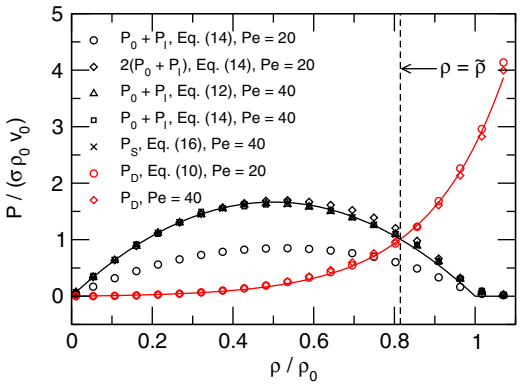


FIG. 1 (color online). Numerical measurements of $P_0 + P_I$, $P_S$, and $P_D$ in single-phase ABP simulations at Péclet number $\mathrm{Pe} \equiv 3v_0/(D_r\sigma) = 40$, where $\sigma$ is the particle diameter. Expressions (12), (14), and (16) for $P_0 + P_I$ and $P_S$ show perfect agreement. Also shown are data for $\mathrm{Pe} = 20$, unscaled and rescaled by factor 2. This confirms that $P_S = P_0 + P_I$ is almost linear in Pe; small deviations arise from the Pe dependence of the correlators. In red is $P_D$ for $\mathrm{Pe} = 20, 40$, with no rescaling. Pe was varied using $D_r$, at fixed $v_0$ and with $D_t = D_r\sigma^2/3$. Solid lines are fits to piecewise parabolic ($P_S$) and exponential ($P_D$) functions used in the semiempirical equation of state. $\rho_0$ is a near-close-packed density at which $v(\rho)$ vanishes and $\tilde{\rho}$ is the threshold density above which $P_D > P_S$. See the Supplemental Material [39] for details.

swim pressure $P_S$ and extends to finite $\rho$ the limiting result $P_S = P_0$ [9,10].

The connections made above are our central findings; they extend statistical thermodynamics concepts from equilibrium far into ABP physics. Before concluding, we ask how far these ideas extend to phase equilibria.

In the following, we ignore for simplicity the $D_t$ term (negligible in most cases [3,5,20,34]). Then, assuming short-range repulsions, we have $P_S = \rho v_0 v(\rho)/(2D_r)$, with $v(\rho) \simeq v_0(1-\rho/\rho_0)$ and $\rho_0$ a near-close-packed density [5,6,20]. $P_D$ should scale as $\sigma\rho v_0 \mathcal{S}(\rho/\rho_0)$, where $\sigma$ is the particle diameter and the function $\mathcal{S}$ diverges at close packing; here, the factor $v_0$ is because propulsive forces oppose repulsive ones, setting their scale [10]. Figure 1 shows that both the approximate expression for $P_S$ (with a fitted $\rho_0 \simeq 1.19$ roughly independent of Pe) and the scaling of $P_D$ hold remarkably well. Defining a threshold value $\tilde{\rho}$ by $P_S(\tilde{\rho}) = P_D(\tilde{\rho})$ (see Fig. 1), it follows that at large enough Péclet numbers $\mathrm{Pe} = 3v_0/(D_r\sigma)$, $P_S$ dominates completely for $\rho < \tilde{\rho}$, with $P_D$ serving *only* to prevent the density from moving above the $\tilde{\rho}$ cutoff. When $\rho < \tilde{\rho}$, $P_D$ is negligible; the criterion $P_S'(\rho) < 0$, used in Refs. [10,38] to identify a mechanical instability, is then via (16) *identical* to the spinodal criterion $(\rho v)' < 0$ used to predict MIPS in systems whose sole physics is a density-dependent speed $v(\rho)$ [2,3]. Thus, for ABPs at large Pe, the mechanical theory reproduces one result of a long-established mapping between MIPS and equilibrium colloids with attractive forces [2,3].

We next address the binodal densities of coexisting phases. According to Refs. [2,3], particles with speed $v(\rho)$ admit an effective bulk free-energy density $f(\rho) = k_BT[\rho(\ln\rho - 1) + \int_0^\rho \ln v(u)du]$. [Interestingly, the equality of $P$ in coexisting phases is equivalent at high Pe and $\rho < \tilde{\rho}$ to the equality of $k_BT\log(\rho v)$, which is the chemical potential in this "thermodynamic" theory [2,4].] The binodals are then found using a common tangent construction (CTC, i.e., global minimization) on $f$, or equivalently an equal-area Maxwell construction (MC) on an effective *thermodynamic* pressure $P_f = \rho f' - f$, which differs from $P$ [11]. Formally, $f$ is a local approximation to a large-deviation functional [41], whose nonlocal terms can (in contrast to equilibrium systems) alter the CTC or MC [11,20]; we return to this issue below.

An appealing alternative is to apply the MC to the mechanical pressure $P$ itself; this was, in different language, proposed in Ref. [38]. (The equivalence will be detailed in Ref. [33].) It amounts to constructing an effective free-energy density $f_P(\rho) \neq f$, defined via $P = \rho f_P' - f_P$, and using the CTC on $f_P$. However, $f_P$ has no clear link to any large-deviation functional [41], and since it differs from $f$, these approaches generically predict different binodals.

To confirm this, we turn to the large Pe limit; here, for ABPs with $v(\rho) = v_0(1-\rho/\rho_0)$ and $\tilde{\rho} = \rho_0$, we can explicitly construct $f(\rho)$ [and hence $P_f(\rho)$] alongside $P(\rho)$ [and hence $f_P(\rho)$], using our hard-cutoff approximation (i.e., a constraint $\rho < \tilde{\rho}$). All four functions are plotted in the Supplemental Material [39]; the two distinct routes indeed predict different binodals at high Pe (see Fig. 2) [43]. Each approach suffers its own limitations. That via $f$ (or $P_f$) appears more accurate, but neglects nonlocal terms that can alter the binodals: although $f'(\rho)$ remains equal in coexisting phases, $P_f$ is not equal once those terms are included [11]. The most serious drawback of this approach, currently, is that it cannot address finite Pe, where $P_D$ no longer creates a sharp cutoff. Meanwhile, the "mechanical" route captures the equality of $P$ in coexisting phases but unjustifiably assumes the MC on $P$, asserting in effect that $f_P$, and not $f$, is the effective free energy [41]. Nonlocal corrections [44] are again neglected.

At finite Pe where the crossover at $\tilde{\rho}$ is soft, (13) shows how $P_I$ and $P_D$ compete, giving Pe-dependent binodals (see Fig. 2). To test the predictions of the mechanical approach (equivalent to Ref. [38]), we set $P_D = \sigma\rho v_0 \mathcal{S}(\rho/\rho_0)$ as above, finding the function $\mathcal{S}$ by numerics on single-phase systems at modest Pe (see Fig. 1). Adding this to $P_S$ (assuming $P_S \propto \mathrm{Pe}$ scaling) gives $P = P(\rho, \mathrm{Pe})$. At each Pe the binodal pressures and densities do lie on this

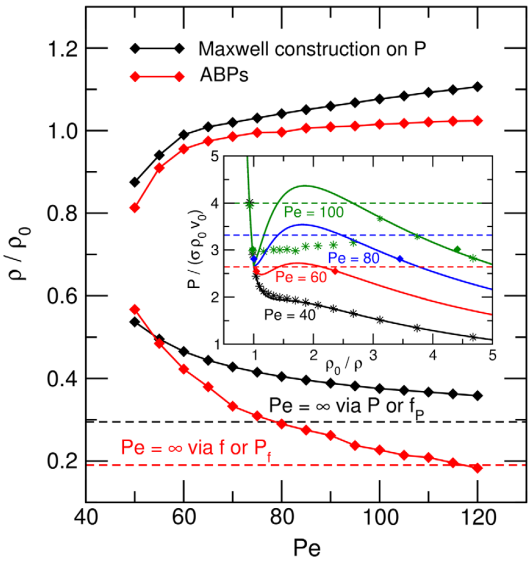


FIG. 2 (color online). Simulated coexistence curves (binodals) for ABPs (red) and those calculated via the Maxwell construction (black) on the mechanical pressure $P$ using the semiempirical equation of state for $P_S$ and $P_D$ fitted from Fig. 1. Dashed lines: predicted high Pe asymptotes for the binodals calculated via $f$ or $P_f$ (lower line) and calculated via $P$ or $f_P$ (upper line). Inset: measured binodal pressures and densities (diamonds) fall on the equation-of-state curves but do not match the MC values (horizontal dashed lines). Stars show the $P(\rho)$ relation across the full density range from simulations at $\mathrm{Pe} = 40$ and $\mathrm{Pe} = 100$. The latter includes two metastable states at low density (high $\rho_0/\rho$) that are yet to phase separate.

equation of state, validating its semiempirical form, but they do not obey the Maxwell construction on $P$, which must therefore be rejected (see Fig. 2, inset). We conclude that, despite our work and that of Ref. [38], no complete theory of phase equilibria in ABPs yet exists.

In summary, we have given in (10)–(13) an exact expression for the mechanical pressure $P$ of active Brownian spheres. This relates $P$ directly to bulk correlation functions and shows it to be a state function, independent of the wall interaction, something not true for all active systems [15]. As well as an ideal term $P_0$, and a direct interaction term $P_D$, there is an indirect term $P_I$ caused by collisional slowing-down of propulsion. We established an exact link between $P_0 + P_I$ and the so-called "swim pressure" [10], allowing a clearer interpretation of that quantity. We showed that when MIPS arises in the regime of high $\mathrm{Pe} = 3v_0/(D_r\sigma)$, the mechanical ($P' < 0$ [10]) and diffusive ($f'' < 0$ [2,3]) instabilities coincide. That equivalence does not extend to the calculation of coexistence curves, for reasons we have explained. For simplicity we have worked in 2D; generalization of our results to 3D is straightforward [33] but notationally cumbersome.

The established description of MIPS as a diffusive instability [2,3,11,20] is fully appropriate in systems whose particles are "programed" to change their dynamics at high density (e.g., via bacterial quorum sensing [45,46]), but it is not yet clear whether the same theory, or one based primarily on the mechanical pressure $P$, is better founded for finite-Pe phase equilibria in ABPs whose slow-down is collisional. Meanwhile, our exact results for $P$ in these systems add significantly to our growing understanding of how statistical thermodynamic concepts can, and cannot, be applied in active materials.

We thank Rosalind Allen, John Brady, Cristina Marchetti, and Xingbo Yang for seminal discussions. This work was funded in part by EPSRC Grant No. EP/J007404. J. S. is supported by the Swedish Research Council (Grant No. 350-2012-274), R. W. is supported by the German Research Foundation (DFG) (Grant No. WI 4170/1-2), Y. K. is supported by the I-CORE Program of the Planning and Budgeting Committee of the Israel Science Foundation, and M. E. C. is supported by the Royal Society. A. P. S. and J. T. are supported by ANR project BACTTERNS. A. P. S., J. S., M. K., M. E. C., and J. T. thank the KITP at the University of California, Santa Barbara, where they were supported through National Science Foundation Grant No. NSF PHY11-25925.

[1] M. C. Marchetti, J.-F. Joanny, S. Ramaswamy, T. B. Liverpool, J. Prost, M. Rao, and R. A. Simha, Rev. Mod. Phys. **85**, 1143 (2013).
[2] J. Tailleur and M. E. Cates, Phys. Rev. Lett. **100**, 218103 (2008).
[3] M. E. Cates and J. Tailleur, Europhys. Lett. **101**, 20010 (2013).
[4] M. E. Cates and J. Tailleur, arXiv:1406.3533 [Annu. Rev. Condens. Matter Phys. (to be published)].
[5] Y. Fily and M. C. Marchetti, Phys. Rev. Lett. **108**, 235702 (2012).
[6] G. S. Redner, M. F. Hagan, and A. Baskaran, Phys. Rev. Lett. **110**, 055701 (2013).
[7] L. F. Cugliandolo, J. Phys. A **44**, 483001 (2011).
[8] T. W. Lion and R. J. Allen, Europhys. Lett. **106**, 34003 (2014); T. W. Lion and R. J. Allen, J. Chem. Phys. **137**, 244911 (2012).
[9] X. B. Yang, L. M. Manning, and M. C. Marchetti, Soft Matter **10**, 6477 (2014).
[10] S. C. Takatori, W. Yan, and J. F. Brady, Phys. Rev. Lett. **113**, 028103 (2014).
[11] R. Wittkowski, A. Tiribocchi, J. Stenhammar, R. J. Allen, D. Marenduzzo, and M. E. Cates, Nat. Commun. **5**, 4351 (2014).
[12] F. Ginot, I. Theurkauff, D. Levis, C. Ybert, L. Bocquet, L. Berthier, and C. Cotton-Bizonne, Phys. Rev. X **5**, 011004 (2015).
[13] S. A. Mallory, A. Saric, C. Valeriani, and A. Cacciuto, Phys. Rev. E **89**, 052303 (2014).
[14] R. Ni, M. A. Cohen-Stuart, and P. G. Bolhuis, Phys. Rev. Lett. **114**, 018302 (2015).
[15] A. P. Solon, Y. Fily, A. Baskaran, M. E. Cates, Y. Kafri, M. Kardar, and J. Tailleur, arXiv:1412.3952.
[16] J. R. Henderson, in *Fundamentals of Inhomogeneous Fluids*, edited by D. Henderson (Marcel Dekker, New York, 1992).
[17] M. P. Allen and D. J. Tildesley, *Computer Simulation of Liquids* (Oxford University Press, Oxford, England, 1987).
[18] M. Doi, *Soft Matter Physics* (Oxford University Press, Oxford, England, 2013).
[19] R. Matas-Navarro, R. Golestanian, T. B. Liverpool, and S. M. Fielding, Phys. Rev. E **90**, 032304 (2014); A. Zöttl and H. Stark, Phys. Rev. Lett. **112**, 118101 (2014).
[20] J. Stenhammar, A. Tiribocchi, R. J. Allen, D. Marenduzzo, and M. E. Cates, Phys. Rev. Lett. **111**, 145702 (2013).
[21] J. Stenhammar, D. Marenduzzo, R. J. Allen, and M. E. Cates, Soft Matter **10**, 1489 (2014).
[22] T. Speck, J. Bialké, A. M. Menzel, and H. Löwen, Phys. Rev. Lett. **112**, 218304 (2014).
[23] A. Wysocki, R. G. Winkler, and G. Gompper, Europhys. Lett. **105**, 48004 (2014).
[24] I. Buttinoni, J. Bialké, F. Kümmel, H. Löwen, C. Bechinger, and T. Speck, Phys. Rev. Lett. **110**, 238301 (2013).
[25] J. R. Howse, R. A. L. Jones, A. J. Ryan, T. Gough, R. Vafabakhsh, and R. Golestanian, Phys. Rev. Lett. **99**, 048102 (2007).
[26] J. Palacci, S. Sacanna, A. P. Stenberg, D. J. Pine, and P. M. Chaikin, Science **339**, 936 (2013).
[27] I. Theurkauff, C. Cottin-Bizonne, J. Palacci, C. Ybert, and L. Bocquet, Phys. Rev. Lett. **108**, 268303 (2012).
[28] S. Thutupalli, R. Seeman, and S. Herminghaus, New J. Phys. **13**, 073021 (2011).
[29] Any self-propelled entity whose motility depends on frictional contact with a support (such as human walking, cell crawling [30], vibrated granular materials [31], or colloids

that move by rolling on a surface [32]) is exchanging momentum with an external reservoir (the support).

[30] E. Tjhung, D. Marenduzzo, and M. E. Cates, Proc. Natl. Acad. Sci. U.S.A. **109**, 12381 (2012).

[31] J. Deseigne, O. Dauchot, and H. Chaté, Phys. Rev. Lett. **105**, 098001 (2010); V. Narayan, S. Ramaswamy, and N. Menon, Science **317**, 105 (2007).

[32] A. Bricard, J. B. Caussin, N. Desreumaux, O. Dauchot, and D. Bartolo, Nature (London) **503**, 95 (2013).

[33] A. P. Solon *et al.* (to be published).

[34] Y. Fily, S. Henkes, and M. C. Marchetti, Soft Matter **10**, 2132 (2014).

[35] F. D. C. Farrell, M. C. Marchetti, D. Marenduzzo, and J. Tailleur, Phys. Rev. Lett. **108**, 248101 (2012).

[36] D. S. Dean, J. Phys. A **29**, L613 (1996).

[37] We assume, without loss of generality, that translational invariance in $y$ is maintained even if the system undergoes phase separation into two or more isotropic phases.

[38] S. C. Takatori and J. F. Brady, Phys. Rev. E **91**, 032117 (2015).

[39] See Supplemental Material at http://link.aps.org/supplemental/10.1103/PhysRevLett.114.198301 for exact proofs of Eqs. (14) and (16), details on numerical simulations citing Ref. [40], and the construction of the binodals of Fig. 2.

[40] S. J. Plimpton, J. Comput. Phys. **117**, 1 (1995).

[41] The large-deviation functional (or effective free energy) $\mathcal{F}[\hat{\rho}(\mathbf{r})]/(Vk_BT)$ for the fluctuating density $\hat{\rho}$ in a nonequilibrium system is defined as $-\ln\{\Pr[\hat{\rho}(\mathbf{r})]\}/V$, where Pr is the steady-state probability distribution [42]. In Refs. [2,3], it is shown that $\int f(\hat{\rho})d^dr/(Vk_BT)$ is, within the local approximation, the large-deviation functional for a system of particles with a density-dependent swim speed $v(\rho)$.

[42] R. S. Ellis, *Entropy, Large Deviations and Statistical Mechanics* (Springer-Verlag, Berlin, 1985).

[43] An additional simulation at $\mathrm{Pe} = 500$ gave a lower binodal value $\rho/\rho_0 \simeq 0.08$. This may be due to the nonlocal gradient terms identified in Ref. [11].

[44] C. Y. D. Lu, P. D. Olmsted, and R. C. Ball, Phys. Rev. Lett. **84**, 642 (2000).

[45] M. B. Miller and B. L. Bassler, Annu. Rev. Microbiol. **55**, 165 (2001).

[46] M. E. Cates, Rep. Prog. Phys. **75**, 042601 (2012).

# Pressure and Phase Equilibria in Interacting Active Brownian Spheres
## Supplemental Material

Alexandre P. Solon,[1] Joakim Stenhammar,[2] Raphael Wittkowski,[2]
Mehran Kardar,[3] Yariv Kafri,[4] Michael E. Cates,[2] and Julien Tailleur[1]

[1] *Laboratoire, Matière et Systèmes Complexes, UMR 7057 CNRS/P7, Université Paris Diderot, 75205 Paris Cedex 13, France*
[2] *SUPA, School of Physics and Astronomy, University of Edinburgh, Edinburgh EH9 3FD, United Kingdom*
[3] *Massachusetts Institute of Technology, Department of Physics, Cambridge, Massachusetts 02139, USA*
[4] *Department of Physics, Technion, Haifa 32000, Israel*

### I. PROOF OF RELATION $P_0 + P_I = P_S$

We prove here (setting $D_t = 0$ for simplicity, and working in $d = 2$ dimensions) that the sum of the ideal pressure $P_0 = \rho v_0^2/(2D_r)$ and the indirect interaction pressure $P_I = v_0 I_2/D_r$ is the swim pressure $P_S = \rho\langle \boldsymbol{r}\cdot\boldsymbol{F}^a\rangle/2$, where the self-propulsion force $\boldsymbol{F}^a = v_0\boldsymbol{u}$ was defined in (16) in the main text. (As in the main text, we set the particle mobility $v_0/F^a = 1$ in this section, where $F^a \equiv \|\boldsymbol{F}^a\|$.) In proving the required result, we also establish that $P_S = \rho v_0 v(\rho)/(2D_r)$, and hence that $v(\rho) = v_0 + 2I_2/\rho$.

We start from (see (6) in the main text)

$$I_2 = \int F_x(\boldsymbol{r}' - \boldsymbol{r})\langle\hat{\rho}(\boldsymbol{r}')\hat{\mathcal{P}}(\boldsymbol{r})\rangle \,\mathrm{d}^2 r' \tag{1}$$

and use[1]

$$\hat{\rho}(\boldsymbol{r}) = \sum_i \delta(\boldsymbol{r} - \boldsymbol{r}_i)\,, \tag{2}$$

$$\hat{\mathcal{P}}(\boldsymbol{r}) = \sum_i \cos(\theta_i)\delta(\boldsymbol{r} - \boldsymbol{r}_i) \tag{3}$$

as well as the fact that the system is isotropic to rewrite (1) in the form

$$I_2 = \frac{1}{L_x L_y}\left\langle \sum_{i,j\neq i} F_x(\boldsymbol{r}_j - \boldsymbol{r}_i)\cos(\theta_i)\right\rangle. \tag{4}$$

We now take the thermodynamic limit: $L_x = L_y = \sqrt{A} \to \infty$. Since the system is isotropic, a similar expression can be written interchanging $x$ and $y$, noting that $\cos(\theta_i) = \boldsymbol{u}_i\cdot\boldsymbol{e}_x$ with $\boldsymbol{u}_i = (\cos(\theta_i), \sin(\theta_i))$ and $\boldsymbol{e}_x = (1, 0)$. Averaging the two results gives

$$P_I = \frac{v_0}{2D_r A}\left\langle \sum_{i,j\neq i} \boldsymbol{F}(\boldsymbol{r}_j - \boldsymbol{r}_i)\cdot\boldsymbol{u}_i\right\rangle. \tag{5}$$

We may also write, using the fact that $\boldsymbol{u}\cdot\boldsymbol{u} = 1$,

$$P_0 = \frac{\rho v_0^2}{2D_r} = \frac{v_0}{2D_r A}\sum_i v_0\langle\boldsymbol{u}_i\cdot\boldsymbol{u}_i\rangle\,. \tag{6}$$

[1] Equations (2) and (3) follow from $\hat{\psi}(\boldsymbol{r},\theta) = \sum_i \delta(\boldsymbol{r}-\boldsymbol{r}_i)\delta(\theta-\theta_i)$ and the definitions of $\hat{\rho}(\boldsymbol{r})$ and $\hat{\mathcal{P}}(\boldsymbol{r})$.

Hence, we obtain

$$P_0 + P_I = \frac{v_0}{2D_r A}\left\langle \sum_i \left(v_0\boldsymbol{u}_i + \sum_{j\neq i}\boldsymbol{F}(\boldsymbol{r}_j - \boldsymbol{r}_i)\right)\cdot\boldsymbol{u}_i\right\rangle. \tag{7}$$

From the Langevin equation (1) in the main text, applied in bulk where the wall force $F_w$ vanishes, and setting $D_t = 0$, we have that the term $v_0\boldsymbol{u}_i + \sum_{j\neq i}\boldsymbol{F}(\boldsymbol{r}_j - \boldsymbol{r}_i)$ in (7) is the instantaneous particle velocity $\dot{\boldsymbol{r}}_i$:

$$P_0 + P_I = \frac{v_0}{2D_r A}\left\langle \sum_i \dot{\boldsymbol{r}}_i\cdot\boldsymbol{u}_i\right\rangle. \tag{8}$$

If we redefine $\langle\cdot\rangle$ to include an average over the particle index, this may be written

$$P_0 + P_I = \frac{\rho v_0}{2D_r}\langle\dot{\boldsymbol{r}}\cdot\boldsymbol{u}\rangle = \frac{\rho v_0}{2D_r}v(\rho)\,. \tag{9}$$

Here, the second equality follows from the definition of $v(\rho) \equiv \langle\dot{\boldsymbol{r}}\cdot\boldsymbol{u}\rangle$ as the average speed of a particle along its propulsive direction (in a bulk system at density $\rho$).

Meanwhile, $P_S$ is defined via (16) in the main text (setting $d = 2$ there) as an equal-time average

$$P_S = \frac{\rho}{2}\langle\boldsymbol{r}\cdot\boldsymbol{F}^a\rangle = \frac{\rho v_0}{2}\langle\boldsymbol{r}\cdot\boldsymbol{u}\rangle\,. \tag{10}$$

We rewrite $\boldsymbol{r}(t) = \boldsymbol{r}(-\infty) + \int_{-\infty}^t \dot{\boldsymbol{r}}(t')\,\mathrm{d}t'$, and use time stationarity and the fact that $\langle\boldsymbol{r}(-\infty)\cdot\boldsymbol{u}(t)\rangle = 0$ to obtain

$$\langle\boldsymbol{r}(t)\cdot\boldsymbol{u}(t)\rangle = \int_0^\infty\langle\dot{\boldsymbol{r}}(0)\cdot\boldsymbol{u}(t')\rangle\,\mathrm{d}t'\,. \tag{11}$$

Next, we use the fact that the angular dynamics of $\boldsymbol{u}$ are autonomous: the rotational diffusion of one particle is unaffected by the location and orientation of any other particle. Then $\dot{\boldsymbol{r}}(0)$ and $\boldsymbol{u}(t')$ are correlated, but only because each is separately correlated with $\boldsymbol{u}(0)$. That separability allows us to write

$$\langle\dot{\boldsymbol{r}}(0)\cdot\boldsymbol{u}(t')\rangle = \frac{1}{2\pi}\int\langle\dot{\boldsymbol{r}}(0)|\boldsymbol{u}(0)\rangle\cdot\langle\boldsymbol{u}(t')|\boldsymbol{u}(0)\rangle\,\mathrm{d}\theta(0)\,, \tag{12}$$

where the integration is over the bulk steady state orientations $\theta(0) = \arccos(u_x(0))$ with uniform probability

density $1/(2\pi)$, and $\langle \boldsymbol{X}|\boldsymbol{Y}\rangle$ denotes the conditional average of $\boldsymbol{X}$ given $\boldsymbol{Y}$. The first conditional average in (12) obeys

$$\langle \dot{\boldsymbol{r}}(0)|\boldsymbol{u}(0)\rangle = v(\rho)\boldsymbol{u}(0) \ , \tag{13}$$

which follows from the definition of $v(\rho)$ [see (9)] and the fact that the mean velocity of a particle must point along its axis $\boldsymbol{u}$, given isotropy of the bulk system. The second conditional average in (12) is found from the autonomous rotational dynamics as

$$\langle \boldsymbol{u}(t')|\boldsymbol{u}(0)\rangle = \boldsymbol{u}(0)\exp(-D_{\rm r}t') \ , \tag{14}$$

which (again given isotropy) is implied by the familiar decay of angular correlations $\langle \boldsymbol{u}(t')\cdot\boldsymbol{u}(0)\rangle = \exp(-D_{\rm r}t')$. It follows from (13) and (14) that the product of the conditional averages in (12) is $v(\rho)\exp(-D_{\rm r}t')$, which is independent of $\boldsymbol{u}(0)$ as befits an isotropic system. This gives finally, upon performing the time integral in (11),

$$\langle \boldsymbol{r}\cdot\boldsymbol{u}\rangle = \frac{v(\rho)}{D_{\rm r}} \ , \tag{15}$$

thus completing the proof that $P_{\rm S}$ defined by (10) is exactly equal to $P_0 + P_{\rm I}$ as given by (9). Note that (15) can also be proved directly, avoiding the use of conditional averages, by a route involving Itō calculus [1].

Having proved in (9) that (with $P_0 = \rho v_0^2/(2D_{\rm r})$) the indirect pressure $P_{\rm I} = v_0 I_2/D_{\rm r}$ obeys

$$P_{\rm I} = \frac{\rho v_0}{2D_{\rm r}}(v(\rho) - v_0) \ , \tag{16}$$

it follows, as stated in the main text, that

$$v(\rho) = v_0 + 2I_2/\rho \ . \tag{17}$$

We know from ABP simulations [2] that, except at very high densities, $v(\rho)$ has the form $v(\rho) = v_0(1-\rho/\rho_0)$ with a constant $\rho_0$, so that $I_2$ scales like $I_2 \propto -v_0\rho^2$.

Although we have set $D_{\rm t} = 0$ when deriving these results, it is simple to establish that the only direct effect of nonzero $D_{\rm t}$ is to add a term $D_{\rm t}\rho$ to $P_0$ [1]. There is also an indirect effect on $P_{\rm D}$ and $P_{\rm I}$ because $D_{\rm t} \neq 0$ alters the correlation functions appearing in $I_1$ and $I_2$.

## II. NUMERICAL METHODS

All simulation results presented in the main text are obtained for spherical particles whose centres are confined to two dimensions (the $xy-$plane) and whose propulsion directions $\boldsymbol{u}$ are constrained to lie in this plane. These particles interact pairwise through a repulsive Weeks-Chandler-Andersen potential:

$$U(r) = 4\varepsilon\left[\left(\frac{\sigma}{r}\right)^{12} - \left(\frac{\sigma}{r}\right)^{6}\right] + \varepsilon \tag{18}$$

with an upper cut-off at $r = 2^{1/6}\sigma$, beyond which $U = 0$. Here $\sigma$ denotes the particle diameter, $\varepsilon$ determines the interaction strength, and $r$ is the center-to-center separation between two particles. The model was studied by solving the fully overdamped translational and rotational Langevin equations. In the current section we restore an explicit particle mobility $v_0/F^{\rm a} = \beta D_{\rm t}$ rather than setting this to unity. The Langevin equations then read:

$$\dot{\boldsymbol{r}}_i = \beta D_{\rm t}(\boldsymbol{F}_i^{\rm tot} + F^{\rm a}\boldsymbol{u}_i) + \sqrt{2D_{\rm t}}\boldsymbol{\eta}_i \ , \tag{19}$$

$$\dot{\theta}_i = \sqrt{2D_{\rm r}}\xi_i \ , \tag{20}$$

where $\boldsymbol{F}_i^{\rm tot}$ is the total conservative force acting on particle $i$, $F^{\rm a}$ is the constant magnitude of the self-propulsion force which acts along $\boldsymbol{u}_i$, $D_{\rm t}$ and $D_{\rm r} = 3D_{\rm t}/\sigma^2$ denote the translational and rotational diffusivities, respectively; $\beta = 1/(k_{\rm B}T)$ is the inverse thermal energy, and $\boldsymbol{\eta}_i(t)$ and $\xi_i(t)$ are zero-mean unit-variance Gaussian white noise random variables. Simulations were carried out using the LAMMPS [3] molecular dynamics package, in a periodic box with $L_x = L_y = 150\sigma$ (corresponding to $N \approx 20000$ particles). The natural simulation units are $\sigma$, $\varepsilon$, and $\tau_{\rm LJ} = \sigma^2/(\varepsilon\beta D_{\rm t})$ for length, energy, and time, respectively. In these units, a time step of $5\times10^{-5}$ was used throughout. As discussed in [2] and in Section III below, the Péclet number ${\rm Pe} \equiv 3v_0/(D_{\rm r}\sigma) = 3\beta D_{\rm t}F^{\rm a}/(D_{\rm r}\sigma)$ was varied by adjusting $D_{\rm r}$ (and hence $D_{\rm t}$), keeping a constant value of $F^{\rm a} = 24\varepsilon/\sigma$.

The value of $\rho_0$, the density where the linearly decreasing swim speed goes to zero, was determined by fitting sampled values at ${\rm Pe} = 40$ (*i.e.*, just outside the phase-separated region) of $v(\rho)$ over the density range $[0, 1.15]$ to the linear function $v(\rho) = v_0(1-\rho/\rho_0)$. The value thus obtained, $\rho_0 \approx 1.19$, was used in reporting the density data presented in the main text as a function of $\rho/\rho_0$.

Binodal densities were determined from simulations by coarse-graining the local density on a grid using a weighting function $w(r) \propto \exp(-r_{\rm cut}^2/(r_{\rm cut}^2 - r^2))$, where $r$ is the distance between the particle and a lattice point, and $r_{\rm cut}$ is a cut-off distance which was taken to be slightly larger than the lattice spacing. The local densities thus obtained were binned and plotted as a probability distribution function, where the maxima of the two density peaks were taken to represent the coexistence densities.

## III. SEMI-EMPIRICAL EQUATION OF STATE

We now revert to our convention that the particle mobility is unity, and rewrite Eq. (14) of the main text as

$$P_{\rm S} = \left(\frac{1}{\rm Pe} + \frac{v(\rho,{\rm Pe})}{6v_0}{\rm Pe}\right)\sigma\rho v_0 \ . \tag{21}$$

Our semi-empirical equation drops the $1/{\rm Pe}$ term (which comes from passive translational diffusion) and assumes that the Pe-dependence in $v(\rho,{\rm Pe})$, which arises from Pe-dependence in the bulk correlators, is negligible. For $v(\rho)$ we use the fitted linear function for $v(\rho)$ described above, with the further assumption that $v = P_{\rm S} = 0$ for

$\rho > \rho_0$ in order to prevent negative swim speeds (see black curve in Fig. 1 of the main text). With these assumptions (which imply that $\rho_0$ is itself Pe-independent), the swim pressure scales as $P_{\rm S} = \sigma\rho v_0 \mathcal{G}(\rho/\rho_0)$Pe with the function $\mathcal{G}(\rho/\rho_0) = v(\rho)/(6v_0)$. This ansatz is confirmed numerically by comparing datasets with two different Pe in Fig. 1 of the main text.

In the main text we also state the scaling hypothesis

$$P_{\rm D} \equiv \sigma\rho v_0 \mathcal{S}(\rho/\rho_0, {\rm Pe}) = \sigma\rho v_0 \mathcal{S}(\rho/\rho_0) \ , \qquad (22)$$

The first identity defines a reduced direct pressure $\mathcal{S}$; the second equality once again requires that Pe has no direct effect on the correlators (which would enter both through the shape of the function $\mathcal{S}$ and through $\rho_0$ itself). Again this is confirmed by comparing $P_{\rm D}$ for two Pe values in Fig. 1 of the main text. Since we choose to vary Pe at fixed $v_0$, a single $P_{\rm D}$ function then describes all our simulations; we fit this as $P_{\rm D}(\rho) = \alpha(1 - \exp(\gamma\rho))$, with $\alpha$ and $\gamma$ fitting parameters. Note that $P_{\rm D}$ is the pressure measured from averaging Eq. (10) of the main text over $\Lambda$ (see red curve in Fig. 1 of the main text) which is mathematically equivalent to using the standard virial relation for pairwise additive forces [4, 5].

The above scaling forms (21) and (22) assume that, once pressures are non-dimensionalized by a factor $\sigma\rho v_0$ (recalling that the mobility is unity), there can be no further dependence on $v_0$ except via the dimensionless combination Pe. This is true for hard particles, but could fail for softened interactions as actually used in our simulations: in particular, at large $v_0$ the effective diameter of the particles seen in collisions will be less than $\sigma$; see [2]. Accordingly the best route for testing the scalings with Pe is to vary this at fixed $v_0$, as we do here.

## IV. CONSTRUCTIONS OF THE BINODALS

As defined in the main text, we consider four routes (in two equivalent pairs) to calculate binodal densities in the high-Pe limit. We use 'thermodynamic' routes (via $f, P_f$) and 'mechanical' routes (via $P, f_P$), relying on the Maxwell equal-area construction (MC) and common tangent construction (CTC) as appropriate.

Method 1 starts from the effective free energy of [6, 7]

$$\tilde{f}(\rho) = k_{\rm B}T\left(\rho(\ln\rho - 1) + \int_0^\rho \ln v(u)\,{\rm d}u\right), \qquad (23)$$

where for ABPs $v = v_0(1 - \rho/\rho_0)$. This we supplement by a hard-core cutoff at $\rho = \rho_0$; hence $f$ obeys

$$f = \tilde{f} \quad \text{for} \quad \rho \le \rho_0 \ , \quad \text{else} \quad f = +\infty \ . \qquad (24)$$

The CTC is then performed on $f$ (see Fig. 1a). Method 2 starts from the mechanical pressure $P = P_{\rm S} + P_{\rm D}$, representing $P_{\rm D}$ as a hard-core cutoff: $P_{\rm D} = 0$ for $\rho \le \rho_0$ and $P_{\rm D} = +\infty$ for $\rho > \rho_0$. $P$ therefore obeys

$$P = \frac{\rho v_0^2}{2D_{\rm r}}(1 - \rho/\rho_0) \ \text{ for } \ \rho \le \rho_0 \ , \ \text{ else } \ P = +\infty \ . \qquad (25)$$

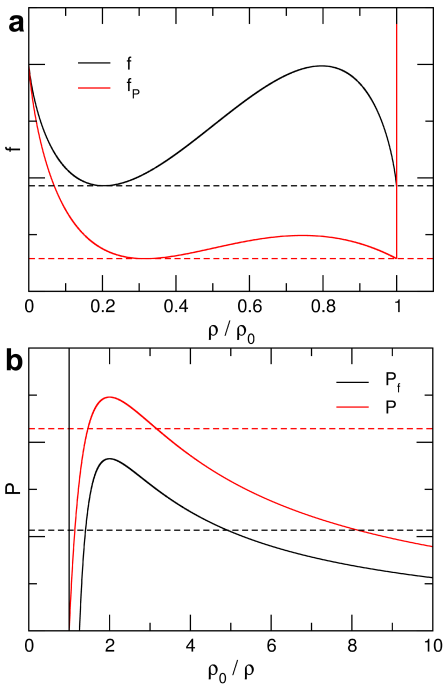


Figure 1. (a) Upper curve: CTC (dashed) on $f$ (solid) based on (24). Lower curve: CTC (dashed) on $f_P$ (solid) based on (27). In each case a linear term has been subtracted to make the common tangent horizontal. (b) Upper curve: MC (dashed) on the mechanical pressure $P = P_{\rm S} + P_{\rm D}$ (solid) based on (25). Lower curve: MC (dashed) on the pressure $P_f$ (solid) based on (26). The curves in (a) and (b) are rescaled/displaced vertically for improved visibility.

The MC is then applied to $P$ (see Fig. 1b). Method 3 constructs the thermodynamic pressure $P_f = \rho f' - \rho$ from $f$, that is

$$P_f = \rho\tilde{f}' - \tilde{f} \quad \text{for} \quad \rho \le \rho_0 \ , \quad \text{else} \quad P_f = +\infty \qquad (26)$$

and then applies the MC to $P_f$. By mathematical necessity, this gives the same binodals as Method 1 (see Fig. 1b). Method 4 constructs a different effective free energy $f_P$ such that $P = \rho f_P' - f_P$. The result is

$$f_P = \frac{\rho v_0^2}{2D_{\rm r}}\left[\rho(\ln\rho - 1) - \frac{\rho^2}{\rho_0}\right] \quad \text{for} \quad \rho \le \rho_0 \ , \quad \text{else} \quad f_P = +\infty \qquad (27)$$

from which binodals are found by the CTC on $f_P$. By mathematical necessity, this gives the same binodals as Method 2 (see Fig. 1a).

As is clear from Fig. 1, Method 1 (or 3) based on $f$ (or $P_f$) gives different binodals from Method 2 (or 4) based on $P$ (or $f_P$). These calculations all use the sharp cutoff approximation and hence the resulting binodals refer to the asymptotic limit of high Pe only. In this limit, Method 1 (or 3) is clearly more accurate than Method 2 (or 4) (see Fig. 2 of the main text).

However, we do not know how to generalize Method 1 (or 3) to the case of finite Pe, since we lack a theory for constructing the direct interaction contributions to $f$ or $P_f$. Method 2 (or 4) does generalize, allowing use of the semi-empirical expressions for $P_{\mathrm{S}}$ and $P_{\mathrm{D}}$ described above and in the main text. However, as shown there (see Fig. 2 of the main text) the results are unsatisfactory.

None of these methods allows for nonlocal contributions, which are shown in [8] to alter the common tangent construction found by Method 1. Similar nonlocal terms are also known to arise in calculations of mechanical force balance at phase coexistence in systems undergoing continuous driving, such as in shear banding [9]; they are likewise unjustifiably neglected by Method 2 (or 4). We conclude, as stated in the main text, that no adequate theory of phase equilibria in ABPs yet exists.

[1] A. P. Solon *et al.* In preparation.
[2] J. Stenhammar, D. Marenduzzo, R. J. Allen and M. E. Cates, *Soft Matter* **10**, 1489-1499 (2014)
[3] S. J. Plimpton, *J. Comp. Phys.* **117**, 1-19 (1995)
[4] M. P. Allen and D. J. Tildesley, *Computer Simulation of Liquids*, Oxford University Press, Oxford (1987)
[5] M. Doi, *Soft Matter Physics*, Oxford University Press, Oxford (2013)
[6] J. Tailleur and M. E. Cates, *Phys. Rev. Lett.* **100**, 218103 (2008)
[7] M. E. Cates and J. Tailleur, *Europhys. Lett.* **101**, 20010 (2013)
[8] R. Wittkowski, A. Tiribocchi, J. Stenhammar, R. J. Allen, D. Marenduzzo and M. E. Cates, *Nature Commun.* **5**, 4351 (2014)
[9] C. Y. D. Lu, P. D. Olmsted and R. C. Ball, *Phys. Rev. Lett.* **84**, 642 (2000)

### 4.4.1 Sphères dures autopropulsées par un processus d'Ornstein-Uhlenbeck

Nous montrons ici que les résultats obtenus pour des sphères dures autopropulsées à vitesse constante sont aussi valables pour des sphères dures autopropulsées par un processus d'Ornstein-Uhlenbeck. En particulier, la pression mécanique satisfait une équation d'état et peut être décomposée en trois termes, similaires à ceux obtenus dans le cas $v = \text{cte}$.

Nous considérons $N$ particules, dont nous notons les positions $\mathbf{r}_i$. La particule $j$ exerce sur la particule $i$ une force répulsive à courte portée $\mathbf{F}(\mathbf{r}_j - \mathbf{r}_i)$. Comme depuis le début de ce chapitre, les particules sont confinées suivant l'axe $\hat{\mathbf{x}}$ par un potentiel $V$. La dynamique de $\mathbf{r}_i$ et de la force $\mathbf{f}_i$ propulsant la particule $i$ s'écrivent

$$\dot{\mathbf{r}_i} = \mu \left[ \mathbf{f}_i - \nabla V(\mathbf{r}_i) + \sum_j \mathbf{F}(\mathbf{r}_j - \mathbf{r}_i) \right], \qquad \tau \dot{\mathbf{f}_i} = -\mathbf{f}_i + \sqrt{2D_f}\boldsymbol{\eta} \tag{4.37}$$

On peut écrire l'équation de Fokker-Planck donnant l'évolution de la probabilité jointe $\mathcal{P}(\{\mathbf{r}_i\},\{\mathbf{f}_i\},t)$ de trouver les $N$ particules aux position $\{\mathbf{r}_i\}$, avec des forces $\{\mathbf{f}_i\}$

$$\partial_t \mathcal{P} = -\sum_i \left\{ \nabla_{\mathbf{r}_i} \cdot \left[ \mu \left( \mathbf{f}_i - \nabla V(\mathbf{r}_i) + \sum_j \mathbf{F}(\mathbf{r}_j - \mathbf{r}_i) \right) \mathcal{P} \right] + \frac{1}{\tau} \nabla_{\mathbf{f}_i} \cdot [\mathbf{f}_i \mathcal{P}] + \frac{D_f}{\tau^2} \Delta_{\mathbf{f}_i} \mathcal{P} \right\} \tag{4.38}$$

Définissons $\langle O \rangle(r_{1,x})$ la moyenne d'une observable $O$ sachant que la particule 1 est à une abscisse $r_{1,x}$. Pour cela, nous intégrons sur toutes les forces, les positions des particules 2 à $N$ et l'ordonnée $r_{1,y}$ de la particule 1

$$\langle O \rangle(r_{1,x}) = \int dr_{1,y} \int d\mathbf{r}_2 \dots d\mathbf{r}_N d\mathbf{f}_1 \dots d\mathbf{f}_N \; O\left(\{\mathbf{r}_i\},\{\mathbf{f}_i\}\right) \mathcal{P}\left(\{\mathbf{r}_i\},\{\mathbf{f}_i\}\right) \tag{4.39}$$

Dans la suite nous noterons $\mathbf{r} = (x, y) = \mathbf{r}_1$ et $\mathbf{f} = (f_x, f_y) = \mathbf{f}_1$ pour alléger les notations. La moyenne de l'équation (4.38) nous donne dans l'état stationnaire

$$0 = -\partial_x \left\langle \mu \left[ f_x - \nabla V + \sum_{j=2}^{N} F_x(\mathbf{r}_j - \mathbf{r}) \right] \right\rangle = -\partial_x J_x \tag{4.40}$$

Le système étant confiné, le flux de particules $J_x$ est nul dans l'état stationnaire. On peut alors utiliser $J_x = 0$ pour exprimer la pression mécanique

$$P = N \int_0^\infty \langle \partial_x V \rangle dx = N \int_0^\infty \left\langle f_x + \sum_{j=2}^{N} F_x(\mathbf{r}_j - \mathbf{r}) \right\rangle dx \tag{4.41}$$

Le facteur $N$ prend en compte le fait que les $N$ particules jouent un rôle symétrique.

En multipliant l'équation (4.38) par $f_x$ et en prenant sa moyenne, on obtient

$$0 = -\partial_x \left[ \mu \left\langle f_x^2 - f_x \partial_x V + f_x \sum_{j=2}^{N} F_x(\mathbf{r}_j - \mathbf{r}) \right\rangle \right] - \frac{\langle f_x \rangle}{\tau} \tag{4.42}$$

En reportant cette expression dans l'équation (4.41) et en effectuant l'intégration spatiale, on obtient pour la pression

$$P = \tau\mu N \langle f_x^2 \rangle_0 + \tau\mu N \langle f_x \sum_{j=2}^{N} F_x(\mathbf{r}_j - \mathbf{r}) \rangle_0 + N \int_0^\infty \left\langle \sum_{j=2}^{N} F_x(\mathbf{r}_j - \mathbf{r}) \right\rangle dx \tag{4.43}$$

où $\langle \cdot \rangle_0$ dénote une moyenne dans le coeur du système, en $x = 0$. Le rôle des particules $j = 2$ à $N$ étant identique dans l'équation (4.43), on peut noter $\mathbf{r}' = \mathbf{r}_2$ et réécrire les deux derniers termes de l'équation (4.43)

$$P_I \equiv \tau\mu N \langle f_x \sum_{j=2}^{N} F_x(\mathbf{r}_j - \mathbf{r}) \rangle_0 = \tau\mu N (N-1) \left\langle f_x F_x(\mathbf{r}' - \mathbf{r}) \right\rangle_0 \tag{4.44}$$

$$P_D \equiv N \int_0^\infty \left\langle \sum_{j=2}^{N} F_x(\mathbf{r}_j - \mathbf{r}_i) \right\rangle dx = N(N-1) \int_0^\infty \langle F_x(\mathbf{r}' - \mathbf{r}) \rangle \, dx \tag{4.45}$$

Comme les notations choisies le suggèrent, les trois termes de l'équation (4.43) sont les équivalents des trois termes obtenus pour des particules autopropulsées à vitesse constante dans l'article D. En notant $P_0$ la pression du gaz parfait actif, $P_0 \equiv \tau\mu N \langle f_x^2 \rangle_0 = \mu D_f \rho_0$, on a alors

$$P = P_0 + P_I + P_D \tag{4.46}$$

Les trois contributions ne dépendent que des propriétés du coeur du système. C'est évident pour la pression de gaz parfait $P_0$ et la pression « indirecte » $P_I$, qui sont des moyennes calculées en $x = 0$. Pour la pression « directe » $P_D$, on peut le voir en utilisant la probabilité de distribution à deux particules

$$\mathcal{P}(\mathbf{r},\mathbf{r}') = \int d\mathbf{r}_3 \ldots d\mathbf{r}_N d\mathbf{f}_1 \ldots d\mathbf{f}_N \; \mathcal{P}\left(\{\mathbf{r}_i\},\{\mathbf{f}_i\}\right) \tag{4.47}$$

La pression directe s'écrit alors

$$P_D = N(N-1) \int_0^\infty dx \int_{-\infty}^\infty dx' \int_{-\infty}^\infty dy \int_{-\infty}^\infty dy' F_x(\mathbf{r}' - \mathbf{r}) \mathcal{P}(\mathbf{r},\mathbf{r}') \tag{4.48}$$

Pour les valeurs $x' > 0$, on peut échanger le rôle des positions $\mathbf{r}$ et $\mathbf{r}'$, $\mathcal{P}(\mathbf{r},\mathbf{r}') = \mathcal{P}(\mathbf{r}',\mathbf{r})$. Leur contribution s'annule par la loi d'action-réaction $F_x(\mathbf{r}'-\mathbf{r}) = -F_x(\mathbf{r}-$

$\mathbf{r}'$). Les seules contributions à l'intégrale de l'équation (4.48) sont donc pour $x > 0$ et $x' < 0$

$$P_D = N(N-1)\int_0^\infty dx \int_{-\infty}^0 dx' \int_{-\infty}^\infty dy \int_{-\infty}^\infty dy' F_x(\mathbf{r}' - \mathbf{r})\mathcal{P}(\mathbf{r},\mathbf{r}') \tag{4.49}$$

Pour des forces $\mathbf{F}$ à courte portée, $P_D$ est donc calculée dans une région finie de l'espace autour de $x = 0$, dans le coeur du système.

Nous avons donc montré que, comme pour les sphères dures autopropulsées à vitesse constante, la pression mécanique admet une équation d'état. Les trois termes qui la composent sont les analogues des trois termes obtenus dans l'article D.

### 4.4.2 Perspectives

Dans l'article D, nous avons étudié les conséquences de l'existence d'une équation d'état satisfaite par la pression mécanique sur les propriétés des phases *homogènes*. Cependant, comme nous l'avons vu pour les particules de déplaçant à une vitesse $v(\rho)$, la deuxième condition fixant les densités de coexistence fait intervenir explicitement les termes de gradients, importants aux interfaces.

Pour aller plus loin, il serait donc nécessaire de calculer les fonctions de corrélations qui entrent dans les définitions de $P_D$ et $P_I$, en particulier les contributions en gradients. L'enjeu sera alors de voir si ces contributions peuvent être capturées par une théorie en $v(\rho)$, par exemple avec un noyau de moyennage asymétrique décrivant bien les collisions. L'équivalence entre les sphères dures et les particules se déplaçant à une vitesse $v(\rho)$ permettrait alors de mieux comprendre les premières en profitant de notre connaissance de la thermodynamique des secondes.

# Chapitre 5

# La transition vers le mouvement collectif

## 5.1 Introduction

L'émergence d'un mouvement collectif est sans doute le phénomène le plus caractéristique de la matière active. En effet, des particules autopropulsées qui interagissent pour aligner leur direction de déplacement peuvent s'auto-organiser pour se déplacer collectivement sur une échelle très grande devant la taille typique des particules. Contrairement à l'application d'un champ extérieur, qui imposerait une direction de déplacement à l'ensemble des particules d'un système, c'est ici une interaction d'alignement locale qui génère un mouvement collectif à grande échelle, dont la direction résulte d'une brisure spontanée de symétrie.

Les exemples de mouvements collectifs sont nombreux dans le monde vivant, les plus évidents étant les déplacements de groupes d'animaux (nuées d'oiseaux, bancs de poissons, troupeaux, etc.). Pour ceux-ci, l'interaction d'alignement est d'origine « sociale », le résultat d'un processus de « décision ». À plus petite échelle, d'autres mécanismes sont en jeu. Les forces exercées entre cellules, ou les signaux biochimiques qu'elles échangent, peuvent être à l'origine de la migration collective de groupes de cellules [124], importante dans la morphogenèse [125] ou le développement de cancers [126]. Des interactions stériques entre particules asymétriques, par exemple entre des bactéries [23] ou des filaments du cytosquelette [22, 24, 30, 31], conduisent également à un alignement effectif et à des mouvements collectifs.

Par ailleurs, il est également possible d'observer des mouvements collectifs avec des particules actives inertes, fabriquées en laboratoire. Les exemples vont de grains vibrés s'alignant par interactions stériques[42] aux « surfeurs » colloïdaux s'alignant

par interaction électrostatique [44] en passant par des gouttes autopropulsées [43] alignées par des interactions hydrodynamiques.

On voit donc que des systèmes variés, à des échelles différentes et avec des mécanismes d'alignement divers, donnent lieu à des mouvements collectifs. En tant que physicien, on peut donc se demander si ces différents mouvements collectifs partagent des propriétés communes, universelles. Pour répondre à cette question, on peut étudier des modèles minimaux qui contiennent seulement les deux ingrédients partagés par tous les systèmes que nous avons évoqués : l'autopropulsion et une interaction locale d'alignement.

Le modèle de Vicsek et collaborateurs [13, 127] a été introduit dans ce but. Il décrit des particules ponctuelles se déplaçant dans un plan continu à vitesse constante $v_0$ suivant leur direction d'autopropulsion $\theta_i$. À chaque pas de temps discret, $\Delta t = 1$, les directions de toutes les particules sont mises à jour en parallèle d'après la règle

$$\theta_i(t+1) = \langle \theta_j \rangle_{j \in \mathcal{N}_i} + \eta \xi_i \tag{5.1}$$

où $\mathcal{N}_i$ est le disque de rayon unité autour de la particule $i$, et $\xi_i$ un nombre aléatoire tiré uniformément dans $[-\pi,\pi]$. Les particules avancent ensuite dans leur nouvelle direction $\mathbf{r}_i(t+1) = \mathbf{r}_i(t) + v_0 \mathbf{e}[\theta_i(t+1)]$ où $\mathbf{e}(\theta) = (\cos\theta, \sin\theta)$. Quand l'amplitude du bruit sur l'alignement $\eta$ est faible, les particules s'ordonnent pour se déplacer en moyenne dans la même direction. Le modèle de Vicsek a donc permis de montrer que l'autopropulsion et un alignement local suffisent à générer un mouvement collectif.

### 5.1.1 Phase homogène ordonnée

Le fait même que le modèle de Vicsek montre un état ordonné apparut comme une surprise aux yeux des physiciens. En effet, le modèle de Vicsek peut être vu comme un modèle XY dynamique, l'interaction d'alignement des vitesses étant analogue à une interaction ferromagnétique entre des spins continus. Or, *à l'équilibre thermique*, le théorème de Mermin-Wagner [14] montre qu'il est impossible de briser spontanément une symétrie continue en 2d lorsque seules des interactions à courte portée sont en jeu. Le modèle XY n'a donc pas de phase ordonnée, contrairement à son homologue actif.

La phase ordonnée du modèle de Vicsek a d'autres propriétés inhabituelles. Elle présente des corrélations à longue portée qui en font un système critique, sans longueur caractéristique. Ces corrélations sont anisotropes et donc difficiles à mesurer numériquement. Une manière simple de les mettre en évidence est d'étudier les fluctuations de densité. Pour cela, on mesure le nombre $n$ de particules dans des boîtes de taille variable et l'on compare la moyenne de $n$ à la taille caractéristique de ses fluctuations $\Delta n = \sqrt{\langle n^2 \rangle - \langle n \rangle^2}$. Pour un système qui possède une

longueur de corrélation $\xi$, des boîtes de taille grande devant $\xi$ peuvent être divisées en sous-boîtes indépendantes. Le nombre moyen de particules dans la boîte est alors une somme de variables aléatoires indépendantes et le théorème central limite impose donc $\Delta n \propto \langle n \rangle^{1/2}$. Au contraire, pour le modèle de Vicsek, on mesure [68] $\Delta n \propto \langle n \rangle^{\alpha}$, avec $\alpha \approx 0.8$. Ces fluctuations « géantes » de densité sont une caractéristique récurrente des systèmes actifs ordonnés, observée numériquement [68, 71] et expérimentalement [40, 128] dans plusieurs systèmes. La phase ordonnée est également caractérisée par une super-diffusion dans la direction $u_\perp$ perpendiculaire à la direction moyenne de déplacement des particules. En effet, une mesure du déplacement quadratique moyen des particules dans cette direction donne [68]

$$\Delta r_\perp = \sqrt{\langle [r_\perp(t) - r_\perp(0)] \rangle} \sim t^\nu \tag{5.2}$$

avec un exposant $\nu \approx 4/3$, au lieu de $\nu = 1$ pour une diffusion normale. Qualitativement, c'est cette super-diffusion qui permet de transmettre efficacement l'information (la direction du mouvement) dans le système, et donc de stabiliser l'ordre à longue portée.

La théorie de Toner et Tu [73–75, 129, 130] permet de prédire les propriétés de la phase homogène ordonnée. Elle part d'équations pour un champ de densité $\rho$ advecté par un champ de vitesse $\mathbf{v}$ qui contiennent tous les termes permis par la symétrie du problème

$$\partial_t \rho + \nabla \cdot (\rho \mathbf{v}) = 0 \tag{5.3}$$

$$\begin{aligned} \partial_t \mathbf{v} + \lambda_1 (\mathbf{v} \cdot \nabla)\mathbf{v} + \lambda_2 (\nabla \cdot \mathbf{v})\mathbf{v} = &\left(\alpha - \beta |\mathbf{v}|^2\right) \mathbf{v} - \nabla P \\ &+ D_L \nabla(\nabla \cdot \mathbf{v}) + D_1 \nabla^2 \mathbf{v} + D_2 \left(\mathbf{v} \cdot \nabla\right)^2 \mathbf{v} + \mathbf{f} \end{aligned} \tag{5.4}$$

où $f$ est un bruit blanc gaussien. L'équation (5.4) est l'analogue d'une équation de Navier-Stokes complétée par un terme de Ginzburg-Landau $(\alpha - \beta|\mathbf{v}|^2)\,\mathbf{v}$ qui tend à imposer une vitesse non nulle $|\mathbf{v}| = \sqrt{\alpha/\beta}$ pour $\alpha$ et $\beta$ positifs. Notons que ce terme brise l'invariance galiléenne de l'équation de Navier-Stokes, ce qui autorise également les termes en $\lambda$ de l'équation (5.4). Ceci peut être vu en posant $\tilde{\mathbf{v}}(\mathbf{r},t) = \mathbf{v}(\mathbf{r} - \mathbf{u}t) + \mathbf{u}$ pour une vitesse constante $\mathbf{u}$. On a alors, pour les termes du membre de gauche de l'équation (5.4)

$$\partial_t \tilde{\mathbf{v}} = \partial_t \mathbf{v} - \mathbf{u} \cdot \nabla \mathbf{v} \tag{5.5}$$

$$\lambda_1 (\tilde{\mathbf{v}} \cdot \nabla)\tilde{\mathbf{v}} = \lambda_1 \left[\mathbf{v} \nabla \cdot \mathbf{v} + \mathbf{u} \cdot \nabla \mathbf{v}\right] \tag{5.6}$$

$$\lambda_2 (\nabla \cdot \tilde{\mathbf{v}})\tilde{\mathbf{v}} = \lambda_2 \left[(\nabla \cdot \mathbf{v})\mathbf{v} + (\nabla \cdot \mathbf{v})\mathbf{u}\right] \tag{5.7}$$

La dynamique de $\tilde{\mathbf{v}}$ est la même que celle de $\mathbf{v}$ uniquement lorsque $\lambda_1 = 1$ et $\lambda_2 = 0$, comme c'est le cas pour l'équation de Navier-Stokes.

Par une méthode de renormalisation dynamique, Toner et Tu sont capables, moyennant certaines approximations [75], de calculer les exposants d'échelle de plusieurs fonctions de corrélation. À notre connaissance, ces exposants n'ont pas été vérifiés numériquement de façon systématique mais leurs prédictions concernant la super-diffusion transverse et les fluctuations géantes de densités l'ont été. Ainsi, la valeur calculée $\nu = 4/3$ pour la super-diffusion transverse correspond bien à la valeur mesurée numériquement [68]. La loi d'échelle anormale des fluctuations de densité peut être obtenue à partir de la fonction de corrélation de la densité, ce que nous détaillons ci-dessous.

La théorie de Toner et Tu prédit, pour la fonction d'autocorrélation de la densité en espace de Fourier $C_\rho(\mathbf{q},t) = \langle|\rho(\mathbf{q},t)|^2\rangle$, des lois d'échelle différentes suivant les régimes ($q_\parallel \gg q_\perp$, $q_\parallel \ll q_\perp$ ou $q_\parallel \sim q_\perp$). À grande échelle, la contribution dominante est donnée par le plus grand exposant, qui correspond aux modes $q_\parallel \sim q_\perp$. L'anisotropie de la fonction de corrélation devient alors sous-dominante. En espace réel, on obtient

$$C_\rho(\mathbf{r},t) = \langle\delta\rho(\mathbf{r},t)\delta\rho(0,t)\rangle \sim r^{-\gamma} \tag{5.8}$$

avec $\gamma = 8/10$ et $\delta\rho = \rho - \rho_0$ où $\rho_0$ est la densité moyenne. On peut alors exprimer la variance du nombre $n$ de particules dans une boîte $\mathcal{B}$ comme

$$\Delta n^2 = \int_{\mathcal{B}} d\mathbf{r} \int_{\mathcal{B}} d\mathbf{r}' C_\rho(\mathbf{r}-\mathbf{r}') \sim \int_{\mathcal{B}} d\mathbf{r} \int_{\mathcal{B}} d\mathbf{r}' |\mathbf{r}-\mathbf{r}'|^{-\gamma} \tag{5.9}$$

En adimensionnant l'équation (5.9) par la taille $\ell$ de la boîte, on trouve finalement

$$\Delta n^2 \sim \ell^{2d-\gamma} \sim n^{\frac{2d-\gamma}{d}} \tag{5.10}$$

où nous avons utilisé $n = \rho_0 \ell^d$. Pour $d = 2$, $(2d-\gamma)/d = 1.6$ ce qui donne bien l'exposant $\alpha = 0.8$ observé numériquement pour $\Delta n$.

### 5.1.2 Transition vers l'état ordonné

Dans ce chapitre, nous nous intéresserons plus particulièrement à la transition de phase qui mène au mouvement collectif, c'est-à-dire au passage entre l'état désordonné et l'état ordonné. Celle-ci a lieu lorsqu'on change un paramètre de contrôle. Traditionnellement, cette transition a été étudiée en variant le bruit, qui joue le rôle d'une température pour une transition ferromagnétique standard, mais nous verrons qu'on peut l'observer également en changeant la densité moyenne de particules ou la vitesse d'autopropulsion.

L'article original de Vicsek et collaborateurs [13] faisait état d'une transition continue, similaire à une transition critique dans un système magnétique passif,

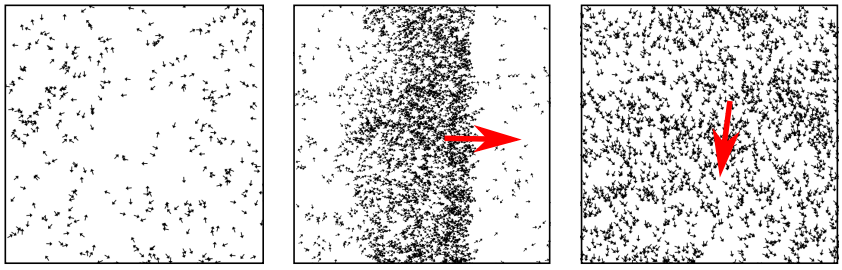

**Figure 5.1** – Les trois phases observées dans le modèle de Vicsek. De gauche à droite : désordonnée, inhomogène (une bande ordonnée se déplaçant dans un gaz désordonné) et ordonnée. Les flèches rouges indiquent la direction de la bande (milieu) ou de l'ensemble des particules (droite).

entre les états homogènes désordonné et ordonné. Toutefois, Grégoire, Chaté et collaborateurs [68, 69] ont montré qu'à des tailles de système suffisamment grandes, la transition est discontinue. En diminuant le bruit à partir de la phase désordonnée, ils observent l'apparition de bandes ordonnées de haute densité qui se propagent dans un gaz désordonné de particules (voir figure 5.1). Ce n'est qu'à plus faible bruit que l'on retrouve la phase homogène ordonnée. De plus, les bandes apparaissent par nucléation et de l'hystérèse est observée entre l'état désordonné et l'état inhomogène, comme pour les transitions du premier ordre à l'équilibre. Comme nous le verrons, la transition « continue » étudiée par Vicsek et collaborateurs est un effet de taille finie observé quand le système n'est pas assez grand pour accommoder une bande de haute densité. La transition étant faiblement du premier ordre, la longueur de corrélation peut être très grande et laisser croire que l'on est en présence d'une transition critique.

À cause de ces effets de taille finie, l'étude du modèle de Vicsek est assez difficile sur le plan numérique, malgré la simplicité apparente du modèle. De plus, les interactions entre bandes dans la phase inhomogène mettent en jeu des échelles de temps très grandes, ce qui rend l'étude de cette phase particulièrement compliquée numériquement. En outre, les règles qui définissent le modèle de Vicsek (temps discret, espace continu) se prêtent mal à la construction d'équations hydrodynamiques. Pour mieux comprendre les propriétés de la transition vers le mouvement collectif, Bertin et collaborateurs ont donc proposé un modèle plus simple, qui ne prend en compte que des collisions binaires entre particules [76, 78, 81]. Ce modèle peut être décrit par une équation de Boltzmann, ce qui permet de construire des équations hydrodynamiques dans la limite de basse densité, où l'on s'attend à ce que l'hypothèse de chaos moléculaire soit justifiée. Ces équations sont similaires dans leur forme à celles de Toner et Tu mais leur construction explicite permet d'obtenir l'expression des coefficients mésoscopiques en fonction des paramètres microscopiques du modèle et de la densité. Les équations rendent compte du dia-

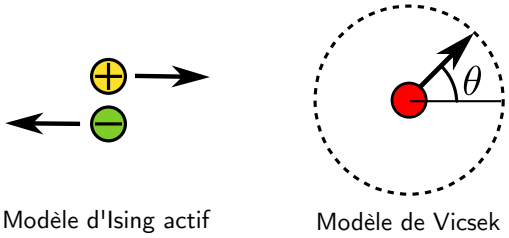


**Figure 5.2** – Illustration de la différence de symétrie entre le modèle d'Ising actif et le modèle de Vicsek. Les flèches noires indiquent la direction d'autopropulsion des particules.

gramme des phases du modèle de Vicsek, en particulier de la présence d'une phase inhomogène. En effet, une étude de stabilité linéaire montre que, dans une région de l'espace des paramètres, aucune phase homogène (ordonnée ou désordonnée) n'est linéairement stable. Pour ces paramètres, la solution stationnaire est donc obligatoirement inhomogène et les équations admettent des solutions propagatives [78]. Toutefois, comme nous le verrons dans l'article F, les équations de Bertin *et al* admettent de nombreuses solutions inhomogènes qu'il n'est pas évident de relier au comportement du modèle de Vicsek.

### 5.1.3 La transition vers le mouvement collectif : une transition liquide-gaz

Le message central de ce chapitre est que la transition vers le mouvement collectif gagne à être interprétée comme une transition liquide-gaz, plutôt qu'une transition ferromagnétique. Cette affirmation fait suite à l'étude du modèle d'Ising actif, présenté en détail dans l'article E, qui permet d'étudier la transition vers le mouvement collectif dans un cadre plus simple que celui du modèle de Vicsek. Ce modèle est basé sur les mêmes ingrédients que le modèle de Vicsek : l'autopropulsion et une interaction d'alignement locale. La principale différence est dans la symétrie du paramètre d'ordre : les particules du modèle d'Ising actif ont deux directions d'autopropulsion possibles, vers la gauche ou vers la droite (et diffusent symétriquement dans la direction verticale), contrairement aux particules du modèle de Vicsek qui peuvent se propulser dans une direction arbitraire du plan (voir figure 5.2 pour une illustration). Le modèle d'Ising actif possède donc, comme le modèle d'Ising standard, une symétrie rotationnelle discrète, tandis que le modèle de Vicsek possède une symétrie rotationnelle continue, comme le modèle XY.

Quand la température, qui contrôle l'efficacité de l'interaction d'alignement, diminue (ou que la densité augmente), on observe dans le modèle d'Ising actif le même type de transition vers le mouvement collectif que dans le modèle de Vic-

sek : d'un état désordonné, on passe à un état inhomogène, où une bande ordonnée dense se déplace dans un gaz dilué désordonné, puis à un état homogène ordonné. Cependant, comme pour les modèles magnétiques d'équilibre, la différence de symétrie entre le modèle de Vicsek et le modèle d'Ising actif entraîne des différences qualitatives importantes, en particulier dans la phase ordonnée. Ainsi, la phase ordonnée du modèle d'Ising actif a des corrélations à courte portée et des fluctuations de densité normales, ce qui la rend plus simple à étudier que celle du modèle de Vicsek.

La transition vers le mouvement collectif dans le modèle d'Ising actif est très similaire à une transition liquide-gaz passive. Dans la phase inhomogène, on observe une séparation de phase entre un liquide ordonné et un gaz désordonné. Les densités de coexistence sont contrôlées par la température et la vitesse d'autopropulsion mais ne dépendent pas de la densité moyenne de particules $\rho_0$. Varier $\rho_0$ change donc simplement la fraction de liquide dans le système, qui est donnée par la loi du levier comme pour une transition liquide-gaz d'équilibre. Cependant, le diagramme des phases dans l'ensemble canonique (température, densité ; voir figure 5.3) diffère d'un diagramme liquide-gaz classique. En effet, le liquide et le gaz ont des symétries différentes (polaire et désordonné) ; le système ne peut donc pas passer continûment de l'un à l'autre, si bien que le diagramme des phases ne peut avoir de région supercritique. Cela se traduit par une asymptote à une température finie sur le diagramme des phases et un déplacement du point critique à une densité infinie (voir figure 5.3). Cette interprétation de la transition vers le mouvement collectif comme transition liquide-gaz n'explique pas simplement le diagramme des phases du modèle. Elle prédit également un grand nombre de caractéristiques de la transition (effets de taille finie, boucles d'hystérèse, variation de l'aimantation, etc.) sur lesquelles nous reviendrons dans l'article E.

De plus, cette image nous a permis de porter un regard nouveau sur le modèle de Vicsek. Comme nous le montrons dans l'article G, le modèle de Vicsek présente également une transition de type liquide-gaz et son diagramme des phases a la même forme que celui du modèle d'Ising actif. La différence majeure entre les deux modèles est la forme des profils de densité dans la phase inhomogène. Alors que le modèle d'Ising actif donne lieu à une séparation de phase complète entre deux domaines de tailles arbitraires, le modèle de Vicsek donne lieu à une séparation en microphases : on observe dans la phase inhomogène des bandes ordonnées *de taille finie* réparties périodiquement dans le système (voir figure 5.3). Nous montrerons dans l'article F que les équations hydrodynamiques supposées décrire ces modèles admettent, de manière équivalente, les deux types de solutions (séparation de phase et microphases). Elles n'expliquent donc pas pourquoi un comportement ou l'autre est observé dans les modèles microscopiques. Pour comprendre cela, nous verrons qu'il faut impérativement tenir compte des fluctuations et donc travailler au niveau

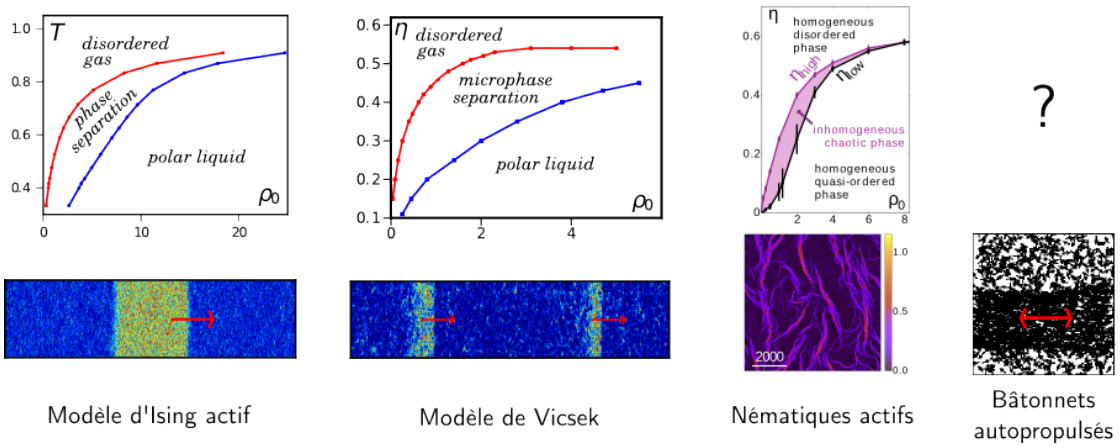


**Figure 5.3** – **Haut** : Diagramme des phases dans l'ensemble canonique (température ou bruit, densité) pour différents modèles microscopiques présentant une transition vers le mouvement collectif. Les diagrammes ont la même forme (celui des bâtonnets autopropulsés n'est pas présent dans la littérature). **Bas** : Instantané dans la phase de coexistence, qui est qualitativement différente pour chaque modèle. Figures reproduites de [71] pour les nématiques actifs et [70] pour les bâtonnets autopropulsés.

des hydrodynamiques *fluctuantes*.

Dans ce chapitre, nous discuterons uniquement des modèles décrivant des particules autopropulsées interagissant via un alignement ferromagnétique. Toutefois, il semble que le scénario de transition liquide-gaz soit plus général. En particulier, le diagramme des phases du modèle de nématiques actifs [71], décrivant des particules vibrant sur place et s'alignant avec une interaction nématique (voir figure 1.6 dans l'introduction de cette thèse), est similaire à ceux du modèle d'Ising actif et du modèle de Vicsek (voir figure 5.3). Un modèle de bâtonnets autopropulsés qui s'alignent nématiquement [70] montre également une séparation de phase entre un domaine liquide ordonné et un gaz désordonné. L'image qui semble se dégager, et qui reste à étayer, est que, dans tous ces modèles minimaux décrivant des particules autopropulsées qui s'alignent localement, la transition vers le mouvement collectif s'inscrit dans le cadre général des transitions liquide-gaz. Dans tous les cas, le liquide et le gaz ont des symétries différentes, ce qui impose la forme du diagramme des phases. Cependant, les phases liquides des différents modèles ont des propriétés différentes (ordre polaire ou nématique, fluctuations de densité géantes ou normales), ce qui conduit à différentes formes de coexistence de phase : séparation de phase dans le modèle d'Ising actif, en microphases dans le modèle de Vicsek, phase « chaotique » dans les nématiques actifs [71] ou bandes immobiles avec un ordre nématique pour les bâtonnets autopropulsés [70] (voir figure 5.3).

Nous commencerons ce chapitre par une étude détaillée du modèle d'Ising actif en deux dimensions à la section 5.2 et montrerons que la transition vers le mouvement collectif dans ce modèle est similaire à une transition liquide-gaz. À la section 5.3, nous montrerons que les équations hydrodynamiques écrites pour décrire les modèles de particules autopropulsées avec alignement (en particulier le modèle d'Ising actif et le modèle Vicsek) admettent génériquement les mêmes types de solutions propagatives. Parmi ces solutions, certaines décrivent une séparation de phase telle qu'observée dans le modèle d'Ising actif, d'autres la séparation en microphases du modèle de Vicsek. Toutefois, les équations hydrodynamiques ne permettent pas de comprendre comment une des solutions est sélectionnée dans chaque modèle microscopique. Nous verrons à la section 5.4, que la transition dans le modèle de Vicsek est également de type liquide-gaz et montrerons que le bruit joue un rôle crucial dans la sélection de la forme des profils inhomogènes. Enfin, à la section 5.5, nous nous intéresserons à des modèles de mouvement collectif en dimension $d = 1$, qui ont une phénoménologie assez différente. En effet, les fluctuations déstabilisent alors l'état ordonné et conduisent à un comportement intermittent que nous analyserons.

Notons que les articles H et I, reproduits en annexes pour éviter des redondances, sont des versions plus condensées des articles E et F inclus dans ce chapitre. Ils peuvent donc constituer une bonne introduction aux sections 5.2 et 5.3, respectivement.

## 5.2 Le modèle d'Ising actif

Dans l'article E, que nous reproduisons ici, le modèle d'Ising actif en dimension $d = 2$ est étudié en détail. Après avoir défini le modèle, nous explorerons numériquement sa phénoménologie : diagramme des phases, dynamique de *coarsening*, boucles d'hystérèse, corrections de taille finie, etc. De plus, nous construirons explicitement des équations hydrodynamiques à partir du modèle microscopique. Celles-ci sont basées sur des équations de champ moyen, corrigées pour tenir compte de l'impact des fluctuations locales sur la dynamique des champs de densité et d'aimantation. Elles permettent alors de reproduire les caractéristiques principales de la phénoménologie du modèle microscopique.

# Flocking with discrete symmetry: the 2d Active Ising Model

A. P. Solon, J. Tailleur
*Université Paris Diderot, Sorbonne Paris Cité, MSC, UMR 7057 CNRS, F75205 Paris, France*
(Dated: September 10, 2015)

We study in detail the active Ising model, a stochastic lattice gas where collective motion emerges from the spontaneous breaking of a discrete symmetry. On a 2d lattice, active particles undergo a diffusion biased in one of two possible directions (left and right) and align ferromagnetically their direction of motion, hence yielding a minimal flocking model with discrete rotational symmetry. We show that the transition to collective motion amounts in this model to a *bona fide* liquid-gas phase transition in the canonical ensemble. The phase diagram in the density/velocity parameter plane has a critical point at zero velocity which belongs to the Ising universality class. In the density/temperature 'canonical' ensemble, the usual critical point of the equilibrium liquid-gas transition is sent to infinite density because the different symmetries between liquid and gas phases preclude a supercritical region. We build a continuum theory which reproduces qualitatively the behavior of the microscopic model. In particular we predict analytically the shapes of the phase diagrams in the vicinity of the critical points, the binodal and spinodal densities at coexistence, and the speeds and shapes of the phase-separated profiles.

## CONTENTS



## I. INTRODUCTION

Active matter systems, defined as large assemblies of interacting particles consuming energy to self-propel, exhibit a variety of elaborate collective behaviors. Among them, collective motion—a term referring to the coherent displacement of large groups of individuals over length scales much larger than their individual size—has played a leading role in active matter studies. It can be observed in a wide range of biological systems such as bird flocks [1], fish schools [2, 3], bacterial swarms [4, 5], actin [6] or microtubule [7] motility assays, but also in inert matter that is artificially self-propelled, for example in assemblies of vibrated polar disks [8], rolling colloids [9] or self-propelled liquid droplets [10].

On the theoretical side, the transition to collective motion—hereafter referred to as the "flocking" transition—has attracted the attention of the physics community because simple models have proved useful to describe its generic properties, highlighting the possibility of universal behaviours. The model introduced by Vicsek and collaborators two decades ago [11] is prototypical of this line of research, containing only two ingredients: self-propulsion at a constant speed and aligning interactions. It has often been described as a dynamical XY model [12] since the alignment of the particle directions of motion resemble the ferromagnetic alignment of XY spins.

The phenomenology of the Vicsek model is now well es-

tablished [11, 13, 14]. When decreasing the noise on the aligning interaction, or increasing the density, a transition takes place from a disordered gas into an ordered state of collective motion. Between these two homogeneous phases lays a region of parameter space where particles gather in dense ordered bands travelling in a dilute disordered background. These bands, which are a robust feature of flocking models [13, 15–20], are a signature of the first-order nature of the transition, together with intermittency, metastability and hysteresis [13, 14]. Unfortunately, they are seen only in large systems and strong finite size effects render the numerical study of the Vicsek model (VM) very costly in computing power.

To overcome these numerical difficulties and gain more insight into the flocking transition, a number of analytical approaches have been followed. Hydrodynamic equations for Vicsek-like models have been either derived by coarse-graining [19, 20] or proposed phenomenologically [12, 15, 21]. These equations predict phase diagrams in qualitative agreement with the microscopic models, including the existence of inhomogeneous bands [14, 15, 19, 20]. Their analytical study is however so complicated that little can be done beyond working with their linearized version. Nevertheless, some progress was made to account for the long range order and giant density fluctuations observed in the ordered phase of the Vicsek model [12]. Interestingly, it was also recently shown that all hydrodynamic equations derived for polar flocking models [15, 19, 20, 22] admit the same family of 1d propagative solutions [23]. A complete analytical study of the Vicsek model, from micro to macro, however remains elusive.

An alternative strategy to gain insight into the flocking transition relied on the introduction of an Active Ising Model (AIM) [22] which circumvents both the numerical and analytical pitfalls of the Vicsek model. Using non-equilibrium versions of ferromagnetic models has indeed often proven a useful strategy [17, 24–26]. The AIM, which we study in detail in this paper, contains the two key ingredients for flocking: self-propulsion and aligning interactions. The continuous rotational symmetry of the Vicsek model is however replaced by a discrete symmetry; In the AIM, particles diffuse in the 2d plane but are self-propelled in only one of two possible directions (left or right). It is thus akin to a dynamical Ising model where particles have a discrete rotational symmetry. The AIM is found to have a simpler, more tractable, behavior than the Vicsek-like models with continuous symmetry while still retaining a large part of their physics. Using a lattice-based model also simplifies both numerical and analytical studies.

After introducing the model in section II, we present a numerical study of the 2d AIM in section III. Our main conclusion is that the transition in the AIM amounts to a liquid-gas transition in the canonical ensemble. At fixed orientational noise, the system can be in two "pure" states: a disordered gas or an ordered liquid, the latter leading to a collective migration of all particles to the left or to the right. When constraining the system's density to lie between two 'spinodal lines', no homogeneous phase can be observed and the system phase separates, with an ordered travelling liquid band coexisting with a disordered gas background. A key difference with the usual equilibrium liquid-gas transition is that liquid and gas have different symmetries; A supercritical region is thus prohibited since one has to break a symmetry to take the system from a gas to a liquid state, which explains the atypical shape of the phase diagram.

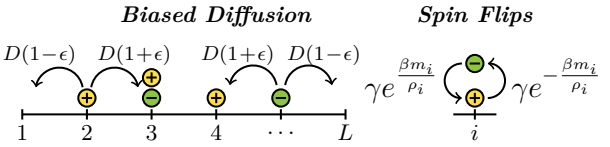


FIG. 1. Sketch of the two possible actions and their rates of occurrence. The ferromagnetic interaction between particles is purely on-site and particles diffuse freely. Beyond the biased diffusion shown here, particles also hop symmetrically up or down, with equal rates $D$ in both directions.

In section IV, we complement our numerical approach by deriving a set of hydrodynamic equations for the dynamics of the local density and magnetisation fields. Interestingly, a simple mean-field theory wrongly predicts a continuous transition, failing to account for the phase-separated profiles. A refined mean-field model, taking into account the fluctuations of the density and magnetisation fields, reproduces qualitatively the phenomenology of the AIM. In section V, we use the hydrodynamic equations to compute at large densities the shape of the phase-separated profiles, the coexisting densities, the velocity of the liquid domain and account for the finite-size scalings observed in the microscopic model. Finally, we argue in section VI in favor of the robustness of our results by considering an off-lattice version of the model and different boundary conditions.

## II. DEFINITION OF THE MODEL

We consider $N$ particles moving on a 2D lattice of $L_x \times L_y$ sites with periodic boundary conditions. Each particle carries a spin $\pm 1$ and there are no excluded volume interactions between the particles: there can thus be an arbitrary number $n_i^{\pm}$ of particles with spins $\pm 1$ on each site $i \equiv (i_1, i_2)$. The local densities and magnetizations are then defined as $\rho_i = n_i^+ + n_i^-$ and $m_i = n_i^+ - n_i^-$. We consider a continuous-time Markov process in which particles can both flip their spins and hop to neighboring lattice sites at rates that depend on their spins. The hopping and flipping rates, detailed in the next subsections, are such that our model is endowed with self-propulsion and inter-particle alignment, hence consituting a flocking model with discrete symmetry.

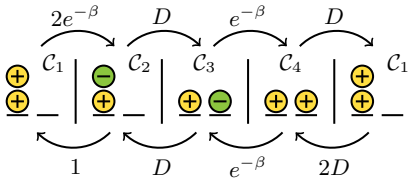


FIG. 2. A loop of four configurations involving 2 particles on 2 sites breaking Kolmogorov's criterion[27] showing that the system does not satisfy detailed balance even when $\varepsilon = 0$. The numbers associated to the arrows are the transition rates for $\varepsilon = 0$. The product of the transition rates along $\mathcal{C}_1 \to \mathcal{C}_2 \to \mathcal{C}_3 \to \mathcal{C}_4 \to \mathcal{C}_1$ (left to right) is $2D^2e^{-2\beta}$, whereas the reverse order (right to left) yields $2D^2e^{-\beta}$.

### A. Alignment: Fully connected Ising models

A particle with spin $s$ on site $i$ flips its spin at rate

$$W(s \to -s) = \gamma \exp\left(-s\beta \frac{m_i}{\rho_i}\right), \qquad (1)$$

where $\beta = 1/T$ plays the role of an inverse temperature. These rates satisfy detailed balance with respect to an equilibrium distribution $P \propto \exp[-\beta H]$ where $H$ is the sum over the $L_xL_y$ lattice sites of the Hamiltonians of fully connected Ising models:

$$H = -\sum_{\text{sites } i} \frac{1}{2\rho_i} \sum_{j=1}^{\rho_i} \sum_{k \neq j} S_j^i S_k^i = -\sum_{\text{sites } i} \left[\frac{m_i^2}{2\rho_i} - \frac{1}{2}\right] \qquad (2)$$

The first sum runs over the lattice site index $i = (i_1, i_2)$, the next two over the particles $j, k$ present on site $i$, and $S_j^i = \pm 1$ is the value of spin $j$. (The factor $1/2$ simply avoids double counting.) The rate $\gamma$ can always be absorbed in a change of time unit so that we take $\gamma = 1$, silently omitting it from now on.

This interaction is purely local: particles only align with other particles on the same site and, without particle hopping, the model amounts to $L^2$ independent fully connected Ising models. The factor $1/\rho_i$ in $W$ makes the Hamiltonian $H$ extensive with $N$ and keeps the interaction rates bounded: the rate $W(s \to -s)$ at which a particle of spin $s$ flips its spin varies between $\exp(-\beta)$ if all the other particles on the same site have spins $s$ to $\exp[\beta(1 - 2/\rho_i)]$ if they all have spins $-s$.

### B. Self-propulsion: Biased diffusion

Particles also undergo free diffusion on the lattice, with a left/right bias depending on the sign of their spins: a particle with spin $s$ hops with rate $D(1 + s\varepsilon)$ to its right, $D(1 - s\varepsilon)$ to its left, and $D$ in both the up and down directions. There is thus a mean drift, which plays the role of self-propulsion, with particles of spins $\pm 1$ moving along the horizontal axis with an average velocity $\pm 2D\varepsilon$.

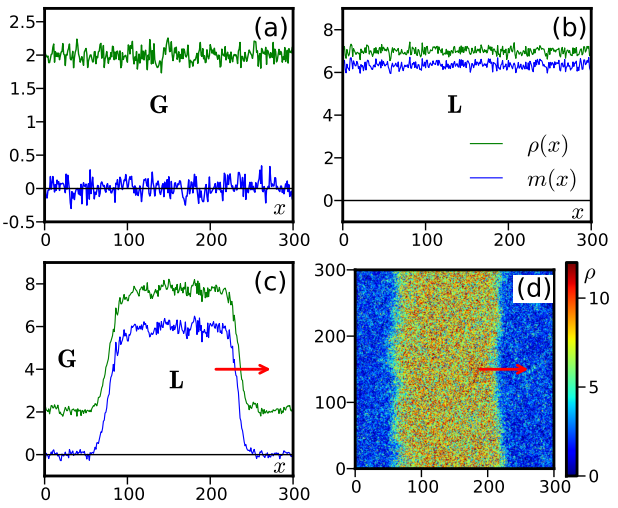


FIG. 3. Examples of density profiles (green line) and magnetization profiles (blue line) averaged along vertical direction for the three phases. (a) Disordered gas, $\beta = 1.4$, $\rho_0 = 2$. (b) Polar liquid, $\beta = 2$, $\rho_0 = 7$. (c) Liquid-gas coexistence, $\beta = 1.6$, $\rho_0 = 5$. (d) 2d snapshot corresponding to (c). (for all figures $D = 1$, $\varepsilon = 0.9$)

The model is designed to have the self-propulsion entering in a minimal and tunable way through the parameter $\varepsilon$. Importantly, the limit of vanishing self-propulsion $\varepsilon \to 0$ is well-defined because the spins still diffuse on the lattice. This dynamics should thus allow us to interpole continuously between 'totally self-propelled' ($\varepsilon = 1$), self-propelled ($\varepsilon \in ]0, 1[$), weakly self-propelled ($\varepsilon \sim 1/L$) and purely diffusive ($\varepsilon = 0$) particles.

This differs from the Vicsek model where the zero-velocity limit corresponds to immobile particles undergoing an equilibrium dynamics resembling that of the XY model, with a quenched disorder on the bonds (only particles closer than a fixed distance interact).

Let us note, however, that even when $\varepsilon = 0$ the model is not at equilibrium *i.e.* it does not satisfy detailed balance with respect to any distribution. This is easily shown using Kolmogorov's criterion [27]. In Fig. 2, we exhibit a loop of four configurations such that the products of the transition rates for visiting the loop in one order, $\mathcal{C}_1 \to \mathcal{C}_2 \to \mathcal{C}_3 \to \mathcal{C}_4 \to \mathcal{C}_1$, and the reverse order are different, whence a violation of detailed balance. To make the $\varepsilon = 0$ limit an equilibrium dynamics, one strategy could be to choose hopping rates satisfying detailed balance with respect to the Hamiltonian H defined in (2), replacing $D$ by $D\exp(-\beta\Delta H/2))$. The steady-state distribution would however be factorized and not very interesting. An alternative would be to further add to (2) nearest neighbours interactions but we have not followed this cumbersome path here. Actually, as we show in section III B, this microscopic irreversibility when $\varepsilon = 0$ is irrelevant at large scales and we recover in this limit a phase transition belonging to the Ising universality class.

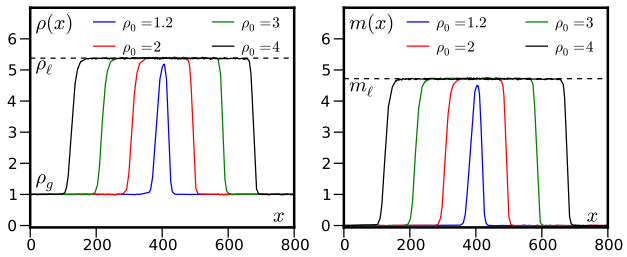


FIG. 4. Phase-separated density (left) and magnetization (right) profiles as the density increases. Parameters: $\beta = 2$, $D = 1$, $\varepsilon = 0.9$, system of size 800x100. The profiles have been averaged over time and along the $y$ axis.

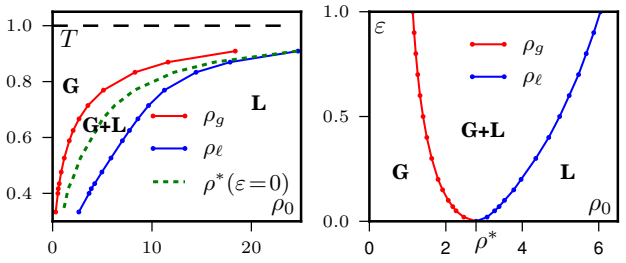


FIG. 5. Phase diagrams of the AIM. The red and blue lines delimit the region of existence of phase-separated profiles. **Left**: Parameter spaces ($T = 1/\beta$, $\rho_0$) for $D = 1$. Red and blue coexistence lines correspond to $\varepsilon = 0.9$ while the green dashed line indicates the critical points at $\varepsilon = 0$. **Right**: Parameter space ($\varepsilon$, $\rho_0$) for $D = 1$, $\beta = 1.9$. At $\varepsilon = 0$ we recover critical point in the Ising universality class.

### C. Simulations

To simulate the dynamics of the model, we used a random-sequential-update algorithm. We discretized the time in small time-steps $\Delta t$. A particle is then chosen at random; it flips its spin $s$ with probability $W(s \to -s)\Delta t$, hops upwards or downwards with probabilities $D\Delta t$, to its right or to its left neighboring sites with probabilities $D(1 \pm s\varepsilon)\Delta t$. Finally, it does nothing with probability $1 - [4D + W(s \to -s)]\Delta t$. Time is then incremented by $\Delta t/N$ and we iterate up to some final time. In practice we used $\Delta t = [4D + \exp(\beta)]^{-1}$ to minimize the probability that nothing happens while keeping all probabilities smaller than one.

Note that this algorithm does not allow a particle to be updated twice (on average) during $\Delta t$ and is thus an approximation of our continuous-time Markov process. We also used continuous-time simulations, associating clocks to each particle or each site and pulling updating times from the corresponding exponential laws. In practice we did not find any difference in the simulation results but the continuous time simulations were often slower so that we mostly used the random sequential update algorithm.

In most of this article we use simulation boxes with $L_x \times L_y$ lattice sites and periodic boundary conditions. In section VI A we discuss what happens for closed boundary conditions.

## III. A LIQUID-GAS PHASE TRANSITION

We explored the phase diagram using three control parameters: the temperature $T = \beta^{-1}$, the average density $\rho_0 = N/(L_x L_y)$, and the self-propulsion 'speed' $\varepsilon$. Doing so, we observed three different phases shown in Fig. 3. For $\varepsilon \neq 0$, at high temperatures and low densities, the particles fail to organize and we observe a homogeneous gas of particles with local magnetization $\langle m_i \rangle \approx 0$. On the contrary, for large densities and small temperatures, the particles move collectively either to the right or to the left, forming a polar liquid state with $\langle m_i \rangle = m_0 \neq 0$. For intermediate densities, when $\rho_0 \in [\rho_g(T, \epsilon), \rho_\ell(T, \epsilon)]$,

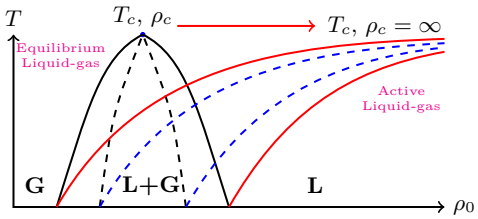


FIG. 6. Schematic picture of the differences between the phase diagrams of the passive and active liquid gas transition. In the active case, because the liquid and the gas have different symmetries, the critical point is sent to $\rho = \infty$, thus suppressing the supercritical region.

the system phase separates into a band of polar liquid traveling to the left or to the right through a disordered gaseous background.

The lines $\rho_g(T, \epsilon)$ and $\rho_\ell(T, \epsilon)$ both delimit the domain of existence of the phase-separated profiles and play the role of coexistence lines: As shown in Fig. 4, for all phase-separated profiles at fixed $T$, $\epsilon$, the densities in the gas and liquid part of the profiles are $\rho_g$ and $\rho_\ell$, respectively. Correspondingly, the magnetization are 0 and $m_\ell(T, \epsilon) \neq 0$. Thus, varying the density $\rho_0$ at constant temperature and propulsion speed solely changes the width of the liquid band. Consequently, in the phase coexistence region, the lever rule can be used to determine the liquid fraction $\Phi$ in the same way as for an equilibrium liquid-gas phase transition in the canonical ensemble:

$$\Phi = \frac{\rho_0 - \rho_g}{\rho_\ell - \rho_g} \tag{3}$$

As we shall see below, this analogy goes beyond the sole shape of the phase separated profiles and the phase-transition to collective motion of the active Ising model is best described as a liquid-gas phase transition rather than an order-disorder one.

### A. Temperature-density 'canonical' ensemble

The phase diagram in the $(T,\ \rho_0)$ parameter plane, computed for $\varepsilon = 0.9$, is shown in the left panel of Fig. 5. While the general structure of the phase diagram, with a gas phase, a liquid phase, and a coexistence region, is reminiscent of an equilibrium liquid-gas phase diagram, the shapes of the transition lines are unusual. This difference can be understood using a symmetry argument. Since the disordered gas and the polar liquid have different symmetries, the system cannot continuously transform from one homogeneous phase to the other without crossing a transition line. There is thus no super-critical region and the critical point is sent to $T_c = 1$ and $\rho_c = \infty$. (See Fig. 6 for a schematic picture.)

This symmetry argument should be rather general for flocking transitions separating a disordered state and a symmetry-broken state of collective motion. Indeed, in Vicsek-like models, where the role of the inverse temperature is played by the noise intensity, the phase diagrams are qualitatively similar to the one shown in Fig. 5. This is true both for the full phase diagram recently computed in [14] as well as for earlier results [13], for a slightly different kinetic model and its hydrodynamic theory [19], but also for an active nematic Vicsek-like model [28] and a hydrodynamic theory of self-propelled rods [29].

### B. Velocity-density ensemble

Conversely, one can change the strength of the self-propulsion $\varepsilon$ while keeping the temperature fixed. Again, one obtains a phase diagram with three regions. The difference with the canonical ensemble is that in this parameter plane, the two coexistence lines merge at $\varepsilon = 0$, where self-propulsion vanishes, yielding a critical point at a finite density $\rho^*(T)$ (See the right panel of Fig. 5). The curve $\rho^*(T)$ is reported in the left panel of Fig. 5 and satisfies $\rho^*(T) \in [\rho_g(T,\varepsilon), \rho_\ell(T,\varepsilon)]$. In section III F we show that this critical point belongs to the Ising universality class.

The shape of this phase diagram is identical to the one computed in [15] for a phenomenological hydrodynamic description of self-propelled particles with polar alignment. The comparison with other microscopic models in the literature is however hard to make since there seems to be very few studies in the $(\varepsilon, \rho_0)$ plane, probably because very few models admit a well-defined zero velocity limit.

### C. Nucleation vs spinodal decomposition

As for an equilibrium liquid-gas transition, the coexistence lines $\rho_g(T,\varepsilon)$ and $\rho_\ell(T,\varepsilon)$ are complemented by spinodal lines $\varphi_g(T,\varepsilon)$ and $\varphi_\ell(T,\varepsilon)$ that mark the limit of linear stability of the homogeneous gas and liquid phases,

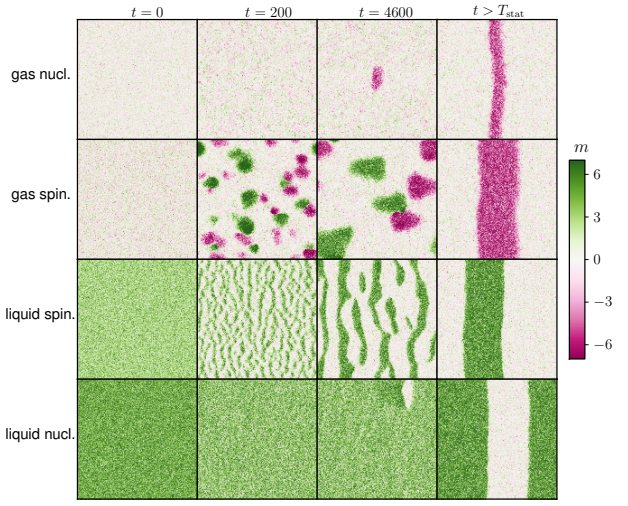


FIG. 7. Successive snapshots following quenches from homogeneous gas and liquid phases inside and outside the spinodal region. Parameters: $D = 1, \varepsilon = 0.9, \beta = 1.8$, system sizes 400x400 and 1000x1000 for the quenches from the gas and liquid phases. From top to bottom, $\rho_0 = 1.84$, 3, 3, 4.7. See Supplementary Movies in [49].

respectively. While $\rho_g$ and $\rho_\ell$ are easily measured in simulations, $\varphi_g$ and $\varphi_\ell$ are much harder to access numerically at non-zero temperature: When the system is in the coexistence region but outside the putative spinodal lines, the homogeneous phases are metastable and finite fluctuations make the system phase-separate. The closer to the spinodal line, the faster this nucleation occurs and it is then difficult to pinpoint precisely the transition from a 'fast' nucleation to a spinodal decomposition. Nevertheless, the differences between the coexistence and spinodal regions are clearly seen when, starting from a homogeneous phase, one quenches the system in the coexistence region but relatively far away from the spinodal lines.

Quenching outside the spinodal region, the homogeneous phases are metastable. The closer to the binodals, the longer it takes for a liquid (resp. gas) domain to be nucleated in the gas (resp. liquid) background. The convergence to the phase-separated steady-state then results from the coarsening of this domain.

Quenching inside the spinodal region, the different symmetries between gas and liquid result in different spinodal decomposition dynamics when starting from ordered and disordered phases. Starting from a disordered gas, the linear instability almost immediately results in the formation of an extensive number of small clusters of negative and positive spins. The coarsening then stems from the merging of these clusters, until a single, macroscopic domain remains. The late stage of the coarsening is thus dominated by the long-lived competition between a small number of right- and left-moving macroscopic clusters. Their shapes (see Fig. 8) are reminiscent of the counter-propagating arrays of bands reported in [30],

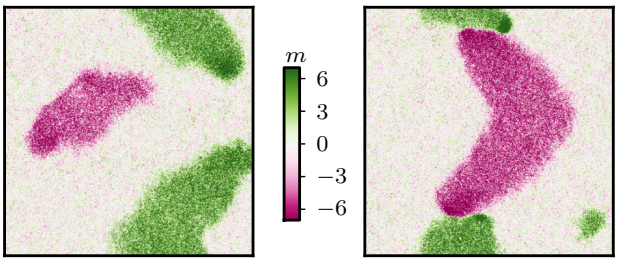


FIG. 8. Snashots in the late stage of coarsening taken from the same simulation as the first row of fig. 7 at time $t = 283000$ (left) and $t = 310000$ (right). Parameters: $D = 1, \varepsilon = 0.9, \beta = 1.8, \rho_0 = 3$, system sizes 400x400.

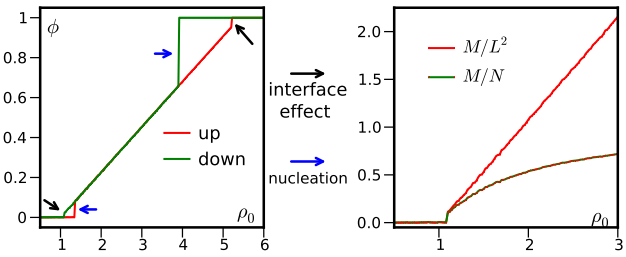


FIG. 9. **Left:** Evolution of the liquid fraction $\phi$ upon changing continuously $\rho_0$. Large jumps in $\Phi$ correspond to the nucleation of bands in meta-stable homogeneous profiles while small jumps are finite-size effects due to the finite width of the interfaces connecting the gas and liquid regions. The density is increased by $\delta\rho_0 = 0.02$ every $\Delta t = 2000$. $L_x \times L_y = 800 \times 100$, $\beta = 2$, $\varepsilon = 0.9$, $D = 1$. **Right** Evolution of the magnetisations per particles and per sites as the density is varied. The linear scaling typical of liquid-gas phase transition is seen using $m_L = M/L^2$.

where it was suggested, using deterministic simulations of the Boltzmann equation derived for kinetic flocking models, that such profiles could constitute a new phase of flocking models. In our simulations, we always observed a coarsening process leading to a single band, which seems to indicate that the apparent stability of these solutions in [30] could be due to the lack of fluctuation terms. It would nevertheless be interesting to make a more detailed study of the coarsening dynamics to see if these alternating bands could indeed form a stable phase (for instance at low temperatures, where the coarsening seems to become slower and slower).

Starting from the ordered phase, the linear instability results in many liquid domains which all move in the same direction. The coarsening then results from the collision of liquid bands that move in the same direction, but with slightly different speeds. See Fig. 7 and SI movies [49] for examples of these four possible dynamics.

### D. Hysteresis loops

Another similarity with a liquid-gas transition is the presence of hysteresis loops obtained by varying slowly the density at constant $\beta$ and $\varepsilon$ in finite-size systems. Such loops are shown in the left panel of Fig. 9, where the liquid fraction $\Phi$ is reported as the density is continuously ramped up and down. To measure $\Phi$ numerically, a first strategy, followed in [22], is to compute average density profiles at fixed $\rho_0$, as shown in the left panel of Fig. 4 and use an arbitrary density treshold between $\rho_g$ and $\rho_\ell$ to associate each site to the gas or liquid regions.

Since the interfaces between gas and liquids are not perfectly straight, this is slightly artefactual for finite-size systems. Here we decided to measure $\Phi$ numerically through:

$$\Phi_{\text{num.}} = \frac{1}{m_\ell L_x L_y} \sum_i m_i \tag{4}$$

where $m_\ell$ is the magnetization of the plateau in the liquid part of the profile. ($m_\ell$ is independent of $\rho_0$ as long as the system is phase-separated and corresponds to the magnetization of a uniform liquid phase at the coexistence density $\rho_\ell$.) The results are very similar to those obtained in [22] but first (4) is faster to measure and second it does not rely on an arbitrary density treshold.

Starting in the gas phase and increasing the density, the system remains disordered, with a liquid fraction $\phi = 0$, until a band of liquid is nucleated, at which point $\phi$ jumps to a finite value. Increasing again $\rho_0$, the liquid region widens until the two interfaces between gas and liquid almost touch and the liquid phase almost fills the system. At that point, the system jumps to a homogeneous liquid phase with $\phi = 1$.

Upon decreasing the density, a similar scenario occurs: A homogeneous liquid becomes metastable as the coexistence line is crossed. As the density keeps decreasing, the system thus remains in a liquid state with $\Phi = 1$ until a nucleation event brings it to a phase-separated profile. The liquid region then shrinks until its boundaries almost touch and a second discontinuity of $\Phi$ occurs as the system jumps into a homogeneous gas phase.

### E. Order parameter and finite-size scaling

The liquid-gas transition picture suggests different finite-size scaling and order parameter than those associated to magnetic phase transitions previously used to study flocking models. Most studies [13, 31, 32] indeed relied on the mean magnetization per particle

$$m_N = \frac{1}{N} \sum_i m_i \tag{5}$$

rather than the mean magnetization per unit area

$$m_L = \frac{1}{L_x L_y} \sum_i m_i = \rho_0 m_N \tag{6}$$

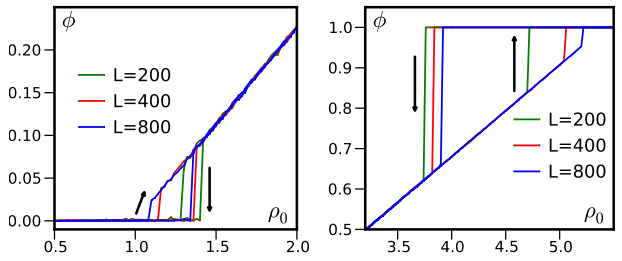


FIG. 10. Hysteresis loops for system sizes 200x100, 400x100 and 800x100. For each system, the density is increased by $\delta\rho_0 = 0.02$ every $\Delta t = 2000$. $T = 0.5$, $\varepsilon = 0.9$.

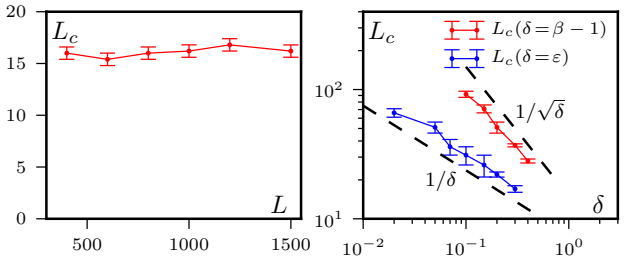


FIG. 11. **Left:** Divergence of the critical nucleus $L_c$ when approaching the critical points $\beta \to 1$ and $\varepsilon \to 0$. To measure $L_c$, we started in the phase-separated state and decreased continuously the density (the errorbars correspond to the density step used) to record the density $\rho_m$ at which the liquid band disappears. $L_c$ is then defined by $L\rho_m = L\rho_g + L_c(\rho_\ell - \rho_g)$, so as the length of a band at density $\rho_\ell$ that can be made with the excess density $\rho_m - \rho_g$. **Right:** Variation of the critical nucleus iwht $L$ showing that, within numerical errors, it does not depend on system size. Parameters: $D = 1$, $\varepsilon = 0.9$, $\beta = 1.9$

For models like the Vicsek model, the former is nothing but the polarisation $\mathbf{m}_N = \mathbf{P}$ while the latter is related to the total momentum $\mathbf{m}_L = \rho_0 \mathbf{P}/v$. In the phase-separated region, both can be related to the liquid fraction $\Phi$ through Eq. (3)

$$m_N = \frac{1}{N}\Phi L_x L_y m_\ell = m_\ell \frac{1-\rho_g/\rho_0}{\rho_\ell - \rho_g} \tag{7}$$

$$m_L = \Phi m_\ell = m_\ell \frac{\rho_0 - \rho_g}{\rho_\ell - \rho_g} \tag{8}$$

The simple linear scaling of $m_L$ with $\rho_0 - \rho_g$ is replaced by a non-linear dependence of $m_N$ with $\rho_0$, as shown in Fig. 9, right panel. An apparently inoccent change of the normalization used to make the magnetisation $M = \sum_i m_i$ intensive can thus turn the simple affine scaling of $m_L$ with $\rho_0$, typical of a liquid-gas transition, into the non-linear dependence of $m_N$ that could make one mistake the transition for a critical one.

Let us now go back to the hysteresis loops and discuss their finite size scaling. As shown in figure 10, the discontinuities of the liquid fraction get closer and closer to the binodals $\rho_g$ and $\rho_\ell$ as the system size increases, leading to vanishingly small hysteresis loops in the thermodynamic limit.

Consider first the transition from gas to phase-separated profiles. The liquid fraction exhibits two different discontinuities when the density is decreased or increased, due to two different effects. As the density is decreased, phase-separated profiles cannot be maintained arbitrarily close to $\rho_g$. There is indeed a critical nucleus, which roughly amounts to two connected domain walls, as can be seen in Fig. 4 for $\rho_0 = 1.2$. As shown on Fig. 11 (left), this critical nucleus $L_c$ is independant of the system size. If the excess mass $L_x L_y(\rho_0 - \rho_g)$ is smaller than a critical value $\varphi_c L_y$, this critical nucleus cannot be accomodated in the system, which thus falls into the gas phase. As the system size increases, the minimal density to observe phase-separated profiles $\rho_0 = \rho_g + \varphi_c/(L_x)$ thus converges to $\rho_g$ as $L_x$ increases and phase-separated profiles are seen closer and closer to the binodal. The second discontinuity, met upon increasing the density, corresponds to the nucleation of a liquid band of width $L_b$ in a gaseous background. Since $L_b$ can be anything between $L_c$ and $L_x$, increasing the system size at fixed density should decrease the mean time until nucleation of such bands, thanks to an entropic contribution due to the number of places where the bands can be nucleated. As shown in 10, this is indeed the case and the transition to phase-separated profiles thus also happens closer and closer to the binodal $\rho_g$.

The same line of reasoning can be used to understand the scaling of the second hysteresis window, close to $\rho_\ell$. Thus, in the thermodynamic limit, all discontinuities disappear and the liquid fraction varies continuously from $\phi = 0$ at $\rho_0 = \rho_g$ to $\phi = 1$ at $\rho_0 = \rho_\ell$, as for an equilibrium liquid-gas transition in the canonical ensemble. Note that the width of the critical nucleus diverges as one gets closer and closer to the critical points ($\varepsilon = 0$ or $\beta = 1$), as shown in the right panel of Fig. 11. This could explain why some studies of the Vicsek model in the small velocity region claim to find a critical transition: as one gets closer and closer to the zero speed limit, the system-size above which one can correctly observe the discontinuous nature of the transition diverges[33].

### F. The $\epsilon = 0$ critical point

While the $\beta = 1$, $\rho_c = \infty$, critical point is out of reach numerically, the study of the $\varepsilon = 0$ critical point is accessible. At $\varepsilon = 0$, there is no self-propulsion and the phase transition is of a completely different nature from the liquid-gas transition described above. As we show below, despite the dynamics being non-equilibrium, it turns out to be a standard critical phase transition belonging to the Ising universality class.

We studied this critical point using a finite-size scaling standard for magnetic systems at criticality [34]. We thus consider the magnetization $m_N \in [0, 1]$. In equilibrium,

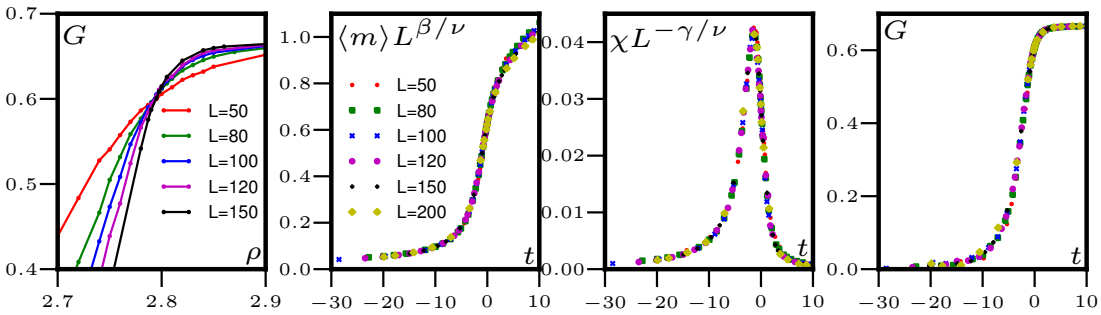


FIG. 12. Left: Binder cumulant $G(\rho)$ from which we find the critical density $\rho^* = 2.798 \pm 0.002$. Other three figures: data collapse on the universal scaling functions $F_m$, $F_\chi$ and $F_G$ (defined in the text) when the data is rescaled with the 2d Ising exponent values $\beta = 1/8$, $\gamma = 7/4$ and $\nu = 1$. $t = L^{1/\nu}(\rho - \rho^*)/\rho^*$. Parameters: $D = 1$, $\varepsilon = 0.9$, $\beta = 1.9$.

around ferromagnetic critical points, the order parameter, susceptibility and Binder cumulant $G = 1 - \frac{\langle m^4 \rangle}{\langle m^2 \rangle^2}$ are known [34] to obey the finite-size scaling relations

$$\langle m \rangle = L^{-\beta/\nu} F_m(tL^{1/\nu}) \tag{9}$$

$$\chi = L^2(\langle m^2 \rangle - \langle m \rangle^2) = L^{\gamma/\nu} F_\chi(tL^{1/\nu}) \tag{10}$$

$$G = F_G(tL^{1/\nu}) \tag{11}$$

where $t = L^{1/\nu}(\rho - \rho^*)/\rho^*$ is the rescaled distance to the critical density $\rho^*$. $F_m$, $F_\chi$ and $F_G$ are universal scaling functions and $\beta$, $\gamma$ and $\nu$ the usual critical exponents.

We used the fact that $G(t = 0)$ is independent of $L$ to find the critical density, which is thus the density where all the curves $G(t)$ for different system sizes intersect (Fig. 12, left). We found that the value at the crossing point is the same universal value $G(t = 0) \simeq 0.61$ as in the 2d Ising model [35]. A very neat data collapse is further observed for the critical exponents of the 2d Ising model $\beta = 1/8$, $\gamma = 7/4$ and $\nu = 1$ (see Fig. 12). We thus conclude that the critical point at $\varepsilon = 0$ is indeed in the Ising universality class.

Note that a direct evalutation of the critical exponents is much harder than for the equilibrium Ising model. Here, the dynamics is fixed so one cannot use alternative dynamics like cluster algorithms to circumvent the problem of critical slowing down.

### G. Number fluctuations

In most flocking models the homogeneous ordered phase exhibits giant density fluctuations [13, 15, 28, 36, 37]. These are quantified by measuring number fluctuations, *i.e* by counting the number of particles $n(\ell)$ in boxes of increasing sizes $\ell < L$ and computing its root mean square $\Delta n(\ell)$. When the correlation length $\mathcal{L}$ is finite, a box of size $\ell \gg \mathcal{L}$ can be divided in $(\ell/\mathcal{L})^2$ independant boxes. The total number of particles in the large box in then the sum of independent identically distributed random variables; The central limit theorem applies and the probability distribution of $n(\ell)$ tends to a Gaussian. This yields the "normal" scaling $\Delta n \sim n^{1/2}$. On the contrary, one finds in the Vicsek model the anomalous scaling $\Delta n \sim n^{0.8}$ [13].

In the Active Ising model the number fluctuations are found to be normal in the liquid and gas phases, where $\Delta n \sim n^{1/2}$, and trivially 'giant' in the phase-separated regime where $\Delta n \sim n$ (see Fig. 13).

Note that the scaling $\Delta n \sim n$ is a simple consequence of phase-separation and one should thus distinguish this scaling from the 'anomalous' scaling of the Vicsek model, which is a signature of long-range correlations. Let us consider a system with liquid fraction $\phi$ that is large enough that we can find a range of box sizes $\ell$ such that: 1) $\ell \ll L$ so that we can neglect the contribution of the interfaces (a box is either in the liquid or the gas phase); 2) $\ell$ is large enough that $n(\ell)$ takes only two possible values and we can neglect the fluctuations around these two values. With these assumptions,

$$P(n) \simeq \phi\delta(n - \rho_\ell \ell^2) + (1 - \phi)\delta(n - \rho_g \ell^2) \tag{12}$$

where $\rho_\ell$ and $\rho_g$ are the densities in the gas and liquid domains. Then one finds

$$\langle n \rangle = (\phi\rho_\ell + (1 - \phi)\rho_g)\ell^2 = \rho_0 \ell^2 \tag{13}$$

$$\Delta n = \sqrt{\langle n^2 \rangle - \langle n \rangle^2} = \sqrt{\phi(1 - \phi)} \frac{\rho_\ell - \rho_g}{\rho_0} \langle n \rangle \tag{14}$$

which is a simple hand-waving explanation of the scaling observed in the coexistence region of the active Ising model, as well as in other phase-separating systems [38, 39].

## IV. HYDRODYNAMIC DESCRIPTION OF THE ACTIVE ISING MODEL

In this section we derive and analyze a continuous description of the AIM based on two coupled partial differential equations accounting for the spatio-temporal evolutions of the density and magnetization fields.

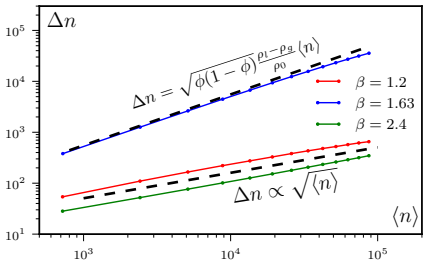


FIG. 13. Number fluctuations in the three different phases: gas (red), liquid (green) and at coexistence (blue). $n$ is the number of particles in boxes of size $\ell$ and $\Delta n$ its root mean square. $D = 1$, $\varepsilon = 0.9$, $L = 400$, $\rho_0 = 5$

We first show in section IV A that a standard mean-field treatment wrongly predicts a continuous transition between the disordered gas and the ordered liquid. In section IV B we show that local fluctuations, which are neglected in the mean-field approximations, are necessary to correctly account for the physics of the system when the density is finite and $\varepsilon \neq 0$. We show in particular that as soon as the density is finite, fluctuations make the transition first order. We then use our hydrodynamic description in section V to study the inhomogeneous profiles.

### A. Mean-field equations

The simplest way to account analytically for a non-equilibrium lattice gas is probably to derive mean-field equations. These are known to be quantitatively wrong, but they often capture phase diagrams correctly [40, 41].

Their derivations follow a standard procedure which can be applied to the AIM and which, for simplicity, we first present in 1D. Starting from the master equation, one first derives the time-evolution of the mean number of $\pm 1$ spins on site $i$

$$\langle \dot{n}_i^{\pm}\rangle = D(1\pm\varepsilon)\langle n_{i-1}^{\pm}\rangle + D(1\mp\varepsilon)\langle n_{i+1}^{\pm}\rangle - 2D\langle n_i^{\pm}\rangle \pm \langle n_i^{-}\exp(\beta\frac{m_i}{\rho_i})\rangle \mp \langle n_i^{+}\exp(-\beta\frac{m_i}{\rho_i})\rangle \quad (15)$$

which can then be rewritten for the density and magnetisation

$$\langle \dot{\rho}_i\rangle = D(\langle\rho_{i+1}\rangle + \langle\rho_{i-1}\rangle - 2\langle\rho_i\rangle) - D\varepsilon(\langle m_{i+1}\rangle - \langle m_{i-1}\rangle) \quad (16)$$

$$\langle \dot{m}_i\rangle = D(\langle m_{i+1}\rangle + \langle m_{i-1}\rangle - 2\langle m_i\rangle) - D\varepsilon(\langle\rho_{i+1}\rangle - \langle\rho_{i-1}\rangle) + 2\langle\rho_i\sinh(\beta\frac{m_i}{\rho_i})\rangle - 2\langle m_i\cosh(\beta\frac{m_i}{\rho_i})\rangle \quad (17)$$

One can then take a continuum limit using the rescaled variable $\tilde{x} = i/L \in [0,1]$, $\tilde{D} = D/L^2$, $\tilde{v} = 2D\varepsilon/L$ and use the Taylor expansion $\rho_{i\pm1} \equiv \rho(x) \pm L^{-1}\partial_x\rho(x) + L^{-2}\partial_{xx}\rho(x)/2$. We then obtain equations for the continuum fields $\rho(x)$, $m(x)$, which are assumed to smoothly interpolate the discrete occupancies $\rho_i$, $m_i$:

$$\partial_t\langle\rho\rangle = \tilde{D}\partial_{\tilde{x}\tilde{x}}\langle\rho\rangle - \tilde{v}\partial_{\tilde{x}}\langle m\rangle \quad (18)$$

$$\partial_t\langle m\rangle = \tilde{D}\partial_{\tilde{x}\tilde{x}}\langle m\rangle - \tilde{v}\partial_{\tilde{x}}\langle\rho\rangle + \left\langle 2\rho\sinh\frac{\beta m}{\rho} - 2m\cosh\frac{\beta m}{\rho}\right\rangle \quad (19)$$

In higher dimension, the sole difference is that the diffusive terms become $\tilde{D}\Delta\langle\rho\rangle$ and $\tilde{D}\Delta\langle m\rangle$ whereas the $\tilde{v}$ terms still involve solely $\partial_{\tilde{x}}$ since the hopping is biased only horizontally.

In practice, to compare microscopic simulations and hydrodynamic theories it is often easier *not* to rescale space and use a continuous variable $x = L\tilde{x} \in [0, L]$ (and hence $D = \tilde{D}L^2$ and $v = L\tilde{v} = 2D\varepsilon$). Macroscopic and microscopic transport parameters are then expressed in the same units and equations (18) and (19) are then valid, without the tilde variables. This is what we use in the following.

Equations (18) and (19) are exact; they couple the first moments $\langle\rho\rangle$ and $\langle m\rangle$ to higher moments through the averages of the hyperbolic sine and cosine functions. Following the standard procedure established for equilibrium ferromagnetic models, we then make two approximations. First, we take a mean-field approximation by replacing $\langle f(\rho, m)\rangle$ by $f(\langle\rho\rangle, \langle m\rangle)$, for any function $f$. (We then drop the $\langle\ldots\rangle$ notation for clarity.) This amounts to neglecting both the correlations between density and magnetisation and their fluctuations. Second, we expand the hyperbolic functions in power series, up to $m^2/\rho^2$. This further restricts our description to the case where $m \ll \rho$. We then arrive at the mean-field equations

$$\dot{\rho} = D\Delta\rho - v\partial_x m \quad (20)$$

$$\dot{m} = D\Delta m - v\partial_x\rho + 2m(\beta-1) - \alpha\frac{m^3}{\rho^2} \quad (21)$$

where $\alpha = \beta^2(1-\beta/3)$. (For $\beta > 3$, one should expand to higher order to obtain a stabilizing term.)

Let us consider the various terms appearing in the mean-field equations. The first terms on the r.h.s of (20) and (21) are diffusion terms arising from the stochastic particle hopping. Let us stress that these terms do *not* depend on the bias $\varepsilon$ and are thus present even in the totally asymmetric case $\varepsilon = 1$; they do not rely on the possibility for $+1$ and $-1$ particles to hop backwards and forwards, respectively. The second terms, proportional to $v$, are due to the bias. Their physical origin is explained in Fig. 14 where we show how positive gradients in $m$ or $\rho$ yield negative contributions to $\dot{\rho}$ or $\dot{m}$, respectively. Finally, the last two terms in (21) stem from the ferromagnetic interaction and, apart from the $\rho^2$ dependence of the last term, are typical of $\phi^4$ Landau mean-field theory. Note that the alignment terms are the only non-linear ones and thus the only terms for which the mean-field approximation is actually an approximation.

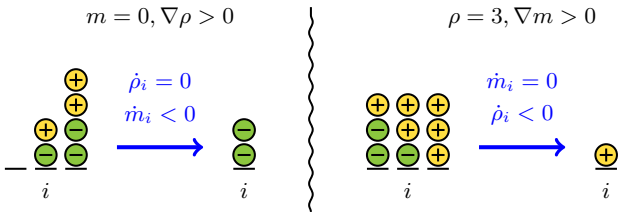


FIG. 14. Schematic account for the role of density and magnetisation gradients in the mean-field equations. **Left**: Initially, $m = 0$ and $\nabla\rho > 0$ around site $i$. Once plus particles jump to the right and minus particles to the left, the density in site $i$ is unchanged but $m_i$ has decreased. **Right**: Initially, $\rho$ is constant and $\nabla m < 0$ around site $i$. Once particles have jumped, the magnetisation of site $i$ is unchanged but the density has decreased.

The mean-field equations always accept the trivial homogeneous solution

$$\rho(x) = \rho_0, \qquad m(x) = 0\,, \tag{22}$$

which is linearly stable for $\beta < 1$. As soon as $\beta > 1$, two ordered homogeneous solutions appear,

$$\rho = \rho_0, \qquad m = \pm\rho_0\sqrt{\frac{2(\beta-1)}{\alpha}}\,, \tag{23}$$

which are linearly stable (see the left panel of Fig. 15). Therefore, at the mean-field level, a linearly stable homogeneous solution exists for all ($\beta$, $\rho_0$). Furthermore, integrating numerically Eqs. (20) and (21) starting from different initial conditions [47], the system always relaxes to a homogeneous solution and inhomogeneous profiles are never observed. Hence, the mean-field equations predict a continuous transition between homogeneous disordered and ordered profiles at $\beta = 1$, just as for the Weiss ferromagnet [42]. The phase diagram is simply split between a high-temperature disordered homogeneous phase, for $T > 1$, and a low temperature ordered homogeneous phase, for $T < 1$. This mean-field approach thus completely misses the phenomenology of the microscopic model; It cannot explain the existence of phase-separated profiles and yield a phase diagram corresponding to a single (continuous) transition line at $T = 1$, in contradiction to the crescent shape observed in the microscopic model (see Fig. 5).

### B. Going beyond the mean-field approximation

Previous coarse-graining approaches of flocking models [18, 19, 43, 44] often relied on neglecting correlations by factorizing probability distributions. For example, in the Boltzmann-Ginzburg-Landau approach of Bertin *et al.* [19] the two-particle probability distribution is replaced by the product of one-particle distributions. In our case, to derive the mean-field equations (20) and (21) we made an even cruder approximation.

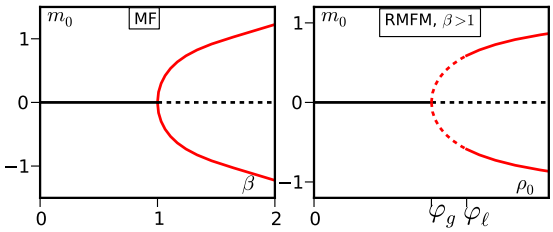


FIG. 15. Linear stability of homogeneous profiles in the naive (left) and refined (right) mean-field models. Plain (resp. dashed) lines denote stable (resp. unstable) solutions. In the RMFM, for $\beta < 1$, only the homogeneous profile exists and is stable at all densities.

When computing, for instance, the first non-linear term $\langle m^3/\rho^2\rangle$, neglecting correlations between $m$ and $\rho$ leads to

$$\langle m^3/\rho^2\rangle = \langle m^3\rangle \left\langle \frac{1}{\rho^2} \right\rangle \tag{24}$$

We went one step further, completely discarding fluctuations and replaced $\langle 1/\rho^2\rangle$, $\langle m^3\rangle$ by $1/\langle\rho\rangle^2$, $\langle m\rangle^3$. As we show below, these fluctuations are crucial to account qualitatively for the physics of the AIM.

The dynamical equations (18) and (19) on the first moments predict how $\langle\rho(x,t)\rangle$ and $\langle m(x,t)\rangle$ evolve in time, given an initial distribution

$$\mathcal{P}[\rho, m] = \delta(\rho(x) - \rho_0)\delta(m(x) - m_0). \tag{25}$$

The mean-field approximation then amounts to compute the averages of hyperbolic functions in (19) by assuming that, as time goes on, $\mathcal{P}$ remains a product of Dirac functions:

$$\begin{aligned}\mathcal{P}[\rho, m; x, t \,|\, \rho_0, m_0] = \delta(\rho(x,t) - \bar{\rho}(x,t)) \\ \times\, \delta(m(x,t) - \bar{m}(x,t))\end{aligned} \tag{26}$$

where $\bar{\rho}(x,t)$ and $\bar{m}(x,t)$ are solutions of the mean-field equations (20) and (21). In practice this means that repeatedly simulating the microscopic model starting from an initial distribution (25) always yields the exact same values $\rho(x,t) = \bar{\rho}(x,t)$ and $m(x,t) = \bar{m}(x,t)$. A better description should allow both $\rho$ and $m$ to fluctuate around their mean values as well as account for their correlations.

We can thus improve our approximation by replacing the dirac functions in (26) by Gaussians of variance $\sigma^2_\rho(x,t)$ and $\sigma^2_m(x,t)$. This still neglects correlations between $\rho$ and $m$ but allows for (small) fluctuations around their mean. Note that the only approximation made in the derivation of the mean-field equations occured at the level of the alignment terms. Since each site of the AIM is a fully connected Ising model, it is reasonnable to assume that in the large density limit, mean-field should be correct. We thus assume that our corrections to mean-field should be small in the high density regions, where it

is reasonnable to assume that the variance of $\rho(x,t)$ and $m(x,t)$ are proportional to $\bar{\rho}$: $\sigma_\rho^2 = \alpha_\rho \bar{\rho}$ and $\sigma_m^2 = \alpha_m \bar{\rho}$ where $\alpha_\rho$ and $\alpha_m$ are functions of $\beta$ and $v$ only.

The probability to observe given values of $\rho(x,t)$ and $m(x,t)$ is then assumed to be

$$\mathcal{P}[\rho, m; x, t \,|\, \rho_0, m_0] = \mathcal{N}(\rho - \bar{\rho}, \alpha_\rho \bar{\rho}) \mathcal{N}(m - \bar{m}, \alpha_m \bar{\rho}) \tag{27}$$

where $\mathcal{N}(x, \sigma^2) = e^{-x^2/\sigma^2}/\sqrt{2\pi\sigma^2}$ is the normal distribution.

Under these assumptions, the alignment term in (19) can still be computed analytically; We show in appendix A that, at leading order in a $\bar{m}/\bar{\rho}$ expansion, the correction to mean-field reads

$$\left\langle 2\rho \sinh \frac{\beta m}{\rho} - 2m \cosh \frac{\beta m}{\rho} \right\rangle \approx 2(\beta - 1 - \frac{r}{\bar{\rho}})\bar{m} - \alpha \frac{\bar{m}^3}{\bar{\rho}^2} \tag{28}$$

where $r = 3\alpha\alpha_m/2$ is a positive function of $\beta$. Intuitively, the fluctuations "renormalize" the transition temperature

$$\beta_t(\rho) = 1 + \frac{r}{\rho} = \beta_t^{MF} + \frac{r}{\rho} \tag{29}$$

In principle, one could expand $\beta_t$ to higher order to obtain a better and better approximation. The correction (29) however suffices to account qualitatively for the most salient features of the microscopic model and we will thus stop our expansion at this order. Furthermore, extending (28) to higher orders does not suffice to provide quantitative agreement between microscopic simulations of the AIM and the "corrected" mean-field equations, probably because we still neglect correlations between $\rho$ and $m$. More details are provided in appendix A for the interested reader.

### C. Refined Mean-Field Model

The correction to mean-field derived in the previous section can thus be seen as a finite-density correction to the transition temperature $\beta_t$, which converges to its mean-field value $\beta_t^{MF} = 1$ as $\rho \to \infty$. As was already recognized in previous studies [15, 19, 29, 43], the density-dependence of $\beta_t$ is the key ingredient to describe phase separation at the level of hydrodynamic equations. With this correction, we obtain a refined mean-field model (RMFM)

$$\dot{\rho} = D\Delta\rho - v\partial_x m \tag{30}$$

$$\dot{m} = D\Delta m - v\partial_x \rho + 2(\beta - 1 - \frac{r}{\rho})m - \alpha \frac{m^3}{\rho^2} \tag{31}$$

which we now study.

The linear stability analysis of homogeneous solutions strongly differs from the mean-field case. For $\beta > 1$ the disordered profile is stable for $\rho_0 \in [0, \varphi_g(\beta)]$ where

$$\varphi_g(\beta) = r/(\beta - 1) \tag{32}$$

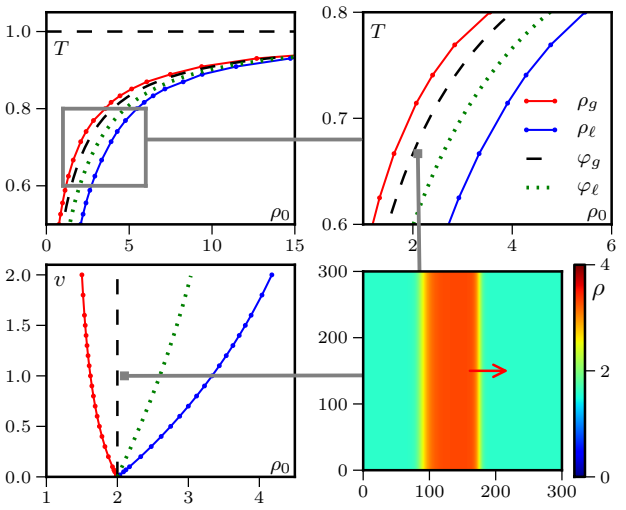


FIG. 16. Phase diagrams in the RMFM. The lines $\varphi_g$ and $\varphi_\ell$ are the spinodal lines denoting the limit of linear stability of homogeneous profiles. The lines $\rho_g$ and $\rho_\ell$ are coexistence lines that limit the domain of existence of phase-separated profiles. **Top row**: temperature/density ensemble. The right plot is a zoom of the region delimited by the grey rectangle. $D = r = v = 1$. **Bottom left**: velocity/density ensemble. $D = r = 1$, $\beta = 1.5$. **Bottom right**: 2d snapshot of the density field in the phase coexistence region. Its position in the phase diagrams is indicated by the grey squares. $D = r = v = 1$, $\beta = 1.5$ and $\rho_0 = 2.1$.

The homogeneous ordered solutions

$$\rho(x) = \rho_0, \quad m(x) = m_0 \equiv \pm\rho_0 \sqrt{2\frac{\beta - 1}{\alpha} - 2\frac{r}{\rho_0 \alpha}} \tag{33}$$

exist for all $\rho_0 > \varphi_g$, but are only stable for $\rho_0 \geq \varphi_\ell > \varphi_g$ (see Fig. 15). The explicit expression of $\varphi_g$ can be found using a standard linear stability analysis, detailed in Appendix B:

$$\varphi_\ell = \varphi_g \frac{v\sqrt{\alpha\,(v^2\kappa + 8D(\beta-1)^2)} + v^2\kappa + 8D\alpha(\beta-1)}{2v^2\kappa + 8D\alpha(\beta-1)}, \tag{34}$$

where $\kappa = 2 + \alpha - 2\beta$.

Close to the critical point at $\beta = 1$,

$$\varphi_\ell = \varphi_g + \frac{r}{2\alpha} + \mathcal{O}(\beta - 1) \tag{35}$$

so that $\varphi_\ell$ and $\varphi_g$ both diverge, while their difference remains constant. Close to the $v = 0$ critical point, we obtain

$$\varphi_\ell = \varphi_g + \frac{rv}{\sqrt{8D\alpha}(\beta - 1)} + \mathcal{O}(v^2) \tag{36}$$

so that $\varphi_\ell \to \varphi_g$ when $v \to 0$.

The homogeneous solutions are linearly unstable in the density range $[\varphi_g, \varphi_\ell]$. Simulating the RMFM [47] for

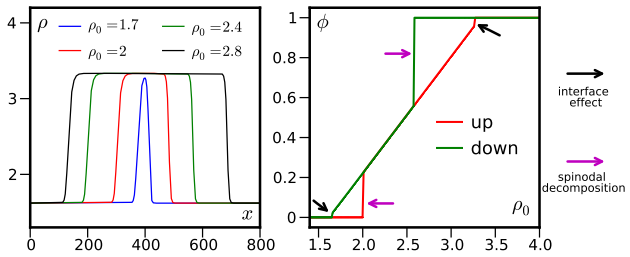


FIG. 17. Hysteresis loops in the RMFM. **Left**: Density profiles along the loop as $\rho_0$ is varied. **Right**: Evolution of the liquid fraction $\phi$ upon changing continuously $\rho_0$. Parameters: $\beta = 1.5$, $D = v = r = 1$, $L = 800$.

such densities yield phase-separated profiles similar to those seen in the AIM, with macroscopic liquid bands travelling in a disordered gas background (see bottom-right panel of fig. 16). The densities in the gas and liquid parts of the profiles remain constant as $\rho_0$ is varied; they thus give access to the coexistence lines $\rho_g$ and $\rho_\ell$.

The phase diagrams of the RMFM in the temperature/density and velocity/density ensembles shown in Fig. 16 are qualitatively similar to those of the AIM, with an asymptote at $T = 1$ when $\rho_0 \to \infty$ in the $(T,\, \rho_0)$ plane, and a critical point at $v = 0$ in the $(v,\, \rho_0)$ plane. As before, the coexistence lines $\rho_g$ and $\rho_\ell$ delimit the domain of existence of phase-separated solutions; they can now be complemented by the spinodals $\varphi_g$ and $\varphi_\ell$ which mark the loss of linear stability of homogeneous disordered and order phases, respectively.

The hysteresis loops observed in the RMFM (see Fig. 17) are similar to those found in the microscopic model (see Fig. 9 and 4). Starting at low density in the gaseous phase and increasing density the system stays in the gas phase until it becomes unstable at $\rho_0 = \varphi_g$, where it phase separates. Increasing again the density, the liquid fraction increases linearly until the liquid almost fills the system. As in the AIM, the finite widths of the interfaces set a minimum and a maximum size for a domain, hence preventing liquid bands from completely filling the system. This results in a discontinuous jump of the liquid fraction close to the binodals, whose height vanishes as the system size diverges (see Fig. 17, right panel). The main difference with the hysteresis loops observed for the AIM is that, given the absence of noise in the RMFM, there is no nucleation and the system phase separates only when the spinodal densities are reached.

### D. Control parameters

To determine how many independent control parameters are needed to describe the behavior of the RMFM, we recast Eqs. (30) and (31) in dimensionless form. To do so, we first have to introduce back the rate $\gamma$ which appeared in the definition of the flipping rates (1) and that we have taken equal to one until now. Introducing the dimensionless variables and constants

$$t = \hat{t}/\gamma,\; x = \sqrt{\frac{D}{\gamma}}\hat{x},\; \rho = r\hat{\rho},\; m = r\hat{m},\; v^2 = \gamma D \hat{v}^2 \quad (37)$$

the refined mean-field equations become

$$\dot{\hat{\rho}} = \hat{\Delta}\hat{\rho} - \hat{v}\partial_{\hat{x}}\hat{m} \quad (38)$$

$$\dot{\hat{m}} = \hat{\Delta}\hat{m} - \hat{v}\partial_{\hat{x}}\hat{\rho} + \left[2(\beta - 1 - \frac{1}{\rho})m - \alpha\frac{m^3}{\rho^2}\right] \quad (39)$$

Since $\alpha$ is a function of $\beta$, there are only two external dimensionless control parameters: $\hat{v}$ is a Peclet number comparing the advection speed $v$ and the diffusivity $D$ at the length scale $v/\gamma$ travelled by a particle between two spin flips; $\beta$ which controls the ordering of the system [48] The average density, which sets an external constraint on the system, constitutes a third independent parameter. Our phase diagrams shown in Fig. 16 thus sample all the relevant parameters of the RMFM.

## V. INHOMOGENEOUS BAND PROFILES

In the previous section we have shown how one can build a refined mean-field model by taking into account the local fluctuations of magnetisations and densities. Numerical simulations of the RMFM exhibit a phenomenology akin to that of the microscopic AIM, confirming the liquid-gas picture of the phase transition. We now focus on the inhomogeneous profiles and show analytically that the RMFM accounts for their shapes and speeds when $\beta \to 1$. Furthermore, the RMFM also correctly predicts the scaling of the width of the critical bands in the vicinity of the critical points $\beta = 1$ and $v = 0$.

### A. Propagative solutions

Let us reduce Eqs. (30) and (31) to a single ordinary differential equation. To do so, we first introduce a new coordinate $z = x - ct$ comoving with the liquid band at an unknown speed $c$. In this comoving frame, the stationnary solutions of the RMFM satisfy

$$D\rho'' + c\rho' - vm' = 0 \quad (40)$$

$$Dm'' + cm' - v\rho' + 2(\beta - 1 - \frac{r}{\rho})m - \alpha\frac{m^3}{\rho^2} = 0 \quad (41)$$

The RMFM is a finite-density correction to the $\rho = \infty$ mean-field limit and should thus work best for large densities. As we can see on the phase diagram shown in Fig 5, the densities $\rho_\ell$ and $\rho_g$ diverge as $\beta \to 1$, as do $\varphi_g$ and $\varphi_\ell$ (see Eqs. (34) and (35)). Furthermore, one can check that $\rho_\ell - \rho_g$ remains finite in this limit, as does $m_\ell$ (see Fig. 18). Close to $\beta = 1$, we can thus

expand Eq. (41) in power of $\epsilon = m/\varphi_g \sim \delta\rho/\varphi_g$, where $\delta\rho \equiv (\rho - \varphi_g)$, to get

$$0 = Dm'' + cm' - v\delta\rho' + \frac{2rm\delta\rho}{\varphi_g^2} - \alpha\frac{m^3}{\varphi_g^2} \tag{42}$$

Besides, Eq. (40) can be solved iteratively to obtain $\rho(z)$ in terms of $m(z)$ and its derivatives

$$\rho(z) = \rho_g + \frac{v}{c}m(z) + \frac{v}{c}\sum_{k=1}^{\infty}\Big(-\frac{D}{c}\Big)^k\frac{d^k m(z)}{dz^k} \tag{43}$$

where $\rho_g$ is an integration constant that equals the density in the gas phase at coexistence, since $\rho(z) = \rho_g$ where $m = 0$. Again, the RMFM should work best close to the critical points, where the width of band fronts diverge (see Fig. 11), we can thus expect the development (43) to rapidly converge in this limit and retain only

$$\rho(z) = \rho_g + \frac{v}{c}m(z) - \frac{Dv}{c^2}m'(z) + \frac{vD^2}{c^3}m''(z) \tag{44}$$

At second order in $\epsilon$, Eqs (42) and (44) then reduces to

$$\hat{D}m'' + (a_0 - a_1 m)m' - b_1 m + b_2 m^2 - b_3 m^3 = 0 \tag{45}$$

where we have introduced the positive constants

$$\begin{aligned} &D = D(1+\frac{v^2}{c^2}), \quad a_0 = c(1-\frac{v^2}{c^2}), \quad a_1 = \frac{4Dvr}{(c^2+v^2)\varphi_g^2} \\ &b_1 = 2r\frac{\varphi_g - \rho_g}{\varphi_g^2}, \quad b_2 = \frac{2rv}{c\varphi_g^2}, \quad b_3 = \frac{\alpha}{\varphi_g^2} \end{aligned} \tag{46}$$

We then look for propagating solutions made of two fronts, connecting an ordered liquid band at $\rho_\ell$, $m_\ell$ to a disordered gas background at $\rho_g$, $m_g = 0$. Precisely, we look for propagating fronts given by:

$$m(z) = \frac{m_\ell}{2}\left[1 + \tanh(kz)\right] \tag{47}$$

To describe phase-separated domains, we need two front solutions, an ascending front $m_a(z)$ with $k_a > 0$ and a descending front $m_d(z)$ with $k_d < 0$, with the same speed $c$, density $\rho_g$ and magnetization $m_\ell$. Since the term $(a_0 - a_1 m)m'$ breaks the symmetry of the equations under $(m, c) \to (-m, -c)$ the fore and rear fronts need not be the same, so that $|k_a| \neq |k_d|$ in general.

The complete solution, specified by ($c$, $\rho_g$, $m_\ell$, $k_{a/d}$) can be obtained by injecting the Ansatz (47) into Eq. (45). Using the equality $\tanh'(kx) = k - k\tanh^2(kx)$, the l.h.s. of Eq. (45) then yields a third order polynomial in $\tanh(kx)$ whose coefficients all have to vanish. Tedious

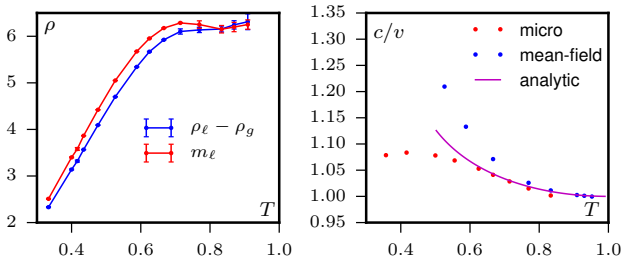


FIG. 18. **Left**: The magnetization $m_\ell$ in the liquid band and $\rho_\ell - \rho_g$ at phase-coexistence, measured in the microscopic simulations, converge to the same constant when $\beta \to 1$ as predicted by the analytical solution. Parameters: $D = 1$, $\varepsilon = 0.9$, $L = 400$ for the microscopic simulations. $r = v = D = 1$, $L = 400$ for the RMFM. **Right**: velocity $c$ of a liquid band propagating in a gas background. As $\beta \to 1$, $c \to v$ in the microscopic model, in 1d simulation of the RMFM (31), and in the analytical solution.

but straightforward algebra then gives

$$\begin{aligned} c &= v\Big(1 + \frac{8r^2 D}{3\alpha v^2 \varphi_g^2}\Big)^{\frac{1}{4}} \\ m_\ell &= \frac{4rv}{3\alpha c} \\ \rho_g &= \varphi_g - \frac{4rv^2}{9\alpha c^2} \\ k_{a/d} &= -\frac{c\gamma_-}{4D\gamma_+}\Big[1 \pm \sqrt{1 + \frac{4\gamma_+^3}{3} + \frac{\gamma_+^3 \alpha v^2 \varphi_g^2}{2Dr^2}}\Big] \end{aligned} \tag{48}$$

where $\gamma_\pm \equiv 1 \pm \frac{v^2}{c^2}$.

The solution is thus completely determined, the density and magnetization profiles being given by Eq. (47) and (44) respectively.

### B. Close to the $\beta = 1$ critical point

At leading orders when $\beta \to 1$, the propagating fronts are characterized by

$$\begin{aligned} &\rho_g = \varphi_g - \frac{4r}{9\alpha}; && \rho_\ell = \varphi_g + \frac{8r}{9\alpha}; \\ &m_\ell = \frac{4r}{3\alpha}; && c = v + \frac{2D(\beta-1)^2}{3v\alpha}; \\ &k_a = \frac{\beta-1}{3\sqrt{D\alpha}} - \frac{(\beta-1)^2}{6v\alpha}; && k_d = -\frac{\beta-1}{3\sqrt{D\alpha}} - \frac{(\beta-1)^2}{6v\alpha}; \end{aligned} \tag{49}$$

Some comments are in order. First, the two coexistence lines $\rho_g$ and $\rho_\ell$ diverge as $\beta \to 1$, as do the spinodals $\varphi_g$ and $\varphi_\ell$, while their difference and the magnetization $m_\ell$ converge to finite constants. This behavior, which is in line with simulations of the microscopic model (see Fig. 18), legitimates the expansion of (41) in powers of $m/\varphi_g$ and $\delta\rho/\varphi_g$.

Then, we can check the validity of the gradient expansion by comparing two successive terms in Eq. (43). When $\beta \to 1$, we have

$$\frac{\left(\frac{D}{c}\right)^{k+1} \frac{d^{k+1}m}{dy^{k+1}}}{\left(\frac{D}{c}\right)^{k} \frac{d^{k}m}{dy^{k}}} \sim \frac{D}{c} k_{a/d} \sim (\beta - 1) \tag{50}$$

so that our approximation becomes exact when $\beta \to 1$.

The front solutions account for a number of interesting features of the propagating liquid bands. First, the front speed $c$ is generally larger than $v$, the maximal mean speed of a single spin. This may seem surprising until one realizes that the front propagation is due both to the spins in the liquid band hopping forward and to the "conversion" of disordered sites into ordered ones at the level of the fore front. There is thus a FKPP-like contribution [45] to the speed of a band, which allows $c$ to be larger than $v$. Interestingly, despite the approximations made in deriving the RMFM, the behavior of $c/v$ as $\beta \to 1$ coincides exactly with what is observed in microscopic simulations of the AIM (see Fig. 18).

Regarding the propagating fronts, the analytical solution predicts $|k_a| < |k_d|$, i.e., that the descending (fore) front is steeper than the ascending (rear) front. The asymmetric term being subleading as $\beta \to 1$, the fore and rear fronts become more and more symmetric as $\beta \to 1$. This is consistent with the microscopic model: In Fig. 19, we show that the fronts are well described by two symmetric tanh functions close to $\beta = 1$. As the temperature decreases, the fronts first remain well approximated by hyperbolic tangents, but with different widths $k_a \neq k_d$, before their functional form deviates from the tanh solution (see Fig. 19).

Let us now be slighlty more quantitative and compare the scalings of the front widths in the AIM with the prediction of our analytical solution (49). In the microscopic model, we fitted the fronts of phase-separated profiles by the hyperbolic tangent solutions (47) to extract their width. Although data is hard to obtain close to critical points, because $m/\rho \to 0$, the measures are consistent with the analytical predictions. As shown in Fig. 20, $k_{a/d} \sim (\beta - 1)$ when $\beta \to 1$. One can also see that in this limit the two fronts become symmetric, i.e., $k_a \to k_d$. The size of the inferfaces, inversely proportional to $k_{a/d}$, can be linked to the size of the critical nucleus. As explained in sec. III D, a liquid domain can form only if the excess number of particles with respect to the gas is sufficient to create a band of minimal size $L_C$. As a first approximation, this minimal size is set by the size of the interfaces so that we expect $L_c \sim 1/k_a + 1/k_d$. Indeed, the same scalings are observed for $L_c$ as for $k_{a/d}$ as shown in Fig. 11.

### C. Close to the $v = 0$ critical points

While our approach was derived to work close to the critical point at $\beta = 1$, the front solution still predicts many correct scalings close to the $v = 0$ critical points. There, the propagating bands are characterized by

$$\begin{aligned}
\rho_g &= \varphi_g - \frac{\sqrt{2} r v}{3(\beta-1)\sqrt{3D\alpha}} \\
\rho_\ell &= \varphi_g + \frac{\sqrt{8} r v}{3(\beta-1)\sqrt{3D\alpha}} \\
m_\ell &= \left(\frac{32 r^4}{27(\beta-1)^2\alpha^3 D}\right)^{1/4} \sqrt{v} \\
c &= \left(\frac{8D(\beta-1)^2}{3\alpha}\right)^{1/4} \sqrt{v} \\
k_a &= \sqrt{\frac{(\beta-1)}{12D\sqrt{6D\alpha}}} (\sqrt{7} - \sqrt{3}) \sqrt{v} \\
k_d &= \sqrt{\frac{(\beta-1)}{12D\sqrt{6D\alpha}}} (-\sqrt{7} - \sqrt{3}) \sqrt{v}
\end{aligned} \tag{51}$$

Again, the two coexisting densities merge with the spinodal lines at $v = 0$ while the magnetization in the liquid vanishes, hence justifying the expansion of Eq. (41) in powers of $m/\varphi_g$ and $\delta\rho/\varphi_g$. While gradients are again expected to vanish as $v \to 0$, the expansion of $\rho$ in derivatives of $m$ includes a diverging prefactor $(D/c)^k \sim 1/v^{k/2}$ at the $k^{\text{th}}$ order. The comparison of two successive terms in the expansion (44) then yields

$$\frac{\left(\frac{D}{c}\right)^{k+1} \frac{d^{k+1}m}{dy^{k+1}}}{\left(\frac{D}{c}\right)^{k} \frac{d^{k}m}{dy^{k}}} \sim \frac{D}{c} k_{a/d} \sim \mathcal{O}(1) \tag{52}$$

Thus, in this limit, the series may still converge but the ratios between two consecutive terms do not vanish as $v \to 0$ and we cannot completely neglect higher order gradients. Nevertheless, as shown in Fig. 20, the analytical solution correctly predicts that the asymmetry between the fore and rear fronts does not disappear in the $v \to 0$ limit. It also correctly predicts the scaling of the front widths $k_{a/d} \sim \sqrt{v}$ and thus the scaling of the critical nucleus in this regime.

Beyond accounting for the shape of the phase diagram and the liquid-gas nature of the transition, the RMFM can thus correctly predict the shape of the band, their speed and the scaling of the critical nucleus in the vicinity of the critical points. In order to get a more quantitative agreement between the RMFM and the microscopic model, beyond the estimation of the unknown parameter $r$, one would probably needs to account for the correlations between $m$ and $\rho$. Apart from quantitative corrections, these correlations however do not seem to play any role in controling the structure of the phase transition and most features of the propagating bands. Interestingly, symmetric hyperbolic tangent front were also observed in hydrodynamic equations for self-propelled rods [29], even though in that case the domains are not moving.

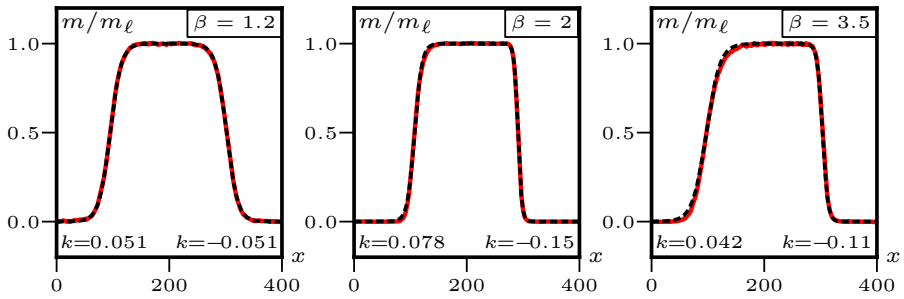


FIG. 19. The fore and rear fronts of propagating bands become more asymmetric as $T$ decreases. The shape of the fronts in the microscopic model (red curves) also deviate more and more from the analytical tanh solution (valid in the limit $\beta \to 1$). Black dashed curves are fits of the rescaled fronts by expression (47), where $k$ is used as a fitting parameter. Parameters: $D = 1$, $\varepsilon = 0.9$. Fronts are averaged over time and along the vertical direction.

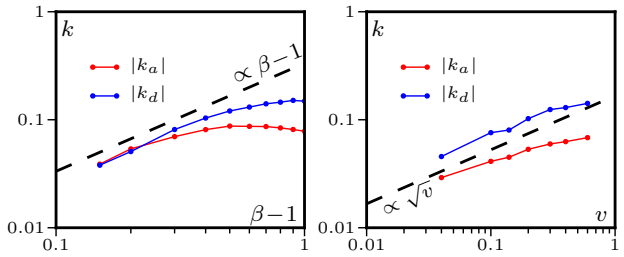


FIG. 20. Scaling of the front widths close to the critical points $\beta \to 1$ (left) and $v \to 0$ (right). The data is consistent with the predictions from the RMFM in these limits Eq. (49) and (51) both for the scaling of $k_{a/d}$ and for the asymmetry between the ascending and descending fronts. $\varepsilon = 0.9$ (left), $\beta = 1.9$ (right) and $D = 1$.

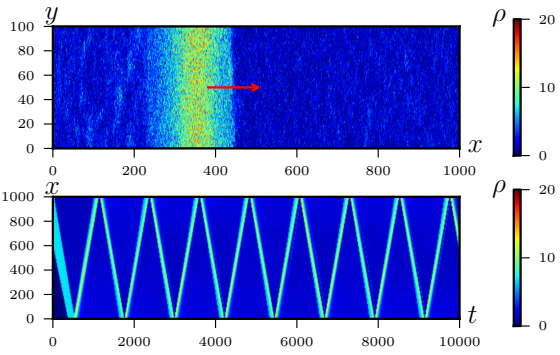


FIG. 21. Active Ising model with closed boundary conditions. Top: snapshot of the density field. Bottom: space-time graph (averaged in the y-direction) showing the liquid domain bouncing back and forth in the box. Parameters: $\beta = 1.9$, $\rho_0 = 3$, $D = 1$, $\varepsilon = 0.9$. See supplementary movies in [49].

## VI. ROBUSTNESS OF THE RESULTS

Let us now discuss how the results presented in the previous sections extend beyond our lattice gas model with periodic boundary conditions. To do so, we consider the case of closed boundary conditions in section VI A and study an off-lattice version of the AIM in section VI B.

### A. Closed boundary conditions

Since the ordered liquid domains always span the whole system in the vertical direction and propagates periodically in the horizontal direction, one could think that their existence and stability relies on the use of periodic boundary conditions. To check this, we simulated the AIM in closed boxes. We tried different conditions at the edges of the box: When particles hit a wall, their spins were either flipped, randomized, or left unaltered.

The same behavior was observed in all cases. First, one notice a small accumulation of particles close to the wall, which is typical of self-propelled particles [46]. Then, the system shows the same type of travelling bands as with periodic boundary conditions, with a macroscopic phase-separation between a liquid domain and a gaseous disordered background (see Fig. 21, top). When the liquid domain reaches a boundary, it accumulates close to the wall until its magnetisation flips, and crosses back the system in the other direction. This leads to the bouncing wave shown on Fig. 21 (bottom), which is reminiscent of what is observed experimentally for the collective motion of colloidal rollers (see supplementary movies of [9]).

### B. Off-lattice version

To show that the phenomenology of the AIM does not rely on the spatial discreteness of this lattice gas, we devised an off-lattice version of our model. To do so, we consider $N$ particles in a continuous space of size $L_x \times L_y$. Each particle carries a spin $\pm 1$, which flips at rate

$$W(s \to -s) = \exp(-\beta \frac{m_i}{\rho_i}) \tag{53}$$

where the local density $\rho_i$ and magnetization $m_i$ are computed in disks of radius 1.

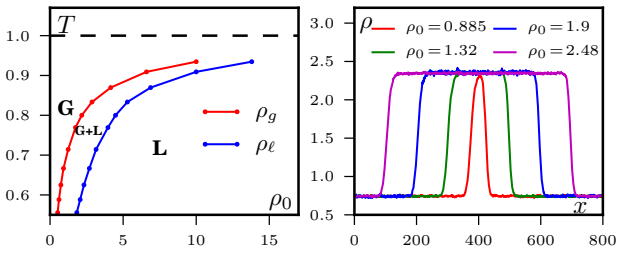


FIG. 22. Phase diagram and phase-separated profiles for the off-lattice model showing the same behavior as the lattice model. Parameters: $D = 1$, $v = 1$ and $\beta = 1.6$ for the profiles.

The position of the particle evolves according to the Langevin equation

$$\dot{\mathbf{r}}_\mathbf{i} = s_i v \mathbf{e}_\mathbf{x} + \sqrt{2D}\boldsymbol{\eta} \tag{54}$$

where $\mathbf{r_i}$ and $s_i$ are the position and spin of particle $i$ and $\boldsymbol{\eta}$ is a Gaussian white noise of unit variance.

The phenomenology of this model is very similar to that of the AIM; Its phase diagram in the temperature-density ensemble shows the same three regions, with an asymptote at $\beta = 1$ as $\rho \to \infty$ (Fig. 22, left). As in the lattice model, only the liquid fraction changes when $\rho_0$ is increased at fixed temperature as shown in Fig. 22 (right).

## VII. DISCUSSION AND OUTLOOK

In this paper we have characterized in detail the transition to collective motion in the 2d active Ising model. For any temperature $T < 1$ and self-propulsion velocity $v > 0$, there is a finite density range for which the system phase-separates into a polar liquid and a disordered gas. The densities at coexistence do not depend on $T$ or $v$ so that changing the average density only changes the liquid fraction. This is one of the many characteristics shared by the flocking transition of the AIM with the equilibrium liquid/gas transition in the canonical ensemble. Others include metastability, hysteresis, and the existence of critical nuclei. More generally, this analogy suggests that the flocking transition should be seen as a phase-separation transition rather than an order-disorder transition. The fact that the liquid phase is ordered however plays a major role by forbidding a supercritical region, which explains the atypical shape of the phase diagram.

To construct a continuous theory for our model we first noticed that one needs to go beyond a standard mean-field approach. The latter indeed fails to capture the phase separation behavior because it lacks a density dependence of the transition temperature. Retaining part of the fluctuations neglected at the mean-field level then allowed us to derive a refined-mean-field model which accounts for the behavior of the microscopic model qualitatively for all parameter values.

The analytical solution for the phase-separated profile that we derived in sec. V is only one of a two-parameter family of solutions, as shown in [23]. Although it is the sole propagating solution accounting for phase separation, the mecanism by which it is selected remains to be investigated. This is particularly interesting since, as shown in [14], most of the picture laid out for the AIM remains valid for the Vicsek model, apart from the shape of the bands in the phase separated region. The full phase separation of the AIM is then replaced by a micro-phase separation, something which cannot be explained at the hydrodynamic level and necessit explicit noise terms.

Beyond the sole case of the AIM, we showed that our results are also valid off lattice. We can thus consider the AIM as a representative example of a flocking model with discrete rotational symmetry. Variants with alignment between nearest neighbours, and not simply on-site, also yield similar results.

Our study of the AIM relies on numerical simulations, microscopic derivation and study of hydrodynamic equations. It says little about the universality of the emerging properties of the Active Ising Model and we strongly believe that developing proper field theoretical approaches of the AIM and more general active spin models could shed light on a number of interesting questions. For instance, is the $\epsilon = 0$ limit of the AIM in the universality class of model C [50], which couples a conserved diffusive field and a non-conserved $\phi^4$ theory? Then, can one study the divergence of the correlation length of the AIM when approaching the $T = 1$ and $v = 0$ critical points? What are the corresponding universality classes? These questions will be addressed in future works.

Last, the analogy of the phase transition in the AIM with an equilibrium liquid/gas transition triggers new questions. For example, could we define a mapping, at some level, with an equilibrium system? And would it be possible to change ensemble in this non-equilibrium system, for example desining a grand-canonical ensemble? These questions, if answered, would certainly improve our theoretical understanding of active matter systems.

## ACKNOWLEDGMENTS

We thank the Kavli Institute for Theoretical Physics, Santa Barbara, USA, and the Galileo Galilei Institute, Firenze, Italy for hositality and financial support. This research was supported by the ANR BACTTERNS project and, in part, by the National Science Foundation under Grant No. NSF PHY11-25915.

### Appendix A: One step beyond mean-field

As shown in section IV A, the mean-field equations, which neglect all fluctuations and correlations, fail to de-

scribe the active Ising model since they predict a continuous phase transition between homogeneous phases. In this appendix we show how one can improve the mean-field approximation. To do so, we take into account the fluctuations of the local magnetisations and densities when computing the dynamics of their first moments $\langle m \rangle$ and $\langle \rho \rangle$.

### 1. Gaussian fluctuations

The simplest assumption that can be made about the fluctuations of $m(x)$ and $\rho(x)$ around their mean values, $\langle m(x) \rangle$ and $\langle \rho(x) \rangle$, is that they are Gaussian. For $m(x)$, this can be seen as resulting from a central limit theorem: In a first approximation, the magnetisation is the sum of many spins fluctuating independently and, indeed, Fig. 23 shows its fluctuations to be well described by a Gaussian. On the contrary, the distribution of the local density is not perfectly Gaussian, as shown in Fig. 23. A better approximation could be obtained by considering a Poisson distribution but, as will be apparent in the following, the first correction to mean-field comes from the fluctuations of $m$ so this would not improve our approximation. Furthermore we believe that, to improve our refined mean-field model, the next step should be to include the correlations between $\rho$ and $m$, that we neglect in the following, and not higher cumulants of the distributions of $\rho$ and $m$.

More formally, the probability to observe a magnetisation $m$ and a density $\rho$ at time $t$ and position $x$ given initial profiles $\rho_0(x)$ and $m_0(x)$ are assumed to be given by

$$\mathcal{P}(\rho, m, x, t \,|\, \rho_0, m_0) = \mathcal{N}(\rho - \bar{\rho}, \sigma_\rho^2)\mathcal{N}(m - \bar{m}, \sigma_m^2) \quad \text{(A1)}$$

where $\mathcal{N}(x, \sigma^2) = e^{-x^2/\sigma^2}/\sqrt{2\pi\sigma^2}$ is the normal distribution and $\bar{\rho}(x,t)$ and $\bar{m}(x,t)$ are the average value of the density and magnetisation fields.

We further assume that the variances of the Gaussian distributions scales linearly with the local density: $\sigma_m^2 = \alpha_m \bar{\rho}(x,t)$ and $\sigma_\rho^2 = \alpha_\rho \bar{\rho}(x,t)$. Again, the underlying assumption is that the fluctuations of the fields $\rho(x)$ and $m(x)$ arise from the sum of $\rho$ independent contributions. As shown in Fig. 24 this is a rather good approximation in the gas phase, close to the critical point at $\beta = 1$, $\rho = \infty$.

### 2. Corrections to mean-field

In deriving hydrodynamic equations from Eq. (18) and (19), the only terms that have to be approximated are the non-linear contributions of the aligning interactions:

$$I = \left\langle 2\rho \sinh \frac{\beta m}{\rho} - 2m \cosh \frac{\beta m}{\rho} \right\rangle = \left\langle \sum_{k=0}^{\infty} a_k \frac{m^{2k+1}}{\rho^{2k}} \right\rangle \quad \text{(A2)}$$

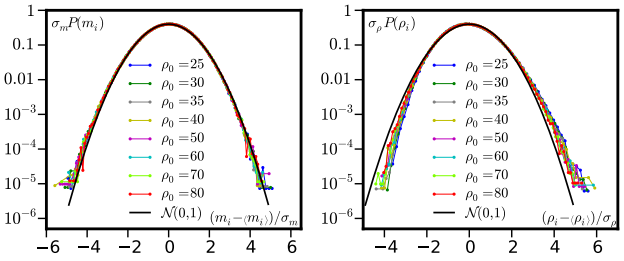


FIG. 23. Rescaled probability distributions of local density (left) and magnetisation (right) in the liquid phase at $\beta = 1.1$ for different densities. $\mathcal{N}(0,1)$ is the Gaussian distribution with zero mean and unit variance. $D = 1$, $\varepsilon = 0.9$, $L = 100$.

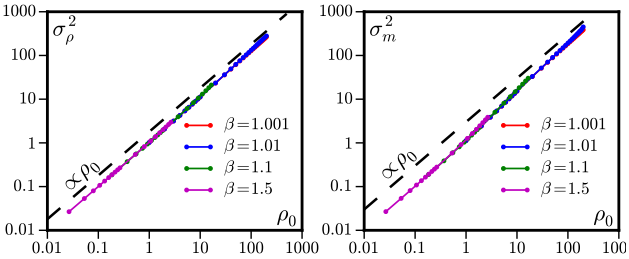


FIG. 24. Variance of the distribution of local density (left) and magnetisation (right) in the gas phase compared to a linear scaling. $D = 1$, $\varepsilon = 0.9$, $L = 100$.

where

$$a_k = 2\left(\frac{\beta^{2k+1}}{(2k+1)!} - \frac{\beta^{2k}}{(2k)!}\right) \quad \text{(A3)}$$

Using the assumption (A1), we can compute $I$ as a sum of Gaussian integrals which can all be evaluated by saddle-point approximation in the limit of large $\bar{\rho}$. We first notice that, since we neglect the correlations between $\rho$ and $m$,

$$\left\langle \frac{m^{2k+1}}{\rho^{2k}} \right\rangle = \left\langle m^{2k+1} \right\rangle \left\langle 1/\rho^{2k} \right\rangle \quad \text{(A4)}$$

To compute $\langle m^{2k+1} \rangle$, we first change variables to $u = m - \bar{m}$ so that

$$\begin{aligned} \left\langle m^{2k+1} \right\rangle &= \int_{-\infty}^{+\infty} dm\, m^{2k+1} \mathcal{N}(m - \bar{m}, \alpha_m \bar{\rho}) \\ &= \int_{-\infty}^{+\infty} du\, (u + \bar{m})^{2k+1} \mathcal{N}(u, \alpha_m \bar{\rho}) \end{aligned} \quad \text{(A5)}$$

We then expand in powers of $u$ and compute the corresponding Gaussian integrals

$$\begin{aligned} \left\langle m^{2k+1} \right\rangle &= \int_{-\infty}^{+\infty} du \sum_{i=0}^{2k+1} \binom{2k+1}{i} u^i \bar{m}^{2k+1-i} \mathcal{N}(u, \alpha_m \bar{\rho}) \\ &= \sum_{j=0}^{k} \binom{2k+1}{2j} \frac{\Gamma(j+1/2)}{\sqrt{\pi}} (2\alpha_m \bar{\rho})^j \bar{m}^{2k+1-2j} \end{aligned} \quad \text{(A6)}$$

Let us now evaluate the terms $\langle \rho^{-2k} \rangle$. First, the integral

$$\langle \rho^{-2k} \rangle = \int_0^{+\infty} d\rho\, \rho^{-2k} \mathcal{N}(\rho - \bar{\rho}, \alpha_\rho \bar{\rho}) \tag{A7}$$

is divergent because of the $\rho = 0$ lower limit. This is a simple discretisation problem which can be bypassed by introducing a cut-off $\zeta$ at small density. For large $\bar{\rho}$, the integrals will be dominated by large values of $\rho$ so this cut-off does not play any role in the following. Changing variable to $s = (\rho - \bar{\rho})/\bar{\rho}$, we find

$$\langle \rho^{-2k} \rangle = \frac{\bar{\rho}^{\frac{1}{2}-2k}}{\sqrt{2\pi\alpha_\rho}} \int_{\frac{\zeta}{\bar{\rho}}-1}^{+\infty} ds\, (1+s)^{-2k} e^{-\bar{\rho}\frac{s^2}{2\alpha_\rho}} \tag{A8}$$

This integral can now be approximated by an asymptotic saddle-point expansion. In the limit of large $\bar{\rho}$, the integral is dominated by $s \simeq 0$. The lower limit of the integral $\frac{\zeta}{\bar{\rho}} - 1 \simeq -1$ can thus be extended to $-\infty$ harmlessly and one can expand $(1+s)^{-2k}$ to get the asymptotic expansion

$$\langle \rho^{-2k} \rangle = \frac{\bar{\rho}^{\frac{1}{2}-2k}}{\sqrt{2\pi\alpha_\rho}} \sum_{i=0}^{2N} \binom{2k+i-1}{i} \int_{-\infty}^{+\infty} ds\, (-s)^i e^{-\bar{\rho}\frac{s^2}{2\alpha_\rho}} + \mathcal{O}(\bar{\rho}^{-2N-2k-1/2}) \tag{A9}$$

All the odd contributions vanish by symmetry. Changing variable to $\omega = \bar{\rho}s^2/(2\alpha_\rho)$, one recognises the integral form of a $\Gamma$ function and finally

$$\langle \rho^{-2k} \rangle = \sum_{j=0}^{N} \binom{2k+2j-1}{2j} \frac{\Gamma(j+\frac{1}{2})}{\sqrt{\pi}} 2^j \alpha_\rho^j \bar{\rho}^{-j-2k} + \mathcal{O}(\bar{\rho}^{-2k-2N-1}) \tag{A10}$$

Putting everything together, we obtain

$$I = \sum_{k=0}^{\infty} \sum_{i=0}^{k} \sum_{j=0}^{N} \Big[ a_k b_{i,k} c_{j,k} \frac{\bar{m}^{1+2k-2i}}{\bar{\rho}^{2k+j-i}} + \mathcal{O}(\frac{1}{\bar{\rho}^{1+N+2k-i}}) \Big] \tag{A11}$$

where

$$b_{i,k} = \binom{2k+1}{2i} \frac{2^i \Gamma(i+1/2)}{\sqrt{\pi}} \alpha_m^i \tag{A12}$$

$$c_{j,k} = \binom{2k+2j-1}{2j} \frac{2^j \Gamma(j+1/2)}{\sqrt{\pi}} \alpha_\rho^j \tag{A13}$$

Keeping only the dominant terms and reordering the sum in increasing powers of $m$ yields

$$I = \sum_{n=0}^{\infty} \frac{\bar{m}^{1+2n}}{\bar{\rho}^{2n}} \Big[ \sum_{i=0}^{N} \sum_{j=0}^{N-i} \frac{a_{n+i} b_{i,n+i} c_{j,n+i}}{\bar{\rho}^{j+i}} + \mathcal{O}(\frac{1}{\bar{\rho}^{1+N}}) \Big] \tag{A14}$$

Expanding up to $m^3$ and $1/\bar{\rho}^2$, we finally obtain

$$I \simeq 2\big(\beta - 1 - \frac{r}{\bar{\rho}} - \frac{r_2}{\bar{\rho}^2}\big)\bar{m} - \alpha \frac{\bar{m}^3}{\bar{\rho}^2} \tag{A15}$$

where

$$\alpha = -a_1 = \beta^2(1 - \frac{\beta}{3}) \tag{A16}$$

$$r = -\frac{a_1 b_{1,1} c_{0,1}}{2} = \frac{3\alpha\alpha_m}{2} \tag{A17}$$

$$r_2 = 3\beta^2(\beta - 3)\alpha_m \alpha_\rho + \frac{\beta^4}{4}(\beta - 5)\alpha_m^2 \tag{A18}$$

In practice, we take $r_2 = 0$ in the RMFM since the first order correction $r/\bar{\rho}$ suffices to account for the phenomenology of the AIM. Expanding (A14) to higher orders is not sufficient to get a *quantitative* agreement between microscopic simulations and our refined mean-field model, probably because the most important correction to (A15) would involve correlations between $m$ and $\rho$. As we show in section IV, however, this first correction to mean-field is sufficient to capture the physics of the model.

## Appendix B: Linear stability analysis

The mean-field and refined mean-field equations read

$$\dot{\rho} = D\Delta\rho - v\partial_x m \tag{B1}$$

$$\dot{m} = D\Delta m - v\partial_x \rho + 2m\mu - \alpha\frac{m^3}{\rho^2} \tag{B2}$$

where $\mu = \beta - 1 - r/\rho$ and $r = 0$ for the mean-field equations. These equations admit three steady homogeneous solutions $\rho(x,t) = \rho_0$, $m(x,t) = m_0$. A disordered solution with $m_0 = 0$ that exists for all $\rho_0$ and $\beta$, and two ordered solutions

$$m_0 = \pm\rho_0\sqrt{\frac{2\mu}{\alpha}} \tag{B3}$$

that exist only when $\mu > 0$.

### 1. Stability of the disordered profile

Let us consider a small perturbation around the disordered profile, $m(\mathbf{r},t) = \delta m(\mathbf{r},t)$, $\rho(\mathbf{r},t) = \rho_0 + \delta\rho(\mathbf{r},t)$. Going into Fourier space,

$$\delta\rho = \int_{-\infty}^{\infty} dx \int_{-\infty}^{\infty} dy\, \delta\rho(\mathbf{q},t) e^{-i(q_x x + q_y y)} \tag{B4}$$

and linearizing Eqs. (B1) and (B2), one finds

$$\partial_t \begin{pmatrix} \delta\rho \\ \delta m \end{pmatrix} = \begin{pmatrix} -D|q|^2 & -iq_x v \\ -iq_x v & -D|q|^2 + 2\mu_0 \end{pmatrix} \begin{pmatrix} \delta\rho \\ \delta m \end{pmatrix} \tag{B5}$$

where we noted $\mu_0 = (\beta - 1 - r/\rho_0)$. The eigenvalues of the 2x2 matrix are

$$\lambda_\pm = -D(q_x^2 + q_y^2) + \mu_0 \pm \sqrt{\mu_0^2 - v^2 q_x^2} \tag{B6}$$

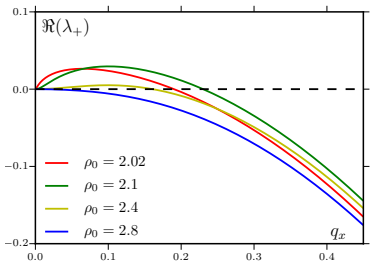


FIG. 25. Real part of the largest eigenvalue $\lambda_+$ related to the stability of the ordered profile $m = m_0$. of Eq. (B8) for $\beta = 1.5$, $D = r = v = 1$ and $q_y = 0$. Ordered profiles exist for all $\rho_0 \geq \varphi_g = 2$ but are unstable for $\varphi_g \leq \rho_0 \leq \varphi_\ell$ (red, green and yellow curves) and stable only for $\rho_0 \geq \varphi_\ell$ (blue curve). For the parameters considered here $\varphi_\ell = 2.598$.

The profile is linearly unstable if one of these eigenvalues has a positive real part. Clearly, the sign of $\mu_0$ controls the stability: the disordered profile is unstable to long wavelength perturbations when $\beta > 1$ and $\rho_0 > \varphi_g = r/(\beta - 1)$ and stable otherwise. This gives the first spinodal line $\varphi_g$ in Fig. 16.

### 2. Stability of the ordered profile

Linearizing the dynamics of a small perturbation around the ordered profile $m(\mathbf{r}, t) = m_0 + \delta m(\mathbf{r}, t)$, $\rho(\mathbf{r}, t) = \rho_0 + \delta\rho(\mathbf{r}, t)$ gives

$$\partial_t \begin{pmatrix} \delta\rho \\ \delta m \end{pmatrix} = \begin{pmatrix} -D|q|^2 & -iq_x v \\ -iq_x v + \frac{m_0}{\rho_0}(\frac{2r}{\rho_0} + 4\mu_0) & -D|q|^2 - 4\mu_0 \end{pmatrix} \begin{pmatrix} \delta\rho \\ \delta m \end{pmatrix} \tag{B7}$$

and the eigenvalues now read

$$\lambda_\pm = -D(q_x^2+q_y^2) - 2\mu_0 \pm \sqrt{4\mu_0^2 - v^2 q_x^2 - \frac{2im_0 q_x v(r + 2\mu_0\rho_0)}{\rho_0^2}} \tag{B8}$$

Equation (B8) shows $q_y$ to have a purely stabilizing effect; Taking $q_y = 0$ thus does not affect the conclusions about the stability of the system. Computing numerically $\Re(\lambda_\pm)$ we observe (Fig. 25) that for small but positive $\mu_0$, $\Re(\lambda_\pm) > 0$ at long wave-length. The value of $\mu_0$ at which the system becomes stable can be determined analytically as the point where $\partial_{qx}^2 \Re(\lambda_\pm)(q_x = 0)$ changes sign (the first derivative being zero at $q_x = 0$). This yields the second spinodal line shown in Fig. 16

$$\varphi_\ell = \varphi_g \frac{v\sqrt{\alpha\,(v^2\kappa + 8D(\beta-1)^2)} + v^2\kappa + 8D\alpha(\beta-1)}{2v^2\kappa + 8D\alpha(\beta-1)} \tag{B9}$$

where $\kappa = 2 + \alpha - 2\beta$.


[1] M. Ballerini, N. Cabibbo, R. Candelier, A. Cavagna, E. Cisbani, I. Giardina, V. Lecomte, A. Orlandi, G. Parisi, A. Procaccini, M. Viale, V. Zdravkovic, Proc. Natl. Acad. Sci. USA **105** 1232 (2008)

[2] Ch. Beccoa, N. Vandewallea, J. Delcourtb and P. Poncinb, Physica A, Volume 367, 15 July 2006, Pages 487–493

[3] Daniel S Calovi et al 2014 New J. Phys. 16

[4] E. B. Steager, C.-B. Kim, M. J. Kim. Physics of Fluids, 20(7):073601, 2008.

[5] F. Peruani, J. Starruss, V. Jakovljevic, L. Sogaard-Andersen, A. Deutsch, M. Bär, Phys. Rev. Lett. **108**, 098102 (2012)

[6] V. Schaller, C. Weber, C. Semmrich, E. Frey, A. R. Bausch, *Nature* **467**, 73-77 (2010).

[7] Y. Sumino, K. H. Nagai, Y. Shitaka, D. Tanaka, K. Yoshikawa, H. Chaté, K. Oiwa, *Nature* **483** 448-452 (2012).

[8] J. Deseigne, O. Dauchot, H. Chaté. Phys. Rev. Lett., **105**, 098001 (2010); Julien Deseigne, Sébastien Léonard, Olivier Dauchot, Hugues Chaté, cond-mat/1201.6021 (2012)

[9] A. Bricard, J-B. Caussin, N. Desreumaux, O. Dauchot, D. Bartolo, Nature 503, 95–98 (2013)

[10] Shashi Thutupalli et al 2011 New J. Phys. 13 073021

[11] T. Vicsek, A. Czirók, E. Ben-Jacob, I. Cohen, O. Shochet, Phys. Rev. Lett. **75**, 1226 (1995)

[12] J. Toner and Y. Tu, Phys. Rev. Lett. **75**, 4326 (1995); Phys. Rev. E **58**, 4828 (1998); J. Toner, Phys.Rev.E **86**, 031918 (2012)

[13] G. Grégoire, H. Chaté, Phys. Rev. Lett. **92** 025702 (2004); H. Chaté, F. Ginelli, G. Grégoire, F. Raynaud, Phys. Rev. E **77** 046113 (2008).

[14] A. P. Solon, H. Chate, J. Tailleur, *Phys. Rev. Lett.* **114** 068101 (2015)

[15] S. Mishra, A. Baskaran, M.C. Marchetti. Phys. Rev. E **81**, 061916. (2010); A. Gopinath, M.F. Hagan, M.C. Marchetti, A. Baskaran. Phys. Rev. E **85**, 061903. (2012)

[16] C. A. Weber, T. Hanke, J. Deseigne, S. Léonard, O. Dauchot, E. Frey, H. Chaté Phys. Rev. Lett. 110, 208001 (2013)

[17] F. Peruani, T. Klauss, A. Deutsch, and A. Voss-Boehme, Phys. Rev. Lett. 106, 128101 (2011)

[18] F. D. C. Farrell, M. C. Marchetti, D. Marenduzzo, and J. Tailleur, Phys. Rev. Lett. 108, 248101 (2012)

[19] E. Bertin, M. Droz, G. Grégoire, Phys. Rev. E **74** 022101 (2006); J. Phys. A **42** 445001 (2009)

[20] T. Ihle, Phys. Rev. E **83**, 030901 (2011); T. Ihle, Phys. Rev. E **88**, 040303(R) (2013)

[21] J. Toner, Y. Tu, and S. Ramaswamy, Ann. Phys. (N.Y.) 318, 170 (2005)

[22] A.P. Solon, J. Tailleur, Phys. Rev. Lett. 111, 078101 (2013)

[23] J-B Caussin, A. Solon, A. Peshkov, H. Chaté, T. Dauxois, J. Tailleur, V. Vitelli, and D. Bartolo, Phys. Rev. Lett. **112**, 148102 (2014)
[24] C. Domb, R. K. Zia, B. Schmittmann, J. L. Lebowitz. *Statistical mechanics of driven diffusive systems.* Academic Press, 1995
[25] M. Kim, S.-C. Park, J. D. Noh. *Phys. Rev. E* **91** 012132 (2015)
[26] K. R. Pilkiewicz, J. D. Eaves. *Phys. Rev. E* **89** 012718 (2014).
[27] A.N. Kolmogorov, *Math. Ann.* **112**, 155-160 (1936)
[28] S. Ngo, A. Peshkov, I.S. Aranson, E. Bertin, F. Ginelli, and H. Chaté, *Phys. Rev. Lett.* **113**, 038302 (2014)
[29] A. Peshkov, I. S. Aranson, E. Bertin, H. Chaté, F. Ginelli, Phys. Rev. Lett. **109**, 268701 (2012)
[30] F. Thüroff, C. A. Weber, and E. Frey, Phys. Rev. X **4**, 041030 (2014)
[31] A. Czirók, H. Stanley, T. Vicsek, J. Phys. A: Math. Gen. **30** 1375 (1997)
[32] O. J. O'Loan, M. R. Evans, J. Phys. A: Math. Gen. **32** L99 (1999)
[33] G. Baglietto, E. V. Albano, J. Candia, *Interface Focus* **2** 708-714 (2012).
[34] K. Binder, Rep. Prog. Phys. **60** 487 (1997)
[35] G. Kamieniarz and H. W. J. Blote, J. Phys. A: Math. Gen. **26** 201 (1993)
[36] F. Ginelli, H. Chaté, Phys. Rev. Lett. **105**, 168103 (2010)
[37] S. Dey, D. Das, and R. Rajesh, Phys. Rev. Lett. 108, 238001 (2012)
[38] I. S. Aranson *et al.*, Science **320** 612 (2008)
[39] Y. Fily, M. Cristina Marchetti, *Phys. Rev. Lett.* **108** 235702 (2012).
[40] R. A. Blythe, M. R. Evans, *J. Phys. A* **40** R333 (2007).
[41] M. R. Evans, Y. Kafri, K. E. P. Sugden, J. Tailleur, J. Stat. Mech. P06009 (2011)
[42] P. Weiss, J. de Phys. 6, pp. 661-690 (1907)
[43] A. Baskaran, M. C. Marchetti, Phys. Rev. E **77**, 011920 (2008)
[44] I. S. Aranson, L. S. Tsimring, Phys. Rev. E **71**, 050901(R) (2005)
[45] W. van Saarloos, *Phys. Rep.* **386**, 29 (2003).
[46] J. Elgeti, G. Gompper, EPL (Europhysics Letters) **85**, 38002 (2009).
[47] To integrate the PDE of the (refined) mean-field model, we used pseudo-spectral methods, computing the linear terms in Fourier space with implicit time stepping.
[48] The definition of the Hamiltonian (2) does not contain any coupling constant $J$ so that $\beta$ is dimensionless.
[49] See Supplemental Material at this URL
[50] P. C. Hohenberg and B. I. Halperin, Rev. Mod. Phys. **49**, 435 (1977)

## 5.3 Équations hydrodynamiques

L'article F va nous permettre d'explorer, de façon approfondie, les solutions inhomogènes des équations hydrodynamiques décrivant les modèles de particules autopropulsées avec alignement ferromagnétique. Pour cela, nous considérerons des équations hydrodynamiques simplifiées que nous comparerons ensuite aux équations décrivant le modèle d'Ising actif (construites dans l'article E) et à celles de Bertin et collaborateurs décrivant une version simplifiée du modèle de Vicsek [76, 78, 81]. Toutes ces équations admettent les mêmes solutions propagatives qui sont de trois types : des solutions décrivant une séparation de phase, des solutions périodiques décrivant une séparation en microphases et des solutions décrivant la propagation d'un objet de taille finie isolé. La dynamique de *coarsening* mène naturellement à une séparation de phase et nous en concluons qu'un ingrédient supplémentaire, qui n'est pas présent au niveau des équations hydrodynamiques, arrête le *coarsening* dans le modèle de Vicsek, où une séparation en microphases est observée.

# Pattern formation in floking models: A hydrodynamic description

Alexandre P. Solon,[1] Jean-Baptiste Caussin,[2] Denis Bartolo,[2] Hugues Chaté,[3,4,5] and Julien Tailleur[1]

[1] *Université Paris Diderot, Sorbonne Paris Cité, MSC, UMR 7057 CNRS, 75205 Paris, France*
[2] *Laboratoire de Physique de l'Ecole Normale Supérieure de Lyon, Université de Lyon, CNRS, 46, allée d'Italie, 69007 Lyon, France*
[3] *Service de Physique de l'État Condensé, CNRS UMR 3680, CEA-Saclay, 91191 Gif-sur-Yvette, France*
[4] *LPTMC, CNRS UMR 7600, Université Pierre & Marie Curie, 75252 Paris, France*
[5] *Beijing Computational Science Research Center, Beijing 100094, China*

(Dated: September 10, 2015)

We study in detail the hydrodynamic theories describing the transition to collective motion in polar active matter, exemplified by the Vicsek and active Ising models. Using a simple phenomenological theory, we show the existence of an infinity of propagative solutions, describing both phase and microphase separation, that we fully characterize. We also show that the same results hold specifically in the hydrodynamic equations derived in the literature for the active Ising model and for a simplified version of the Vicsek model. We then study numerically the linear stability of these solutions. We show that stable ones constitute only a small fraction of them, which however includes all existing types. We further argue that in practice, a coarsening mechanism leads towards phase-separated solutions. Finally, we construct the phase diagrams of the hydrodynamic equations proposed to qualitatively describe the Vicsek and active Ising models and connect our results to the phenomenology of the corresponding microscopic models.

## CONTENTS



## I. INTRODUCTION

Collective motion is the ability of large groups of motile agents to move coherently on scales much larger than their individual sizes. It is encountered at all scales in nature, from macroscopic animal groups, such as bird flocks, fish schools, or sheep herds, down to the cellular scale, where the collective migration of cells [1] or bacteria [2] is commonly observed. At the subcellular level, in vitro motility assays of actin filaments [3] or microtubules [4] have shown the spontaneous emergence of large vortices. Collective motion is also observed in ensemble of man-made motile particles such as shaken polar grains [5], colloidal rollers [6], self-propelled droplets [7] or assemblies of polymers and molecular motors [3, 4, 8]. Despite the differences in their propulsion and interaction mechanisms, these seemingly very different systems

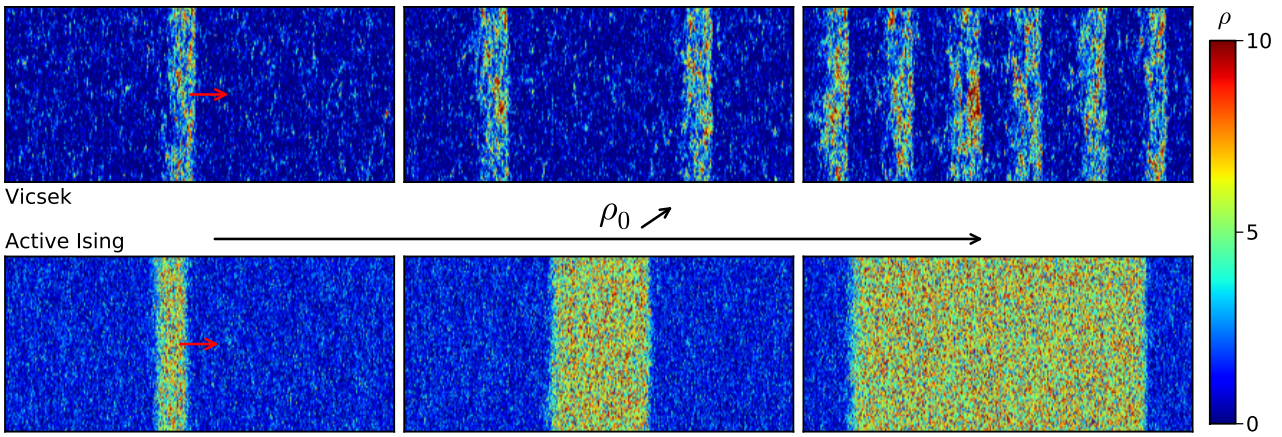


FIG. 1. **Top**: Micro-phase separation in the Vicsek model. $\eta = 0.4$, $v_0 = 0.5$, $\rho_0 = 0.83, 1.05, 1.93$. **Bottom**: Phase separation in the Active Ising model. $D = 1$, $\varepsilon = 0.9$, $\beta = 1.9$, $\rho_0 = 1.5, 2.35, 4.7$. System sizes $800 \times 100$. High-density bands propagate as indicated by the red arrows on the left snashots.

share common macroscopic behaviors that can be captured by minimal physical models. Of particular interest is the emergence of *directed* collective motion, which was first addressed in this context in a seminal work by Vicsek and co-workers [9]. The Vicsek model consists in point particles moving at constant speed and aligning imperfectly with the direction of motion of their neighbors. When the error on the alignment interaction is decreased, or the density of particles increased, a genuine phase transition from a disordered to a symmetry-broken state is observed. This flocking transition gives rise to an emergent ordered phase, with true long-range polar order even in 2D, where all the particles propel on average along the same direction. Toner and Tu showed analytically, using a phenomenological fluctuating hydrodynamic description, how this ordered state, which would be forbidden by the Mermin-Wagner theorem at equilibrium [10], is stabilized by self-propulsion [11]. The transition to collective motion in the Vicsek model has a richer phenomenology than originally thought. As first pointed out numerically in [12], at the onset of collective motion, translational symmetry is broken as well. In periodic simulation boxes, high-density ordered bands of particles move coherently through a low-density disordered background. The transition between these bands and the homogeneous disordered profile is discontinuous, with metastability and hysteresis loops. These spatial patterns and the first-order nature of the transition can be encompassed in a wider framework, which describes the emergence to collective motion as a liquid-gas phase separation [13, 14]. The travelling bands result from the phase coexistence between a disordered gas and an ordered polarized liquid. This framework captures many of the characteristics of the transition, from the scaling of the order parameter to the shape of the phase diagram. This phase-separation picture is robust to the very details of the propulsion and interaction mechanisms. More specifically, it has also been quantitatively demonstrated in the active Ising model [13] in which particles can diffuse in a 2d space but self-propel, and align, only along one axis. However the specifics of the emergent spatial patterns and the type of phase separation depend on the symmetry of the orientational degrees of freedom. While the active Ising model model shows a bulk phase separation, the Vicsek model is akin to an active XY model and is associated with a microphase separation where the coherently moving polar patterns self-organize into smectic structures [14] (see Fig. 1).

In this paper, building on the two prototypical models that are the Vicsek model and the active Ising model, we provide a comprehensive description of the emergent patterns found at the onset of the flocking transition from a hydrodynamic perspective. We first recall the definitions and phenomenologies of these two models in Sec. II. In Sec. III, we provide a simplified hydrodynamic description of the flocking models. In line with [15, 16], we show that these models support non-linear propagative solutions whose shape is described using a mapping onto the trajectories of point-like particles in one-dimensional potentials. Finding such solutions thus reduces to a classical mechanics problem with one degree of freedom. For given values of all the hydrodynamic coefficients, and hence of all underlying microscopic parameters, we find an infinity of solutions, describing both phase and microphase separations, that we fully characterize. We then show that the same results hold specifically for the hydrodynamic equations explicitly derived for the active Ising model [13] and for a simplified version of the Vicsek model [15]. Next, we investigate the linear stability of these solutions as solutions of the hydrodynamic equations in Sec. VI and their coarsening dynamics in Sec. VII. Finally, we provide full phase diagrams constructed from the hydrodynamic model in Sec. VIII. We close by discussing the similarities and differences with the phenomenology of

the agent-based models and conjecture on the role of the hydrodynamic noise in the selection of the band patterns.

## II. PHENOMENOLOGY OF MICROSCOPIC MODELS

Let us first briefly recall the phenomenology of the Vicsek and active Ising models. They are both based on the same two ingredients: Self-propulsion and a local alignment rule. The major differences between the two models are thus the symmetries of the alignment interaction and of the direction of motion.

### A. Vicsek model

In the Vicsek model [9], $N$ point-like particles, labeled by an index $i$, move at constant speed $v_0$ on a rectangular plane with periodic boundary conditions. At each discrete time step $\Delta t = 1$, the headings $\theta_i$ of all particles are updated in parallel according to

$$\theta_i(t+1) = \langle \theta_j(t) \rangle_{j \in \mathcal{N}_i} + \eta\, \xi_i^t \qquad (1)$$

where $\mathcal{N}_i$ is the disk of unit radius around particle $i$, $\xi_i^t$ a random angle drawn uniformly in $[-\pi, \pi]$, and $\eta$ sets the level of noise, playing a role akin to that of a temperature in a ferromagnetic XY model. Then, particles hop along their new headings: $\mathbf{r}_i(t+1) = \mathbf{r}_i(t) + v_0 \mathbf{e}_i^{t+1}$, where $\mathbf{e}_i^{t+1}$ is the unit vector pointing in direction given by $\theta_i(t+1)$.

### B. Active Ising model

In the active Ising model [13], particles carry a spin $\pm 1$ and move on a 2D lattice with periodic boundary conditions. Their dynamics depend on the sign of their spin: A particle with spin $s$ jumps to the site on its right at rate $D(1 + s\varepsilon)$ and to the site on its left at rate $D(1 - s\varepsilon)$, where $0 \leq \varepsilon \leq 1$ measures the bias on the diffusion. On average, $+1$ particles thus self-propel to the right and $-1$ particles to the left at a mean velocity $v_0 \equiv 2D\varepsilon$. Both types of particles diffuse symetrically at rate $D$ in the vertical direction.

The alignment interaction is purely local. On a site $i$, a particle flips its spin $s$ at rate

$$W_i(s \to -s) = \exp\left(-\frac{s}{T}\frac{m_i}{\rho_i}\right) \qquad (2)$$

where $T$ is a temperature, and $m_i$ and $\rho_i$ are the magnetization and number of particles on site $i$. (An arbitrary number of particles is allowed on each site since there is no excluded volume interaction.)

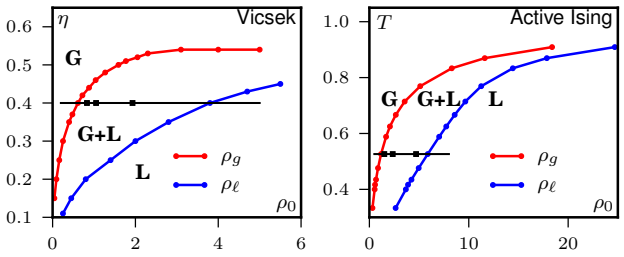


FIG. 2. Phase diagrams of the microscopic models. The red and blue lines delimit the domain of existence of (micro) phase-separated profiles. The black line and squares indicate the position of the snapshots shown in Fig. 1. $v_0 = 0.5$ for the Vicsek model, $D = 1$ and $\varepsilon = 0.9$ for the active Ising model.

### C. A liquid-gas phase transition

The phase diagrams in the temperature/noise-density ensemble are shown for both models in Fig. 2, highlighting their similarity. At high temperature/noise or low density both systems are in a homogeneous disordered gas state. At low temperature/noise and high density they are homogeneous and ordered; in these liquid phases, all particles move in average in the same direction. In the central region of the phase diagram, inhomogeneous profiles are observed, with liquid domains moving in a disordered gaseous background.

The phase transitions of both models have all the features of a liquid-gas transition, exhibiting metastability and hysteresis close to the transition lines [12–14]. The main difference between the two models lies in the coexistence region: In the active Ising model, the particles phase separate in a gaseous background and an ordered liquid band, both of macroscopic sizes [13]. The coexisting densities depend only on temperature and bias, but not on the average density; in the coexistence region, increasing the density at fixed $T, \varepsilon$ thus results in larger and larger liquid domains whose density remains constant, as shown in Fig. 1. Conversely, in the Vicsek model, the system forms arrays of ordered bands arranged periodically in space which have a finite width along their direction of motion: a micro-phase separation occurs [14]. As shown in Fig. 1, increasing the density at constant noise, the number of bands increases but their shape does not change [14].

Three types of propagating patterns can thus be observed at phase coexistence, all shown in Fig. 1: (i) localized compact excitations, (ii) Smectic microphases, and (iii) Phase-separated polar liquid domains. In the vicinity of the left coexistence line, collective motion emerges in the form of localized compact excitations in both models [22]. At higher density, phase-separated domains are found in the active Ising model and periodic "smectic" bands in the Vicsek model. Understanding the emergence of these three types of solutions will be the focus of the rest of the paper.

## III. HYDRODYNAMIC EQUATIONS

A lot of attention has been given in the literature to hydrodynamic equations of flocking models. Two different approaches have been followed, starting from phenomenological equations [11, 16, 17] or deriving explicitly coarse-grained equations from a microscopic model [13, 15, 18–20]. All these equations describe the dynamics of a conserved density field $\rho(\vec{r},t)$ coupled to a non-conserved magnetization field, the latter being a vector $\vec{m}(\vec{r},t)$ for continuous rotational symmetries, as in the Vicsek model, or a scalar $m(\vec{r},t)$, for discrete symmetries, as in the active Ising model.

We first introduce in Sec. III A two sets of hydrodynamic equations derived by coarse-graining microscopic models which will be discussed in this paper. Then, we turn in Sec. III B to a simpler set of phenomenological hydrodynamic equations on which we will establish our general results in Sec. IV.

### A. Coarse-grained hydrodynamic descriptions

We first consider the equations proposed by Bertin *et al.* to describe a simplified version of the Vicsek model [15], in which one solely considers binary collisions between the particles. One can then use, assuming molecular chaos, a Boltzmann equation formalism to arrive at the following hydrodynamic equations for the density field and a vectorial magnetization field [23]

$$\frac{\partial\rho}{\partial t} = -v_0\nabla\cdot\vec{m} \tag{3}$$

$$\frac{\partial\vec{m}}{\partial t} + \gamma(\vec{m}\cdot\nabla)\vec{m} = \nu\nabla^2\vec{m} - \frac{v_0}{2}\nabla\rho + \frac{\kappa}{2}\nabla(|\vec{m}|^2) - \kappa(\nabla\cdot\vec{m})\vec{m} + (\mu-\zeta|\vec{m}^2|)\vec{m} \tag{4}$$

The mass-conservation equation (3) simply describes the advection of the density by the magnetization field. Equation (4) can be seen as a Navier-Stokes equation complemented by a Ginzburg-Landau term $(\mu-\zeta|\vec{m}|^2)\vec{m}$, stemming from some underlying alignment mechanism, and leading to the emergence of a spontaneous magnetization. Because particles are self-propelled in a given frame of reference, these equations break Galilean invariance so that one can have $\gamma\neq 1$ and $\kappa\neq 0$ unlike e.g. in the Navier-Stokes equation.

In Eqs. (3) and (4), to which we refer to as "Vicsek hydrodynamic equations" hereafter, all the coefficients $\gamma$, $\nu$, $\kappa$, $\mu$ and $\zeta$, depend on the local density; see [15] for their exact expression.

The second set of equations, which we refer to as "Ising hydrodynamic equations" in the following, has been derived to describe the large-scale phenomenology of the active Ising model [13]. In this case, the dynamics of the density field and the scalar magnetization—corresponding to the Ising symmetry—are given by

$$\frac{\partial\rho}{\partial t} = D\Delta\rho - v_0\partial_x m \tag{5}$$

$$\frac{\partial m}{\partial t} = D\Delta m - v_0\partial_x\rho + 2\left(\beta - 1 - \frac{r}{\rho}\right)m - \alpha\frac{m^3}{\rho^2} \tag{6}$$

where $\beta = 1/T$, $\alpha$ and $r$ are positive coefficients depending on $\beta$ only and $v_0 = 2D\varepsilon$. The advection term $v_0\nabla\vec{m}$ of Eq. (3) is here replaced by a partial derivative $v_0\partial_x m$ because, in the active Ising model, the density is advected by the magnetization only in the $x$-direction.

### B. Phenomenological hydrodynamic equations with constant coefficients

Coarse-grained hydrodynamic equations derived from microscopic models have the advantage of expressing the macroscopic transport coefficients in terms of microscopic quantities (noise, self-propulsion speed, etc). However, these possibly complicated relations may not be relevant to understand the qualitative behavior of the models. Thus, before discussing the Vicsek and Ising hydrodynamic equations in Sec. V, we first study in detail, in Sec. IV, a simpler model

$$\partial_t\rho = -v_0\nabla\cdot\vec{m} \tag{7}$$

$$\partial_t\vec{m} + \xi(\vec{m}\cdot\nabla)\vec{m} = D\nabla^2\vec{m} - \lambda\nabla\rho + a_2\vec{m} - a_4|\vec{m}|^2\vec{m} \tag{8}$$

where the transport coefficients $v_0$, $\xi$, $D$, $\lambda$ and $a_4$ are constant. In the following, we refer to these equations as the "phenomenological hydrodynamic equations". This simplified model is very similar to that first introduced by Toner and Tu from symmetry considerations [11]. However, unlike the original Toner and Tu model, we keep an explicit density dependence in $a_2$: $a_2(\rho) = \rho - \varphi_g$, which is essential to account for inhomogeneous profiles [13, 15, 17].

The stability criteria of the homogeneous solutions ($\rho(\mathbf{r},t) = \rho_0$, $\vec{m}(\mathbf{r},t) = \vec{m}_0$) of Eqs. (7-8) are readily computed:

- For $\rho_0 < \varphi_g$ ($a_2(\rho_0) < 0$) only the disordered solution ($\rho_0$, $|\vec{m}_0| = 0$) exists and is stable
- For $\rho_0 > \varphi_g$ ($a_2(\rho_0) > 0$) the disordered solution becomes unstable and ordered solutions ($\rho_0$, $|\vec{m}_0| = \sqrt{(\rho_0-\varphi_g)/a_4}$) appear.
- The ordered solutions are linearly stable only when $\rho_0 > \varphi_\ell = \varphi_g + \frac{1}{4a_4v_0+2\lambda}$

Thus, in the range $\rho_0\in[\varphi_g,\varphi_\ell]$, homogeneous solutions are linearly unstable. In the language of the liquid-gas transition, $\varphi_g$ and $\varphi_\ell$ are the gas and liquid spinodals, between which the homogeneous phases are linearly unstable and spinodal decomposition takes place. In the

next section we address the existence of heterogenous ordered excitations propagating through stable disordered (gaseous) backgrounds. This analysis will make it possible both to identify all the possible flocking patterns and to further understand the first-order nature of the flocking transition.

## IV. PROPAGATIVE SOLUTIONS

Let us now establish and classify all the inhomogeneous propagating solutions of Eqs. (7-8). In order to do so, we first recast this problem into a dynamical system framework in section IV A. We then show in section IV B that three types of propagating solutions exist with different celerities $c$ and densities of the gaseous background $\rho_g$. Sections IV C, IV D and IV E are dedicated to a detailed study of how these solutions depend on $c$ and $\rho_g$. Section IV F shows how, once the average density is fixed, we are left with a one-parameter family of solutions. Last, section IV G is devoted to cases where the inhomogeneous profiles can be studied analytically.

### A. Newton Mapping

Following [15], we look for inhomogeneous polar excitations invariant along, say the $y$ direction, and which propagate, and/or relax solely along the $x$ direction. We thus assume, $m_y = 0$ and reduce Eqs. (7-8) to:

$$\partial_t \rho = -v_0 \partial_x m \tag{9}$$

$$\partial_t m + \xi m \partial_x m = D\partial_x^2 m - \lambda \partial_x \rho + (\rho - \varphi_g) m - a_4 m^3 \tag{10}$$

where we wrote $m = m_x$ to ease the notation. We look for solutions propagating steadily at a speed $c$. Introducing the position $z = x - ct$ in the frame moving at $c$: $\rho(x,t) = \rho(z)$, $m(x,t) = m(z)$, we obtain

$$c\dot{\rho} - v_0 \dot{m} = 0 \tag{11}$$

$$D\ddot{m} + (c - \xi m)\dot{m} - \lambda \dot{\rho} + (\rho - \varphi_g) m - a_4 m^3 = 0 \tag{12}$$

where the dots denote derivation with respect to $z$. Solving Eq. (11) gives $\rho(z) = \rho_g + \frac{v_0}{c} m(z)$. If $\rho(z)$ is localized in space, $\rho_g$ has a simple meaning. Since $\rho(z) = \rho_g$ when $m(z) = 0$, the integration constant $\rho_g$ is the density in the gaseous phase surrounding the localized polar excitation. We can then insert the expression of $\rho$ in Eq. (12) and obtain the second-order ordinary differential equation

$$D\ddot{m} + (c - \frac{\lambda v_0}{c} - \xi m)\dot{m} - (\varphi_g - \rho_g) m + \frac{v_0}{c} m^2 - a_4 m^3 = 0 \tag{13}$$

Following [15, 16], we now provide a mechanical interpretation of Equation (13) through the well-known Newton mapping. Rewriting Eq. (13) as:

$$D\ddot{m} = -f(m)\dot{m} - \frac{dH}{dm} \tag{14}$$

$$H(m) = -(\varphi_g - \rho_g)\frac{m^2}{2} + \frac{v_0}{3c} m^3 - \frac{a_4}{4} m^4 \tag{15}$$

$$f(m) = c - \frac{\lambda v_0}{c} - \xi m \tag{16}$$

it is clear that this equation corresponds to the mechanical equation of motion of a point particle. The position of the particle is $m$, $z$ is the time variable, $D$ is the mass of the particle, $H(m)$ is an energy potential and $f(m)$ is a position-dependent friction. The trajectory $m(z)$ of this fictive particle exactly corresponds to the shape of the propagative excitations of our hydrodynamic model in the frame moving at a speed $c$ (see Fig. 3).

We shall stress that for a given hydrodynamic model, Eq. (14) is parametrized by the two unknown parameters $c$ and $\rho_g$ which *a priori* can take any value. Each pair ($c$, $\rho_g$) gives different potential $H$ and friction $f$, and hence different trajectories $m(z)$. We now turn to the study of these trajectories and of the corresponding admissible values for the celerity $c$ and the gas density $\rho_g$.

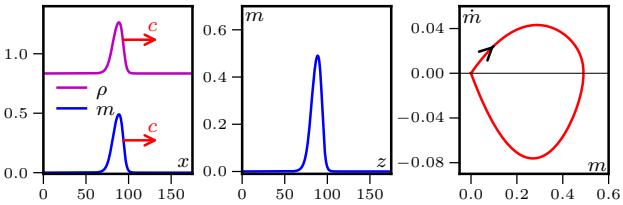


FIG. 3. **Left**: Density and magnetization profiles of a propagative solution of the hydrodynamic Eqs. (7-8). **Center**: Magnetization profile in the comoving frame $z = x - ct$ or, equivalently, trajectory $m(z)$ of a point particle in the spurious time $z$. **Right**: Phase portrait corresponding to the trajectory $m(z)$. Parameters: $D = v_0 = \lambda = \xi = a_4 = \varphi_g = 1$.

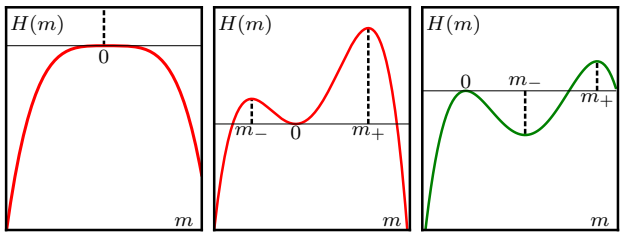


FIG. 4. The green potential can give rise to physical (positive, non-exploding) solutions while the red ones are ruled out by our conditions (C1) (left) and (C2) (center).

### B. Three possible propagating patterns

The original problem of finding all the inhomogeneous propagative solutions $m(x,t)$, $\rho(x,t)$ of the hydrodynamic equations is now reduced to finding all the pairs ($c$,

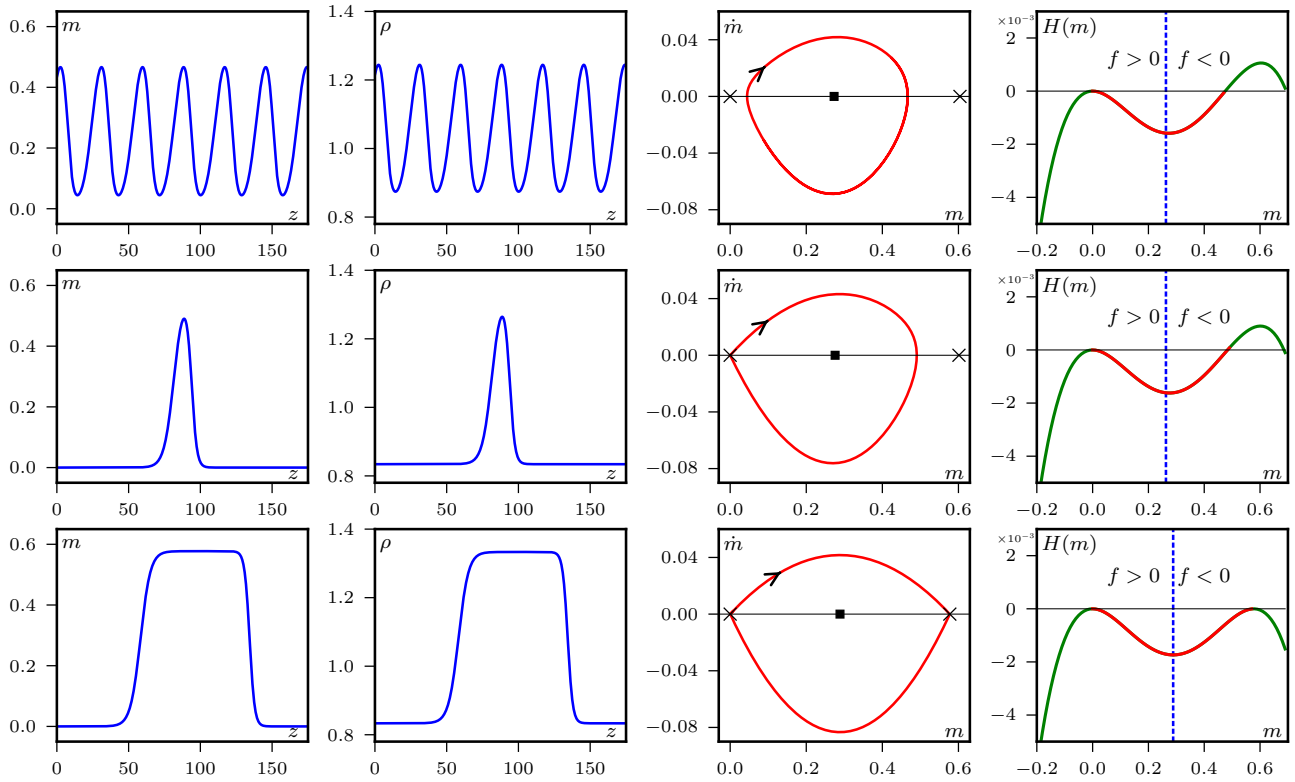


FIG. 5. Example of the three types of trajectories. From left to right: magnetization and density profiles, phase portrait, and potential $H$. **Top row**: Periodic trajectory, $\rho_g = 0.835$, $c = 1.14$. **Center row**: Homoclinic trajectory, $\rho_g = 0.83412$, $c = 1.14$. **Bottom row**: Heteroclinic trajectory, $\rho_g = 0.83333$, $c = 1.1547$. Phase portrait: Crosses indicate saddle points at $m = 0$ and $m = m_+$. Squares indicate stable fixed points at $m = m_-$. Potentials: The blue dashed line indicate where the friction changes sign. The red portion of the potential is the one visited by the trajectory. Parameters: $D = v_0 = \lambda = \xi = a_4 = \varphi_g = 1$.

$\rho_g$) for which the corresponding trajectories $m(z)$ exist. Mass conservation, Eq. (9), imposes the boundary condition $m(z = -\infty) = m(z = +\infty)$ so that we are looking for solutions of (14) which are closed in the $(m, \dot{m})$ plane. An example of propagative solutions $m(x, t)$, $\rho(x, t)$ together with the corresponding trajectory $m(z)$ and its phase portraits is shown in Fig. 3.

To put a first constraint on $\rho_g$ and $c$, let us rule out the potentials which cannot give such physical solutions. The extrema of $H$, solutions of $H'(m) = 0$, are located at $m = 0$ and $m = m_\pm$ with

$$m_\pm = \frac{v_0}{2a_4 c}\left(1 \pm \sqrt{1 - \frac{4a_4(\varphi_g - \rho_g)c^2}{v_0^2}}\right) \tag{17}$$

We can already discard the case where $H'(m)$ has two complex roots since $H$ then has a single maximum at $m = 0$, and all trajectories wander to $m = \pm\infty$ (see Fig. 4, left). This leads to a first condition on $c$, $\rho_g$:

$$(\varphi_g - \rho_g)c^2 < a_4 v_0^2 \tag{C1}$$

Without loss of generality we can assume that $c > 0$ and look only for solutions with $m \geq 0$. This rules out the $(c, \rho_g)$ values for which $m_- < 0$ and $m_+ > 0$ which give oscillations between negative and positive values of $m$ (see Fig. 4, central panel). At the hydrodynamic equation level, such solutions would indeed correspond to different parts of the profiles moving in opposite direction. The corresponding condition

$$\rho_g < \varphi_g \tag{C2}$$

imposes $0 < m_- < m_+$. The potential $H$ then has two maxima, at $m = 0$ and $m = m_+$, and one minimum, at $m = m_-$. The typical shape of potential which gives admissible solutions is shown in Fig. 4 along with examples of potentials ruled out by conditions (C1) and (C2).

>From the admissible shape of the potential $H$, we can now list all possible trajectories $m(z)$ and the corresponding fields $m(x, t)$, $\rho(x, t)$:

- Limit cycles, whose corresponding magnetisation profiles are periodic bands, as shown in the first row of Fig. 5.
- Homoclinic orbits, that start infinitely close to a maximum of $H$, hence spending an arbitrary large time there, before crossing twice the potential well

in a finite time to finally return to the same maximum of $H$ at $z = \infty$. These trajectories correspond to isolated solitonic band profiles, as shown in the second row of Fig. 5.

- Heteroclinic orbits that spend an arbitrary large time close to a first maximum of $H$, cross the potential well in a finite time, spend an arbitrary large time close to the second maximum of $H$, before returning to the first maximum. These trajectories correspond to phase separated profiles. The arbitrary waiting times at the two maxima of $H$ then reflect the arbitrary sizes of two phase-separated domains (see the third row of Fig. 5).

A third condition on $\rho_g, c$ arises from the non-linear friction term. Following the classical mechanics analogy, we define an energy function

$$E = \frac{1}{2} D\dot{m}^2 + H \tag{18}$$

Multiplying the equation of motion (13) by $\dot{m}$, we get

$$\frac{dE}{dz} = -f(m)\dot{m}^2 \tag{19}$$

Energy is injected when $f(m) < 0$ and dissipated when $f(m) > 0$. On a closed trajectory, the friction $f$ must thus change sign. Since $f$ is a decreasing function of $m$, this imposes $f(0) > 0$ for trajectories with $m(z) > 0$, or equivalently

$$c > \sqrt{\lambda v_0} \tag{C3}$$

The conditions (C1), (C2) and (C3) thus provide loose bounds on the subspace of the $(c, \rho_g)$ plane which contains the three types of trajectories $m(z)$ described above. These trajectories correspond to the three types of inhomogeneous profiles seen in the microscopic models [24]. Before studying the stability and coarsening of these propagative solutions, we first need to understand precisely how they are organised in the $(c,\ \rho_g)$ plane. In order to do so, we first analyze the phase portrait of the dynamics (14). We then study how the phase portrait evolves when $\rho_g$ and $c$ are varied.

### C. Stability of the fixed points

The structure of the phase portrait is most easily captured by locating the fixed points of (14) and studying their stability. We first rewrite (14) as a system of two first-order differential equations:

$$\frac{d}{dz}\begin{pmatrix} m \\ \dot{m} \end{pmatrix} = \begin{pmatrix} \dot{m} \\ -\frac{f(m)}{D}\dot{m} - \frac{H'(m)}{D} \end{pmatrix} \tag{20}$$

The fixed points are the solutions satisfying $\dot{m} = 0$ and $H'(m) = 0$, *i.e.*, the constant solutions extremizing $H$. As explained before, because of the condition (C2), the extrema of $H$ at $m = 0, m_-, m_+$ are such that $0 < m_- < m_+$, so that 0 and $m_+$ are two maxima and $m_-$ is a minimum of $H$.

Linearizing the dynamics around one of the fixed points, we define $m = m_0 + \delta m$ with $m_0 = 0,\ m_-, m_+$, so that $\dot{m} = \delta\dot{m}$ and

$$\frac{d}{dz}\begin{pmatrix} \delta m \\ \delta\dot{m} \end{pmatrix} = \begin{pmatrix} 0 & 1 \\ -H''(m_0)/D & -f(m_0)/D \end{pmatrix}\begin{pmatrix} \delta m \\ \delta\dot{m} \end{pmatrix} \tag{21}$$

The stability of the fixed points is given by the eigenvalues $\lambda_{1,2}$ of the $2 \times 2$ matrix which read

$$\lambda_{1,2}(m_0) = \frac{-f(m_0)}{2D} \pm \sqrt{\left(\frac{f(m_0)}{2D}\right)^2 - \frac{H''(m_0)}{D}} \tag{22}$$

- At the maxima $m_0 = 0$ and $m_0 = m_+$ of $H$, $H''(m_0)$ is negative and the two eigenvalues are thus real with opposite signs. These fixed points are saddle points with one unstable direction ($\lambda_1 > 0$) and one stable direction ($\lambda_2 < 0$).

- At the minimum $m_0 = m_-$ of $H$, $H''(m_0)$ is positive and the real part of the two eigenvalues have the same sign, given by $-f(m_-)$. The fixed point is stable when $f(m_-) > 0$ and unstable when $f(m_-) < 0$. Physically, when the friction of the fictive particle is negative around $m = m_-$, small perturbations are amplified, driving the trajectory away from the fixed point. Conversely, a positive friction damps any initial perturbation, leading to trajectories converging towards $m_-$.

  When $c$ and $\rho_g$ are such that $f(m_-) = 0$, $\lambda_{1,2}$ are complex conjugate imaginary numbers. A Hopf bifurcation takes place, leading to the apparition of a limit cycle.

At the onset of a Hopf bifurcation, a limit cycle appears around the fixed point whose stability changes. In the following sections we elucidate how the interplay between the saddle-point and the Hopf dynamics rules the non-linear dynamics of the fictive particle and hence the polar-band shape.

### D. Hopf bifurcation

Let us first provide a comprehensive characterization of the Hopf bifurcation. It happens when the real part of $\lambda_{1,2}$ vanishes, *i.e.*, when

$$f(m_-) = c - \frac{\lambda v_0}{c} - \xi m_-(c, \rho_g) = 0 \tag{23}$$

where $m_-$, which depends on both $c$ and $\rho_g$, is given by Eq. (17). Equation (23) is satisfied on the line

$$\rho_g^H(c) = \varphi_g + \frac{(-c^2 + v_0\lambda)(-a_4c^2 + a_4v_0\lambda + v_0\xi)}{c^2\xi^2} \tag{24}$$

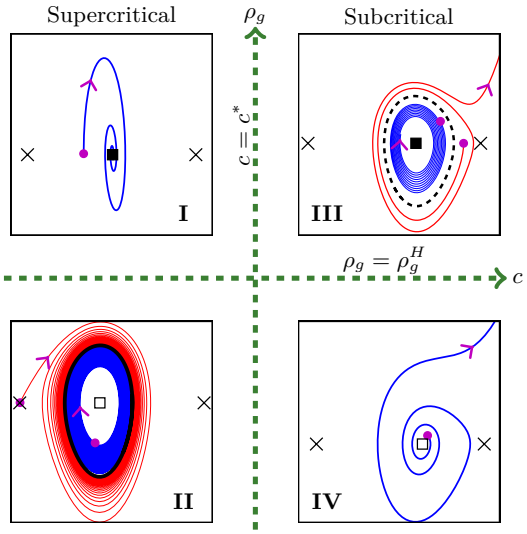


FIG. 6. The four types of phase portrait $(m, \dot{m})$ obtained in our system when changing $\rho_g$ and $c$. The line $\rho_g = \rho_g^H$ is where the Hopf bifurcation takes place. The bifurcation is supercritical for $c < c^*$ and subcritical for $c > c^*$. The plain (resp. open) black squares denote stable (resp. unstable) fixed points at $m = m_-$. The plain (resp. dashed) black lines denote stable (resp. unstable) limit cycles. The crosses denote the saddle points at $m = 0$ and $m = m_+$. The initial condition of each trajectory is marked by a magenta disk and the direction of "time" $z$ indicated by a magenta arrow.

which we call the Hopf transition line.

Following standard text books in bifurcation theory [21], the type of Hopf bifurcation (super- or subcritical) is given by the sign of

$$\Delta = \frac{\xi^2}{16\omega D^3} H'''(m_-, \rho_g^H) \frac{\partial m_-}{\partial \rho_g}(\rho_g^H) \tag{25}$$

where $\omega = \sqrt{H''(m_-, \rho_g^H)/D} > 0$ is the imaginary part of the eigenvalues at the bifurcation point. Moreover

$$\frac{\partial m_-}{\partial \rho_g} = \frac{-1}{\sqrt{\frac{v_0^2}{c^2} - 4a_4(\varphi_g - \rho_g)}} \tag{26}$$

is always negative because of condition (C1). The sign of $\Delta$ is thus given by the sign of $H'''(m_-, \rho_g^H)$, which changes at $c = c^*$ with

$$c^* = \frac{\sqrt{v_0(3a_4\lambda + \xi)}}{\sqrt{3a_4}} \tag{27}$$

Two different scenarios occur depending on whether $c$ is larger or smaller than $c^*$.

- When $c < c^*$, the Hopf bifurcation is supercritical ($\Delta > 0$). The system branches from a stable fixed point for $\rho_g > \rho_g^H$ (case I, Fig. 6) to a stable limit cycle surrounding an unstable fixed point for $\rho_g < \rho_g^H$ (case II, Fig. 6).
- When $c > c^*$, the Hopf bifurcation is subcritical ($\Delta < 0$). The system branches from an unstable fixed point when $\rho_g < \rho_g^H$ (case IV, Fig. 6) to an unstable limit cycle surrounding a stable fixed point when $\rho_g > \rho_g^H$ (case III, Fig. 6).

The organisation of these four typical cases in the $(c, \rho_g)$ plane is illustrated in Fig. 6. We thus see that, when $c < c^*$, limit cycles exist for $\rho_g$ *smaller* than $\rho_g^H$, whereas when $c > c^*$, they exist for $\rho_g$ *larger* than $\rho_g^H$. The Hopf bifurcation line is thus a boundary of the domain of existence of periodic propagative solutions of the hydrodynamic equations. Let us now consider what happens when we explore the $c, \rho_g$ plane further away from the Hopf bifurcation line.

### E. Structure of the $(c, \rho_g)$ solution space

So far, we have shown that three different types of trajectories $m(z)$ (periodic, homoclinic and heteroclinic) can be found by varying the values of $c$, $\rho_g$. The subspace where these physical solutions can be found was first bounded by the conditions (C1), (C2), and (C3). In the previous section, we further found that the Hopf transition line $\rho_g^H(c)$ given by Eq. (24) is the upper boundary for the admissible values of $\rho_g$ when $c < c^*$ and the lower boundary when $c > c^*$.

To explore the remaining $(c, \rho_g)$ space, we numerically integrated the dynamical system (20) using a Runge-Kutta scheme of order 4. Starting from different initial conditions, one easily finds the basins of attraction of the different solutions. To locate unstable fixed points and limit cycles, we integrated the dynamics backward in time since they are attractors when $z \to -\infty$. As $c$ and $\rho_g$ vary, so do the shapes and sizes of the limit cycles. To quantify these variations, we measured the "amplitude" of a cycle, defined as the difference between the two extrema of $m(z)$

$$\Delta m \equiv \max_z[m(z)] - \min_z[m(z)] \tag{28}$$

We systematically vary $\rho_g$ at fixed $c$, first focussing on the case $c < c^*$ where the Hopf bifurcation is supercritical. Decreasing $\rho_g$, a stable limit cycle of vanishing amplitude appears at $\rho_g = \rho_g^H$ (Fig. 7, panel A). The amplitude of the cycle then increases as $\rho_g$ decreases (Fig. 7, panel B) until it hits the fixed point at $m = 0$ where the limit cycle becomes an homoclinic trajectory (Fig. 7, panel C). For even lower $\rho_g$ the particle escapes to $m = -\infty$. The variation of the cycle amplitude with $\rho_g$ shown in Fig. 7 can be qualitatively explained. When $\rho_g$ decreases, the distance $m_- - m_f$ increases, where $m_f = \frac{1}{\xi}(c - \lambda v_0/c)$ is the value of $m$ where the friction changes sign, i.e., $f(m_f) = 0$. More energy is thus injected in the system and, to dissipate this energy, the trajectory need to go closer to $m = 0$.

A symmetric behavior is observed when $c > c^*$, for the subcritical Hopf bifurcation. Increasing $\rho_g$, an unstable

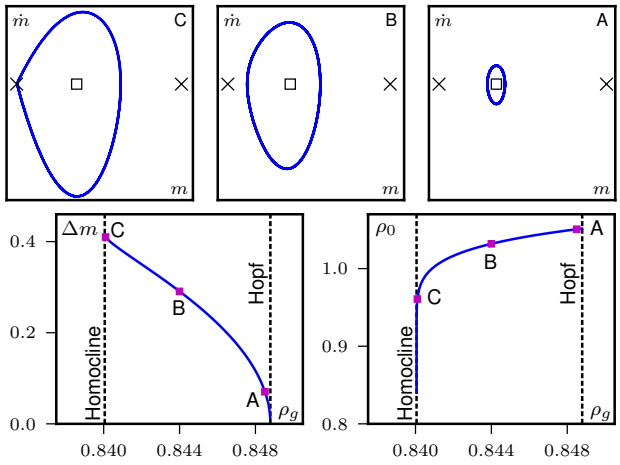


FIG. 7. Line at fixed $c = 1.12$ in the $(c, \rho_g)$ space, for $c < c^*$. **Top**: Three phase portraits along the line, from the vicinity of the Hopf bifurcation line (A) until the homoclinic is found (C) **Bottom-left**: Size of the limit cycle $\Delta m$ defined in Eq. (28). The limit cycle disappears when $\Delta m$ is large enough that the orbit reaches $m = 0$, where the trajectory is homoclinic. **Bottom-right**: Average density $\rho_0$ of the solutions. Parameters: $D = v_0 = \lambda = \xi = a_4 = \varphi_g = 1$.

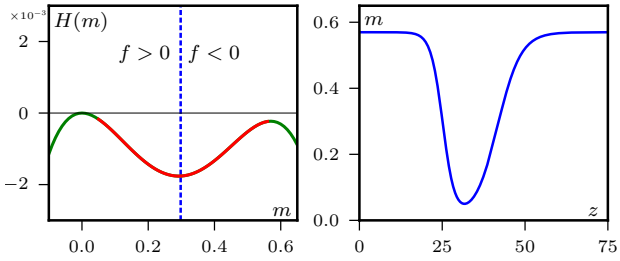


FIG. 8. Unstable homoclinic trajectory starting from $m = m_+$ for $c = 1.16$. Parameters: $D = v_0 = \lambda = \xi = a_4 = \varphi_g = 1$.

limit cycle of vanishing amplitude appears at $\rho_g = \rho_g^H$. The amplitude of the cycle then increases with $\rho_g$ until the trajectory hits the point $m = m_+$ where we have an (unstable) homoclinic solution that starts from $m = m_+$ as shown in Fig. 8. Physically, when increasing $\rho_g$, $m_f - m_-$ increases so that the friction around the stable fixed point at $m = m_-$ becomes larger and thus its basin of attraction (whose boundary is the unstable limit cycle, see Fig. 6) becomes larger.

All in all, the central results of this section is that all the admissible solutions lie in a band delimited by the Hopf bifurcation line $\rho_g^H(c)$ and a line where the homoclinic trajectories are found, as shown in Fig. 9. Inside this band there exists stable non-degenerate limit cycles, corresponding to periodic propagating profiles. The unique heteroclinic trajectory is located exactly at $c = c^*$ where the Hopf bifurcation changes from supercritical to subcritical. We thus observe a 2-parameter family of periodic solutions, a line of homoclinic trajectories and a

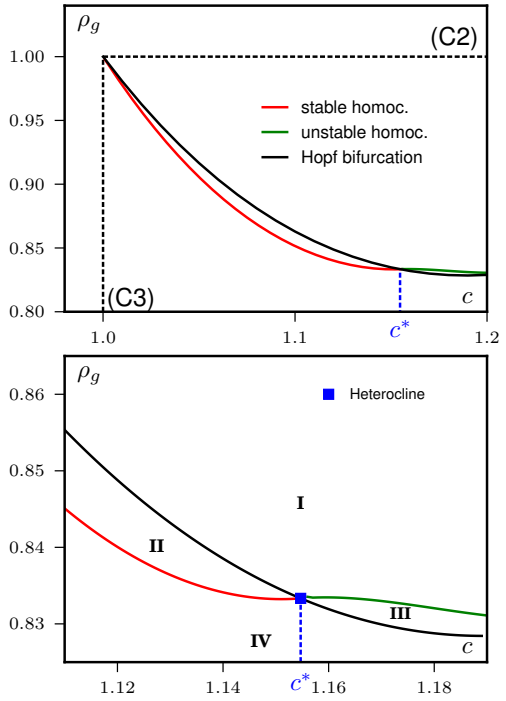


FIG. 9. Space of all solutions. A 2-parameter family of periodic orbits is found inside the band delimited by the Hopf bifurcation and the homoclinic trajectories. The constraints (C2) and (C3) are indicated by the black dashed lines. The constraint (C1) lies out the range of this plot. **Bottom**: Zoom of the plot above around the point $c = c^*$ where the Hopf bifurcation changes from supercritical to subcritical. This is also where the unique heteroclinic trajectory is found. The roman numbers refer to Fig. 6, indicating the type of phase portrait found in each region. Parameters: $D = v_0 = \lambda = \xi = a_4 = \varphi_g = 1$.

unique heteroclinic trajectory. Going back to the original pattern formation problem, they correspond to a 2-parameter family of micro-phase separated profiles, a line of isolated solitonic bands and a unique phase-separated state where a macroscopic polar liquid domain cruises through a disordered gas.

### F. Working at fixed average density

In the microscopic models and the original hydrodynamic equations the average density $\rho_0$ is a conserved quantity fixed by the initial condition. On the contrary, when considering the trajectories of the fictive particle $m(z)$, $\rho_0$ is not *a priori* fixed and varies between the different solutions. To compute the mean density on a trajectory $m(z)$ we simply average $\rho(z) = \rho_g + v_0 m(z)/c$ over time.

As shown in Fig. 7 (bottom-right), we find that at fixed $c < c^*$, $\rho_0$ decreases when $\rho_g$ decreases. It ranges from $\rho_0 = \rho_g + \frac{v_0}{c} m_-$ when $\rho_g = \rho_g^H$ to $\rho_0 = \rho_g$ at the homo-

clinic trajectory where the portion of the trajectory with $m(z) \neq 0$ becomes negligibly small. Note that, at the heteroclinic trajectory, $\rho_0$ can take a large range of values. Since the size of the gas and liquid domains are arbitrary, the average density can take any value in $[\rho_g^h, \rho_\ell^h]$ where $\rho_g^h$ and $\rho_\ell^h$ are the densities in the gas and liquid domains respectively.

Fixing $\rho_0$ adds a constraint that selects a line of solutions in the $(c,\, \rho_g)$ space, as shown in Fig. 10 (left). For all $\rho_0 \in [\rho_g^h, \rho_\ell^h]$ these lines end at the heteroclinic trajectory. We also observe that, at fixed $\rho_0$, the closer the trajectories are to the heteroclinic solution, the larger their amplitude (see Fig. 10, right). This means that along a line $\rho_0 = \text{cst}$, the higher the amplitude the faster the band excitations propagate. This point will turn out to be crucial when discussing the coarsening dynamics at the hydrodynamic level in Sec. VII.

Until now, we have shown that three different types of possible trajectories $m(z)$ exist, which correspond to all the propagative solutions observed in the microscopic models of flying spins. We have further identified the subset of values of the propagation speed $c$ and the gas density $\rho_g$ for which these solutions exist. We can now turn to the study of their dynamical stability at the hydrodynamic equation level. However, we first discuss analytically in the next section the shape of inhomogeneous solutions.

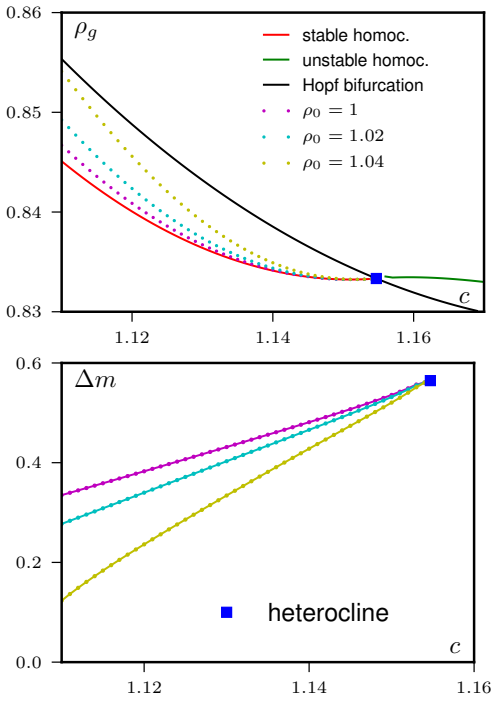


FIG. 10. **Top**: Lines of solutions having a fixed average density $\rho_0$ in the space of all solutions. **Bottom**: the amplitude $\Delta m$ of the cycles, defined in Eq. (28), along the lines $\rho_0 = \text{cst}$ increases when $c$ increases. Parameters: $D = v_0 = \lambda = \xi = a_4 = \varphi_g = 1$.

### G. Exact solution for the heterocline

There are no general analytic solutions for the propagating inhomogeneous profiles. However, progress is possible for some limiting cases. In the following we show that a complete solution for the heterocline – its position in the $(c,\, \rho_g)$ plane and its shape – can be determined exactly [13]. In A, we then show that, although exact solutions are not available, progress regarding the shape of the homoclinic solutions is achievable in the small $D$ limit.

To compute the shape of the heterocline, let us start from the ansatz

$$m_{1,2}(z) = \frac{m_\ell}{2}\Big[1 + \tanh\left(k_{1,2}(z - z_{1,2})\right)\Big] \tag{29}$$

Each of $m_1(z)$ and $m_2(z)$ describe an interface centered around $z = z_{1,2}$ between a disordered phase with $m = 0$ and an ordered phase with $m = m_\ell$. The complete heteroclinic trajectory then consists of two fronts glued together: An ascending front $m_1(z)$ with $k_1 > 0$ and a descending front $m_2(z)$ with $k_2 < 0$, with $z_2 \gg z_1$ (see Fig. 11); Being part of the same profile, the two fronts share the same celerity $c$ and density $\rho_g$.

Moreover we know that $m_\ell$ must be located at the second maximum of $H$ so that

$$m_\ell = m_+ = \frac{v_0}{2a_4 c}\left(1 + \sqrt{1 - \frac{4a_4(\varphi_g - \rho_g)c^2}{v_0^2}}\right) \tag{30}$$

Plugging $m_1$ and $m_2$ in Eq. (13) and replacing $m_\ell$ by its expression, one obtains for each of the fronts

$$g(c, \rho_g, k_{1,2}) + h(c, \rho_g, k_{1,2}) \tanh\left(k_{1,2}(z - z_{1,2})\right) = 0 \tag{31}$$

where $g$ and $h$ are complicated functions that we omit for conciseness. Eq. (31) can be true only if $g$ and $h$ vanish independently, for both $k_1$ and $k_2$.

We can express $k_1$ and $k_2$ as functions of $c$ and $\rho_g$ by linearizing the ansatz (29) around $m = 0$. When $k_{1,2}(z - z_{1,2}) \to -\infty$, one has $m_{1,2} \sim \exp(2k_{1,2}(z - z_{1,2}))$ so that we can identify $k_{1,2}$ with the two eigenvalues of the linear stability analysis Eq. (22). The ascending front is associated with the unstable direction $k_1 = \lambda_1/2$ and the descending front with the stable direction $k_2 = \lambda_2/2$.

Replacing $k_{1,2}$ by their values in Eq. (31), we have four equations for the two unknowns $c$ and $\rho_g$. After some algebra, one obtains a unique solution $(c^h,\, \rho_g^h)$ with

$$c^h = c^* = \frac{\sqrt{v_0(3a_4\lambda + \xi)}}{\sqrt{3a_4}} \tag{32}$$

$$\rho_g^h = \varphi_g - \frac{2v_0}{9a_4\lambda + 3\xi} \tag{33}$$

This gives us the magnetization $m_\ell$ and the the fronts

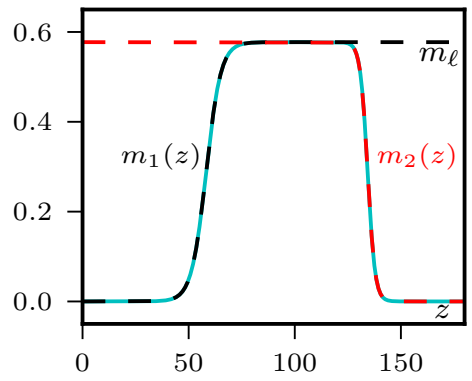


FIG. 11. Comparison between the exact solution for the heterocline (dashed lines) and the result from numerical integration of Eq. (20) (blue line). Parameters: $D = v_0 = \lambda = \xi = a_4 = \varphi_g = 1$.

steepness $k_{1,2}$ as

$$m_\ell = \frac{2v_0}{\sqrt{3a_4 v_0(3a_4\lambda + \xi)}} \tag{34}$$

$$k_1 = \frac{\sqrt{v_0(8a_4 D + \xi^2)} - \sqrt{v_0}\xi}{4D\sqrt{3a_4(3a_4\lambda + \xi)}} \tag{35}$$

$$k_2 = \frac{-\sqrt{v_0(8a_4 D + \xi^2)} - \sqrt{v_0}\xi}{4D\sqrt{3a_4(3a_4\lambda + \xi)}} \tag{36}$$

In Fig. 11, we show that this solution matches exactly the heteroclinic orbit found by numerical integration of Eq. (20).

## V. BACK TO THE VICSEK-LIKE AND THE ACTIVE ISING MODELS: NON-LINEAR SOLUTIONS OF THE HYDRODYNAMIC EQUATIONS

In Sec. III and IV we consider phenomenological hydrodynamic equations and assumed the simplest possible dependences of their coefficients with density. Here we extend our study to the more realistic hydrodynamic equations presented in Sec III A. We first consider in Sec. V A the Vicsek hydrodynamic equations before turning to the Ising hydrodynamic equations in Sec. V B. For sake of completeness, we also consider in Appendix B a more general case where the potential $H$ appearing in the dynamical system for $m(z)$ is not a polynomial in $m$. While not directly relevant for the hydrodynamic equations studied in this paper for the Vicsek and active Ising model, such Hamiltonians cannot be ruled out and may arise, for instance, from a density-dependence of the coefficient $a_4$ in the phenomenological hydrodynamic equations (8).

### A. Vicsek like equations

Let us consider the hydrodynamic equations (3-4) introduced by Bertin and co-workers to describe a simplified version of the Vicsek model [15]. These equations have the same structure as the phenomenological equations (7-8) with two additional gradient terms $\frac{\kappa}{2}\nabla(|\vec{m}|^2)$ and $-\kappa(\nabla\cdot\vec{m})\vec{m}$. Importantly, all the coefficients $\gamma$, $\nu$, $\kappa$, $\mu$ and $\zeta$ depend on the density.

We follow the same approach as before. Looking for propagative solutions invariant in the transverse direction we set $m_y = 0$, write $m_x = m$, and go to the comoving frame $z = x - ct$, to obtain

$$c\dot{\rho} - v_0\dot{m} = 0 \tag{37}$$

$$\nu\ddot{m} + \left(c - \frac{v_0^2}{2c}\right)\dot{m} - \gamma m\dot{m} - \frac{v_0}{2}\dot{\rho} + \mu m - \zeta m^3 = 0 \tag{38}$$

Note that after setting $m_y = 0$ the two $\kappa$ gradient terms of Eq. (4) cancel each other.

As before, Eq. (37) directly yields

$$\rho(z) = \rho_g + \frac{v_0}{c}m(z) \tag{39}$$

As we show in Appendix C, Eq. (38) can also be greatly simplified using the explicit density-dependence of its coefficients. Introducing $\tilde{\gamma} = \gamma/\nu$, $\tilde{\zeta} = \zeta/\nu$, and writing $\mu = \mu_1\rho - \mu_2$ and $\nu^{-1} = \nu_1\rho + \nu_2$, one obtains the second-order ordinary differential equation

$$\ddot{m} + (\alpha - \xi m)\dot{m} - a_2 m + a_3 m^2 - a_4 m^3 = 0 \tag{40}$$

where the coefficients are all function of $c$ and $\rho_g$

$$\alpha = \left(c - \frac{v_0^2}{2c}\right)(\nu_1\rho_g + \nu_2) \qquad \xi = \frac{v_0^3}{2c^2}\nu_1 + \tilde{\gamma} \tag{41}$$

$$a_2 = \mu_2\nu_2 + (\mu_2\nu_1 - \mu_1\nu_2)\rho_g - \mu_1\nu_1\rho_g^2$$

$$a_3 = \frac{v_0}{c}\left(2\rho_g\mu_1\nu_1 + \mu_1\nu_2 - \mu_2\nu_1\right)$$

$$a_4 = \tilde{\zeta} - \frac{v_0^2}{c^2}\mu_1\nu_1$$

Interestingly, Eq. (40) has exactly the same form as Eq. (13)—the dynamical system stemming from the phenomenological hydrodynamic equations studied in Sec IV—although with coefficients depending in a more complicated way on $\rho_g$ and $c$. Their propagative solutions will thus be the same, up to a slightly different organisation in the $c, \rho_g$ plane.

However, an important difference between the Vicsek and phenomenological hydrodynamic equations, is the scaling of the magnetization with density in the ordered phase. The Vicsek hydrodynamic equations (3-4) of Bertin and co-workers indeed predict that the homogeneous ordered solution satisfies

$$\frac{|\vec{m}_0|}{\rho_0} = \frac{1}{\rho_0}\sqrt{\frac{\mu}{\zeta}} \xrightarrow[\rho_0\to\infty]{} \sqrt{\frac{\mu_1\nu_1}{\tilde{\zeta}}} \tag{42}$$

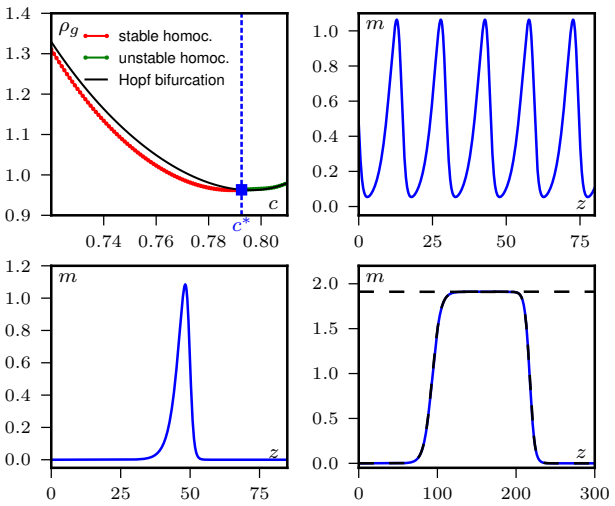


FIG. 12. **Top left**: Phase diagram for the propagative solutions of the hydrodynamic equations of Bertin *et al.* Eq. (40). The color code and different phases are the same as for the $a_4 = \text{cst}$ case Fig. 9. We obtain the same three types of inhomogeneous profiles: periodic, homoclinic and heteroclinic. $\sigma = 0.7$.

which is consistent with what is observed in microscopic models such as the Vicsek model. On the contrary, because the coefficient $a_4$ in Eq. (8) does not depend on density, the phenomenological equations (7-8) would yield $\frac{m_0}{\rho_0} \to 0$ as $\rho_0$ increases. In this region of parameter space, which is not the main focus of this paper, the Vicsek hydrodynamic equations are thus more faithful to the phenomenology of microscopic models studied in Sec. II than the phenomenological equations (7-8). As we show in Appendix B, however, these phenomenological equations can recover a scaling akin to that of the Vicsek model if the coefficient $a_4$ of Eq. (8) is allowed to depend on density. This leads to a slightly more complicated dynamical system [16] that we study in the appendix for completeness.

Coming back to the dynamical system (40), following the same method as that introduced in Sec. IV, one can derive analytical expressions for the Hopf bifurcation line $\rho_g^H(c)$ and the speed $c^*$ where the bifurcation becomes subcritical. We show in Fig. 12 the phase diagram in the ($c$, $\rho_g$)-plane and examples for the three types of inhomogeneous trajectories. Again an exact solution for the heteroclinic trajectory can be derived and (the dashed lines in Fig. 12) is found at speed $c^h = c^*$. As expected, there is no qualitative difference with the simpler case studied in Sec. III.

### B. Active Ising model equations

The active-Ising hydrodynamic equations [13] seem *a priori* different since they contain none of the non-linear gradient terms found in the phenomenological and Vicsek hydrodynamic equations. However, these terms are in fact generated by the diffusion term in the dynamical equation (5) for the density field [13], so that we will once again recover the same types of propagative solutions.

Looking for stationary profiles in the comoving frame $z = x - ct$, Eq. (5) and (6) reduce to

$$D\ddot{\rho} + c\dot{\rho} - v_0\dot{m} = 0 \tag{43}$$

$$D\ddot{m} + c\dot{m} - v_0\dot{\rho} + 2\left(\beta - 1 - \frac{r}{\rho}\right)m - \alpha\frac{m^3}{\rho^2} = 0 \tag{44}$$

Equation (43) can be solved by expanding $\rho$ in gradients of $m$. Introducing the ansatz

$$\rho(z) = \rho_g + \sum_{k=0}^{\infty} \alpha_k \frac{d^k m}{dz^k} \tag{45}$$

into Eq. (43), and solving order by order, we get the following recursion relation

$$a_0 = \frac{v_0}{c} \qquad a_{k+1} = -\frac{D}{c}a_k \tag{46}$$

from which we obtain

$$\rho(z) = \rho_g + \frac{v_0}{c}\sum_{k=0}^{\infty}\left(-\frac{D}{c}\right)^k \frac{d^k m}{dz^k} \tag{47}$$

In the following we retain only the first order terms in gradient:

$$\rho(z) = \rho_g + \frac{v_0}{c}m(z) - \frac{Dv_0}{c^2}\dot{m}(z) + \frac{D^2 v_0}{c^3}\ddot{m}(z) \tag{48}$$

To simplify Eq. (44) we linearize around the density $\varphi_g = r/(\beta - 1)$ where the disordered profile becomes linearly unstable. As shown in [13], this is a good approximation when $\beta \gtrsim 1$ because $\varphi_g \to \infty$ while $\rho - \varphi_g$ remains finite for inhomogeneous solutions. We then obtain

$$D\ddot{m} + c\dot{m} - v_0\dot{\rho} + \frac{2r}{\varphi_g^2}(\rho - \varphi_g)m - \alpha\frac{m^3}{\varphi_g^2} = 0 \tag{49}$$

Finally, inserting Eq. (48) in the previous equation we obtain a second-order ordinary differential equation with exactly the same terms as those obtained from the phenomenological and Vicsek hydrodynamic equations, Eq. (13) and (40):

$$\tilde{D}\ddot{m} + \left(c - \frac{v_0^2}{c} - \xi m\right)\dot{m} - a_2 m + a_3 m^2 - a_4 m^3 = 0 \tag{50}$$

with

$$\tilde{D} = D\left(1 + \frac{v_0^2}{c^2}\right) \qquad \xi = \frac{4rDv_0}{(c^2 + v_0^2)\varphi_g^2} \tag{51}$$

$$a_2 = \frac{2r(\varphi_g - \rho_g)}{\varphi_g^2} \qquad a_3 = \frac{2rv_0}{c\rho_g^2} \qquad a_4 = \frac{\alpha}{\rho_g^2} \tag{52}$$

This equation has again the same qualitative behavior as in the phenomenological theory and the same three types of inhomogeneous solutions are found with the same organization in the ($c$, $\rho_g$) parameter space.

## VI. LINEAR STABILITY OF THE PROPAGATIVE SOLUTIONS IN THE 1D HYDRODYNAMIC EQUATIONS

In sections IV and V, we have found and classified all the propagative solutions of different hydrodynamic equations. We have shown that in all cases three types of such solutions *exist*: periodic patterns of finite-size bands, solitary band solutions, and phase-separated solutions. These solutions were found as stable limit cycles, homoclinic, and heteroclinic orbits $m(z)$ of the reduced dynamical system (13). This study does *not* tell us anything about the local and a fortiori global *stability* of these solutions as solutions $m(x-ct)$ and $\rho(x-ct)$ of the original hydrodynamic partial differential equations. Indeed, a stable orbit of the reduced dynamical system can very well be unstable to spatiotemporal perturbations when re-expressed as an inhomogeneous propagative solution of the hydrodynamic equations. For example, consider the fixed point at $m = m_-$ which is stable for $\rho_g > \rho_g^H$, in the region I and III in Fig. 9. Without performing any calculation, we know that the corresponding homogeneous solution ($\rho_0 = \rho_g + \frac{v_0}{c} m_-$, $m_0 = m_-$) is unstable in the hydrodynamic equations because it lies inside the spinodal region where no homogeneous solution is linearly stable.

In this section we study the linear (local) stability of these solutions at the hydrodynamic level. Although, it is a well-defined linear problem, determining the stability of inhomogeneous solutions of nonlinear partial differential equations cannot be done analytically even in the (rare) cases where these solutions are known analytically. A direct numerical study is possible (for an example, see, e.g. [25]), but is rather tedious, all the more so as we deal with 2D hydrodynamic equations. In the following, we study mostly the linear stability of the hydrodynamic equations reduced to one dimension (that of propagation), using a simple numerical procedure explained below. For an account of some fully 2D preliminary investigation, see the end of this section.

### A. Numerical procedure

We investigated numerically the stability of the propagative solutions of the phenomenological hydrodynamic equations Eq. (7-8) reduced to one space dimension, that of propagation. To do so, we select a solution of the corresponding classical mechanics problem. (13) and use it as initial condition of the numerical integration of Eqs. (7) and (8).

The numerical integration is done using a semi-spectral algorithm, the linear terms being computed in Fourier space, the non-linear ones in real space and a semi-implicit time-stepping. This method, where the fields $\rho$ and $m$ are represented by their $N$ first Fourier modes (with $N$ large enough that the simulation has converged), is well suited to simulate systems with diffusion terms and periodic boundary conditions.

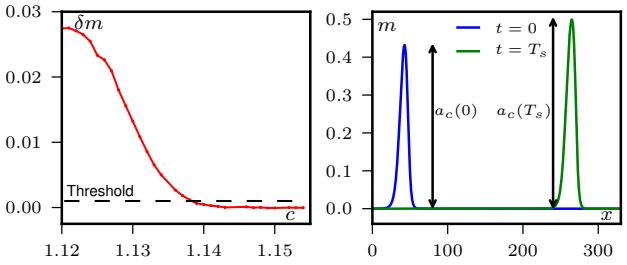


FIG. 13. Stability of homoclinic orbits in the hydrodynamic equations. $\Delta a_c$ is the difference in the amplitude of the solution measured between $t = 0$ and $t = T_s$. The solution is declared to be linearly stable if $\delta m(T_s)$, defined in Eq. (53) is smaller than a threshold that we take at $10^{-3}$. $v_0 = \lambda = \xi = a_4 = \varphi_g = 1$, $c = 1.125$ (right)

Preparing the initial condition of the hydrodynamic equations always brings in discretization errors. Indeed, because of the periodic boundary conditions in the hydrodynamic equations, we need to select a portion of the solution $m(z)$ which is a multiple of the period. This is done with an error of order $dx$, the space discretization step used in the numerical integration of (7) and (8).

Accordingly, we observe a rapid relaxation at short times due to the discretization errors. Subsequently, we find that the original solution is either stable at long times or is quickly destabilized and converges to another solution. To analyze systematically the stability of the propagative solutions, we defined a quantitative criterion for the stability: We choose a time $T_s = 2000$ much larger than the relaxation time of the initial perturbation (which happens in a time $\sim 100$) but not too large to test solely the linear stability regardless of a possible long-time coarsening dynamics that could be induced by numerical noise. We then measure the amplitude of the solution $|\Delta m|(t)$ defined in Eq. (28) as a function of time. If

$$\delta m(T_s) \equiv |\Delta m(T_s) - \Delta m(0)| \tag{53}$$

is smaller than $10^{-3}$, the solution is said to be stable and unstable otherwise (see Fig. 13). This protocol does not give exact answers to the question of linear stability, since in particular the small but finite initial perturbations may take the initial condition out of the basin of attraction of a (stable) solution. But the results presented below are relatively robust to changing our numerical resolution and the conditions used to decide stability, and we are thus confident that they represent well the 'true' subset of linear stable solutions.

The precise criterion does not matter much for the results since we find an abrupt transition from stable to unstable trajectories (see Fig. 13) which is visible on a variety of observables (norm of the fields, period, max and min values, etc).

### B. Results

Figure 14 contains one of the central results of our paper: only a very small subset of the propagative solutions are stable at the hydrodynamic level. However this subset includes the three possible types of trajectories: periodic bands, solitonic bands, and phase-separated profiles. The linearly stable solutions are all found in the region of the $(c,\ \rho_g)$ plane close to the heteroclinic trajectory and close to the line of homoclinic orbits. Examples of stable and unstable solutions are shown in Fig. 15.

To understand why only the vicinity of the heteroclinic and homoclinic solutions is stable, one can argue that the solutions must have a large enough amplitude to be dynamically stable. Indeed, the periodic solutions oscillate around $m = m_-$ which lies inside the spinodal region of the hydrodynamic equations, where no homogeneous solutions is stable. Small-amplitude oscillations around this point should thus also by dynamically unstable and only large enough amplitude cycles, found near the homoclinic line and the heteroclinic trajectories, are stable.

Note that the region where stable solutions are found has a rather rough boundary in Fig. 14. This is most probably an artefact due to the initial discretization error which is not controlled and varies from one propagative solution to another. Close to the threshold of linear instability, this can easily make a (linearly) stable trajectory unstable.

We report finally on fully 2D simulations performed on rectangular boxes of width $L_y = 100$, with small noise added to each grid point on a 1D solution extended trivially along $y$. These yielded essentially no change with respect to the results presented above. While this encourages us to believe that no unstable mode has components along $y$, and thus that the subset determined above corresponds to the linearly stable solutions of the full 2D hydrodynamic equations, we remain cautious. As a matter of fact, recent results obtained in the case of hydrodynamic equations for active nematics have revealed the existence of (very) long wavelength instability along the homogeneous direction of band solutions. [26] A similar investigation is left for future studies.

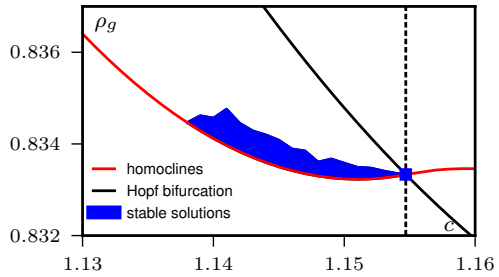


FIG. 14. The blue region is the subset of admissible propagative solutions which are linearly stable. None of the solutions for $c > c^*$ is stable in the hydrodynamic equations. $v_0 = \lambda = \xi = a_4 = \varphi_g = 1$. We use system sizes $L_x = 300$ or more (adapted to fit the solution) with resolution $dx = 0.5$ and $dt = 0.1$.

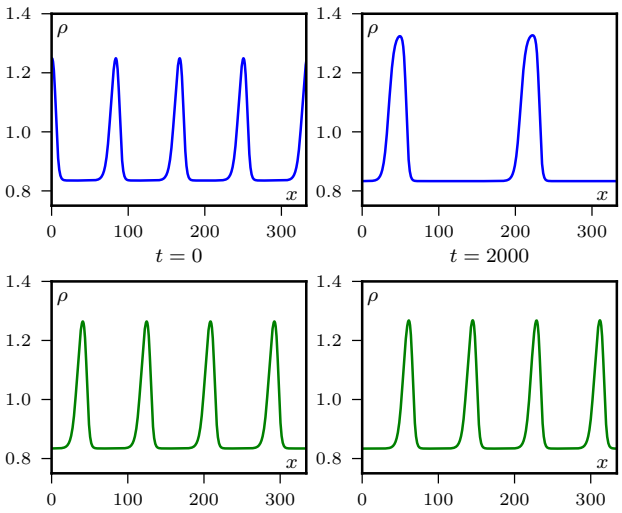


FIG. 15. Evolution of two propagative solutions in the hydrodynamic equations (7-8). The initial conditions are stable limit cycles of the dynamical system (13) for $m(z)$. **Top row**: unstable solution with $c = 1.135$, $\rho_g = 0.8351$. **Bottom row**: stable solutions with $c = 1.14$, $\rho_g = 0.8341$. System size $340 \times 100$, $dt = 0.1$, $dx = 0.4$. $v_0 = \lambda = \xi = a_4 = \varphi_g = 1$.

## VII. COARSENING IN THE HYDRODYNAMIC EQUATIONS

The two-dimensional subset of propagative solutions that are linearly stable still contains an infinity of solutions, including smectic patterns, solitary bands, and phase-separated profiles. We can thus wonder whether a single solution is selected in the hydrodynamic equation starting from a random initial condition.

One can obtain some insight into this question by studying the lines of propagative solutions having a given average density $\rho_0$, shown in Fig. 10. Indeed, $\rho_0$ is conserved in the hydrodynamic equations and any stable propagative solutions has to lie on such a line. As discussed earlier, the larger the amplitude of a solution, the faster the propagation. We can thus expect that if several travelling bands coexist, they will encounter and merge because of their different speeds. This will in turn increase the sizes of the surviving objects and hence their speed. This mechanism would naturally lead the system toward the heteroclinic solution, *i.e.*, to the phase-separated state.

We checked this scenario by simulating the phenomenological hydrodynamic equations (7-8) with three different initial conditions, as shown in Fig. 16:

- We build an initial condition made of two homoclines glued together, both solutions of the differential equation (13) for different speed $c$ and inside the stability domain of Fig. 14. To avoid discon-

tinuities we interpolate smoothly between the gas densities of the two solutions using a hyperbolic tangent function. We then observe that the two travelling bands get closer until, when close enough (though not in contact), the smaller one evaporates, its mass being transfered to the second band. The final solution is hence a single larger isolated band.

- Starting from a random ordered solution with constant $\rho$ and a magnetization $m$ fluctuating around $m_0 \neq 0$, several bands form at short times that all go in the same direction. The system then coarsens because of the speed differences between the liquid droplets until only "phase-separated domains", that all have the same speed, remain. In practice, because the band speeds can be very close, a final state with a single phase-separated profile may not be reached within the time-scales of our simulations and a precise study of this coarsening regime is beyond our numerical capacities.

- Starting from a disordered initial condition with $m(x)$ fluctuating around 0 and a density inside the spinodal region, many domains of positive and negative magnetization form. These objects then encounter and merge yielding a rapid coalescence process. Because of the periodic boundary conditions, this process typically yields a single phase-separated state for the system sizes we considered. For larger systems, the coalescence process could result in a larger number of bands propagating in the same direction. We should then observe the same type of coarsening as in the second case discussed above.

At the level of hydrodynamic equations, the fact that larger ordered domains travel faster leads to a natural coarsening towards the phase-separated states. This coarsening relies both on a coalescence process and, when bands travelling in the same direction are close enough, on a ripening during which a smaller band evaporates and is "swallowed" by its larger neighbour.

Note that we studied the stability of propagative solutions and their coarsening process using the phenomenological hydrodynamic equations (7-8). While the precise results will depend on the set of hydrodynamic equations under study, our simulations of the Vicsek and Ising hydrodynamic equations, (3-4) and (5-6), did not suggest any qualitative difference. Their comprehensive investigation, which is beyond the scope of this paper, would nevertheless be interesting, especially to quantifiy the role played by the non-linearities in the vectorial hydrodynamic equations (4).

## VIII. PHASE DIAGRAM OF COARSE-GRAINED HYDRODYNAMIC EQUATIONS

We can now construct the full phase diagram for the Ising and Vicsek hydrodynamic equations in the temperature-density ensemble (or noise-density for Vicsek), Fig. 17. It is composed of two spinodal lines, which are the limit of linear stability of the homogeneous disordered and ordered profiles, and two binodal lines outside which inhomogeneous solutions cannot be observed.

### A. Spinodal lines

The spinodal lines can be determined analytically from a linear stability analysis, as was previously done for the Vicsek model [15] and the active Ising model [13]. The lower spinodal line $\varphi_g$ is simply the density at which the coefficient of the term linear in $m$ in the hydrodynamic equations changes sign (in our phenomenological equation, when $a_2 = 0$). It reads for the Ising and Vicsek hydrodynamic equations

$$\varphi_g^I(T) = r/(\beta - 1) \tag{54}$$

$$\varphi_g^V(\sigma) = \frac{\mu_2}{\mu_1} = \frac{\pi(1 - e^{-\sigma^2/2})}{4(e^{-\sigma^2/2} - 2/3)} \tag{55}$$

where $\beta = 1/T$. The higher spinodal $\varphi_\ell$ can be determined exactly for the Ising hydrodynamic equations

$$\varphi_\ell^I(T) = \varphi_g \frac{v_0\sqrt{\alpha\,(v_0^2\kappa + 8D(\beta-1)^2)} + v_0^2\kappa + 8D\alpha(\beta-1)}{2v_0^2\kappa + 8D\alpha(\beta-1)} \tag{56}$$

where $\kappa = 2 + \alpha - 2\beta$ and $\alpha = \beta^2(1 - \beta/3)$. For the Vicsek hydrodynamic equation, the exact determination of $\varphi_\ell$ is much more cumbersome [15]. In Fig. 17 we show the line $\varphi_\ell^V(\sigma)$ computed numerically by simulating the Vicsek hydrodynamic equations at different densities in the homogeneous ordered state and looking at the growth of a small perturbation.

### B. Binodal lines

The binodal lines $\rho_g$ and $\rho_\ell$ are defined as the minimum and maximum global densities beyond which inhomogeneous propagative profiles cannot be observed in simulations of the hydrodynamic equations. As explained in Sec. IV F, at the heteroclinic trajectory the size of the liquid and gas domains are arbitrary so that phase-separated solutions can have any density in the range $[\rho_g^h, \rho_\ell^h]$. We find that, for all parameters we tested, $\rho_\ell^h = \rho_\ell$, i.e., no other stable solution has a larger density than the liquid domain of the heteroclinic solution.

The situation is more subtle for the lower binodal $\rho_g$. Depending on the external parameters, the line of homoclinic trajectories solution of the dynamical system

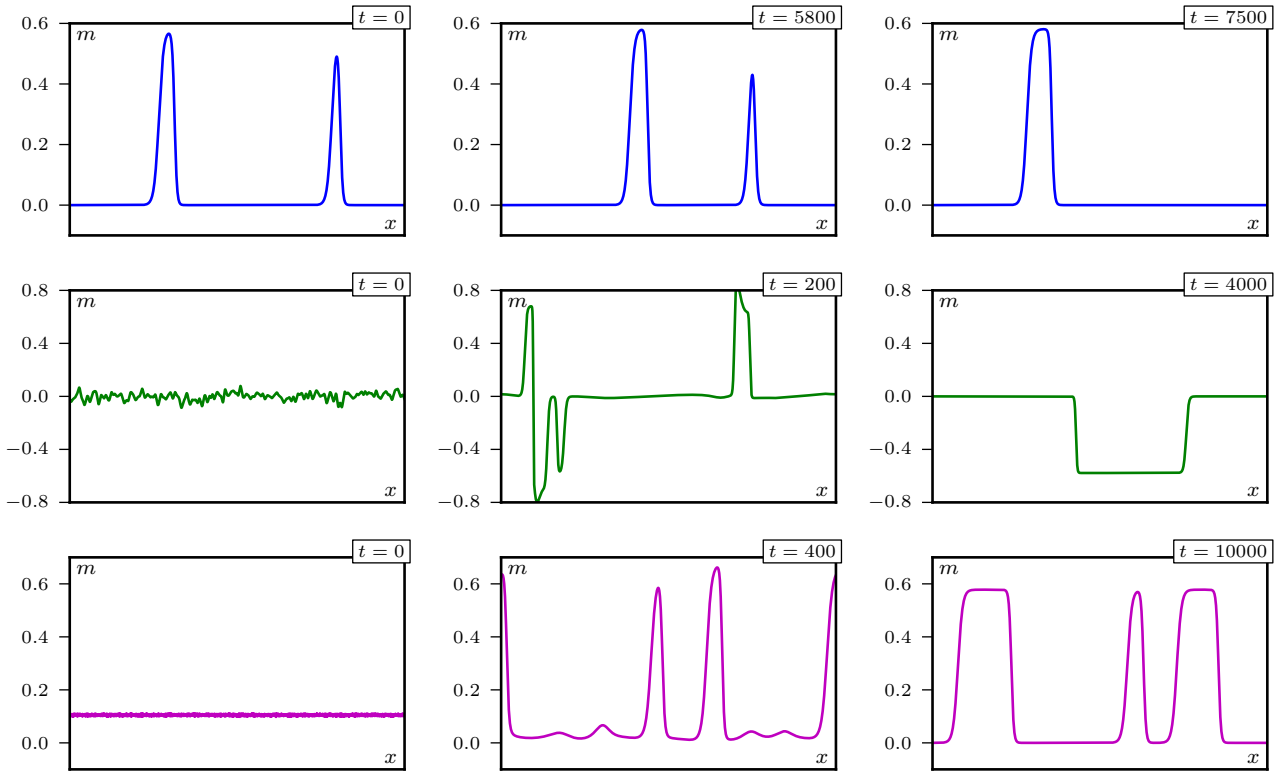


FIG. 16. Coarsening in the phenomenological hydrodynamic equations (7-8) from three different initial conditions. **Top**: Two homoclinic trajectories glued together. **Middle**: Disordered initial condition. **Bottom**: Ordered initial condition. System size $500 \times 100$ (top and bottom), $1000 \times 100$ (middle). The profiles are averaged along the $y$-direction in which the system is invariant. $v_0 = \lambda = \xi = a_4 = \varphi_g = 1$, $dt = 0.1$, $dx = 0.1$.

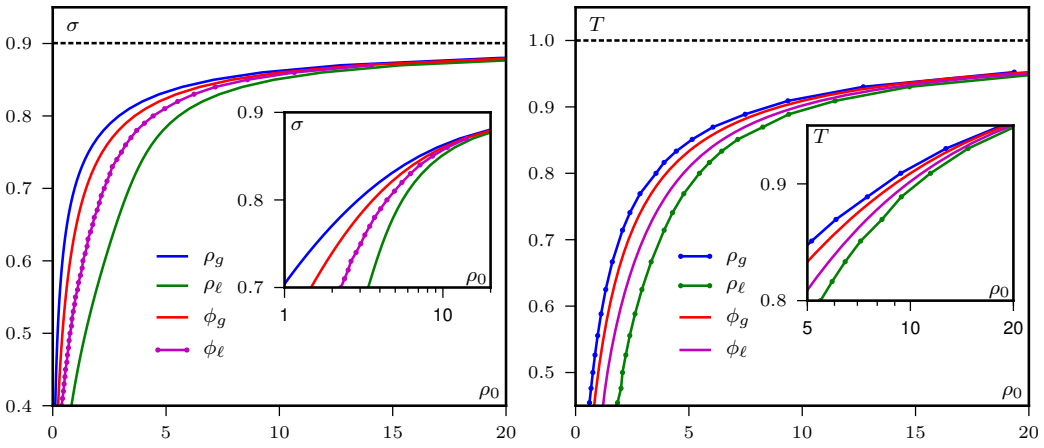


FIG. 17. Phase diagram of the Visek (left) and Ising (right) hydrodynamic equations. The spinodal lines $\varphi_g$ and $\varphi_\ell$ are known exactly except $\varphi_\ell$ in the Vicsek hydrodynamic equation which we computed numerically by looking at the stability of systems of size $50 \times 50$. The binodals $\rho_g$ and $\rho_\ell$ are the coexisting densities of phase-separated (heteroclinic) solutions as explained in the text. The dashed line indicate the asymptote above which only disordered solutions exist. Insets are close-ups on the high-density regions with a logarithmic scale on the $x$-axis. Parameters: $v_0 = D = 1 = r = 1$ (Ising), $v_0 = 1$ (Vicsek).

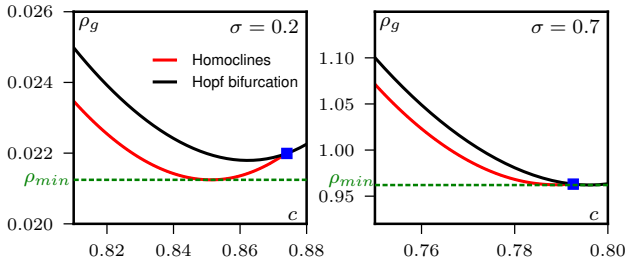


FIG. 18. Propagative solutions of the Vicsek hydrodynamic equations for $\sigma = 0.2$ and 0.7. The solution with the lower mean density $\rho_{\min}$ is found at the minimum of the line of homoclinic solutions. At low noise, it does not coincide with the heteroclinic solution (blue squares). $v_0 = 1$.

is not always monotonous as a function of $c$. For example, in the Vicsek hydrodynamic equation it is not monotonous at low noise, as shown in Fig. 18. In this case the minimum density accessible to propagative solutions is the minimum of the homoclinic line. This solution need not be stable in the hydrodynamic equations so that one should repeat the stability analysis done in Sec. VI for each value of the noise to determine exactly the binodal line. For simplicity, the lower binodal of the Vicsek hydrodynamic equation shown in Fig. 17 is the gas density read from the phase-separated profile, which is true at high noise and a good approximation of $\rho_g$ at lower noise values.

For the Vicsek hydrodynamic equations, the coexisting densities of the heteroclinic trajectory are known exactly whereas in the Ising case they can be determined analytically only after linearizing Eq. (44) around $\rho = \varphi_g$. The binodal lines in the phase diagram of the Ising hydrodynamic equations shown in Fig. 17 are thus determined by integrating numerically the hydrodynamic equations and measuring the density of the liquid and gas domain of a phase-separated solution whereas we plot the analytical solution in the Vicsek case.

## IX. CONCLUSION

Before summarizing our results, let us discuss how the study of the hydrodynamic equations presented in this article compares with the phenomenology of the microscopic models. The phase diagrams of the Ising and Vicsek hydrodynamic equations shown in Fig. 17 are qualitatively similar. They are also consistent with the phase diagrams of the microscopic models shown in Fig. 2. The hydrodynamic equations thus provide a picture which is consistent with the liquid-gas framework discussed in Sec. II C. For instance, the asymptote at finite noise (or temperature) can again be seen as the simplest way of forcing the system to cross a transition line to go from its gas to liquid phase.

The comparison between the phase-separated regions of the microscopic models and hydrodynamic equations is however more subtle. We have indeed shown, using the phenomenological hydrodynamic equation (7-8), that the coarsening leads, at the hydrodynamic level, to the phase-separated solution. This is true in the active Ising model but not in the Vicsek model, which only shows micro-phase separation and thus a coarsening leading to a periodic solution (see Fig. 1). This difference between microscopic models and hydrodynamic equations is however not surprising since it was recently shown that fluctuations are essential to account for the selection of micro-phase separated profiles in the Vicsek model [14].

More precisely, phase-separated and micro-phase-separated solutions are both linearly stable in the hydrodynamic equations for vectorial order parameters. As noise is added to these equations, though, large bands are destabilized and break in periodic array of finite-size bands, in agreement with what is seen in microscopic simuations of the Vicsek model [14]. We can now tentatively put together these results to propose a coarsening process that would lead to the micro-phase separated states seen in the Vicsek model. Starting from a profile with many coexisting bands, the coarsening *at fixed* $\rho_0$ would tend to lead to the formation of larger and larger bands. This coarsening would however be arrested by the fact that the fluctuations in the Vicsek model set a maximal size beyond which bands are (non-linearly) unstable. How this size is selected however remains to be determined.

All in all, we have shown in this paper that the hydrodynamic equations describing polar flocking models generically share the same propagative solutions. We found three types of solutions that are all observed in microscopic models: periodic orbits that describe microphase separation, homoclinic orbits describing solitonic objects and heteroclinic trajectories that correspond to phase separation. Only a subset is stable in the hydrodynamic equations, but it still contains the three types of solutions.

The coarsening in the hydrodynamic equations favors the fastest solutions which are also the largest patterns. It thus leads naturally to the phase-separated solution which controls the phase diagram of the hydrodynamic equations. The same behavior is observed in the microscopic active Ising model whereas one can understand the microphase separation of the Vicsek model as an arrested coarsening, the largest pattern being non-linearly unstable to the (giant) fluctuations of the liquid phase.

## ACKNOWLEDGMENTS

We thank T. Dauxois, A. Peshkov, J. Toner, V. Vitelli for many illuminating discussions. This project was supported through ANR projects BACTTERNS and MiTra.

### Appendix A: Limit of small $D$

While we do not have an analytic solution for the homoclinic profiles, lots of insight on their physics can be gained by studying the limit of small diffusion coefficient $D$. This is most easily done by introducing the auxiliary variable $Z = D\dot{m} + F(m)$ where

$$F(m) = \left(c - \frac{\lambda v_0}{c}\right) m - \frac{\xi}{2} m^2 \tag{A1}$$

such that $F'(m) = f(m)$. Our dynamical system can then be recast as

$$\frac{d}{dz}\begin{pmatrix} m \\ Z \end{pmatrix} = \begin{pmatrix} \frac{1}{D}(Z - F(m)) \\ -H'(m) \end{pmatrix} \tag{A2}$$

Let us consider a large-amplitude orbits that start close to $m = 0$. An example of such orbits and the corresponding phase portrait for the $(m,\ Z)$ variables is shown in Fig. 19. When $D$ is small, $\dot{m}$ relaxes quickly to zero so that $Z$ relaxes to the parabola $Z = F(m)$ in a time $\sim D$. Following the trajectory in Fig. 19, starting from point A at $m \approx 0$, the trajectory between A and B is above the parabola $F(m)$. The distance with the parabola first increases when $m < m_-$, which implies $H'(m) < 0$ and $\dot{Z} > 0$, and decreases afterwards when $m > m_-$. The distance with the parabola stays of order $D$, set by the relaxation time of $\dot{m}$. When $Z = f(m)$ at point $B$, $m$ relaxes to $m = 0$ in a time $\sim D$. This gives profiles with sharp leading fronts and long exponential tails, which are indeed consistent with the profiles seen at small temperature in the Vicsek model and its putative hydrodynamic description [12, 15, 18].

This picture is consistent with the fact that at leading order in $D$ the eigenvalues at point $(m = 0,\ \dot{m} = 0)$ read

$$\lambda_1 = \frac{\varphi_g - \rho_g}{c - \lambda v_0/c} \qquad \lambda_2 = -\frac{c - \lambda v_0/c}{D} \tag{A3}$$

so that we have a slow unstable direction $\lambda_1$ and a fast stable direction $\lambda_2$. These two eigenvalues indeed control a large part of the trajectory, as shown in the right panel of Fig. 19.

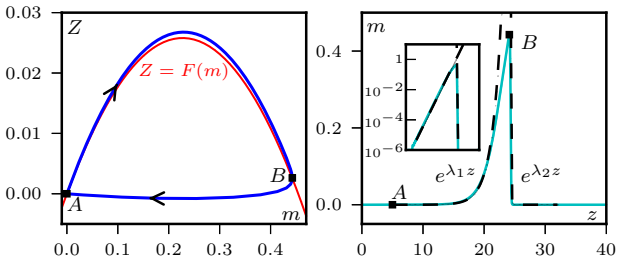


FIG. 19. **Left**: Phase portrait for the variables $m$ and $Z = D\dot{m}+F(m)$ where $F(m)$ is the red parabola. **Right**: The corresponding trajectory. The dashed lines are the linear approximation around $m = 0$. The inset in semi-log scale shows the exponential tail close to $m = 0$. Parameters: $D = 0.01$, $v_0 = \lambda = \xi = a_4 = \varphi_g = 1$.

### Appendix B: Phenomenological equations with $a_4(\rho)$

In the hydrodynamic equation (8) the homogeneous ordered solutions have a magnetization $|\vec{m}_0| = \sqrt{a_2/a_4}$. Thus, in the simplified case studied in Sec. III where $a_2 = \rho - \varphi_g$ and $a_4 = \text{cst}$, one observes that

$$\frac{|\vec{m}_0|}{\rho} = \sqrt{\frac{\rho - \varphi_g}{a_4 \rho^2}} \xrightarrow[\rho\to\infty]{} 0 \tag{B1}$$

On the contrary we observe in the microscopic Vicsek and active Ising models that, at large densities, $|\vec{m}_0|/\rho_0$ reaches a constant $P_0 \leq 1$ (set by the noise intensity in the microscopic models). This can be achieved by assuming that $a_4 = (\rho P_0^2)^{-1}$ as in [16] so that

$$\frac{|\vec{m}_0|}{\rho} = P_0 \sqrt{\frac{\rho - \varphi_g}{\rho}} \xrightarrow[\rho\to\infty]{} P_0 \tag{B2}$$

Repeating the same treatment as before, we look for 1d propagative solutions with speed $c$ which are the solutions of

$$D\ddot{m} + (c - \frac{\lambda v_0}{c} - \xi m)\dot{m} - (\varphi_g - \rho_g)m + \frac{v_0}{c} m^2 - \frac{m^3}{P_0^2(\rho_g + \frac{v_0}{c} m)} = 0 \tag{B3}$$

which can be written in the same form as Eq. (14) with a different potential

$$D\ddot{m} = -f(m)\dot{m} - H'(m) \tag{B4}$$

$$H(m) = -\frac{c^3 \rho_g^2}{P_0^2 v_0^3} m + \left[\frac{c^2 \rho_g}{2P_0^2 v_0^2} - \frac{(\varphi_g - \rho_g)}{2}\right] m^2 - \left[\frac{c}{3P_0^2 v} - \frac{v_0}{3c}\right] m^3 + \frac{c^4 \rho_g^3}{P_0^2 v_0^2} \log(v_0 m + c\rho_g) \tag{B5}$$

$$f(m) = c - \frac{\lambda v_0}{c} - \xi m \tag{B6}$$

We find a behavior very similar to the case $a_4 = \text{cst}$ discussed in section IV. Under the same constraints (C1-3), the potential $H(m)$ has the same form with maxima in $m = 0$ and $m = m_+$ and a minimum at $m = m_-$ given by

$$m_\pm = \frac{c v_0 P_0^2 (2\rho_g - \varphi_g) \pm c P_0 \sqrt{(P_0 v_0 \varphi_g)^2 - 4c^2 \rho_g (\varphi_g - \rho_g)}}{2(c^2 - P_0^2 v_0^2)} \tag{B7}$$

One observes the same three types of trajectories already shown in Fig. 5: periodic, homoclinic and heteroclinic. The phase diagram $(\rho_g,\ c)$, shown in Fig. 20, is also similar to the case $a_4 = \text{cst}$ except in a very small region close to the heteroclinic trajectory. We find again a

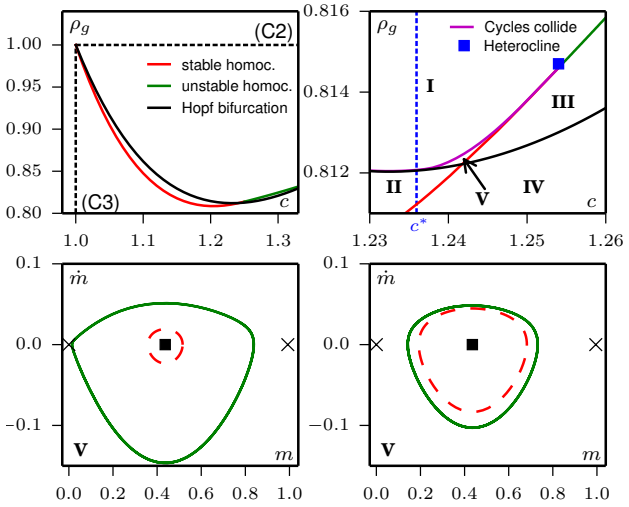


FIG. 20. **Top row**: Phase diagram for the propagative solutions of Eq. (B4). The right plot is a zoom on the region $c^* < c < c^h$. Phase I to IV are the same as in the case $a_4 = \text{cst}$ (see Fig. 6). **Bottom row**: Phase portraits of the solutions in phase V for the same $c = 1.2421$ and $\rho_g = 0.81228$ (left) and $\rho_g = 0.81248$ (right). When $\rho_g$ increases, the size of the stable cycle decreases while the size of the unstable cycle increases, until they collide as indicated on the phase diagram. $v_0 = \lambda = \xi = P_0 = \varphi_g = 1$.

2-parameter family of periodic orbits and a line of homoclinic solutions which terminates at a unique heteroclinic trajectory.

As before, we can compute analytically the line $\rho_g^H(c)$ where the Hopf bifurcation takes place and the speed $c^*$ such that the bifurcation is supercritical for $c < c^*$ and subcritical for $c > c^*$. The difference with the previous case is that the heteroclinic trajectory, for which we do not have an exact solution anymore, is not found at $c = c^*$ but at $c^h > c^*$. As a consequence, we observe a new phase (shown as number V in Fig. 20) in which two limit cycles are found. A large stable cycle surrounds a smaller unstable limit cycle which itself encapsulates the stable fixed point $m = m_-$. As seen from the phase portraits in Fig. 20, when increasing $\rho_g$ the size of the stable cycle decreases whereas the size of the unstable one increases. Thus the upper limit of existence of this phase (the magenta line in the phase diagram) is the moment where the cycles collide and annihilate.

### Appendix C: Propagative solutions of the Vicsek hydrodynamic equations

Here we show how the study of propagative solutions in the Vicsek hydrodynamic equations leads to the same dynamical system as for the phenomenological equations, but with coefficients depending in a more complicated way on $\rho_g$ and $c$.

We start from the hydrodynamic equations (3-4) in the comoving frame $z = x - ct$:

$$c\dot{\rho} - v_0\dot{m} = 0 \tag{C1}$$

$$\nu\ddot{m} + \left(c - \frac{v_0^2}{2c}\right)\dot{m} - \gamma m\dot{m} - \frac{v_0}{2}\dot{\rho} + \mu m - \zeta m^3 = 0 \tag{C2}$$

The coefficients in Eq. (C2) are greatly simplified by dividing the equation by $\nu$, thus getting

$$\ddot{m} + \frac{1}{\nu}\left(c - \frac{v_0^2}{2c}\right)\dot{m} - \tilde{\gamma} m\dot{m} - \frac{v_0}{2\nu}\dot{\rho} + \frac{\mu}{\nu}m - \tilde{\zeta}m^3 = 0 \tag{C3}$$

where $\tilde{\gamma} = \gamma/\nu$ and $\tilde{\zeta} = \zeta/\nu$ depend only on the noise $\sigma$ on the alignment interaction [15]

$$\tilde{\gamma} = \frac{8}{\pi}\left(\frac{16}{15} + 2e^{-2\sigma^2} - e^{-\sigma^2/2}\right) \tag{C4}$$

$$\tilde{\zeta} = \frac{64}{\pi^2}\left(e^{-\sigma^2/2} - \frac{2}{5}\right)\left(\frac{1}{3} + e^{-2\sigma^2}\right) \tag{C5}$$

while $\mu$ and $\nu$ depend also on the density

$$\mu = \frac{4v_0\rho}{\pi}\left(e^{-\sigma^2/2} - \frac{2}{3}\right) - v_0\left(1 - e^{-\sigma^2/2}\right) \tag{C6}$$

$$\nu^{-1} = \frac{4}{v_0^2}\left[\frac{8\rho}{3\pi}\left(\frac{7}{5} + e^{-2\sigma^2}\right) + \left(1 - e^{-2\sigma^2}\right)\right] \tag{C7}$$

One can solve Eq. (C1) to get $\rho(z) = \rho_g + \frac{v_0}{c}m(z)$ as before and use it in Eq. (C3) to obtain the second-order ordinary differential equation

$$\ddot{m} + (\alpha - \xi m)\dot{m} - a_2 m + a_3 m^2 - a_4 m^3 = 0 \tag{C8}$$

where the coefficients are all function of $c$ and $\rho_g$

$$\alpha = \left(c - \frac{v_0^2}{2c}\right)(\nu_1\rho_g + \nu_2) \qquad \xi = \frac{v_0^3}{2c^2}\nu_1 + \tilde{\gamma} \tag{C9}$$

$$a_2 = \mu_2\nu_2 + (\mu_2\nu_1 - \mu_1\nu_2)\rho_g - \mu_1\nu_1\rho_g^2$$

$$a_3 = \frac{v_0}{c}\left(2\rho_g\mu_1\nu_1 + \mu_1\nu_2 - \mu_2\nu_1\right)$$

$$a_4 = \tilde{\zeta} - \frac{v_0^2}{c^2}\mu_1\nu_1$$

where $\mu_{1,2}$ are defined by $\mu = \mu_1\rho - \mu_2$ and $\nu_{1,2}$ by $\nu^{-1} = \nu_1\rho + \nu_2$.

[1] Sepúlveda, N., Petitjean, L., Cochet, O., Grasland-Mongrain, E., Silberzan, P., Hakim, V. PLoS Comp. Biol., 9(3), e1002944 (2013)

[2] F. Peruani, J. Starruss, V. Jakovljevic, L. Sogaard-Andersen, A. Deutsch, M. Bär, Phys. Rev. Lett. **108**, 098102 (2012)
[3] V. Schaller, C. Weber, C. Semmrich, E. Frey, A. R. Bausch, *Nature* **467**, 73-77 (2010).
[4] Y. Sumino, K. H. Nagai, Y. Shitaka, D. Tanaka, K. Yoshikawa, H. Chaté, K. Oiwa, *Nature* **483** 448-452 (2012).
[5] J. Deseigne, O. Dauchot, H. Chaté. Phys. Rev. Lett., **105**, 098001 (2010); J. Deseigne, *et al.* Soft Matter **8**, 5629 (2012); C.A. Weber, *et al.* Phys. Rev. Lett., **110**, 208001 (2013).
[6] A. Bricard, J.B. Caussin, N. Desreumaux, O. Dauchot, and D. Bartolo, *Nature*, **503**, 95 (2013)
[7] Shashi Thutupalli et al 2011 New J. Phys. 13 073021
[8] T. Sanchez; D. T. N. Chen, S. J. DeCamp, M. Heymann, Z. Dogic, *Nature* **491** 431 (2012).
[9] T. Vicsek, A. Czirók, E. Ben-Jacob, I. Cohen, and O. Shochet, *Phys. Rev. Lett.* **75**, 1226 (1995)
[10] Mermin, N. D., Wagner, H. *Phys. Rev. Lett.* **17**, 1133 (1966)
[11] J. Toner, and Y. Tu, *Phys. Rev. Lett.* **75**, 4326 (1995). J. Toner, Y. Tu, and M. Ulm, *Phys. Rev. Lett.* **80**, 4819 (1998)
[12] G. Grégoire, and H. Chaté, *Phys. Rev. Lett.* **92**, 025702 (2004) ; H. Chaté, F. Ginelli, G. Grégoire, and F. Raynaud, *Phys. Rev. E* **77**, 046113 (2008)
[13] A.P. Solon, and J. Tailleur, *Phys. Rev. Lett.* **111**, 078101 (2013)
[14] A. P. Solon, H. Chaté, J. Tailleur, *Phys. Rev. Lett.* **114**, 068101 (2015)
[15] E. Bertin, M. Droz, G. Grégoire, *Phys. Rev. E* **74** 022101 (2006); *J. Phys. A* **42** 445001 (2009); A. Peshkov, E. Bertin, F. Ginelli and H. Chaté, *Eur. Phys. J Special Topics* **223**, 1315 (2014).
[16] J-B Caussin, A. Solon, A. Peshkov, H. Chaté, T. Dauxois, J. Tailleur, V. Vitelli, and D. Bartolo, Phys. Rev. Lett. **112**, 148102 (2014)
[17] S. Mishra, A. Baskaran, M.C. Marchetti. *Phys. Rev. E* **81**, 061916. (2010); A. Gopinath, M.F. Hagan, M.C. Marchetti, A. Baskaran. *Phys. Rev. E* **85**, 061903. (2012)
[18] T. Ihle, *Phys. Rev. E* **83**, 030901 (2011); T. Ihle, *Phys. Rev. E* **88**, 040303(R) (2013).
[19] F. D. C. Farrell, J. Tailleur, D. Marenduzzo, M. C. Marchetti, *Phys. Rev. Lett.* **108**, 248101 (2012)
[20] R. Großmann, L. Schimansky-Geier, and P. Romanczuk, *New Journal of Physics* **15**, 085014 (2013)
[21] Y. A. Kuznetsov, Elements of Applied Bifurcation Theory, Second Edition. Springer. (2004)
[22] In the Vicsek model, the region in which solitary bands can be seen vanishes as the system size is taken to infinity. At fixed intensive parameters, doubling the system size indeed doubles the number of bands and increasing the system size hence asymptotically leads, in principle, to a smectic arrangements of bands.
[23] Note that $m$ is actually a momemtum field in this context.
[24] Again, in the infinite-size limit, the homoclinic orbits/solitary wave solutions are only observable in a codimension one subset of parameter space.
[25] H. Chaté, and P. Manneville, *Phys. Lett. A* **171**, 183 (1992).
[26] S. Ngo, *et al.* Phys. Rev. Lett. **113**, 038302 (2014).

## 5.4 Séparation de phase ou microphases

Depuis l'article original de Vicsek *et al* [13] et les travaux de Grégoire, Chaté et collaborateurs [68, 69], peu de progrès ont été réalisés, sur le plan numérique, dans l'étude du modèle de Vicsek. Dans l'article G, guidés par l'intuition acquise grâce au modèle d'Ising actif, nous proposons une image relativement complète de la transition dans le modèle de Vicsek : forme du diagramme des phases, boucles d'hystérèse, variations du paramètre d'ordre, etc. Cependant, au lieu de la séparation de phase observée dans le modèle d'Ising actif, nous montrerons que la région de coexistence est le lieu d'une séparation en microphases. On ne peut alors plus définir simplement une fraction de liquide et c'est le nombre de bandes qui joue à présent ce rôle. De plus, nous montrons que, pour expliquer cette forme de coexistence de phase, il faut prendre en compte des termes de bruit dans les équations hydrodynamiques. Pour des modèles ayant une symétrie rotationnelle continue, comme le modèle de Vicsek, le bruit génère des fluctuations géantes de densité. Celles-ci semblent empêcher une séparation de phase complète en déstabilisant des domaines liquides de trop grande taille. L'origine de cette instabilité (non-linéaire) est probablement le seul ingrédient qui manque pour obtenir une compréhension complète du modèle de Vicsek.

À la section 5.4.1, nous comparerons plus en détail la dynamique des bandes ordonnées du modèle de Vicsek et du modèle d'Ising actif. Cela nous permettra de mieux comprendre ce qui mène aux deux formes de coexistence, entre phases ou microphases. Finalement, nous étudierons à la section 5.4.2 d'autres modèles de spins actifs contenant les mêmes ingrédients. Il semble que ces derniers puissent chacun être associé à l'une des deux classes d'universalité représentées par le modèle d'Ising actif et le modèle de Vicsek.

PRL 114, 068101 (2015) PHYSICAL REVIEW LETTERS week ending 13 FEBRUARY 2015

# From Phase to Microphase Separation in Flocking Models: The Essential Role of Nonequilibrium Fluctuations

Alexandre P. Solon,[1] Hugues Chaté,[2,3,4] and Julien Tailleur[1]
[1]Université Paris Diderot, Sorbonne Paris Cité, MSC, UMR 7057 CNRS, 75205 Paris, France
[2]Service de Physique de l'État Condensé, CNRS UMR 3680, CEA-Saclay, 91191 Gif-sur-Yvette, France
[3]LPTMC, CNRS UMR 7600, Université Pierre et Marie Curie, 75252 Paris, France
[4]Beijing Computational Science Research Center, 3 Heqing Road, Haidian District, Beijing 100080, China
(Received 23 June 2014; revised manuscript received 11 September 2014; published 12 February 2015)

We show that the flocking transition in the Vicsek model is best understood as a liquid-gas transition, rather than an order-disorder one. The full phase separation observed in flocking models with $Z_2$ rotational symmetry is, however, replaced by a microphase separation leading to a smectic arrangement of traveling ordered bands. Remarkably, continuous deterministic descriptions do not account for this difference, which is only recovered at the fluctuating hydrodynamics level. Scalar and vectorial order parameters indeed produce different types of number fluctuations, which we show to be essential in selecting the inhomogeneous patterns. This highlights an unexpected role of fluctuations in the selection of flock shapes.

DOI: 10.1103/PhysRevLett.114.068101 PACS numbers: 87.23.Cc, 05.65.+b, 47.27.ed, 47.54.-r

Many of the phenomena heretofore only invoked to illustrate the many facets of active matter are now being investigated in careful experiments, and more and more sophisticated models are built to account for them. For flocking alone, by which we designate the collective motion of active agents, spectacular results have been obtained on both biological systems [1–9] and man-made self-propelled particles [10–12]. Nevertheless, it is fair to say that the current excitation about flocking takes place while our understanding of the simplest situations remains unsatisfactory. This is true even for idealized self-propelled particles interacting only via local alignment rules, as epitomized by the Vicsek model (VM) [13], which stands out for its minimality and popularity. Twenty years after the introduction of this seminal model for the flocking transition and despite the subsequent extensive literature [14], we still lack a global understanding of the transition to collective motion.

It took a decade to show that the transition to collective motion in the VM, initially thought to be critical [13], was discontinuous [15]: upon increasing the density or reducing the noise strength, high-density bands of spontaneously aligned particles form suddenly [15] (Fig. 1). The homogeneous, ordered "Toner-Tu" phase [16] is only observed after a second transition at significantly lower noise and/or higher density [15]. Since then, hydrodynamic-level deterministic descriptions have been established and shown to support bandlike solutions [17–19], but it was recently proved [20] that many such different solutions generically coexist. In fact, the connection of these results to microscopic models remains elusive. More generally, we lack a unifying framework encompassing the two transitions (between disordered and band phases, and between band and Toner-Tu phases).

Such a global picture was recently proposed for the active Ising model (AIM), where rotational invariance is replaced by a discrete symmetry [21]: particles carrying Ising spins diffuse in space with a constant-amplitude bias along one arbitrarily fixed direction $\pm\mathbf{u}_x$, the sign being given by the local magnetization (see Ref. [22] for a detailed definition). The emergence of flocking in this model is akin to a liquid-gas transition between an ordered liquid and a disordered gas. Unlike the traveling bands of the VM, inhomogeneous profiles in the AIM are fully phase separated, with a single macroscopic liquid domain traveling in the gas (Fig. 1). More generally, the symmetry difference between the two models questions the relevance of this framework for the VM.

In this Letter, we show that the flocking transition in the Vicsek model is also best understood in terms of a liquid-gas transition—rather than an order-disorder one—but with *microphase* separation in the coexistence region. Contrary to what was previously believed, we indeed show that the dense ordered bands discovered in Ref. [15] for the VM are arranged *periodically* in space, leading to an effectively "smectic" phase. We define an appropriate "liquid fraction"

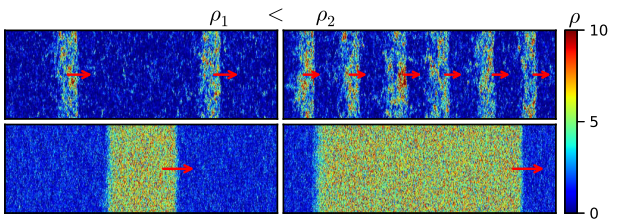


FIG. 1 (color online). Top: Microphase separation in the Vicsek model. $\eta = 0.4$, $v_0 = 0.5$, $\rho_1 = 1.05$ (left), $\rho_2 = 1.93$ (right). Bottom: Phase separation in the active Ising model. $D = 1$, $\varepsilon = 0.9$, $\beta = 1.9$, $\rho_1 = 2.35$ (left), $\rho_2 = 4.7$ (right). System sizes $800 \times 100$. Red arrows indicate the direction of motion.

 

which allows us to recover the linear scaling across the coexistence region of a liquid-gas transition, hence closing a long-standing debate on the nature of the transition in the VM. But our most important results concern the hydrodynamic descriptions of flocking models. Surprisingly, deterministic hydrodynamic equations for scalar (AIM) and vectorial (VM) order parameters *both* support many different coexisting *stable* inhomogeneous solutions selected by initial conditions, including single-domain and microphase smectics. They thus do not account for the differences observed in the microscopic models. We then show that the two scenarios are, however, discriminated at the *fluctuating* hydrodynamic level: the different symmetries result in qualitatively different density fluctuations, effectively providing a selection criterion. Scalar and vectorial stochastic partial differential equations indeed generically lead to different, unique profiles, in agreement with the microscopic models.

We first recall the definition of the Vicsek model. $N$ pointlike particles, labeled by index $i$, move at constant speed $v_0$ on a rectangular plane of surface $S = L_x L_y$ with periodic boundary conditions. At each discrete time step $\Delta t = 1$, the headings $\theta_i$ of all particles are updated in parallel according to [23]

$$\theta_i(t+1) = \langle \theta_j(t) \rangle_{j \in \mathcal{N}_i} + \eta \xi_i^t, \qquad (1)$$

where $\mathcal{N}_i$ is the disk of unit radius around particle $i$, $\xi_i^t$ is a random angle drawn uniformly in $[-\pi, \pi]$, and $\eta$ sets the noise intensity. Then, particles hop along their new headings: $\mathbf{r}_i(t+1) = \mathbf{r}_i(t) + v_0 \mathbf{e}_i^{t+1}$, where $\mathbf{e}_i^{t+1}$ is the unit vector pointing in the direction given by $\theta_i(t+1)$.

In agreement with Ref. [15], we find, varying the noise $\eta$ and the density $\rho_0 = N/S$, three different phases: a disordered gas at high noise and low density, a polar liquid at low noise and high density, and an intermediate region where ordered bands travel in a disordered background. In the thermodynamic limit, the homogeneous phases are separated from the coexistence phase by two "binodals": $\rho_l(\eta)$ and $\rho_h(\eta)$, which are reported in Fig. 2(a). One could in principle add spinodal lines in the coexistence region, marking the limits of linear stability of the homogeneous phases. At finite "temperature" $\eta$, nucleation prevents us from computing them directly, but quenching the system into the coexistence region, we see two distinct behaviors: metastability and nucleation close to the coexistence lines and spinodal decomposition deeper in the coexistence region (see movies in Ref. [22]). As for the AIM, an important difference with the phase diagram of a liquid-gas phase transition in the canonical ensemble is its unusual shape, which stems from the different symmetries of the two phases. Since it is impossible to go continuously from the polar liquid to the disordered gas, there is no supercritical region and the critical point is sent to $\rho_c = \infty$.

While the phase diagrams of VM and AIM have similar shapes, their coexistence regions are fundamentally

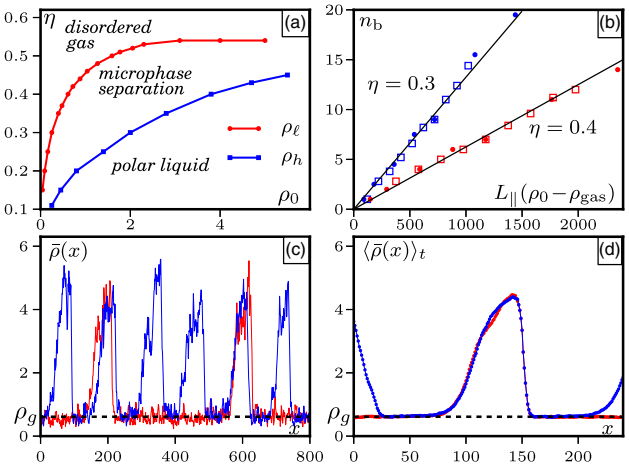


FIG. 2 (color online). (a) Phase diagram of the Vicsek model. The binodals $\rho_\ell(\eta)$ and $\rho_h(\eta)$ mark the limit of the coexistence region. (b) Number of bands vs $L_\parallel(\rho_0 - \rho_{gas})$ varying either the excess density for $Lx \times Ly = 2000 \times 100$ (squares) or the system size along the direction of propagation (dots) for $\rho_0 = 0.6$ ($\eta = 0.3$) or $\rho_0 = 1.2$ ($\eta = 0.4$). The straight black lines are guides for the eyes. (c) Density profiles of Fig. 1 averaged along the transverse direction $\mathbf{e}_\perp$, $\bar{\rho}(x_\parallel) = \langle \rho(x_\perp, x_\parallel) \rangle_{x_\perp}$. (d) Time average of the band profiles shown in (c). A threefold increase of the excess density changes the number of bands but not the gas density or the shape of the bands. $v = 0.5$, $\eta = 0.4$, $\rho_0 = 1.05$ (red/light grey lines), $\rho_0 = 1.93$ (blue/dark grey lines).

different. Starting from random initial conditions, the dynamics of the VM rapidly leads to randomly spaced ordered bands propagating along a direction $e_\parallel$ and spanning the system along $e_\perp$, as reported before [15,17]. On much longer time scales, unreached in previous studies, the relaxation of compression modes actually leads to *regularly* spaced bands [see Fig. 2(c) and the movie in Ref. [22]]. In the thermodynamic limit, the bands have well-defined profiles, independent from the average density and the system size. In this limit, increasing $\rho_0$ at constant $\eta$ thus does not change the density $\rho_{gas}$ of the gaseous background or the celerity or the shape of the bands. Only the band number $n_b$ increases, proportionally to $L_\parallel(\rho_0 - \rho_{gas})$ [Figs. 2(b) and 2(d)]. For finite systems, the quantization of the liquid fraction has some interesting consequences. An excess mass $S(\rho_0 - \rho_{gas})$ which is not a multiple of the excess mass $m_b$ of a single band does not allow the system to relax to its asymptotic band shape. To accommodate this excess mass, the bands are slightly deformed, but $c$ and $\rho_{gas}$ barely change as $\rho_0$ is varied (not shown).

This smectic arrangement of finite-width bands markedly differs from the more conventional liquid-gas phase separation seen in the AIM, where increasing the density simply widens the single liquid domain. One may thus wonder whether all features of the liquid-gas scenario survive. The global polarization $|\mathbf{P}| = (1/N)|\sum_i \mathbf{e_i}|$, used

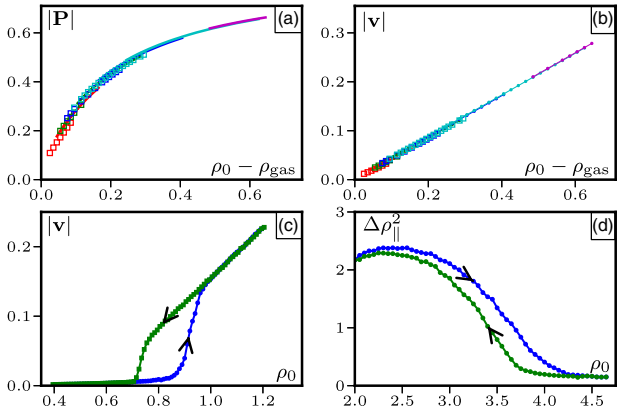


FIG. 3 (color online). (a) Polarization and (b) mean velocity vs $\rho_0$ for $L = 2048$ (squares) and $L = 1024$ (lines). Red, green, blue, cyan, and magenta correspond to solutions with 1 to 5 bands. (c) Hysteresis loop between gas and microphase states. (d) Hysteresis loop between microphase and liquid states. The variance $\Delta\rho_\parallel^2$ quantifies inhomogeneity along the direction of motion. 100 runs are used for (c) and (d), with $\eta = 0.4$, system size $400 \times 400$.

in previous studies of the VM to characterize the onset of ordering [13,15,17], does not show a linear increase of the liquid fraction with density [Fig. 3(a)]. Such a scaling is, however, recovered by considering $|\mathbf{v}| \equiv (1/S)|\sum_i v_0 \mathbf{e_i}| = v_0\rho_0|\mathbf{P}|$ [Fig. 3(b)]. Indeed, for a propagating band of celerity $c$, integrating the continuity equation $\dot{\rho} = -\nabla \cdot \mathbf{W}$, where $\mathbf{W}(\mathbf{r}) = \sum_i \delta(\mathbf{r} - \mathbf{r_i}) v_0 \mathbf{e_i}$ is the momentum field, yields $c[\rho(\mathbf{r}) - \rho_{gas}] = W_\parallel(\mathbf{r})$ [17]. Averaging over space, this gives $|\mathbf{v}| = c(\rho_0 - \rho_{gas})$. Since $c$ and $\rho_{gas}$ barely depend on $\rho_0$, $|\mathbf{v}|$ scales linearly with $\rho_0 - \rho_{gas}$, even for finite systems where nearby values of $n_b$ coexist [see Fig. 3(b)]. This is yet another signature of the first-order nature of the transition and confirms the analogy with the canonical liquid-gas transition; the apparent singularity of $|\mathbf{P}|$ close to $\rho_{gas}$ is a simple consequence of its normalization, not of criticality (as often assumed in the literature).

Close to $\rho_\ell(\eta)$, we observe expected hysteresis loops [15] when ramping $\rho_0$ up and down, with two sharp jumps in the mean velocity $|\mathbf{v}|$ [Fig. 3(c)]. Their interpretation is now much clearer: if the ramping is slow enough, they correspond to the nucleation and vanishing of a single band which acts as a critical nucleus. Indeed, a band can only be observed if the excess density $\rho_0 - \rho_{gas}$ is of the order of $m_b/S$. As the system size increases, bands are hence seen closer and closer to $\rho_{gas}$, which thus coincide with the binodal $\rho_\ell$, as in a standard liquid-gas transition. Moreover, the critical nucleus contains a smaller and smaller fraction of the particles as $L$ increases so that $|\mathbf{v}|$ and $|\mathbf{P}|$ vary *continuously* to 0 in the infinite-size limit [cf. Figs. 3(a) and 3(b)], something which had been missed before.

The second transition line $\rho_\ell(\eta)$ between the smectic microphase and the ordered liquid is harder to locate accurately. For $\rho_0 \lesssim \rho_h(\eta)$, the bands are indeed closely packed and interact strongly. Although global orientational order remains high, they break and merge in a chaotic manner (see the movie in Ref. [22]). The resulting dynamics is thus difficult to distinguish from the giant density fluctuations of the homogeneous phase. Following Ref. [15], we use $\Delta\rho_\parallel^2 \equiv \langle[\bar{\rho}(x_\parallel) - \rho_0]^2\rangle_{x_\parallel}$, the variance along $L_\parallel$ of $\bar{\rho}$, the density profile averaged in the transverse direction. Figure 3(d) shows that hysteresis loops also exist around the transition line $\rho_\ell(\eta)$, which we define as the high-density end point of the loops. This allows us to provide for the first time a complete phase diagram of the VM in Fig. 2.

To account for the differences between the coexistence phases of the VM and AIM, we now connect the above results to the more theoretical level of continuous descriptions. There are two important differences between the hydrodynamic equations of VM and AIM: the nature of the ordering field (vectorial in the VM, scalar in the AIM) and the functional dependencies of the transport coefficients on density and momentum fields. When looking for one-dimensional traveling solutions, the dimension of the ordering field, however, becomes irrelevant. Furthermore, it was recently shown [20] that hydrodynamic equations of flocking models admit such traveling solutions with both smectic microphases and phase-separated profiles. We have checked that both types of solutions exist for both the equation proposed for the AIM [21] and for those proposed for Vicsek-like models [17].

Since Ref. [20] only established the existence of these solutions, a possibility to account for the different inhomogeneous profiles seen in VM and AIM could be that these solutions have different *stability* in the corresponding two-dimensional equations, where the dimension of the order parameter can play a role. To test this hypothesis, we consider scalar and vectorial versions of the "same" minimal two-dimensional partial differential equations (PDEs). The first one, the sPDE, has a scalar magnetization field $W$ corresponding to the AIM discrete symmetry

$$\partial_t \rho = -\partial_x W, \tag{2}$$

$$\partial_t W = \left[(\rho - \rho_t) - \frac{W^2}{P_0^2 \rho}\right] W + \nu \nabla^2 W - \partial_x \rho - \lambda W \partial_x W. \tag{3}$$

The second set, the vPDE, has a vectorial momentum $\vec{W}$ in line with the continuous rotational symmetry of the VM

$$\partial_t \rho = -\nabla \cdot \vec{W}, \tag{4}$$

$$\partial_t \vec{W} = \left[(\rho - \rho_t) - \frac{|\vec{W}|^2}{P_0^2 \rho}\right] \vec{W} + \nu \nabla^2 \vec{W} - \nabla\rho - \lambda(\vec{W} \cdot \nabla)\vec{W}. \tag{5}$$

Clearly, the disordered solution $|W| = 0$ becomes linearly unstable for $\rho_0 > \rho_t$. As in all active matter systems with


FIG. 4 (color online). Density field in the PDEs after integration over $t = 10^5$. Left: scalar PDE, ordered initial condition with a periodic perturbation. Right: vectorial PDE, disordered initial condition. Parameters: $\lambda = \rho_c = D = P_0 = 1$, $\rho_0 = 1.2$. System size $800 \times 100$.

metric interactions, the homogeneous ordered solution $|W|^2 = \rho_0(\rho_0 - \rho_t)P_0^2$ that emerges from this mean-field transition is itself linearly unstable to long wavelengths until $\rho_0 > \rho_s$ [17,18,20]. Note that $\rho_t$ and $\rho_s$ correspond to the spinodal lines mentioned above. Most of the inhomogeneous solutions classified in Ref. [20] exist in a $\rho_0$ range wider than $[\rho_t, \rho_s]$. It is possible to estimate $\rho_{\min}$ and $\rho_{\max}$, the extremal values of $\rho_0$ between which solutions exist. For instance, setting all parameters including $\rho_t$ to unity as in Fig. 4, one finds $\rho_{\min} \simeq 0.808$, $\rho_s \simeq 1.25$, and $\rho_{\max} \simeq 1.74$.

We integrated numerically these two sets of equations for various parameter values inside and outside the $[\rho_t, \rho_s]$ interval [24]. After transients, we end up with effectively one-dimensional solutions taking constant values along $\mathbf{e}_\perp$. In all cases, we found both smectic microphases and phase-separated profiles. Which solution is observed depends only on the initial condition and not on the symmetry of the ordering field. Figure 4 shows a periodic solution in the sPDE and a single traveling domain in the vPDE obtained for the same parameter values, striking evidence that the (deterministic) hydrodynamic equations alone *cannot* explain the selection of different patterns observed in microscopic models. This result was found robust to modifications of Eqs. (2)–(5).

We call sSDE and vSDE the stochastic versions of Eqs. (2)–(5) obtained by adding a zero-mean scalar (or vectorial) Gaussian white noise of variance $\gamma^2\rho[1 - (|W|^2/\rho^2)]$ in the $W$ (or $\vec{W}$) equation [25]. Integrating first sSDE and vSDE in the homogeneous liquid phase, we recover the same density fluctuations as in the corresponding microscopic models (Fig. 5, left): normal fluctuations in sSDE and giant ones in vSDE (with the same scaling as in microscopic models). More importantly, we recover the correct type of inhomogeneous profiles in each case, irrespective of the initial conditions. For instance, starting from a large liquid domain as initial condition in both sets of equations with the same parameters, we find that sSDE keeps this configuration while it breaks down in vSDE, eventually leading to a periodic array of bands (Fig. 5, right). In the converse experiment, starting from a configuration with many bands, we observe initially merging events in both cases, but this process stops in vSDE, leading to an asymptotic periodic state with a finite number of bands, while coarsening proceeds for sSDE.

We conclude that fluctuations play an essential role in selecting the phase-separated patterns. Note that similar experiments performed in microscopic models yield similar results. For instance, in the VM at relatively high noise large liquid domains are metastable for a long enough time to be observed before fluctuations break them and lead the system to the smectic microphase state (see the movie in Ref. [22]). Giant density fluctuations break large liquid domains and arrest band coarsening while normal fluctuations do not. Two different scenarios emerge: In the active Ising class, magnetization is a scalar quantity, density fluctuations are normal, and the system undergoes bulk phase separation. In the active $XY$ or Vicsek class, magnetization is vectorial and density fluctuations in the liquid are anomalously large and drive the system to the microphase-separated state.

To summarize, we have shown that the flocking transition in the Vicsek model amounts to a microphase liquid-gas transition in the canonical ensemble exhibiting metastability, hysteresis, and coexistence between a disordered gas and a smectic arrangement of liquid bands. This is in contrast with the bulk phase separation exhibited by the active Ising model [21]. We found that while (deterministic) hydrodynamic equations do *not* explain this difference, their stochastic counterparts do: the different nature of the order parameter produces different types

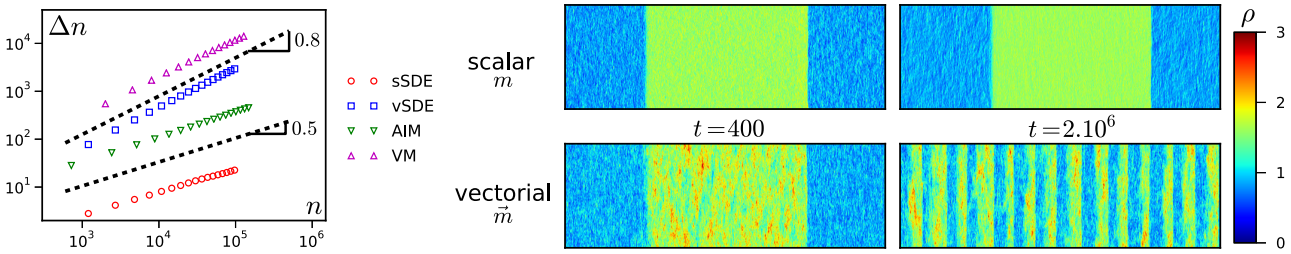


FIG. 5 (color online). Left: Number fluctuations $\Delta n = \sqrt{\langle n^2 \rangle - \langle n \rangle^2}$ where $n$ is the number of particles in boxes of different sizes. Measures are done in the homogeneous liquid phase. Parameters: size $400 \times 400$ (all), $\rho_0 = 5$, $\beta = 2.4$ (AIM), $\rho_0 = 5$, $\eta = 0.4$ (VM), $\lambda = \rho_c = D = P_0 = 1$, $\gamma^2 = 0.4$, $\rho_0 = 3$ (sSDE and vSDE). Right: Numerical integration of sSDE (top) and vSDE (bottom). Parameters: $\rho_c = \lambda = D = P_0 = 1$, $\gamma^2 = 0.4$, system size $2000 \times 100$.

of number fluctuations, which are essential in selecting the phase-separated patterns. This unexpected role of fluctuations in the selection of flock shapes calls for greater care when trying to account for active systems based on purely deterministic continuum equations.

Interesting questions remain open. For example, the mechanism by which the bands interact in the VM to reach a periodic spacing and the chaotic behavior of closely packed bands are still to be investigated. Further, we so far have no analytical approach and limited numerical results to ascertain the stability of the smectic pattern in the direction along the bands. It is not inconceivable that, like recently found in active nematics [26], the coexistence phase is asymptotically disordered. Last, in the large density region, the finite sizes of real flocking agents are not negligible and steric effects such as motility-induced phase separation [27–29] could enrich the simple liquid-gas scenario [30].

We thank the Max Planck Institute for the Physics of Complex Systems, Dresden, Germany, and the Kavli Institute for Theoretical Physics, Santa Barbara, U.S.A., for hospitality. This research was supported in part by the National Science Foundation under Grant No. NSF PHY11-25915.

[1] V. Schaller, C. Weber, C. Semmrich, E. Frey, and A. R. Bausch, Nature (London) **467**, 73 (2010); V. Schaller and A. R. Bausch, Proc. Natl. Acad. Sci. U.S.A. **110**, 4488 (2013).

[2] Y. Sumino, K. H. Nagai, Y. Shitaka, D. Tanaka, K. Yoshikawa, H. Chaté, and K. Oiwa, Nature (London) **483**, 448 (2012).

[3] M. Ballerini, N. Cabibbo, R. Candelier, A. Cavagna, E. Cisbani, I. Giardina, V. Lecomte, A. Orlandi, G. Parisi, A. Procaccini, M. Viale, and V. Zdravkovic, Proc. Natl. Acad. Sci. U.S.A. **105**, 1232 (2008).

[4] T. Sanchez, D. T. Chen, S. J. DeCamp, M. Heymann, and Z. Dogic, Nature (London) **491**, 431 (2012).

[5] S. Zhou, A. Sokolov, O. D. Lavrentovich, and I. S. Aranson, Proc. Natl. Acad. Sci. U.S.A. **111**, 1265 (2014).

[6] A. Sokolov, I. S. Aranson, J. O. Kessler, and R. E. Goldstein, Phys. Rev. Lett. **98**, 158102 (2007).

[7] F. Peruani, J. Starruss, V. Jakovljevic, L. Sogaard-Andersen, A. Deutsch, and M. Bär, Phys. Rev. Lett. **108**, 098102 (2012).

[8] Y. Katz, K. Tunstrøm, C. C. Ioannou, C. Huepe, and I. D. Couzin, Proc. Natl. Acad. Sci. U.S.A. **108**, 18720 (2011).

[9] J. Gautrais, F. Ginelli, R. Fournier, S. Blanco, M. Soria, H. Chaté, and G. Theraulaz, PLoS Comput. Biol. **8**, e1002678 (2012).

[10] J. Deseigne, O. Dauchot, and H. Chaté, Phys. Rev. Lett. **105**, 098001 (2010); J. Deseigne, S. Léonard, O. Dauchot, and H. Chaté, Soft Matter **8**, 5629 (2012); C. A. Weber, T. Hanke, J. Deseigne, S. Léonard, O. Dauchot, E. Frey, and H. Chaté, Phys. Rev. Lett. **110**, 208001 (2013).

[11] S. Thutupalli, R. Seemann, and S. Herminghaus, New J. Phys. **13**, 073021 (2011).

[12] A. Bricard, J.-B. Caussin, N. Desreumaux, O. Dauchot, and D. Bartolo, Nature (London) **503**, 95 (2013).

[13] T. Vicsek, A. Czirók, E. Ben-Jacob, I. Cohen, and O. Shochet, Phys. Rev. Lett. **75**, 1226 (1995).

[14] T. Vicsek and A. Zafeiris, Phys. Rep. **517**, 71 (2012).

[15] G. Grégoire and H. Chaté, Phys. Rev. Lett. **92**, 025702 (2004); H. Chaté, F. Ginelli, G. Grégoire, and F. Raynaud, Phys. Rev. E **77**, 046113 (2008).

[16] J. Toner and Y. Tu, Phys. Rev. Lett. **75**, 4326 (1995); J. Toner and Y. Tu, Phys. Rev. E **58**, 4828 (1998); J. Toner, Phys. Rev. E **86**, 031918 (2012).

[17] E. Bertin, M. Droz, and G. Grégoire, Phys. Rev. E **74**, 022101 (2006); E. Bertin, M. Droz, and G. Grégoire, J. Phys. A **42**, 445001 (2009); A. Peshkov, E. Bertin, F. Ginelli, and H. Chaté, Eur. Phys. J. Spec. Top. **223**, 1315 (2014).

[18] S. Mishra, A. Baskaran, and M. C. Marchetti, Phys. Rev. E **81**, 061916 (2010); A. Gopinath, M. F. Hagan, M. C. Marchetti, and A. Baskaran, Phys. Rev. E **85**, 061903 (2012).

[19] T. Ihle, Phys. Rev. E **83**, 030901 (2011); T. Ihle, Phys. Rev. E **88**, 040303(R)(2013).

[20] J.-B. Caussin, A. Solon, A. Peshkov, H. Chaté, T. Dauxois, J. Tailleur, V. Vitelli, and D. Bartolo, Phys. Rev. Lett. **112**, 148102 (2014).

[21] A. P. Solon and J. Tailleur, Phys. Rev. Lett. **111**, 078101 (2013).

[22] See Supplemental Material at http://link.aps.org/supplemental/10.1103/PhysRevLett.114.068101 for movies and more information.

[23] This defines the angular noise dynamics of the Vicsek model. Vectorial noise dynamics do not introduce any qualitative difference [15].

[24] For PDEs, we used a pseudospectral integration scheme (linear terms are computed in Fourier space, nonlinear ones in real space) using semi-implicit time stepping. The stochastic PDEs were integrated following Itō's interpretation.

[25] This structure of the noise variance is one of the simplest that accounts for the observed fact that the amplitude of fluctuations decreases when polarization $|W|/\rho$ increases while respecting the symmetry of the ordering field. However, our results are not sensitive to this particular form and hold for simpler choices such as $\gamma^2\rho$ or even additive noise.

[26] S. Ngo, A. Peshkov, I. S. Aranson, E. Bertin, F. Ginelli, and H. Chaté, Phys. Rev. Lett. **113**, 038302 (2014); X. Shi, H. Chaté, and Y. Ma, New J. Phys. **16**, 035003 (2014).

[27] J. Tailleur and M. E. Cates, Phys. Rev. Lett. **100**, 218103 (2008).

[28] Y. Fily and M. C. Marchetti, Phys. Rev. Lett. **108**, 235702 (2012).

[29] G. S. Redner, M. F. Hagan, and A. Baskaran, Phys. Rev. Lett. **110**, 055701 (2013).

[30] F. D. C. Farrell, J. Tailleur, D. Marenduzzo, and M. C. Marchetti, Phys. Rev. Lett. **108**, 248101 (2012).

### 5.4.1 Dynamique des bandes

Nous voulons, dans cette section, compléter l'article G en étudiant plus en détail la dynamique des bandes ordonnées observées dans la région de coexistence des modèles de Vicsek et d'Ising actif.

La figure 5 de l'article G montre l'évolution d'un large domaine ordonné dans les hydrodynamiques fluctuantes avec aimantation scalaire ou vectorielle. La bande de liquide est stable lorsque l'aimantation est scalaire. Au contraire, elle se fractionne lorsque l'aimantation est vectorielle. On peut réaliser l'expérience inverse : partir d'un système séparé en microphases, contenant de nombreuses bandes, et regarder comment le nombre de bandes $N_b$ évolue. L'évolution de $N_b$ pour quatre simulations (en partant d'une ou de 25 bandes, pour une aimantation scalaire ou vectorielle) est tracée à la figure 5.4. Dans les équations avec aimantation vectorielle, le nombre de bandes semble converger vers une valeur finie, entre 15 et 18, ce qui est compatible avec la sélection d'une taille caractéristique. Au contraire, avec une aimantation scalaire, le système semble tendre vers un domaine liquide unique, bien que des simulations beaucoup plus longues seraient nécessaires pour arriver à ce résultat en partant d'une séparation en microphases.

La dynamique des bandes dans les modèles microscopiques (Ising actif et Vicsek) confirme les résultats obtenus pour les équations hydrodynamiques fluctuantes. Dans le modèle d'Ising actif, comme dans les équations hydrodynamiques avec aimantation scalaire, un large domaine liquide est toujours stable. De plus, comme on peut le voir à la figure 5.5, deux bandes ordonnées séparées d'une distance relativement grande finissent, aux temps longs, par fusionner. C'est l'échange de particules entre les deux bandes, plus que les fluctuations de leur vitesse, qui semble mener à cette fusion. En effet, la largeur des deux bandes effectue une marche aléatoire (voir figure 5.5, centre). Cela conduit à des différences de vitesse (comme nous l'avons vu dans l'article F, la vitesse d'une bande est corrélée à sa taille), qui *in fine* les amènent à se rencontrer.

La dynamique des bandes du modèle de Vicsek est très différente. Tout d'abord, un large domaine liquide est métastable, comme dans les équations hydrodynamiques avec aimantation vectorielle. Aux temps longs, il se fractionne en plusieurs bandes. Contrairement à ce qu'on observe dans le modèle d'Ising actif, les bandes échangent des particules pour égaliser leurs masses (voir figure 5.5, centre et droite). Ainsi, dans l'état final, on observe des bandes approximativement de même taille. De plus, une interaction répulsive entre bandes les amène à se répartir périodiquement dans l'espace. La figure 5.6 montre la distance $\Delta x$ entre deux bandes en fonction du temps. On voit qu'une force répulsive, dont l'amplitude décroît avec la distance, tend à éloigner les deux bandes.

Tous ces résultats semblent montrer que, dans le modèle d'Ising actif (ou pour les équations hydrodynamiques avec aimantation scalaire), le système converge

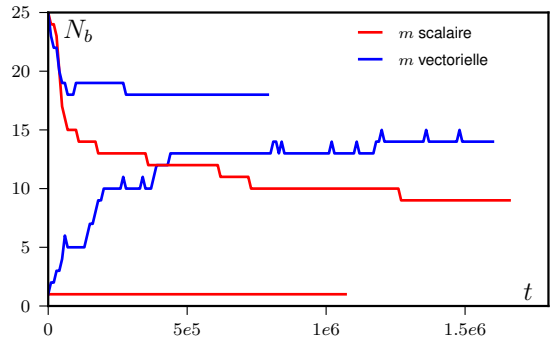


**Figure 5.4** – Évolution du nombre de bandes dans des simulations des équations hydrodynamiques fluctuantes (définies dans l'article G), en partant soit d'un unique domaine liquide, soit d'une séparation en 25 microphases. Les paramètres, identiques pour les quatre simulations, sont ceux de la figure 5 de l'article G.

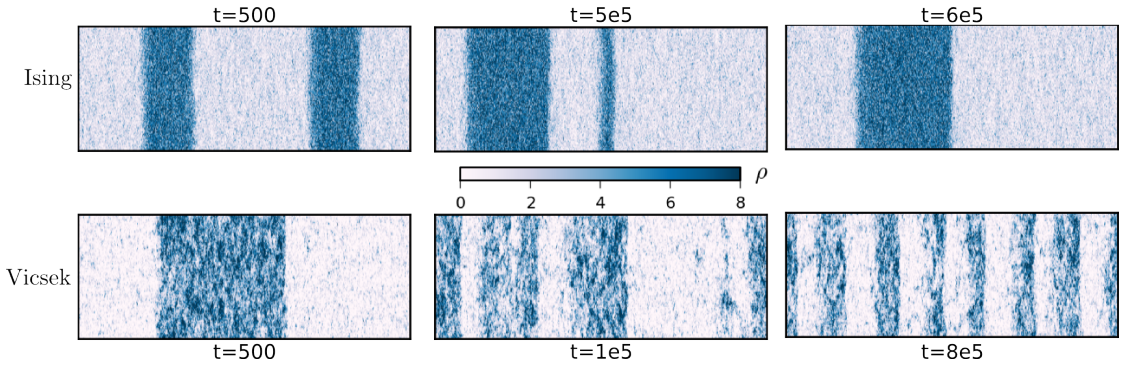


**Figure 5.5** – Dynamique des bandes dans le modèle d'Ising actif (haut) et dans le modèle de Vicsek (bas). **Haut** : dans le modèle d'Ising actif, les échanges de masse entre bandes (centre) conduisent à des variations de vitesse, si bien que deux bandes fusionnent aux temps longs (droite). Paramètres : $\beta = 1.8$, $\rho_0 = 2.8$, $D = 1$, $\varepsilon = 1.9$, taille du système $800 \times 100$. **Bas** : dans le modèle de Vicsek, un domaine liquide est métastable (gauche). Il se fractionne en plusieurs bandes. Les bandes échangent de la masse pour égaliser leur taille et une interaction répulsive conduit à un arrangement périodique (droite). Paramètres : $v = 0.5$, $\eta = 0.4$ (bruit angulaire), $\rho_0 = 2.25$, taille du système $800 \times 100$.

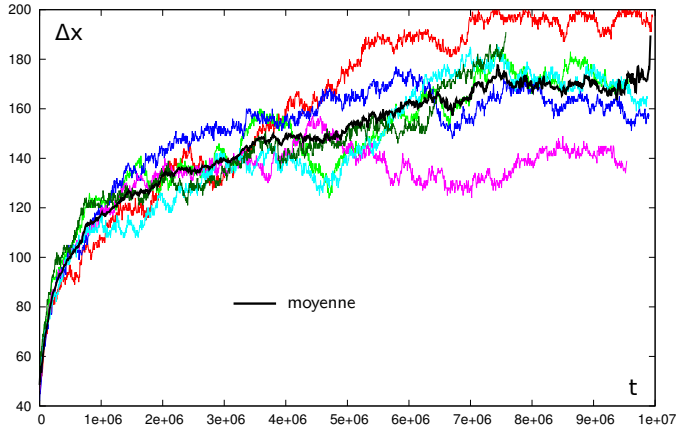


**Figure 5.6** – Évolution de la distance $\Delta x$ entre deux bandes dans le modèle de Vicsek. Le temps $t = 0$ correspond au moment où une bande plus large s'est fractionnée en deux bandes dont on suit la position. Les courbes en couleur correspondent à six événements et la courbe épaisse noire à la moyenne des six. Paramètres : $v = 0.5$, $\eta = 0.6$ (bruit vectoriel), $\rho_0 = 1$, taille du système $400 \times 100$.

toujours vers un domaine ordonné unique se déplaçant dans un gaz désordonné. Au contraire, dans le modèle de Vicsek (ou les équations hydrodynamiques avec aimantation vectorielle), une taille caractéristique de bande est sélectionnée et le système converge vers un arrangement périodique de ces microphases. Notons que, au-delà des observations faites ici, les interactions entre bandes restent à étudier. En particulier, le mécanisme générant une interaction répulsive entre bandes dans le modèle de Vicsek est un problème complètement ouvert.

### 5.4.2 Deux classes d'universalité pour la transition vers le mouvement collectif

Les résultats des sections précédentes montrent que l'on peut obtenir deux types de comportement pour la transition vers le mouvement collectif. Ceux-ci semblent intimement liés à la présence (ou non) de fluctuations géantes de densité. Dans le modèle d'Ising actif, comme dans les équations hydrodynamiques fluctuantes avec une aimantation scalaire, les fluctuations de densité sont normales et on observe une séparation de phase complète. Dans le modèle de Vicsek, comme dans les équations hydrodynamiques avec aimantation vectorielle, les fluctuations de densité sont géantes et s'accompagnent d'une séparation en microphases.

Dans cette section, nous voulons tester la généralité de ces deux classes d'universalité en étudiant d'autres modèles de spins actifs. En particulier, nous intro-

duirons un modèle XY actif, qui a la même symétrie que le modèle de Vicsek mais une dynamique microscopique différente. Nous introduirons également un modèle de Potts actif dans lequel chaque particule porte une « couleur » parmi $n$. En associant chaque couleur à une direction d'autopropulsion, on peut modifier le nombre de directions possibles et ainsi obtenir des cas intermédiaires entre le modèle d'Ising actif (deux directions) et le modèle XY actif (une infinité). Nous étudierons ces modèles sur réseau, ce qui ne semble pas introduire de différences qualitatives par rapport à des modèles similaires en espace continu (voir l'article E, section VI.B, pour une version du modèle d'Ising actif en espace continu).

### *Modèle XY actif*

On peut définir un modèle XY actif sur un réseau 2d d'une façon similaire au modèle d'Ising actif. Chaque particule porte un spin continu $\mathbf{S}_i$ donnant sa direction d'autopropulsion. Elles sautent alors vers le site voisin dans la direction $\mathbf{u}$ (avec $\mathbf{u} = (\pm 1,0)$ ou $\mathbf{u} = (0, \pm 1)$ pour les directions horizontales et verticales) avec un taux $D(1 + \varepsilon \mathbf{u} \cdot \mathbf{S}_i)$. Les particules alignent également leur direction de déplacement avec les particules présentes sur le même site. La dynamique de l'angle $\theta_i$, paramétrant le spin $\mathbf{S}_i$ de la particule $i$, est donnée par l'équation de Langevin

$$\dot{\theta}_i = -\frac{\partial \mathcal{H}}{\partial \theta_i} + \sqrt{2T}\xi \tag{5.11}$$

où $\xi$ est un bruit blanc gaussien de variance unité. L'Hamiltonien $\mathcal{H}$ est similaire à celui d'un modèle XY dans lequel tous les spins sur un même site $k$ sont couplés

$$\mathcal{H} = -\sum_k \frac{1}{\rho_k} \sum_{i \neq j} \mathbf{S}_i \cdot \mathbf{S}_j \tag{5.12}$$

où la première somme porte sur les sites du réseau et la deuxième sur les particules présentes au site $k$. Comme pour le modèle d'Ising actif, on utilise un algorithme de mise à jour séquentielle aléatoire dans les simulations.

On retrouve dans ce modèle XY actif la phénoménologie du modèle de Vicsek. En particulier, on mesure des fluctuations géantes de densité qui ont la même loi d'échelle que celles du modèle de Vicsek (voir figure 5.8). De plus, l'expérience numérique de l'article 5.4 (figure 5) donne le même résultat que dans le modèle de Vicsek : une large bande ordonnée de haute densité est métastable. Aux temps longs, celle-ci se casse en bandes de taille finie, réparties périodiquement dans l'espace (voir figure 5.7). Cela n'est au contraire jamais observé dans le modèle d'Ising actif, dans lequel un domaine liquide de taille arbitraire est stable.

### *Modèles de Potts actifs*

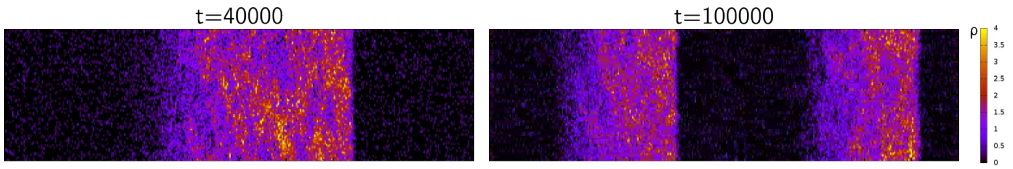


**Figure 5.7** – Modèle XY actif. Un grand domaine liquide ordonné est métastable. Aux temps longs il se brise pour former plusieurs bandes. Paramètres : $T = 0.3$, $\rho_0 = 0.6$, $D = 1$, $\varepsilon = 0.9$, taille de système $2000 \times 100$.

Introduisons maintenant un modèle de Potts qui va nous permettre d'interpoler entre le comportement du modèle d'Ising actif (deux directions d'autopropulsion) et celui du modèle XY actif (une continuité de directions). Dans celui-ci, $n$ « couleurs », portées par les particules, sont couplées à $n$ directions d'autopropulsion possibles. L'Hamiltonien contrôlant l'alignement des particules s'écrit

$$\mathcal{H} = -\sum_k \frac{1}{\rho_k} \sum_{i \neq j} \delta_{c(i)c(j)} \tag{5.13}$$

où $c(i)$ est la couleur de la particule $i$. Une particule change alors sa couleur de $c_1$ en $c_2$ avec une probabilité

$$W\left(c_1 \to c_2\right) = \exp\left(-\beta \frac{\Delta \mathcal{H}}{2}\right) \tag{5.14}$$

Notons que ce type d'alignement est légèrement différent de l'alignement ferromagnétique considéré précédemment : deux particules ayant des couleurs (*i.e.* directions) différentes contribuent à $\mathcal{H}$ de la même façon, qu'elles que soient leurs couleurs (qu'elles correspondent à des directions proches ou opposées).

Nous avons considéré les deux cas les plus évidents sur réseau : les modèles de Potts à quatre et huit couleurs. Dans le modèle à quatre couleurs, quatre directions (haut, bas, gauche et droite) sont possibles. Avec huit couleurs, nous rajoutons les diagonales. Une particule saute alors dans la direction donnée par sa couleur avec un taux $D(1 + \varepsilon)$ et dans toutes les autres directions avec un taux $D(1 - \varepsilon)$.

Les comportements des modèles à quatre et huit couleurs sont qualitativement différents. En particulier, les fluctuations de densité dans la phase ordonnée sont normales pour le cas $n = 4$ et géantes, avec la loi d'échelle des modèles de Vicsek et XY, pour $n = 8$ (voir figure 5.8). De plus, le modèle à quatre couleurs montre une séparation de phase entre un domaine gazeux et un domaine liquide stable arbitrairement grand, un comportement similaire à celui du modèle d'Ising actif (voir figure 5.9).

Notons que ces résultats sont préliminaires. Les modèles de Potts sont gourmands en temps de calcul (qui est proportionnel au nombre de couleurs) et leurs

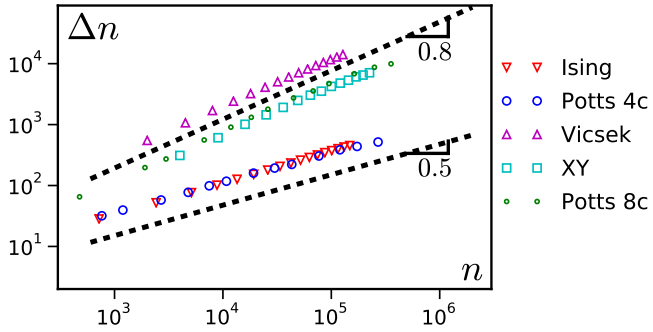


**Figure 5.8** – Fluctuations de densité dans les modèles microscopiques étudiés. On distingue deux comportements : des fluctuations normales dans les modèles d'Ising actif et de Potts actif à quatre couleurs, des fluctuations anormales données par le même exposant $\alpha = 0.8$ pour les modèles de Vicsek, XY actif et Potts actif à huit couleurs.

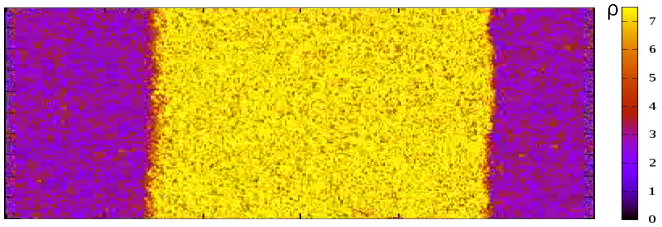


**Figure 5.9** – Séparation de phase dans le modèle de Potts actif à quatre couleurs. Paramètres : $\beta = 4.5$, $\rho_0 = 5.5$, $\varepsilon = 0.9$, $D = 1$, taille du système $600 \times 200$.

propriétés restent à étudier plus en détail, en particulier la coexistence de phase dans le modèle à huit couleurs.

### *Classes d'universalité*

La conclusion qui semble se dégager de ces résultats est qu'on peut organiser les modèles de particules autopropulsées avec alignement ferromagnétique en deux classes d'universalité, qui correspondent à deux types de coexistence de phase. La forme de la coexistence de phase est contrôlée par les propriétés de la phase ordonnée. En particulier, la présence ou non de fluctuations anormales de densité semble cruciale. Des fluctuations normales dans la phase liquide donnent lieu à une séparation de phase complète dans la région de coexistence. Au contraire, des fluctuations géantes entraînent une séparation en microphases.

La présence de ces fluctuations géantes de densité est liée à la symétrie rotationnelle du système. Lorsqu'un faible nombre de directions d'autopropulsion

($\leq 4$) sont possibles, le comportement est celui du modèle d'Ising actif. Lorsque les directions possibles sont nombreuses ($\geq 8$), il semble que l'on retrouve le comportement du modèle de Vicsek. Cela reste à confirmer en étudiant la phase de coexistence du modèle de Potts à huit couleurs. De plus, il serait intéressant de voir si l'on peut affiner la limite entre les deux classes en considérant des modèles ayant entre 4 et 8 directions d'autopropulsion.

On peut relier l'existence des deux classes d'universalité à des observations expérimentales. Dans l'expérience réalisée par Bartolo et collaborateurs [44], des colloïdes isolants plongés dans un liquide conducteur sont autopropulsés par une instabilité électro-hydrodynamique. De plus, ils interagissent pour aligner leur direction de déplacement par des interactions hydrodynamiques. Les colloïdes peuvent se déplacer dans une direction arbitraire du plan mais il a été montré que, dans ce système, les interactions hydrodynamiques suppriment les fluctuations géantes de densité [44]. En ligne avec notre analyse, on observe alors une séparation de phase complète entre un liquide ordonné et un gaz désordonné (voir figure 5.10, gauche). Au contraire, dans un *motility assay* utilisant des filaments d'actine [22], des fluctuations géantes de densité sont observées [128], avec une loi d'échelle proche de celle observée dans nos modèles. On observe alors la propagation de bandes ordonnées de taille finie, réminiscentes de la séparation en microphases que nous avons décrite (voir figure 5.10, droite).

## 5.5 Mouvement collectif en dimension 1

Nous terminons ce chapitre par l'étude de la transition vers le mouvement collectif en 1d. Nous nous baserons pour cela sur le modèle d'Ising actif, défini de la même façon que pour $d = 2$. Comme pour le modèle d'Ising d'équilibre, en dimension 1, les fluctuations jouent un rôle prépondérant. En particulier, nous verrons qu'elles modifient la phénoménologie de la coexistence de phase. Au lieu d'une séparation de phase entre deux domaines liquide et gazeux, on observe un agrégat ordonné qui se déplace dans un gaz désordonné en changeant de forme au cours du temps et qui inverse sa direction de déplacement de façon aléatoire. Ce phénomène d'intermittence a été observé sur des sauterelles placées dans une arène circulaire [131]. Les insectes tournent alors collectivement dans l'arène en changeant spontanément et aléatoirement leur sens de rotation. Nous étudierons la dynamique de ces « retournements » à la section 5.5.1. L'autre effet majeur des fluctuations est de rendre la phase ordonnée métastable, comme nous le montrerons à la section 5.5.2. On observe alors seulement une transition entre un état désordonné et l'état inhomogène intermittent.

La littérature sur le mouvement collectif en 1d est plus restreinte qu'en dimensions supérieures. Deux modèles assez similaires ont toutefois été étudiés [132,

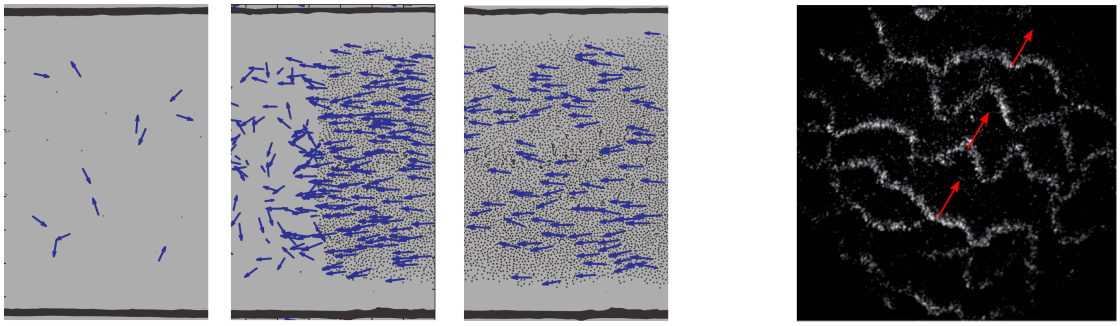

**Figure 5.10** – Deux expériences montrant une phase inhomogène de mouvement collectif. **Gauche** : Image reproduite de [44]. Des colloïdes autopropulsés montrent une séparation de phase entre un domaine gazeux désordonné et un liquide ordonné, les deux étant arbitrairement grands. De façon importante, les fluctuations de densité anormales sont absentes de ce système qui a une phénoménologie proche de celle du modèle d'Ising actif. **Droite** : Image reproduite de [22]. Des filaments d'actine dans un *motility assay* forment des bandes propagatives de taille finie. Ici, des fluctuations anormales de densité ont été observées dans la phase homogène ordonnée. Le comportement à la coexistence de phase est alors proche de la phénoménologie des modèles de Vicsek ou XY actif.

133]. Dans ces deux modèles, l'interaction d'alignement est une règle de majorité : les particules prennent la direction qui est majoritaire parmi leurs voisins, avec une probabilité qui dépend d'un paramètre de bruit. Les deux permettent d'observer la phase inhomogène intermittente décrite plus haut. Concernant la transition entre l'état désordonné et la phase intermittente, les deux études [132, 133] concluent à une transition continue, et utilisent les outils développés pour les systèmes magnétiques d'équilibre pour calculer des exposants critiques (différents pour les deux modèles). Nous montrerons à la section 5.5.3 que la transition n'est en fait pas critique mais discontinue, comme en 2d. À cause des retournements causés par les fluctuations, cela n'apparaît clairement que pour des valeurs de paramètres non explorées précédemment.

### 5.5.1 Retournements

La figure 5.11 montre en détail la dynamique du retournement d'un agrégat. Une fluctuation à l'avant de l'agrégat, si elle est d'amplitude suffisante et d'aimantation opposée à celle de l'agrégat, peut se propager dans celui-ci en retournant le spin de toutes les particules qu'elle rencontre. En 1d, une telle fluctuation localisée a une probabilité finie, c'est-à-dire indépendante de la taille du système, de

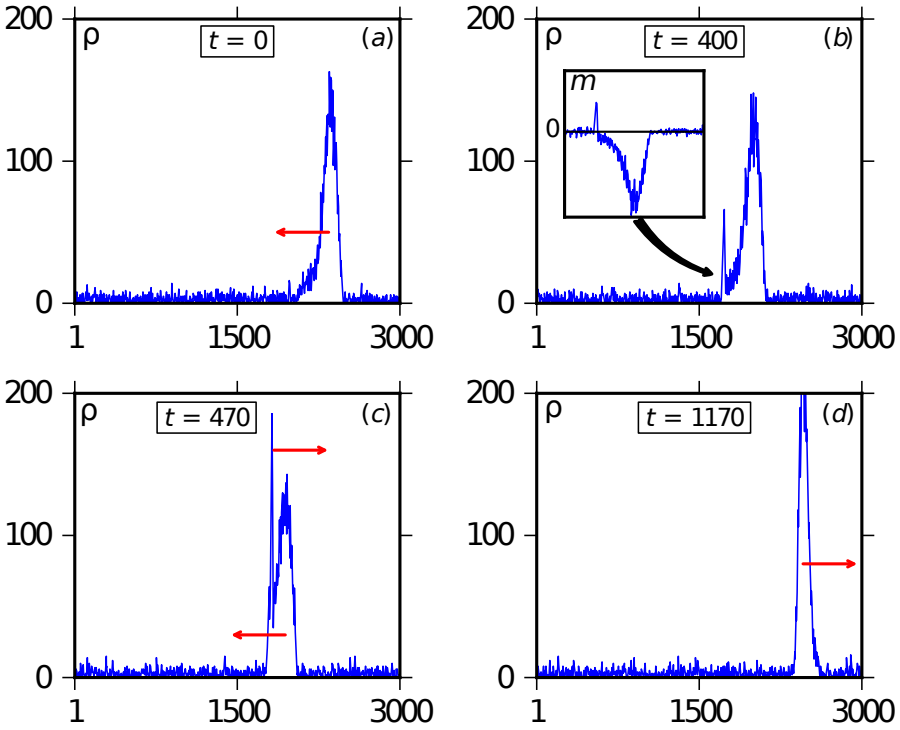


**Figure 5.11** – Dynamique de retournement des agrégats ordonnés. Une fluctuation locale d'aimantation à l'avant de l'agrégat (b, encart) se propage dans l'agrégat en retournant progressivement le spin de toutes les particules (c). On obtient finalement un agrégat se déplaçant dans la direction opposée (d). Paramètres : $D = 1$, $\varepsilon = 0.5$, $\beta = 1.6$, $\rho_0 = 10$.

se produire par unité de temps. Au contraire, dans le modèle d'Ising actif en 2d, une ligne de fluctuations serait nécessaire pour retourner un domaine liquide. L'occurrence d'une telle fluctuation a une probabilité par unité de temps qui décroît exponentiellement avec la taille du système, ce qui explique que les retournements ne jouent pas un rôle prépondérant en 2d.

Comme on peut le voir sur la figure 5.11, après un retournement, l'agrégat est condensé sur quelques sites du réseau. Il s'étale ensuite en se propageant. On peut mesurer la taille $L_c(t)$ de l'agrégat en définissant un seuil de densité *ad hoc*. On trouve qu'elle augmente linéairement entre deux retournements, qui la ramènent à une valeur plus basse (voir figure 5.12, gauche).

On peut s'intéresser également au temps moyen entre deux retournements $\tau_R$, en particulier à sa dépendance avec la taille du système, importante pour déterminer si le système présente une brisure spontanée de symétrie. Dans le modèle d'O'Loan et collaborateurs [133], une divergence très lente $\tau_R(L) \sim \ln L$ est observée. Dans notre modèle, on observe que, suivant les paramètres, $\tau_R(L)$ peut être une fonction croissante ou décroissante, qui semble converger vers une valeur finie aux grands $L$ (voir figure 5.12, panneau central).

Un argument simple permet de montrer que, tant que $\tau_R(L)$ croît moins vite que $\tau_R \sim L$, la fraction du temps passée par le système dans des retournements est finie. En effet, la durée d'un retournement est proportionnelle à taille $L_c$ de l'agrégat ; elle est donnée par la durée de la propagation balistique de la fluctuation dans l'agrégat. De plus, nous avons montré que la taille $L_c$ est proportionnelle à $\tau_R$, la taille de l'agrégat augmentant linéairement dans le temps. Le système passe donc un temps proportionnel à $L_c/\tau_R \sim \mathcal{O}(1)$ dans des retournements. (Si $\tau_R$ croît plus vite que $\tau_R \sim L$, la situation change car l'agrégat, dont la masse est proportionnelle à $L$, a alors le temps de s'étaler complètement.) On peut vérifier l'argument précédent en traçant l'histogramme de l'aimantation par unité de longueur $m = \frac{1}{L}\sum_i S_i$, où $S_i = \pm 1$ est le spin de la particule $i$. Dans la limite $L \to \infty$, on observe que la probabilité de trouver $m$ proche de $m = 0$ (*i.e.* dans un retournement) converge vers une valeur finie (voir figure 5.12, droite). Il n'y a donc pas de brisure spontanée de symétrie : l'agrégat continue à changer de direction dans la limite thermodynamique.

### 5.5.2 Phase ordonnée instable

Le diagramme des phases du modèle d'Ising actif en 1d dans l'espace (température, densité) est présenté à la figure 5.13 (gauche). À la différence du cas $d = 2$, il ne comporte pas de phase homogène ordonnée, celle-ci étant seulement métastable. En effet, une fluctuation locale de l'aimantation dans la phase ordonnée (disons une fluctuation négative dans une phase homogène d'aimantation positive) peut se propager et ainsi retourner toute la phase homogène positive. Le système arrive

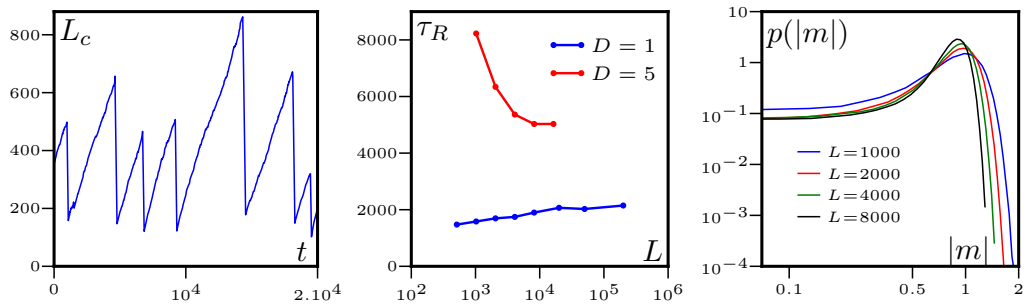


**Figure 5.12** – **Gauche** : Taille de l'agrégat intermittent en fonction du temps. On observe un étalement linéaire entre les retournements. Paramètres : $D = 1$, $\varepsilon = 0.9$, $\beta = 2$, $\rho_0 = 3$. **Centre** : Temps moyen entre deux retournements en fonction de la taille du système. Paramètres : $\varepsilon = 0.9$, $\beta = 1.7$, $\rho_0 = 3$. **Droite** : Probabilité d'observer une aimantation $|m|$ dans le système. $P(m \approx 0)$ ne s'annule pas lorsque $L \to \infty$, signifiant que l'on n'observe pas de brisure de symétrie. Paramètres : $D = 1$, $\varepsilon = 0.9$, $\beta = 1.538$, $\rho_0 = 4$.

alors dans l'état intermittent décrit plus haut. Une telle fluctuation, bien qu'improbable à basse température et haute densité, a une probabilité $\alpha$ finie de se produire par unité de longueur et de temps.

On peut calculer, à partir de ce taux $\alpha$, le temps de vie de la phase ordonnée. La probabilité que la phase ordonnée survive un temps $\tau_s$ est égale à la probabilité (i) qu'aucune fluctuation ne survienne pendant un temps $\tau_s$ et (ii) qu'une fluctuation retourne la phase homogène à $t = \tau_s$. Pour un système de taille $L$ et de longueur de corrélation finie, une fluctuation survient à un taux $\alpha L$ par unité de temps. On a donc

$$\mathcal{P}(\tau_s) = \alpha L e^{-\alpha L \tau_s} \tag{5.15}$$

Le temps moyen de métastabilité est alors donné par

$$\langle \tau_s \rangle = \int_0^\infty \tau_s \mathcal{P}(\tau_s) d\tau_s = \frac{1}{\alpha L} \tag{5.16}$$

La loi d'échelle $\langle \tau_s \rangle \sim 1/L$ est très bien vérifiée numériquement, comme on peut le voir à la figure 5.13. On voit également que le taux $\alpha$ diminue quand la densité augmente, ce qui est conforme à notre intuition : plus la phase ordonnée est dense, plus les fluctuations à même de la déstabiliser sont rares.

### 5.5.3 Transition liquide-gaz

Comme nous l'avons évoqué dans l'introduction de cette section, les études précédentes sur la transition entre l'état désordonné et l'état intermittent [132,

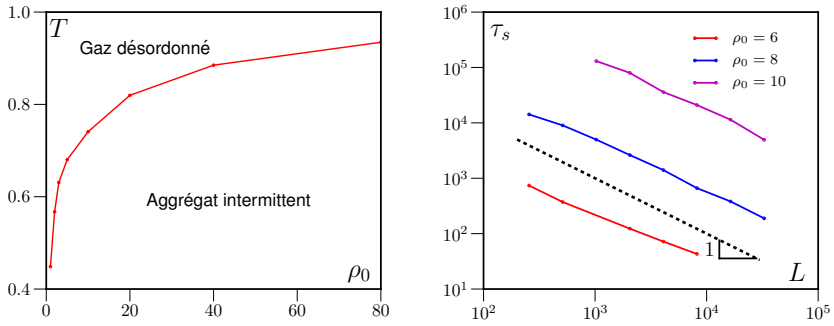


**Figure 5.13** – **Gauche** : Diagramme des phases du modèle d'Ising actif en 1d. Paramètres : $D = 1$, $\varepsilon = 0.9$. **Droite** : Temps moyen de métastabilité de la phase homogène ordonnée. Paramètres : $D = 1$, $\varepsilon = 0.9$, $\beta = 2.2$.

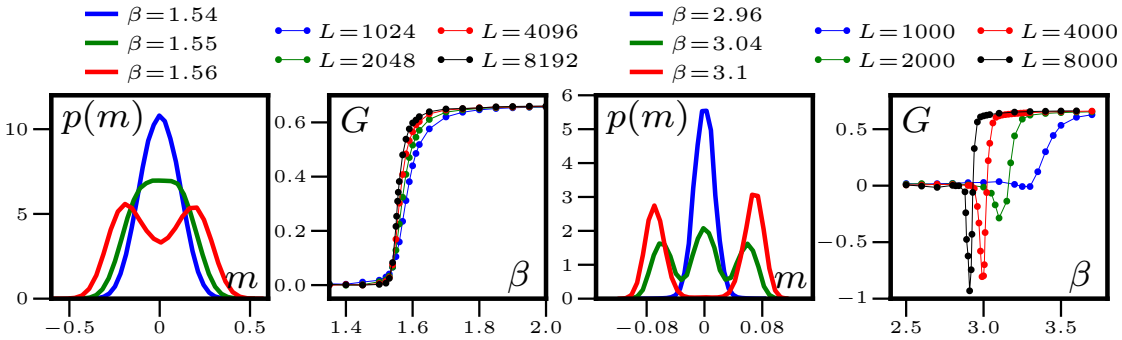


**Figure 5.14** – Histogrammes et cumulant de Binder de l'aimantation totale. **Gauche** : $D = 1$, $\rho_0 = 3$. **Droite** : $D = 10$, $\rho_0 = 0.2$. Pour les deux : $\varepsilon = 0.9$ et $L = 8000$ pour les histogrammes.

133] concluent à une transition de phase continue. Pour cela, elles utilisent les observables habituellement étudiées dans les transitions de phase des systèmes magnétiques d'équilibre. En particulier, le cumulant de Binder [134], défini par $G = 1 - \langle m^4 \rangle / (3 \langle m^2 \rangle^2)$ (voir article E) a un comportement différent pour des transitons continues ou discontinues. Pour une transition continue, il est monotone et les courbes $G_L$ pour différentes tailles de système se croisent toutes en un point. Pour une transition discontinue, $G$ présente un pic négatif à la transition, de plus en plus marqué pour des tailles de système de plus en plus grandes. Ce comportement peut être relier aux histogrammes de l'aimantation totale $P(m)$ : le pic négatif de $G$ apparaît lorsque $P(m)$ a une forme « à trois bosses », caractéristique de la métastabilité observée dans les transitions de phase discontinues.

Nous montrons à la figure 5.14 que les deux comportements du cumulant de Binder et de $P(m)$ peuvent être observés, pour différents paramètres. En effet, en augmentant le coefficient de diffusion, on diminue l'effet des fluctuations. Cela

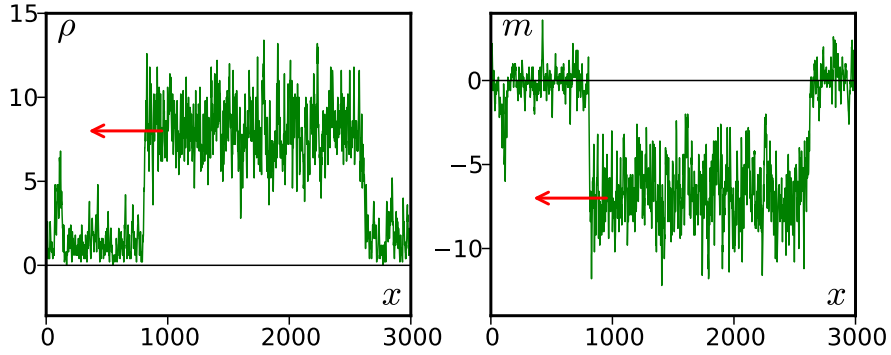


**Figure 5.15** – Profils de densité (gauche) et d'aimantation (droite). Lorsque le coefficient de diffusion est assez élevé, les retournements sont rares. L'agrégat ordonné peut alors converger vers sa forme finale, qui est similaire à celle des domaines liquides du modèle d'Ising actif en 2d. Paramètres : $D = 5$, $\rho_0 = 5.5$. $\varepsilon = 0.5$, $L = 3000$.

se traduit notamment par l'augmentation du temps entre les retournements de l'agrégat ordonné (voir figure 5.12). Pour un $D$ suffisamment grand, on observe alors un comportement similaire au cas $d = 2$ : une transition discontinue montrant de la métastabilité entre l'état désordonné et l'état inhomogène (voir figure 5.14, droite). Lorsque le temps entre les retournements est assez grand, l'agrégat a le temps de s'étaler complètement. Il a alors le même profil que les domaines liquides du modèle 2d (voir figure 5.15).

Au contraire, pour des valeurs plus petites de $D$, les histogrammes de l'aimantation et le cumulant de Binder ressemblent à ce que l'on trouverait pour une transition continue. Les fluctuations masquent alors la métastabilité entre les deux phases. La transition n'est pas critique pour autant. En particulier, aucune longueur caractéristique ne diverge à la transition.

# Conclusion

La phénoménologie des systèmes actifs est diverse, tantôt proche de comportements observés à l'équilibre thermique, tantôt radicalement différente. Comme nous l'avons vu tout au long de cette thèse, des modèles simplifiés permettent de comprendre l'essence de certains phénomènes caractéristiques de la matière active, et de mettre en évidence leur généralité.

Le cas exploré au chapitre 2 d'une particule active dans un potentiel extérieur, le plus simple que nous ayons étudié, est déjà intéressant pour comprendre la différence entre particules actives et passives. Lorsque l'échelle caractéristique du potentiel est grande devant la longueur de persistance des particules autopropulsées, celles-ci se comportent comme des colloïdes passifs ; l'effet de l'activité est alors complètement pris en compte par une température effective. Au contraire, lorsque le potentiel extérieur varie sur une échelle comparable à la longueur de persistance, l'activité a des effets plus originaux comme l'accumulation de particules actives observée sur les bords d'un piège harmonique. De plus, différentes dynamiques d'autopropulsion conduisent dans ce cas à des comportements différents.

Notre étude de la pression mécanique d'un fluide de particules actives, au chapitre 3, nous a permis de mettre en évidence une propriété générique des systèmes actifs : l'absence d'une équation d'état. Plus généralement, la pression mécanique des systèmes actifs possède de nombreuses propriétés contre-intuitives. Nous avons vu, par exemple, qu'elle peut être anisotrope ou inhomogène dans l'état stationnaire, sans engendrer d'écoulement. Ce travail est récent ; l'étude des propriétés de la pression mécanique, et des possibilités nouvelles qu'elles offrent, reste donc à approfondir. En particulier, il serait intéressant de voir si notre compréhension des forces exercées par des particules actives modèles peut nous permettre de nous pencher sur des situations plus complexes. Par exemple, des cellules ont la capacité de mesurer très précisément la rigidité de leur substrat [135]. On peut donc imaginer que la réponse différente des particules actives à des matériaux de rigidités différentes puisse jouer un rôle dans cette mesure.

Les cas exceptionnels où la pression mécanique satisfait une équation d'état nous permettent de mieux comprendre la thermodynamique des systèmes actifs. Par exemple, nous avons vu comment la pression mécanique intervient dans la séparation de phase induite par la motilité dans un fluide de sphères dures autopropulsées. Elle permet alors d'expliquer en partie l'équilibre des phases observé. Toutefois, une compréhension globale de la coexistence de phase dans ce système nous échappe toujours. Au contraire, les travaux détaillés au chapitre 4 montrent que la transition de phase induite par la motilité est très bien comprise dans des fluides de particules autopropulsées à une vitesse $v(\rho)$ dépendant explicitement de la densité. On peut, dans ces systèmes, construire des fonctions thermodynamiques prédisant quantitativement les binodales observées dans les simulations microscopiques. Le succès inhabituel de ces théories (même en comparaison de systèmes à l'équilibre thermique) nous permet d'espérer arriver à une compréhension générale de la séparation de phase induite par la motilité, incluant les fluides de sphères dures.

Enfin, l'introduction du modèle d'Ising actif au chapitre 5 nous a permis de poser de nouvelles bases pour la compréhension de la transition vers le mouvement collectif. Son interprétation comme une coexistence liquide-gaz permet de comprendre certaines propriétés générales de la transition, en particulier la forme du diagramme des phases. On peut ensuite dégager plusieurs types de coexistence de phase qui correspondent à des liquides ayant des propriétés différentes. Nous avons ainsi défini deux classes d'universalité, basées sur la symétrie des systèmes, pour les modèles de particules autopropulsées avec alignement ferromagnétique. Ce travail reste à poursuivre de façon plus systématique pour inclure d'autres types d'interactions générant une transition vers le mouvement collectif.

Dans cette thèse, nous avons étudié la transition induite par la motilité et celle vers le mouvement collectif de façons quelque peu déconnectées. Elles présentent pourtant des points communs, les deux étant des coexistences entre une phase liquide dense et un gaz dilué. On peut donc se demander si une théorie plus générale pourrait rendre compte des deux types de transition de façon unifiée. L'approche de la physique statistique par les fonctions de grande déviation [136] permet, conceptuellement, de généraliser les potentiels thermodynamiques à des systèmes hors d'équilibre. Une étude des systèmes actifs par la théorie des grandes déviations pourrait donc nous permettre de comprendre s'il est possible de définir des ensembles statistiques hors d'équilibre et d'étudier leur (in)équivalence. Dans cette optique, les coexistences de phase observées dans les systèmes actifs, qui sont de mieux en mieux comprises, semblent un bon objet d'étude.

# Annexe A

# Diffusion rotationnelle en trois dimensions

Dans cette annexe, nous voulons clarifier la relation entre l'équation de la diffusion rotationnelle en coordonnées sphériques, l'équation de Fokker-Planck et l'équation de Langevin associée dans l'interprétation d'Itō.

On considère une particule dont l'orientation $\mathbf{u}$ subit une diffusion rotationnelle avec un temps de persistance $\tau = D_r^{-1}$. L'équation maîtresse du problème est donnée par

$$\dot{P}(\mathbf{u}) = \Delta_{\mathbf{u}} D_r P(\mathbf{u}) \tag{A.1}$$

où $\Delta_{\mathbf{u}}$ est la partie angulaire du Laplacien écrit en coordonnées sphériques. En utilisant l'expression standard du Laplacien, l'équation (A.1) se réécrit

$$\dot{P}(\theta,\varphi) = D_r \left[ \frac{1}{\sin\theta} \frac{\partial}{\partial\theta} \sin\theta \frac{\partial}{\partial\theta} + \frac{1}{\sin^2\theta} \frac{\partial^2}{\partial\varphi^2} \right] P(\theta,\varphi) \tag{A.2}$$

On peut remarquer que, dans cette équation, $P(\theta,\varphi)$ n'est pas la densité de probabilité de trouver la particule avec une direction donnée par des angles dans $[\theta,\theta+d\theta]$ et $[\varphi,\varphi+d\varphi]$. En particulier, $\int d\theta d\varphi P(\theta,\varphi)$ n'est pas conservée par l'équation (A.2). $P(\theta,\varphi)$ est en fait la probabilité de trouver les composantes du vecteur $\mathbf{u}$ dans $[u_i,u_i+du_i]$, mais écrite en coordonnées sphériques. La normalisation appropriée est donc

$$\int d\theta d\varphi \sin\theta P(\theta,\varphi) = 1 \tag{A.3}$$

au lieu de la normalisation habituelle $\int d\theta d\varphi P(\theta,\varphi) = 1$ d'une densité de probabilité. Cette différence est importante. Elle signifie que l'équation (A.2) n'est pas une

équation de Fokker-Planck, et ne peut donc pas être utilisée pour lire l'équation de Langevin correspondante.

Pour obtenir l'équation de Langevin décrivant l'évolution des angles $\theta$ et $\varphi$, il nous faut écrire l'équation de Fokker-Planck donnant l'évolution de la densité de probabilité $\rho(r,\theta,\varphi)$ définie par

$$\rho(r,\theta,\varphi)drd\theta d\varphi = P(u_x,u_y,u_z)du_x du_y du_z \tag{A.4}$$

Puisque $du_x du_y du_z = r^2 \sin\theta drd\theta d\varphi$, on a sur la sphère unité

$$\rho(\theta,\varphi) = P(u_x,u_y,u_z)\sin\theta = P(\theta,\varphi)\sin\theta. \tag{A.5}$$

On peut en déduire l'équation sur $\rho$

$$\dot{\rho} = \sin\theta\dot{P} = D_r\left[\frac{\partial}{\partial\theta}\sin\theta\frac{\partial}{\partial\theta} + \frac{1}{\sin\theta}\frac{\partial^2}{\partial\varphi^2}\right]\frac{\rho(\theta,\varphi)}{\sin\theta} \tag{A.6}$$

qui se réécrit

$$\dot{\rho} = D_r\left[\frac{\partial}{\partial\theta^2} - \frac{\partial}{\partial\theta}\frac{\cos\theta}{\sin\theta} + \frac{\partial^2}{\partial\varphi^2}\frac{1}{\sin\theta^2}\right]\rho(\theta,\varphi) \tag{A.7}$$

L'équation (A.7) est bien une équation de Fokker-Planck. L'équation de Langevin associée s'écrit alors

$$\dot{\theta} = \sqrt{2D_r}\eta_\theta + \frac{\cos\theta}{\sin\theta}D_r; \qquad \dot{\varphi} = \sqrt{\frac{2D_r}{\sin^2\theta}}\eta_\varphi \tag{A.8}$$

où $\eta_\theta$ et $\eta_\varphi$ sont des bruits blancs gaussiens de variance unité.

L'équation (A.8) n'est clairement pas la mieux adaptée aux simulations numériques à cause de la divergence de $1/\sin\theta$. Il est alors plus simple de revenir aux coordonnées cartésiennes

$$u_x = \sin\theta\cos\varphi; \qquad u_y = \sin\theta\sin\varphi; \qquad u_z = \cos\theta \tag{A.9}$$

On peut écrire leur dynamique en utilisant le calcul d'Itō. On obtient

$$\begin{aligned}
\dot{u}_x &= -2Du_x + \sqrt{2D_r}\cos\theta\cos\varphi\eta_\theta - \sqrt{2D_r}\sin\varphi\eta_\varphi \\
\dot{u}_y &= -2Du_y + \sqrt{2D_r}\cos\theta\sin\varphi\eta_\theta + \sqrt{2D_r}\cos\varphi\eta_\varphi \\
\dot{u}_z &= -2Du_z - \sqrt{2D_r}\sin\theta\eta_\theta
\end{aligned} \tag{A.10}$$

Notons que les trois termes de bruit peuvent également s'écrire

$$\xi \wedge \mathbf{u} = (\xi_y p_z - \xi_z p_y, \xi_z p_x - \xi_x p_z, \xi_x p_y - \xi_y p_x) \tag{A.11}$$

où $\xi_x$,$\xi_y$,$\xi_z$ sont des bruits blancs gaussiens de variance unité. Cette forme, plus compacte, fait intervenir trois bruits et semble donc moins bien adaptée aux simulations numériques. Toutefois, l'équation (A.10) nécessite de calculer des fonctions trigonométriques, également coûteuses en temps de calcul. On peut vérifier facilement que les corrélations des bruits satisfont, pour les deux équations (A.10) et (A.11)

$$\begin{aligned} &\sigma_{xx} = u_y^2 + u_z^2; \quad \sigma_{yy} = u_x^2 + u_z^2; \quad \sigma_{zz} = u_x^2 + u_y^2; \\ &\sigma_{xy} = -u_x u_y; \quad \sigma_{yz} = -u_y u_z; \quad \sigma_{xz} = -u_x u_z \end{aligned} \tag{A.12}$$

L'équation d'Itō-Langevin s'écrit finalement

$$\dot{\mathbf{u}} = \xi \wedge \mathbf{u} - 2D_r \mathbf{u} \tag{A.13}$$

Le dernier terme du membre de droite correspond à l'advection due à la discrétisation d'Itō. Il est souvent omis dans la littérature [62, 64, 66], où la convention de Stratonovich est (implicitement) utilisée. Toutefois, l'équation (A.13) ayant un bruit multiplicatif, son implémentation numérique est bien plus aisée dans l'interprétation d'Itō que celle de Stratonovich.

# Annexe B

# Hydrodynamique fluctuante et moyennage asymétrique de la densité

Le formalisme présenté dans l'article C permet d'obtenir l'hydrodynamique fluctuante de particules se déplaçant à une vitesse $v[\rho(\mathbf{r})]$ dépendant de la densité locale. Ci-dessous, nous étendons ce formalisme à des particules qui mesurent la densité de façon asymétrique par rapport à leur direction de déplacement et se déplacent alors à une vitesse $v[\rho(\mathbf{r},\mathbf{u})]$. Plus précisément, nous considérons le cas où la densité est mesurée à une distance $\varepsilon\mathbf{u}$ de la particule. Au premier ordre en gradient (voir section 4.3.2), les particules se déplacent alors à la vitesse

$$v\left[\rho(\mathbf{r}+\varepsilon\mathbf{u})\right] \approx v\left[\rho(\mathbf{r})\right] + \nabla v\left[\rho(\mathbf{r})\right]\cdot\varepsilon\mathbf{u} \tag{B.1}$$

Pour décrire cette situation, il nous faut tout d'abord construire l'équation d'advection-diffusion d'une particule se déplaçant avec un $v(r,\mathbf{u})$, comme dans l'annexe A de l'article C où nous avons considéré des particules avec un $v(\mathbf{r})$. Cette étape constitue la principale difficulté technique ; la suite de la construction de l'hydrodynamique fluctuante suivra le même chemin que dans l'article C et la section 4.3.1.

# B.1 Équation d'advection-diffusion

## Moments de la distribution de probabilité $\psi$

Notre point de départ est l'équation maîtresse donnant la probabilité $\psi(\mathbf{r},\mathbf{u})$ de trouver une particule à la position $\mathbf{r}$, avec l'orientation $\mathbf{u}$

$$\dot{\psi}(\mathbf{r},\mathbf{u}) = -\nabla\cdot[v(\mathbf{r},\mathbf{u})\mathbf{u}\psi - D_t\nabla\psi] + D_r\Delta_u\psi - \alpha\psi + \frac{\alpha}{\Omega}\int d\Omega'\psi \tag{B.2}$$

Nous décomposons tout d'abord $\psi$ en harmoniques sphériques

$$\psi(\mathbf{r},\mathbf{u}) = \phi + \mathbf{p}\cdot\mathbf{u} + Q : M + \Theta[\psi], \qquad \text{avec} \quad M_{ab} = u_a u_b - \delta_{ab}/d \tag{B.3}$$

où la densité $\phi$ et les deux premiers moments $\mathbf{p}$ et $Q$ ne dépendent que de $\mathbf{r}$. L'opérateur $\Theta$ projette $\psi$ sur les harmoniques sphériques d'ordre supérieur. En projetant l'équation (B.2) sur 1, $\mathbf{u}$ and $M$, on obtient les équations d'évolution de $\phi$, $\mathbf{p}$ et $Q$

$$\Omega\dot{\phi} = -\langle 1,\nabla\cdot v\mathbf{u}\psi\rangle + \Omega\nabla\cdot(D_t\nabla\phi) \tag{B.4}$$

$$\frac{\Omega}{d}\dot{\mathbf{p}} = -\langle \mathbf{u},\nabla\cdot v\mathbf{u}\psi\rangle + \frac{\Omega}{d}\nabla\cdot(D_t\nabla\mathbf{p}) - \frac{\Omega}{d}(D_r(d-1)+\alpha)\mathbf{p} \tag{B.5}$$

$$\tilde{\Omega}\dot{Q}_{ab} = -\langle M_{ab},\nabla\cdot v\mathbf{u}\psi\rangle + \tilde{\Omega}\nabla\cdot(D_t\nabla Q_{ab}) - \tilde{\Omega}(2dD_r+\alpha)Q_{ab} \tag{B.6}$$

où $\tilde{\Omega} \equiv \frac{2\Omega}{d(d+2)}$. Le produit scalaire est défini sur la sphère unité

$$\langle f,g\rangle = \int d\Omega f(u)g(u) \tag{B.7}$$

et permet d'obtenir les relations d'orthogonalité (voir l'annexe A de l'article C pour plus de détails)

$$\langle 1,\psi\rangle = \Omega\phi; \qquad \langle \mathbf{u},\psi\rangle = \frac{\Omega}{d}\mathbf{p}; \qquad \langle M_{ab},\psi\rangle = \tilde{\Omega}Q_{ab} \tag{B.8}$$

## Développement de $v$

Les équations (B.4), (B.5) et (B.6) sont valables pour une vitesse générique $v(\mathbf{r},\mathbf{u})$. Pour calculer explicitement les produits scalaires apparaissant dans ces équations, il nous faut développer également la vitesse $v$ en harmoniques sphériques. On ne prendra en considération que la première harmonique de $v$, qui est suffisante pour décrire la vitesse asymétrique de nos particules donnée par l'équation (B.1). On pose alors

$$v(\mathbf{r},\mathbf{u}) = v^0(\mathbf{r}) + \mathbf{v}^1(\mathbf{r})\cdot\mathbf{u} \tag{B.9}$$

Le premier terme du membre de droite de l'équation (B.4) peut maintenant s'écrire

$$\langle 1,\nabla\cdot v\mathbf{u}\psi\rangle = \partial_a\left\langle 1,(v^0+v_b^1u_b)u_a(\phi+p_cu_c+Q_{de}M_{de}+\Theta[\psi])\right\rangle \tag{B.10}$$

$$= \frac{\Omega}{d}\partial_a v^0 p_a + \frac{\Omega}{d}\partial_a v_a^1\phi + \tilde{\Omega}\partial_a v_b^1 Q_{ab} + \partial_a\langle 1,u_a v\Theta[\psi]\rangle \tag{B.11}$$

où, pour passer à la dernière ligne, nous avons calculé explicitement $\langle u_au_b,M_{de}\rangle$ et utilisé le fait que l'on peut toujours choisir le tenseur $Q$ symétrique et de trace nulle. De même, le premier terme du membre de droite de l'équation (B.5) donne

$$\langle \mathbf{u},\nabla\cdot v\mathbf{u}\psi\rangle = \partial_a\langle u_a,(v^0+v_b^1u_b)u_c(\phi+p_du_d+Q_{ef}M_{ef}+\Theta[\psi])\rangle \tag{B.12}$$

$$= \frac{\Omega}{d}\partial_c v^0\phi + \tilde{\Omega}\partial_a v^0 Q_{ac} + \tilde{\Omega}\partial_a(v_a^1p_c+v_c^1p_a) + \tilde{\Omega}\partial_c v_b^1 p_b \tag{B.13}$$

$$+\partial_a\langle u_a,vu_c\Theta[\psi]\rangle$$

Et pour l'équation (B.6), on obtient

$$\langle M_{ab},\nabla\cdot v\mathbf{u}\psi\rangle = \langle M_{ab},\partial_c(v^0+v_d^1u_d)u_c(\phi+p_eu_e+Q_{fg}M_{fg}+\Theta[\psi])\rangle \tag{B.14}$$

$$= \frac{\Omega}{d}\partial_c v^0 p_e B_{abce} + \frac{\Omega}{d}\partial_c v_d^1\phi B_{abcd} + \frac{\Omega}{d}\partial_c v_d^1 Q_{fg}C_{abcdfg} \tag{B.15}$$

$$+\partial_c\langle M_{ab},vu_c\Theta[\psi]\rangle$$

où nous avons défini $B_{abcd}=\frac{d}{\Omega}\langle M_{ab},M_{cd}\rangle$ et $C_{abcdfg}=\frac{d}{\Omega}\langle M_{ab},u_cu_dM_{fg}\rangle$.

Les équations (B.4), (B.5) et (B.6) se réécrivent alors (on permutera les indices pour qu'ils apparaissent dans l'ordre alphabétique)

$$\dot{\phi} = -\frac{1}{d}\partial_a\left(v^0p_a+v_a^1\phi+\frac{2}{d+2}v_b^1Q_{ab}\right)+\partial_aD_t\partial_a\phi+\partial_a\chi_a^\phi \tag{B.16}$$

$$\dot{p}_a = -\partial_a v^0\phi - \frac{2}{d+2}\partial_b v^0 Q_{ab} + \frac{d}{d+2}\left(\partial_b v_b^1 p_a+\partial_b v_a^1 p_b+\partial_a v_b^1 p_b\right) \tag{B.17}$$

$$+\partial_bD_t\partial_bp_a-(D_r(d-1)+\alpha)\,p_a+\partial_b\chi_{ab}^p$$

$$\dot{Q}_{ab} = -\frac{d+2}{2}\left(\partial_c(v^0p_d+v_d^1\phi)B_{abcd}+\partial_cv_d^1Q_{ef}C_{abcdef}\right) \tag{B.18}$$

$$+\partial_cD_t\partial_cQ_{ab}-(2dD_r+\alpha)\,Q_{ab}+\partial_c\chi_{abc}^Q$$

où nous avons défini les fonctions

$$\chi_a^\phi=\frac{\langle 1,u_av\Theta[\psi]\rangle}{\Omega};\qquad \chi_{ab}^p=\frac{d\langle u_a,u_bv\Theta[\psi]\rangle}{\Omega};\qquad \chi_{abc}^Q=\frac{\langle M_{ab},u_cv\Theta[\psi]\rangle}{\tilde{\Omega}} \tag{B.19}$$

### Développement en gradient

Contrairement à $\phi$, $Q$ et $\mathbf{p}$ sont des modes rapides, qui relaxent en un temps de l'ordre du temps de persistance d'une particule. On peut donc poser $\dot{Q} = 0$ et $\dot{\mathbf{p}} = 0$. Au premier ordre en gradient, on a alors

$$p_a = -\frac{1}{D_r(d-1)+\alpha}\partial_a v^0 \phi + O(\nabla^2) \tag{B.20}$$

$$Q_{ab} = -\frac{d+2}{d(2dD_r+\alpha)}\partial_c v_d^1 \phi B_{abcd} + O(\nabla^2) \tag{B.21}$$

En reportant ces expressions dans l'équation (B.16), on a, à l'ordre 2 en gradient,

$$\dot{\phi} = -\partial_a \left[ -\left( D_t + \frac{(v^0)^2}{d(D_r(d-1)+\alpha)} \right) \partial_a \phi + \left( \frac{v_a^1}{d} - \frac{v^0 \partial_a v^0}{d(D_r(d-1)+\alpha)} \right) \phi \right.$$
$$\left. - \frac{2}{2dD_r+\alpha} v_b^1 v_d^1 B_{abcd} \partial_c \phi \right] \tag{B.22}$$

Pour la vitesse que nous considérons, donnée par l'équation (B.1), $v^0 = v(\mathbf{r})$ et $\mathbf{v}^1 = \varepsilon \nabla v(\mathbf{r})$. Lorsque $\nabla v \ll v$, on peut négliger le dernier terme de l'équation (B.22). On obtient alors l'équation d'advection-diffusion

$$\dot{\phi} = -\nabla \cdot [\mathbf{V}\phi - D\nabla\phi] \tag{B.23}$$

où

$$\mathbf{V} = \frac{\varepsilon \nabla v}{d} - \frac{\tau v \nabla v}{d}; \qquad D = D_t + \frac{\tau v^2}{d} \tag{B.24}$$

avec $\tau = D_r(d-1)+\alpha$. L'effet de l'asymétrie apparaît donc comme une contribution supplémentaire au potentiel $\mathbf{V}$.

## B.2 Densité asymétrique non-locale

L'équation (B.23) d'advection-diffusion pour une particule peut être traitée de la même façon que dans l'article C pour obtenir l'hydrodynamique fluctuante du champ de densité pour des particules se déplaçant à une vitesse $v[\rho(\mathbf{r}+\varepsilon\mathbf{u})]$. La dynamique du champ de densité est alors la même que pour le cas $v[\rho(\mathbf{r})]$, au terme additionel dans $\mathbf{V}$ près.

On peut également ajouter l'effet, discuté à la section 4.3.2, d'un moyennage isotrope de la densité, qui est effectué ici autour de la position $\mathbf{r}+\varepsilon\mathbf{u}$. Les particules se déplacent alors à une vitesse

$$v\left[\tilde{\rho}(\mathbf{r}+\varepsilon\mathbf{u})\right] \approx v\left[\tilde{\rho}(\mathbf{r})\right] + \nabla v\left[\tilde{\rho}(\mathbf{r})\right] \cdot \varepsilon\mathbf{u} \tag{B.25}$$

Par rapport au cas $\varepsilon = 0$, l'asymétrie apporte une contribution supplémentaire à la tension de surface. Prenons $D_t = 0$ pour simplifier. On trouve

$$\frac{\mathbf{V}}{D} = -\frac{\nabla v(\tilde{\rho})}{v(\tilde{\rho})} + \frac{\varepsilon \nabla v(\tilde{\rho})}{\tau v(\tilde{\rho})^2} = -\nabla \left[ \ln v(\tilde{\rho}) - \frac{\varepsilon}{\tau v(\tilde{\rho})} \right] \tag{B.26}$$

que l'on peut développer comme précédemment en un terme local, dérivant d'une énergie libre, et un terme de tension de surface $\kappa(\rho)$

$$\frac{\mathbf{V}}{D} = -\nabla \left[ f'(\rho) - \kappa(\rho) \Delta \rho \right] \tag{B.27}$$

avec

$$f'(\rho) = \ln v(\rho) - \frac{\varepsilon}{\tau v(\rho)}; \qquad \kappa(\rho) = -\gamma^2 \frac{v'(\rho)}{v(\rho)} \left( 1 - \frac{\varepsilon}{\tau v(\rho)} \right) \tag{B.28}$$

L'effet de l'asymétrie entre donc comme une contribution supplémentaire dans $\mathcal{F}$ et $\kappa$. La dynamique du champ de densité est alors donnée par la même équation de Langevin que dans le cas $\varepsilon = 0$

$$\dot{\rho} = \nabla \cdot \left[ \rho D(\tilde{\rho}) \nabla \left( \frac{\delta \mathcal{F}}{\delta \rho} - \kappa(\rho) \Delta \rho \right) + \sqrt{2 \rho D(\tilde{\rho})} \boldsymbol{\eta} \right], \tag{B.29}$$

PRL 111, 078101 (2013) PHYSICAL REVIEW LETTERS week ending 16 AUGUST 2013

# Revisiting the Flocking Transition Using Active Spins

A. P. Solon and J. Tailleur
*Université Paris Diderot, Sorbonne Paris Cite, MSC, UMR 7057 CNRS, F75205 Paris, France*
(Received 16 March 2013; published 13 August 2013)

We consider an active Ising model in which spins both diffuse and align on lattice in one and two dimensions. The diffusion is biased so that plus or minus spins hop preferably to the left or to the right, which generates a flocking transition at low temperature and high density. We construct a coarse-grained description of the model that predicts this transition to be a first-order liquid-gas transition in the temperature-density ensemble, with a critical density sent to infinity. In this first-order phase transition, the magnetization is proportional to the liquid fraction and thus varies continuously throughout the phase diagram. Using microscopic simulations, we show that this theoretical prediction holds in 2D whereas the fluctuations alter the transition in 1D, preventing, for instance, any spontaneous symmetry breaking.

DOI: 10.1103/PhysRevLett.111.078101 PACS numbers: 87.18.Gh, 05.65.+b, 45.70.Vn

Active matter systems are driven out of equilibrium by the injection of energy at the single particle level [1–4]. This microscopic breakdown of detailed balance results in a wide range of phenomena that have aroused the interest of physicists, from bacterial ratchets [5–8] to self-propelled clusters [9–11]. Furthermore, this rich phenomenology is often captured by simple models. For instance, simple flocking models account for the patterns found in motility assays [12,13] while bacterial clustering was successfully modeled using self-propelled rods [14].

Nevertheless, despite the successful description of many experiments, a full understanding of the underlying mechanisms sometimes remains elusive. For instance, even though the flocking transition is a central feature of active matter, it remains one of the most debated questions in the field. In their seminal work, Vicsek and co-workers [15] showed that self-propelled particles that align locally can exhibit a transition to long-range order in 2D. Initially thought to be continuous [15], this transition was later shown to be first order using large scale simulations and a finite size scaling akin to that of magnetic phase transitions [16]. Many works were also devoted to nematic [17–19] or metric-free interactions [20], the latter yielding a continuous transition [21]. Flocking models were also studied in 1D [22,23] where, surprisingly, the transition was found to be critical.

Obtaining conclusive numerical evidence for flocking models is notoriously difficult due to strong finite-size effects and the lack of a theoretical framework to analyze them. In parallel to numerical studies, much effort was thus devoted to construct such an analytical description of the flocking transition. While the Vicsek model (VM) is among the simplest to simulate, it is one of the hardest to coarse grain, being defined off lattice, in discrete time and involving manybody interactions. Many approaches were thus either phenomenological [24–26] or focused on simpler models [27], and progress is slower for the VM [28]. Lots of effort was also devoted to the nematic case [29–31] or to topologic interactions [30,32]. The existence of long-range order in 2D for polar alignment was established [24] but progress is difficult since the coarse-grained equations are hard to solve. Most analytical studies were thus restricted to the linear stability analysis of homogeneous solutions or the simulation of continuous equations [25–27]. While nonlinear profiles for a model with nematic alignment could be computed explicitly [30], closed analytical solutions are still missing for polar models despite recent progress [25,27,28]. All in all, despite the important progresses made during the last few years, a unifying theoretical framework of the flocking transition is still missing.

We present below a tentative step in this direction through the introduction of a microscopic lattice model with discrete symmetry, which is much simpler to study numerically and analytically than traditional flocking models. By bridging micro and macro, we show the transition of our model to amount to a standard liquid-gas transition in the canonical ensemble with an infinite critical density. This sheds new light on the finite-size scaling of the transition and predicts the order parameter to vary *continuously* in the temperature-density plane, in the thermodynamic limit. Furthermore, we show that there is no critical transition in 1D, where fluctuations strongly alter the transition.

We consider $N$ particles carrying Ising spins $s = \pm 1$ on a 1D lattice of $L$ sites. Each particle hops at rate $D(1 + s\varepsilon)$ and $D(1 - s\varepsilon)$ to its right and left neighboring site. (In higher dimensions, the hopping rates are symmetric in all but one directions.) There is no exclusion between particles and we note $n_i^{\pm}$ the numbers of $\pm$ spins on site $i$ so that the local densities and magnetizations are given by $\rho_i = n_i^+ + n_i^-$ and $m_i = n_i^+ - n_i^-$. The particles also align their spins: on site $i$ each spin $s$ flips at rate $\exp(-sm_i/T\rho_i)$ where the temperature $T$ plays a role similar to the orientational noise in the VM [16]. When $D = 0$, the system thus amounts to $L^d$ independent fully connected Ising models. When $D > 0$ and $\epsilon \neq 0$, three different configurations are typically observed (see Fig. 1): at low temperature a uniform ordered phase, at high temperature a uniform disordered phase,

 

and phase-separated profiles in between, with narrow interfaces connecting ordered high density bands ($\rho_i \simeq \rho_h$, $m_i \simeq m_h \neq 0$) to disordered homogeneous backgrounds ($\rho_i \simeq \rho_\ell$, $m_i \simeq 0$). These profiles are all long-lived in finite systems even though their stability in the thermodynamic limit depends on the number of spatial dimensions. Let us now show how a simple theoretical framework can be constructed to account for the phase diagram of Fig. 1.

Previous coarse-graining approaches often relied on factorization approximation of kinetic equations [27,29,33,34]. On a 1D lattice, this amounts to a mean-field approximation: $f(\langle n_i^{\pm}\rangle) = \langle f(n_i^{\pm})\rangle$, which may be quantitatively wrong but often captures phase diagrams exactly [35,36]. Introducing $x = i/L$, $v = 2D\varepsilon/L$, $\tilde{D} = D/L^2$, and $\beta = T^{-1}$, the mean-field dynamics of the coarse-grained fields $\rho(x) = \langle \rho_i \rangle$ and $m(x) = \langle m_i \rangle$ is given, in the large $L$ limit, by

$$\dot{\rho} = \tilde{D}\partial_{xx}\rho - v\partial_x m \tag{1}$$

$$\dot{m} = \tilde{D}\partial_{xx} m - v\partial_x \rho + 2\rho \sinh\frac{\beta m}{\rho} - 2m\cosh\frac{\beta m}{\rho}. \tag{2}$$

In higher dimensions $\partial_{xx}$ becomes a Laplacian $\Delta$, and we use this more general form hereafter.

Looking for the onset of a flocking transition, we linearize the dynamics for $m \ll \rho$, which yields [37]

$$\dot{m} = \tilde{D}\Delta m - v\partial_x \rho + 2m(\beta - 1) - \alpha\frac{m^3}{\rho^2} \tag{3}$$

where $\alpha = \beta^2[1 - (\beta/3)]$. The line $\beta = 1$ separates the linear stability regions of homogeneous ordered and disordered profiles while simulations of Eqs. (1) and (2) never show stable phase-separated profiles [38]. The mean-field

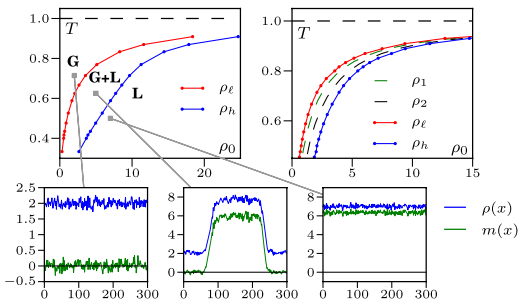


FIG. 1 (color online). Top left: Phase diagram in 2D with ordered liquid ($L$), disordered gas ($G$), and coexistence region ($G + L$). The red and blue lines correspond to low and high densities of phase separated profiles; they enclose the region where such profiles can be seen. $D = 1$, $\epsilon = 0.9$, $L = 300$, $\rho_0 = N/L$. Bottom: Snapshots of the different profiles averaged over the transverse direction. Top right: Phase diagram predicted by the RMFM. In addition to $\rho_h$ and $\rho_\ell$, black and green dashed spinodal lines signal the loss of linear stability of the homogeneous profiles. $D = v = r = 1$.

approximation thus predicts a continuous transition from $m \equiv (1/L)\sum_i m_i = 0$ to $m = m_0(\beta)$ at $\beta_c = 1$, in contradiction with Fig. 1. As often [39,40], the mean-field approximation is only valid for $\rho \to \infty$; for finite densities we thus expand the mean-field critical temperature to include $1/\rho$ corrections [41,42] and use $\beta_c \equiv 1 + (r/\rho)$ in Eq. (3):

$$\dot{m} = \tilde{D}\Delta m - v\partial_x \rho + 2m\left(\beta - 1 - \frac{r}{\rho}\right) - \alpha\frac{m^3}{\rho^2}. \tag{4}$$

The phase diagram corresponding to Eqs. (1) and (4), which form our refined mean-field model (RMFM), is presented in the top-right corner of Fig. 1. When $T < 1$, homogeneous disordered (resp. ordered) profiles are always linearly stable at low enough density $\rho_0 < \rho_1$ (resp. high enough density $\rho_0 > \rho_2$). Since $\rho_1 < \rho_2$, there is a finite intermediate region $[\rho_1, \rho_2]$ where neither homogeneous profiles are stable. In this region, the system separates into two homogeneous phases connected with sharp fronts: a disordered region with low density $\rho_\ell < \rho_1$ and an ordered region with high density $\rho_h > \rho_2$ and $m_h \neq 0$.

Propagating shocks can be computed analytically when $\beta$ is close to 1 by linearizing Eq. (4) around the density $\rho_1 = r/(\beta - 1)$ at which the homogeneous disordered profile becomes linearly unstable. We first solve Eq. (1), by neglecting the diffusion term in a reference frame moving at speed $c$, to get $\rho$ as a function of $m$:

$$\rho(\mathbf{r}) = \rho_\ell + \frac{v}{c}m(\mathbf{r}). \tag{5}$$

Equations (4) and (5) then yields for $m$

$$\tilde{D}\Delta m + c\left(1 - \frac{v^2}{c^2}\right)\partial_x m + \mu\left[\rho_l - \rho_1 + \frac{v}{c}m\right]m - \alpha\frac{m^3}{\rho_1^2} = 0 \tag{6}$$

where $\mu = 2r/\rho_1^2$. Looking for ascending ($q^+ > 0$) and descending ($q^- < 0$) front solutions

$$m(\mathbf{r}) = \frac{m_h}{2}[1 + \tanh(q^{\pm}x)] \tag{7}$$

one gets

$$c = v; \qquad q^{\pm} = \frac{\pm m_h\sqrt{\alpha}}{\sqrt{8\tilde{D}\rho_1}}; \qquad m_h = \frac{4r}{3\alpha}; \qquad \rho_\ell = \rho_1 - \frac{4r}{9\alpha}. \tag{8}$$

Such solutions are consistent with our approximations since $[(\rho - \rho_1)/\rho_1] \ll 1$ and $\tilde{D}\Delta\rho \ll v\partial_x\rho$ when $\beta \to 1$ [42]. In this regime, Eqs. (5)–(8) and simulations of the RMFM yield the same profiles and band velocities. For larger $\beta$, the $\tilde{D}\Delta\rho$ term makes fore and rear fronts asymmetric and $c > v$: the flocks fly faster than the birds [42].

Since $\rho_\ell$, $\rho_h$, and $m_h$ do not depend on $\rho_0$, increasing the density at fixed temperature only increases the width of the high-density bands. In the thermodynamic limit, phase separated profiles can be seen from $\rho_\ell$ to $\rho_h$. One always has $\rho_\ell < \rho_1 < \rho_2 < \rho_h$ so that clusters and homogeneous profiles are linearly stable when $\rho_0 \in [\rho_\ell, \rho_1] \cup [\rho_2, \rho_h]$.

The refined mean-field scenario thus resembles an equilibrium liquid-gas transition in the canonical ensemble, the total magnetization being proportional to the fraction of the liquid phase. Varying the density at fixed temperature, one indeed observes hysteresis loops (see Fig. 2). Increasing $\rho_0$, homogeneous disordered profiles are seen up to $\rho_1$ where the system discontinuously jumps into a phase-separated profile. Further density increases result in a widening of the liquid phase until it almost fills the system for $\rho \lesssim \rho_h$. (The widths of the fronts connecting $\rho_\ell$ and $\rho_h$ prevent phase-separated profiles for $\rho_0 \simeq \rho_{\ell/h}$ in finite systems.) Decreasing $\rho_0$, the homogeneous ordered phase remains metastable until $\rho_0 = \rho_2$ before discontinuously jumping to a coexistent state. The fraction of gas then increases until it fills the system at $\rho \simeq \rho_l$.

Unlike equilibrium liquid-gas transitions, dense and dilute phases in flocking models have different symmetries. One thus cannot circumvent the transition and continuously transform the system from a gas to a liquid: the transition line cannot stop at a finite point in the $(T, \rho_0)$ plane and, indeed, the critical density is infinite. As far as we are aware, this has not been described for other flocking models [43] even though it should be generic and is consistent with numerical results on the VM [16,27].

Simulations of the 2D active Ising model confirm both the structure of the phase diagram (see Fig. 1) and the nature of the transition predicted by the RMFM. The coexistence between homogeneous and phase-separated profiles is observed and changing $\rho_0$ at fixed $T$ in the coexistence region only changes the fraction of the liquid phase (see Fig. 2); the velocity of the high density bands, for instance, remains constant [42]. Since high density bands have a minimal size $\ell_c$, the apparition of a flock in a finite-size system corresponds to a discontinuous jump to a nonzero magnetization $m_0 \simeq m_h \ell_c / L$ which vanishes as

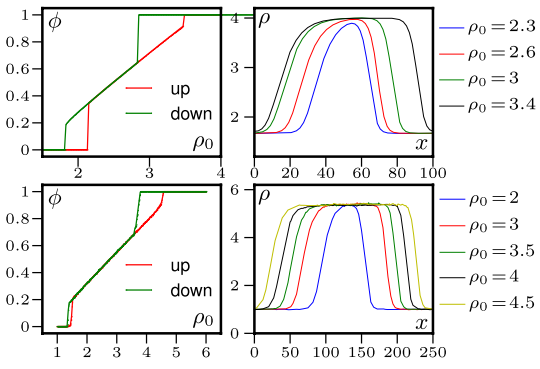


FIG. 2 (color online). Left: Fraction of the ordered liquid phase when $\rho_0$ is either increased or decreased for the RFMF (top) and in 2D microscopic simulations (bottom). Right Corresponding profiles of the system. Parameters: RMFM $L = 100$, $v = D = 1$, $r = 1.6$, $\beta = 1.75$, $\Delta\rho_0 = 10^{-2}$ every $\Delta t = 15000$; 2D lattice model $L = 250$, $\beta = 2$, $D = 1$, $\varepsilon = 0.9$, $\Delta\rho_0 = 10^{-2}$ every $\Delta t = 500$.

$L \to \infty$. In this limit, as for a liquid-gas transition in the canonical ensemble, the order parameter varies *continuously* throughout the phase diagram.

The scenario presented here can be related to the measurement of the binder cumulant $G = 1 - (\langle m^4 \rangle / 3 \langle m^2 \rangle^2)$ done in the literature [16,31]. The coexistence between phase-separated profiles ($m = \pm m_0$) and supercooled gas phase ($m = 0$) yields three peaks in $P(m)$ whose weights vary across the transition. (The same holds for the coexistence with superheated liquid.) Assuming a sum of three Gaussians of variance $\sigma$, the minimum of $G$, $G_{\min} = -[12(\sigma/m_0)^2 + 36(\sigma/m_0)^4]^{-1}$, is only markedly negative when $m_0 \gg \sigma$. When $L \to \infty$, contrary to what happens in a grand-canonical ensemble, both $m_0$ and $\sigma$ vanish, the negative peak need not become more pronounced, and the transition may appear critical if $\sigma$ remains comparable to $m_0$ (see the 1D case below).

Let us now show that fluctuations strongly alter the transition in 1D. First, all three profiles shown on Fig. 1 exist and are linearly stable in finite systems [44]. The general scenario predicted by the RMFM thus holds: homogeneous profiles are linearly unstable for $\rho_1(T) < \rho_0 < \rho_2(T)$ and phase-separate between linearly stable low-density disordered and high-density ordered regions.

To assess the impact of fluctuations, let us consider the stability of an ordered band in the coexistence region. In 1D, an excess of, say, positive spins on a single site suffices to flip an approaching negative cluster (see Fig. 3); this happens frequently and the total magnetization keeps flipping in this region. The 2D counterpart of such a fluctuation is an excess of positive spins on a transverse band of $\sim L$ sites in front of the approaching cluster, which has a negligible probability when $L \to \infty$. Similarly, the $m = m_0$ homogeneous profile is unstable in the thermodynamic limit in 1D, which may be why it has not been observed before [44]. Indeed, although a fluctuation leading to a small negative cluster in a uniform profile with $m > 0$ is rare, its probability does not decay exponentially fast with $L$ since only a finite number of sites have to be flipped. When $L$ increases, so does the entropy of such local perturbations; the time it takes to exit the homogeneous state thus vanishes when $L \to \infty$.

In 1D, only two phases thus survive in the thermodynamic limit: homogeneous disordered profiles and flipping

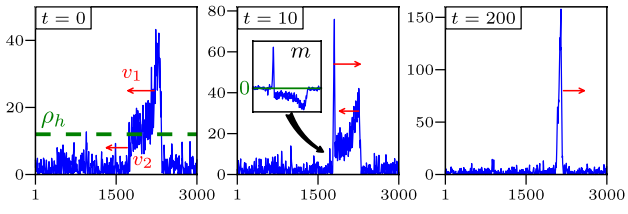


FIG. 3 (color online). Reversal of a 1D cluster due to a localized fluctuation. $v_2$ is greater than $v_1$ until $\rho(x) = \rho_h$ in the whole cluster. (See movies in [42].) $\rho_0 = 5$, $D = 1$, $\varepsilon = 0.9$, $\beta = 1.7$.

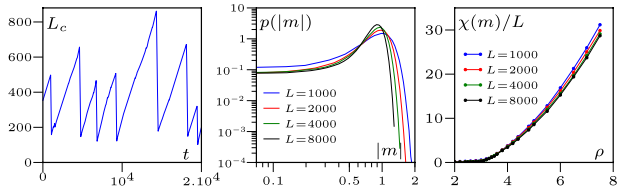


FIG. 4 (color online). Left: Cluster length as a function of time, showing a linear spreading between reversals. $D = 1$ $\varepsilon = 0.9$ $\beta = 2$ $\rho_0 = 3$. Center and Right: $P(|m|)$ for $\rho_0 = 4$; $\chi_m(\rho)/L$; $\beta = 1.538$, $D = 1$, $\varepsilon = 0.9$.

clusters, whose dynamics we now describe (see Fig. 3 and movies in [42]). Starting from a localized cluster, the ordered region spreads at constant speed: the fore front is initially faster than the rear front, their velocity becoming equal when the density in the band has uniformly spread to $\rho_h$. The mean cluster size before a reversal $L_c^R$ is thus proportional to the mean time between reversals. A reversal corresponds to the progression of a fluctuation from the front to the rear of a cluster, progressively flipping all its sites. The average *duration* of a reversal is thus proportional to $L_c^R$ and hence to the mean time *between* reversals. When $L \to \infty$, there is a nonzero probability to find the system in a reversal, $P(m)$ does not vanish between $\pm m_0$, and $\langle m \rangle = 0$ (see Fig. 4): there is no spontaneous symmetry breaking in 1D. Since the reversals capture a finite part of the steady-state measure, one cannot replace $m$ by $|m|$ when computing the susceptibility $\chi_m = L(\langle m^2 \rangle - \langle m \rangle^2)$, as is frequently done for the Ising model. In agreement with the lack of ergodicity breaking, and contrary to earlier results in 1D, $\chi_m$ is simply extensive in the cluster region.

The difficulty of analyzing Binder cumulants can be clearly seen in 1D, where the large $L$ limit is easily reached and the three peaks in $P(m)$ at the transition can be hard to discriminate. If the width of the peaks is larger than their separation, no negative peak in $G$ is observed. Increasing $L$ does not help since the peaks get closer as they get narrower. In Fig. 5 we show two extreme cases: without the RMFM to analyze the data, it would be very difficult to realize that they correspond to the same transition. This may explain why previous studies of 1D flocking models with similar—though not identical—dynamics concluded to a second-order transition [22,23].

*Conclusion.*—We have introduced a lattice model of self-propelled Ising spins whose phenomenology is similar to that of traditional flocking models. The simplicity of our model allows us to show that its flocking transition amounts to a liquid-gas transition in the canonical ensemble with an infinite critical density. The total magnetization is proportional to the liquid fraction and thus varies *continuously* through this first-order transition in the thermodynamic limit, a rather counterintuitive result. This scenario, confirmed numerically in 2D, is altered by fluctuations in 1D, where neither spontaneous symmetry breaking nor critical transitions are observed.

Despite fundamental differences between our model and others found in the literature, such as the symmetry of the order parameter, many features of the flocking transition observed here seem consistent with existing numerical results on either microscopic models [16,19,30] or continuous descriptions [25–28] of self-propelled particles. For instance, the phase diagram seems compatible with those of nematic [19,30] or VM [16,27], even though the high density regions have not been studied in these models. This suggests that the analogy between the flocking transition and a canonical liquid gas transition could be generic, while the symmetry of the order parameter would mostly control features of the ordered phase. For instance, giant-number fluctuations, which have been reported in flocking models, are trivially present in the coexistence region of our model. There, $P(\rho_i)$ is peaked around $\rho_\ell$ and $\rho_h$, and the variance of the number of particles in a box of finite size satisfies $\langle N^2 \rangle - \langle N \rangle^2 \propto \langle N \rangle^2$ [45]. They are, however, absent from the homogeneous ordered phase [42], showing that such fluctuations are not intrinsic to polar flocking states.

Active spin models are mostly aimed at improving our theoretical understanding of the flocking transition. One can nevertheless wonder whether such models could be relevant experimentally. The discrete symmetry of the order parameter can for instance stem out of a geometry allowing only two flocking directions, as for locusts in a ring-shaped arena [46,47]. Then, as for the VM, the high density region can only be attained if the interaction range between particles is much larger than their size, as for

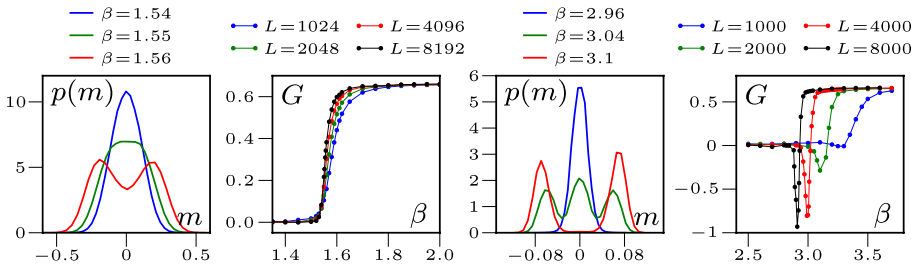


FIG. 5 (color online). Histograms and Binder cumulant of the total magnetization for $\rho_0 = 3$, $D = 1$ (left) and $\rho_0 = 0.2$, $D = 10$ (right). $\varepsilon = 0.9$. $L = 8000$ for $P(m)$.

electrostatic, hydrodynamic, or social interactions. In other cases, such as hard rods, the steric exclusion between particles and other density-induced effects may alter the flocking transition [33]. Lastly, thanks to recent progress on the manipulation of cold atoms in optical lattices, physicists now have a large freedom to control the interactions in spin chains [48]. This could provide an interesting path towards a quantum version of active spin models.

The authors thank H. Chaté, M. Cheneau, G. Grégoire, P. Krapivksy, F. Peruani, H. Touchette, and F. van Wijland for useful discussions.

[1] S. Ramaswamy, Annu. Rev. Condens. Matter Phys. **1**, 323 (2010).
[2] P. Romanczuk, M. Br, W. Ebeling, B. Lindner, and L. Schimansky-Geier, Eur. Phys. J. Special Topics **202**, 1 (2012).
[3] T. Vicsek and A. Zafeiris, Phys. Rep. **517**, 71 (2012).
[4] M. E. Cates, Rep. Prog. Phys. **75**, 042601 (2012).
[5] P. Galajda, J. Keymer, P. Chaikin, and R. Austin, J. Bacteriol. **189**, 8704 (2007); P. Galajda, J. Keymerb, J. Dallandc, S. Parkd, S. Koud, and Rob. Austin, J. Mod. Opt. **55**, 3413 (2008).
[6] J. Tailleur and M. E. Cates, Europhys. Lett. **86**, 60 002 (2009).
[7] L. Angelani, R. Di Leonardo, and G. Ruocco, Phys. Rev. Lett. **102**, 048104 (2009); R. Di Leonardo, L. Angelani, D. Dell'Arciprete, G. Ruocco, V. Iebba, S. Schippa, M. P. Conte, F. Mecarini, F. De Angelis, and E. Di Fabrizio, Proc. Natl. Acad. Sci. U.S.A. **107**, 9541 (2010).
[8] A. Sokolov, M. M. Apodaca, B. A. Grzybowski, and I. S. Aranson, Proc. Natl. Acad. Sci. U.S.A. **107**, 969 (2009).
[9] J. Schwarz-Linek, C. Valeriani, A. Cacciuto, M. E. Cates, D. Marenduzzo, A. N. Morozov, and W. C. K. Poon, Proc. Natl. Acad. Sci. U.S.A. **109**, 4052 (2012).
[10] I. Theurkauff, C. Cottin-Bizonne, J. Palacci, C. Ybert, and L. Bocquet, Phys. Rev. Lett. **108**, 268303 (2012).
[11] J. Palacci, S. Sacanna, A. P. Steinberg, D. J. Pine, and P. M. Chaikin, Science **339**, 936 (2013).
[12] V. Schaller, C. Weber, C. Semmrich, E. Frey, and A. R. Bausch, Proc. Natl. Acad. Sci. U.S.A. **108**, 19 183 (2011).
[13] Y. Sumino, K. H. Nagai, Y. Shitaka, D. Tanaka, K. Yoshikawa, H. Chaté, and K. Oiwa, Nature (London) **483**, 448 (2012).
[14] F. Peruani, J. Starruss, V. Jakovljevic, L. Sogaard-Andersen, and A. Deutsch, M. Bär, Phys. Rev. Lett. **108**, 098102 (2012).
[15] T. Vicsek, A. Czirók, E. Ben-Jacob, I. Cohen, and O. Shochet, Phys. Rev. Lett. **75**, 1226 (1995).
[16] G. Grégoire and H. Chaté, Phys. Rev. Lett. **92**, 025702 (2004); H. Chaté, F. Ginelli, G. Grégoire, and F. Raynaud, Phys. Rev. E **77**, 046113 (2008).
[17] F. Peruani, A. Deutsch, and M. Bär, Phys. Rev. E **74**, 030904 (2006).
[18] A. Baskaran and M. C. Marchetti, Phys. Rev. Lett. **101**, 268101 (2008); J. Stat. Mech. (2010) P04019.
[19] F. Ginelli, F. Peruani, M. Bär, and H. Chaté, Phys. Rev. Lett. **104**, 184502 (2010).
[20] M. Ballerini, N. Cabibbo, R. Candelier, A. Cavagna, E. Cisbani, I. Giardina, V. Lecomte, A. Orlandi, G. Parisi, A. Procaccini, M. Viale, and V. Zdravkovic, Proc. Natl. Acad. Sci. U.S.A. **105**, 1232 (2008).
[21] F. Ginelli and H. Chaté, Phys. Rev. Lett. **105**, 168103 (2010).
[22] A. Czirók, A.-L. Barabási, and T. Vicsek, Phys. Rev. Lett. **82**, 209 (1999).
[23] O. J. O'Loan and M. R. Evans, J. Phys. A **32**, L99 (1999).
[24] J. Toner and Y. Tu, Phys. Rev. Lett. **75**, 4326 (1995); Phys. Rev. E **58**, 4828 (1998); J. Toner, Phys. Rev. Lett. **108**, 088102 (2012); Phys. Rev. E **86**, 031918 (2012).
[25] S. Mishra, A. Baskaran, and M. C. Marchetti, Phys. Rev. E **81**, 061916 (2010).
[26] A. Gopinath, M. F. Hagan, M. C. Marchetti, and A. Baskaran, Phys. Rev. E **85**, 061903 (2012).
[27] E. Bertin, M. Droz, and G. Grégoire, Phys. Rev. E **74**, 022101 (2006); J. Phys. A **42**, 445001 (2009).
[28] T. Ihle, Phys. Rev. E **83**, 030901 (2011); arXiv:1304.0149.
[29] A. Baskaran and M. C. Marchetti, Phys. Rev. E **77**, 011920 (2008).
[30] A. Peshkov, I. S. Aranson, E. Bertin, H. Chaté, and F. Ginelli, Phys. Rev. Lett. **109**, 268701 (2012).
[31] S. Ngo, F. Ginelli, and H. Chaté, Phys. Rev. E **86**, 050101(R) (2012).
[32] Y.-L. Chou, R. Wolfe, and T. Ihle, Phys. Rev. E **86**, 021120 (2012).
[33] F. D. C. Farrell, M. C. Marchetti, D. Marenduzzo, and J. Tailleur, Phys. Rev. Lett. **108**, 248101 (2012).
[34] I. S. Aranson and L. S. Tsimring, Phys. Rev. E **71**, 050901 (R) (2005).
[35] R. A. Blythe and M. R. Evans, J. Phys. A **40**, R333 (2007).
[36] M. R. Evans, Y. Kafri, K. E. P. Sugden, and J. Tailleur, J. Stat. Mech. (2011) P06009.
[37] For $\beta > 3$, should be expanded to higher orders.
[38] We used spectral methods and fully implicit time stepping to simulate the continuous equations.
[39] J. Tailleur, J. Kurchan, and V. Lecomte, J. Phys. A **41**, 505001 (2008).
[40] A. G. Thompson, J. Tailleur, M. E. Cates, and R. A. Blythe, J. Stat. Mech. (2011) P02029.
[41] W. Ketterle and N. J. van Druten, Phys. Rev. A **54**, 656 (1996).
[42] See Supplemental Material at http://link.aps.org/supplemental/10.1103/PhysRevLett.111.078101 for movies and complementary technical details.
[43] The phenomenological equations of [25,26] focus on the role of propulsion speed and assume finite spinodal densities. Here, we account for the effect of temperature and can thus describe the full phase diagram in the $\rho$, $T$ plane, hence predicting the $\rho_c = \infty$ critical point.
[44] Homogeneous ordered phases were not observed in earlier studies of 1D flocking models [22,23]; we numerically checked that they are also present in these models.
[45] I. S. Aranson, A. Snezhko, J. S. Olafsen, and J. S. Urbach, Science **320**, 612 (2008).
[46] J. Buhl, D. J. T. Sumpter, I. D. Couzin, J. J. Hale, E. Despland, E. R. Miller, and S. J. Simpson, Science **312**, 1402 (2006).
[47] Particles hopping forward correspond to $\varepsilon = 1$.
[48] T. Fukuhara *et al.*, Nat. Phys. **9**, 235 (2013).

PRL 112, 148102 (2014) PHYSICAL REVIEW LETTERS week ending 11 APRIL 2014

# Emergent Spatial Structures in Flocking Models: A Dynamical System Insight

Jean-Baptiste Caussin,[1] Alexandre Solon,[2] Anton Peshkov,[3,4,5] Hugues Chaté,[4,5,3] Thierry Dauxois,[1] Julien Tailleur,[2] Vincenzo Vitelli,[6] and Denis Bartolo[1]

[1]*Laboratoire de Physique de l'Ecole Normale Supérieure de Lyon, Université de Lyon, CNRS, 46, Allée d'Italie, 69007 Lyon, France*
[2]*Université Paris Diderot, Sorbonne Paris Cité, MSC, CNRS, 75205 Paris, France*
[3]*LPTMC, CNRS, Université Pierre et Marie Curie, 75252 Paris, France*
[4]*Service de Physique de l'Etat Condensé, CEA-Saclay, CNRS, 91191 Gif-sur-Yvettes, France*
[5]*Max Planck Institute for Physics of Complex Systems, Nöthnitzer Straße 38, 01187 Dresden, Germany*
[6]*Instituut-Lorenz for Theoretical Physics, Universiteit Leiden, 2300 RA Leiden, Netherlands*

(Received 23 December 2013; revised manuscript received 25 February 2014; published 8 April 2014)

We show that hydrodynamic theories of polar active matter generically possess inhomogeneous traveling solutions. We introduce a unifying dynamical-system framework to establish the shape of these intrinsically nonlinear patterns, and show that they correspond to those hitherto observed in experiments and numerical simulation: periodic density waves, and solitonic bands, or polar-liquid droplets both cruising in isotropic phases. We elucidate their respective multiplicity and mutual relations, as well as their existence domain.

DOI: 10.1103/PhysRevLett.112.148102 PACS numbers: 87.23.Cc, 05.65.+b, 47.27.ed, 47.54.−r

Could the emergence of collective motion in fish schools, bird flocks, and insect swarms be understood within a unified physical framework? A growing stream of works has approached this provocative question following the seminal work of Vicsek *et al.*, who considered self-propelled point particles interacting solely via local velocity-alignment rules [1]. This model displays a spontaneous rotational-symmetry breaking leading to orientational order [1–3]. In addition, a number of subsequent simulations and experiments have revealed an even more surprising feature. At the onset of collective motion, despite the lack of any attractive interactions, polar active matter self-organizes in the form of band-shape swarms [4–12]. However, depending on the specifics of the systems, these dynamical patterns take three different forms: (i) delocalized density waves [5,6], as exemplified in Fig. 1(a), (ii) solitonic structures [7–9], Fig. 1(b), and (iii) phase-separated states [10–12], Fig. 1(c). Although it is now clear that they are responsible for the first-order nature of the transition toward collective motion [4,9,10], no unifying theory exists to account for the origin and the variety of these band patterns.

In this Letter, we convey a comprehensive description of the propagative excitations of polar active matter. Using a hydrodynamic description and dynamical system concepts, we establish the shape of these intrinsically nonlinear band structures, and show that they correspond to those observed in all the available experiments and numerical simulation; see, e.g., Refs. [5–14].

Our starting point is a hydrodynamic description of compressible polar active fluids [3,15]. Since we are chiefly interested in structures varying only along the main direction of motion, we focus here on a one-dimensional problem. The local density field $\rho(x,t)$ obeys a conservation equation which complements the equation governing the momentum field $W(x,t)=\rho(x,t)P(x,t)$, where $P(x,t)\in[0,1]$ is a polarization field. Following Toner and Tu [15] these equations read

$$\partial_t\rho+\partial_x W=0, \tag{1}$$

$$\partial_t W+\xi W\partial_x W=a_2 W-a_4 W^3-\lambda\partial_x\rho+D\partial_{xx}W, \tag{2}$$

where all the coefficients *a priori* depend both on $\rho$ and $W^2$. These phenomenological equations were introduced to account for a continuous mean-field transition from a homogeneous isotropic state with $\rho=\rho_0$ and $P=0$ when $a_2<0$, to a homogeneous polarized state with $P=\rho_0^{-1}\sqrt{a_2/a_4}$, when $a_2>0$. In addition, the $\lambda$ term reflects the pressure gradient induced by density heterogenities. $\xi$ and $D$ are two transport coefficients associated, respectively, with the

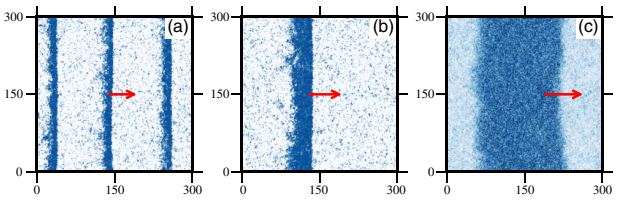


FIG. 1 (color online). Band patterns observed in agent-based simulations. (a) Smectic arrangement of polar bands in the Vicsek model with vectorial noise [5]. Speed $v=0.5$, noise intensity $\eta=0.6$, and density $\rho=1.1$. (b) A solitary band observed for the same model and same parameters as in (a). (c) Polar-liquid droplet in an isotropic phase observed in the active Ising model [10], with inverse temperature $\beta=6$, density $\rho=5$, hopping rate $D=1$, and bias $\epsilon=0.9$. More simulation details can be found in the Supplemental Material [16].

 

advection and the diffusion of the local-order parameter. Following [7], we now look for propagating solutions of Eqs. (1) and (2): $\rho = \rho(x - ct)$ and $W = W(x - ct)$, where $c$ is the propagation speed [7,11]. This ansatz reduces Eq. (1) to an algebraic relation,

$$\rho = \rho^\star + \frac{1}{c} W. \tag{3}$$

When a band moves in an isotropic gas [see, e.g., Fig. 1(b)], the constant $\rho^\star$ corresponds to the gas density. Inserting the latter expression in Eq. (2) leads to a second-order ordinary differential equation,

$$D\ddot{W} + \dot{W}\frac{dF}{dW} + \frac{dH}{dW} = 0, \tag{4}$$

where $H(W)$ is defined via $dH/dW = a_2 W - a_4 W^3$, $F(W) = (c - (\lambda/c))W - \frac{1}{2}\xi W^2$, and the dot symbol denotes the derivative with respect to $\tau \equiv x - ct$. Therefore, the band-pattern problem is recast into a dynamical system framework: establishing the shape of the bands amounts to describing the motion of a particle of mass $D$ and position $W$ in a potential $H(W)$, and experiencing a nonlinear friction $F(W)$; see Fig. 2(a). Note that the particle gains (losses) energy when $F'(W) < 0$ [$F'(W) > 0$].

Mass conservation in the original problem, Eq. (1), constrains the boundary conditions of Eq. (4) as $W(x \to -\infty) = W(x \to +\infty)$. Given this simple observation, without any further calculation, we can anticipate all the possible band patterns: the solutions of Eq. (4) correspond to closed trajectories in the $(W, \dot{W})$ plane. Therefore, they necessarily belong to one of the three following classes: (i) periodic orbits, (ii) homoclinic cycles (the trajectory includes one saddle point), or (iii) heteroclinic cycles (the trajectory includes two saddle points). Back in real space, as exemplified in Fig. 3, these trajectories, respectively, correspond to three possible propagating patterns

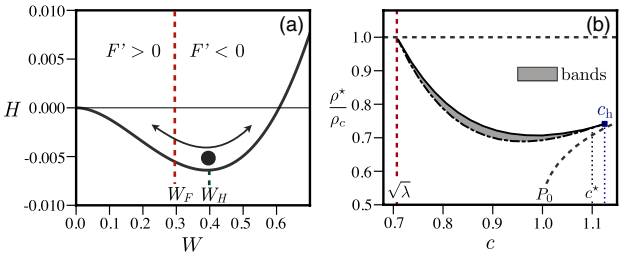


FIG. 2 (color online). (a) Sketch of the motion of an oscillating point particle in the effective potential $H(W)$ for $P_0 = 1$, $\rho_c = 1$, $\lambda = 0.5$, $\xi = 1$, $c = 0.9$, and $\rho^\star = 0.7$. The system loses or gains energy $H$ when $F'(W) > 0$ or $F'(W) < 0$. (b) Band phase diagram for the same parameters. Nonlinear bands exist only in the gray region. The dashed lines correspond to the conditions $W_H > 0$, and $W_F > 0$. For $c < c^*$, the black solid line corresponds to the supercritical Hopf bifurcation. Polar-liquid droplet states are observed only at $c = c_h$.

$W(x - ct)$: (i) a smectic phase composed of ordered bands ($W$ varies periodically with $x - ct$), (ii) a localized solitary wave, the length of which being set by the "time" taken to explore the homoclinic cycle, (iii) a polar-liquid droplet separated by domain walls from an isotropic gaseous phase, the fraction of polar liquid being given by the ratio between the waiting times at the two saddle points. These three patterns exactly correspond to those *hitherto* observed in model experiments, and in numerical simulations at the onset of collective motion.

Motivated by this pivotal observation, we now turn to the study of Eq. (4). For sake of clarity we henceforth specify the functional dependence of the phenomenological coefficients in Eq. (2). As the density is a control parameter of the transition to collective motion for all models based on short-range alignment interactions, $a_2(\rho)$ has to change sign at a finite density $\rho_c$ [2,3]. Different systems may result in different functions $a_2(\rho)$. We choose a simple linear dependence $a_2 = \rho - \rho_c$ which is consistent, close to $\rho_c$, with all existing kinetic theories [7,8,10,17,18]. In addition, having, for example, the original Vicsek model in mind, we want to capture the saturation of the average polarization of a homogeneous polar state of density $\rho = \rho_0$, when $\rho_0 \gg \rho_c$, at a nonzero value $P_0$. In agent-based models, $P_0$ is set by the noise amplitude. Here, since $P \sim \rho_0^{-1}[(\rho_0 - \rho_c)/a_4]^{1/2}$, the simplest possible choice yielding the correct saturation is $a_4(\rho) = (\rho P_0^2)^{-1}$. This choice simplifies the equations studied numerically in [11]. In all that follows $\xi$, $\lambda$, and $D$ are kept constant.

Now that Eqs. (1) and (2) have been fully defined, we can obtain their propagative solutions explicitly by solving Eq. (4). We stress that the two functions $H(W)$ and $F(W)$ are parametrized by two independent parameters: $\rho^\star$ and $c$, which specify the shape of the bands. Their explicit forms are provided in the Supplemental Material [16] and $H$ is plotted in Fig. 2(a) for a given set of parameters. The existence of closed trajectories in the $(W, \dot{W})$ plane requires that the system has at least one fixed point [19]. Hence, keeping in mind that Eq. (4) describes the motion of a massive particle in a potential, we look for trajectories that display at least one oscillation. This obviously requires (i) that $H$ has a local minimum at a finite value $W_H > 0$ (and thus a local maximum at $W = 0$), and (ii) that the friction $F'(W)$ changes sign at a finite $W_F > 0$ so that the particle does not fall to, and remains stuck at, $W_H$, where $H$ is minimum. It is straightforward to show that the former condition implies $\rho^\star < \rho_c$, and the latter $c > \sqrt{\lambda}$. In order to establish the shape of the periodic trajectories of the dynamical system, and in turn the shape of the bands, we need to go beyond this simple picture. We introduce the auxiliary variable $Z \equiv D\dot{W} + F(W)$ and recast Eq. (4) into the two-dimensional dynamical system,

$$\dot{W} = \frac{1}{D}[Z - F(W)], \tag{5}$$

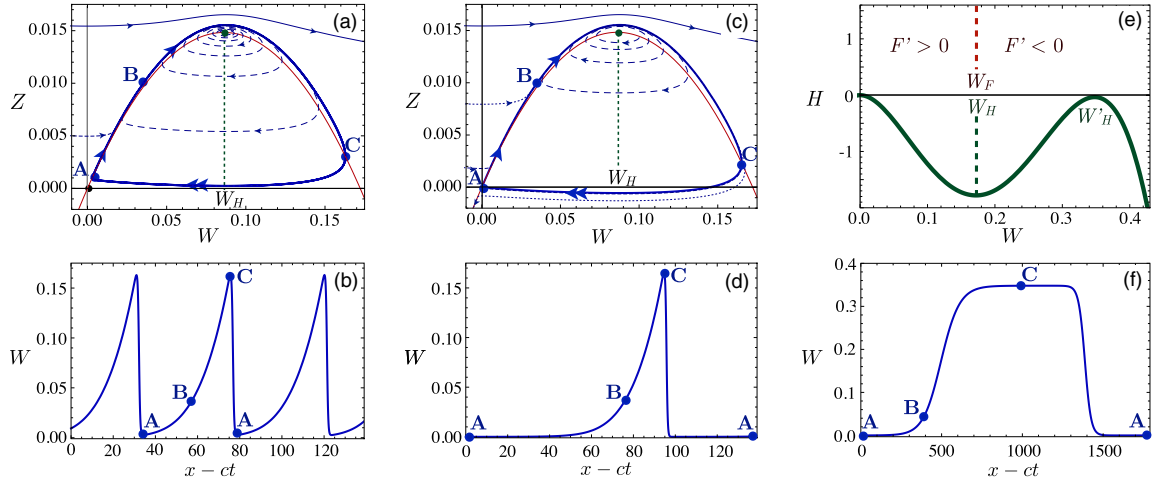


FIG. 3 (color online). (a) Dashed lines: dynamical system trajectories, for $P_0 = 1$, $\rho_c = 0.1$, $\lambda = 0.5$, $\xi = 4$, $D = 0.1$, $c = 0.9$. $\rho^\star$ was chosen such that $W_H \gtrsim W_F$. Thick line: stable limit cycle. Thin line: $Z = F(W)$ curve. (b) Polar smectic corresponding to the limit cycle shown in (a). (c) Homoclinic orbit; same parameters as in (a) but for a lower value of $\rho^\star$. (d) Solitonic band corresponding to the limit cycle shown in (c). (e) $H(W)$, solid line, plotted for $P_0 = 1$, $\rho_c = 1$, $\lambda = 1$, $\xi = 10$, and $D = 50$. The dashed lines show the positions of $W_F$ and $W_H$. The values of $c$ and $\rho^\star$ give rise to a heteroclinic cycle [16]. (f) Polar-liquid droplet for the same values of the parameters as in (e); see also the Supplemental Material [16].

$$\dot{Z} = -\frac{dH}{dW}. \tag{6}$$

This change of variable greatly simplifies the investigation of the fixed points of the dynamical system now defined by Eqs (5)–(6) [20]. It has at least two fixed points: (0,0) and $(W_H, F(W_H))$. A conventional linear stability analysis shows that (0,0) is always a saddle point. Conversely, the second fixed point $(W_H, F(W_H))$ calls for a more careful discussion. It undergoes a Hopf bifurcation as $W_H - W_F$ changes sign, as can be seen on the eigenvalues of the Jacobian matrices (see the Supplemental Material [16]). This bifurcation, which we will thoroughly characterize elsewhere [21], is supercritical (subcritical) if $c < c^*$ ($c > c^*$), where the critical velocity $c^*$ is defined implicitly by $H'''(W_H) = 0$. Both the bifurcation line and $c^*$ can be computed analytically and are shown in Fig. 2(b). More importantly, regardless of its sub- or supercritical nature the Hopf bifurcation results in an unstable spiral trajectory which can lead the system toward a cyclic attractor. We now describe how these limit cycles are explored in the $(W, Z)$ plane, and relate these nonlinear trajectories to the morphologies of the band patterns.

*Polar smectic phase or periodic orbits.*— To gain more quantitative insight, we consider large-amplitude cycles in the limit of small $D$ [22]. For small $W$, Eq. (5) implies that the system quickly relaxes toward the curve $Z = F(W)$ in a time $\sim D^{-1}$. Close to the origin, the dynamics is controlled by the linear properties of the saddle point (0,0), which defines two well-separated scales. It can be easily shown that the stable direction is nearly horizontal, it is associated with a fast relaxation at the rate $\tau_-^{-1} \sim D^{-1}(c - \lambda/c)$. Conversely, the unstable direction is nearly tangent to the curve $Z = F(W)$, and corresponds, again in the small-$D$ limit, to a much slower growth at the rate $\tau_+^{-1} \sim (\rho_c - \rho^\star)/(c - \lambda/c)$. The shape of large-amplitude cycles immediately follows from this discussion and from the parabolic shape of $F(W)$. Let us start from the left of the cycle, point $A$ in Fig. 3(a), close to the origin. We call $W_{\min}$ the abscissa of this point, which is the minimum value of $W$ in the cycle. As noted above, the trajectory first remains near the parabola $Z = F(W)$. If $A$ is close enough to the origin, this part of the cycle is explored slowly, in a time $\sim\tau_+$. Then the trajectory approaches the unstable point $(W_H, F(W_H))$. It therefore leaves the parabola and starts spiraling, at a point labeled $B$ in Fig. 3(a) [$B$ is here defined as the point where the trajectory deviates from the $Z = F(W)$ curve by 5%]. It finally crosses the parabola again, at point $C$, and $\dot{W}$ changes sign; see Eq. (5). $W$ then decreases and the system quickly goes back to point $A$ in a time typically set by $\sim\tau_-$. To further check this picture we have numerically computed the phase portraits of Eqs. (5) and (6), Fig. 3(a) (dotted lines). The typical periodic orbit shown in Fig. 3(a) (solid line) is in excellent agreement with the scenario described above. From this analysis, we infer the shape of the steadily propagating band pattern $W(x - ct)$. As anticipated, periodic orbits correspond to a polar smectic phase composed of equally spaced bands, in qualitative agreement with the experimental pictures reported in [6], and Fig. 1(a). The numerical shape of a smectic pattern is shown in Fig. 3(b). It is composed of strongly asymmetric excitations, which reflects the time-scale separation in the underlying dynamical system close to the origin; the large-amplitude bands are composed of a

long exponential tail, and of a sharp front at the head. Note that we describe here the propagation of large-amplitude excitations in a polarized environment. However, the minimum polarization in the regions separating the bands, $W_{\min}$, can be vanishingly small. In this limit the period of the crystalline structure would diverge logarithmically as $\tau_+ \log(W_F/W_{\min})$.

*Solitary bands or homoclinic cycles.*—In the limiting case where the minimal value of $W$ goes to 0 ($W_{\min} = 0$), point $A$ then corresponds to the saddle located at the origin. Consequently, the orbits followed by the dynamical system become homoclinic. As exemplified in Fig. 3(c), they are not periodic anymore, as the trajectory remains stuck at (0,0). In real space, the associated pattern is a solitary wave emerging out of a disordered gas, Fig. 3(d). We stress that the existence of solitonic structures at the onset of collective motion is one of the more robust observations made in agent-based simulations [5,7,9]; see Fig. 1(b).

*Polar liquid droplets or heteroclinic cycles.*—Until now, we have restricted our analysis to the case where the dynamical system only probes the first two extrema of $H$. However, looking for high-speed solutions ($c > P_0$), $H$ displays an additional extremum at $W'_H > W_H$; see Fig. 3(e). $(W'_H, F(W'_H))$ is a second saddle point. Therefore, heteroclinic cycles are found when $A$ is located at the origin and $C$ at the second saddle. The cycles are not periodic as the dynamics freezes both at $A$ and $C$. In real space, the corresponding structure $W(x - ct)$ is a localized domain, a polar-liquid droplet, traveling in a disordered gas, whose length is given by the residence at point $C$; see Fig. 3(f). This phase-separation pattern corresponds to the one numerically observed in the active spin model, Fig. 1(c), and in a generalization of the 2D Toner and Tu model [10,12]. In the small $P_0$ limit, the shapes of the asymmetric domain walls bounding the polar-liquid droplets can be computed exactly (see the Supplemental Material [16]).

Several comments are in order. First, we emphasize that the salient features of the swarming patterns do not depend on the specific functional forms of the hydrodynamic coefficients in Eq. (2). The limit-cycle solutions solely require the existence of a Hopf bifurcation, and the dynamics along this cycle is chiefly controlled by the stability of the other fixed points. Therefore, at a qualitative level, only the global shapes of the effective potential $H(W)$ and the friction curve $F(W)$ matter. For instance, we shall stress that a hydrodynamic theory where $a_4 = \text{cst}$ in Eq. (2) would yield nonlinear patterns qualitatively identical to those shown in Fig. 1 (not shown). Only the sign reversal of $a_2(\rho)$ at $\rho_c$ was necessary to observe band patterns, in agreement with [23].

Second, we emphasize that a traveling band can exist when the average density $\rho_0$ is smaller than $\rho_c$, though the linear stability of Eqs. (1) and (2) predicts that no small-amplitude wave can propagate [3]. The fundamental propagative excitations of polar active matter are intrinsically nonlinear below $\rho_c$.

Third, we come back to the status of the solutions described above. Until now we have identified an infinite family of band-type solutions, located in the vicinity of the Hopf-bifurcation line in the $(c, \rho^\star)$ plane, gray region in Fig. 2(b). The boundaries of this region are found by looking for nondegenerate solutions satisfying $W > 0$ [21], and its extent is an increasing function of the diffusivity $D$. The domain of existence of the bands collapses on the Hopf-bifurcation line in the limit $D \to 0$. The homoclinic cycles, corresponding to solitary waves, are constrained to include one saddle point. Therefore, they define a one-parameter ensemble of band-type solutions. This ensemble corresponds to the lower boundary of the phase diagram, Figure 2(b) (dashed-dotted line), and is established by taking the infinite-period limit. The heteroclinic solution, polar-liquid droplet, is constrained by the existence of two saddles along a cycle. Therefore, if any, the heteroclinic cycle is unique. It is a limiting case of the one-parameter homoclinic family, point $c_h$ in Fig. 2(b).

Finally, we discuss the pattern-selection problem. The ensemble of band-type solutions described above is actually restrained by the mass-conservation law. The mean density $\rho_0$ in the system is fixed; therefore, only band shapes compatible with this value exist. However, we are *a priori* left with an infinite family of solutions, which is parametrized by one free parameter. Hence, we predict that, for a given value of $\rho_0$, several solutions propagating at different speeds may coexist. This conjecture is again supported by numerical evidences. In Fig. 1 the three-band and single-band patterns correspond to identical values of all the simulation parameters. The full resolution of the challenging pattern-selection problem obviously goes beyond the scope of this Letter. However, a tentative picture for the nucleation of stationary swarms from a disordered state can be attempted from Eq. (2). The emergence of sharp fronts is natural since the left-hand side of (2) has the form of a Burgers equation, which supports rarefaction shocks [24]. A density fluctuation above $\rho_c$ grows and polarizes via the generic coupling between density and order embodied in the $\rho$ dependence of $a_2$ in Eq. (2). When these two competing effects balance each other, the density at the top of the shock is pinned, and a constant-shape asymmetric band steadily propagates. In the transient regime, we therefore expect several bands to form and collide, until the system reaches one of the possible steady states. This mechanism might favor large-amplitude or fast bands via coalescence events, in agreement with the experiments reported in [8].

To close this Letter we comment on the role of fluctuations on the transition toward collective motion [2]. Equation (2) predicts a second-order transition for homogeneous systems. Here, we have evidenced that stationary polarized excitations (solitary bands, and polar-liquid droplets) can coexist with a homogeneous isotropic phase, which in turn confirms the first-order scenario evidenced in numerical simulations [4,5]. This coexistence does not rely

on any fluctuation-induced mechanism, unlike all the conventional equilibrium scenarios making first order a mean-field second-order transition (e.g., Brazovskii [25] and Halperin, Lubensky, and Ma [26]). However, beyond the mean-field deterministic picture, fluctuations are very likely to play a major role in the stability, the selection, and the ordering of the band patterns. These difficult but crucial problems are a topic for future work.

We thank J. Toner for valuable comments and suggestions. D. B. acknowledges support from Institut Universitaire de France, and ANR project MiTra. H. C., A. P., A. S., and J. T. thank the Max Planck Institute for the Physics of Complex Systems, Dresden, for providing the framework of the Advanced Study Group "Statistical Physics of Collective Motion" within which part of this work was performed.

[1] T. Vicsek, A. Czirók, E. Ben-Jacob, I. Cohen, and O. Shochet, Phys. Rev. Lett. **75**, 1226 (1995).
[2] T. Vicsek and A. Zafeiris, Phys. Rep. **517**, 71 (2012).
[3] M. C. Marchetti, J. F. Joanny, S. Ramaswamy, T. B. Liverpool, J. Prost, M. Rao, and R. A. Simha, Rev. Mod. Phys. **85**, 1143 (2013).
[4] G. Grégoire and H. Chaté, Phys. Rev. Lett. **92**, 025702 (2004).
[5] H. Chaté, F. Ginelli, G. Grégoire, and F. Raynaud, Phys. Rev. E **77**, 046113 (2008); H. Chaté, F. Ginelli, G. Grégoire, F. Peruani and F. Raynaud, Eur. Phys. J. B **64**, 451 (2008).
[6] V. Schaller, C. Weber, C. Semmrich, E. Frey, and A. R. Bausch, Nature (London) **467**, 73 (2010).
[7] E. Bertin, M. Droz, and G. Grégoire, Phys. Rev. E **74**, 022101 (2006); J. Phys. A **42**, 445001 (2009).
[8] A. Bricard, J. B. Caussin, N. Desreumaux, O. Dauchot, and D. Bartolo, Nature (London) **503**, 95 (2013).
[9] T. Ihle, Phys. Rev. E **88**, 040303 (2013).
[10] A. P. Solon and J. Tailleur, Phys. Rev. Lett. **111**, 078101 (2013).
[11] S. Mishra, A. Baskaran, and M. C. Marchetti, Phys. Rev. E **81**, 061916 (2010).
[12] A. Gopinath, M. F. Hagan, M. C. Marchetti, and A. Baskaran, Phys. Rev. E **85**, 061903 (2012).
[13] C. A. Weber, T. Hanke, J. Deseigne, S. Léonard, O. Dauchot, E. Frey, and H. Chaté, Phys. Rev. Lett. **110**, 208001 (2013).
[14] P. Romanczuk and L. Schimansky-Geier, Ecological Complexity **10**, 83 (2012).
[15] J. Toner and Y. Tu, Phys. Rev. Lett. **75**, 4326 (1995); Y. Tu, J. Toner, and M. Ulm, Phys. Rev. Lett. **80**, 4819 (1998).
[16] See Supplemental Material at http://link.aps.org/supplemental/10.1103/PhysRevLett.112.148102 for details of the simulations of Fig. 1, expressions of $H$ and $F$, eigenvalues of the Jacobian matrix evaluated at $(W_H, F(W_H))$, and the exact expression for the shape of the polar-liquid droplets.
[17] F. D. C. Farrell, M. C. Marchetti, D. Marenduzzo, and J. Tailleur, Phys. Rev. Lett. **108**, 248101 (2012).
[18] A. Baskaran and M. C. Marchetti, Phys. Rev. E **77**, 011920 (2008).
[19] V. I. Arnold, *Ordinary Differential Equations* (MIT Press, Cambridge, MA, 1980).
[20] S. H. Strogatz, *Nonlinear Dynamics and Chaos* (Addison-Wesley, New York, 1994).
[21] A. Solon *et al.* (unpublished).
[22] More precisely, we consider $D \ll [(c^2-\lambda)^2/4c^2(\rho_c-\rho^\star)]$.
[23] A. Peshkov, S. Ngo, E. Bertin, H. Chaté, and F. Ginelli, Phys. Rev. Lett. **109**, 098101 (2012).
[24] G. B. Whitham, *Linear and Nonlinear Waves* (John Wiley & Sons, New York, 1974).
[25] S. A. Brazovskii, Zh. Eksp. Teor. Fiz. **68**, 175 (1975); [, Sov. Phys. JETP **41**, 85 (1975)].
[26] B. I. Halperin, T. C. Lubensky, and S.-K. Ma, Phys. Rev. Lett. **32**, 292 (1974).

# Bibliographie


[1] J. W. Gibbs. *Elementary principles in statistical mechanics*. Courier Corporation, 2014. isbn : 0486789950.

[2] B. Diu, C. Guthmann, D. Lederer et B. Roulet. *Physique statistique*. 1989.

[3] H. Risken. *Fokker-Planck Equation*. Springer, 1984. isbn : 3642968090.

[4] L. Berthier et G. Biroli. « Theoretical perspective on the glass transition and amorphous materials ». *Reviews of Modern Physics* 83.2 (2011), p. 587.

[5] C. Domb, R. K. Zia, B. Schmittmann et J. L. Lebowitz. *Statistical mechanics of driven diffusive systems*. T. 17. Academic Press, 1995. isbn : 0080538746.

[6] M. Kardar, G. Parisi et C. Zhang. « Dynamic scaling of growing interfaces ». *Physical Review Letters* 56.9 (1986), p. 889.

[7] H. Hinrichsen. « Non-equilibrium critical phenomena and phase transitions into absorbing states ». *Advances in physics* 49.7 (2000), p. 815–958.

[8] F. Juelicher, K. Kruse, J. Prost et J.-F. Joanny. « Active behavior of the cytoskeleton ». *Physics Reports* 449.1 (2007), p. 3–28.

[9] S. Ramaswamy. « The mechanics and statistics of active matter ». *The Mechanics and Statistics of Active Matter* 1 (2010), p. 323–345.

[10] P. Romanczuk, M. Bär, W. Ebeling, B. Lindner et L. Schimansky-Geier. « Active brownian particles ». *The European Physical Journal Special Topics* 202.1 (2012), p. 1–162.

[11] T. Vicsek et A. Zafeiris. « Collective motion ». *Physics Reports* 517.3 (2012), p. 71–140.

[12] M. C. Marchetti, J. F. Joanny, S. Ramaswamy, T. B. Liverpool, J. Prost, M. Rao et R. A. Simha. « Hydrodynamics of soft active matter ». *Reviews of Modern Physics* 85.3 (2013), p. 1143.

[13] T. Vicsek, A. Czirók, E. Ben-Jacob, I. Cohen et O. Shochet. « Novel type of phase transition in a system of self-driven particles ». *Physical review letters* 75.6 (1995), p. 1226.

[14] N. D. Mermin et H. Wagner. « Absence of ferromagnetism or antiferromagnetism in one-or two-dimensional isotropic Heisenberg models ». *Physical Review Letters* 17.22 (1966), p. 1133.

[15] M. Ballerini et al. « Interaction ruling animal collective behavior depends on topological rather than metric distance: Evidence from a field study ». *Proceedings of the national academy of sciences* 105.4 (2008), p. 1232–1237.

[16] A. Cavagna, A. Cimarelli, I. Giardina, G. Parisi, R. Santagati, F. Stefanini et M. Viale. « Scale-free correlations in starling flocks ». *Proceedings of the National Academy of Sciences* 107.26 (2010), p. 11865–11870.

[17] W. Bialek, A. Cavagna, I. Giardina, T. Mora, E. Silvestri, M. Viale et A. M. Walczak. « Statistical mechanics for natural flocks of birds ». *Proceedings of the National Academy of Sciences* 109.13 (2012), p. 4786–4791.

[18] J. L. Silverberg, M. Bierbaum, J. P. Sethna et I. Cohen. « Collective motion of humans in mosh and circle pits at heavy metal concerts ». *Physical review letters* 110.22 (2013), p. 228701.

[19] Y. Katz, K. Tunstrøm, C. C. Ioannou, C. Huepe et I. D. Couzin. « Inferring the structure and dynamics of interactions in schooling fish ». *Proceedings of the National Academy of Sciences* 108.46 (2011), p. 18720–18725.

[20] J. Gautrais, F. Ginelli, R. Fournier, S. Blanco, M. Soria, H. Chaté et G. Theraulaz. « Deciphering interactions in moving animal groups ». *Plos computational biology* 8.9 (2012), e1002678.

[21] D. S. Calovi, U. Lopez, S. Ngo, C. Sire, H. Chaté et G. Theraulaz. « Swarming, schooling, milling: phase diagram of a data-driven fish school model ». *New Journal of Physics* 16.1 (2014), p. 015026.

[22] V. Schaller, C. Weber, C. Semmrich, E. Frey et A. R. Bausch. « Polar patterns of driven filaments ». *Nature* 467.7311 (2010), p. 73–77.

[23] F. Peruani, J. Starruss, V. Jakovljevic, L. Søgaard-Andersen, A. Deutsch et M. Bär. « Collective motion and nonequilibrium cluster formation in colonies of gliding bacteria ». *Physical review letters* 108.9 (2012), p. 098102.

[24] Y. Sumino, K. H. Nagai, Y. Shitaka, D. Tanaka, K. Yoshikawa, H. Chaté et K. Oiwa. « Large-scale vortex lattice emerging from collectively moving microtubules ». *Nature* 483.7390 (2012), p. 448–452.

[25] N. Sepúlveda, L. Petitjean, O. Cochet, E. Grasland-Mongrain, P. Silberzan et V. Hakim. « Collective cell motion in an epithelial sheet can be quantitatively described by a stochastic interacting particle model ». *PLoS computational biology* 9.3 (2013), e1002944.

[26] C. Liu et al. « Sequential establishment of stripe patterns in an expanding cell population ». *Science* 334.6053 (2011), p. 238–241.

[27] T. Risler. « Cytoskeleton and Cell Motility ». *Encyclopedia of Complexity and Systems Science*. Springer, 2009, p. 1738–1774. isbn : 0387758887.

[28] H. Yamaguchi, J. Wyckoff et J. Condeelis. « Cell migration in tumors ». *Current opinion in cell biology* 17.5 (2005), p. 559–564.

[29] J. Dunkel, S. Heidenreich, K. Drescher, H. H. Wensink, M. Bär et R. E. Goldstein. « Fluid dynamics of bacterial turbulence ». *Physical review letters* 110.22 (2013), p. 228102.

[30] T. Sanchez, D. T. Chen, S. J. DeCamp, M. Heymann et Z. Dogic. « Spontaneous motion in hierarchically assembled active matter ». *Nature* 491.7424 (2012), p. 431–434.

[31] G. Henkin, S. J. DeCamp, D. T. Chen, T. Sanchez et Z. Dogic. « Tunable dynamics of microtubule-based active isotropic gels ». *Philosophical Transactions of the Royal Society A: Mathematical, Physical and Engineering Sciences* 372.2029 (2014), p. 20140142.

[32] A. Brown et W. Poon. « Ionic effects in self-propelled Pt-coated Janus swimmers ». *Soft matter* 10.22 (2014), p. 4016–4027.

[33] A. Walther et A. H. E. Müller. « Janus particles ». *Soft Matter* 4.4 (2008), p. 663.

[34] J. R. Howse, R. A. Jones, A. J. Ryan, T. Gough, R. Vafabakhsh et R. Golestanian. « Self-motile colloidal particles: from directed propulsion to random walk ». *Physical review letters* 99.4 (2007), p. 048102.

[35] I. Theurkauff, C. Cottin-Bizonne, J. Palacci, C. Ybert et L. Bocquet. « Dynamic clustering in active colloidal suspensions with chemical signaling ». *Physical review letters* 108.26 (2012), p. 268303.

[36] J. Palacci, C. Cottin-Bizonne, C. Ybert et L. Bocquet. « Sedimentation and effective temperature of active colloidal suspensions ». *Physical Review Letters* 105.8 (2010), p. 088304.

[37] J. Palacci, S. Sacanna, A. P. Steinberg, D. J. Pine et P. M. Chaikin. « Living crystals of light-activated colloidal surfers ». *Science* 339.6122 (2013), p. 936–940.

[38] I. Buttinoni, G. Volpe, F. Kümmel, G. Volpe et C. Bechinger. « Active Brownian motion tunable by light ». *Journal of Physics: Condensed Matter* 24.28 (2012), p. 284129.

[39] F. Ginot, I. Theurkauff, D. Levis, C. Ybert, L. Bocquet, L. Berthier et C. Cottin-Bizonne. « Nonequilibrium equation of state in suspensions of active colloids ». *Physical Review X* 5.1 (2015), p. 011004.

[40] V. Narayan, S. Ramaswamy et N. Menon. « Long-lived giant number fluctuations in a swarming granular nematic ». *Science* 317.5834 (2007), p. 105–108.

[41] A. Kudrolli, G. Lumay, D. Volfson et L. S. Tsimring. « Swarming and swirling in self-propelled polar granular rods ». *Physical review letters* 100.5 (2008), p. 058001.

[42] J. Deseigne, O. Dauchot et H. Chaté. « Collective motion of vibrated polar disks ». *Physical Review Letters* 105.9 (2010), p. 098001.

[43] S. Thutupalli, R. Seemann et S. Herminghaus. « Swarming behavior of simple model squirmers ». *New Journal of Physics* 13.7 (2011), p. 073021.

[44] A. Bricard, J.-B. Caussin, N. Desreumaux, O. Dauchot et D. Bartolo. « Emergence of macroscopic directed motion in populations of motile colloids ». *Nature* 503.7474 (2013), p. 95–98.

[45] M. Rubenstein, A. Cornejo et R. Nagpal. « Programmable self-assembly in a thousand-robot swarm ». *Science* 345.6198 (2014), p. 795–799.

[46] F. Peruani, A. Deutsch et M. Bär. « Nonequilibrium clustering of self-propelled rods ». *Physical Review E* 74.3 (2006), p. 030904.

[47] R. Wittkowski, A. Tiribocchi, J. Stenhammar, R. J. Allen, D. Marenduzzo et M. E. Cates. « Scalar phi4 field theory for active-particle phase separation ». *Nature communications* 5 (2014).

[48] A. Tiribocchi, R. Wittkowski, D. Marenduzzo et M. E. Cates. « Active Model H: Scalar Active Matter in a Momentum-Conserving Fluid ». *ArXiv e-prints* (avr. 2015).

[49] P. C. Hohenberg et B. I. Halperin. « Theory of dynamic critical phenomena ». *Reviews of Modern Physics* 49.3 (1977), p. 435.

[50] R. W. Nash, R. Adhikari, J. Tailleur et M. E. Cates. « Run-and-tumble particles with hydrodynamics: sedimentation, trapping, and upstream swimming ». *Physical review letters* 104.25 (2010), p. 258101.

[51] J. R. Blake. « A spherical envelope approach to ciliary propulsion ». *Journal of Fluid Mechanics* 46.1 (1971), p. 199–208.

[52] M. E. Cates et J. Tailleur. « Motility-Induced Phase Separation ». *Annual Review of Condensed Matter Physics* 6.1 (2015), p. 219–244.

[53] H. C. Berg et D. A. Brown. « Chemotaxis in Escherichia coli analysed by three-dimensional tracking ». *Nature* 239.5374 (1972), p. 500–504.

[54] G. Szamel. « Self-propelled particle in an external potential: Existence of an effective temperature ». *Physical Review E* 90.1 (2014), p. 012111.

[55] D. Levis et L. Berthier. « Clustering and heterogeneous dynamics in a kinetic Monte Carlo model of self-propelled hard disks ». *Physical Review E* 89.6 (2014), p. 062301.

[56] C. Maggi, U. Marini Bettolo Marconi, N. Gnan et R. Di Leonardo. « Multidimensional Stationary Probability Distribution for Interacting Active Particles ». *ArXiv e-prints* (mar. 2015).

[57] J. Tailleur et M. E. Cates. « Statistical mechanics of interacting run-and-tumble bacteria ». *Physical review letters* 100.21 (2008), p. 218103.

[58] Y. Fily et M. C. Marchetti. « Athermal phase separation of self-propelled particles with no alignment ». *Physical review letters* 108.23 (2012), p. 235702.

[59] G. S. Redner, M. F. Hagan et A. Baskaran. « Structure and dynamics of a phase-separating active colloidal fluid ». *Physical review letters* 110.5 (2013), p. 055701.

[60] J. Stenhammar, A. Tiribocchi, R. J. Allen, D. Marenduzzo et M. E. Cates. « Continuum theory of phase separation kinetics for active brownian particles ». *Physical review letters* 111.14 (2013), p. 145702.

[61] J. Bialké, H. Löwen et T. Speck. « Microscopic theory for the phase separation of self-propelled repulsive disks ». *EPL (Europhysics Letters)* 103.3 (2013), p. 30008.

[62] J. Stenhammar, D. Marenduzzo, R. J. Allen et M. E. Cates. « Phase behaviour of active Brownian particles: the role of dimensionality ». *Soft Matter* 10.10 (2014), p. 1489–1499.

[63] J. Bialké, H. Löwen et T. Speck. « Negative interfacial tension in phase-separated active suspensions ». *arXiv preprint arXiv:1412.4601* (2014).

[64] A. Wysocki, R. G. Winkler et G. Gompper. « Cooperative motion of active Brownian spheres in three-dimensional dense suspensions ». *EPL (Europhysics Letters)* 105.4 (2014), p. 48004.

[65] S. C. Takatori, W. Yan et J. F. Brady. « Swim Pressure: Stress Generation in Active Matter ». *Physical review letters* 113.2 (2014), p. 028103.

[66] S. A. Mallory, A. Šarić, C. Valeriani et A. Cacciuto. « Anomalous thermomechanical properties of a self-propelled colloidal fluid ». *Physical Review E* 89.5 (2014), p. 052303.

[67] X. Yang, M. L. Manning et M. C. Marchetti. « Aggregation and segregation of confined active particles ». *Soft matter* 10.34 (2014), p. 6477–6484.

[68] H. Chaté, F. Ginelli, G. Grégoire et F. Raynaud. « Collective motion of self-propelled particles interacting without cohesion ». *Physical Review E* 77.4 (2008), p. 046113.

[69] G. Grégoire et H. Chaté. « Onset of collective and cohesive motion ». *Physical review letters* 92.2 (2004), p. 025702.

[70] F. Ginelli, F. Peruani, M. Bär et H. Chaté. « Large-scale collective properties of self-propelled rods ». *Physical Review Letters* 104.18 (2010), p. 184502.

[71] S. Ngo, A. Peshkov, I. S. Aranson, E. Bertin, F. Ginelli et H. Chaté. « Large-scale chaos and fluctuations in active nematics ». *Physical review letters* 113.3 (2014), p. 038302.

[72] P. Zhang, A. Be'er, E.-L. Florin et H. L. Swinney. « Collective motion and density fluctuations in bacterial colonies ». *Proceedings of the National Academy of Sciences* 107.31 (2010), p. 13626–13630.

[73] J. Toner et Y. Tu. « Long-range order in a two-dimensional dynamical XY model: how birds fly together ». *Physical Review Letters* 75.23 (1995), p. 4326.

[74] J. Toner et Y. Tu. « Flocks, herds, and schools: A quantitative theory of flocking ». *Physical review E* 58.4 (1998), p. 4828.

[75] J. Toner. « Reanalysis of the hydrodynamic theory of fluid, polar-ordered flocks ». *Physical Review E* 86.3 (2012), p. 031918.

[76] E. Bertin, M. Droz et G. Grégoire. « Boltzmann and hydrodynamic description for self-propelled particles ». *Physical Review E* 74.2 (2006), p. 022101.

[77] F. Thüroff, C. A. Weber et E. Frey. « Numerical treatment of the Boltzmann equation for self-propelled particle systems ». *Physical Review X* 4.4 (2014), p. 041030.

[78] E. Bertin, M. Droz et G. Grégoire. « Hydrodynamic equations for self-propelled particles: microscopic derivation and stability analysis ». *Journal of Physics A: Mathematical and Theoretical* 42.44 (2009), p. 445001.

[79] A. Peshkov, S. Ngo, E. Bertin, H. Chaté et F. Ginelli. « Continuous theory of active matter systems with metric-free interactions ». *Physical review letters* 109.9 (2012), p. 098101.

[80] A. Peshkov, I. S. Aranson, E. Bertin, H. Chaté et F. Ginelli. « Nonlinear field equations for aligning self-propelled rods ». *Physical review letters* 109.26 (2012), p. 268701.

[81] A. Peshkov, E. Bertin, F. Ginelli et H. Chaté. « Boltzmann-Ginzburg-Landau approach for continuous descriptions of generic Vicsek-like models ». *The European Physical Journal Special Topics* 223.7 (2014), p. 1315–1344.

[82] T. Ihle. « Kinetic theory of flocking: Derivation of hydrodynamic equations ». *Physical Review E* 83.3 (2011), p. 030901.

[83] T. Ihle. « Invasion-wave-induced first-order phase transition in systems of active particles ». *Physical Review E* 88.4 (2013), p. 040303.

[84] A. P. Berke, L. Turner, H. C. Berg et E. Lauga. « Hydrodynamic attraction of swimming microorganisms by surfaces ». *Physical Review Letters* 101.3 (2008), p. 038102.

[85] J. Elgeti et G. Gompper. « Self-propelled rods near surfaces ». *EPL (Europhysics Letters)* 85.3 (2009), p. 38002.

[86] J. Elgeti et G. Gompper. « Wall accumulation of self-propelled spheres ». *EPL (Europhysics Letters)* 101.4 (2013), p. 48003.

[87] J. Elgeti et G. Gompper. « Run-and-tumble dynamics of self-propelled particles in confinement ». *EPL (Europhysics Letters)* 109.5 (2015), p. 58003.

[88] K. Drescher, J. Dunkel, L. H. Cisneros, S. Ganguly et R. E. Goldstein. « Fluid dynamics and noise in bacterial cell–cell and cell–surface scattering ». *Proceedings of the National Academy of Sciences* 108.27 (2011), p. 10940–10945.

[89] D. Saintillan et M. J. Shelley. « Orientational order and instabilities in suspensions of self-locomoting rods ». *Physical review letters* 99.5 (2007), p. 058102.

[90] D. Saintillan et M. J. Shelley. « Instabilities and pattern formation in active particle suspensions: Kinetic theory and continuum simulations ». *Physical Review Letters* 100.17 (2008), p. 178103.

[91] R. Matas-Navarro, R. Golestanian, T. B. Liverpool et S. M. Fielding. « Hydrodynamic suppression of phase separation in active suspensions ». *Physical Review E* 90.3 (2014), p. 032304.

[92] A. Zöttl et H. Stark. « Hydrodynamics determines collective motion and phase behavior of active colloids in quasi-two-dimensional confinement ». *Physical review letters* 112.11 (2014), p. 118101.

[93] E. Lauga, W. R. DiLuzio, G. M. Whitesides et H. A. Stone. « Swimming in circles: motion of bacteria near solid boundaries ». *Biophysical journal* 90.2 (2006), p. 400–412.

[94] Y. Hatwalne, S. Ramaswamy, M. Rao et R. A. Simha. « Rheology of active-particle suspensions ». *Physical review letters* 92.11 (2004), p. 118101.

[95] A. Sokolov et I. S. Aranson. « Reduction of viscosity in suspension of swimming bacteria ». *Physical Review Letters* 103.14 (2009), p. 148101.

[96] S. Rafaï, L. Jibuti et P. Peyla. « Effective viscosity of microswimmer suspensions ». *Physical Review Letters* 104.9 (2010), p. 098102.

[97] R. Voituriez, J.-F. Joanny et J. Prost. « Spontaneous flow transition in active polar gels ». *EPL (Europhysics Letters)* 70.3 (2005), p. 404.

[98] R. Voituriez, J. F. Joanny et J. Prost. « Generic phase diagram of active polar films ». *Physical review letters* 96.2 (2006), p. 028102.

[99] H. Turlier, B. Audoly, J. Prost et J.-F. Joanny. « Furrow constriction in animal cell cytokinesis ». *Biophysical journal* 106.1 (2014), p. 114–123.

[100] J. Tailleur et M. Cates. « Sedimentation, trapping, and rectification of dilute bacteria ». *EPL (Europhysics Letters)* 86.6 (2009), p. 60002. issn : 0295-5075.

[101] M. E. Cates et J. Tailleur. « When are active Brownian particles and run-and-tumble particles equivalent? Consequences for motility-induced phase separation ». *EPL (Europhysics Letters)* 101.2 (2013), p. 20010.

[102] A. P. Solon et J. Tailleur. « Revisiting the flocking transition using active spins ». *Physical review letters* 111.7 (2013), p. 078101.

[103] J.-B. Caussin, A. Solon, A. Peshkov, H. Chaté, T. Dauxois, J. Tailleur, V. Vitelli et D. Bartolo. « Emergent spatial structures in flocking models: a dynamical system insight ». *Physical review letters* 112.14 (2014), p. 148102.

[104] M. Enculescu et H. Stark. « Active colloidal suspensions exhibit polar order under gravity ». *Physical review letters* 107.5 (2011), p. 058301.

[105] L. F. Cugliandolo. « The effective temperature ». *Journal of Physics A: Mathematical and Theoretical* 44.48 (2011), p. 483001.

[106] M. Deforet, V. Hakim, H. G. Yevick, G. Duclos et P. Silberzan. « Emergence of collective modes and tri-dimensional structures from epithelial confinement ». *Nature communications* 5 (2014).

[107] A.-K. Marel, A. P. Alberola et J. O. Rädler. « Proliferation and Collective Migration of Small Cell Groups Released from Circular Patches ». *Biophysical Reviews and Letters* 7.1 (2012), p. 15–28.

[108] S. C. Takatori et J. F. Brady. « Towards a thermodynamics of active matter ». *Phys. Rev. E* 91.3 (mar. 2015), p. 032117.

[109] Y. Fily, A. Baskaran et M. F. Hagan. « Dynamics of self-propelled particles under strong confinement ». *Soft matter* 10.30 (2014), p. 5609–5617.

[110] Y. Fily, A. Baskaran et M. F. Hagan. « Dynamics and density distribution of strongly confined noninteracting nonaligning self-propelled particles in a nonconvex boundary ». *Phys. Rev. E* 91.1 (jan. 2015), p. 012125.

[111] F. Alarcon et I. Pagonabarraga. « Spontaneous aggregation and global polar ordering in squirmer suspensions ». *Journal of Molecular Liquids* 185 (2013), p. 56–61.

[112] D. Ray, C. Reichhardt et C. O. Reichhardt. « Casimir effect in active matter systems ». *Physical Review E* 90.1 (2014), p. 013019.

[113] T. F. F. Farage, P. Krinninger et J. M. Brader. « Effective interactions in active Brownian suspensions ». *Physical Review E* 91.4 (2015), p. 042310.

[114] A. G. Thompson, J. Tailleur, M. E. Cates et R. A. Blythe. « Lattice models of nonequilibrium bacterial dynamics ». *Journal of Statistical Mechanics: Theory and Experiment* 2011.2 (2011), P02029.

[115] B. M. Mognetti, A. Šarić, S. Angioletti-Uberti, A. Cacciuto, C. Valeriani et D. Frenkel. « Living clusters and crystals from low-density suspensions of active colloids ». *Physical review letters* 111.24 (2013), p. 245702.

[116] G. S. Redner, A. Baskaran et M. F. Hagan. « Reentrant phase behavior in active colloids with attraction ». *Physical Review E* 88.1 (2013), p. 012305.

[117] I. Buttinoni, J. Bialké, F. Kümmel, H. Löwen, C. Bechinger et T. Speck. « Dynamical clustering and phase separation in suspensions of self-propelled colloidal particles ». *Physical review letters* 110.23 (2013), p. 238301.

[118] L. Hall-Stoodley, J. W. Costerton et P. Stoodley. « Bacterial biofilms: from the natural environment to infectious diseases ». *Nature Reviews Microbiology* 2.2 (2004), p. 95–108.

[119] M. E. Cates, D. Marenduzzo, I. Pagonabarraga et J. Tailleur. « Arrested phase separation in reproducing bacteria creates a generic route to pattern formation ». *Proceedings of the National Academy of Sciences* 107.26 (2010), p. 11715–11720.

[120] M. P. Brenner. « Chemotactic patterns without chemotaxis ». *Proceedings of the National Academy of Sciences* 107.26 (2010), p. 11653–11654.

[121] X. Fu, L.-H. Tang, C. Liu, J.-D. Huang, T. Hwa et P. Lenz. « Stripe formation in bacterial systems with density-suppressed motility ». *Physical review letters* 108.19 (2012), p. 198102.

[122] D. S. Dean. « Langevin equation for the density of a system of interacting Langevin processes ». *Journal of Physics A: Mathematical and General* 29.24 (1996), p. L613.

[123] M. E. Cates et M. R. Evans. *Soft and Fragile Matter: Nonequilibrium Dynamics, Metastability and Flow (PBK)*. CRC Press, 2000. isbn : 1420033514.

[124] P. Rørth. « Collective Cell Migration ». *Annual Review of Cell and Developmental Biology* 25.1 (2009), p. 407–429.

[125] D. J. Montell. « Morphogenetic cell movements: diversity from modular mechanical properties ». *Science* 322.5907 (2008), p. 1502–1505.

[126] P. Friedl et D. Gilmour. « Collective cell migration in morphogenesis, regeneration and cancer ». *Nature reviews Molecular cell biology* 10.7 (2009), p. 445–457.

[127] A. Czirók, H. E. Stanley et T. Vicsek. « Spontaneously ordered motion of self-propelled particles ». *Journal of Physics A: Mathematical and General* 30.5 (1997), p. 1375.

[128] V. Schaller et A. R. Bausch. « Topological defects and density fluctuations in collectively moving systems ». *Proceedings of the National Academy of Sciences* 110.12 (2013), p. 4488–4493.

[129] Y. Tu, J. Toner et M. Ulm. « Sound waves and the absence of Galilean invariance in flocks ». *Physical review letters* 80.21 (1998), p. 4819.

[130] J. Toner, Y. Tu et S. Ramaswamy. « Hydrodynamics and phases of flocks ». *Annals of Physics* 318.1 (2005), p. 170–244.

[131] J. Buhl, D. J. Sumpter, I. D. Couzin, J. J. Hale, E. Despland, E. R. Miller et S. J. Simpson. « From disorder to order in marching locusts ». *Science* 312.5778 (2006), p. 1402–1406.

[132] A. Czirók, A.-L. Barabási et T. Vicsek. « Collective motion of self-propelled particles: Kinetic phase transition in one dimension ». *Physical Review Letters* 82.1 (1999), p. 209.

[133] O. J. O'Loan et M. R. Evans. « Alternating steady state in one-dimensional flocking ». *Journal of Physics A: Mathematical and General* 32.8 (1999), p. L99.

[134] K. Binder. « Applications of Monte Carlo methods to statistical physics ». *Reports on Progress in Physics* 60.5 (1997), p. 487.

[135] T. Luo, K. Mohan, P. A. Iglesias et D. N. Robinson. « Molecular mechanisms of cellular mechanosensing ». *Nature materials* 12.11 (2013), p. 1064–1071.

[136] H. Touchette. « The large deviation approach to statistical mechanics ». *Physics Reports* 478.1 (2009), p. 1–69.

# Publications

**P1.** A. P. Solon, J. Tailleur
« Revisiting the flocking transition using active spins »
*Phys. Rev. Lett.* 111, 078101 (2013)

**P2.** J.-B. Caussin, A. P. Solon, A. Peshkov, H. Chaté, T. Dauxois, J. Tailleur, V. Vitelli, D. Bartolo
« Emergent spatial structures in flocking models : a dynamical system insight »
*Phys. Rev. Lett.* 112, 148102 (2014)

**P3.** A. P. Solon, H. Chaté, J. Tailleur
« From Phase to Micro-Phase Separation in Flocking Models : The Essential Role of Fluctuations »
*Phys. Rev. Lett.* 114, 068101 (2015)

**P4.** A. P. Solon, Y. Fily, A. Baskaran, M. E. Cates, Y. Kafri, M. Kardar and J. Tailleur
« Pressure is not a state function for generic active fluids »
*Nature Physics*, sous presse. arXiv :1412.3952

**P5.** A. P. Solon, J. Stenhammar, R. Wittkowski, M. Kardar, Y. Kafri, M. E. Cates and J. Tailleur
« Pressure and Phase Equilibria in Interacting Active Brownian Spheres »
*Phys. Rev. Lett.* 114, 198301 (2015)

**P6.** A. P. Solon, M. E. Cates and J. Tailleur
« Active Brownian Particles and Run-and-Tumble Particles : a Comparative Study »
*Eur. Phys. J. Special Topics*, sous presse. arXiv :1504.07391

Les articles E et F, inclus dans le chapitre 5, ont été écrits pendant la rédaction de cette thèse. Ils seront soumis prochainement pour publication dans *Phys. Rev. E* et sur arXiv.

**P7.** A. P. Solon, J. Tailleur
« Flocking with discrete symmetry : the 2d Active Ising Model »

**P8.** A. P. Solon, J.-B. Caussin, D. Bartolo, H. Chaté and J. Tailleur
« Generic behavior of the hydrodynamic equations for flocking models »

# Résumé

Les systèmes actifs, composés de particules capables de transformer l'énergie stockée dans leur environnement pour s'autopropulser, sont omniprésents dans la nature. On les trouve à toutes les échelles : des moteurs moléculaires aux groupes d'animaux, en passant par les tissus cellulaires et les colonies de bactéries. Ces systèmes hors d'équilibre ont attiré l'attention des physiciens car ils présentent une phénoménologie plus riche que les systèmes passifs, que l'on peut cependant comprendre à partir de modèles simples.

Dans cette thèse, nous avons étudié analytiquement et numériquement des modèles minimaux de particules actives. Ceux-ci nous ont permis de comprendre différents phénomènes spécifiques à la matière active et d'étudier le comportement à grand échelle de plusieurs classes de systèmes.

La thermodynamique des systèmes actifs est fondamentalement différente de celle des systèmes d'équilibre. Nous montrons en particulier que la pression mécanique d'un fluide de particules actives n'est pas donnée par une équation d'état. La pression n'est donc pas seulement une propriété du fluide et dépend du détail des interactions avec les parois du récipient dans lequel il est confiné.

Nous étudions également deux transitions de phase propres à la matière active : la séparation de phase induite par la motilité et la transition vers le mouvement collectif. Dans les deux cas, on observe une séparation de phase entre un liquide et un gaz dont nous étudions la coexistence. Pour la transition vers le mouvement collectif on distingue deux classes d'universalité, en fonction de la symétrie des particules, qui ont des coexistences de phase différentes.

# Abstract

Active systems, composed of particles capable of using the energy stored in their medium to self-propel, are ubiquitous in nature. They are found at all scales : from molecular motors to cellular tissues, bacterial colonies and animal groups. These out-of-equilibrium systems have attracted a lot of attention from the physics community because they show a richer phenomenology than passive systems that we can still understand using simple models.

In this thesis, we study analytically and numerically minimal models of active particles. They allow us to understand different phenomena that are characteristic of active matter and to study the large-scale behavior of several classes of systems.

The thermodynamics of active systems is fundamentally different from that of equilibrium systems. In particular, we show that the mechanical pressure of an active particle fluid is not given by an equation of state. The pressure is thus

not a property of the fluid and depends on the details of the interaction with the containing vessel.

We also study two phase transitions that specific to active matter : The motility-induced phase separation and the transition to collective motion. In both cases, we observe a phase separation between a liquid and a gas and study their coexistence. For the transition to collective motion, we exhibit two universality classes, based on the particles' symmetry, which have different types of coexistence phases.